Magnetic Materials Based on Layered Double Hydroxides:
Chemical Design, Processing and Electrochemical Applications

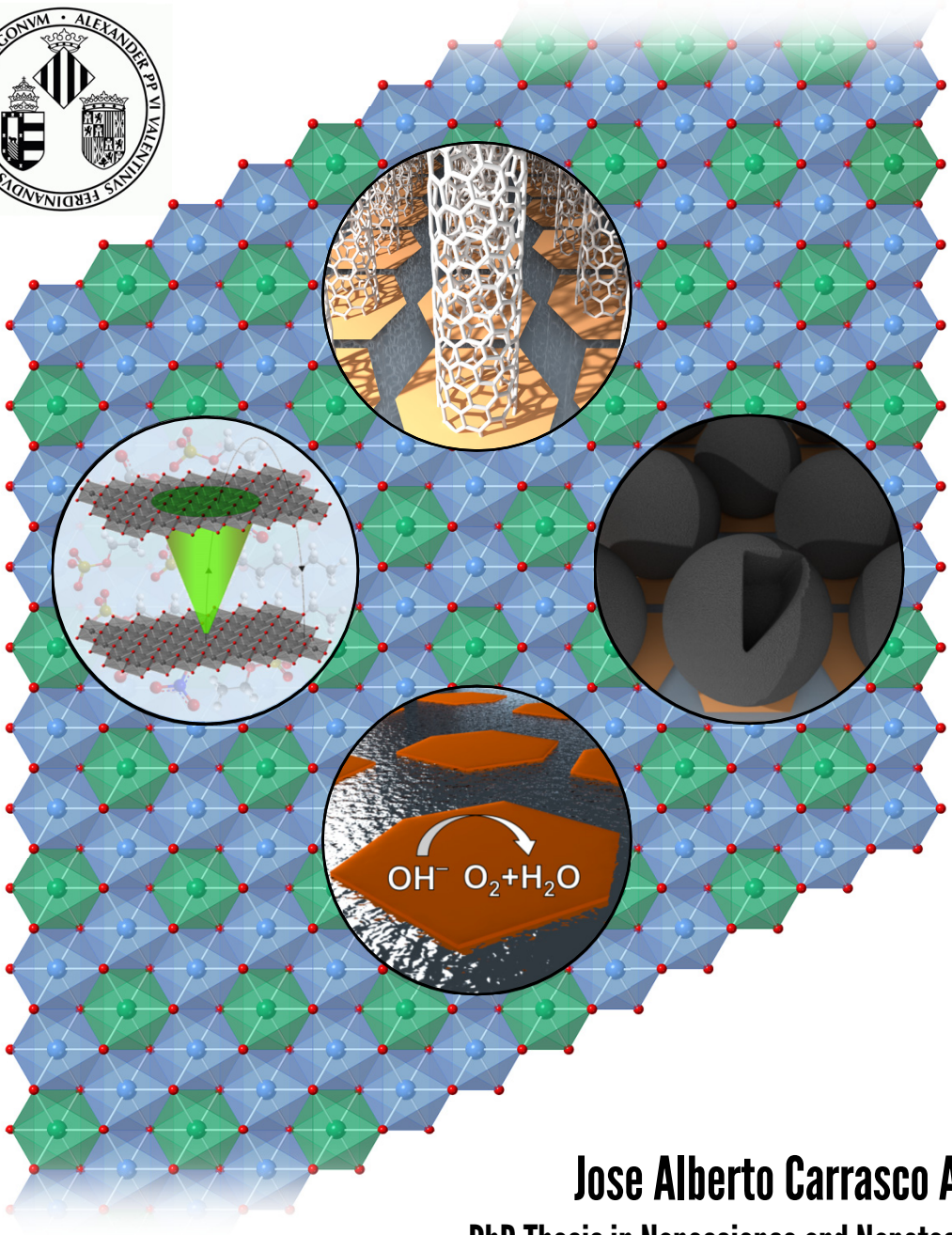

Jose Alberto Carrasco Andrés

PhD Thesis in Nanoscience and Nanotechnology

June 2018

Supervised by:
Prof. Eugenio Coronado Miralles
Dr. Gonzalo Abellán Sáez

Magnetic Materials Based on Layered Double Hydroxides: Chemical Design, Processing and Electrochemical Applications

Universidad de Valencia

Instituto de Ciencia Molecular (ICMol)

****

Memoria presentada por Jose Alberto Carrasco Andrés para aspirar al grado de Doctor en Nanociencia y Nanotecnología

****

Dirigida por:

Prof. Eugenio Coronado Miralles

Dr. Gonzalo Abellán Sáez

D. Eugenio Coronado Miralles, Profesor Catedrático del Departamento de Química Inorgánica de la Universidad de Valencia, y D. Gonzalo Abellán Sáez, doctor por la Universidad de Valencia.

Certifican: Que la presente Tesis Doctoral, titulada “Magnetic Materials Based on Layered Double Hydroxides: Chemical Design, Processing and Electrochemical Applications” ha sido desarrollada por Jose Alberto Carrasco Andrés bajo la dirección de ambos en el Instituto de Ciencia Molecular (ICMol), autorizando mediante este escrito la presentación de la misma para optar al grado de Doctor.

En Paterna, a 13 de Junio de 2018.

Dr. Eugenio Coronado Miralles

Dr. Gonzalo Abellán Sáez

Agradecimientos

A mi madre y a mi padre, por su amor incondicional, su apoyo, confianza y fe en mí. Por haberme convertido en la persona que soy ahora y haberme transmitido su valentía, determinación y valores. Este éxito es también vuestro. Gracias por creer en mí.

A mi familia, por haber estado unidos todos estos años, saber disfrutar los momentos felices y superar las adversidades juntos.

A Eugenio Coronado, por darme la oportunidad de formarme científica y personalmente en su grupo de investigación. Por haberme hecho mejorar académicamente y haber depositado en mí su confianza para llevar a cabo una tesis doctoral.

A Gonzalo Abellán, por todo lo aprendido bajo su tutela. Esta tesis está impregnada de tus enseñanzas. Un científico excelente y una persona admirable, un modelo a seguir que me ha permitido crecer como científico y como persona, y cuya pasión por la ciencia irradia cada uno de sus trabajos.

A todos mis compañeros en la UIMM por haberme hecho sentir siempre como en casa. Por todos los grandes momentos vividos durante todos estos años que han convertido este viaje en una experiencia inolvidable.

Mención especial para los nuevos amigos que he conocido a lo largo del doctorado y con los que he podido compartir un tiempo fantástico: Roger Sanchis, José Navarro, Eugenia Miguel, Néstor Calvo y Javier López. Convivir a diario con vosotros ha resultado ser increíblemente gratificante y enriquecedor. Coincidir en aficiones, humor y vivencias hacía empezar cada día con una sonrisa.

También quisiera dedicar esta tesis a mis amigos de la carrera Alberto Lopera, Elena Salvador y Alexis Rodríguez. Compartir los años de carrera, máster y doctorado juntos ha sido un regalo de valor incalculable. Gracias por acompañarme durante algunas de las etapas más felices de mi vida y estar siempre a mi lado. Sé que puedo contar con vosotros para cualquier cosa, que sois unos amigos estupendos y me enorgullezco de teneros a mi lado.

A mis amigos del colegio y del instituto José Carlos Balaguer y Fernando Medina, por haber crecido juntos y continuar haciéndolo tras más de dos décadas. Me siento muy afortunado de haberos conocido.

Por último, quisiera dedicar estas líneas finales a la que se ha convertido en una de mis pasiones. Durante mis años de instituto y especialmente en la universidad tuve el placer de conocer a docentes brillantes cuyo entusiasmo por la enseñanza era capaz de inspirar verdadera predilección por sus asignaturas. A lo largo de mi doctorado, y motivado por estos profesores ejemplares, decidí impartir clases durante varios años a casi un centenar de alumnos, despertando en mí una vocación docente y convirtiéndose en una de las experiencias más satisfactorias que he tenido el honor de disfrutar desde el punto de vista académico. Quisiera agradecerles a todos, profesores y alumnos, haber sido partícipes de ello.

Jose Alberto.

Table of Contents

Abbreviations

AC	Alternate Current
APTS	(3-Aminopropyl)triethoxysilane
AQ	Anthraquinone
ARR	Ammonium Releasing Reagent
CA	Contact Angle
ca.	Circa (approximately)
CHP	N-Cyclohexyl-2-pyrrolidone
CNF	Carbon Nanoform
CNT	Carbon Nanotube
CVD	Chemical Vapour Deposition
DC	Direct Current
EDLC	Electrical Double Layer Capacity
et al.	et alia (and others)
FESEM	Field Emission Scanning Electron Microscopy
FIB-SEM	Focused Ion Beam Scanning Electron Microscopy
FTIR	Fourier Transform Infrared
HRTEM	High Resolution Transmission Electron Microscopy
i.e.	id est (that is)
JCPDS	Joint Committee on Powder Diffraction Standards
LDH	Layered Double Hydroxide
OER	Oxygen Evolution Reaction
RMS	Root Mean Squared (Roughness)
rpm	Revolutions per Minute

SAED	Selected Area Electron Diffraction
SDS	Sodium Dodecyl Sulfate
SES	Sodium Ethyl Sulfate
SODS	Sodium Octadecyl Sulfate
SOS	Sodium Octyl Sulfate
STEM-EELS	Scanning Transmission Electron Microscopy and Electron Energy-Loss Spectroscopy
TEA	Triethanolamine
TGA	Thermogravimetric Analysis
TG-MS	Thermogravimetric Analysis coupled with Mass Spectrometry
T_M	Temperature for the onset of the Spontaneous Magnetization
TOF	Turnover Frequency
VRH	Variable Range Hopping
XRD	X-ray Diffraction

Chapter 1:

Introduction

1.1. Introduction.

With the rise of graphene in 2004,[1,2] two-dimensional (2D) materials have attracted enormous attention from the scientific community in the recent years. In addition to the paradigmatic graphene, other inorganic 2D materials have emerged showing a plethora of physical and chemical properties, consolidating the growing interest around these systems.[3–5] These materials exhibit anisotropic bonds, combining in-plane covalent bonding between the atoms with weaker van der Waals interactions between the layers. Transition metal dichalcogenides,[6,7] boron nitride,[8,9] black phosphorus (in the single-layer form phosphorene)[10,11] or antimonene[12,13] are some examples of this class of materials. In addition to neutral 2D materials, the existence of other compounds formed by ionic layers, where electrostatic interactions play a crucial role, are also known. This is the case of the layered double hydroxides (LDHs).[14,15]

LDHs are a wide class of layered anionic clays with exchangeable anions in the interlayer space (**Fig. 1.1**). Their chemical structure is analogous to that of the hydrotalcite, $Mg_6Al_2(OH)_{16}(CO_3)\cdot 4H_2O$, first discovered by Hochstetter in 1842 as a white mass of waxy or pearly lustre in serpentinite from Snarum, Norway. Afterwards, the characterization of this material was gradually unveiled by authors such as Foshag (1920) or Frodel (1941), among others, who described their currently accepted formula. X-ray patterns contributed to the characterization of this material.[16] Typically, LDHs are made up of positively charged 2D brucite-like layers with an interlayer region that contains the charge compensating anions as well as the solvation molecules. One of the main aspects of the LDHs is their ability to be exfoliated into 2D nanosheets retaining the properties of their pristine bulk precursors such as 2D magnetism or redox chemistry.[15] This feature allows them to act as macromolecular building blocks in the design of more complex architectures. From the point of view of the intralayer structure, the metal cations occupy the centres of edge-sharing octahedra, whose vertices depict hydroxide anions that serve as bridges for the connection with neighbouring metallic cations, assembling the infinite 2D sheets.[15,17] The general formula for these materials is the following: $[M^{2+}_{1-x}\, M^{3+}_{x}\, (OH)_2][A^{n-}]_{x/n}\cdot yH_2O$, where M stands for the cationic metal ions and A for

the interlayer anion. One of the main features of LDHs relies in their outstanding ability to tune their chemical composition by modifying the nature of their fundamental components. For example, the most common divalent metals (M^{2+}) are Mg^{2+}, Ni^{2+}, Co^{2+}, Fe^{2+}, Zn^{2+}, Ca^{2+}, Cu^{2+} or Mn^{2+}, whereas the trivalent metals (M^{3+}) are generally Al^{3+}, Fe^{3+}, Ni^{3+}, Cr^{3+}, Fe^{3+}, Ga^{3+}, Mn^{3+} or In^{3+}.[14,18,19] Although the presence of a divalent and a trivalent metal is the most common in the synthesis of most LDH phases, there are also additional arrangements that involve the mixture of different divalent and trivalent metal cations to give rise to ternary or quaternary LDHs.[20–22] Furthermore, some authors have reported the synthesis of LDHs with monovalent or tetravalent cations such as Li^{+} or Ti^{4+}, respectively.[23–26] Regarding the atomic ratio between both metals (M^{2+}/M^{3+}), χ usually ranges between 0.2 – 0.4, hence implying a M^{2+}/M^{3+} ratio between 4:1 to 1.5:1, respectively.[18,19,27] Concerning the interlayer non-framework charge compensating anion (A), there is an incredible wide range of possibilities that vary from inorganic to organic anions, simple and complex ones. For example, one can find halides (Cl^{-}, F^{-}, etc.), non-metallic oxoanions (CO_3^{2-}, NO_3^{2-}, SO_4^{2-}, BrO_4^{-}, ClO_4^{-}, AsO_4^{3-}, etc.), oxometalate anions (CrO_4^{2-}, MnO_4^{-}, $Cr_2O_7^{2-}$, VO_4^{3-}, etc.) organic anions ($C_2O_4^{2-}$, $C_6H_5SO_3^{-}$, CH_3COO^{-}, $C_6H_5COO^{-}$, surfactants like $C_{12}H_{25}SO_4^{-}$ etc.), as well as more exotic anions such as porphyrins, photoactive molecules, anionic polymers, anionic complexes of transition metals or biological molecules, among others.[14,18,19,28] When the synthesis of a given LDH is made under ambient conditions, the intralayer anion is the carbonate, which can be exchanged *via* intercalation reactions.[29] These anion exchange reactions are crucial in order to modify the chemical, electronic, optical and magnetic properties of the host lattice.[30] The ease of these procedures is related with the charge density of the layers and the anions, which affect the intensity of the electrostatic interactions in the global system. For example, the presence of a high number of M^{3+} cations increases the positive charge density of the hydroxide sheet, whereas divalent anions exhibit higher charge densities than the monovalent ones. In this context, the affinity of carbonate anions for the LDH layers is higher than that observed for other analogues, thus hindering subsequent delamination procedures.[29,30] In order to favour the exfoliation of these materials, a previous replacement of the CO_3^{2-} anion is mandatory by means of anion exchange reactions to molecules with lesser charge

density such as nitrate, halides or surfactants, which also facilitates delamination procedures thanks to their aliphatic chain and the formation of micelles.[31]

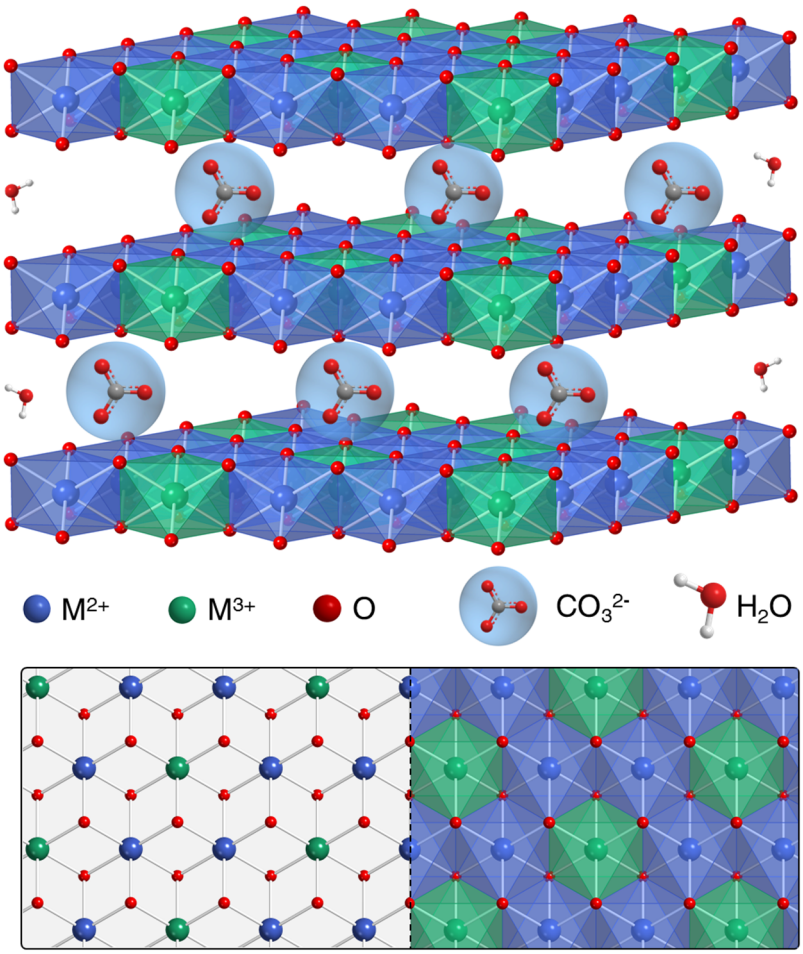

Figure 1.1. Top image depicts a schematic illustration of a general LDH system with M^{2+}/M^{3+} ratio of 2:1, highlighting the layered structured and exhibiting CO_3^{2-} as the interlayer anion. In addition, H_2O solvent molecules can be found along the structure. On the other hand, bottom scheme depicts the view of a cationic sheet from above, exhibiting the octahedral environment of each metal and the hydroxo bridges that connect them.

From the point of view of the synthetic methodologies, LDHs are usually synthesized by means of a traditional coprecipitation method, where the two soluble metal salts are mixed simultaneously in water in the presence of a base in order to control the pH of the solution to favour the formation of the final hydroxide phase.

This synthetic approach usually leads to small particles with undefined morphologies. In order to avoid the presence of impurities, keeping a constant pH is highly recommended by adding reagents such as NaOH, NH_3 or KOH, among others.[18,32] Ammonium releasing reagent (ARR) such as urea can also be used for carefully controlling the pH of the mixture improving the morphology of these materials.[33] The addition of a base retardant such as urea as a precipitating agent allows the separation between nucleation and particle growth, therefore avoiding ageing effects derived from continuous nucleation of the mixed hydroxides which results in a wide particle size distribution. This improved coprecipitation synthesis in aqueous media is the main way to give rise to hexagonal and pure -Al^{3+} LDHs nowadays, thanks to the amphoteric behaviour of the trivalent cation.[28,30,34–37] The hexagonal morphology is formed *via* a circle-like growth motion mechanism starting from M^{3+} hydroxide or oxide seeds.[38,39] In this context, the final LDH phase can be obtained with different interlayer anions according to the starting metallic salts as well as by inducing an inert atmosphere during the reaction.[40] On the other hand, the synthesis of crystalline non-Al^{3+}-based LDHs is highly disfavoured for the traditional coprecipitation methods due to the absence of amphoteric behaviour in transition-metal cations like Fe^{3+}. To overcome this problem, the main strategies rely in two approaches: the use of chelating reagents such as triethanolamine (TEA)[27,39] or the use of a topochemical approach.[41–43] In this context, hydrothermal or solvothermal treatments using autogenous conditions can be used for improving the crystallinity of non-Al^{3+}-LDHs. Alongside with these methodologies, one can find other alternative approaches such as electrosynthesis,[44] microwave[45] or ultrasound-assisted methods.[46]

After the experimental synthesis of the material, a precise characterization becomes crucial in order to identify the LDH phase and confirm the quality of the sample. Regarding the general characterization of a LDH, **Fig. 1.2** depicts the X-ray powder diffraction patter (XRPD), Fourier transferred infrared spectra (FTIR), thermogravimetric analysis (TGA) and microscopy images for a typical CoAl-CO_3 LDH. In the following chapters and the included papers,[28,33,39,47,48] different LDH compositions (such as CoFe- and NiFe-) and intercalated systems (nitrate or surfactant-intercalated materials) are thoroughly described.

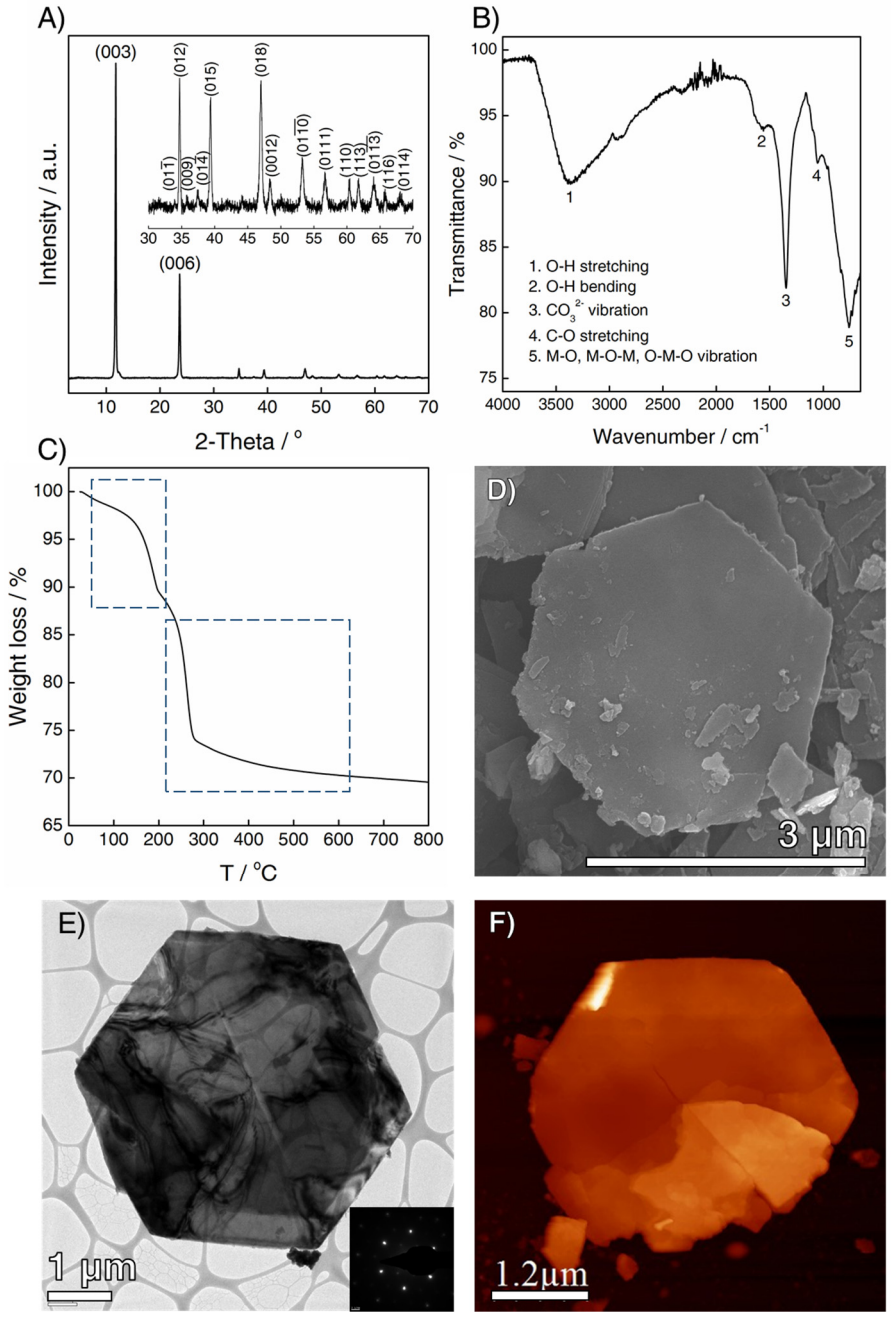

Figure 1.2. Characterization of a typical CoAl-CO_3 LDH: XRPD zooming the 30 – 70º region (A), FTIR spectrum highlighting the main peaks (B), TGA carried out under air, pointing out the two different regions (C), FESEM (D), HRTEM (E) and AFM (F) images of the material. The inset in (D) indicates the SAED pattern of the sample.

XRPD (**Fig 1.2A**) confirmed the LDH phase highlighting the main basal reflections for hydrotalcite-like compounds (JCPDS 22-700).[49] A typical diffractogram exhibits well-defined and intense peaks at low 2-theta (2θ) values, the first (003) basal reflection ascribed to the basal space of the system. In this context, basal space takes into account the interlayer distance as well as the half width of the adjacent layers, as depicted in **Fig. 1.3**.[28] The 2θ value of *ca.* 11º is related with a basal space of 7.6 Å, hence implying the presence of carbonate as interlayer anion. Alongside with that reflection, the characteristic (006), (009), (012), (015) and (018) peaks are found between 23º and 47º, as well as the typical doublet (110) – (113) observed in these materials near 60º.[39,50,51] For these materials, the quality of (00*l*) peaks are related with the stacking among the layers, whereas (*h*0*l*) and (*hk*0) reflections indicate the presence of in-plane turbostatic structures and disorder effects.[19,33]

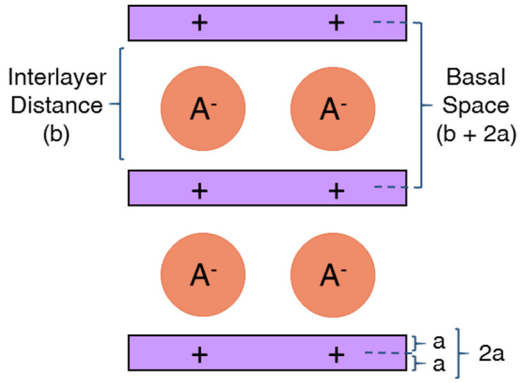

Figure 1.3. Schematic illustration of the differences between interlayer distance, which only takes into account the gallery height of the system, and the basal space, which also considers the thickness of the cationic sheet (purple). Interlayer anion is depicted by the orange circle between the layers.

On the other hand, FTIR spectroscopy arises as a powerful technique in order to characterise the interlayer anion found in the material. In a typical LDH, FTIR spectrum (**Fig. 1.2B**) presents a broad peak at *ca.* 3400 cm^{-1} related to the stretching vibrations of the OH groups that are found in the LDH structure whereas the peak at *ca.* 1590 cm^{-1} is ascribed to the bending vibrations of H_2O molecules placed between the layers.[51,52] At *ca.* 1347 cm^{-1} we can observe the band that confirms the presence

of carbonate anions in the interlayer space,[27,53] while the peak at *ca.* 1050 cm^{-1} corresponds to the C–O stretching vibrations.[50] Finally, the range of 800 – 500 cm^{-1} is related with the metallic vibrational bands M–O, M–O–M and O–M–O.[54,55] Regarding the TGA, this technique results useful in the monitoring of the decomposition steps of a LDH sample. In a typical profile carried out under air atmosphere (**Fig. 1.2C**), one can find an initial weight loss in the 25 – 220 ºC range, related with the elimination of the physisorbed water molecules by the LDH structure (solvation molecules),[51] followed by a second and most intense weight loss between *ca.* 220 – 600 ºC, which matches with the overlapping between the dehydroxylation of the layered system, the elimination of the chemisorbed water and the decomposition of the interlayer anion.[53]

In order to study the morphology of a LDH, electronic microscopy arises as the most powerful technique of characterization in the form of emission scanning electron microscopy (FESEM) and high resolution transmission microscopy (HRTEM) (**Fig. 1.2D** and **1.2E**, respectively). The CoAl-CO_3 LDH exhibits a conventional hexagonal morphology[56] with well-defined and regular hexagonal shape whose average lateral dimensions are *ca.* 3.5 μm and 80 – 100 nm in thickness. HRTEM confirms the morphology, depicting a low contrast due to the low thickness of the flake, and the selected area electron diffraction (SAED) pattern evidences the high crystalline quality of the sample.[30,57] Finally, the atomic force microscopy (AFM) on SiO_2 substrates also confirms the hexagonal and well-defined morphology of the LDH (**Fig 1.2F**).

Whereas the characterization and synthetic methodologies here presented usually refers to micrometric hexagonal LDHs synthesized under aqueous conditions, by modification of the experimental parameters such as the synthetic methodology or the use of additional reagents in combination with the metallic salts, the resulting material can present strong deviations from the typical structure due to dislocations in the edges of the nanostructures.[58] For example, with the addition of ethylene glycol in a hydrothermal treatment we can obtain flower-like LDHs,[33] and the use of a non-aqueous route based on methanol leads to the synthesis of nanometric LDHs with a high degree of crystallinity at the light of electronic

microscopy (**Fig. 1.4**).[50,59] Both changes affect the internal properties of the LDH as well as the magnetic behaviour as we will discuss in detail later.

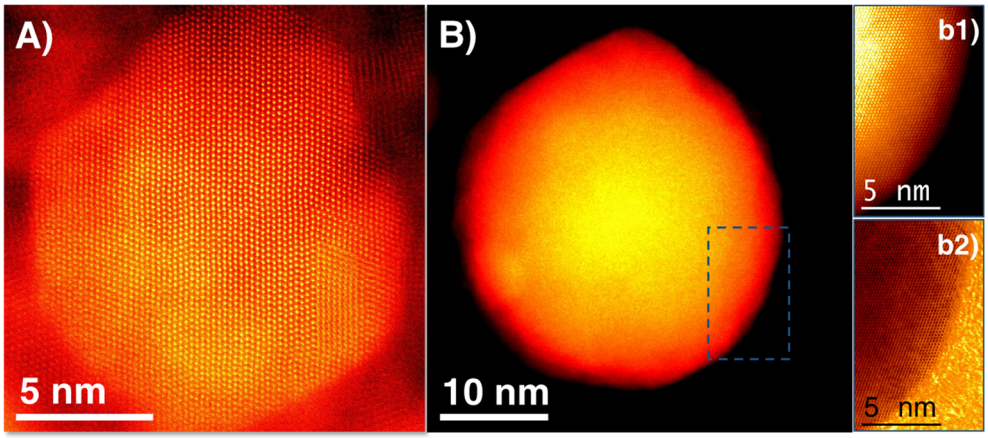

Figure 1.4. Low magnification high angle annular dark field images of the nanometric CoFe-Methoxide (A) and NiFe-Methoxide (B) samples, synthesized *via* a methanolic route. The highlighted region in (B) is zoomed in high magnification annular dark field (b1) and bright field (b2). The images show the high quality of the crystallites of both materials.

Besides the structural and morphological characterization, deciphering the magnetic behaviour results in a key aspect for LDHs composed by magnetic metals such as the compositions depicted in the present thesis: CoAl-, CoFe- and NiFe-LDHs. In this context, a thorough magnetic study highlighting the main parameters and the basis of the magnetic response of these materials can be found in the next Chapter.

Alongside with this general introduction to LDH materials, additional key aspects of them are thoroughly detailed in the following chapters, including a specific introduction of the topic for each one of them. Chapter 2 is focused on the magnetic properties of these systems, exhibiting the two main contributions (intralayer and interlayer) to the overall magnetism of the material, and unveils some of the main aspects that surround the understanding of the magnetic behaviour. Aspects such as a meticulous synthesis to avoid the presence of extrinsic magnetic impurities, as well as the importance of morphology in the overall magnetic response, or the role played by the interlayer distance in the dipolar interactions. Chapter 3 addresses the

functionalization and exfoliation procedures, introducing a non-aqueous methodology that gives rise to nanometric LDHs with superparamagnetic behaviour and enhanced electrochemical features. In line with that, this methanolic route allows the exfoliation of the materials in water, hence overcoming processability disadvantages related to common delaminating agents such as formamide. Furthermore, unpublished studies on ultrasonic tip sonication as well as covalent functionalization are also portrayed, highlighting new promising steps in both topics. Finally, Chapter 4 is centred on the applications of these materials, pointing out the catalytic behaviour of NiFe-LDHs by means of chemical vapour deposition (CVD) and depicting a thorough study of the catalytic response towards the synthesis of carbon nanoforms. The catalytic procedures were carried out in bulk and with the LDHs deposited on films at different temperatures, hence exhibiting the synthesis of distinct carbon nanoforms according to the arrangement and temperature studied. In addition, the formation mechanism of the LDH flakes was also unveiled.

In summary, this work provides further characterization and comprehensive understanding for this type of layered materials, expanding some of the boundaries in aspects such as magnetism, functionalization or applications, and highlights the importance of LDHs as a key material in materials science with a bright present and a promising future.

1.2. Motivation.

This thesis is motivated by the recent advances of layered materials. Inspired by the discovery and posterior research of graphene, layered inorganic materials have gained significant attention throughout the scientific community. In this context, layered double hydroxides have recently shown exceptional results in fields such as catalysis or electrochemistry, turning into excellent alternatives to more expensive materials. Nevertheless, there are still unexplored territories related with the electronic properties of these materials that need to be addressed.

This work is divided in three main chapters, composed by the state-of-the-art of each topic, followed by a summary of the most important results and highlighting the main contributions of the author to the field and the included papers.

Fundamental aspects of LDHs such as their magnetic nature (Chapter 1), exfoliation and functionalization procedures (Chapter 2) and catalytic applications (Chapter 3) are thoroughly discussed in depth, shedding light to new results in the ongoing learning of these layered materials and their impact in the field of materials science.

Regarding the articles attached to this thesis, they were selected based on their main topic. Chapter 1 includes three papers focused on the magnetic behaviour of LDHs: "*Room Temperature Magnetism in Layered Double Hydroxides due to Magnetic Nanoparticles*" (*Inorg. Chem.* **2013**, *52*, 7828–7830), "*Influence of Morphology in the Magnetic Properties of Layered Double Hydroxides*" (*J. Mater. Chem. C* **2018**, *6*, 1187–1198) and "*Deciphering the Role of Dipolar Interactions in Magnetic Layered Double Hydroxides*" (*Inorg. Chem.* **2018**, *57*, 2013–2022). Chapter 2 aims to exfoliation, functionalization and electrochemistry of the 2D LDH nanosheets, with two papers based on a non-aqueous synthesis of nanometric LDHs: "*Alkoxide-intercalated CoFe-Layered Double Hydroxides as Precursors of Colloidal Nanosheet Suspensions: Structural, Magnetic and Electrochemical Properties*" (*J. Mater. Chem. C* **2014**, *2*, 3723–3731) and "*Alkoxide-intercalated NiFe-Layered Double Hydroxides Magnetic Nanosheets as Efficient Water Oxidation Electrocatalysts*" (*Inorg. Chem. Front.* **2016**, *3*, 478–487). Finally, Chapter 3 is focused on to the catalytic applications of NiFe-LDHs in the CVD synthesis of carbon

nanoforms, both as powder material and deposited on ultrathin films: "*In-Situ Growth of Ultrathin Films of NiFe-LDHs: Towards a Hierarchical Synthesis of Bamboo-Like Carbon Nanotubes*" (*Adv. Mater. Interfaces* **2014**, *1*, 1400184) and "*CVD Synthesis of Carbon Spheres using NiFe-LDHs as Catalytic Precursors: Structural, Electrochemical and Magnetoresistive Properties*" (*J. Mater. Chem. C* **2016**, *4,* 440–448). Alongside with these two papers, a book chapter focused on "*Layered Double Hydroxide Nanocomposites Based on Carbon Nanoforms*" (Chapter 9 in *Layered Double Hydroxide Polymer Nanocomposites*; Ed. Woodhead Publishing, Cambridge, 2019) is also included.

1.3. Publications during the PhD.

1) Room Temperature Magnetism in Layered Double Hydroxides due to Magnetic Nanoparticles. Abellán, G.; Carrasco, J. A.; Coronado, E. *Inorg. Chem.* **2013**, *52*, 7828–7830.

2) Alkoxide-intercalated CoFe-Layered Double Hydroxides as Precursors of Colloidal Nanosheet Suspensions: Structural, Magnetic and Electrochemical Properties. Abellán, G.; Carrasco, J. A.; Coronado, E.; Romero, J.; Varela, M. *J. Mater. Chem. C* **2014**, *2*, 3723–3731.

3) Synthesis of $FeNi_3$ Nanoparticles in Benzyl Alcohol and their Electrical and Magnetic Properties. Abellán, G.; Carrasco, J. A.; Coronado, E.; Prima-García, H. *J. Sol-Gel Sci. Techn.* **2014**, *70*, 292–299.

4) In-Situ Growth of Ultrathin Films of NiFe-LDHs: Towards a Hierarchical Synthesis of Bamboo-Like Carbon Nanotubes. Abellán, G.; Carrasco, J. A.; Coronado, E.; Prieto-Ruiz, J. P.; Prima-García, H. *Adv. Mater. Interfaces* **2014**, *1*, 1400184.

5) CVD Synthesis of Carbon Spheres using NiFe-LDHs as Catalytic Precursors: Structural, Electrochemical and Magnetoresistive Properties. Carrasco, J. A.; Prima-Garcia, H.; Romero, J.; Hernández-Saz, J.; Molina, S. I.; Abellán, G.; Coronado, E. *J. Mater. Chem. C* **2016**, *4*, 440–448.

6) Alkoxide-intercalated NiFe-Layered Double Hydroxides Magnetic Nanosheets as Efficient Water Oxidation Electrocatalysts. Carrasco, J. A.; Romero, J.; Varela, M.; Hauke, F.; Abellán, G.; Hirsch, A.; Coronado, E. *Inorg. Chem. Front.* **2016**, *3*, 478–487.

7) Small-pore Driven High Capacitance in a Hierarchical Carbon *via* Carbonization of Ni-MOF-74 at Low Temperatures. Carrasco, J. A.; Romero, J.; Abellán, G.; Hernández-Saz, J.; Molina, S. I.; Martí-Gastaldo, C.; Coronado, E. *Chem. Commun.* **2016**, *52*, 9141–9144.

8) Influence of Morphology in the Magnetic Properties of Layered Double Hydroxides. Carrasco, J. A.; Abellán, G.; Coronado, E. *J. Mater. Chem. C* **2018**, *6*, 1187–1198.

9) Deciphering the Role of Dipolar Interactions in Magnetic Layered Double Hydroxides. Carrasco, J. A.; Cardona-Serra, S.; Clemente-Juan, J. M.; Gaita-Ariño, A.; Abellán, G.; Coronado, E. *Inorg. Chem.* **2018**, *57*, 2013–2022.

10) Layered Double Hydroxide Nanocomposites Based on Carbon Nanoforms (Chapter 9). Carrasco, J. A.; Abellán, G.; Coronado, E. *Layered Double Hydroxide Polymer Nanocomposites*; Ed. Woodhead Publishing, Cambridge, 2019.

11) Covalent Functionalization of Magnetic Layered Double Hydroxides. Carrasco, J.A.; Vieira, B. J. C.; Waerenborgh, J. C.; Márkus, B. G.; Simon, F.; Abellán, G.; Coronado, E. (*manuscript in preparation*).

12) Liquid Phase Exfoliation of Layered Double Hydroxides. Carrasco, J.A.; Harvey, A.; Hanlon, D.; Abellán, G.; Coleman, J. N.; Coronado, E. (*manuscript in preparation*).

1.4. References.

(1) Geim, A. K.; Novoselov, K. S. The Rise of Graphene. *Nat. Mater.* **2007**, *6*, 183–191.

(2) Geim, A. K. Graphene: Status and Prospects. *Science* **2009**, *324*, 1530–1534.

(3) Duong, D. L.; Yun, S. J.; Lee, Y. H. Van der Waals Layered Materials: Opportunities and Challenges. *ACS Nano* **2017**, *11*, 11803–11830.

(4) Novoselov, K. S.; Mishchenko, A.; Carvalho, A.; Castro Neto, A. H. 2D Materials and van der Waals Heterostructures. *Science* **2016**, *353*, aac9439.

(5) Miró, P.; Audiffred, M.; Heine, T. An Atlas of Two-Dimensional Materials. *Chem. Soc. Rev.* **2014**, *43*, 6537–6554.

(6) Ganatra, R.; Zhang, Q. Few-Layer MoS_2: A Promising Layered Semiconductor. *ACS Nano* **2014**, *8*, 4074–4099.

(7) Tan, C.; Zhang, H. Two-Dimensional Transition Metal Dichalcogenide Nanosheet-Based Composites. *Chem. Soc. Rev.* **2015**, *44*, 2713–2731.

(8) Ci, L.; Song, L.; Jin, C.; Jariwala, D.; Wu, D.; Li, Y.; Srivastava, A.; Wang, Z. F.; Storr, K.; Balicas, L.; et al. Atomic Layers of Hybridized Boron Nitride and Graphene Domains. *Nat. Mater.* **2010**, *9*, 430–435.

(9) Golberg, D.; Bando, Y.; Huang, Y.; Terao, T.; Mitome, M.; Tang, C.; Zhi, C. Boron Nitride Nanotubes and Nanosheets. *ACS Nano* **2010**, *4*, 2979–2993.

(10) Kou, L.; Chen, C.; Smith, S. C. Phosphorene: Fabrication, Properties, and Applications. *J. Phys. Chem. Lett.* **2015**, *6*, 2794–2805.

(11) Li, L.; Yu, Y.; Ye, G. J.; Ge, Q.; Ou, X.; Wu, H.; Feng, D.; Chen, X. H.; Zhang, Y. Black Phosphorus Field-Effect Transistors. *Nat. Nanotechnol.* **2014**, *9*, 372–377.

(12) Gibaja, C.; Rodriguez-San-Miguel, D.; Ares, P.; Gómez-Herrero, J.; Varela, M.; Gillen, R.; Maultzsch, J.; Hauke, F.; Hirsch, A.; Abellán, G.; et al. Few-Layer Antimonene by Liquid-Phase Exfoliation. *Angew. Chem. Int. Ed.* **2016**, *55*, 14345–14349.

(13) Zhang, S.; Yan, Z.; Li, Y.; Chen, Z.; Zeng, H. Atomically Thin Arsenene and Antimonene: Semimetal-Semiconductor and Indirect-Direct Band-Gap Transitions. *Angew. Chem. Int. Ed.* **2015**, *54*, 3112–3115.

(14) *Layered Double Hydroxides: Present and Future*; Rives, V., Ed.; Nova Science Publishers: Huntington, N.Y, 2001.

(15) Wang, Q.; O'Hare, D. Recent Advances in the Synthesis and Application of Layered Double Hydroxide (LDH) Nanosheets. *Chem. Rev.* **2012**, *112*, 4124–4155.

(16) Mills, S. J.; Christy, A. G.; Génin, J.-M. R.; Kameda, T.; Colombo, F. Nomenclature of the Hydrotalcite Supergroup: Natural Layered Double Hydroxides. *Mineral. Mag.* **2012**, *76*, 1289–1336.

(17) Guo, X.; Zhang, F.; Evans, D. G.; Duan, X. Layered Double Hydroxide Films: Synthesis, Properties and Applications. *Chem. Commun.* **2010**, *46*, 5197–5210.

(18) Cavani, F.; Trifirò, F.; Vaccari, A. Hydrotalcite-Type Anionic Clays: Preparation, Properties and Applications. *Catal. Today* **1991**, *11*, 173–301.

(19) *Layered Double Hydroxides*; Duan, X., Evans, D. G., Eds.; Structure and Bonding; Springer-Verlag: Berlin/Heidelberg, 2006; Vol. 119.

(20) Kim, S.; Fahel, J.; Durand, P.; André, E.; Carteret, C. Ternary Layered Double Hydroxides (LDHs) Based on Co-, Cu-Substituted ZnAl for the Design of Efficient Photocatalysts. *Eur. J. Inorg. Chem.* **2017**, *2017*, 669–678.

(21) Wang, T.; Xu, W.; Wang, H. Ternary NiCoFe Layered Double Hydroxide Nanosheets Synthesized by Cation Exchange Reaction for Oxygen Evolution Reaction. *Electrochim. Acta* **2017**, *257*, 118–127.

(22) Das, N. N.; Das, R. Synthesis, Characterization and Activation of Quaternary Layered Double Hydroxides for the One-Pot Synthesis of Methyl Isobutyl Ketone. *React. Kinet. Mech. Catal.* **2010**, *99*, 397–408.

(23) Wang, S. L.; Hseu, R. J.; Chang, R. R.; Chiang, P. N.; Chen, J. H.; Tzou, Y. M. Adsorption and Thermal Desorption of Cr(VI) on Li/Al Layered Double Hydroxide. *Colloids Surf. Physicochem. Eng. Asp.* **2006**, *277*, 8–14.

(24) Liu, Y. T.; Wang, M. K.; Chen, T. Y.; Chiang, P. N.; Huang, P. M.; Lee, J. F. Arsenate Sorption on Lithium/Aluminum Layered Double Hydroxide Intercalated by Chloride and on Gibbsite: Sorption Isotherms, Envelopes, and Spectroscopic Studies. *Environ. Sci. Technol.* **2006**, *40*, 7784–7789.

(25) Zhang, W. H.; Guo, X. D.; He, J.; Qian, Z. Y. Preparation of Ni(II)/Ti(IV) Layered Double Hydroxide at High Supersaturation. *J. Eur. Ceram. Soc.* **2008**, *28*, 1623–1629.

(26) Shu, X.; Zhang, W.; He, J.; Gao, F.; Zhu, Y. Formation of Ni–Ti-Layered Double Hydroxides Using Homogeneous Precipitation Method. *Solid State Sci.* **2006**, *8*, 634–639.

(27) Abellán, G.; Coronado, E.; Martí-Gastaldo, C.; Waerenborgh, J.; Ribera, A. Interplay between Chemical Composition and Cation Ordering in the Magnetism of Ni/Fe Layered Double Hydroxides. *Inorg. Chem.* **2013**, *52*, 10147–10157.

(28) Carrasco, J. A.; Cardona-Serra, S.; Clemente-Juan, J. M.; Gaita-Ariño, A.; Abellán, G.; Coronado, E. Deciphering the Role of Dipolar Interactions in Magnetic Layered Double Hydroxides. *Inorg. Chem.* **2018**, *57*, 2013–2022.

(29) Khan, A. I.; O'Hare, D. Intercalation Chemistry of Layered Double Hydroxides: Recent Developments and Applications. *J. Mater. Chem.* **2002**, *12*, 3191–3198.

(30) Liu, Z.; Ma, R.; Osada, M.; Iyi, N.; Ebina, Y.; Takada, K.; Sasaki, T. Synthesis, Anion Exchange, and Delamination of Co−Al Layered Double Hydroxide: Assembly of the Exfoliated Nanosheet/Polyanion Composite Films and Magneto-Optical Studies. *J. Am. Chem. Soc.* **2006**, *128*, 4872–4880.

(31) Wang, C. J.; Wu, Y. A.; Jacobs, R. M. J.; Warner, J. H.; Williams, G. R.; O'Hare, D. Reverse Micelle Synthesis of Co−Al LDHs: Control of Particle Size and Magnetic Properties. *Chem. Mater.* **2011**, *23*, 171–180.

(32) Miyata, S.; Kumura, T. Synthesis of New Hydrotalcite-like Compounds and Their Physico-Chemical Properties. *Chem. Lett.* **1973**, *2*, 843–848.

(33) Carrasco, J. A.; Abellán, G.; Coronado, E. Influence of Morphology in the Magnetic Properties of Layered Double Hydroxides. *J. Mater. Chem. C* **2018**, *6*, 1187–1198.

(34) Adachi-Pagano, M.; Forano, C.; Besse, J.-P. Synthesis of Al-Rich Hydrotalcite-like Compounds by Using the Urea Hydrolysis Reaction—control of Size and Morphology. *J. Mater. Chem.* **2003**, *13*, 1988–1993.

(35) Arai, Y.; Ogawa, M. Preparation of Co–Al Layered Double Hydroxides by the Hydrothermal Urea Method for Controlled Particle Size. *Appl. Clay Sci.* **2009**, *42*, 601–604.

(36) Inayat, A.; Klumpp, M.; Schwieger, W. The Urea Method for the Direct Synthesis of ZnAl Layered Double Hydroxides with Nitrate as the Interlayer Anion. *Appl. Clay Sci.* **2011**, *51*, 452–459.

(37) Rao, M. M.; Reddy, B. R.; Jayalakshmi, M.; Jaya, V. S.; Sridhar, B. Hydrothermal Synthesis of Mg–Al Hydrotalcites by Urea Hydrolysis. *Mater. Res. Bull.* **2005**, *40*, 347–359.

(38) Okamoto, K.; Iyi, N.; Sasaki, T. Factors Affecting the Crystal Size of the MgAl-LDH (Layered Double Hydroxide) Prepared by Using Ammonia-Releasing Reagents. *Appl. Clay Sci.* **2007**, *37*, 23–31.

(39) Abellán, G.; Carrasco, J. A.; Coronado, E.; Prieto-Ruiz, J. P.; Prima-García, H. In-Situ Growth of Ultrathin Films of NiFe-LDHs: Towards a Hierarchical Synthesis of Bamboo-Like Carbon Nanotubes. *Adv. Mater. Interfaces* **2014**, *1*, 1400184.

(40) Forano, C.; Costantino, U.; Prévot, V.; Gueho, C. T. Layered Double Hydroxides (LDH). In *Developments in Clay Science*; Elsevier, 2013; Vol. 5, pp 745–782.

(41) Lee, J.-H.; O'Hare, D.; Jung, D.-Y. Topochemical Oxidation of Transition Metals in Layered Double Hydroxides by Anthraquinone-2-Sulfonate. *Bull. Korean Chem. Soc.* **2012**, *33*, 725–727.

(42) Li, Y.; Li, H.; Yang, M.; He, X.; Ni, P.; Kang, L.; Liu, Z.-H. Topochemical Synthesis of Ni^{2+}–Fe^{3+} Layered Double Hydroxides with Large Size. *Appl. Clay Sci.* **2011**, *52*, 51–55.

(43) Liang, J.; Ma, R.; Iyi, N.; Ebina, Y.; Takada, K.; Sasaki, T. Topochemical Synthesis, Anion Exchange, and Exfoliation of Co−Ni Layered Double Hydroxides: A Route to Positively Charged Co−Ni Hydroxide Nanosheets with Tunable Composition. *Chem. Mater.* **2010**, *22*, 371–378.

(44) Prevot, V.; Forano, C.; Khenifi, A.; Ballarin, B.; Scavetta, E.; Mousty, C. A Templated Electrosynthesis of Macroporous NiAl Layered Double Hydroxides Thin Films. *Chem Commun* **2011**, *47*, 1761–1763.

(45) Benito, P.; Herrero, M.; Labajos, F. M.; Rives, V. Effect of Post-Synthesis Microwave–hydrothermal Treatment on the Properties of Layered Double Hydroxides and Related Materials. *Appl. Clay Sci.* **2010**, *48*, 218–227.

(46) Lee, J. H.; Lee, Y. S.; Kim, H.; Jung, D.-Y. Ultrasound-Induced Rapid Intercalation of Biselenite in Layered Double Hydroxides. *Eur. J. Inorg. Chem.* **2011**, *2011*, 3334–3339.

(47) Abellán, G.; Carrasco, J. A.; Coronado, E. Room Temperature Magnetism in Layered Double Hydroxides Due to Magnetic Nanoparticles. *Inorg. Chem.* **2013**, *52*, 7828–7830.

(48) Carrasco, J. A.; Prima-Garcia, H.; Romero, J.; Hernández-Saz, J.; Molina, S. I.; Abellán, G.; Coronado, E. CVD Synthesis of Carbon Spheres Using NiFe-LDHs as Catalytic Precursors: Structural, Electrochemical and Magnetoresistive Properties. *J. Mater. Chem. C* **2016**, *4*, 440–448.

(49) Sharma, U.; Tyagi, B.; Jasra, R. V. Synthesis and Characterization of Mg−Al−CO_3 Layered Double Hydroxide for CO_2 Adsorption. *Ind. Eng. Chem. Res.* **2008**, *47*, 9588–9595.

(50) Carrasco, J. A.; Romero, J.; Varela, M.; Hauke, F.; Abellán, G.; Hirsch, A.; Coronado, E. Alkoxide-Intercalated NiFe-Layered Double Hydroxides Magnetic Nanosheets as Efficient Water Oxidation Electrocatalysts. *Inorg. Chem. Front.* **2016**, *3*, 478–487.

(51) Zhang, J.; Xie, X.; Li, C.; Wang, H.; Wang, L. The Role of Soft Colloidal Templates in the Shape Evolution of Flower-like MgAl-LDH Hierarchical Microstructures. *RSC Adv.* **2015**, *5*, 29757–29765.

(52) Zhou, L.-J.; Huang, X.; Chen, H.; Jin, P.; Li, G.-D.; Zou, X. A High Surface Area Flower-like Ni–Fe Layered Double Hydroxide for Electrocatalytic Water Oxidation Reaction. *Dalton Trans.* **2015**, *44* (25), 11592–11600.

(53) Xiao, T.; Tang, Y.; Jia, Z.; Li, D.; Hu, X.; Li, B.; Luo, L. Self-Assembled 3D Flower-like Ni^{2+}–Fe^{3+} Layered Double Hydroxides and Their Calcined Products. *Nanotechnology* **2009**, *20*, 475603.

(54) Fang, J.; Li, M.; Li, Q.; Zhang, W.; Shou, Q.; Liu, F.; Zhang, X.; Cheng, J. Microwave-Assisted Synthesis of CoAl-Layered Double Hydroxide/Graphene Oxide Composite and Its Application in Supercapacitors. *Electrochim. Acta* **2012**, *85*, 248–255.

(55) Sun, H.; Chu, Z.; Hong, D.; Zhang, G.; Xie, Y.; Li, L.; Shi, K. Three-Dimensional Hierarchical Flower-like Mg–Al-Layered Double Hydroxides: Fabrication, Characterization and Enhanced Sensing Properties to NO_x at Room Temperature. *J. Alloys Compd.* **2016**, *658*, 561–568.

(56) Abellán, G.; Coronado, E.; Martí-Gastaldo, C.; Ribera, A.; Jordá, J. L.; García, H. Photo-Switching in a Hybrid Material Made of Magnetic Layered Double Hydroxides Intercalated with Azobenzene Molecules. *Adv. Mater.* **2014**, *26*, 4156–4162.

(57) Hobbs, C.; Jaskaniec, S.; McCarthy, E. K.; Downing, C.; Opelt, K.; Güth, K.; Shmeliov, A.; Mourad, M. C. D.; Mandel, K.; Nicolosi, V. Structural Transformation of Layered Double Hydroxides: An in Situ TEM Analysis. *Npj 2D Mater. Appl.* **2018**, *2*, 4.

(58) Ni, B.; Wang, X. Edge Overgrowth of Spiral Bimetallic Hydroxides Ultrathin-Nanosheets for Water Oxidation. *Chem. Sci.* **2015**, *6*, 3572–3576.

(59) Abellán, G.; Carrasco, J. A.; Coronado, E.; Romero, J.; Varela, M. Alkoxide-Intercalated CoFe-Layered Double Hydroxides as Precursors of Colloidal Nanosheet Suspensions: Structural, Magnetic and Electrochemical Properties. *J. Mater. Chem. C* **2014**, *2*, 3723–3731.

Chapter 2:

Magnetism in Layered Double Hydroxides

2.1. Introduction.

One of the main features of LDH materials is their potential interest as magnetic materials, supported by the fact that this magnetic behaviour is retained after exfoliation procedures, therefore acting as macromolecular magnetic building blocks. The magnetic properties of LDHs as well as their hybrids are determined by two main contributions: the in-plane (intralayer) magnetic superexchange between metallic centres through the hydroxo bridges across the cationic sheets, and the weaker inter-plane (interlayer) dipolar interactions.[1] **Fig. 2.1** displays a schematic illustration of a LDH highlighting these contributions.

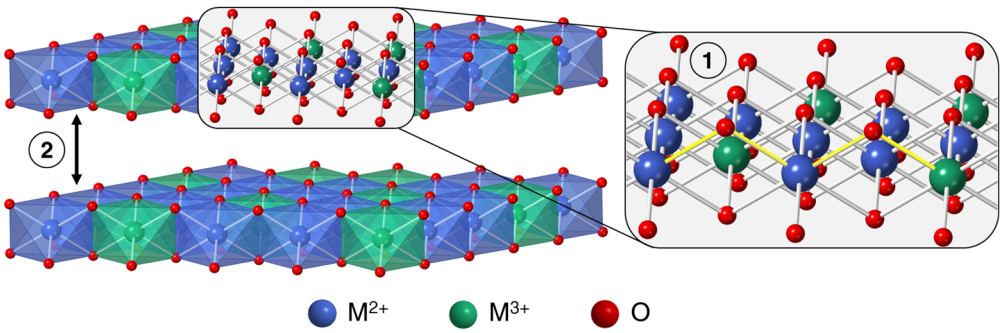

Figure 2.1. Schematic illustration of a LDH system with M^{2+}/M^{3+} ratio of 2:1, highlighting the two magnetic contributions in these materials: The intralayer superexchange reactions between metallic centres mediated hydroxo bridges (1) and the less intense interlayer dipolar interactions (2). A couple of superexchange interactions are highlighted as a visual guide.

Even though this promising feature, there are barely reports in the literature focusing on the magnetic properties of LDH materials, which are usually set aside as precursors for metal oxides since their thermal decomposition gives rise to the formation of mixed metal oxides with high surface area and metal dispersion, depicting catalytic activity.[2–7]

Traditionally, the magnetic properties of LDHs are studied by using magnetometric and calorimetric procedures. On one hand, one can analyse the static susceptibility measurements (direct current, DC) to unveil the nature and strength of the magnetic interactions. On the other hand, dynamic measurements (alternate current, AC) are needed in order to acquire information on the presence

of net spontaneous magnetization at low temperatures, linked to the appearance of an out-of-phase signal below an ordering temperature (temperature for the onset of the spontaneous magnetization, T_M). From the out-of-phase signal, we can confirm the frequency dependence by the Mydosh parameter (ϕ) in order to estimate the glassy behaviour of the system.[8,9] Finally, heat capacity measurements are useful to corroborate the origin of the spontaneous magnetization distinguishing between real magnetic ordering and other magnetic anomalies.

The first exhaustive study on the magnetism of LDHs dates from 2002 by the group of Coronado *et al.*[3] In this work, three different LDHs of CoAl-, NiAl-, and MgAl- were synthesized in a metallic ratio M^{2+}/M^{3+} of 3:1 being characterized *via* DC and AC magnetic susceptibility measurements. It was observed that CoAl- and NiAl-LDHs exhibited spontaneous magnetization at low temperatures due to the ferromagnetic coupling between M^{2+} cations across the layers. The superexchange mechanism occurs between neighbouring edge-sharing octahedra (as highlighted in **Fig. 2.2**). The M^{2+}–OH–M^{2+} angle for these LDHs is close to 90º, hence leading to the orthogonality of the M^{2+} magnetic orbitals, resulting in a weak coupling of ferromagnetic nature between the high-spin metallic centres (Co^{2+}, d^7, S = 3/2 and Ni^{2+}, d^8, S = 1), responsible for the low temperature magnetic nature.[10,11] Diamagnetic Al^{3+} cations do not show magnetic behaviour due to the absence of unpaired electrons. By replacing Al^{3+} ions with paramagnetic transition-metal cations such as Fe^{3+} or Cr^{3+} an overall ferrimagnetic behaviour takes place as a consequence of the addition of antiferromagnetic M^{2+}–OH–M^{3+} and M^{3+}–OH–M^{3+} coupled pairs to the previous M^{2+}–OH–M^{2+} ferromagnetic pairs. This antiferromagnetism comes from the overlapping between nonorthogonal magnetic orbitals such as M^{2+} e_g and M^{3+} t_{2g}. Moreover, the pressure of competing magnetic interactions throughout the layers leads to the appearance of a glassy behaviour.[12–15] This magnetic behaviour is also related with M^{3+} cation clustering, which favours the in-plane spin frustration.[1] In addition to the intralayer interactions, weaker dipolar interactions occur between the layers, presumably dependent on the interlayer distance between the cationic sheets, when innocent interlayer anions are used.[16–18] Remarkably, in the development of this chapter, we describe that interlayer distance does not play a crucial role in the dipolar interactions which affect the overall

magnetism. On the contrary, the parameter that governs the interlayer interactions is the layer size (domain size in the limit case).[19–21] For nanosized CoFe- and NiFe-LDHs,[20,21] we observed superparamagnetic size effects and spin glass-like behaviour, with temperatures for the onset of the spontaneous magnetization that are lower than that observed for some LDHs synthesized by means of most typical ammonium releasing reagent methods.[14] Comparing the ordering temperature of a nanosized NiFe-LDH (*ca.* 35 nm) with the observed for a typical NiFe-LDH synthesized by a hydrothermal approach[1] (platelet size of *ca.* 900 – 1700 nm), we estimated values of 7.8 K and 16.8 K, respectively, in good agreement with the expected for size effects and in line with spin glass-like materials, according to the Mydosh parameter.[8]

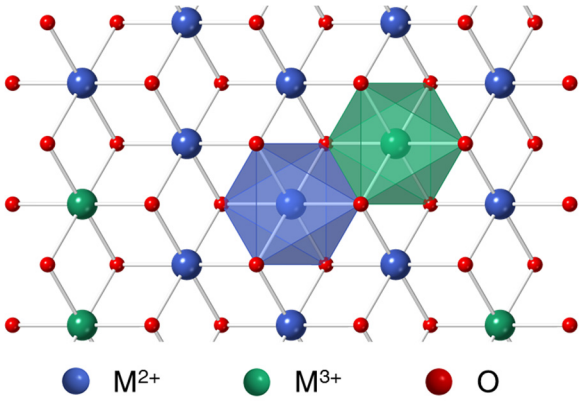

Figure 2.2. LDH layer from above, depicting the neighbouring edge-sharing octahedral. The coordination environment of two metals is highlighted as a visual guide.

Regarding the insertion of magnetic anions such as metallic oxalates,[22] phtalocyanines[23] or Co^{2+}-tetraphenylprophirine complexes[24] in the interlayer space, it has also been studied with both nonmagnetic and magnetic LDHs.[22,23,25–27] In the first case, no major effects on the magnetic behaviour were observed due to the absence of magnetic properties in the LDH system. In the second case, the main magnetic properties are inherited from the LDH host, whereas the intercalated anion may affect the overall magnetism.[18] Stimuli-responsive molecules can also be exchanged, resulting in a change in the assembly of the layers (like the displacement effect induced by a thermoresponsive molecule)[17]. Nevertheless, magnetic

behaviour of the LDH hybrid does not suffer extreme deviations from the pristine LDH host.

Finally, we have recently demonstrated that morphology can affect the overall magnetism of a LDH material.[28] By the careful control of the experimental parameters during the synthetic procedure, LDHs can adopt more exotic morphologies such as dahlia flowers,[29] cones,[30] or even spirals,[31] among others. It was observed that the distortion of the layers in the flower morphology led to a more disordered magnetic behaviour, with higher ordering temperature or saturation magnetization, as well as a marked spin glass-like character.[28]

2.2. Summary of the most important results.

The key point relies in the understanding and analysis of three different parameters that can affect the global magnetism of a LDH system. Firstly, the magnetic impurities that can mislead in the intrinsic magnetic behaviour of the LDHs. Secondly, the importance of the morphology and how is able to affect the magnetic behaviour giving rise to a more disordered material from the magnetic point of view, and finally, the effect of the interlayer distance on the dipolar interactions of the system. Three systems are described and studied in the articles here presented: NiFe-LDH with Ni^{2+}/Fe^{3+} ratio of 2:1, a CoFe-LDH with Co^{2+}/Fe^{3+} ratio of 3:1 and CoAl-LDH with Co^{2+}/Al^{3+} ratio of 2:1. Their schematic structures are depicted in **Fig. 2.3**.

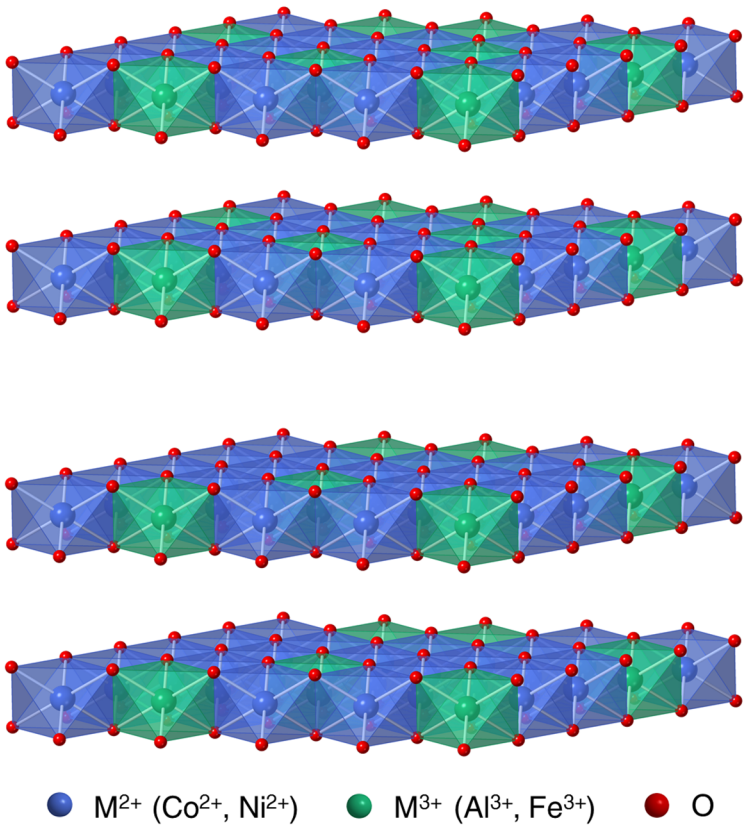

Figure 2.3. Schematic illustration of a general LDH with M^{2+}/M^{3+} ratio of 2:1 (top) and 3:1 (bottom).

In spite of the presence of LDHs with magnetic response at low temperatures, no room temperature magnetic LDHs have been ever reported to date in literature, being no examples of spontaneous magnetization above 20 K. However, some authors claimed the synthesis of iron-containing LDHs that behave as magnets at room temperature.[32,33] A thorough synthetic study allowed us to found out that this room temperature magnetism came from extrinsic sources, such as spinel or iron oxide nanoparticles, that is, impurities that are formed during the synthesis.[34] In stark contrast, by controlling the experimental parameters in order to achieve pure LDH phases, no room temperature magnetic behaviour is observed. The synthesis of non-Al^{3+}-based LDHs (like NiFe- or CoFe-LDHs) is very disfavoured by means of the most typical homogeneous precipitation method used for the Al^{3+}-containing counterparts due to the absence of amphoteric behaviour in transition-metal cations such as Fe^{3+}. To overcome this problem, one can use different strategies such as the addition of chelating agents or a topochemical approach. Otherwise, the synthesis of iron-based LDHs usually leads to the presence of amorphous phases such as ferrihydrite (FeOOH) or iron oxide nanoparticles (maghemite or magnetite, Fe_2O_3 or Fe_3O_4, respectively). In the case of CoFe-LDHs, the typical coprecipitation method leads also to the partial oxidation of Co^{2+} to Co^{3+}, hence giving rise to spinel impurities in form of $Co^{2+}Co^{3+}{}_2O_4$, $Co^{2+}Fe^{3+}{}_3O_4$ or $Co^{2+}Co^{3+}Fe^{3+}O_4$, exhibiting room temperature magnetism. These impurities may be undetectable *via* XRD if they are in low amount, although can be detected by techniques such as HRTEM. However, the decorated LDHs with those nano impurities retain most of their chemical properties. Magnetic characterization becomes the crucial divergent point between pure and impure phases. Impure samples are attracted to a magnet and both direct current (DC) and alternate current (AC) are sensitive to those impurities. As an example, hysteresis curves for pure samples do show neither coercive field nor remanent magnetization above the critical temperature, whereas impure phases do.

Morphology in LDHs also plays a determinant role in the overall magnetism of the system.[28] As reported previously in the literature, the flexible nature of LDHs allows the synthesis of these materials in different morphologies others than the most typical hexagonal one,[35] such as cones,[30] spirals[31] or dahlia flowers.[29] Nevertheless, it was not reported how the change in morphology can affect the overall magnetism

of the material. By means of a hydrothermal approach, we were able to synthesize NiFe- and CoAl-LDHs with M^{2+}/M^{3+} ratio of 2:1 in two different morphologies: the hexagonal and the dahlia flower. **Fig. 2.4** displays a schematic illustration of the two samples alongside with some electron microscopy images (FESEM and HRTEM), highlighting the ordered nature of the hexagonal sample in contrast with the disordered flower-like sample.

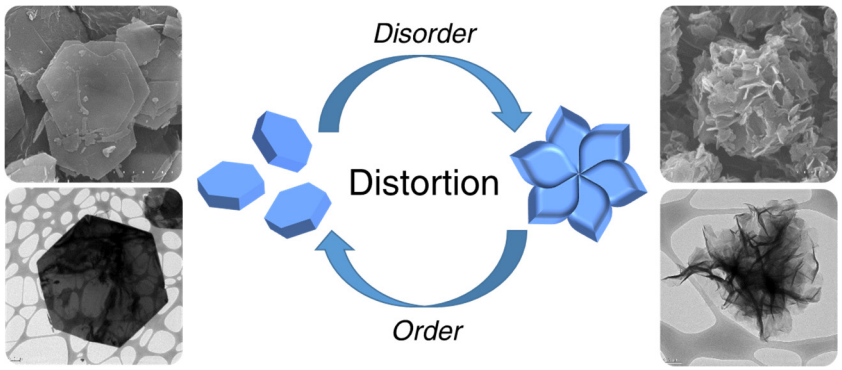

Figure 2.4. Scheme with the hexagonal and dahlia flower morphologies supported by FESEM and HRTEM images.

While some of the characterization techniques do not show major differences between the two morphologies (although variations, such as an increase in the surface area or broader diffractograms for the flower samples, were observed), the magnetism of the system was deeply affected by the increased distortion of the layers. These results were noticed regardless the metallic composition of the LDH. Compared to the hexagonal samples, Weiss constant depicted a stronger anfiferromagnetic behaviour for the flower samples, with a saturation magnetization being *ca.* 50% higher. This increment is related with the increase in the paramagnetic contribution of non-compensated spins, as a consequence of the pronounced disorder of the system. Regarding AC measurements, we found an increase of the temperature for the onset of the spontaneous magnetization (defined as the point where the out-of-phase signal becomes different to zero, $\chi'' \neq 0$, and acts as a guide for the magnetic transition of the system) of *ca.* 3 and 1 K for CoAl- and NiFe-LDH samples, respectively. In addition, Mydosh parameter for flower samples were lower than those calculated for the hexagonal materials, hence pointing out to a more

disordered behaviour of the system, which is close to that of canonical spin glasses.[8] Finally, the fitting of the out-of-phase signal to an Arrhenius law displayed higher activation energies for the flower samples, in good agreement with the spin glass type behaviour. All these results indicate that the distortion of the layers induces a magnetically more disordered behaviour.

The last factor to be studied was the influence of the interlayer distance on the dipolar interactions that occur between magnetic layers, and the role exerted by those interactions in their overall magnetic behaviour.[36] In this context, a family of highly crystalline and hexagonal-shaped CoAl-LDHs (keeping intact the Co^{2+}/Al^{3+} ratio of 2:1) with increasing basal space was synthesized by means of anion exchange reactions with different surfactants starting from the pristine carbonate material. **Fig. 2.5** displays a schematic illustration depicting the increase in the interlayer distance after the successive anion exchange reactions. Basal spaces ranging from 7.5 to 34 Å for the smallest (carbonate) to the largest (octadecyl sodium sulfate) intercalated molecule, respectively, were confirmed *via* XRPD measurements.

Followed by a complete characterization *via* XRPD, FTIR, TGA and electron microscopy, where we unequivocally confirmed the successful synthesis of all samples with the corresponding interlayer anion, an exhaustive magnetic analysis was carried out on the CoAl-LDH family. Due to the strong radial dependence of dipole-dipole interaction, we could expect that dipolar interactions are intrinsically dependent on the distance between the cationic sheets. Hence, an increase in the interlayer space should affect the overall magnetism of the system. Nevertheless, there are different parameters that also affect the magnetism of a LDH, such as particle size, flexibility (as seen before) or cation clustering. Regarding the interlayer magnetic contribution, only dipolar interactions should modulate the interlayer interactions, due to the absence of covalent connection between layers. Interestingly, what we observed with the experimental magnetic data was a puzzling situation in which a systematically increase in the interlayer spacing does not afford a clear dependence of the magnetic behaviour, except for the coercive field, which increases with the interlayer distance. In order to support these results, we complemented them with a theoretical approach. The qualitative revelations of this

study were that the factor governing dipolar interactions between the layers is the layer size and, in the limit case, the domain size. Only for tiny domain sizes (or high cation disorder), the interlayer distance played a dominant role. In addition, for single-domain layers, the sign of the dipolar magnetic coupling was independent of the interlayer distance, which may change for multi-domain layers. Finally, in order to further validate our results, we synthesized nanometric alkoxide-intercalated CoAl-LDH by following a methanolic route in the form of CoAl-OMe (methoxide).[20,37] In this sample we found the highest coercive field (80 Oe) and temperature for the onset of the spontaneous magnetization (8.3 K) found in the CoAl-LDH family here reported, suggesting a much more intense influence of the dipolar interactions, as expected in comparison with their micrometric counterparts. For LDHs with two magnetic metals (such as NiFe- or CoNi-LDHs) we should expect a bigger influence of the dipolar interactions due to the competing magnetic interactions, smaller correlation domains or spin frustration.[1,13,18,24]

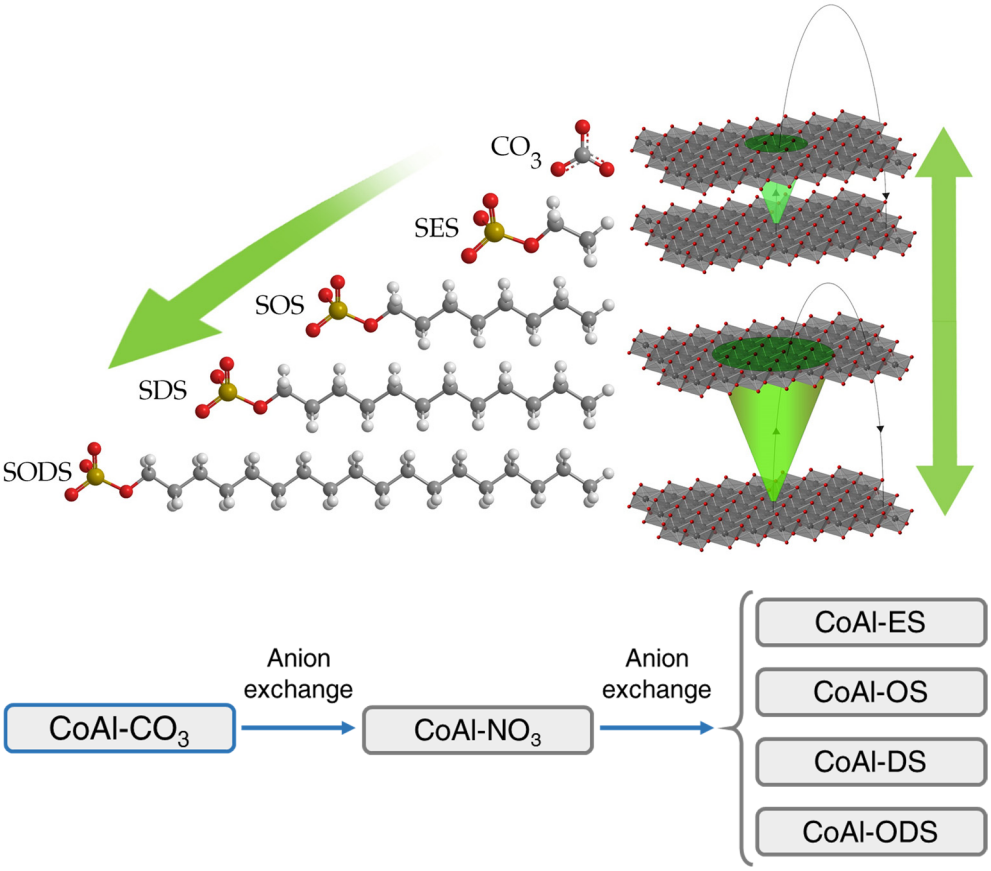

Figure 2.5. Schematic view of the increase in the interlayer distance of a LDH material by enlarging the interlayer anion of the system. The green flashlight indicates ferromagnetic coupling between metals of each layer (top). Synthetic pathway scheme for the synthesis of the surfactant-intercalated samples, starting from the carbonate material and using nitrate-LDH as intermediate, all based in anion exchange reactions (bottom). SES stands for sodium ethyl sulfate, SOS for sodium octyl sulfate, SDS for sodium dodecyl sulfate and SODS for sodium octadecyl sulfate.

2.3. Contribution of the author.

2.3.1. Article 1: "*Room Temperature Magnetism in Layered Double Hydroxides due to Magnetic Nanoparticles.*"

The main contribution of this communication was to highlight the care that must be taken during the synthesis of an iron-containing LDH phase in order to avoid the generation of magnetic impurities (in the form of spinel and iron oxide nanoparticles) that can lead to wrong claims in the assignment of room temperature spontaneous magnetization to a LDH material. With the synthesis of NiFe- and CoFe-LDHs both as pure and impure phase (in presence of room temperature magnetic impurities), we carefully analyse the impact in the overall magnetism that these impurities have.

The author synthesized all samples, contributed in the experimental characterization and collaborated in the writing of the paper.

2.3.2. Article 2: "*Influence of Morphology in the Magnetic Properties of Layered Double Hydroxides.*"

In this paper, we studied for the very first time the effect of morphology in the magnetic behaviour of LDHs. Thanks to the flexible nature of LDHs, one can modulate their morphology from the most typical hexagonal shape to more exotic forms by controlling the synthetic parameters. Two different families of LDHs (CoAl- and NiFe-) were synthesized by means of a hydrothermal approach in two distinct morphologies: the hexagonal and the flower-like one. We found that the distortion of the layers of the flower-like samples induced a magnetically more disordered behaviour of the LDH, reflected in lower coercive field and higher ordering temperature, activation energy or saturation magnetization. This effect is independent of the metallic composition of the LDH.

The author synthesized and characterised all samples, performed the discussion of the results and wrote the paper supervised by the other authors.

2.3.3. Article 3: "*Deciphering the Role of Dipolar Interactions in Magnetic Layered Double Hydroxides*."

The most relevant contribution of this article to the literature was the study of the role exerted by the dipolar interactions in the overall magnetism of a LDH material, which has not been reported before. An in-depth study based on increasing the basal space of surfactant-intercalated CoAl-LDHs revealed that the interlayer distance had a very weak influence on the magnetism of a LDH, in stark contrast to what is expected from a naïve point of view. However, by combining the experimental data with theoretical models, it was observed that the main factor that governs the dipolar interaction between the layers is the lateral dimension of the layers (related with the domain size), therefore becoming a crucial point in the design of magnetic LDHs.

The author synthesized, characterised and discussed the results of all samples from the experimental point of view. Theoretical approach was performed by other authors. The author wrote the paper in collaboration with the other authors.

2.4. References.

(1) Abellán, G.; Coronado, E.; Martí-Gastaldo, C.; Waerenborgh, J.; Ribera, A. Interplay between Chemical Composition and Cation Ordering in the Magnetism of Ni/Fe Layered Double Hydroxides. *Inorg. Chem.* **2013**, *52*, 10147–10157.

(2) Abellán, G.; Carrasco, J. A.; Coronado, E.; Prieto-Ruiz, J. P.; Prima-García, H. In-Situ Growth of Ultrathin Films of NiFe-LDHs: Towards a Hierarchical Synthesis of Bamboo-Like Carbon Nanotubes. *Adv. Mater. Interfaces* **2014**, *1*, 1400184.

(3) Pérez-Ramírez, J.; Ribera, A.; Kapteijn, F.; Coronado, E.; Gómez-García, C. J. Magnetic Properties of Co-Al, Ni-Al, and Mg-Al Hydrotalcites and the Oxides Formed upon Their Thermal Decomposition. *J. Mater. Chem.* **2002**, *12*, 2370–2375.

(4) Abellán, G.; Coronado, E.; Martí-Gastaldo, C.; Ribera, A.; Sánchez-Royo, J. F. Layered Double Hydroxide (LDH)–organic Hybrids as Precursors for Low-Temperature Chemical Synthesis of Carbon Nanoforms. *Chem. Sci.* **2012**, *3*, 1481–1485.

(5) Li, F.; Liu, J.; Evans, D. G.; Duan, X. Stoichiometric Synthesis of Pure MFe_2O_4 (M = Mg, Co, and Ni) Spinel Ferrites from Tailored Layered Double Hydroxide (Hydrotalcite-Like) Precursors. *Chem. Mater.* **2004**, *16*, 1597–1602.

(6) Heredia, A. C.; Oliva, M. I.; Agú, U.; Zandalazini, C. I.; Marchetti, S. G.; Herrero, E. R.; Crivello, M. E. Synthesis, Characterization and Magnetic Behavior of Mg–Fe–Al Mixed Oxides Based on Layered Double Hydroxide. *J. Magn. Magn. Mater.* **2013**, *342*, 38–46.

(7) Agú, U. A.; Oliva, M. I.; Marchetti, S. G.; Heredia, A. C.; Casuscelli, S. G.; Crivello, M. E. Synthesis and Characterization of a Mixture of $CoFe_2O_4$ and $MgFe_2O_4$ from Layered Double Hydroxides: Band Gap Energy and Magnetic Responses. *J. Magn. Magn. Mater.* **2014**, *369*, 249–259.

(8) Mydosh, J. A. *Spin Glasses: An Experimental Introduction*; Taylor & Francis: London ; Washington, DC, 1993.

(9) Mulder, C. A. M.; Van Duyneveldt, A. J.; Mydosh, J. A. Frequency and Field Dependence of the Ac Susceptibility of the Au Mn Spin-Glass. *Phys. Rev. B* **1982**, *25*, 515.

(10) Kahn, O. *Molecular Magnetism*; VCH Publishers: New York, 1993.

(11) Rabu, P.; Drillon, M. Layered Organic–Inorganic Materials: A Way towards Controllable Magnetism. *Adv. Eng. Mater.* **2003**, *5*, 189–210.

(12) Coey, J. M. D. *Magnetism and Magnetic Materials*; Cambridge University Press: Cambridge, 2010.

(13) Coronado, E.; Galán-Mascarós, J. R.; Martí-Gastaldo, C.; Ribera, A.; Palacios, E.; Castro, M.; Burriel, R. Spontaneous Magnetization in Ni−Al and Ni−Fe Layered Double Hydroxides. *Inorg. Chem.* **2008**, *47*, 9103–9110.

(14) Almansa, J. J.; Coronado, E.; Martí-Gastaldo, C.; Ribera, A. Magnetic Properties of $Ni^{II}Cr^{III}$ Layered Double Hydroxide Materials. *Eur. J. Inorg. Chem.* **2008**, *2008*, 5642–5648.

(15) Intissar, M.; Segni, R.; Payen, C.; Besse, J.-P.; Leroux, F. Trivalent Cation Substitution Effect into Layered Double Hydroxides $Co_2Fe_y\ Al_{1-y}(OH)_6Cl{\cdot}nH_2O$: Study of the Local Order. *J. Solid State Chem.* **2002**, *167*, 508–516.

(16) Abellán, G.; Coronado, E.; Martí-Gastaldo, C.; Ribera, A.; Jordá, J. L.; García, H. Photo-Switching in a Hybrid Material Made of Magnetic Layered Double Hydroxides Intercalated with Azobenzene Molecules. *Adv. Mater.* **2014**, *26*, 4156–4162.

(17) Abellán, G.; Jordá, J. L.; Atienzar, P.; Varela, M.; Jaafar, M.; Gómez-Herrero, J.; Zamora, F.; Ribera, A.; García, H.; Coronado, E. Stimuli-Responsive Hybrid Materials: Breathing in Magnetic Layered Double Hydroxides Induced by a Thermoresponsive Molecule. *Chem Sci* **2015**, *6*, 1949–1958.

(18) Zhang, C.; Tsuboi, T.; Namba, H.; Einaga, Y.; Yamamoto, T. Enhancement of the Coercivity in Co–Ni Layered Double Hydroxides by Increasing Basal Spacing. *Dalton Trans* **2016**, *45*, 13324–13331.

(19) Wang, C. J.; Wu, Y. A.; Jacobs, R. M. J.; Warner, J. H.; Williams, G. R.; O'Hare, D. Reverse Micelle Synthesis of Co−Al LDHs: Control of Particle Size and Magnetic Properties. *Chem. Mater.* **2011**, *23*, 171–180.

(20) Carrasco, J. A.; Romero, J.; Varela, M.; Hauke, F.; Abellán, G.; Hirsch, A.; Coronado, E. Alkoxide-Intercalated NiFe-Layered Double Hydroxides Magnetic Nanosheets as Efficient Water Oxidation Electrocatalysts. *Inorg. Chem. Front.* **2016**, *3*, 478–487.

(21) Abellán, G.; Carrasco, J. A.; Coronado, E.; Romero, J.; Varela, M. Alkoxide-Intercalated CoFe-Layered Double Hydroxides as Precursors of Colloidal Nanosheet Suspensions: Structural, Magnetic and Electrochemical Properties. *J. Mater. Chem. C* **2014**, *2*, 3723–3731.

(22) Coronado, E.; Martí-Gastaldo, C.; Navarro-Moratalla, E.; Ribera, A.; Galán-Mascarós, J. R. Intercalation of Two-Dimensional Oxalate-Bridged Molecule-Based Magnets into Layered Double Hydroxide Hosts. *J. Mater. Chem.* **2010**, *20*, 9476–9483.

(23) Abellán, G.; Busolo, F.; Coronado, E.; Martí-Gastaldo, C.; Ribera, A. Hybrid Magnetic Multilayers by Intercalation of Cu(II) Phthalocyanine in LDH Hosts. *J. Phys. Chem. C* **2012**, *116*, 15756–15764.

(24) Abellán, G.; Coronado, E.; Gómez-García, C. J.; Martí-Gastaldo, C.; Ribera, A. Intercalation of Cobalt(II)-Tetraphenylporphine Tetrasulfonate Complex in Magnetic NiFe-Layered Double Hydroxide. *Polyhedron* **2013**, *52*, 216–221.

(25) Wang, Q.; O'Hare, D. Recent Advances in the Synthesis and Application of Layered Double Hydroxide (LDH) Nanosheets. *Chem. Rev.* **2012**, *112*, 4124–4155.

(26) Coronado, E.; Martí-Gastaldo, C.; Navarro-Moratalla, E.; Ribera, A. Intercalation of $[M(Ox)_3]^{3-}$ (M=Cr, Rh) Complexes into $Ni^{II}Fe^{III}$-LDH. *Appl. Clay Sci.* **2010**, *48*, 228–234.

(27) Bourzami, R.; Eyele-Mezui, S.; Delahaye, E.; Drillon, M.; Rabu, P.; Parizel, N.; Choua, S.; Turek, P.; Rogez, G. New Metal Phthalocyanines/Metal Simple Hydroxide Multilayers: Experimental Evidence of Dipolar Field-Driven Magnetic Behavior. *Inorg. Chem.* **2014**, *53*, 1184–1194.

(28) Carrasco, J. A.; Abellán, G.; Coronado, E. Influence of Morphology in the Magnetic Properties of Layered Double Hydroxides. *J. Mater. Chem. C* **2018**, *6*, 1187–1198.

(29) Xiao, T.; Tang, Y.; Jia, Z.; Li, D.; Hu, X.; Li, B.; Luo, L. Self-Assembled 3D Flower-like Ni^{2+}–Fe^{3+} Layered Double Hydroxides and Their Calcined Products. *Nanotechnology* **2009**, *20*, 475603.

(30) Liu, X.; Ma, R.; Bando, Y.; Sasaki, T. A General Strategy to Layered Transition-Metal Hydroxide Nanocones: Tuning the Composition for High Electrochemical Performance. *Adv. Mater.* **2012**, *24*, 2148–2153.

(31) Ni, B.; Wang, X. Edge Overgrowth of Spiral Bimetallic Hydroxides Ultrathin-Nanosheets for Water Oxidation. *Chem. Sci.* **2015**, *6*, 3572–3576.

(32) Shao, M.; Xu, X.; Han, J.; Zhao, J.; Shi, W.; Kong, X.; Wei, M.; Evans, D. G.; Duan, X. Magnetic-Field-Assisted Assembly of Layered Double Hydroxide/Metal Porphyrin Ultrathin Films and Their Application for Glucose Sensors. *Langmuir* **2011**, *27*, 8233–8240.

(33) Dou, Y.; Liu, X.; Shao, M.; Han, J.; Wei, M. Flexible and Transparent Free-Standing Films with Enhanced Magnetic and Luminescent Anisotropy. *J. Mater. Chem. A* **2013**, *1*, 4786–4792.

(34) Abellán, G.; Carrasco, J. A.; Coronado, E. Room Temperature Magnetism in Layered Double Hydroxides Due to Magnetic Nanoparticles. *Inorg. Chem.* **2013**, *52*, 7828–7830.

(35) Liu, Z.; Ma, R.; Osada, M.; Iyi, N.; Ebina, Y.; Takada, K.; Sasaki, T. Synthesis, Anion Exchange, and Delamination of Co−Al Layered Double Hydroxide: Assembly of the Exfoliated Nanosheet/Polyanion Composite Films and Magneto-Optical Studies. *J. Am. Chem. Soc.* **2006**, *128*, 4872–4880.

(36) Carrasco, J. A.; Cardona-Serra, S.; Clemente-Juan, J. M.; Gaita-Ariño, A.; Abellán, G.; Coronado, E. Deciphering the Role of Dipolar Interactions in Magnetic Layered Double Hydroxides. *Inorg. Chem.* **2018**, *57*, 2013–2022.

(37) Gursky, J. A.; Blough, S. D.; Luna, C.; Gomez, C.; Luevano, A. N.; Gardner, E. A. Particle−Particle Interactions between Layered Double Hydroxide Nanoparticles. *J. Am. Chem. Soc.* **2006**, *128*, 8376–8377.

Article 1:

Room Temperature Magnetism in Layered Double Hydroxides due to Magnetic Nanoparticles

Inorganic Chemistry **2013**, *52*, 7828–7830

Inorganic Chemistry

Communication

pubs.acs.org/IC

Room Temperature Magnetism in Layered Double Hydroxides due to Magnetic Nanoparticles

Gonzalo Abellán, Jose A. Carrasco, and Eugenio Coronado*

Instituto de Ciencia Molecular (ICMol), Universidad de Valencia, c/Catedrático José Beltrán, 2, 46980 Paterna, Spain

Supporting Information

ABSTRACT: Some recent reports claiming room temperature spontaneous magnetization in layered double hydroxides (LDHs) have been published; however, the reported materials cause serious concern as to whether this cooperative magnetic behavior comes from extrinsic sources, such as spinel iron oxide nanoparticles. The syntheses of crystalline Fe^{3+}-based LDHs with and without impurities have been developed, highlighting the care that must be taken during the synthetic process in order to avoid misidentification of magnetic LDHs.

Numerous reports claiming ferromagnetic behavior exceeding room temperature in organic and metal−organic molecular magnets exist. However, for the most part, the source of magnetism is of extrinsic origin. A typical case is that of pure organic materials in which magnetism is often caused by the presence of metals, like iron, or metal oxide impurities.[1] The issue of intrinsic versus extrinsic sources of magnetism has also been pointed out more recently in some claims about room temperature magnetism in metal−organic Ni-TCNE charge-transfer salts.[2]

In the case of pure inorganic materials, this issue can also be present, although the intrinsic cooperative magnetism arising from the interacting metals often overcomes the extrinsic magnetism coming from impurities. Still, when intrinsic cooperative magnetism occurs at low temperatures, the presence of magnetic impurities can be dominant at high temperatures, thus leading to wrong claims. An illustrative example in this context is provided by the magnetic layered double hydroxides (LDHs), as we will show in this paper.

LDHs are a family of layered materials traditionally used in fields of utmost importance such as catalysis, absorbents, medicine, or industrial applications.[3] The structure of these anionic clays is related to that of the brucite, in which the partial substitution of divalent cations leads to an excess of positive charge, compensated for by the presence of interlamellar anions. The typical formula for these materials is $[M^{II}_{1-x}M^{III}_{x}(OH)_2]^{x+}(A^{n-})_{x/n}\cdot yH_2O$, thus offering the possibility of a wide tuning of the chemical composition.

Recently, these layered systems have been postulated both as functional hosts and as building blocks for the preparation of organic−inorganic hybrid magnetic materials.[4] In this sense, the introduction of magnetic metal cations within the layers can lead to ferro- or ferrimagnetic behavior, operating through superexchange interactions mediated by hydroxo bridges, in addition to the less intense dipolar interactions operating through the space between the magnetic layers. These magnetic properties are inherently designed to be manifested at low temperatures because of the low intensity of the involved exchange interactions. In fact, as a result of the structural features of these layers (MO_6 octahedra sharing edges), the M−O−M superexchange path is always close to orthogonality, leading to weak exchange interactions.[5]

Surprisingly, Wei and co-workers recently claimed in several works that iron-containing LDHs behave as magnets at room temperature.[6] In fact, they found that highly crystalline colloidal LDH suspensions obtained after the coprecipitation of nickel, cobalt, and iron nitrate or chloride salts, followed by a hydrothermal treatment at moderate temperatures, led to the synthesis of NiFe- or CoFe-LDHs, which were attracted by a conventional laboratory magnet. Although their applications as sensors are very appealing, this room temperature spontaneous magnetization is due to magnetic impurities, as we will demonstrate in this work.

Generally, the synthesis of highly crystalline non-Al^{3+}-based LDHs is very disfavored via a homogeneous precipitation route mainly because of the absence of a specific amphoteric behavior in transition-metal cations like Fe^{3+}. Recent work has developed novel synthetic strategies to address these problems, including the use of additional chelating reagents[7] or the smart topochemical approach developed by Sasaki and co-workers.[8] More concretely, the synthesis of iron-based LDHs has usually led to the presence of some amorphous phases like ferrihydrite (FeOOH), or even iron oxide nanoparticles (Fe_2O_3 or Fe_3O_4 maghemite and magnetite, respectively), that exhibit room temperature magnetism (see Figure 1).[8b,9] These impurities sometimes are not detectable through powder X-ray diffraction (PXRD). Thus, it is possible to obtain LDHs maintaining their chemical properties despite being decorated with spinel "nano impurities". As can be observed in Figure 1, highly crystalline NiFe-LDH phases with the highest iron content (i.e., Ni:Fe ratio equal to 2:1) can be prepared following a modified homogeneous precipitation method reported by our group using triethanolamine and urea as chelating and hydrolysis reagents, respectively, at 125 °C over 48 h (section SI-1 in the Supporting Information, SI).[7a,4i] The PXRD pattern shows the typical profile expected for a LDH. It presents sharp intense peaks at low θ values and less intense peaks at higher angular values, with no signature of contaminant phases. Despite the crystallinity exhibited by the apparently pure bulk sample, it is attracted by a conventional laboratory magnet.

Received: April 9, 2013
Published: June 24, 2013

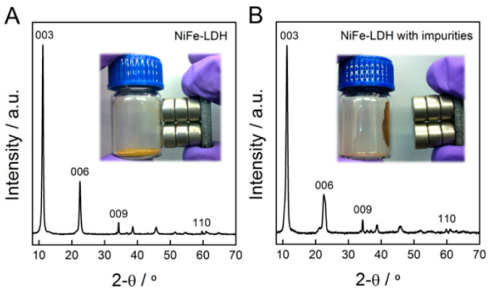

Figure 1. (A) PXRD of a NiFe-LDH (2:1 ratio) without room temperature magnetic impurities. (B) PXRD of a NiFe-LDH exhibiting a similar profile but decorated with nondetectable spinel impurities. The insets show digital photographs of the samples under an external magnetic field.

Sometimes these spinel peaks are seen as very weak signals of small intensity in the PXRD experiments. This can be observed in Figure 2A for samples of NiFe and CoFe prepared by the

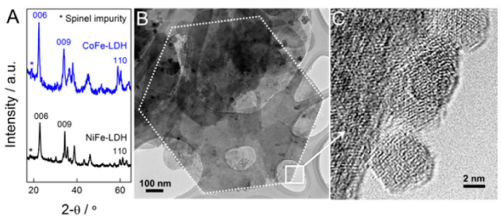

Figure 2. (A) PXRD patterns and peaks indexation of NiFe-LDH and CoFe-LDH at high angles highlighting the spinel impurities. (B) HRTEM image of a hexagonal crystal of the impure NiFe-LDH. (C) Magnified image showing some nanoparticles decorating the LDH surface.

hydrothermal approach (sections SI-1−SI-3 in the SI). In this case, the broad peak at around a 2θ value ranging from 17 to 19° can be detected and is related to the presence of Co and Fe spinel impurities. In addition, a detailed inspection of the crystals through high-resolution transmission electron microscopy (HRTEM) shows the presence of very small nanoparticles of ca. 4 nm on the surface of the NiFe-LDH crystals (Figure 2B,C). Moreover, Rives et al.[10] reported that when CoFe-LDH is synthesized through a traditional coprecipitation method, Co^{II} can become partially oxidized to Co^{III}, being a possible source of spinel impurities (probably $Co^{II}Co^{III}{}_2O_4$, $Co^{II}Fe^{III}{}_2O_4$, or $Co^{II}Co^{III}Fe^{III}O_4$), which also exhibits room temperature magnetic properties (section SI-2 in the SI). In contrast, the nonaqueous method reported by Gardner et al.[11] leads to pure CoFe-LDHs (sections SI-2 and SI-4 in the SI).

These impure LDHs are immediately attracted to a magnet (as previously observed in the inset of Figure 1B). Moreover, the temperature-dependent magnetic susceptibility, χ, of NiFe and CoFe decorated with impurities reported as χT versus T shows an almost linear increase above ca. 25 K, suggesting a partial temperature-independent component that could be ferromagnetic or superparamagnetic in origin (Figure 3).[2b]

The drop observed in both the pure and "decorated" LDH phases in the χT plot below 20 K defining a maximum

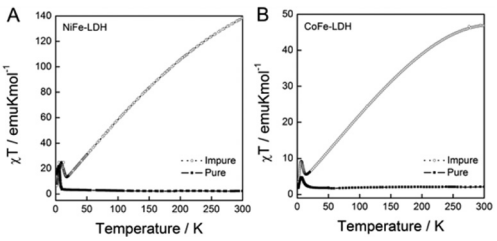

Figure 3. Temperature dependence of the $\chi_M T$ product for (A) impure NiFe-LDH (open symbols) and (B) impure CoFe-LDH. $\chi_M T$ values for pure NiFe- and CoFe-LDHs are shown for comparison (closed symbols).

corresponds to the intrinsic cooperative magnetism in the LDH layers and is accompanied by steep jumps in the χ_M signals.[4] This intrinsic spontaneous magnetization at low temperature is confirmed by alternating-current (ac) dynamic susceptibility measurements (see Figure 4), which show the presence of

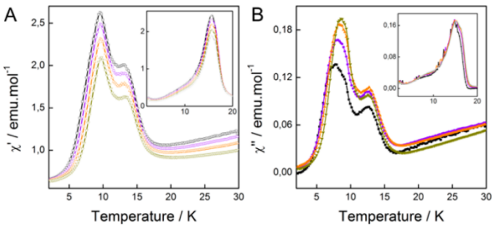

Figure 4. Measurements of ac susceptibility for the NiFe-LDH isolated compounds: (A) in-phase and (B) out-of-phase signals at 10, 100, 1000, and 10000 Hz (black, purple, orange, and green data points, respectively). The inset represents the signals of a pure LDH phase.

defined peaks in both the in-phase (χ_M') and out-of-phase (χ_M'') signals (see the insets in Figure 4).[4] From the position of the χ_M'' signal, one can extract the critical temperature below which the spontaneous magnetization of the LDH material appears. In the case of NiFe, this temperature is about 16 K, while for CoFe, it is ca. 10 K.

These dynamic experiments are strongly sensitive to the presence of magnetic impurities in the samples. In fact, in both NiFe and CoFe, these measurements show a peak at very low temperatures that is frequency-dependent and whose intensity increases with the amount of impurity. This peak is probably due to the presence of very small superparamagnetic nanoparticles anchored to the LDH surface, which undergo superparamagnetic blocking at these low temperatures. In fact, the blocking temperature for Fe_3O_4 nanoparticles of 4 nm in size is close to 8 K.[12] In the examples reported in the present paper (NiFe- and CoFe-LDHs with small intercalate anions such as CO_3^{2-} or NO_3^-), one can notice that this low-T signal only appears when impurities are present. Still, we should remark that, in other pure LDH materials presenting a higher interlamellar space due to the intercalation of bulky anions, a similar frequency-dependent signal has also been observed at this temperature. In these cases, this signal is intrinsic and has been attributed to the movement of the domain walls in the ordered state[4a,b,f,g,i] or even to the presence of metallic disorder within the layers, which can give rise to spin-glass-like behavior or to superparamagnetism coming

dx.doi.org/10.1021/ic400883k | Inorg. Chem. 2013, 52, 7828−7830

from metal clustering within the layers.[4f,i] The conclusion is that not always can this low-T and frequency-dependent χ_M'' signal be taken as proof of the presence of magnetic impurities. Other experiments, such as, for example, the presence of a hysteretic behavior in the magnetization versus field plot, can be more conclusive. In this context, we have plotted the M versus H curves at various temperatures for a pure NiFe-LDH (Figure 5). For the

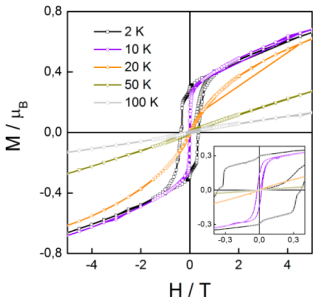

Figure 5. Field-dependent magnetization of pure NiFe-LDH at different temperatures ranging from 2 to 100 K. The inset shows enlarged partial hysteresis curves.

hysteresis cycle measured at 20 K, just above the critical temperature for the onset of the spontaneous magnetization, neither significant coercive field nor remnant magnetization can be measured.

In addition, the M versus H curve for $T > 50$ K does not show any hysteresis, as expected. In turn, the impure sample exhibits hysteretic behavior, even at room temperature, as has already been observed.[6]

In conclusion, attention should be paid to the synthesis and characterization of iron-containing LDHs because of the possibility of having magnetic impurities that can induce wrong claims such as room temperature magnetism in LDHs. To date, there are no examples of spontaneous magnetization in LDHs exceeding ca. 20 K. Having said that, it is worth mentioning that the presence of ferromagnetic or superparamagnetic spinel nanoparticles in these kinds of layered materials could be of interest in the preparation of new hybrids combining the intrinsic properties of LDHs with the room temperature magnetic properties of metal oxide nanoparticles. This possibility opens the door for the use of LDHs as building blocks of new multifunctional materials, taking advantage of the flexibility and chemical versatility of these hosts.

■ ASSOCIATED CONTENT

Supporting Information

Experimental information and additional PXRD patterns. This material is available free of charge via the Internet at http://pubs.acs.org.

■ AUTHOR INFORMATION

Corresponding Author

*E-mail: Eugenio.Coronado@uv.es. Tel: +34 96 354 4415.

Notes

The authors declare no competing financial interest.

■ ACKNOWLEDGMENTS

Financial support from the EU (Projects HINTS and ERC Advanced Grant SPINMOL), the Spanish Ministerio de Economía y Competitividad (Projects Consolider-Ingenio in Molecular Nanoscience, MAT2007-61584 and MAT2011-22785), and the Generalitat Valenciana (Prometeo Program) is gratefully acknowledged. We also acknowledge J. M. Martínez and G. Agustí for magnetic measurements.

■ REFERENCES

(1) (a) Miller, J. S. *Adv. Mater.* **1992**, *4*, 298. (b) Miller, J. S. *Adv. Mater.* **1992**, *6*, 435. (c) Lefebvre, J.; Trudel, S.; Hill, R. H.; Leznoff, D. B. *Chem.—Eur. J.* **2008**, *14*, 7156. (d) Buckelew, A.; Galán-Mascarós, J. R.; Dunbar, K. R. *Adv. Mater.* **2002**, *14*, 1646.

(2) (a) Jain, R.; Kabir, K.; Gilroy, J. B.; Mitchell, K. A. R.; Wong, K.-c.; Hicks, R. G. *Nature* **2007**, *445*, 291. (b) Miller, J. S.; Pokhodnya, K. I. *J. Mater. Chem.* **2007**, *17*, 3585.

(3) (a) Cavani, F.; Trifiro, F.; Vaccari, A. *Catal. Today* **1991**, *11*, 173. (b) Forano, C.; Hibino, T.; Leroux, F.; Taviot-Guého, C. *Handbook of Clay Science*; Bergaya, F., Theng, B. K. G., Lagaly, G., Eds.; Elsevier: Amsterdam, The Netherlands, 2006; Vol. *1*, p 1021. (c) Rives, V. *Layered Double Hydroxides: Present and Future*; Nova Science Publishers: New York, 2001.

(4) (a) Coronado, E.; Galán-Mascarós, J. R.; Marti-Gastaldo, C.; Ribera, A.; Palacios, E.; Castro, M.; Burriel, R. *Inorg. Chem.* **2008**, *47*, 9103. (b) Almansa, J. J.; Coronado, E.; Marti-Gastaldo, C.; Ribera, A. *Eur. J. Inorg. Chem.* **2008**, 5642. (c) Trujillano, R.; Holgado, M. J.; Pigazo, F.; Rives, V. *Phys. B* **2006**, *373*, 267. (d) Intissar, M.; Segni, R.; Payen, C.; Besse, J.-P.; Leroux, F. J. *Solid State Chem.* **2002**, *167*, 508. (e) Giovannelli, F.; Zaghrioui, M.; Autret-Lambert, C.; Delorme, F.; Seron, A.; Chartier, T.; Pignon, B. *Mater. Chem. Phys.* **2012**, *137*, 55−60. (f) Wang, C. J.; Wu, Y. A.; Jacobs, R. M. J.; Warner, J. H.; Williams, G. R.; O'Hare, D. *Chem. Mater.* **2011**, *23*, 171. (g) Abellán, G.; Coronado, E.; Gómez-García, C. J.; Martí-Gastaldo, C.; Ribera, A. *Polyhedron* **2013**, *52*, 216. (h) Abellán, G.; Busolo, F.; Coronado, E.; Martí-Gastaldo, C.; Ribera, A. *J. Phys. Chem. C* **2012**, *116*, 15756. (i) Abellán, G.; Coronado, E.; Martí-Gastaldo, C.; Ribera, A.; Waerenboug, J. C., submitted for publication. (j) Abellán, G.; Latorre-Sanchez, M.; Fornes, V.; Ribera, A.; Garcia, H. *Chem. Commun.* **2012**, *48*, 11416. (k) Layrac, G.; Tichit, D.; Larionova, J.; Guari, Y.; Guérin, C. *J. Phys. Chem. C* **2011**, *115*, 3263.

(5) (a) Kahn, O. *Molecular magnetism*; VCH Publishers, Inc.: New York, 1993. (b) Fujita, W.; Awaga, K. *Inorg. Chem.* **1996**, *35*, 1915. (c) Rogez, G.; Massobrio, C.; Rabu, P.; Drillon, M. *Chem. Soc. Rev.* **2011**, *40*, 1031.

(6) (a) Dou, Y.; Liu, X.; Shao, M.; Han, J.; Wei, M. *J. Mater. Chem. A* **2013**, *1*, 4786. (b) Shao, M.; Wei, M.; Evans, D. G.; Duan, X. *Chem. Commun.* **2011**, *47*, 3171. (c) Shao, M.; Xu, X.; Han, J.; Zhao, J.; Shi, W.; Kong, X.; Wei, M.; Evans, D. G.; Duan, X. *Langmuir* **2011**, *27*, 8233.

(7) (a) Abellán, G.; Coronado, E.; Marti-Gastaldo, C.; Pinilla-Cienfuegos, E.; Ribera, A. *J. Mater. Chem.* **2010**, *20*, 7451. (b) Han, Y.; Liu, Z.-H.; Yang, Z.; Wang, Z.; Tang, X.; Wang, T.; Fan, L.; Ooi, K. *Chem. Mater.* **2008**, *20*, 360.

(8) (a) Ma, R.; Liu, Z.; Takada, K.; Iyi, N.; Bando, Y.; Sasaki, T. *J. Am. Chem. Soc.* **2007**, *129*, 5257. (b) Ma, R.; Liang, J.; Takada, K.; Sasaki, T. *J. Am. Chem. Soc.* **2011**, *133*, 613.

(9) Manohara, G. V.; Prasanna, S. V.; Kamath, V. P. *Eur. J. Inorg. Chem.* **2011**, 2624.

(10) del Arco, M.; Trujillano, R.; Rives, V. *J. Mater. Chem.* **1998**, *8*, 761.

(11) (a) Gardner, E.; Huntoon, K. M.; Pinnavaia, T. J. *Adv. Mater.* **2001**, *13*, 1236. (b) Gursky, J. A.; Blough, S. D.; Luna, C.; Gomez, C.; Luevano, A. N.; Gardner, E. *J. Am. Chem. Soc.* **2006**, *128*, 8376.

(12) Park, J.; Lee, E.; Hwang, N.-M.; Kang, M.; Kim, S. C.; Hwang, Y.; Park, J.-G.; Noh, H.-J.; Kim, J.-Y.; Park, J.-H.; Hyeon, T. *Angew. Chem.* **2005**, *117*, 2932.

Supplementary Information

Room Temperature Magnetism in Layered Double Hydroxides Due to Magnetic Nanoparticles

G. Abellán, J. A. Carrasco and E. Coronado*

Instituto de Ciencia Molecular (ICMol), Universidad de Valencia. Catedrático José Beltrán 2, 46890 Paterna, Spain. Fax: +34 96 354 3273. Telf: +34 96 354 4415. E-mail: eugenio.coronado@uv.es.

Contents

SI-1 Synthesis of NiFe-LDHs

All Chemicals $Ni(NO_3)_2 \cdot 6H_2O$, $Fe(NO_3)_3 \cdot 9H_2O$, $NaNO_3$, HNO_3, $C_6H_{15}NO_3$ (triethanolamine, TEA) and $CO(NH_2)_2$ (urea) were used as received without further purification. LDHs were synthesized following a modified homogeneous precipitation method by using urea and TEA as ammonium releasing reagent (ARR) and chelating agent, respectively.

In a typical procedure, the nitrate salts of the metals were dissolved in 50 mL of Milli-Q purged water together with TEA, in order to reach a total metal cation concentration of 20 mM in the final solution, adjusting the stoichiometric coefficient x = Fe/(Ni + Fe) to x = 0.33. The concentration of TEA was equimolar with iron concentration. Then, 50 mL of an aqueous solution of urea (35 mM) were added. The amount of urea was fixed to be 1.75 times the total metal concentration. The resulting dark brown mixture was placed in a 125 mL stainless steel Teflon lined autoclave and heated in an oven. In order to study the effect of the temperature of the hydrothermal step in the purity of the final material, the temperature of the oven was ranged from 125 (pure) to 150 °C (impure). After 48 hours, the autoclave was cooled on a bench to room temperature and the resulting yellowish fine powder was filtered, washed thoroughly with Milli-Q water and dried in a vacuum. The pH value of the remaining solution was found to be around 7.5 – 8.0.

SI-2 Synthesis of CoFe-LDHs

All chemicals $Co(NO_3)_2.6H_2O$, $CoCl_2{\cdot}6H_2O$, $Fe(NO_3)_3.9H_2O$, $FeCl_3{\cdot}6H_2O$, NaOH, Na_2CO_3 and MeOH were used as received without further purification.

CoFe-hydrothermal.

Synthesized following the method described by Wei et al [1].

In a typical procedure, the salts of the metals $CoCl_2{\cdot}6H_2O$ (0.16 M) and $Fe(NO_3)_3.9H_2O$ (0.055 M) were dissolved in 150 mL double-distilled water and the pH was adjusted to 8.0 by using a NaOH solution (1.5 M). The resulting mixture was placed in a 125 mL stainless steel Teflon lined autoclave and heated in an oven and was aged at 130 ^oC for 24 h. After 24 h, the autoclave was cooled on a bench to room temperature and the resulting dark brown fine powder was filtered, washed thoroughly with Milli-Q water and dried in a vacuum. The pH value of the remaining solution was found to be around 8.

CoFe-coprecipitation

Synthesized following the method described by Rives et al [2].

In a typical procedure, the nitrate salts of the metals 0.012 mol $Co(NO_3)_2.6H_2O$ and 0.006 mol of $Fe(NO_3)_3.9H_2O$ were dissolved in 25 mL double-distilled water and then the solution was dropwise added (*ca*. 30 drops min^{-1}) to a solution containing 0.031 mol Na_2CO_3 in 50 ml double-distilled water.

The resulting mixture was stirred at 70 ^oC for 30 h. After that, the light brown fine powder was filtered and dried in a vacuum.

CoFe-alkoxide

Synthesized following the method described by Gardner et al [3,4].

In a typical procedure, the chloride salts of the metals, $CoCl_2{\cdot}6H_2O$ (30 mM) and $FeCl_3{\cdot}6H_2O$ (10 mM), were added into a three-neck flask and then dissolved with 100 mL of methanol, reaching a total metal cation concentration of 40 mM. The solution was stirred and heated at 65 ^oC during 1h. Then, a solution containing 3.8 g of NaOH in 100 mL of MeOH was added to the previous solution and the mixture was left 72 h under stirring at 65 ^oC. After that, the resultant light brown fine powder product was filtered and dried in a vacuum.

SI-3 Physical Characterization

Metallic atomic composition of bulk samples was determined by means of electron probe microanalysis (EPMA) performed in a Philips SEM-XL30 equipped with an EDAX microprobe. NiFe-LDH X-ray powder diffraction patterns were collected with a Siemens d-500 X-ray diffractometer (Cu-Kα radiation; λ_α = 1.5418 Å) equipped with a rotating anode D-max Rigaku operating at 80 mA and 45 kV. Samples were mounted on a flat sample plate. Profiles were collected in the 2.5° < 2θ < 70° range with a step size of 0.05°. CoFe-LDH X-ray powder diffraction patterns were obtained using a Phillips X'Pert-MPD diffractometer provided with a graphite monochromator, operating at 40 kV and 20 mÅ and employing nickel-filtered Cu Kα radiation (λ = 0.1542 nm). Profiles were collected in the 5° < 2θ < 70° range. Carbon, hydrogen and nitrogen contents were determined by microanalytical procedures using an EA 1110 CHNS-O elemental analyzer from CE Instruments. HRTEM studies of the selected samples were carried out on a JEM-2010 microscope (JEOL, Japan) operating at 200 kV. Samples were prepared by dropping a suspension of the sample in ethanol on a carbon-coated copper grid. The digital analysis of the HRTEM micrographs was done using DigitalMicrographTM 1.80.70 for GMS 1.8.0 by Gatan.

Magnetic susceptibility measurements were performed on polycrystalline samples with a Quantum Design (SQUID) Magnetometer MPMS-XL-5. The susceptibility data were corrected by removing the diamagnetic contributions as deduced by using Pascal's constant tables. The *dc* data were collected in the range 2 – 300 K upon decreasing temperatures with an applied field in the range 100 – 5000 G, and hysteresis loops were collected between –5 and +5 T at 2, 10, 20, 50 and 100 K. The *ac* data were collected in the range 2 – 30 K with an applied alternating field of 3.95 G at different frequencies in the range 10 – 10000 Hz with a Quantum Design PPMS-9 equipment.

SI-4 Powder X-ray diffraction patterns of CoFe-LDHs

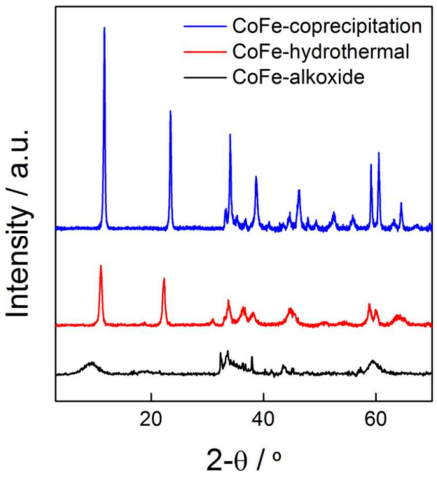

SI-5 References

[1] Shao, M.; Wei, M.; Evans, D.G.; Duan, X. *Chem. Commun.,* **2011**, *47*, 3171 – 3173.

[2] Del Arco, M.; Trujillano, R.; Rives, V. *J. Mater. Chem*., **1998**, *8*, 761–767.

[3] Gursky, J.A.; Blough, S.D.; Luna, C.; Gomez, C.; Luevano, A.N.; Gardner, E. *J. Am. Chem. Soc,* **2006**, *128,* 8376 – 8377.

[4] Gardner, E.; Huntoon, K.M.; Pinnavaia, T.J. *Adv. Mater.,* **2001**, *13*, 1236 – 1266.

Article 2:

Influence of Morphology in the Magnetic Properties of Layered Double Hydroxides

Journal of Materials Chemistry C **2018**, *6*, 1187–1198

Journal of Materials Chemistry C

PAPER

View Article Online
View Journal | View Issue

Cite this: J. Mater. Chem. C, 2018, 6, 1187

Influence of morphology in the magnetic properties of layered double hydroxides†

Jose A. Carrasco,[a] Gonzalo Abellán *[b] and Eugenio Coronado *[a]

Received 4th December 2017,
Accepted 9th January 2018

DOI: 10.1039/c7tc05569b

rsc.li/materials-c

We report the controlled synthesis of magnetic CoAl and NiFe layered double hydroxides (LDHs) endowed with well-defined morphology (hexagonal and flower-like shapes) by means of modified homogeneous precipitation. These layered magnets display high crystallinity and micrometric size, thus offering a perfect scenario for the elucidation of the role exerted by distortion of the layers in their magnetic behaviour. The magnetic properties have been investigated by means of DC and AC magnetic susceptibility measurements and isothermal magnetization, demonstrating that the distortion of the nanosheets induces a magnetically more disordered behaviour, with marked spin-glass nature, independently of the composition of the layers. This is reflected in a more antiferromagnetic character, lower coercive fields, higher values of saturation magnetization and higher activation energies. Moreover, the temperatures for the onset of the spontaneous magnetization of the distorted systems reached the highest values reported so far. This work highlights for the very first time the importance of the morphology on the magnetic behaviour of LDHs and will serve as a guide in the design of new switchable magnetic hybrids.

Introduction

Two dimensional (2D) materials have attracted enormous attention in the last few years. Beyond graphene,[1] other van der Waals layered solids have emerged like for example, layered chalcogenides,[2,3] boron nitride,[4] black phosphorus[5,6] or antimonene,[7,8] expanding the range of physical properties and applications. 2D materials are not limited to neutral systems, in fact other compounds formed by ionic layers like the layered double hydroxides[9] (LDHs) can be exfoliated down to the monolayer limit offering a plethora of interesting properties in energy storage, catalysis, sensing or magnetism, to name a few.[10–14] These layered hosts display a brucite-like structure composed of positively charged sheets consisting of edge shared $M(OH)_6$ octahedra. They exhibit the following general formula: $[M^{II}_{1-x}M^{III}_{x}(OH)_2]^{x+}(A^{n-})_{x/n}\cdot mH_2O$,[11,15] where the two metals can vary in a wide stoichiometry range (usually between $0.20 \leq \chi \leq 0.33$) giving rise to a great variety of isostructural layered systems.[12,16] Moreover, through the rational choice of the transition metals, layered materials with controlled composition can be easily obtained and their magnetic properties can be conveniently tuned by modifying the interlayer distance.[16–18] Indeed, by insertion of functional molecules that respond to light or temperature stimulus, the magnetic properties of LDH can be reversibly switched.[19,20] We have demonstrated that by changing the bonding motif of these molecules (connected through one side or through the two sides to the layers) it is possible to: (i) induce layer distortion, strongly influencing the magnetic properties, or (ii) induce a softer layer sliding with a less acute modification of the magnetism. In the former case this behaviour was ascribed to the interplay between the contraction of the interlayer space (increasing the extent of interlayer antiferromagnetic dipolar interactions), and the modification of the exchange pathways within the layer due to structural distortions.[19] Interestingly, it has been recently demonstrated that LDHs can be synthesized exhibiting permanent distortion within the layers, which results in the formation of LDH crystals endowed with morphologies different from the (most typical) hexagonal one,[15] such as betlike, rodlike,[21] dahlia flowers,[22] cones[23] or even spirals.[24] However, the influence of this distortion in the magnetic properties of pristine LDHs remains unexplored. This remarkable morphological complexity can be accessed thanks to the relatively flexible character of LDHs (which exhibit an interlayer rigidity parameter, $p \sim 5$). In fact, they exhibit much more interlayer rigidity than graphite ($p \sim 2$) and graphene, but much less rigidity than conventional phyllosilicate clays ($p \sim 7$),[25–27] behaving similarly to metal dichalcogenides ($p \sim 3.5$).[28] Among others, the flower-like morphology is particularly interesting because of its marked curved or contoured nanosheets, exhibiting sharp layer distortions, and represents an

[a] Instituto de Ciencia Molecular (ICMol), Universidad de Valencia, Catedrático José Beltrán 2, 46980 Paterna, Valencia, Spain. E-mail: eugenio.coronado@uv.es
[b] Department of Chemistry and Pharmacy and Joint Institute of Advanced Materials and Processes (ZMP), Friedrich-Alexander-Universität Erlangen-Nürnberg, Henkestr. 42, 91054 Erlangen and Dr-Mack Str. 81, 90762 Fürth, Germany. E-mail: gonzalo.abellan@fau.de

† Electronic supplementary information (ESI) available. See DOI: 10.1039/c7tc05569b

excellent candidate for the direct comparison of distorted LDH crystals with conventional strain-free hexagonal-shaped LDHs.

Herein we propose for the very first time a thorough magnetic study of morphologically well-defined micrometric LDHs (hexagonal and flower-like) endowed with the same stoichiometry and interlayer anion, synthesized using a hydrothermal approach, thus offering a perfect scenario for the elucidation of the role exerted by distortion of the layers in their magnetic behaviour.[13,16,29–34] Moreover, the influence of competing magnetic interactions within the layers has been also tackled, comparing ferromagnetic CoAl-LDHs with ferrimagnetic NiFe-LDHs. These studies demonstrated that the distortion of the layers strongly influences the magnetism of LDHs, creating more disordered magnetic systems with increased glassiness, stronger antiferromagnetic (AF) interactions and exhibiting increased critical temperatures and activation energies, as well as lower coercive fields, independently of the chemical composition.

Experimental section

Chemicals

All chemicals $CoCl_2{\cdot}6H_2O$, $AlCl_3{\cdot}6H_2O$, $Ni(NO_3)_2{\cdot}6H_2O$, $Fe(NO_3)_3{\cdot}9H_2O$, $Co(NO_3)_2{\cdot}6H_2O$, $Al(NO_3)_3{\cdot}9H_2O$, $FeCl_2$, triethanolamine (TEA, $C_6H_{15}NO_3$), urea ($CO(NH_2)_2$) and ethylene glycol (EtGly, $C_2H_6O_2$) were purchased and used as-received from Sigma-Aldrich. Ethanol absolute (EtOH) was purchased from Panreac and the formamide (99%) from ACROS organics. Milli-Q water was obtained from a Millipore Milli-Q equipment.

Synthesis

Synthesis of CoAl-LDH (hexagonal morphology). This sample was synthesized following a modification of the method described by Sasaki *et al.*[15] In a typical procedure, 20 mM of $CoCl_2{\cdot}6H_2O$, 10 mM of $AlCl_3{\cdot}6H_2O$ and 70 mM of urea (excess) were dissolved with Milli-Q water in a 125 cm^3 Teflon lined autoclave and the reaction was set at 100 °C for 24 h. Afterwards, the autoclave was cooled down to room temperature and the solid obtained was filtered and washed with H_2O and EtOH several times. pH of the solution was found to be *ca.* 8. After the filtration, the pink sample was dried under vacuum overnight and then grinded and collected as the final product. This sample was labelled as CoAl-H.

Synthesis of CoAl-LDH (flower morphology). This sample was synthesized following a modification of the method described by Huang *et al.*[35] In a typical procedure, 10 mM of $Co(NO_3)_2{\cdot}6H_2O$, 5 mM of $Al(NO_3)_3{\cdot}9H_2O$ and 75 mM of urea (excess) were dissolved in a mixture of EtGly and Milli-Q water (9 : 1 ratio in volume) in a 125 cm^3 Teflon lined autoclave and the reaction was set at 160 °C for 12 h. Afterwards, the autoclave was cooled down to room temperature and the solid obtained was filtered and washed with H_2O and EtOH several times. pH of the solution was found to be *ca.* 8. After the filtration, the pink sample was dried in an oven at 100 °C for 12 h and then grinded and collected as the final product. This sample was labelled as CoAl-F.

Synthesis of NiFe-LDH (hexagonal morphology). This sample was synthesized following the method described by Abellán *et al.*[36] In a typical procedure, 13.33 mM of $Ni(NO_3)_2{\cdot}6H_2O$, 6.67 mM of $Fe(NO_3)_3{\cdot}9H_2O$, 6.67 mM of TEA (equimolar to Fe content) and 35 mM of urea (excess) were dissolved with Milli-Q water in a 125 cm^3 Teflon lined autoclave and the reaction was set at 125 °C for 48 h. Afterwards, the autoclave was cooled down to room temperature and the solid obtained was filtered and washed with H_2O and EtOH several times. pH of the solution was found to be around 8. After the filtration, the yellowish sample was dried under vacuum overnight and then grinded and collected as the final product. This sample was labelled as NiFe-H.

Synthesis of NiFe-LDH (flower morphology). This sample was synthesized following a modification of the method described by Luo *et al.*[22] In a typical procedure, 10 mM of $Ni(NO_3)_2{\cdot}6H_2O$ and 5 mM of $FeCl_2$ were dissolved under bath sonication in 50 mL of a mixture of EtGly and Milli-Q water (3 : 2 ratio in volume). After that, 400 mM of urea (excess) was added followed by stirring during 10–15 min. The resulting solution was poured in a 125 cm^3 Teflon lined autoclave and the reaction was set at 85 °C for 6 h. Afterwards, the autoclave was cool down to room temperature and the solid obtained was filtered and washed with H_2O and EtOH several times. The pH of the solution was found to be *ca.* 8. After the filtration, the yellowish sample was dried in an oven at 50 °C for 12 h and then grinded and collected as the final product. This sample was labelled as NiFe-F.

Physical characterization

X-ray powder diffraction (XRPD) patterns were obtained with a Philips X'Pert diffractometer using the copper radiation (Cu-Kα = 1.54178 Å) in the 2–70° region with a step size of 0.05°. Attenuated total reflectance Fourier transform infrared spectroscopy (ATR-FTIR) were collected in an Agilent Cary 630 FTIR spectrometer in the 4000–650 cm^{-1} range in absence of KBr pellets. Thermogravimetric analysis (TGA) of all samples were carried out in a Mettler Toledo TGA/SDTA 851 apparatus in the 25–800 °C temperature range, using a 5 °C min^{-1} scan rate and an air flow of 100 mL min^{-1}. Nitrogen adsorption/desorption isotherms were collected in an AUTOSORB-6 apparatus. Samples were previously degased at 353 K for 6 h under vacuum with an AUTOSORB DEGASSER. Carbon, nitrogen and hydrogen contents were determined by microanalytical procedures by using a LECO CHNS. Field emission scanning electron microscopy (FESEM) studies were carried out on a Hitachi S-4800 microscope at an accelerating voltage of 20 kV and 30 seconds of Au/Pd metallization of the samples. High resolution transmission electron microscopy (HRTEM) studies were carried out in a Tecnai G^2 F20 operating at 200 kV. The samples were prepared by drop casting of a sonicated sample solution in ethanol on a lacey Formvar/carbon copper grid (300 mesh). Magnetic data were collected over the bulk material with a Quantum Design superconducting quantum interference device (SQUID) MPMS-XL-5. The magnetic susceptibility of the samples was corrected from the diamagnetic contributions of their atomic constituents as deduced from Pascal's constant tables

and the sample holder. The DC data were obtained under an external applied field of 100 or 1000 Oe in the 2–300 K temperature range. Magnetization studies were performed between −5 and +5 T at a constant temperature of 2 K. The AC data were collected under an applied field of 3.95 Oe at 997, 333, 110, 10 and 1 Hz.

Results and discussion

There are different synthetic routes and methodologies for the preparation of LDHs; the most commonly used are: (i) the direct co-precipitation from mixed metal solutions either at constant or variable pH control, (ii) the use of urea as base retardant, (iii) the development of reverse microemulsion, and (iv) the non-aqueous approaches. In overall, these routes provide platelet-like morphologies; nevertheless, the use of surfactants or complexation reagents can induce the formation of LDH crystallites endowed with a great variety of morphologies. Particularly, the ethylene glycol (EtGly) assisted solvothermal method has been proven to be successful in the synthesis of flower-like LDH systems. This is due to the complexation of metal cations by EtGly, which reduces the reaction rate, causing the separation of the nucleation and growth steps, preventing the development of bigger crystallites during the crystallization process.[22,35] Then, probably due to Ostwald ripening, the surface of aggregates becomes smooth, and in order to minimize the surface energy and release the stress, the aggregates split into smaller curved nanosheets. Finally, under external conditions like electrostatic and dipolar fields associated with H-bonds, hydrophobic interactions, crystal-face attraction and van der Waals forces, the curved LDH nanosheets self-assemble into irregular 3D flower-like structures (in short $M^{II}M^{III}$-F). Herein, we adapted these procedures to synthesize flower-like CoAl and NiFe-LDH. Moreover, the hexagonal shaped LDHs (in short $M^{II}M^{III}$-H) have been synthesized by following the same hydrothermal approach, using urea as ammonia releasing reagent (ARR) in the absence of EtGly, which has been proven to be a very efficient route.[15,36] It is worth to remark here that the chosen synthetic protocol may have important implications in the cation ordering of the LDHs, as recently reported by Nielsen and co-workers for ZnAl-LDHs.[37]

The syntheses of the different LDH phases (whose general structure is depicted in Fig. 1a) were confirmed *via* XRPD (Fig. 1b), highlighting the main basal reflections for hydrotalcite-like materials (JCPDS 22-700).[38] All diffractograms recorded exhibited well-defined and intense peaks at low 2θ values. The main (003) basal reflection at around 11° can be ascribed to the presence of carbonate anions in the interlayer space of the LDHs, giving rise to basal spaces values of 7.5, 8.0, 7.6 and 7.6 Å for the CoAl-H, CoAl-F, NiFe-H and NiFe-F LDHs samples, respectively. Alongside with that initial reflection, we can found the characteristic (006), (009), (012), (015) and (018) peaks at *ca.* 23°, 34.3°, 39° and 46.5°, respectively, as well as the doublet (110)–(113) near 60°.[32,36,39] As expected, the hexagonal counterparts (CoAl-H and NiFe-H) are the most crystalline samples attending to the intensity, broadening and definition of the peaks.[15] On the other hand, it is worth noting the fact that the flower-like morphology exhibits broader (00*l*) peaks with lower intensity, indicative of more disorder and fewer stacking layers in these systems. Moreover, the increased broadening of the (*h*0*l*) reflections, as well as the (*hk*0) reflections showing a "shark's fin" line shape, rising sharply and displaying an asymmetry of the high angle side, are a clear indication of increased disorder and the presence of turbostratic structures, which is a first proof of the appearance of distortion in the systems.[11] Moreover, the presence of EtGly in the interlamellar space induces a small shift of *ca.* 0.5° for the (003) peak in the CoAl-F sample. Nevertheless, the observed basal space of *ca.* 8 Å, matches well with that expected for a carbonate sample; in turn, an EtGly-intercalated LDH usually exhibits a basal space of *ca.* 9 Å.[40,41] For the NiFe-F sample, no displacement was observed probably due to the fact that the quantity of EtGly during its synthesis was lower than that of the CoAl-F (EtGly : H_2O ratio of 3 : 2 for NiFe-F *versus* 9 : 1 for CoAl-F). A magnified image of the XRPD can be found in Fig. S1, ESI.† Molecular formula of every sample can be found in Table 1.

ATR-FTIR spectra of the different samples are depicted in Fig. 1c, exhibiting a similar spectrum in each case. The broad peak at 3396 cm^{-1} is ascribed to the stretching vibrations of the OH groups, whereas the peak at 1590 cm^{-1} is related with their bending vibrations due to the presence of water molecules within the layered structure.[38,39] The intense band centred at 1347 cm^{-1} confirmed the presence of carbonate anions in the interlayer space.[16,22] On the other hand, the peak found at 1051 cm^{-1} can be ascribed to C–O stretching vibrations.[32] Finally, in the range of 800–500 cm^{-1} we can find the metallic vibrational bands M–O, M–O–M and O–M–O (M = Co, Al, Ni and Fe).[42,43] As previously mentioned, the presence of some molecules of EtGly in the interlayer space of the CoAl-F LDH can be confirmed from the small shoulder found at 2889 cm^{-1}, related with the stretching vibrations of C–H groups.[40] Along with that, TGA analysis under air atmosphere were also carried out in order to give further information regarding the chemical nature of the intercalated anions in the LDH structure (Fig. 1d and Fig. S2, ESI†).[32] The typical profile of a LDH material exhibits a first weight loss in the 25–220 °C range, related with the elimination of the physisorbed water molecules by the LDH structure (solvation molecules).[39] This loss is *ca.* 8%, 7%, 11% and 9% for CoAl-H, CoAl-F, NiFe-H and NiFe-F samples, respectively. The following and most intense weight loss is the one observed between 220–600 °C, which matches with the overlapping between the dehydroxylation of the layered system, the elimination of the chemisorbed water and the decomposition of CO_3^{2-} to CO_2.[22] Moreover, for the flower-like samples CoAl-F and NiFe-F the second step also includes the decomposition of the trapped EtGly molecules,[40] which results in a final weight loss for these samples that is slightly higher (4%) than that observed for the hexagonal counterparts.

Finally, N_2 adsorption–desorption isotherms were also measured in order to investigate the effect of the different morphologies in the surface area of the LDHs (Fig. 1e and Fig. S3, ESI†). All isotherms can be classified as type IV,[35] exhibiting a surface BET area of *ca.* 51, 54, 88 and 90 $m^2\ g^{-1}$ for CoAl-H, CoAl-F, NiFe-H and NiFe-F, respectively. In view of

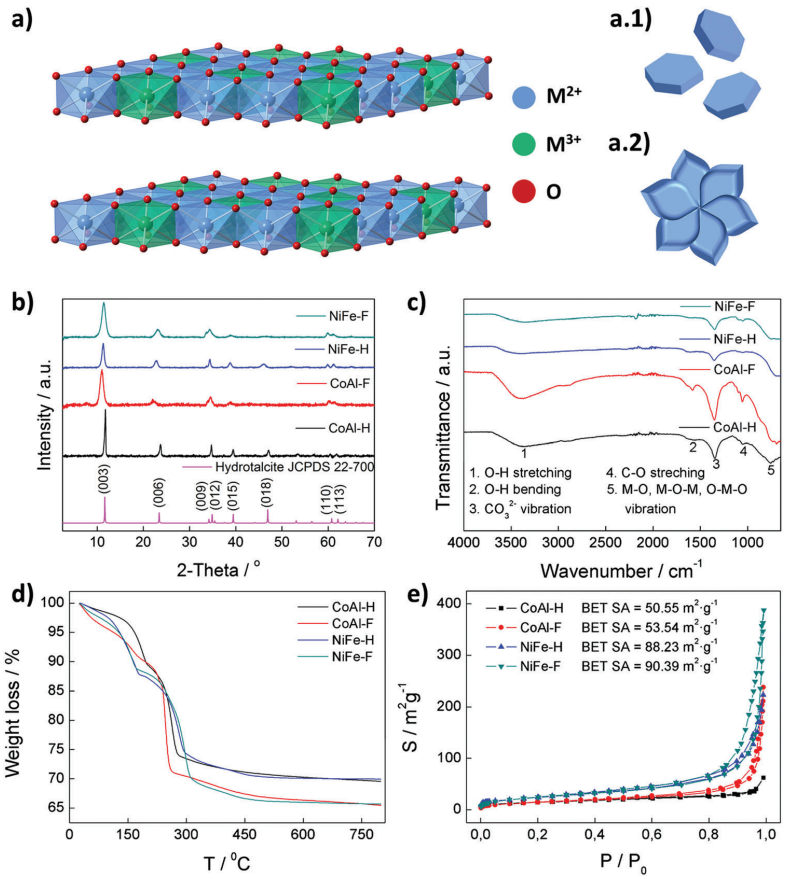

Fig. 1 Schematic illustration of a LDH with M^{2+}/M^{3+} ratio of 2 : 1 (a), hexagonal (a.1) and flower-like (a.2) LDH scheme. XRPD (b), FTIR spectra (c), TGA (d) and N_2 adsorption–desorption isotherms (e) for the synthesized LDH samples.

Table 1 Molecular formula for the hexagonal and flower-like synthesized LDHs

		EA found			EA calculated		
Sample	Molecular formula[a]	C	H	N	C	H	N
CoAl-H	$Co_{0.69}Al_{0.31}(OH)_2(CO_3)_{0.155}(H_2O)_{0.3}$	2.46	2.69	0.01	1.9	2.68	0.0
CoAl-F	$Co_{0.70}Al_{0.30}(OH)_2(CO_3)_{0.15}(H_2O)_{0.394}(C_2H_6O_2)_{0.189}$	5.56	3.17	0.07	5.38	3.45	0.0
NiFe-H	$Ni_{0.67}Fe_{0.33}(OH)_2(CO_3)_{0.165}(H_2O)_{0.4}$	2.39	2.57	0.72	1.82	2.59	0.0
NiFe-F	$Ni_{0.69}Fe_{0.31}(OH)_2(CO_3)_{0.155}(H_2O)_{0.556}(C_2H_6O_2)_{0.143}$	4.37	2.56	0.74	4.41	3.33	0.0

[a] Molecular formulas were estimated from the EDAX microanalysis alongside with TGA and elemental analysis results. The *N* value in NiFe-LDHs most likely comes from a residual nitrate contribution (<0.05 per molecular formula) from the initial metallic salts.

the results, the flower-like samples display slightly higher values of surface BET area (therefore higher adsorption capacity), confirming the formation of more intricate structures with higher specific surface areas.[44,45]

The morphology of the LDHs have been studied by field-emission scanning electron microscopy (FESEM) and high-resolution transmission electron microscopy (HRTEM). Regarding the CoAl-LDH family, Fig. 2a–d display the FESEM images at low and high magnifications. The CoAl-H exhibits a conventional hexagonal morphology (Fig. 2a and Fig. S4, ESI†),[19] with a very well-defined and regular hexagonal shape whose average lateral dimensions are *ca.* 3.5 μm and 80–100 nm in thickness. On the contrary, Fig. 2b and Fig. S4 (ESI†) reveal the morphology of the CoAl-F, composed by irregular ensembles consisting of LDH crystallites

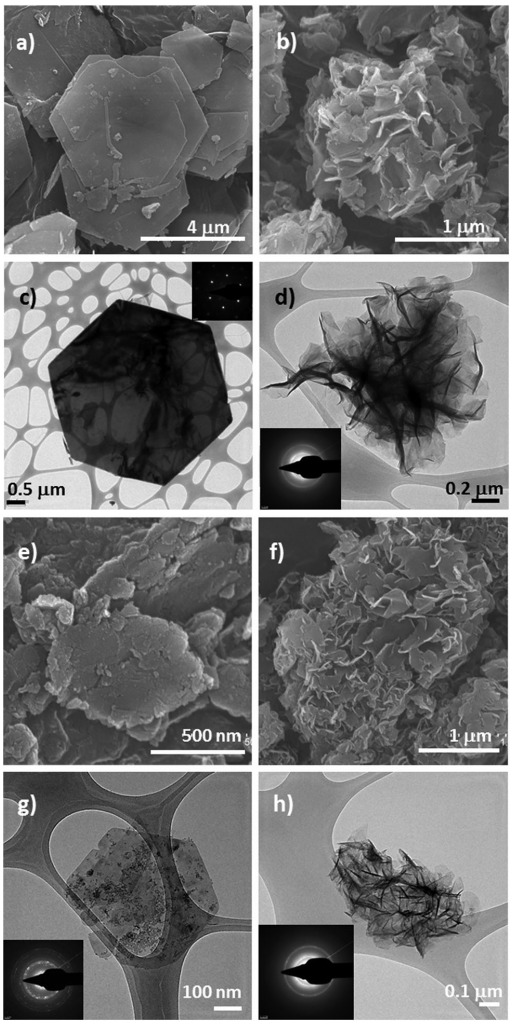

Fig. 2 FESEM images of the CoAl-H (a), CoAl-F (b), NiFe-H (e) and NiFe-F (f) samples. HRTEM images highlighting the different morphologies of CoAl-H (c), CoAl-F (d), NiFe-H (g) and NiFe-F (h). The inset in (c), (d), (g) and (h) correspond to the SAED pattern of the samples.

adopting the shape of a dahlia flower.[46] The dimensions of the platelets are *ca.* 300–400 nm in size and 20–30 nm in thickness, whereas the diameter of the macrostructures is close to 1.5 μm. A size histogram for CoAl-H can be found in Fig. S5 (ESI†). HRTEM images highlights the different morphology between both samples (Fig. 2c and d), showing low contrast due to its low thickness, being more pronounced in the case of CoAl-F (Fig. 2d),[16] which exhibits hierarchical structures composed by small contoured LDH platelets, giving rise to the flower structure. Selected area electron diffraction (SAED) pattern (inset of Fig. 2c and d) suggests different orientations and lower crystallinity than that observed for the hexagonal counterpart, in good accordance with XRPD results.

In line with that, EDAX microanalysis was also carried out, depicting an experimental ratio Co : Al of 2.2 : 1 and 2.3 : 1 for CoAl-H and CoAl-F, respectively, in good agreement with the calculated one. Mapping analysis revealed a completely homogeneous distribution of both metals throughout the whole sample (Fig. 3a and b).

In the case of the NiFe-LDH family, a similar scenario can be found. NiFe-H sample exhibits the typical hexagonal morphology,[13,16] with smaller lateral dimensions (*ca.* 800 nm) and thickness below 30 nm (Fig. 2e, g and Fig. S4, S5, ESI†).[47] NiFe-F sample shows the expected dahlia-like morphology, composed by an ensemble of small curved LDH platelets (thickness of *ca.* 15 nm) which gather themselves giving rise to spherical structures of about 2 μm, similarly to that previously observed for the CoAl-F (Fig. 2f, h and Fig. S4, ESI†).[48] A size histogram for NiFe-H can be found in Fig. S5 (ESI†). Finally, EDAX microanalysis of the NiFe-LDH family displays a Ni : Fe metal ratio of 2.0 : 1 and 2.2 : 1 for NiFe-H and NiFe-F, respectively, in good agreement with the expected one. Mapping of the samples (Fig. 3c and d) depicts a homogeneous distribution of both metals.

By combining the TGA data, EDAX and elemental analysis, we can estimate the molecular formula for the studied LDHs, as shown in Table 1.

Once the LDH materials have been successfully synthesized, a complete magnetic study was carried out to unveil how the distortion of the layers may affect the magnetic behaviour of the samples. In general, the magnetic behaviour of a LDH system is controlled by two main contributions: the intralayer superexchange interactions between metallic centres mediated by –OH bridges, and the interlayer dipolar interactions between the double hydroxide layers.[13] Moreover, there are several factors that may influence the magnetic behaviour of LDHs, *i.e.* dipolar interactions, chemical composition, cation ordering or particle size. In order to achieve comparable systems, we kept constant the stoichiometry, the interlayer space and the solvothermal synthetic protocol.

Table 2 summarizes all the experimental magnetic parameters calculated for the CoAl-LDH and NiFe-LDH families, respectively. The collected magnetic data for the CoAl-LDH family is depicted in Fig. 4 and 5. In the case of CoAl-LDH, DC measurements exhibit spontaneous magnetization at low temperatures (Fig. 4a and 5a). χ_M remains nearly constant upon cooling down until *ca.* 50 K, followed by a sharp increase reaching a maximum value of 0.99 and 3.3 emu mol^{-1} at 2 K for CoAl-H and CoAl-F, respectively. On the other hand, $\chi \cdot T_{rt}$ product displays its maximum value of 3.4 emu K mol^{-1} at 4.5 K for CoAl-H, and 15.0 emu K mol^{-1} at 6.0 K for the CoAl-F sample, followed by an abrupt decrease until 1.6 emu K mol^{-1} (CoAl-H) and 6.5 emu K mol^{-1} (CoAl-F) at 2 K. The inverse of the magnetic susceptibility (χ_M^{-1}) can be fitted to a Curie–Weiss law in the high temperature region (50–300 K). From the fitting, we can estimate the Curie constant for each sample, resulting in 2.11 emu K mol^{-1} for CoAl-H and 2.62 emu K mol^{-1} for CoAl-F,

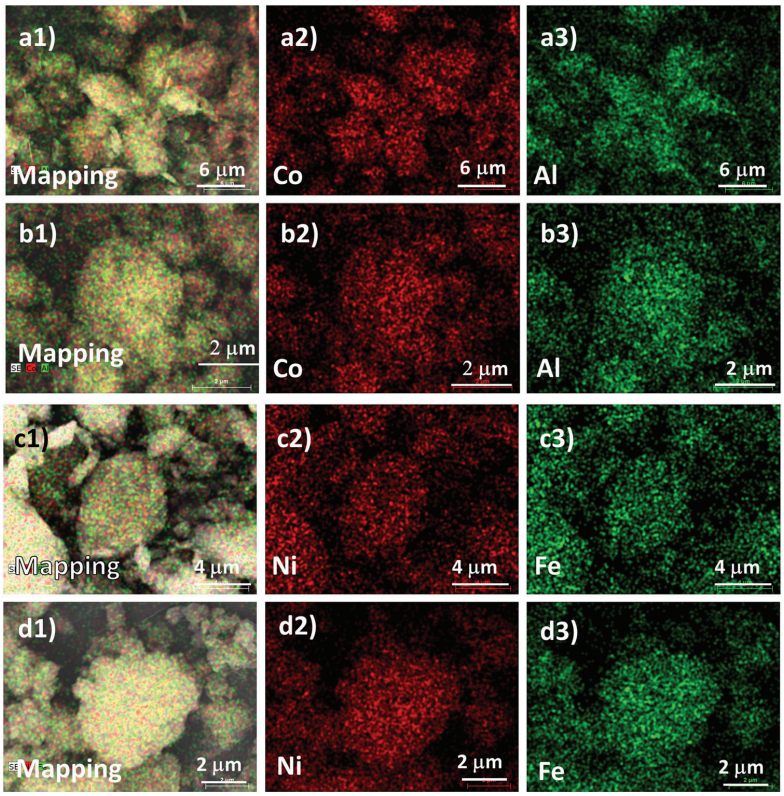

Fig. 3 Mapping analysis of CoAl-H (a1–a3), CoAl-F (b1–b3), NiFe-H (c1–c3) and NiFe-F (d1–d3) samples, highlighting the homogeneous distribution of the metals in all samples.

Table 2 Magnetic data of CoAl-H, CoAl-F, NiFe-H and NiFe-F LDHs[a]

Sample	$\chi \cdot T_{rt}$ (emu K mol^{-1})	C_{SO} (emu K mol^{-1})	C (emu K mol^{-1})	θ (K)	T_{irr} (K)	T_M (K)	M_S (μ_B)	H_C (Oe)	E_a/k_B (K)	ϕ
CoAl-H	2.06	1.29	2.11	8.80	2.56	4.7	1.04	9.46	85.70	0.068–0.085
CoAl-F	2.65	1.31	2.62	−2.97	4.09	7.2	1.54	4.64	213.37	0.039–0.045
NiFe-H	2.40	2.11	2.30	29.11	16.25	17.8	0.66	3613.45	1381.0	0.019–0.021
NiFe-F	2.11	2.05	2.13	4.30	15.05	18.5	1.05	1509.85	2301.26	0.013–0.014

[a] $\chi \cdot T_{rt}$ at room temperature; C_{SO} expected value for the spin-only Curie constant; C experimental estimated Curie constant; θ Weiss constant; T_{irr} irreversible temperature extracted from the bifurcation between ZFC and FC. T_M temperature for the onset of the spontaneous magnetization, extracted from the out-of-phase signal in the AC measurements; M_S saturation magnetization; H_c coercive field; E_a/k_B activation energy estimated by fitting the χ_M'' signal to an Arrhenius law; ϕ Mydosh parameter. $S(Co^{2+}) = 3/2$, $S(Al^{3+}) = 0$, $(Ni^{2+}) = 1$, $S(Fe^{3+}) = 5/2$.

in both cases slightly higher than that expected for the spin-only value (C_{SO}) for a magnetically diluted combination of Co^{2+} ($S = 3/2$) and Al^{3+} ($S = 0$) ions, indicating that a significant orbital contribution is involved. Moreover, Weiss constant (θ) results in a positive value (8.80 K) for the CoAl-H sample, suggesting predominant ferromagnetic interactions in the system, and a negative value of −2.97 K for the CoAl-F material, indicative of an increased contribution of the antiferromagnetic interactions. Field cooled (FC) and zero-field cooled (ZFC) experiments point out the presence of cooperative interactions (Fig. 4b and 5b), showing a clear bifurcation below an irreversible temperature of 2.56 K and 4.09 K for the CoAl-H and CoAl-F, respectively.[31] Field dependent magnetization cycles at 2 K (Fig. 4c and 5c) present coercive fields (H_c) of 9.46 and 4.64 Oe for CoAl-H and CoAl-F, respectively, which highlights the soft magnetic character of these materials. The saturation magnetization (M_s) of the CoAl-H sample was found to be 1.04 μ_B, and 1.5 μ_B for CoAl-F. This increment in the M_s is related with increased paramagnetic contribution of non-compensated spins, as a consequence of the pronounced disorder of the system. Moreover, in order to exclude

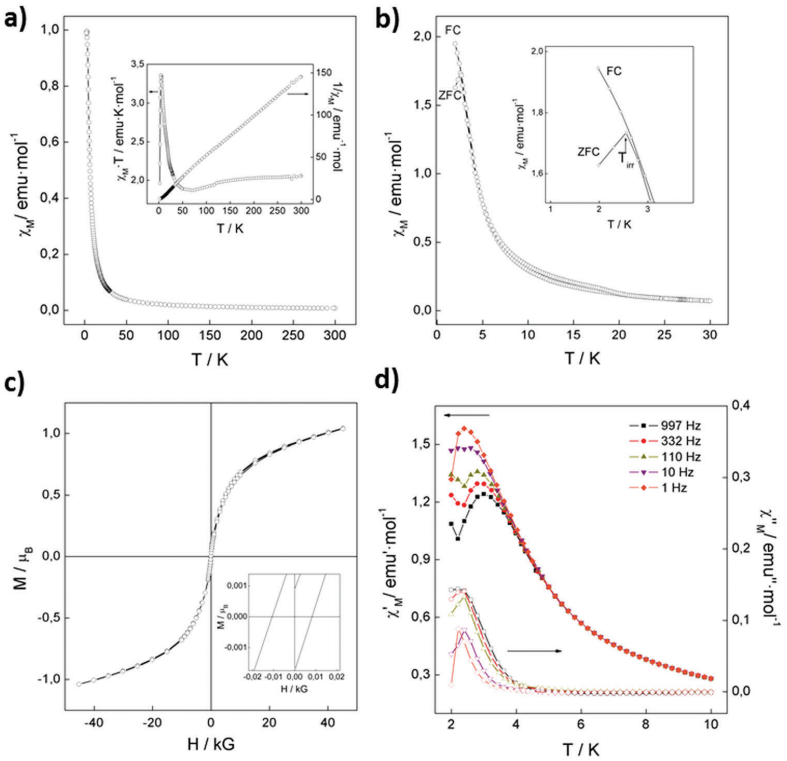

Fig. 4 (a) Magnetic properties of the CoAl-H sample. χ_M *vs.* *T* with an external applied field of 1000 Oe. The inset represents the thermal dependence of χ_M·*T* and the fitting of the χ_M^{-1} to a Curie–Weiss law; (b) FC/ZFC with an external applied field of 100 Oe. The inset highlights the low temperature region remarking the irreversible temperature; (c) hysteresis cycle at 2 K. The inset depicts the low field region; (d) frequency dependence with the temperature for the in-phase (χ_M') and the out-of-phase (χ_M'') signals at 1, 10, 110, 332 and 997 Hz.

the influence of the experimental stoichiometry deviations in the magnetic properties, we have synthesized and characterized several CoAl-H and CoAl-F exhibiting slight variations in the metal content, and showing negligible fluctuations in the M_s values, thus confirming the intrinsic nature of the observed magnetic properties (see Fig. S6, ESI†).

On the other hand, dynamic AC susceptibility measurements with an external applied field of 3.95 Oe oscillating at different frequencies allow us to confirm the spontaneous magnetization at low temperatures (Fig. 4d and 5d). Both the in-phase (χ_M') and the out-of-phase (χ_M'') signals exhibit a defined and frequency-dependent peak at low temperature. From the out-of-phase signal, we can estimate the temperature for the onset of the spontaneous magnetization (T_M) as the point where $\chi_M'' \neq 0$ and can be used as a guide for the magnetic transition of the system. Interestingly, a remarkable increase from 4.7 K for the CoAl-H sample to 7.2 K for the CoAl-F LDH was observed. To the best of our knowledge, this is the highest T_M value ever measured for a CoAl-LDH.[13] Moreover, we can also estimate the frequency dependence of the χ_M'' maxima with the calculation of the Mydosh parameter (ϕ).[49,50]

$$\phi = \Delta T_{max}/T_{max}\Delta(\log \nu) \quad (1)$$

The range obtained for CoAl-H was 0.068–0.085, typical of spin glass-like materials (0.06–0.08), whereas the CoAl-F exhibited remarkably lower values between 0.039–0.045, pointing to a more disordered behaviour (*i.e.* closer to that of canonical spin glasses).[49] Further information of the spin relaxation can be obtained by fitting the frequency dependence of the out-of-phase signal to an Arrhenius law (Fig. S7, ESI†) with the following equation:

$$\nu = \nu_0 \exp(-E_a/k_B T) \quad (2)$$

This fitting allows the estimation of the activation energy of the system (E_a/k_B), showing a value of 85.7 K for the CoAl-H, which may be ascribed to the movement of the domain walls in the ferromagnetic phase, as previously observed in other 2D magnets. In turn, CoAl-F exhibits a significantly higher activation energy of 213.4 K, in line with a marked spin glass-like character, in agreement with the calculated Mydosh parameters.[49]

With respect to the NiFe-LDH family, a more complex magnetic scenario arises as a consequence of the combined action of ferromagnetic Ni–OH–Ni and antiferromagnetic Ni–OH–Fe and

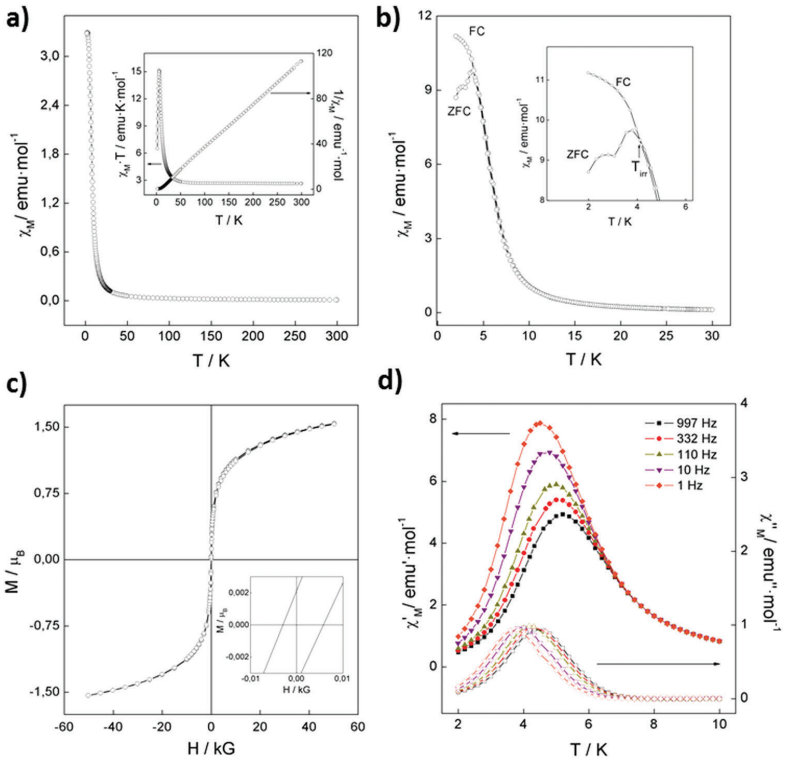

Fig. 5 (a) Magnetic properties of the CoAl-F sample. χ_M *vs.* *T* with an external applied field of 1000 Oe. The inset represents the thermal dependence of $\chi_M \cdot T$ and the fitting of the χ_M^{-1} to a Curie–Weiss law; (b) FC/ZFC with an external applied field of 100 Oe. The inset highlights the low temperature region remarking the irreversible temperature; (c) hysteresis cycle at 2 K. The inset depicts the low field region; (d) frequency dependence with the temperature for the in-phase (χ_M') and the out-of-phase (χ_M'') signals at 1, 10, 110, 332 and 997 Hz.

Fe–OH–Fe pairs across the layers, as well as the dipolar interactions operating between the layers. Furthermore, for the highest Fe concentrations, like in the present case (Ni : Fe, 2 : 1), significant Fe clustering (AF Fe–OH–Fe pairs) occurs enabling the presence of spin frustration and exhibiting increased coercive fields and T_M.[16] The DC susceptibility depicts a sharp increase of χ_M near 50 K up to 2.4 and 1.4 emu mol^{-1} at 2 K for the NiFe-H and the NiFe-F samples, respectively (Fig. 6a and 7a). $\chi_M \cdot T$ presents a similar trend with maximum values of 20.3 and 11.0 emu K mol^{-1} at *ca.* 10 K, with an abrupt decrease until 4.8 and 2.8 emu K mol^{-1} at 2 K for NiFe-H and NiFe-F, respectively. From the Curie–Weiss fitting in the high temperature region we can estimate a Curie constant of 2.30 and 2.13 emu K mol^{-1} for NiFe-H and NiFe-F, respectively, in good agreement with that expected for the spin-only value of a magnetically diluted combination of Ni^{2+} ($S = 1$) and Fe^{3+} ($S = 5/2$) ions. Weiss constant is positive for both samples (29.11 K for NiFe-H and 4.30 K for NiFe-F), indicative of the predominance of ferromagnetic interactions within the layers. Interestingly, the θ value of NiFe-F is remarkably smaller than that of the hexagonal counterpart and similar to that exhibited by nanosized (*ca.* 110 nm) alkoxide-intercalated NiFe-LDH.[32] Fig. 6b and 7b display the FC/ZFC magnetic measurements, with a T_{irr} of 16.25 K for the NiFe-H sample and 15.05 K for the NiFe-F. Hysteresis cycles measured at 2 K exhibit an abrupt decrease in the coercive fields from *ca.* 3600 (NiFe-H) to 1500 Oe for NiFe-F (Fig. 6c and 7c). The saturation magnetization found for NiFe-H was lower (0.66 μ_B) than that for the NiFe-F (1.05 μ_B), in excellent agreement with that previously observed for the CoAl-LDHs, indicative of an increased contribution of non-compensated spins. Furthermore, several control experiments have ruled out the influence of slight experimental fluctuations in the metallic ratio on the magnetic behavior, as depicted in Fig. S6 (ESI†).

AC susceptibility measurements (Fig. 6d and 7d) give rise to a slight increase in the T_M values from 17.8 K (NiFe-H) to 18.5 K (NiFe-F) that again, is the highest reported for a NiFe-LDH so far. Furthermore, Mydosh parameters depict a range of 0.019–0.021 for the NiFe-H sample, and 0.013–0.014 for the NiFe-F material which perfectly match those expected for canonical spin glasses ($\phi = 0.005$–0.018). In order to shed light on the spin relaxation dynamics, we have fitted the frequency dependence of χ_M'' to both an Arrhenius law and a 3D critical scaling law. The fitting of the maximum values to an Arrhenius law

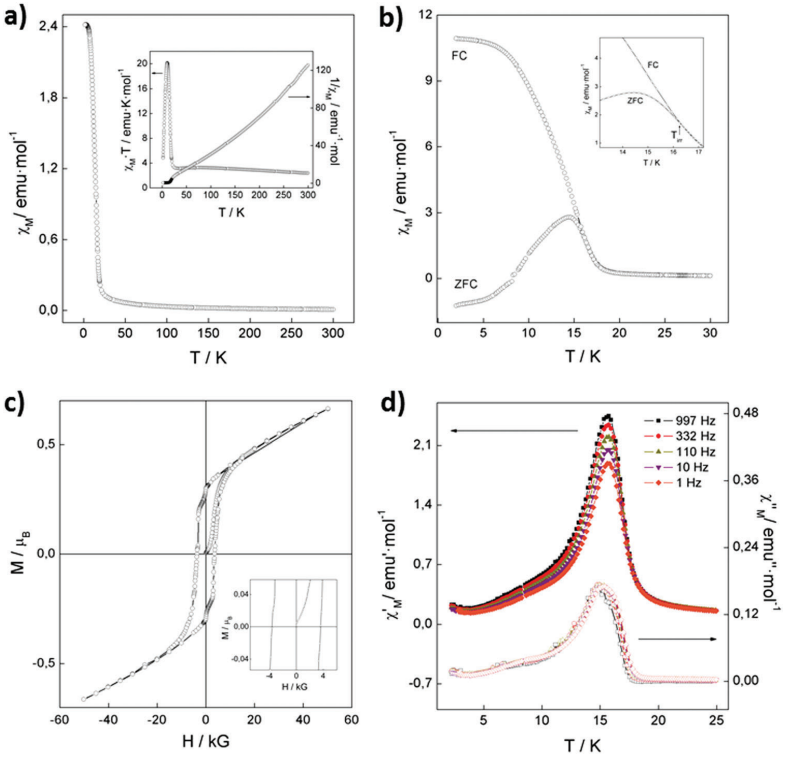

Fig. 6 (a) Magnetic properties of the NiFe-H sample. χ_M *vs.* *T* with an external applied field of 1000 Oe. The inset represents the thermal dependence of χ_M·*T* and the fitting of the $\chi_M{}^{-1}$ to a Curie–Weiss law; (b) FC/ZFC with an external applied field of 100 Oe. The inset highlights the low temperature region remarking the irreversible temperature; (c) hysteresis cycle at 2 K. The inset depicts the low field region; (d) frequency dependence with the temperature for the in-phase (χ_M') and the out-of-phase (χ_M'') signals at 1, 10, 110, 332 and 997 Hz.

(eqn (2) and Fig. S7, ESI†) exhibited an activation energy of 1381 and 2301 K for NiFe-H and NiFe-F, respectively. These meaningless physical values for E_a/k_B agree with the spin glass type behaviour. Moreover, we have fitted the frequency dependence of χ_M'' to the 3D critical scaling law for spin dynamics, in which the relaxation time diverges at finite temperature ($T_g \neq 0$ K), following the equation:

$$\tau = \tau_0[T_g/(T_g/T_{max} - T_g)]^{z\nu} \quad (3)$$

where T_g is the critical glass temperature, τ_0 the attempt time and zν a critical exponent. For NiFe-H the best fit of our data to a linear form of the eqn (3) (Fig. 8a) was obtained for T_g = 15.6 K, $\tau_0 = 6.01 \times 10^{-12}$ s and a zν = 3.5. For NiFe-F, the best fit (see Fig. 8b) was found for T_g = 8 K, $\tau_0 = 2.95 \times 10^{-12}$ s and zν = 70.3. For both cases the obtained τ_0 value falls in the range for canonical spin glasses (from 10^{-7} to 10^{-12}), in turn zν is out of this range (from 4 to 12).[32,49,51] Interestingly NiFe-F exhibits a remarkably lower T_g, suggesting the appearance of aging phenomena at lower temperatures, and confirming the increased glassines in the NiFe-F.

In overall, both static and dynamic magnetic measurements of CoAl- and NiFe-LDH families indicate that the distortion of the layers induces a magnetically more disordered behaviour, independently of the chemical composition. This is reflected in a more antiferromagnetic character, lower coercive fields, higher values of M_s, T_M and activation energies, and lower Mydosh parameters. These results clearly reflect an increase in the glassiness of the distorted systems, approaching the behaviour of canonical spin glasses. The observed magnetic behaviour is in good agreement with previous results in azobenzene-intercalated CoAl-LDH hybrids, exhibiting reversible magnetic switching upon *cis–trans* photoisomerization.[19] In this case, changes of the exchange pathways and magnetic correlation at a local level as a consequence of the structural distortion in the layers resulted in increased antiferromagnetic interactions leading to a higher T_M value. Moreover, recent studies on the influence of dipolar interactions revealed that the most important factor governing the dipolar interactions is the spin correlation size, or, in the limit case, the lateral dimensions of the layer, rather than the interlayer distance.[52] In our case, size effects can be ruled out due to the micrometric

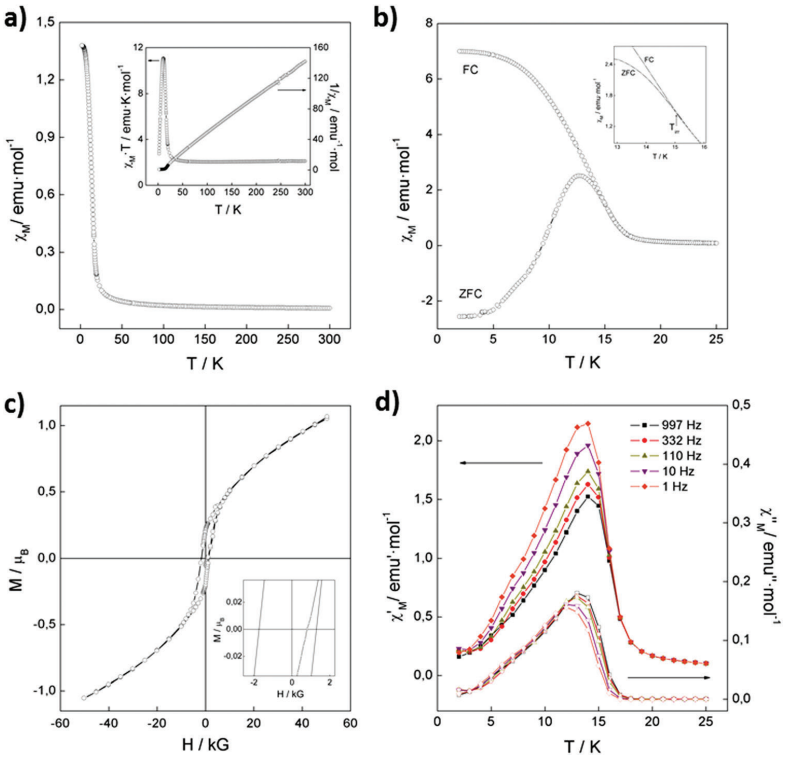

Fig. 7 (a) Magnetic properties of the NiFe-F sample. χ_M *vs.* *T* with an external applied field of 1000 Oe. The inset represents the thermal dependence of χ_M·*T* and the fitting of the χ_M^{-1} to a Curie–Weiss law; (b) FC/ZFC with an external applied field of 100 Oe. The inset highlights the low temperature region remarking the irreversible temperature; (c) hysteresis cycle at 2 K. The inset depicts the low field region; (d) frequency dependence with the temperature for the in-phase (χ_M') and the out-of-phase (χ_M'') signals at 1, 10, 110, 332 and 997 Hz.

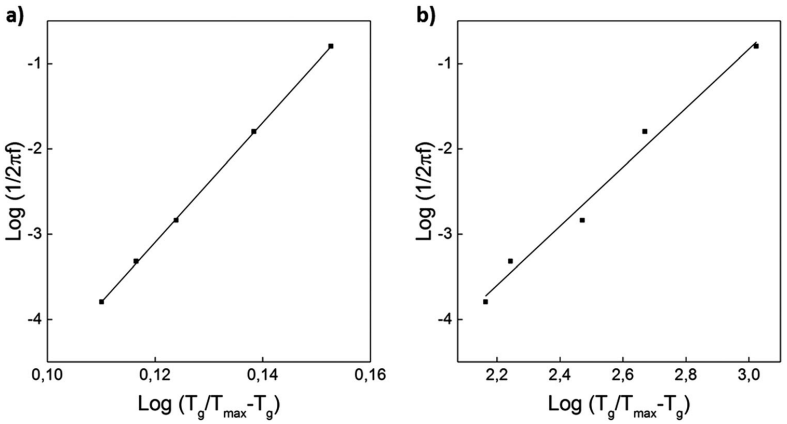

Fig. 8 Frequency dependence of χ_M'' fitted with the 3D scaling low model $\tau = \tau_0[T_g/(T_g/T_{max} - T_g)]^{zv}$ for the NiFe-H (a) and NiFe-F (b) samples.

character of the studied LDHs. On the other hand, as previously mentioned, we recently reported that the influence of interlayer distance in the magnetic properties of flexible CoAl-LDH hybrid systems having only one anchoring group is remarkably lower

than in the rigid ones (connected through two anchoring groups to the layers).[20] Herein we have demonstrated that the distortion of the layers induce a dramatic increase in the glassiness of the system, and this can be correlated with the presence of structural changes in the coordination environment of the metal octahedra across the layers, thus affecting angles and bond distances, which ultimately, will induce changes in magnetism. These results highlight the importance of layer distortion, morphology and flexibility in the overall magnetic behaviour of LDHs and pave the way for the rational design of hybrid systems with switchable morphological and magnetic control.

Conclusions

Two different families of magnetic LDHs (CoAl- and NiFe-) have been synthesized *via* a hydrothermal approach with two distinct morphologies: hexagonal and flower-like. All samples were fully characterized by XRPD, ATR-FTIR, TGA/DTA and adsorption–desorption nitrogen isotherms. Detailed microscopy studies with FESEM and TEM on these samples revealed the inherent curvature of the platelets, which gather themselves like petals into spherical microstructures assembling the flower-like shapes. We observed that this distortion of the layers induces a magnetically more disordered behaviour regardless the chemical composition of the LDH, effect that is reflected in a stronger antiferromagnetic character, lower coercive fields, higher values of saturation magnetization, ordering temperatures and activation energies, and lower Mydosh parameters. Our results demonstrate that the distortion of the layers induces a crystalline disorder that translates into more pronounced spin glass behaviour. This work paves the way for the development of smart stimuli-responsive magnetic hybrid materials in which the inherent flexibility of LDH may exert a key role.

Conflicts of interest

There are no conflicts to declare.

Acknowledgements

The research reported here was supported by the Spanish MINECO (grants MAT 2014-56143-R, CTQ 2014-52758-P, and Excellence Unit María de Maeztu MDM-2015-0538), the European Union (COST 15128 Molecular Spintronics Project) and the Generalitat Valenciana (Prometeo Program of Excellence, 2017/066). J. A. C. thanks the Universidad de Valencia for a predoctoral grant. G. A. thanks the FAU for the Emerging Talents Initiative (ETI) grant #WS16-17_Nat_04. The authors strongly thank Maria Teresa Pérez Chiva for her assistance with the experimental work.

References

1 A. K. Geim and K. S. Novoselov, *Nat. Mater.*, 2007, **6**, 183–191.
2 A. K. Geim and I. V. Grigorieva, *Nature*, 2013, **499**, 419–425.
3 Q. H. Wang, K. Kalantar-Zadeh, A. Kis, J. N. Coleman and M. S. Strano, *Nat. Nanotechnol.*, 2012, **7**, 699–712.
4 V. Nicolosi, M. Chhowalla, M. G. Kanatzidis, M. S. Strano and J. N. Coleman, *Science*, 2013, **340**, 1226419.
5 D. Hanlon, C. Backes, E. Doherty, C. S. Cucinotta, N. C. Berner, C. Boland, K. Lee, A. Harvey, P. Lynch, Z. Gholamvand, S. Zhang, K. Wang, G. Moynihan, A. Pokle, Q. M. Ramasse, N. McEvoy, W. J. Blau, J. Wang, G. Abellan, F. Hauke, A. Hirsch, S. Sanvito, D. D. O'Regan, G. S. Duesberg, V. Nicolosi and J. N. Coleman, *Nat. Commun.*, 2015, **6**, 8563.
6 G. Abellán, S. Wild, V. Lloret, N. Scheuschner, R. Gillen, U. Mundloch, J. Maultzsch, M. Varela, F. Hauke and A. Hirsch, *J. Am. Chem. Soc.*, 2017, **139**, 10432–10440.
7 C. Gibaja, D. Rodriguez-San-Miguel, P. Ares, J. Gómez-Herrero, M. Varela, R. Gillen, J. Maultzsch, F. Hauke, A. Hirsch, G. Abellán and F. Zamora, *Angew. Chem., Int. Ed.*, 2016, **55**, 14345–14349.
8 P. Ares, J. J. Palacios, G. Abellán, J. Gómez-Herrero and F. Zamora, *Adv. Mater.*, 2017, 1703771.
9 S. M. Auerbach, K. A. Carrado and P. K. Dutta, *Handbook of Layered Materials*, CRC Press, 2004.
10 V. Rives, *Layered Double Hydroxides: Present and Future*, Nova Publishers, 2001.
11 X. Duan and D. G. Evans, *Layered Double Hydroxides*, Springer, 2006.
12 Q. Wang and D. O'Hare, *Chem. Rev.*, 2012, **112**, 4124–4155.
13 G. Abellán, C. Martí-Gastaldo, A. Ribera and E. Coronado, *Acc. Chem. Res.*, 2015, **48**, 1601–1611.
14 J. Yu, Q. Wang, D. O'Hare and L. Sun, *Chem. Soc. Rev.*, 2017, **46**, 5950–5974.
15 Z. Liu, R. Ma, M. Osada, N. Iyi, Y. Ebina, K. Takada and T. Sasaki, *J. Am. Chem. Soc.*, 2006, **128**, 4872–4880.
16 G. Abellán, E. Coronado, C. Martí-Gastaldo, J. Waerenborgh and A. Ribera, *Inorg. Chem.*, 2013, **52**, 10147–10157.
17 E. Coronado, J. R. Galán-Mascarós, C. Martí-Gastaldo, A. Ribera, E. Palacios, M. Castro and R. Burriel, *Inorg. Chem.*, 2008, **47**, 9103–9110.
18 C. Zhang, T. Tsuboi, H. Namba, Y. Einaga and T. Yamamoto, *Dalton Trans.*, 2016, **45**, 13324–13331.
19 G. Abellán, E. Coronado, C. Martí-Gastaldo, A. Ribera, J. L. Jordá and H. García, *Adv. Mater.*, 2014, **26**, 4156–4162.
20 G. Abellán, J. L. Jordá, P. Atienzar, M. Varela, M. Jaafar, J. Gómez-Herrero, F. Zamora, A. Ribera, H. García and E. Coronado, *Chem. Sci.*, 2015, **6**, 1949–1958.
21 G. Hu and D. O'Hare, *J. Am. Chem. Soc.*, 2005, **127**, 17808–17813.
22 T. Xiao, Y. Tang, Z. Jia, D. Li, X. Hu, B. Li and L. Luo, *Nanotechnology*, 2009, **20**, 475603.
23 X. Liu, R. Ma, Y. Bando and T. Sasaki, *Adv. Mater.*, 2012, **24**, 2148–2153.
24 B. Ni and X. Wang, *Chem. Sci.*, 2015, **6**, 3572–3576.
25 S. A. Solin, D. Hines, S. K. Yun, T. J. Pinnavaia and M. F. Thorpe, *J. Non-Cryst. Solids*, 1995, **182**, 212–220.
26 M.-A. Thyveetil, P. V. Coveney, J. L. Suter and H. C. Greenwell, *Chem. Mater.*, 2007, **19**, 5510–5523.
27 B. Li, J. He and D. G. Evans, *Chem. Eng. J.*, 2008, **144**, 124–137.

28 T.-R. Park, T. Y. Park, H. Kim and P. Min, *J. Phys.: Condens. Matter*, 2002, **14**, 11687.
29 P. Rabu, E. Delahaye and G. Rogez, *Nanotechnol. Rev.*, 2015, **4**, 557–580.
30 C. J. Wang, Y. A. Wu, R. M. J. Jacobs, J. H. Warner, G. R. Williams and D. O'Hare, *Chem. Mater.*, 2011, **23**, 171–180.
31 G. Abellán, J. A. Carrasco, E. Coronado, J. Romero and M. Varela, *J. Mater. Chem. C*, 2014, **2**, 3723.
32 J. A. Carrasco, J. Romero, M. Varela, F. Hauke, G. Abellán, A. Hirsch and E. Coronado, *Inorg. Chem. Front.*, 2016, **3**, 478–487.
33 J. J. Almansa, E. Coronado, C. Martí-Gastaldo and A. Ribera, *Eur. J. Inorg. Chem.*, 2008, 5642–5648.
34 G. Abellán, E. Coronado, C. J. Gómez-García, C. Martí-Gastaldo and A. Ribera, *Polyhedron*, 2013, **52**, 216–221.
35 X.-Y. Yu, T. Luo, Y. Jia, R.-X. Xu, C. Gao, Y.-X. Zhang, J.-H. Liu and X.-J. Huang, *Nanoscale*, 2012, **4**, 3466.
36 G. Abellán, J. A. Carrasco, E. Coronado, J. P. Prieto-Ruiz and H. Prima-García, *Adv. Mater. Interfaces*, 2014, **1**, 1400184.
37 S. S. C. Pushparaj, C. Forano, V. Prevot, A. S. Lipton, G. J. Rees, J. V. Hanna and U. G. Nielsen, *J. Phys. Chem. C*, 2015, **119**, 27695–27707.
38 L.-J. Zhou, X. Huang, H. Chen, P. Jin, G.-D. Li and X. Zou, *Dalton Trans.*, 2015, **44**, 11592–11600.
39 J. Zhang, X. Xie, C. Li, H. Wang and L. Wang, *RSC Adv.*, 2015, **5**, 29757–29765.
40 C. Wang, X. Zhang, X. Sun and Y. Ma, *Electrochim. Acta*, 2016, **191**, 329–336.
41 C. Wang, X. Zhang, Z. Xu, X. Sun and Y. Ma, *ACS Appl. Mater. Interfaces*, 2015, **7**, 19601–19610.
42 J. Fang, M. Li, Q. Li, W. Zhang, Q. Shou, F. Liu, X. Zhang and J. Cheng, *Electrochim. Acta*, 2012, **85**, 248–255.
43 H. Sun, Z. Chu, D. Hong, G. Zhang, Y. Xie, L. Li and K. Shi, *J. Alloys Compd.*, 2016, **658**, 561–568.
44 T. Yan, R. Li and Z. Li, *Mater. Res. Bull.*, 2014, **51**, 97–104.
45 D. C. Carvalho, N. A. Ferreira, J. M. Filho, O. P. Ferreira, J. M. Soares and A. C. Oliveira, *Catal. Today*, 2015, **250**, 155–165.
46 Y. Li, S. Li, Y. Zhang, M. Yu and J. Liu, *Mater. Lett.*, 2015, **142**, 137–140.
47 C. Carteret, B. Grégoire and C. Ruby, *Solid State Sci.*, 2011, **13**, 146–150.
48 Y. Wei, X. Zhang, X. Wu, D. Tang, K. Cai and Q. Zhang, *RSC Adv.*, 2016, **6**, 39317–39322.
49 J. A. Mydosh, *Spin glasses: an experimental introduction*, Taylor & Francis, London, Washington, DC, 1993.
50 C. A. M. Mulder, A. J. Van Duyneveldt and J. A. Mydosh, *Phys. Rev. B: Condens. Matter Mater. Phys.*, 1982, **25**, 515.
51 G. Layrac, D. Tichit, J. Larionova, Y. Guari and C. Guérin, *J. Phys. Chem. C*, 2011, **115**, 3263–3271.
52 J. A. Carrasco, S. Cardona-Serra, J. M. Clemente-Juan, A. Gaita-Ariño, G. Abellán and E. Coronado, submitted.

Electronic Supplementary Material (ESI) for Journal of Materials Chemistry C.

Influence of Morphology in the Magnetic Properties of Layered Double Hydroxides

Jose A. Carrasco,[a] Gonzalo Abellán*,[b] Eugenio Coronado*[a]

[a] Instituto de Ciencia Molecular (ICMol), Universidad de Valencia, Catedrático José Beltrán 2, 46980 Paterna, Valencia, Spain.

[b] Department of Chemistry and Pharmacy and Joint Institute of Advanced Materials and Processes (ZMP), Friedrich-Alexander-Universität Erlangen-Nürnberg, Henkestr. 42, 91054 Erlangen and Dr.-Mack Str. 81, 90762 Fürth, Germany.

*Corresponding authors: Gonzalo Abellán (gonzalo.abellan@fau.de) and Eugenio Coronado (eugenio.coronado@uv.es)

Contents

SI 1. Magnified XRPD patterns.

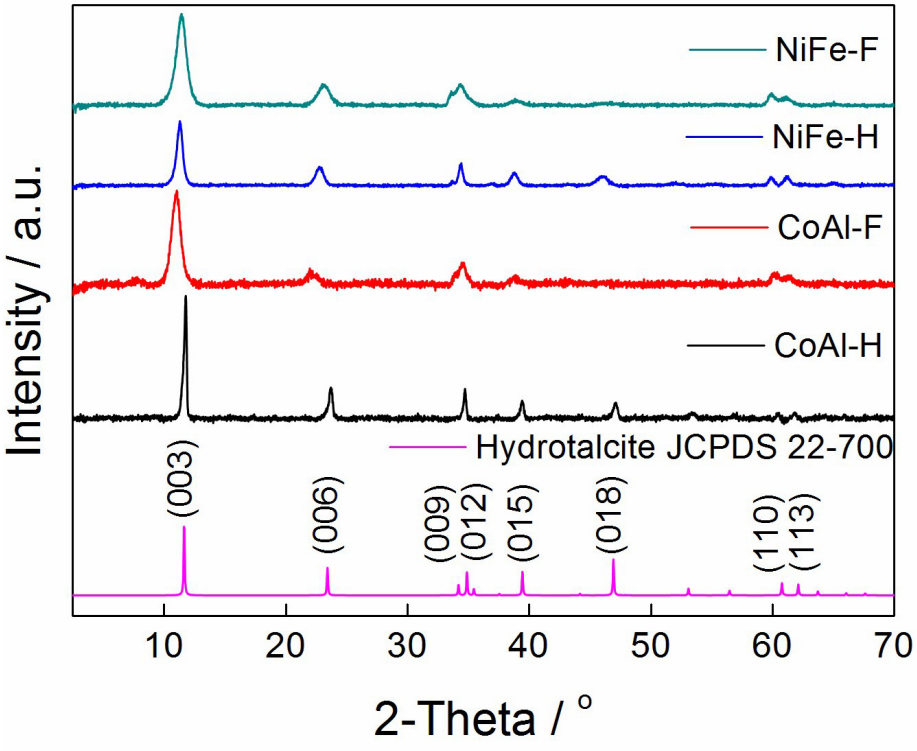

SI 2. Individual TGA/DTA curves.

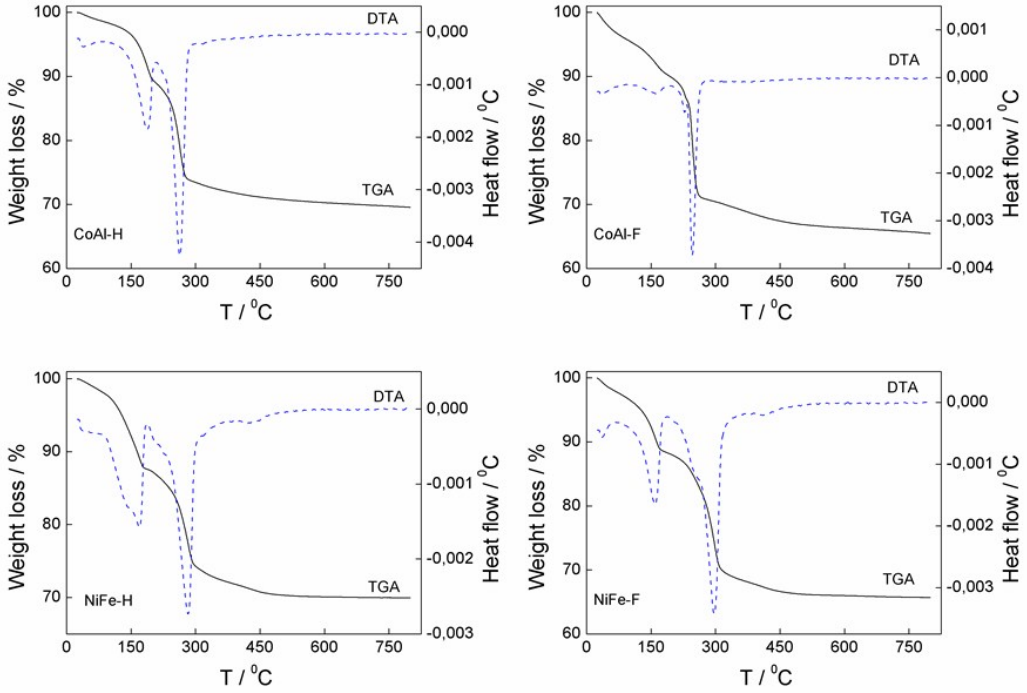

SI 3. Individual N_2 adsorption-desorption isotherms.

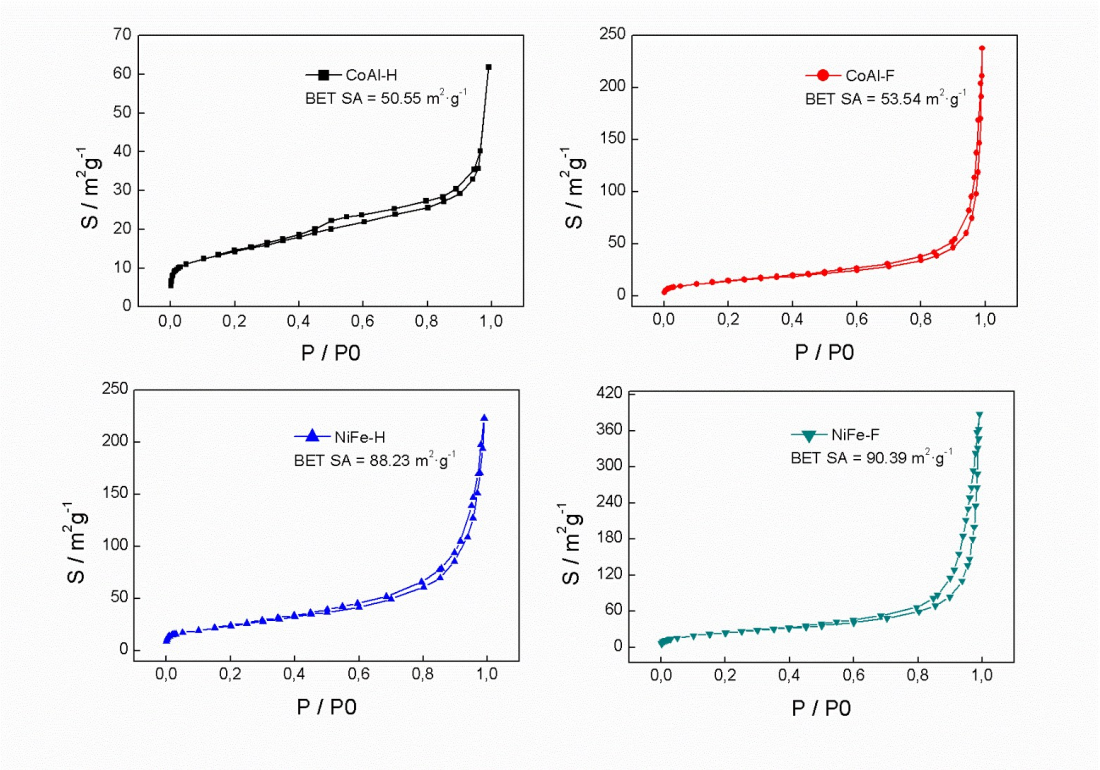

SI 4. Additional FESEM images.

CoAl-H (a and b), CoAl-F (c and d), NiFe-H (e and f) and NiFe-F (g and h).

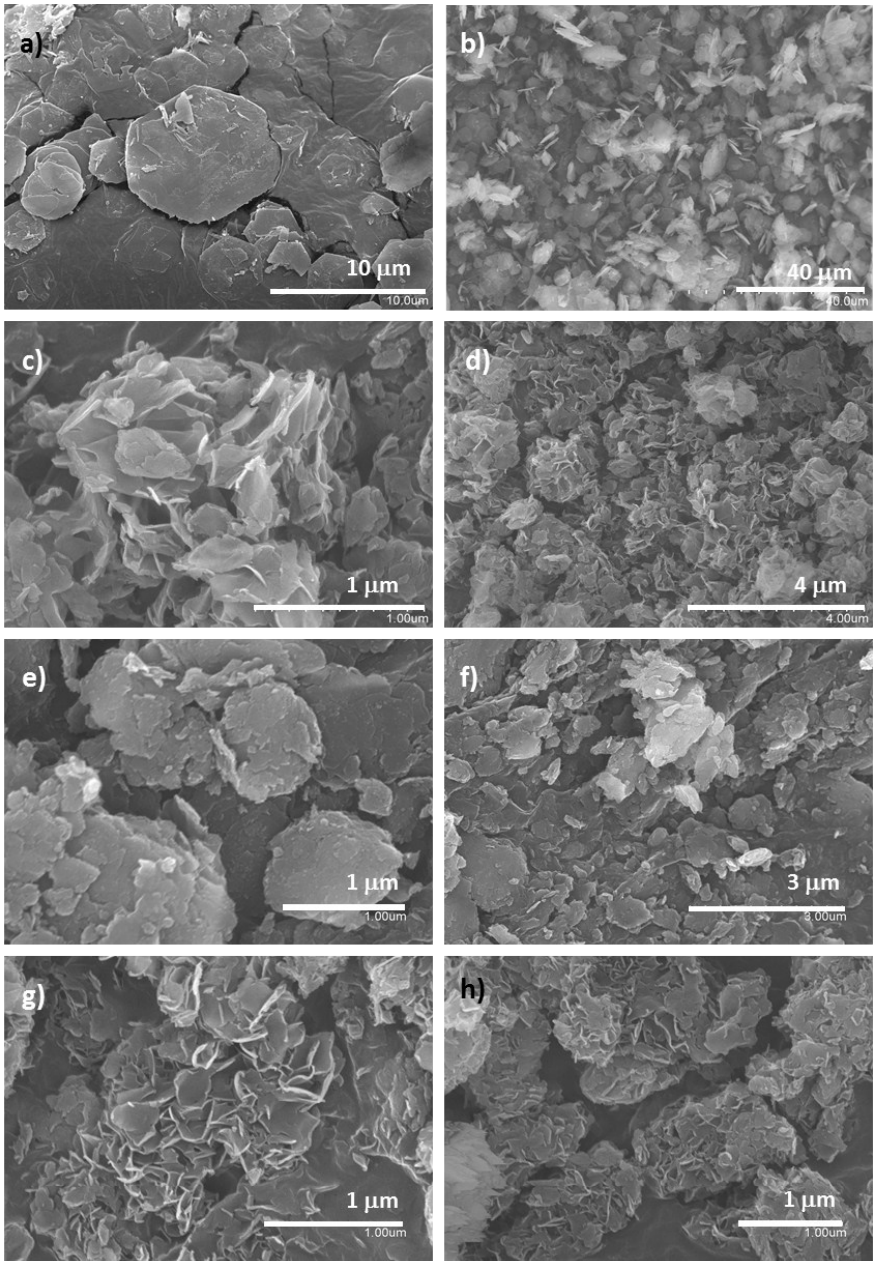

SI 5. Size histograms for the hexagonal samples.

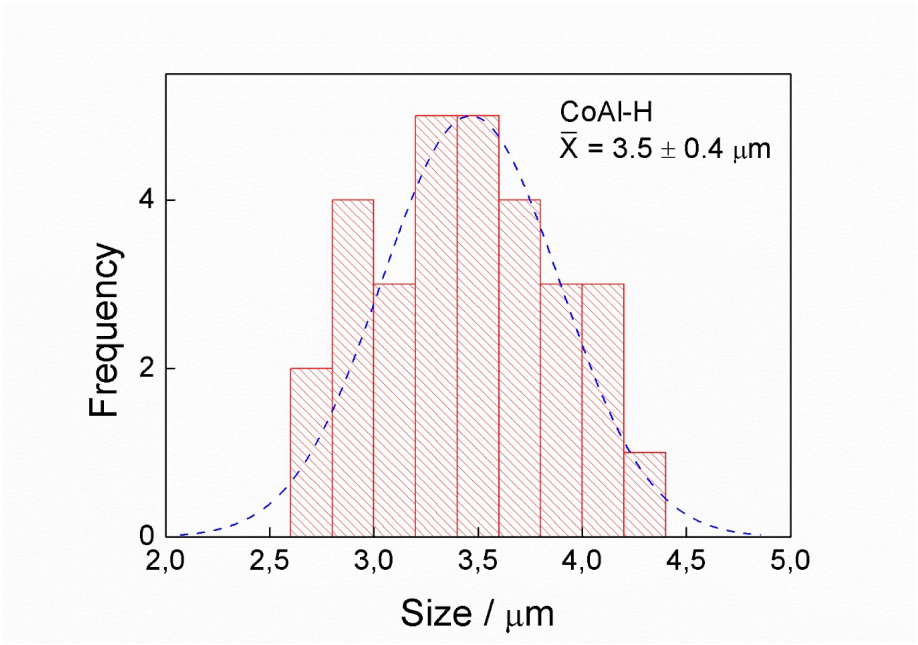

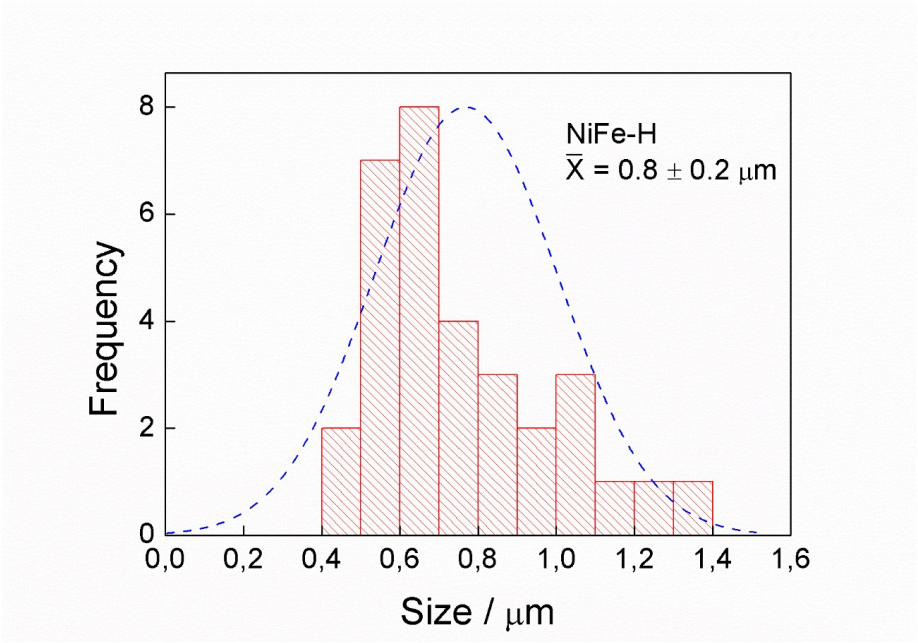

SI 6. Hysteresis cycles of flower-like samples with small variations in their M^{2+}/M^{3+} ratio.

Sample	EDAX ratio M^{2+}/M^{3+}	Saturation Magnetization (M_s) at 2 K
CoAl-F (main text)	(0.70/0.30) = 2.3	1.54 μ_B
CoAl-F_2	(0.68/0.32) = 2.1	1.45 μ_B
CoAl-F_3	(0.67/0.33) = 2.0	1.42 μ_B
NiFe-F (main text)	(0.69/0.31) = 2.2	1.05 μ_B
NiFe-F_2	(0.70/0.30) = 2.3	1.10 μ_B
NiFe-F_3	(0.68/0.32) = 2.1	1.12 μ_B

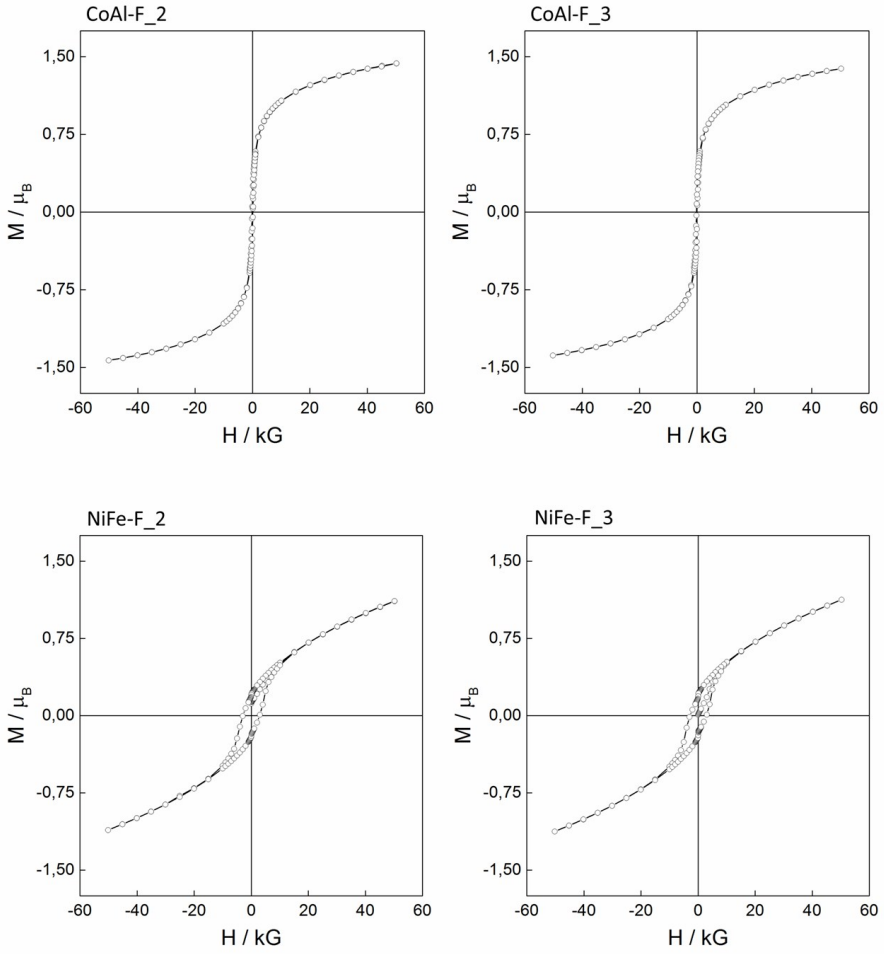

SI 7. Arrhenius fitting of the out-of-phase (χ''_M) signal.

Arrhenius fitting of the out-of-phase (χ''_M) signal for CoAl-H (a), CoAl-F (b), NiFe-H (c) and NiFe-F (d).

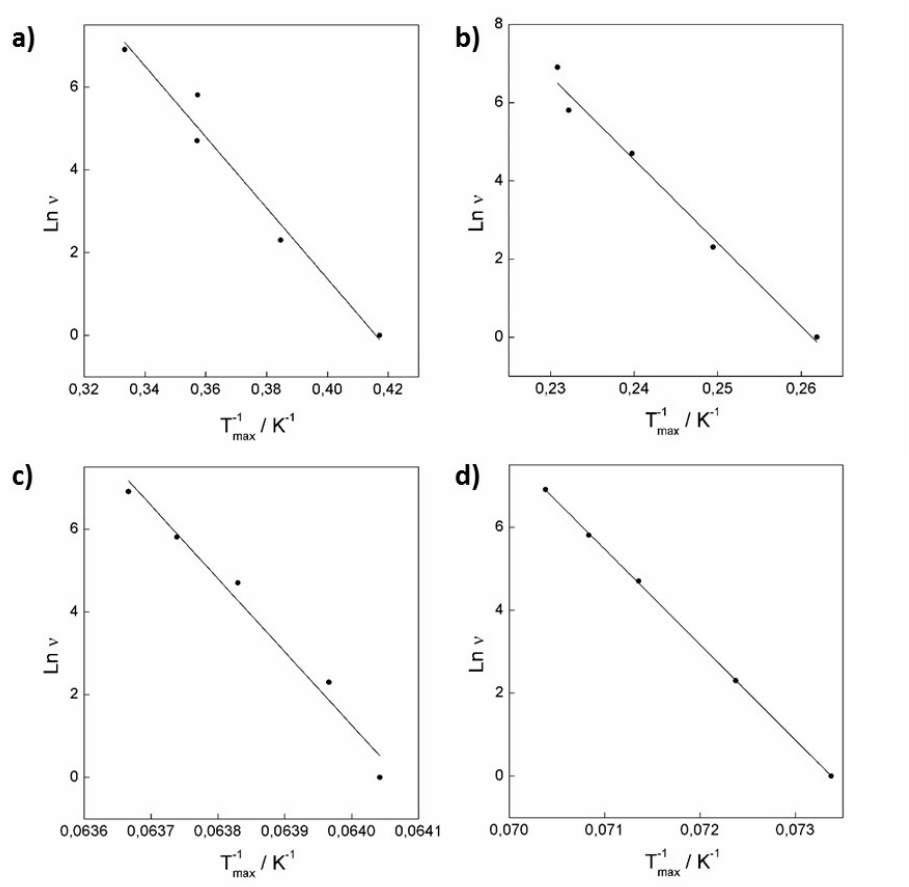

Article 3:

Deciphering the Role of Dipolar Interactions in Magnetic Layered Double Hydroxides

Inorganic Chemistry **2018**, *57*, 2013–2022

Inorganic Chemistry
Article
Cite This: Inorg. Chem. 2018, 57, 2013−2022
pubs.acs.org/IC

Deciphering the Role of Dipolar Interactions in Magnetic Layered Double Hydroxides

Jose A. Carrasco,[†,∥] Salvador Cardona-Serra,[†,∥] Juan Modesto Clemente-Juan,[†] Alejandro Gaita-Ariño,[*,†] Gonzalo Abellán,[*,†,§] and Eugenio Coronado[*,†]

[†]Instituto de Ciencia Molecular (ICMol), Universidad de Valencia, Catedrático José Beltrán 2, 46980, Paterna, Valencia, Spain
[§]Department of Chemistry and Pharmacy and Joint Institute of Advanced Materials and Processes (ZMP), University Erlangen-Nürnberg, Henkestr. 42, 91054 Erlangen and Dr.-Mack Str. 81, 90762 Fürth, Germany

Supporting Information

ABSTRACT: Layered double hydroxides (LDHs) exhibit unparalleled anion exchange properties and the ability to be exfoliated into 2D nanosheets, which can be used as a building block to fabricate a wide variety of hybrid functional nanostructured materials. Still, if one wants to use LDHs as a magnetic building blocks in the design of complex architectures, the role played by the dipolar magnetic interactions in these layered materials needs to be understood. In this work, we synthesized and characterized a five-membered CoAl-LDH series with basal spacing ranging from 7.5 to 34 Å. A detailed experimental characterization allows us to conclude that the main factor governing the dipolar interactions between magnetic layers cannot be the interlayer spacing. Supporting theoretical modeling suggests instead a relevant role for spin correlation size, which, in the limit, is related to the lateral dimension of the layer. These results highlight the importance of cation ordering in the magnetic behavior of LDHs, and underpin the differences with homometallic-layered hydroxides.

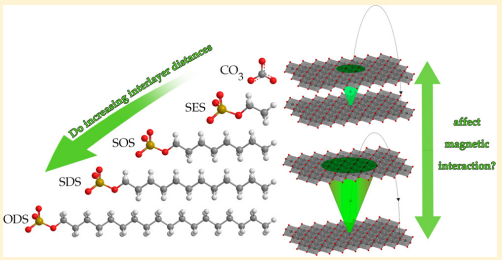

INTRODUCTION

The search for multifunctional materials is one of the most appealing topics in materials science.[1] Among the different strategies, the so-called hybrid approach stands as the most interesting route for the preparation of hybrids by combining organic/molecular and inorganic building blocks.[2−6] Beyond the coexistence of properties, which is nowadays almost standard, the development of hybrid stimuli-responsive materials has emerged, being a sophisticated tool to control the physical properties of a certain host at will.[7,8] Among the different available inorganic building blocks, layered metal hydroxides are outstanding candidates due to their chemical versatility and wide range of possible applications. Layered double hydroxides (LDHs) are a special class of anionic clays consisting of positively charged brucite-type inorganic layers interleaved with anions.[9,10] They can be formulated as $[M^{II}_{1-x}M^{III}_{x}(OH)_2]^{x+}$ $[A^{n-}]_{x/n}\cdot mH_2O$ (A^{n-} = organic or inorganic anions). They exhibit unparalleled anion exchange properties and a wide chemical versatility. One of their most interesting properties is the ability to be exfoliated into 2D nanosheets, which can be used as macromolecular building blocks in the design of more complex architectures, as they retain the properties of the pristine bulk precursor like redox behavior or 2D magnetism.[11] LDHs can be synthesized using first row paramagnetic transition metal ions that, in combination with the ability to confine guest molecules, originate a plethora of magnetic behaviors; however, dipolar effects have never been studied in detail. In brief, the magnetic properties of LDH and their hybrids are determined by two main contributions: the in-plane superexchange mechanism mediated by −OH bridges on the one hand, and the interplane weaker dipolar interactions on the other hand.[12,13] While the replacement of the diamagnetic Al(III) centers by paramagnetic cations provides a rich magnetic behavior due to the competition between ferro- (F) and antiferromagnetic (AF) interactions, the role of dipolar interactions is much less understood.[10] Indeed, we recently reported that, when a photoactive molecule is rigidly connected to two adjacent LDH layers, the magnetic properties change strongly as a consequence of the distortion induced within the layers when the hybrid material is irradiated. Still, one expects that, during this process, the dipolar interactions remain unchanged since the interlayer distances do not significantly change.[12] In contrast, when these linkers are only connected by one side to the LDH layers, these layers are not distorted and, as a consequence, there is only a slight change in the magnetic properties exclusively affected by dipolar interactions.[13]

While interlayer distances could be a straightforward path to control magnetic properties in layered materials,[14] the factors

Received: November 16, 2017
Published: February 8, 2018

DOI: 10.1021/acs.inorgchem.7b02928
Inorg. Chem. 2018, 57, 2013−2022

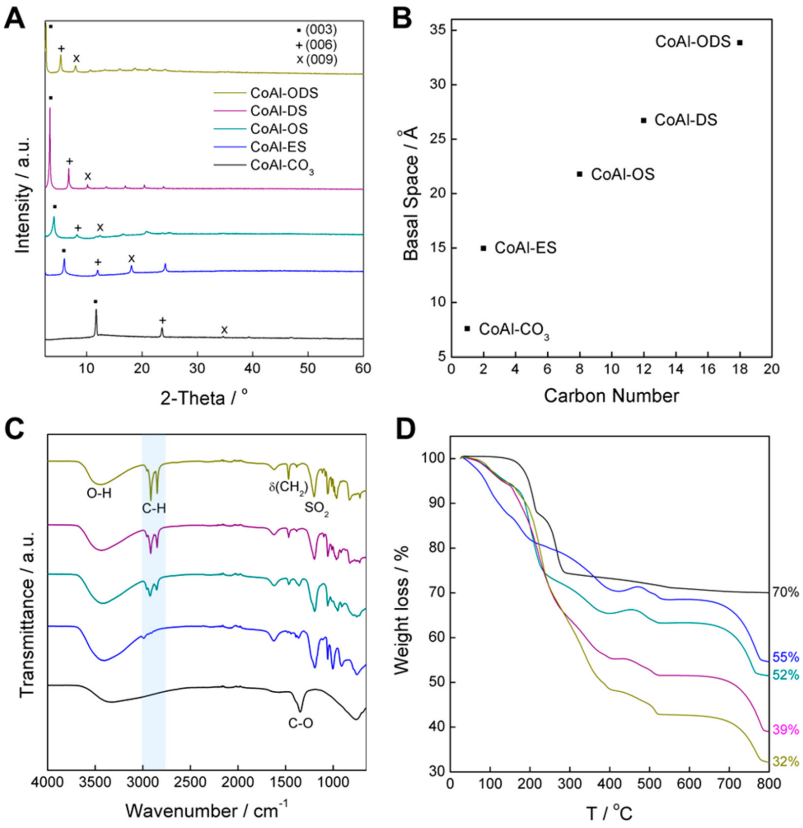

Figure 1. (A) XRPD patterns of the CoAl-LDHs in the 2−60° region. (B) Basal space versus carbon number. (C) FTIR spectra of the CoAl-LDH family in the absence of KBr pellet. Main vibrational bands are pointed out and alkyl bands associated with the surfactants are highlighted. (D) TGA in air for the synthesized samples, highlighting the total weight loss according to the anion intercalation.

governing dipolar interactions in LDH remain unclear for the scientific community despite some recent remarkable efforts.[15,16] Such an understanding and its relationship with the structural features of the layered material is a matter of utmost importance for designing stimuli-responsive systems. To fill this gap, herein we propose a combined experimental and theoretical study using as model system a highly crystalline CoAl−LDH with well-defined hexagonal shapes intercalated with a series of *n*-alkyl sulfates of different length (from 2 to 18). This allows us to modify the basal space (*BS*) in a wide range (from ca. 7.6 to 33.8 Å), while keeping the most simple magnetic scenario for LDHs, consisting of only one magnetic element (i.e., Co(II)). Thus, a systematic study of the influence of the dipolar interactions on the magnetism of LDHs can be performed, shedding light on their complex magnetic behavior and paving the way for tuning its magnetic properties at will.

EXPERIMENTAL SECTION

Chemicals. $CoCl_2{\cdot}6H_2O$, $AlCl_3{\cdot}6H_2O$, urea (CH_4N_2O), $NaNO_3$, sodium ethyl sulfate ($C_2H_5NaO_4S$), sodium octyl sulfate ($C_8H_{17}NaO_4S$), sodium dodecyl sulfate ($C_{12}H_{25}NaO_4S$), and sodium octadecyl sulfate ($C_{18}H_{37}NaO_4S$) were purchased from Sigma-Aldrich. Ethanol absolute was purchased from Panreac. All chemicals were used as received. Ultrapure water was obtained from a Millipore Milli-Q equipment.

Synthesis of CoAl-CO_3 LDH. Following the method described by Liu et al.,[17] in a typical procedure, 0.02 M of $CoCl_2{\cdot}6H_2O$, 0.01 M of $AlCl_3{\cdot}6H_2O$, and 0.07 M of urea were dissolved in 500 mL of Milli-Q water. The mixture was set under Ar atmosphere and magnetic stirring for 48 h at the refluxing temperature of 97 °C. Then, the mixture was filtered, washed with Milli-Q water and EtOH, and dried at room temperature. The resulting pink pale powder was grinded and collected as the final product.

Synthesis of CoAl-NO_3 LDH. 1.5 M of $NaNO_3$ and 0.005 M of HNO_3 were dissolved in 500 mL of Milli-Q water. Then, 500 mg of CoAl-CO_3 LDH was added to the mixture and the reaction was set under Ar atmosphere and magnetic stirring for 96 h. Finally, the mixture was filtered, washed with Milli-Q water and EtOH, and dried in a vacuum. The resulting pink pale powder was grinded and collected as the final product.

Synthesis of CoAl-ES and CoAl-OS LDHs. 90 mL of Milli-Q water was placed in a two-neck flask and set under Ar atmosphere and magnetic stirring at 50 °C. After 30 min, sodium ethyl sulfate or sodium octyl sulfate (SES or SOS, respectively) was added to the solution (0.03 M), followed by the addition of 200 mg of CoAl-NO_3 LDH right after the SES/SOS was completely dissolved. The reaction was kept for 48 h. Finally, the mixture was filtered, washed with Milli-

DOI: 10.1021/acs.inorgchem.7b02928
Inorg. Chem. 2018, 57, 2013−2022

Table 1. Compositional Information of the Studied CoAl-LDH Family[b]

sample	carbon number	basal space (Å)	molecular formula[a]	ratio Co:Al
CoAl-CO_3	–	7.59	$[Co_{0.67}^{2+}Al_{0.33}^{3+}(OH)_2]^{0.33+}(CO_3^{2-})_{0.17}\cdot 0.33\ H_2O$	2.03
CoAl-ES	2	14.96	$[Co_{0.67}^{2+}Al_{0.33}^{3+}(OH)_2]^{0.33+}(ES^-)_{0.33}\cdot 1.51\ H_2O$	2.03
CoAl-OS	8	21.76	$[Co_{0.66}^{2+}Al_{0.34}^{3+}(OH)_2]^{0.34+}(OS^-)_{0.34}\cdot 1.49\ H_2O$	1.94
CoAl-DS	12	26.68	$[Co_{0.66}^{2+}Al_{0.34}^{3+}(OH)_2]^{0.34+}(DS^-)_{0.34}\cdot 1.70\ H_2O$	1.94
CoAl-ODS	18	33.84	$[Co_{0.67}^{2+}Al_{0.33}^{3+}(OH)_2]^{0.33+}(ODS^-)_{0.33}\cdot 1.49\ H_2O$	2.03

[a]Molecular formula was estimated from the EDAX microanalysis alongside with TGA and elemental analysis results. [b]The alkyl-sufates used are ethyl sulfate (ES), octyl sulfate (OS), dodecyl sulfate (DS), and octadecyl sulfate (ODS).

Q water and EtOH, and dried in a vacuum. The resulting pink pale powder was grinded and collected as the final product.

Synthesis of CoAl-DS LDH. 50 mL of Milli-Q water was placed in a two-neck flask and set under Ar atmosphere and magnetic stirring at 50 °C. After 30 min, sodium dodecyl sulfate (SDS) was added to the solution (0.2 M), followed by the addition of 200 mg of CoAl-NO_3 LDH right after the SDS was completely dissolved. The reaction was kept for 12 h. Finally, the mixture was filtered, washed with Milli-Q water and EtOH, and dried in a vacuum. The resulting pink pale powder was grinded and collected as the final product.

Synthesis of CoAl-ODS LDH. 50 mL of Milli-Q water was placed in a two-neck flask and set under Ar atmosphere and magnetic stirring at 65 °C. After 30 min, octadecyl sodium sulfate (ODS) was added to the solution (0.01 M), followed by the addition of 200 mg of CoAl-NO_3 LDH right after the OSS was completely dissolved. The temperature was set at 50 °C. The reaction was kept for 12 h. Finally, the mixture was filtered, washed with Milli-Q water and EtOH, and dried in a vacuum. The resulting pink pale powder was grinded and collected as the final product.

Physical Characterization. X-ray powder diffraction (XRPD) patterns were obtained with a Bruker D8 Advance A25 using the copper radiation (Cu−Kα = 1.54178 Å) in the 2−40° region. Field emission scanning electron microscopy (FESEM) studies were carried out on a Hitachi S-4800 microscope at an accelerating voltage of 20 kV and 60 s of Au/Pd metallization of the samples. ATR Infrared spectra were collected in an Agilent Cary 630 FTIR spectrometer in the 4000−650 cm^{-1} range in absence of KBr pellets. Thermogravimetric analysis (TGA) of all samples was carried out in a Mettler Toledo TGA/SDTA 851 apparatus in the 25−800 °C temperature range at 10 °C·min^{-1} scan rate and an air flow of 30 mL·min^{-1}. Carbon, nitrogen, hydrogen, and sulfur contents were determined by microanalytical procedures by using a LECO CHNS. Magnetic data were collected over the bulk material with a Quantum Design superconducting quantum interference device (SQUID) MPMS-XL-5. The magnetic susceptibility of the samples was corrected considering the diamagnetic contributions of their atomic constituents as deduced from Pascal's constant tables and the sample holder. The dc data were obtained under an external applied field of 100 or 1000 Oe in the 2−300 K temperature range. Magnetization studies were performed between −5 and +5 T at a constant temperature of 2, 4, 6, 8, 12 or 30 K, depending on the sample. The ac data were collected under an applied field of 3.95 Oe at 997, 333, 110, 10, and 1 Hz.

RESULTS AND DISCUSSION

In order to have a material with a high crystallinity and well-defined morphology, we selected the CoAl-LDH prepared by a modified homogeneous precipitation method using urea as the ammonia-releasing reagent (ARR).[13] This LDH exhibits an excellent anion exchange capability, being possible to obtain the NO_3^- form under mild acid-salt treatment. By subsequent anion exchange of the nitrate form with four different *n*-alkyl-sulfate derivatives, we obtained a family of materials with an increasing number of carbon atoms: 2 for the ethyl (-ES), 8 for the octyl (-OS), 12 for the dodecyl (-DS), and 18 for the octadecyl (-ODS) form.[13,17] It is worth to highlight the importance of the synthetic conditions for each sample, since the synthesis for every surfactant-intercalated material requires some specific conditions. Moreover, to the best of our knowledge, the -ES and -ODS CoAl-LDH derivatives have never been reported so far. The complete characterization of the CoAl-NO_3 precursor can be found in the Supporting Information (Figure S10 and Table S2). X-ray powder diffraction (XRPD) patterns of the studied CoAl-LDH family exhibit the characteristic basal reflections observed in these class of materials, showing an excellent crystallinity for all of them and a concomitant shift toward lower 2-θ values as the length of the intercalated anion is increased.[18] The values of the observed *BS* varied from. 7.6 Å for the CoAl-CO_3 sample to 33.8 Å for the CoAl-ODS sample (Figure 1A and Table 1).[13,19] It is worth to mention that, for large surfactants like DS or ODS, there is an enhancement of the crystallinity, leading to better-defined crystallographic peaks, showing up to 10 basal reflections.[20−22] This effect is attributed to the stabilization during the synthesis of the LDH nanoplatelets thanks to the electrostatic interactions between the cationic sheets and the anionic polar head of the surfactant, whereas the hydrocarbonated apolar chain creates a micelle system in the reaction media.[23,24] The graphic correlation between basal space and 2-θ values can be found in Figure 1B.

FTIR spectra (Figure 1C) were collected to provide further information regarding the anionic intercalation. Among the different vibrational bands appearing in the spectra, it is interesting to highlight the C−H stretching doublet at ca. 2917 and 2845 cm^{-1}. This band is associated with the presence of the surfactant,[25] and gains intensity as the length of the molecule is increased. Concretely, methylene scissoring vibrational mode (2845 cm^{-1}) and sulfate asymmetric and symmetric stretching bands (1184 and 1050 cm^{-1}) can be clearly detected in the surfactant-intercalated compounds.[25] According to the model stated by Lagaly, we can expect a bilayer arrangement of the surfactants within the LDH sheets exhibiting tilt angles in the ca. 9−24° range.[26]

TGA and elemental analysis were carried out to gain further evidence of the successful exchange procedures. Figure 1D depicts the TGA patterns of the whole CoAl-LDH family (see Figure S1 for individual TGA/DTA plots). These TGA can be split out in two main segments including several processes:[27−29] First of all, a low-temperature weight loss between 25 and 220 °C associated with the removal of hydrated and intercalated (physisorbed) water molecules, followed by a second weight loss in the 220−600 °C range associated with the evaporation of the interlamellar (chemisorbed) water molecules and the dehydroxylation of the layers, as well as the decomposition of the organic molecule.[28,30] Interestingly, an increase in the final weight loss can be observed after the exchange of larger surfactant molecules, in accordance with the theoretical molecular formula. EDAX microanalysis was used to confirm the experimental ratio between Co and Al atoms (Co/Al ratio

DOI: 10.1021/acs.inorgchem.7b02928
Inorg. Chem. 2018, 57, 2013−2022

of 2). The structural information on all samples is summarized in Table 1. Comparison between calculated and experimental elemental analysis values can be found in Table S1, exhibiting excellent agreement.

In order to study the morphology of these materials and the influence of the successive anion exchange process in the shape and size of the crystals, we have used field-emission scanning electron microscopy (FESEM).[31,32] Figure 2 reveals that their

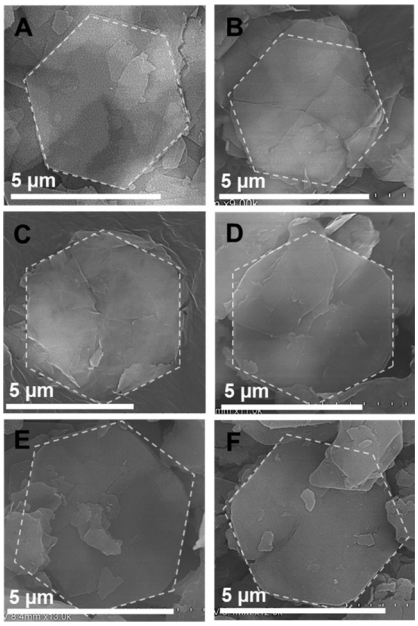

Figure 2. FESEM images of the CoAl-LDH family, highlighting that the hexagonal morphology is retained after the anionic exchange reaction. (A) CoAl-CO_3, (B) CoAl-NO_3, (C) CoAl-ES, (D) CoAl-OS, (E) CoAl-DS, and (F) CoAl-ODS.

well-defined hexagonal shape is maintained independent of the selected interlamellar anion. Figures S2 and S3 depict low-magnification FESEM images as well as a mapping analysis of CoAl-CO_3, respectively, to check the homogeneous distribution of Co and Al atoms throughout the layers.

Average lateral sizes and thicknesses values for all samples were also compared in Figure 3A,B, respectively. Whereas the lateral dimensions of the platelets remain constant in every case, an increase in the platelet thickness is observed as the carbon number of the sample is increased, from a minimum of ca. 120 nm for the carbonate sample to a maximum of ca. 250 nm for the octadecyl sample. This effect is clearly related to the continuous expanding of the LDH system with the inclusion of larger anions within their layered cationic sheets, confirming the topochemical reaction of intercalation, as previously reported by Ogawa et al.[13,33] Figure 3C depicts the chemical structure of the different surfactant molecules here studied.

An exhaustive magnetic study has been made on these CoAl-LDH intercalated compounds. The overall magnetism in this class of materials is controlled by two main contributions,[10] namely, magnetic superexchange interactions, which occur between neighboring metallic centers mediated by hydroxyl bridges (−OH) within each single layer (intralayer interaction), and dipolar magnetic interactions that take place between different layers (interlayer interaction). Because of the strong radial dependence of dipole−dipole interaction, one could expect the dipolar interactions to be intrinsically dependent on the distance between the cationic sheets in the global system; therefore, an increase in the spacing between the layers should affect the overall magnetism of the material. However, several parameters like particle size and morphology, flexibility of the layers, or cation clustering affect the magnetic behavior of LDHs as well. According to the reported studies, Al-containing−, NiMn− and NiCr−LDHs exhibit AF dipolar interactions, whereas NiFe−LDHs reveal dipolar interactions of ferromagnetic character.[10] This is in sharp contrast to the results reported for homometallic-layered hydroxides, in which the hydroxide layers are covalently connected to the interlamellar anions.[6,34,35] This strong bond seems to exert an important role in their interlayer magnetic interactions. In fact, for shorter interlayer distances of less than 1 nm, through-bond AF interactions appear, promoting metamagnetic behavior. On the other hand, for higher interlayer distances (>1 nm), dipolar F through-space interactions predominate, with a significant distance dependence between individual spins, likely proportional to BS^{-3}.[34,36−38,35] Concerning LDHs, only dipolar interactions should appear, due to the noncovalent connection between the layers and the anions. In this sense, related precedents reporting on the influence of *BS* on the overall magnetism exhibited disparate results. First, a family of subnanometric hybrid coprecipitated NiFe−LDHs, suggesting F dipolar interactions, in which the temperature for the spontaneous magnetization (T_M) and the coercivity decrease proportionally to BS^{-3}.[16] Still, the nature of the interlamellar anion could promote some divergences to this tendency, as observed for mononuclear macrocyclic-intercalated LDHs.[39−41] Second, a family of micrometric *n*-alkylsulfonates intercalated CoNi-LDHs with interlayer distances up to 22.41 Å, showing a variation in the coercive field with the basal space with no clear trend, and an increase for the maximum interlayer distances.

Herein, we will try to unveil how the system is affected by a continuous displacement of the layers in a unprecedented wide range due to the anion exchange of successive larger molecules (in the form of surfactants), keeping intact the metallic composition, lateral dimensions, and morphology of the crystals.

Table 2 summarizes all the experimental magnetic parameters calculated for the CoAl-LDH family. For the sake of clarity, only the magnetic graphs for the sample exhibiting the maximum *BS* value, CoAl-ODS, are included in the main text (Figure 4). The complete magnetic data of each sample can be found in Figures S5−S9 (CoAl-CO_3, CoAl-ES, CoAl-OS, and CoAl-DS) and Figure S11 (CoAl-NO_3).

The DC susceptibility measurements (Figure 4A) (χ_M) for the CoAl-ODS sample exhibit a continuous increase upon cooling down, which becomes very sharp at low *T* (below 20 K), reaching a maximum value of 2.63 emu·mol^{-1} at 2 K. In addition, the $\chi_M \cdot T$ product also increases, exhibiting a sharp peak in the low *T* range. Thus, the thermal variation of $\chi_M \cdot T$ slightly increases from a value of 2.48 emu·K·mol^{-1} at room temperature to a value of 2.60 emu·K·mol^{-1} at 70 K, followed by a sharp increase up to 8.03 emu·K·mol^{-1} at 4.6 K and a rapid decrease to 5.2 emu·K·mol^{-1} at 2 K. The inset of Figure 4A also presents the fitting of the inverse of the χ_M to a Curie−Weiss

DOI: 10.1021/acs.inorgchem.7b02928
Inorg. Chem. 2018, 57, 2013−2022

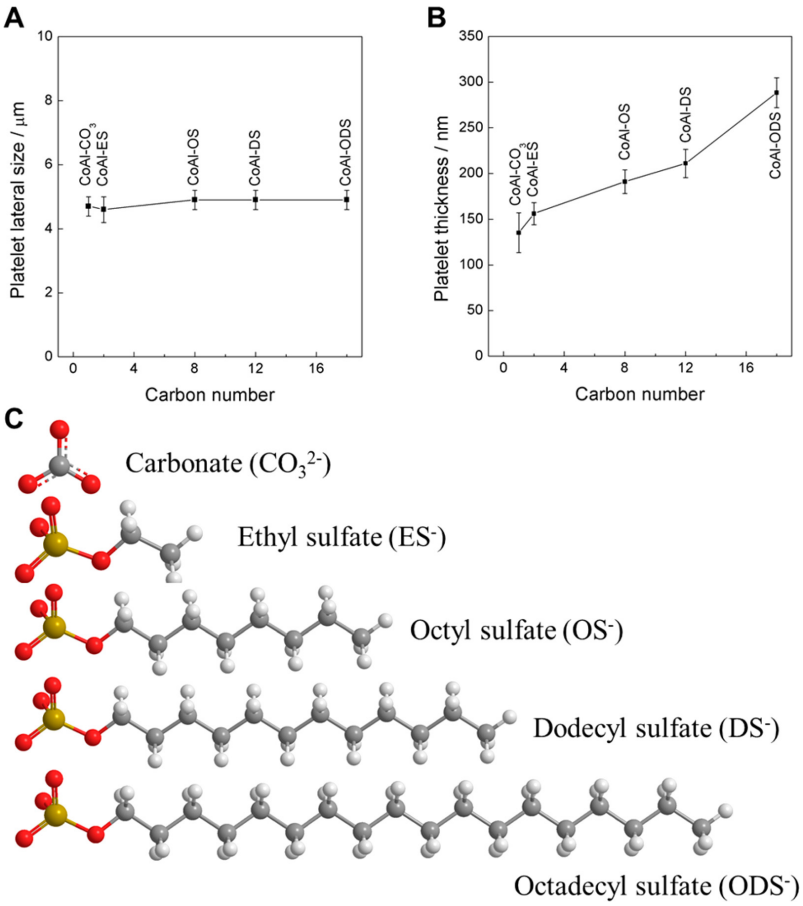

Figure 3. (A) Mean platelet lateral size with its standard deviation and (B) approximated platelet thickness values for every CoAl-LDH sample determined by FESEM. Individual histograms for each sample highlighting their lateral size distribution can be found in Figure S4. (C) Surfactant molecules used as separation bridges.

Table 2. Main Magnetic Data and Parameters for the Magnetic CoAl-LDHs[a]

sample	$\chi \cdot T_{RT}$ (emu·K·mol^{-1})	C_{SO} (emu·K·mol^{-1})	C (emu·K·mol^{-1})	θ (K)	T_B (K)	T_M (K)	M_S (μ_B)	H_c (Oe)
CoAl-CO_3	2.00	1.26	2.02	−0.04	2.81	4.80	1.26	13.66
CoAl-ES	2.48	1.26	2.49	4.04	2.35	5.41	1.56	20
CoAl-OS	2.48	1.24	2.49	−0.45	2.18	5.00	1.52	30
CoAl-DS	2.50	1.24	2.51	3.13	2.29	4.80	1.52	40
CoAl-ODS	2.48	1.26	2.47	−5.85	5.60	4.81	1.66	48

[a]From left to right: $\chi \cdot T_{RT}$ value at room temperature; expected spin-only value of the Curie constant (C_{so}); experimental Curie constant (C); Weiss constant (θ); temperature of the divergence of the ZFC and FC magnetic susceptibility (T_B); temperature for the onset of spontaneous magnetization extracted from the χ''_M plot (T_M); saturation magnetization (M_S); coercive field (H_C). $S(Co^{2+}) = 3/2$, $S(Al^{3+}) = 0$.

law above 50 K, resulting in a Curie constant (C) of 2.47 emu·K·mol^{-1}, higher than that expected for a spin-only value of a magnetically diluted combination of Co^{2+} ($S = 3/2$) and Al^{3+} ($S = 0$), and a small and negative value of the Weiss constant (θ). All of these results are consistent with the presence of dominant ferromagnetic interactions within the layers. In the present case, the weak negative value of θ does not seem to be due to the predominance of antiferromagnetic interactions but to the orbital contribution coming from octahedral Co(II).

In different samples, one observes no apparent correlation between the $\chi_M \cdot T$ vs T plots and the interlayer distance (see also Figures S5−S9). It is worth noting that, according to Table 2, θ does not show a linear trend with the increase of the anion allocated within the layers. Moreover, in the case of the sample

DOI: 10.1021/acs.inorgchem.7b02928
Inorg. Chem. 2018, 57, 2013−2022

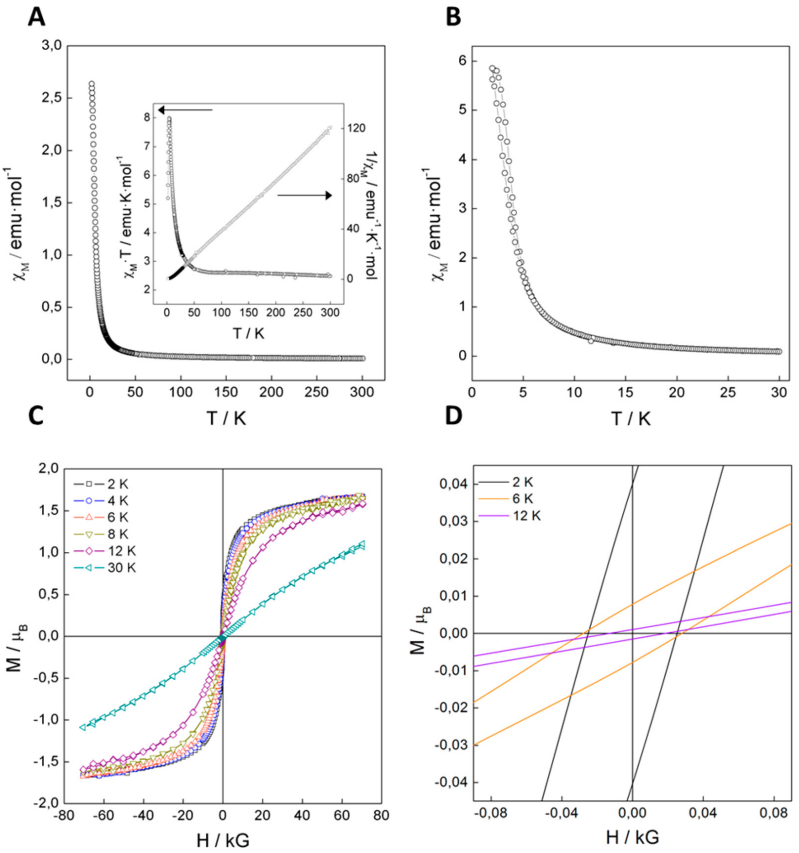

Figure 4. Magnetic properties of the CoAl-ODS sample: (A) χ_M vs T with an external applied field of 1000 Oe. The inset represents the temperature dependence of the $\chi_M \cdot T$ product and χ_M^{-1} vs T. (B) FC/ZFC with an external applied field of 100 Oe. (C) Magnetization curves at different temperatures. (D) Zoom of the low field region for 2, 6, and 12 K.

with the smallest interlamellar space (CoAl-CO_3), we also measured the field dependence of χ vs T between 100 and 5000 G to rule out any possible metamagnetic behavior (see Figure S6). This result clearly differentiates the LDH behavior to that of the monometallic hydroxides as pointed out previously.[18,35]

For the CoAl-ODS sample, field-cooled and zero-field-cooled (FC/ZFC) data (Figure 4B) allow us to extract a value for blocking temperature of 5.60 K, which is the highest value of the family. A hysteresis loop was recorded at different temperatures (Figure 4C), depicting spontaneous magnetization at low temperatures with a value of 48 Oe at 2 K (Figure 4D), which is also the highest value of the family. Interestingly, a clear trend was observed for the values of coercive field (H_C), which increase with the basal space. The relative low values (ca. 10−50 Oe) are indicative of soft magnets, and are far from other LDHs with hard magnetic behavior (>1000 Oe as H_C).[10,18] In addition, we have studied the influence of the temperature on the presence of hysteretic behavior in the magnetization vs field plot for the CoAl-ODS sample (Figure 4C,D). Below the blocking temperature (T_B = 5.6 K), the curves can be superimposed, exhibiting the same coercive field. Above this value, a progressive decrease in the coercive field and the remnant magnetization can be measured.[42−44] In sum, experimentally we have a somewhat puzzling situation in which a systematic increase in the interlayer spacing does not afford a clear dependence of the magnetic behavior, except for the coercive field.

To complement this study from the theoretical point of view, we have proposed two approaches to understand the correlation (if any) between the static magnetic behavior and the interlayer distance: (i) a semiempirical fitting of the experimental magnetic susceptibility with an anisotropic spin Hamiltonian including an effective interlayer coupling parameter between minimal hexagonal networks, and (ii) a purely theoretical study which considers the magnetic dipolar interaction along a range of interlayer distances and magnetic domain sizes. We make no attempt to reproduce the dynamic magnetic behavior. Even so, because of the enormous magnetic complexity of these systems and the limited experimental data available, theoretical models are necessarily oversimplifications which may have limited validity. Thus, we include here only a summary and collection of the most robust conclusions, with all

DOI: 10.1021/acs.inorgchem.7b02928
Inorg. Chem. 2018, 57, 2013−2022

details being available in the SI sections and Figures S13–S16 for the semiempirical fitting model and Figures S17 and S18 for the dipolar layer study.

Satisfactory fittings of the thermal dependences of the magnetic susceptibility were obtained using the first previously mentioned semiempirical model (see Figure S13). A minimal six-member network was used to model each layer since larger models were either inadequate for symmetry reasons or unsolvable for computational reasons (see Figure S14). The Hamiltonian considers anisotropic exchange between effective spin Kramers doublets (allowing $J_z \neq J_{xy}$), an effective interlayer coupling, and a Zeeman term, also allowing $g_z \neq g_{xy}$ (see Figure S15 for the complete fitting set and Table S6 for the parameters obtained on each case). Fittings with a smaller number of degrees of freedom were attempted but were not successful (see Figure S16). While overparametrization impedes extracting fine details of these fits, a few main trends seem stable among different fitting attempts, namely, (i) the Co(II) ions, which are here in a very axially distorted environment, behave as Ising spins, (ii) Co(II)-O-Co(II) superexchange interactions are in the usual range reported for oxo-bridged complexes of similar geometries, and (iii) the interlayer exchange interaction is 2 orders of magnitude weaker compared with the superexchange interaction.

Furthermore, we used a completely different approach based on purely dipolar interactions. In this case, we estimate the interaction between two ferromagnetic monolayers, with each layer containing between 25 and 10^6 spins (rather than just 6). Within this approach, we get some general understanding about the importance of dipolar interactions in LDHs and correlate them with the information obtained in the previous model (see Figures S17 and S18). The numerical results for a wide window of interlayer distances and spin correlation sizes are summarized in Figure 5. One observes that the dipolar

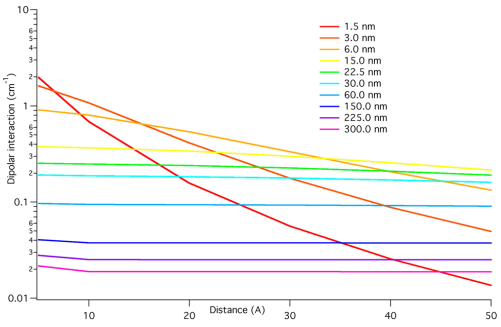

Figure 5. Dipolar interaction variation with the interlayer distance and the spin correlation size on each layer.

interactions vary very little with the interlayer distance for spin correlation sizes above 15 nm. Only when these spin correlation sizes become really small does the interlayer distance need to be taken into account. The first qualitative conclusion is the fact that the factor governing dipolar interaction between magnetic layers is the layer size or, for more realistic multidomain layers, the domain size; only for tiny domain sizes (or high cation disorder) does the interlayer distance play a dominant role. The second main conclusion is that, for single-domain layers, increasing distances cannot change the sign of the dipolar magnetic coupling; this possibly changes for multidomain layers. These results suggest that highly disordered layers showing cation clustering will be significantly affected by dipolar interactions. Furthermore, submicrometric LDH particles like those typically obtained through coprecipitation routes or using reverse microemulsion approaches will be more susceptible to suffer a stronger dipolar influence. This is supported by previous reports on carbonate-intercalated CoAl-LDH (basal space: 7.59 Å) of ca. 15 nm in lateral dimensions synthesized through coprecipitation, which exhibit ordering temperatures of ca. 6 K, T_{irr} of 5.7 K, and coercive fields of ca. 55 Oe.[45] Moreover, the introduction of two magnetic cations within the layers (e.g., NiFe- or NiCo-LDHs) will lead to competing intralayer magnetic interactions and cation clustering as previously reported by our group,[18] resulting in a more complex behavior in which, presumably, dipolar interactions will play a key role.

Additionally, we have also performed AC dynamic susceptibility measurements in the presence of an applied field of 3.95 Oe in the 1–10 000 Hz frequency range. The results confirm a cooperative magnetic behavior in all the samples, as seen in Figure 6 and Figures S5–S9 and S11. Both

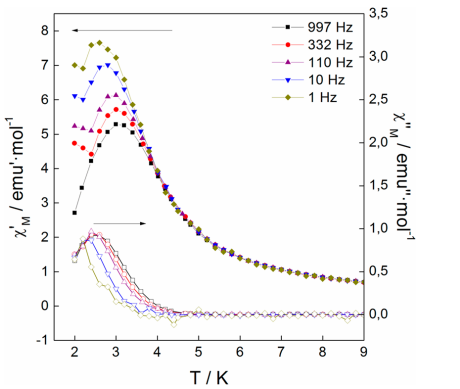

Figure 6. CoAl-ODS sample: Thermal dependence of the χ'_M (in-phase) and χ''_M (out-of-phase) signals at 1, 10, 110, 332, and 997 Hz.

the in-phase (χ'_M) and the out-of-phase signals (χ''_M) display defined peaks at low temperatures exhibiting frequency dependence. From the out-of-phase signal, one can deduce the temperature for the onset for the spontaneous magnetization (T_M), defined as the point where $\chi''_M \neq 0$. All the values fall in the 4.8–5.4 K range, as expected for this sort of CoAl-LDH. This small variation in T_M indicates that the dominant factor controlling the cooperative behavior is not the interlayer distance. For the CoAl-ODS, $T_M \approx 4.8$ K, which is not the highest value ($T_M \approx 5.4$ K in CoAl-ES). The frequency dependence in this sort of materials is related to its intrinsically disordered nature and glassy behavior.[18,46,47] We have confirmed the spin-glass nature of these compounds by extracting the frequency-shift parameter (also known as the Mydosh parameter ϕ) from the out-of-phase signal.[48]

$$\Phi = \Delta T_{max}/[T_{max}\Delta(\log \upsilon)] \quad (1)$$

DOI: 10.1021/acs.inorgchem.7b02928
Inorg. Chem. 2018, 57, 2013–2022

We have found $\phi < 0.1$ for all the samples, in good agreement with that reported for related hybrid CoAl-LDHs and spin-glass-like materials previously reported.[12,43,48,49]

Last, but not least, and in order to further validate our results, we have synthesized nanometric alkoxide-intercalated CoAl-LDH by following our previously reported methanolic route (CoAl-OMe).[28,30] These preliminary results exhibit the highest coercive field (80 Oe) and T_M values (8.3 K) of the series, thus suggesting a much more intense influence of the dipolar interactions than in their micrometric counterparts, in excellent accordance with our experiments and calculations (see Figure S12). Overall, the main conclusion from the magnetic properties is that, for ferromagnetic LDHs having only one magnetic metal, the influence of dipolar interactions is very small unless the lateral dimensions of the layers are a few nanometers. Furthermore, in these limit cases, several aspects for the magnetic responses are also dependent on the size of the nanoplatelets.[28,30,43] On the other hand, the presence of two magnetic cations within the layers lead to competing magnetic interactions, spin frustration, and smaller correlation domains, resulting in a bigger influence of the dipolar interactions, as previously observed for NiFe- and CoNi-LDHs.[15,16,18,41] In the future, the influence of the size effect on the magnetic properties of these layered materials will be fully developed and analyzed in a separate study to check if the expected predictions are fulfilled for all kinds of LDHs.

CONCLUSIONS

A family of highly crystalline, hexagonal-shaped hybrid CoAl-LDH with increasing basal spacing up to 34 Å has been synthesized, in order to investigate the role exerted by the dipolar interactions in their overall magnetic behavior. The successful anion exchange reactions of the different surfactants in the interlayer space of the LDH system has been demonstrated by means of XRPD, FTIR, or TGA analysis. The hexagonal morphology and platelet sizes are kept in every member of the CoAl-LDH family. Magnetometry evidenced a markedly different behavior compared to homometallic layered hydroxides. Conversely to what could be expected from a naive point of view, the study revealed that an increase in the interlayer distance has a very weak influence on the dipolar interaction, with both the static magnetic properties and the cooperative behavior observed in these materials being largely unaffected. These experimental conclusions were supported by simple theoretical models that indicate that the main governing parameter for the dipolar interaction between ferromagnetic single-domain monolayers is the lateral dimension of the layer, with the interlayer spacing having a minor effect. For the design of magnetic LDHs, this suggests that a more effective strategy could be playing with the particle size—which limits the maximum domain size—and/or with competing intralayer magnetic interactions and cation clustering, which could also result in smaller magnetic domains.

ASSOCIATED CONTENT

Supporting Information

The Supporting Information is available free of charge on the ACS Publications website at DOI: 10.1021/acs.inorgchem.7b02928.

Additional characterization of the CoAl-LDH samples including TG, EA, FESEM, EDX, and magnetic measurements, as well as complete physical characterization of the CoAl-NO_3 sample. Additional theoretical calculations information (PDF)

AUTHOR INFORMATION

Corresponding Authors

*E-mail: gaita@uv.es (A.G.-A.).
*E-mail: gonzalo.abellan@fau.de (G.A.).
*E-mail: eugenio.coronado@uv.es (E.C.).

ORCID

Salvador Cardona-Serra: 0000-0002-5328-7047
Juan Modesto Clemente-Juan: 0000-0002-3198-073X
Alejandro Gaita-Ariño: 0000-0002-1600-8627
Gonzalo Abellán: 0000-0003-1564-6210

Author Contributions

‖These authors contributed equally to this work.

Notes

The authors declare no competing financial interest.

ACKNOWLEDGMENTS

The research reported here was supported by the Spanish MINECO (grants MAT 2017-89993-R, CTQ 2017-89528-P, and Excellence Unit María de Maeztu MDM-2015-0538), the European Union (ERCCoG DECRESIM 647301, and COST 15128 Molecular Spintronics Project) and the Generalitat Valenciana (Prometeo Program of Excellence). A.G.-A. thanks the Spanish MINECO for a Ramón y Cajal Fellowship. J.A.C. thanks the Universidad de Valencia for a predoctoral grant. S.C.-S. thanks the Universitat de Valencia for an 'Atracción del talento' postdoctoral grant. G.A. thanks the FAU for the Emerging Talents Initiative (ETI) grant #WS16-17_Nat_04 as well as support by the Deutsche Forschungsgemeinschaft (DFG) and FLAG-ERA (AB 694/2-1).

REFERENCES

(1) *Functional Hybrid Materials*; Gómez-Romero, P., Sanchez, C., Eds.; Wiley-VCH: Weinheim, 2004.
(2) Ma, W.; Ma, R.; Wang, C.; Liang, J.; Liu, X.; Zhou, K.; Sasaki, T. A Superlattice of Alternately Stacked Ni−Fe Hydroxide Nanosheets and Graphene for Efficient Splitting of Water. *ACS Nano* **2015**, *9*, 1977−1984.
(3) Sanchez, C.; Julián, B.; Belleville, P.; Popall, M. Applications of Hybrid Organic−inorganic Nanocomposites. *J. Mater. Chem.* **2005**, *15*, 3559−3592.
(4) Delahaye, É.; Eyele-Mezui, S.; Bardeau, J.-F.; Leuvrey, C.; Mager, L.; Rabu, P.; Rogez, G. New Layered Organic-Inorganic Magnets Incorporating Azo Dyes. *J. Mater. Chem.* **2009**, *19*, 6106−6115.
(5) Laget, V.; Hornick, C.; Rabu, P.; Drillon, M.; Ziessel, R. Molecular Magnets. *Coord. Chem. Rev.* **1998**, *178−180*, 1533−1553.
(6) Rabu, P.; Drillon, M. Layered Organic−Inorganic Materials: A Way towards Controllable Magnetism. *Adv. Eng. Mater.* **2003**, *5*, 189−210.
(7) Clemente-León, M.; Coronado, E.; Martí-Gastaldo, C.; Romero, F. M. Multifunctionality in Hybrid Magnetic Materials Based on Bimetallic Oxalate Complexes. *Chem. Soc. Rev.* **2011**, *40*, 473−497.
(8) Coronado, E.; Mínguez Espallargas, G. Dynamic Magnetic MOFs. *Chem. Soc. Rev.* **2013**, *42*, 1525−1539.
(9) Rives, V. *Layered Double Hydroxides: Present and Future*; Nova Science Publishers: New York, 2001.
(10) Abellán, G.; Martí-Gastaldo, C.; Ribera, A.; Coronado, E. Hybrid Materials Based on Magnetic Layered Double Hydroxides: A Molecular Perspective. *Acc. Chem. Res.* **2015**, *48*, 1601−1611.
(11) Wang, Q.; O'Hare, D. Recent Advances in the Synthesis and Application of Layered Double Hydroxide (LDH) Nanosheets. *Chem. Rev.* **2012**, *112*, 4124−4155.

(12) Abellán, G.; Coronado, E.; Martí-Gastaldo, C.; Ribera, A.; Jordá, J. L.; García, H. Photo-Switching in a Hybrid Material Made of Magnetic Layered Double Hydroxides Intercalated with Azobenzene Molecules. *Adv. Mater.* **2014**, *26*, 4156−4162.
(13) Abellán, G.; Jordá, J. L.; Atienzar, P.; Varela, M.; Jaafar, M.; Gómez-Herrero, J.; Zamora, F.; Ribera, A.; García, H.; Coronado, E. Stimuli-Responsive Hybrid Materials: Breathing in Magnetic Layered Double Hydroxides Induced by a Thermoresponsive Molecule. *Chem. Sci.* **2015**, *6*, 1949−1958.
(14) Monteiro, B.; Coutinho, J. T.; Pereira, C. C. L.; Pereira, L. C. J.; Marçalo, J.; Almeida, M.; Baldoví, J. J.; Coronado, E.; Gaita-Ariño, A. Magnetic Properties of the Layered Lanthanide Hydroxide Series $Y_xDy_{8-x}(OH)_{20}Cl_4 \cdot 6H_2O$: From Single Ion Magnets to 2D and 3D Interaction Effects. *Inorg. Chem.* **2015**, *54*, 1949−1957.
(15) Zhang, C.; Tsuboi, T.; Namba, H.; Einaga, Y.; Yamamoto, T. Enhancement of the Coercivity in Co−Ni Layered Double Hydroxides by Increasing Basal Spacing. *Dalton Trans* **2016**, *45*, 13324−13331.
(16) Coronado, E.; Galán-Mascarós, J. R.; Martí-Gastaldo, C.; Ribera, A.; Palacios, E.; Castro, M.; Burriel, R. Spontaneous Magnetization in Ni−Al and Ni−Fe Layered Double Hydroxides. *Inorg. Chem.* **2008**, *47*, 9103−9110.
(17) Liu, Z.; Ma, R.; Osada, M.; Iyi, N.; Ebina, Y.; Takada, K.; Sasaki, T. Synthesis, Anion Exchange, and Delamination of Co−Al Layered Double Hydroxide: Assembly of the Exfoliated Nanosheet/Polyanion Composite Films and Magneto-Optical Studies. *J. Am. Chem. Soc.* **2006**, *128*, 4872−4880.
(18) Abellán, G.; Coronado, E.; Martí-Gastaldo, C.; Waerenborgh, J.; Ribera, A. Interplay between Chemical Composition and Cation Ordering in the Magnetism of Ni/Fe Layered Double Hydroxides. *Inorg. Chem.* **2013**, *52*, 10147−10157.
(19) Ahmed, A. A. A.; Talib, Z. A.; Hussein, M. Z. Influence of Sodium Dodecyl Sulfate Concentration on the Photocatalytic Activity and Dielectric Properties of Intercalated Sodium Dodecyl Sulfate into Zn−Cd−Al Layered Double Hydroxide. *Mater. Res. Bull.* **2015**, *62*, 122−131.
(20) Yang, T.; Xia, D.; Chen, G.; Chen, Y. Influence of the Surfactant and Temperature on the Morphology and Physico-Chemical Properties of Hydrothermally Synthesized Composite Oxide BiVO4. *Mater. Chem. Phys.* **2009**, *114*, 69−72.
(21) Lee, J. W.; Choi, W. C.; Kim, J.-D. Size-Controlled Layered Zinc Hydroxide Intercalated with Dodecyl Sulfate: Effect of Alcohol Type on Dodecyl Sulfate Template. *CrystEngComm* **2010**, *12*, 3249−3254.
(22) Yin, H. Y.; Wang, L.; Sun, Y. F.; Shi, D. J.; Wang, X. X. Enhancement of Crystalization and Photocatalysis of Bi_2MoO_6 Nanoplates by SDS Assisted Hydrothermal Method. *Adv. Mater. Res.* **2011**, *233*−*235*, 2091−2097.
(23) Mazlan, N. A.; Osman, N.; Md Jani, A. M.; Yaakob, M. H. Role of Ionic and Nonionic Surfactant on the Phase Formation and Morphology of Ba(Ce,Zr)O3 Solid Solution. *J. Sol-Gel Sci. Technol.* **2016**, *78*, 50−59.
(24) Wang, C. J.; Wu, Y. A.; Jacobs, R. M. J.; Warner, J. H.; Williams, G. R.; O'Hare, D. Reverse Micelle Synthesis of Co−Al LDHs: Control of Particle Size and Magnetic Properties. *Chem. Mater.* **2011**, *23*, 171−180.
(25) Viana, R. B.; da Silva, A. B. F.; Pimentel, A. S. Infrared Spectroscopy of Anionic, Cationic, and Zwitterionic Surfactants. *Adv. Phys. Chem.* **2012**, *2012*, 1−14.
(26) Meyn, M.; Beneke, K.; Lagaly, G. Anion-Exchange Reactions of Hydroxy Double Salts. *Inorg. Chem.* **1993**, *32*, 1209−1215.
(27) Zhang, J.; Xu, Y. F.; Qian, G.; Xu, Z. P.; Chen, C.; Liu, Q. Reinvestigation of Dehydration and Dehydroxylation of Hydrotalcite-like Compounds through Combined TG-DTA-MS Analyses. *J. Phys. Chem. C* **2010**, *114*, 10768−10774.
(28) Carrasco, J. A.; Romero, J.; Varela, M.; Hauke, F.; Abellán, G.; Hirsch, A.; Coronado, E. Alkoxide-Intercalated NiFe-Layered Double Hydroxides Magnetic Nanosheets as Efficient Water Oxidation Electrocatalysts. *Inorg. Chem. Front.* **2016**, *3*, 478−487.
(29) Zhang, J.; Yang, Z.; Qiu, J.; Lee, H.-W. Design and Synthesis of Nitrogen and Sulfur Co-Doped Porous Carbon via Two-Dimensional Interlayer Confinement for a High-Performance Anode Material for Lithium-Ion Batteries. *J. Mater. Chem. A* **2016**, *4*, 5802−5809.
(30) Abellán, G.; Carrasco, J. A.; Coronado, E.; Romero, J.; Varela, M. Alkoxide-Intercalated CoFe-Layered Double Hydroxides as Precursors of Colloidal Nanosheet Suspensions: Structural, Magnetic and Electrochemical Properties. *J. Mater. Chem. C* **2014**, *2*, 3723−3731.
(31) Abellán, G.; Coronado, E.; Martí-Gastaldo, C.; Pinilla-Cienfuegos, E.; Ribera, A. Hexagonal Nanosheets from the Exfoliation of Ni^{2+}-Fe^{3+} LDHs: A Route towards Layered Multifunctional Materials. *J. Mater. Chem.* **2010**, *20*, 7451−7455.
(32) Okamoto, K.; Iyi, N.; Sasaki, T. Factors Affecting the Crystal Size of the MgAl-LDH (Layered Double Hydroxide) Prepared by Using Ammonia-Releasing Reagents. *Appl. Clay Sci.* **2007**, *37*, 23−31.
(33) Ogawa, M.; Hiramine, M. Direct Correlation between Nanostructure and Particle Morphology during Intercalation. *Cryst. Growth Des.* **2014**, *14*, 1516−1519.
(34) Laget, V.; Hornick, C.; Rabu, P.; Drillon, M. Hybrid Organic-Inorganic Layered Compounds Prepared by Anion Exchange Reaction: Correlation between Structure and Magnetic Properties. *J. Mater. Chem.* **1999**, *9*, 169−174.
(35) Rabu, P.; Delahaye, E.; Rogez, G. Hybrid Interfaces in Layered Hydroxides: Magnetic and Multifunctional Superstructures by Design. *Nanotechnol. Rev.* **2015**, *4*, 557−580.
(36) Rogez, G.; Massobrio, C.; Rabu, P.; Drillon, M. Layered Hydroxide Hybrid Nanostructures: A Route to Multifunctionality. *Chem. Soc. Rev.* **2011**, *40*, 1031−1058.
(37) Rall, J. D.; Seehra, M. S. The Nature of the Magnetism in Quasi-2D Layered α-Ni(OH)2. *J. Phys.: Condens. Matter* **2012**, *24*, 076002.
(38) Seehra, M. S.; Singh, V. Magnetic Ordering of Nickel Hydroxide Layers 30 Å Apart Obtained by Intercalating Dodecyl Sulfate. *J. Phys.: Condens. Matter* **2013**, *25*, 356001.
(39) Abellán, G.; Busolo, F.; Coronado, E.; Martí-Gastaldo, C.; Ribera, A. Hybrid Magnetic Multilayers by Intercalation of Cu(II) Phthalocyanine in LDH Hosts. *J. Phys. Chem. C* **2012**, *116*, 15756−15764.
(40) Layrac, G.; Tichit, D.; Larionova, J.; Guari, Y.; Guérin, C. Controlled Growth of Cyano-Bridged Coordination Polymers into Layered Double Hydroxides. *J. Phys. Chem. C* **2011**, *115*, 3263−3271.
(41) Abellán, G.; Coronado, E.; Gómez-García, C. J.; Martí-Gastaldo, C.; Ribera, A. Intercalation of Cobalt(II)-Tetraphenylporphine Tetrasulfonate Complex in Magnetic NiFe-Layered Double Hydroxide. *Polyhedron* **2013**, *52*, 216−221.
(42) Kobayashi, Y.; Ke, X.; Hata, H.; Schiffer, P.; Mallouk, T. E. Soft Chemical Conversion of Layered Double Hydroxides to Superparamagnetic Spinel Platelets. *Chem. Mater.* **2008**, *20*, 2374−2381.
(43) Wang, C. J.; Wu, Y. A.; Jacobs, R. M. J.; Warner, J. H.; Williams, G. R.; O'Hare, D. Reverse Micelle Synthesis of Co−Al LDHs: Control of Particle Size and Magnetic Properties. *Chem. Mater.* **2011**, *23*, 171−180.
(44) Abellán, G.; Carrasco, J. A.; Coronado, E. Room Temperature Magnetism in Layered Double Hydroxides Due to Magnetic Nanoparticles. *Inorg. Chem.* **2013**, *52*, 7828−7830.
(45) Pérez-Ramírez, J.; Ribera, A.; Kapteijn, F.; Coronado, E.; Gómez-García, C. J. Magnetic Properties of Co-Al, Ni-Al, and Mg-Al Hydrotalcites and the Oxides Formed upon Their Thermal Decomposition. *J. Mater. Chem.* **2002**, *12*, 2370−2375.
(46) Cadars, S.; Layrac, G.; Gérardin, C.; Deschamps, M.; Yates, J. R.; Tichit, D.; Massiot, D. Identification and Quantification of Defects in the Cation Ordering in Mg/Al Layered Double Hydroxides. *Chem. Mater.* **2011**, *23*, 2821−2831.
(47) Pushparaj, S. S. C.; Forano, C.; Prevot, V.; Lipton, A. S.; Rees, G. J.; Hanna, J. V.; Nielsen, U. G. How the Method of Synthesis Governs the Local and Global Structure of Zinc Aluminum Layered Double Hydroxides. *J. Phys. Chem. C* **2015**, *119*, 27695−27707.
(48) Mydosh, J. A. *Spin Glasses: An Experimental Introduction*; Taylor & Francis: London, 1993.
(49) Tanaka, N.; Okazawa, A.; Sugahara, A.; Kojima, N. Development of a Photoresponsive Organic−Inorganic Hybrid Magnet:

DOI: 10.1021/acs.inorgchem.7b02928
Inorg. Chem. 2018, 57, 2013−2022

Layered Cobalt Hydroxides Intercalated with Spiropyran Anions. *Bull. Chem. Soc. Jpn.* **2015**, *88*, 1150−1155.

DOI: 10.1021/acs.inorgchem.7b02928
Inorg. Chem. 2018, 57, 2013−2022

Supplementary Information

Deciphering the Role of Dipolar Interactions in Magnetic Layered Double Hydroxides

Jose A. Carrasco,[a,†] Salvador Cardona-Serra,[a,†] Juan Modesto Clemente-Juan,[a] Alejandro Gaita-Ariño,[a,*] Gonzalo Abellán,[a,b,*] and Eugenio Coronado[a,*]

[a] *Instituto de Ciencia Molecular (ICMol), Universidad de Valencia, Catedrático José Beltrán 2, 46980, Paterna, Valencia, Spain.*

[b] *Department of Chemistry and Pharmacy and Joint Institute of Advanced Materials and Processes (ZMP), University Erlangen-Nürnberg, Henkestr. 42, 91054 Erlangen and Dr.-Mack Str. 81, 90762 Fürth, Germany.*

[†] These authors contributed equally to this work.

Corresponding authors: Alejandro Gaita-Ariño (gaita@uv.es), Gonzalo Abellán (gonzalo.abellan@fau.de) and Eugenio Coronado (eugenio.coronado@uv.es).

Contents

Section III. References.

Section I. Additional experimental data.

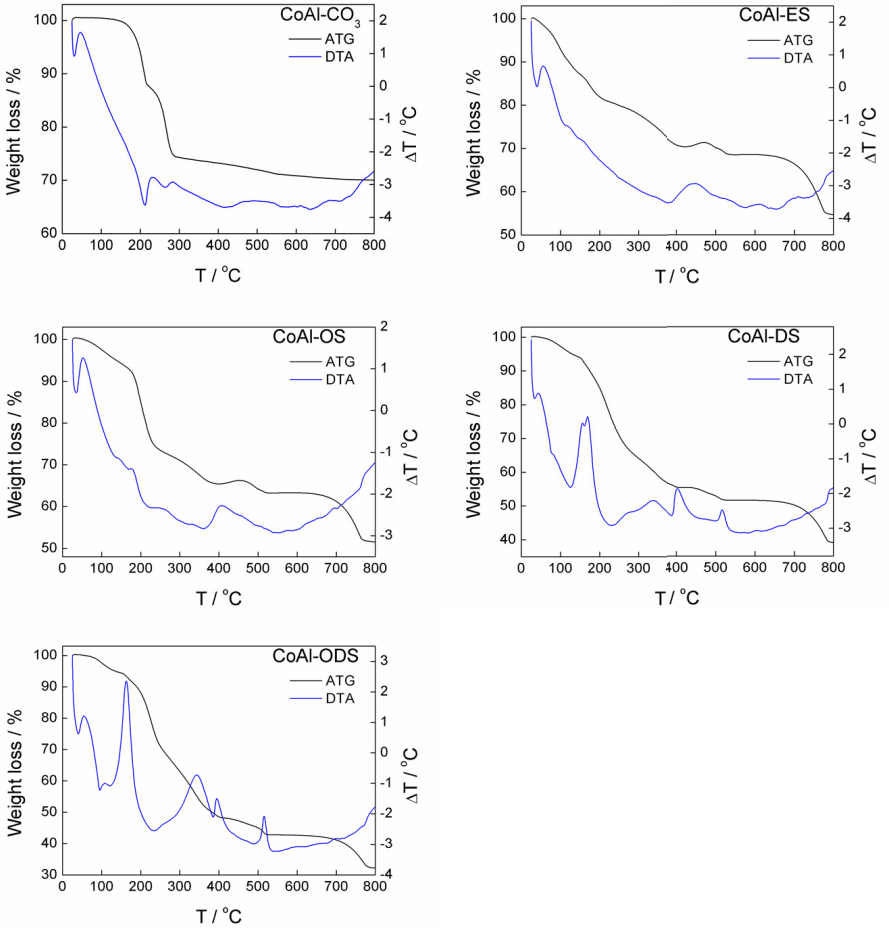

Figure S1. Thermogravimetric analysis for the as-synthesized CoAl-LDH family.

Table S1. Comparison between calculated and experimental elemental analysis

Sample	Molecular formula	C_{found}	H_{found}	N_{found}	S_{found}	$C_{calculated}$	$H_{calculated}$	$N_{calculated}$	$S_{calculated}$
CoAl-CO_3	$[Co_{0,67}^{2+}Al_{0,33}^{3+}(OH)_2]^{0,33+}(CO_3^{2-})_{0,17}\cdot 0.33\ H_2O$	1.98	2.58	0.15	0.12	2.03	2.70	0.00	0.00
CoAl-ES	$[Co_{0,67}^{2+}Al_{0,33}^{3+}(OH)_2]^{0,33+}(ES^-)_{0,33}\cdot 1.51\ H_2O$	5.18	4.12	0.21	6.31	5.22	4.64	0.00	6.96
CoAl-OS	$[Co_{0,66}^{2+}Al_{0,34}^{3+}(OH)_2]^{0,34+}(OS^-)_{0,34}\cdot 1.49\ H_2O$	17.23	5.86	0.15	5.48	17.95	5.96	0.00	5.98
CoAl-DS	$[Co_{0,66}^{2+}Al_{0,34}^{3+}(OH)_2]^{0,34+}(DS^-)_{0,34}\cdot 1.70\ H_2O$	25.49	6.29	0.16	5.18	24.32	6.87	0.00	5.40
CoAl-ODS	$[Co_{0,67}^{2+}Al_{0,33}^{3+}(OH)_2]^{0,33+}(ODS^-)_{0,33}\cdot 1.49\ H_2O$	33.00	7.42	0.13	4.56	31.97	7.68	0.00	4.74

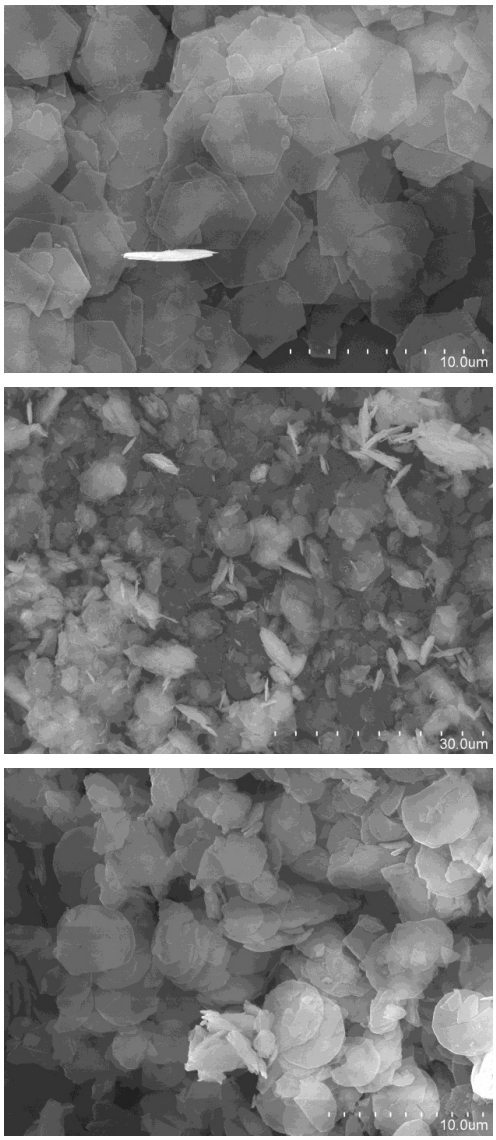

Figure S2. Low magnification FESEM images of CoAl-LDHs. From up to bottom: CoAl-CO_3, CoAl-OS and CoAl-DS.

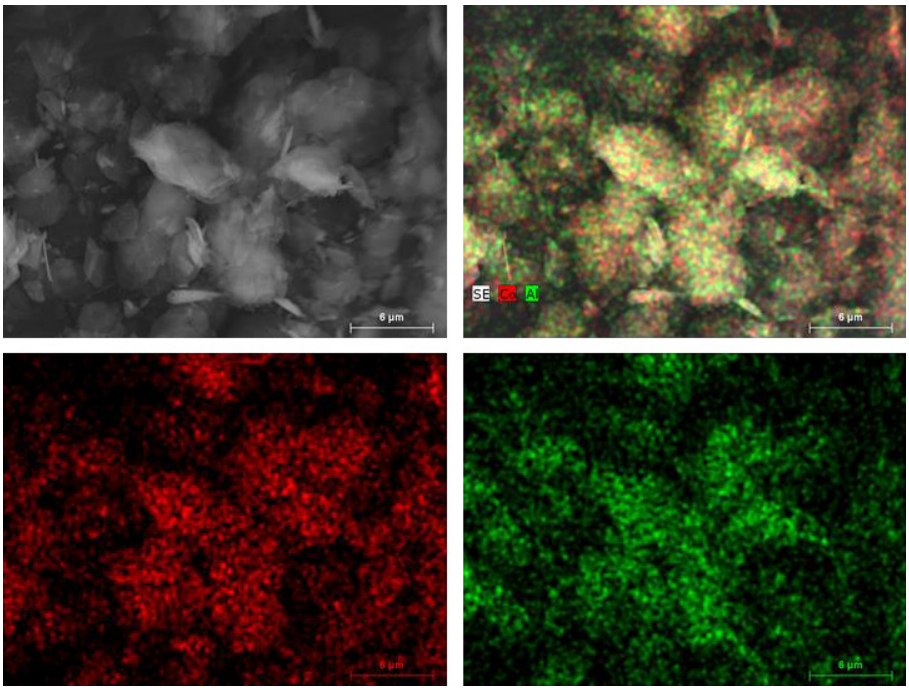

Figure S3. Mapping analysis of CoAl-CO_3 sample.

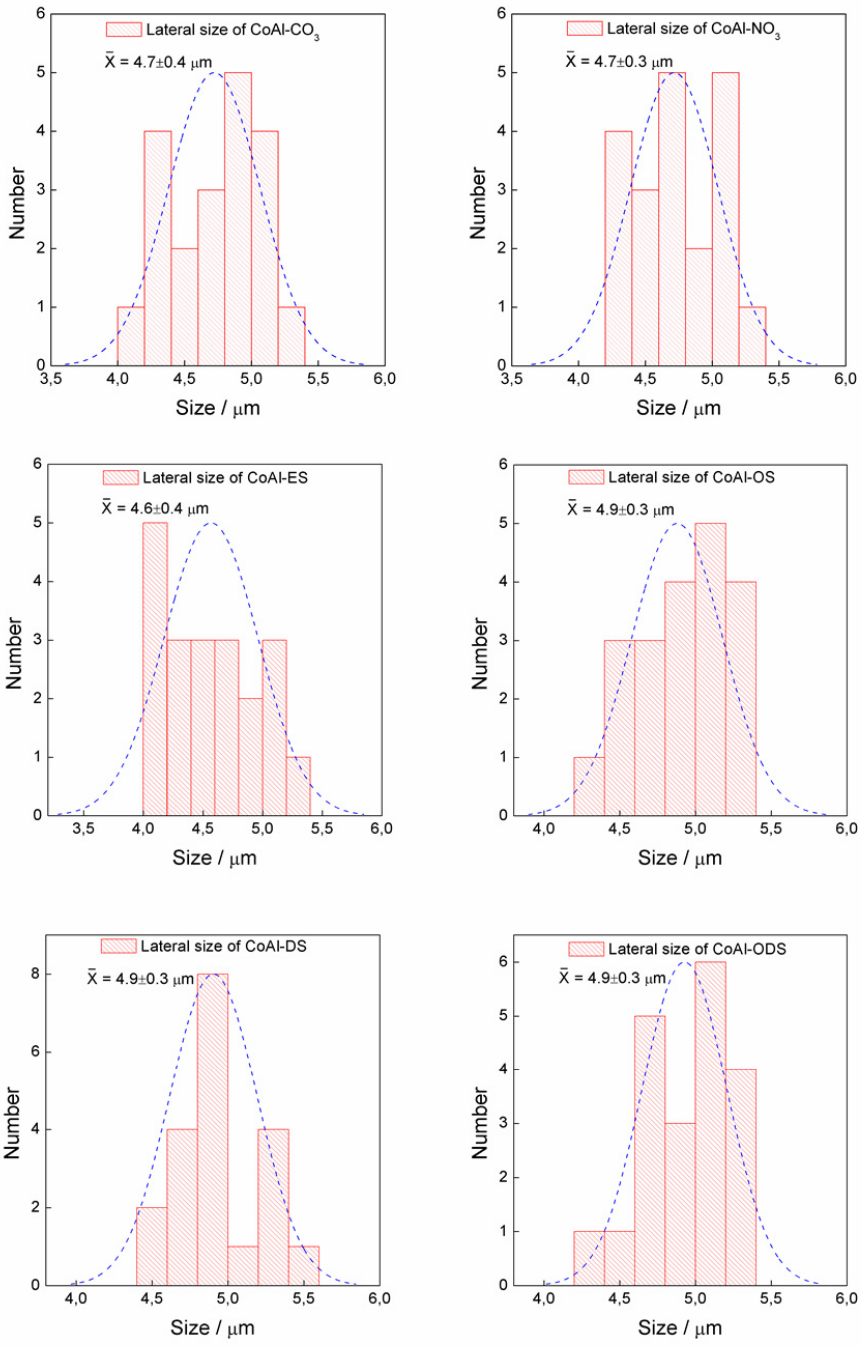

Figure S4. CoAl-LDHs lateral size histograms. All histograms have been made measuring 20 different crystallites in every sample.

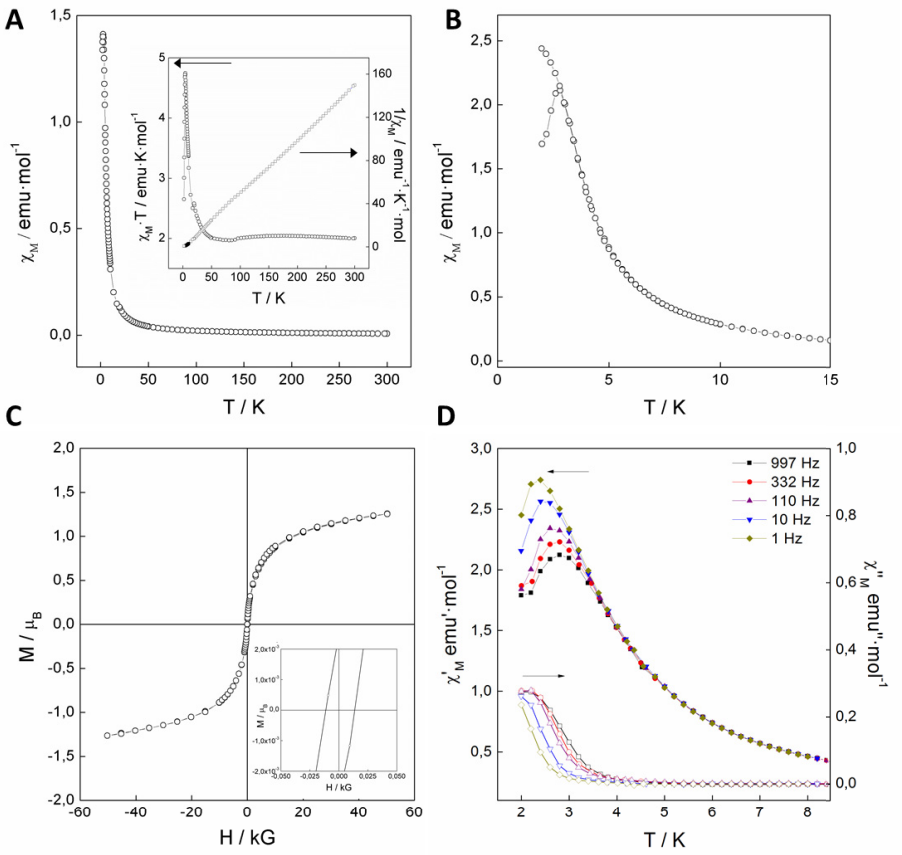

Figure S5. Magnetic characterization of CoAl-CO_3. (A) χ_M *vs.* T plot at 1000 Oe. The inset represents the temperature dependence of the $\chi_M \cdot T$ product and χ_M^{-1} vs. T. (B) FC/ZFC plot at 100 Oe. (C) Magnetization curve at 2 K. The inset shows the low field region. (D) Thermal dependence of the χ'_M (in-phase) and χ''_M (out-of-phase) signals at 1, 10, 110, 332 and 997 Hz.

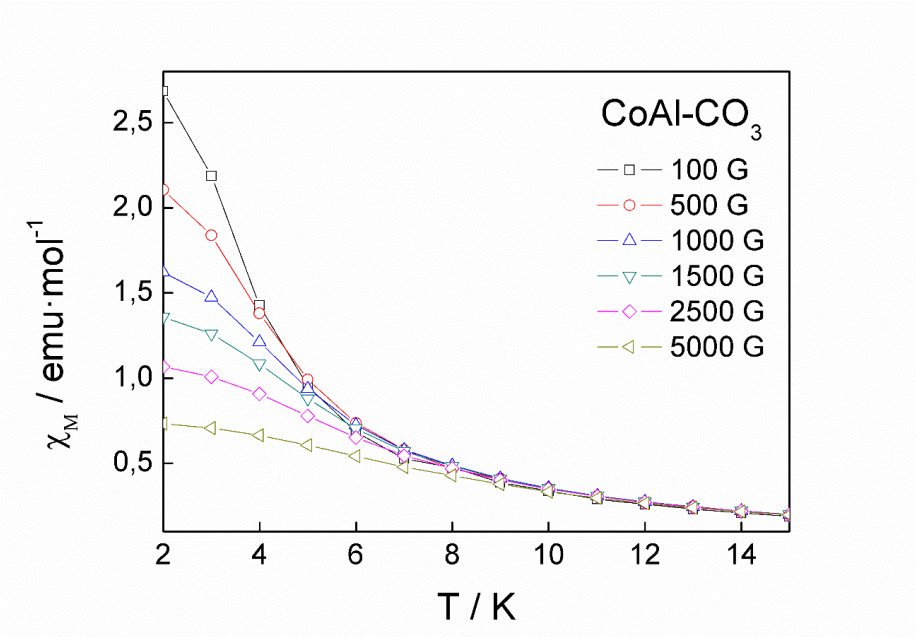

Figure S6. Thermal variation of the magnetic susceptibility (χ) of CoAl-CO_3 for different magnetic fields. The absence of a defined peak at any applied field discards a metamagnetic behavior for the sample.[1]

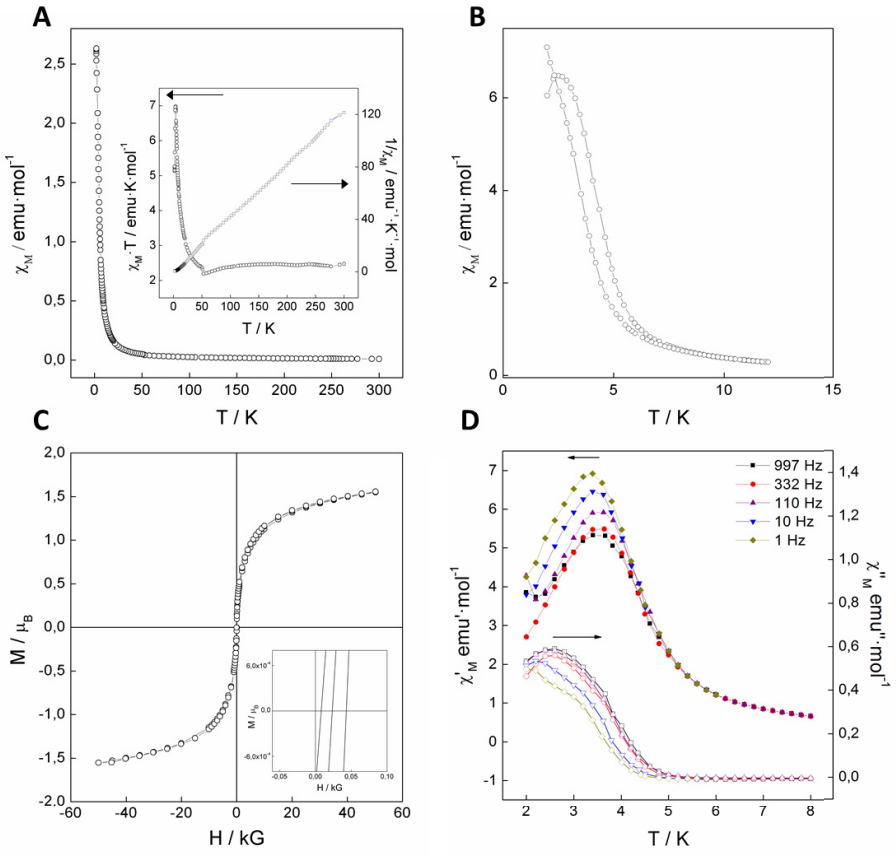

Figure S7. Magnetic characterization of CoAl-ES. (A) χ_M *vs*. T plot at 1000 Oe. The inset represents the temperature dependence of the $\chi_M \cdot T$ product and χ_M^{-1} vs. T. (B) FC/ZFC plot at 100 Oe. (C) Magnetization curve at 2 K. The inset shows the low field region. (D) Thermal dependence of the χ'_M (in-phase) and χ''_M (out-of-phase) signals at 1, 10, 110, 332 and 997 Hz.

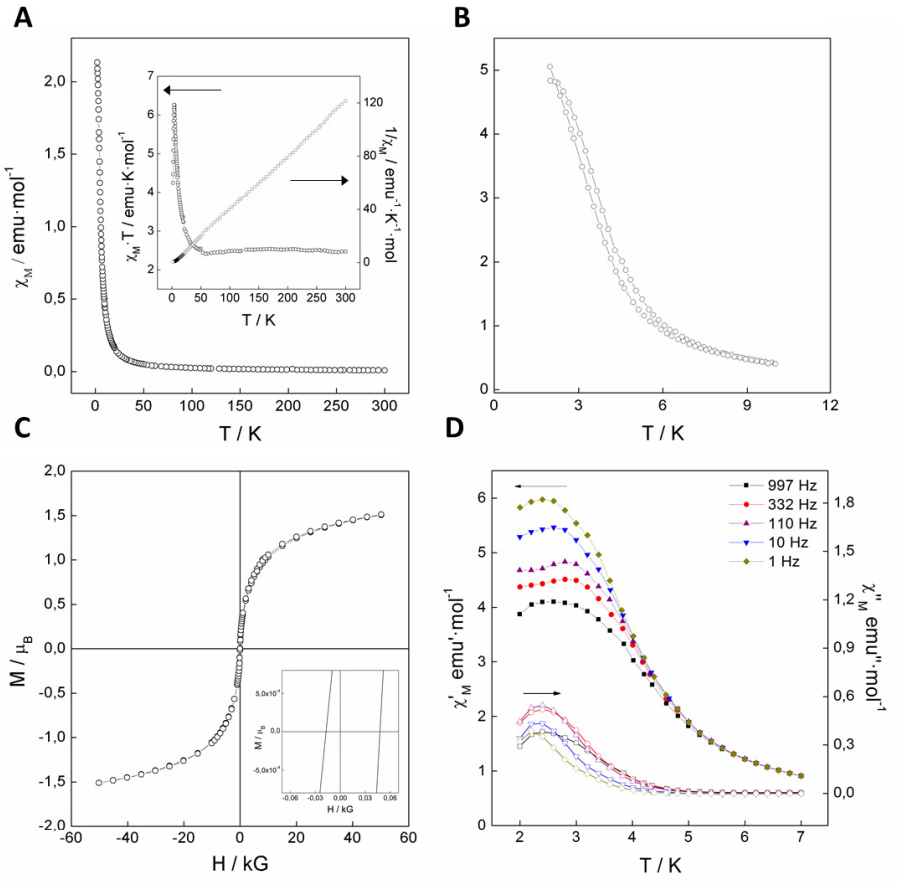

Figure S8. Magnetic characterization of CoAl-OS. (A) χ_M *vs*. T plot at 1000 Oe. The inset represents the temperature dependence of the $\chi_M \cdot T$ product and χ_M^{-1} vs. T. (B) FC/ZFC plot at 100 Oe. (C) Magnetization curve at 2 K. The inset shows the low field region. (D) Thermal dependence of the χ'_M (in-phase) and χ''_M (out-of-phase) signals at 1, 10, 110, 332 and 997 Hz.

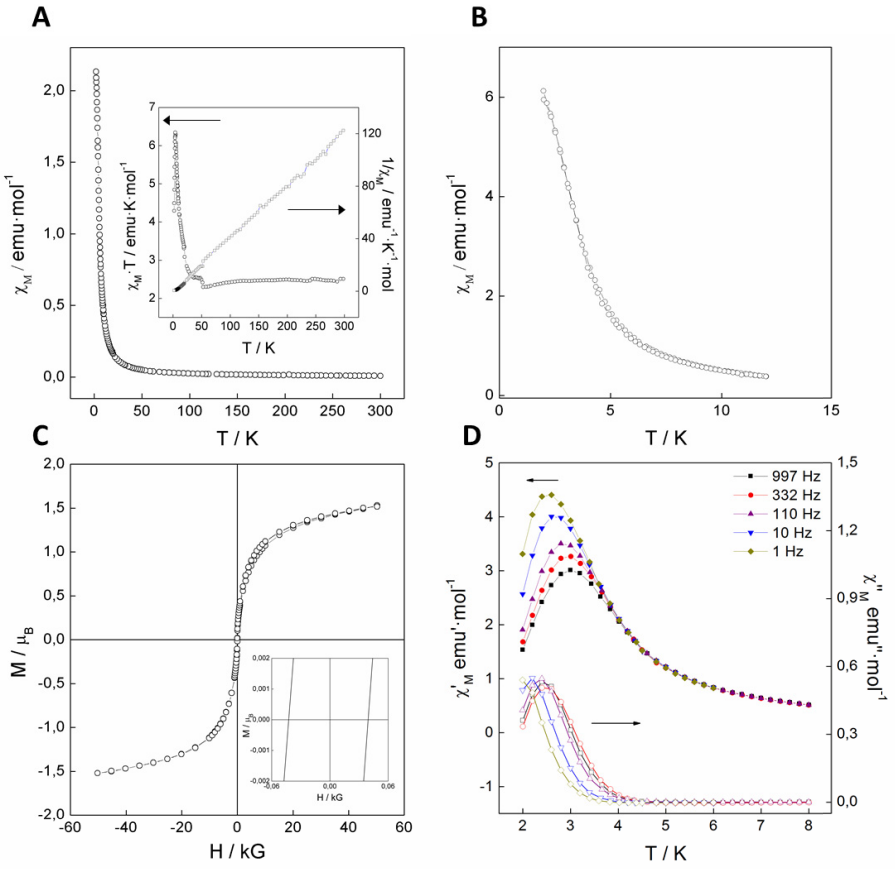

Figure S9. Magnetic characterization of CoAl-DS. (A) χ_M *vs*. T plot at 1000 Oe. The inset represents the temperature dependence of the $\chi_M \cdot T$ product and χ_M^{-1} vs. T. (B) FC/ZFC plot at 100 Oe. (C) Magnetization curve at 2 K. The inset shows the low field region. (D) Thermal dependence of the χ'_M (in-phase) and χ''_M (out-of-phase) signals at 1, 10, 110, 332 and 997 Hz.

All data extracted from these plots can be seen in **Table 2** in the main text.

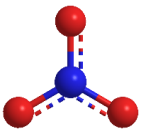

Nitrate (NO_3^-)

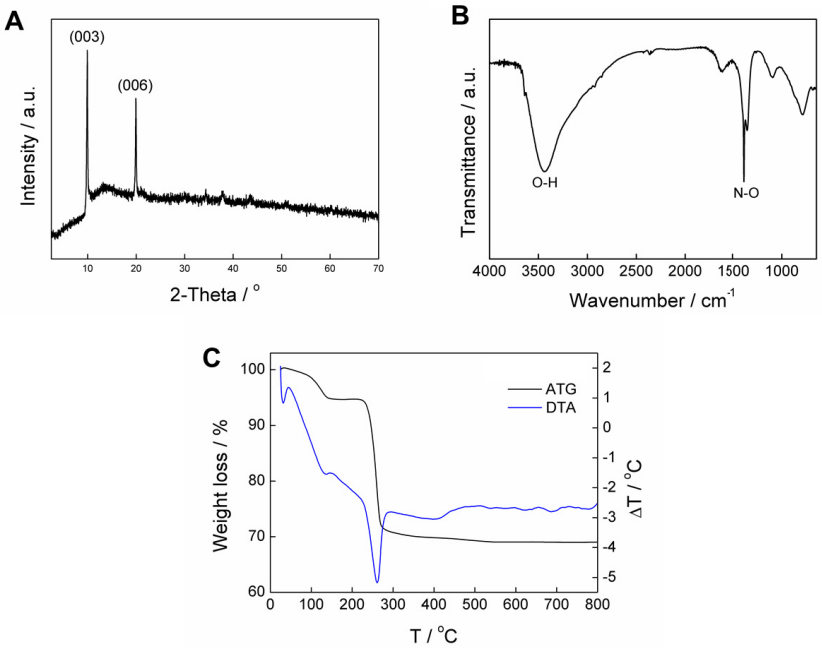

Figure S10. CoAl-NO_3 physical characterization. (A) XRPD pattern, (B) FTIR and (C) TGA/DTA.

Table S2. Molecular formula, basal space and elemental analysis of CoAl-NO_3.

Sample	Molecular formula	Basal space (Å)	C_{found}	H_{found}	N_{found}	S_{found}	$C_{calculated}$	$H_{calculated}$	$N_{calculated}$	$S_{calculated}$
CoAl-NO_3	$[Co_{0,67}^{2+}Al_{0,33}^{3+}(OH)_2]^{0,33+}(NO_3^-)_{0,33}\cdot 0.33\ H_2O$	8.95	0.18	2.27	4.12	0.12	0.00	2.43	4.22	0.00

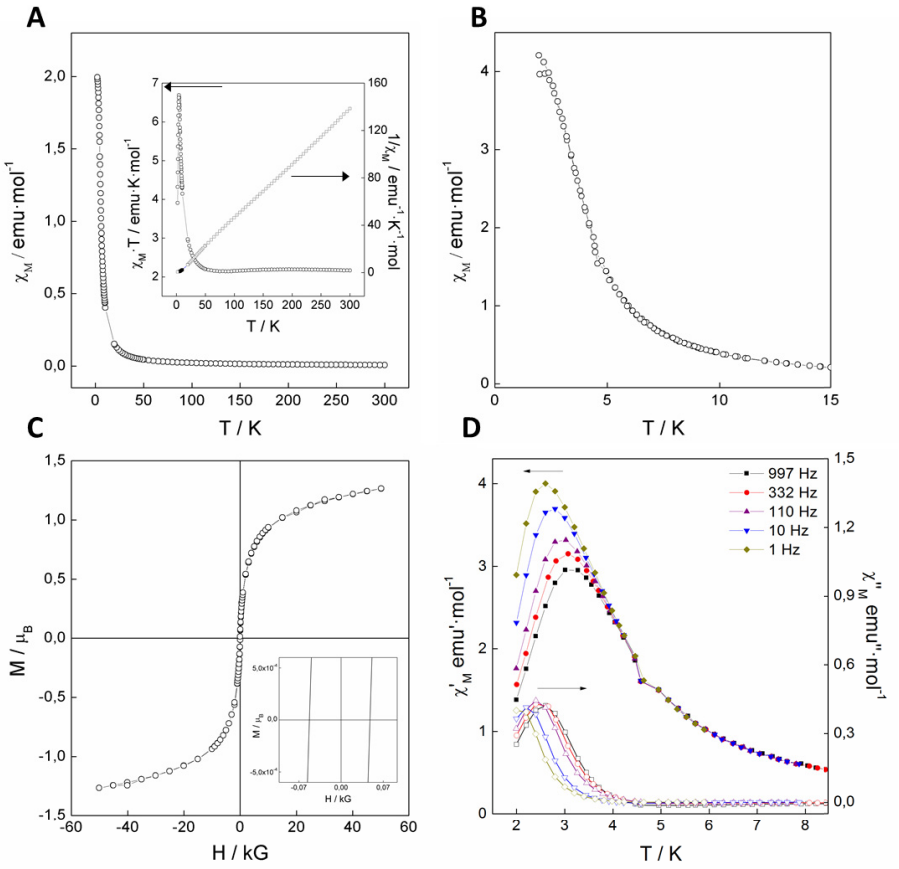

Figure S11. Magnetic characterization of CoAl-NO_3. (A) χ_M *vs*. T plot at 1000 Oe. The inset represents the temperature dependence of the $\chi_M \cdot T$ product and χ_M^{-1} vs. T. (B) FC/ZFC plot at 100 Oe. (C) Magnetization curve at 2 K. The inset shows the low field region. (D) Thermal dependence of the χ'_M (in-phase) and χ''_M (out-of-phase) signals at 1, 10, 110, 332 and 997 Hz.

Table S3. Main magnetic data of CoAl-NO_3.[a]

Sample	$\chi \cdot T_{rt}$ (emu·K·mol^{-1})	C_{SO} (emu·K·mol^{-1})	C (emu·K·mol^{-1})	θ (K)	T_B (K)	T_M (K)	M_S (μ_B)	H_c (Oe)
CoAl-NO_3	2.17	1.26	2.19	0.73	3.05	4.76	1.27	45.00

[a] From left to right: $\chi \cdot T_{rt}$ value at room temperature; expected spin-only value of the Curie constant (C_{so}); experimental Curie constant (C); Weiss constant (θ); temperature of the divergence of the ZFC and FC magnetic susceptibility (T_B); temperature for the onset of spontaneous magnetization extracted from the χ''_M plot (T_M); saturation magnetization (M_S); coercive field (H_C). $S(Co^{2+}) = 3/2$, $S(Al^{3+}) = 0$.

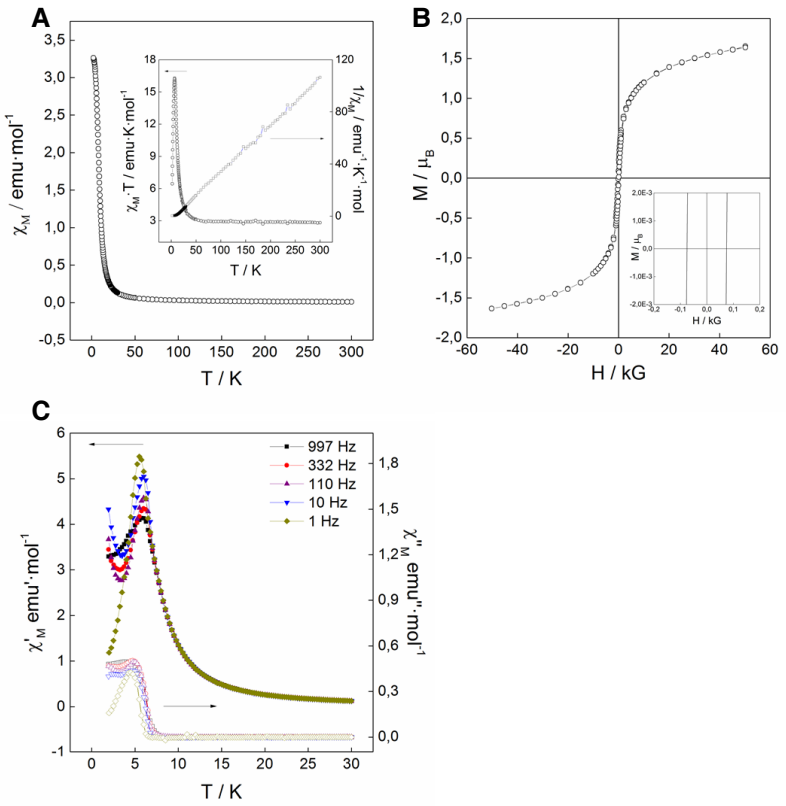

Figure S12. Magnetic characterization of CoAl-OMe. (A) χ_M vs. T plot at 1000 Oe. The inset represents the temperature dependence of the $\chi M \cdot T$ product and χ_M^{-1} vs. T. (B) Magnetization curve at 2 K. The inset shows the low field region. (C) Thermal dependence of the χ'_M (in-phase) and χ''_M (out-of-phase) signals at 1, 10, 110, 332 and 997 Hz.

Table S4. Main magnetic data of CoAl-OMe.[a]

Sample	$\chi \cdot T_{rt}$ ($emu \cdot K \cdot mol^{-1}$)	C_{SO} ($emu \cdot K \cdot mol^{-1}$)	C ($emu \cdot K \cdot mol^{-1}$)	θ (K)	T_M (K)	M_S (μ_B)	H_c (Oe)
CoAl-OMe	2.80	1.26	2.81	-4.19	8.32	1.65	80

[a] From left to right: $\chi \cdot T_{rt}$ value at room temperature; expected spin-only value of the Curie constant (C_{so}); experimental Curie constant (C); Weiss constant (θ); temperature for the onset of spontaneous magnetization extracted from the χ''_M plot (T_M); saturation magnetization (M_S); coercive field (H_C). $S(Co^{2+}) = 3/2$, $S(Al^{3+}) = 0$.

Section II. Theoretical approach.

Considering the symmetry at the Co(II) sites, the term $^4T_1$ splits into six anisotropic Kramers doublets. Previous studies using thermal neutrons showed that only the ground Kramers doublet is significantly populated up to 50K in similar oxo-cobalt complexes.[2,3] Magnetic susceptibility and EPR results clearly indicate the anisotropic nature of this Kramers doublet. One can therefore describe the coupling within the layer by the pairwise coupling of highly anisotropic Kramers doublets with effective spin S=1/2.

The simplification of the network is necessarily more dramatic. Although we studied several arrangements to extend the model size (details in **Fig. S14**), we have decided to describe the full LDH sheet with an hexagonal array of Co(II) ions by including its fundamental interactions. Within this hexagonal array, the parameters used to describe this coupling were: 'In-plane' (J_{xy}) and 'out-of-plane' (J_z) magnetic exchange coupling, Landé g-factors (g_{xy} and g_z), and an interlayer interaction (zJ). The effective parameter zJ aims to account for the interaction among layers, and in particular it quantifies the interaction energy of a single copy of our hexagonal array with the mean magnetic field generated by other layers. (**Fig. S13**).[4]

$$\mathrm{H} = -2\sum_{i,f}\sum_{\alpha=xy,z} J_{ij}^{\alpha}\hat{S}_i^{\alpha}\hat{S}_j^{\alpha} - \sum_{\alpha=xy,z} g_{\alpha}\beta H_{\alpha}\hat{S}_{\alpha} - 2zJ\hat{S^z}\left\langle\hat{S^z}\right\rangle \quad (1)$$

Within this model, the susceptibility of the whole family has been well reproduced ($r<0.006$ for the worst case, see **Table S5.**). In **Fig. S13** the fitting of the compound with a longer interlayer distance is shown (see the rest of the fittings also in **Fig. S15**).

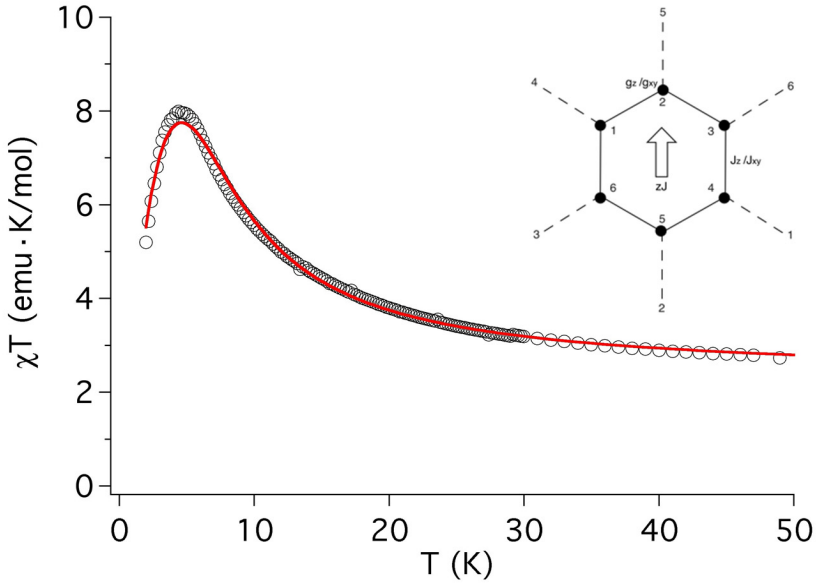

Figure S13. χ·T vs T fitting of the magnetic susceptibility for the ODS material using the previously described anisotropic effective Hamiltonian. The inset shows the basic structure of the hexagonal model used in the effective Hamiltonian model. Other non-functional structures can be found in **Fig. S14**.

Analysing the fitting results one can find a dominant ferromagnetic interaction between the Co(II) spins. The ratio $g_z/g_{xy} \approx 20$ confirms that the system shows an Ising type behaviour. The fitting is achieved with a range of parameters shown below (a complete set parameters for each system is shown in **Table S6** with each compound individually fitted). The obtained results for the exchange parameters J are in good agreement to those reported for other Co(II) oxo-complexes, while the parameter zJ is two orders of magnitude lower than J (between 0.0152 cm^{-1} for ODS and 0.0239 cm^{-1} for CO_3^{2-}).

Table S5. Parameters obtained from the simultaneous fitting of the complete family of materials.

J_z	2.48 – 3.63 cm^{-1}
J_{xy}	3.63 – 4.81 cm^{-1}
g_z	8.27 – 11.39 cm^{-1}
g_{xy}	0.50 – 0.62 cm^{-1}

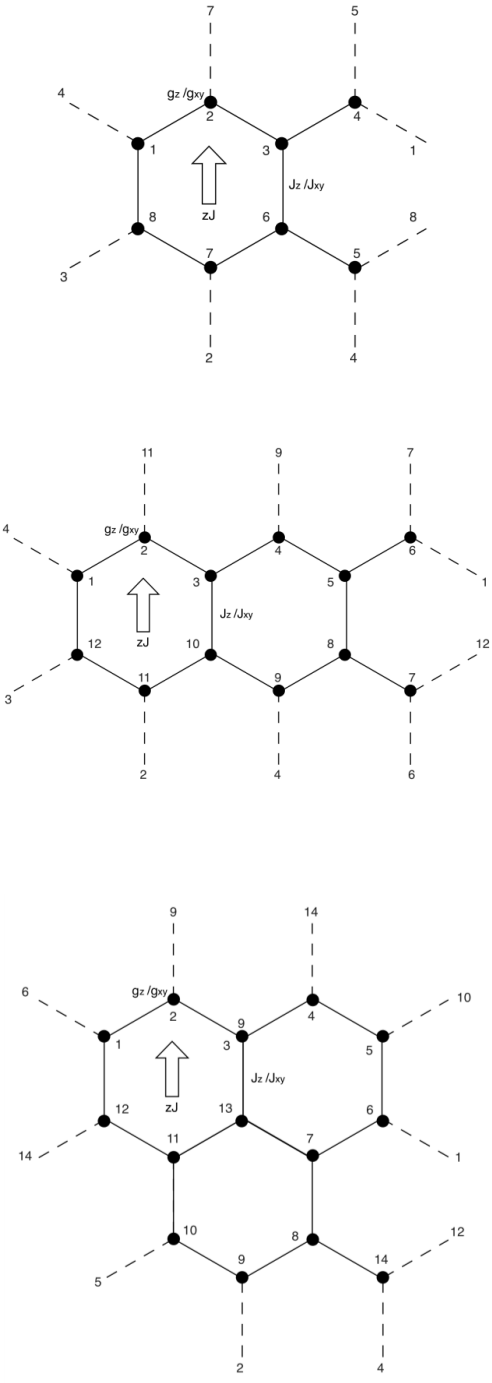

Figure S14. Non-functional structures of the hexagonal model used in the effective Hamiltonian model.

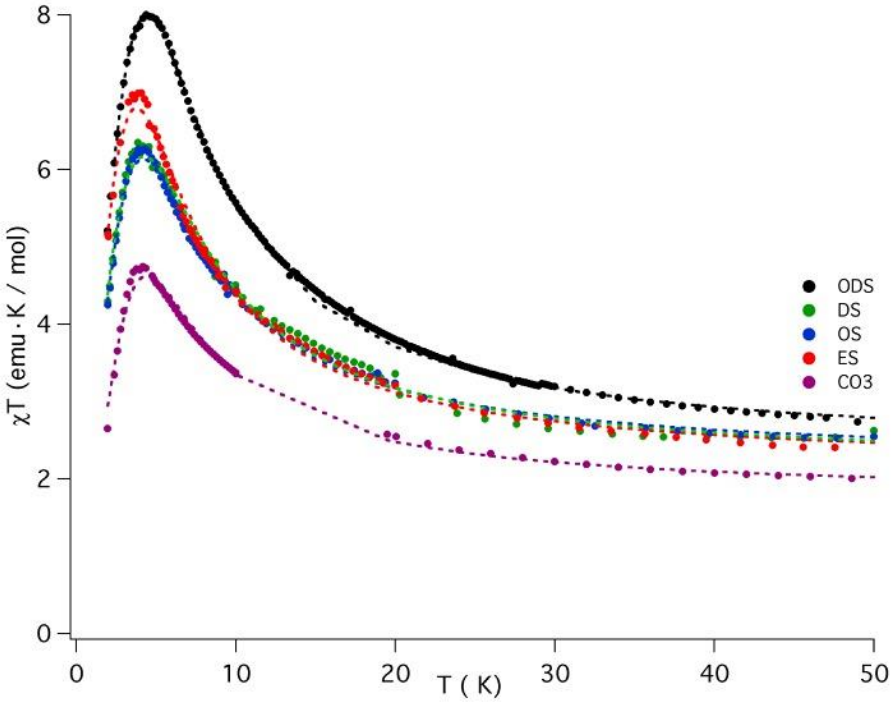

Figure S15. χ·T vs T fitting of the magnetic susceptibility for the CoAl-LDH family studied.

Table S6. Description of the parameters used for the fittings using the 6-atom model.

Sample	zJ(cm^{-1})	J_z(cm^{-1})	g_z	J_{xy}(cm^{-1})	scal	g_{xy}
CoAl-CO3	0.0239	2.48	8.27	3.63	1.21	0.625
CoAl-ES	0.0174	3.03	9.29	3.97	1.15	0.535
CoAl-OS	0.0166	2.94	9.24	3.92	1.21	0.537
CoAl-DS	0.0166	3.33	9.13	4.28	1.19	0.549
CoAl-ODS	0.0152	3.63	11.39	4.81	0.84	0.500

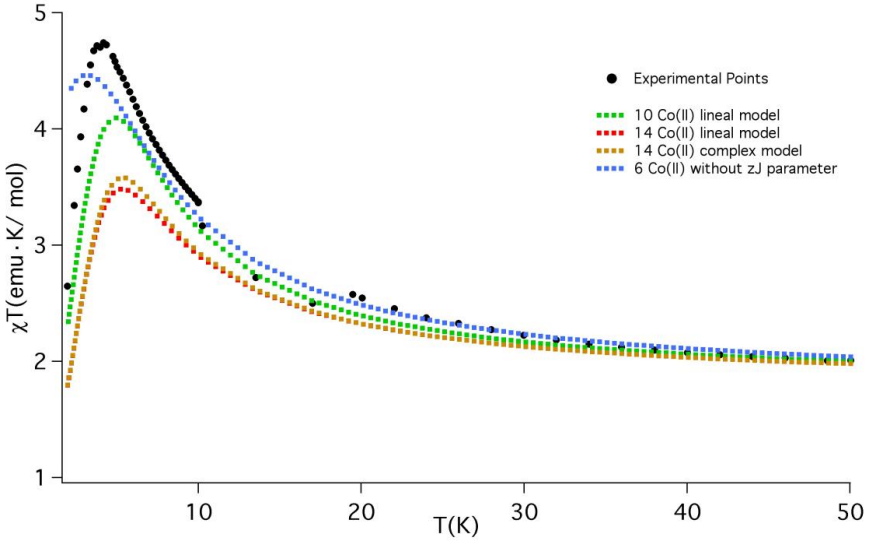

Figure S16. χT vs T plot representing unsuccessful fittings using other models with higher nuclearity or different spatial arrangement.

Calculations enlarging the minimal model resulted in a subsequent increase of the energy matrix size. The first approach consisted in adding a second (third) hexagon adjacent to the initial one (**Fig. S14**). This increases the matrix size from (64x64) to (1024x1024) and (16384x16384) making all of them still affordable sequentially in a typical processor. This way of increasing the model size proved to be of limited utility since the symmetry of the total plane is reproduced with decreasing accuracy in each step (different plane directions get increasingly inequivalent). Alternate approaches are depicted in **Fig. S14**. The model with nuclearity n=14 was calculated, although it still presents an assymetry that makes it unadequate. The model with nuclearity n=18 is already beyond our computational means. The results are depicted in **Fig. S16**. Models that maintain the symmetry in higher nuclearity are much beyond reasonable computational cost, thus we are restricted to the minimal approach with n=6.

To extend the previous analysis of the interlayer dependence, a fully-theoretical approach was proposed. This model employs classical magnetic dipoles and calculates the interaction felt between a distribution of parallel (Ising) magnetic moments in two bidimensional layers. For simplicity, each Co(II) ion has been represented by an effective moment pointing in the direction perpendicular to each sheet. In this model, the magnetic moment is again simplified as a Krammers doublet with spin S=1/2 with an effective $g_{z\text{-eff}}$ containing the information about the real total spin. Thanks to the axial compression ($d_{shortO\text{-}O}$=1.958Å vs. $d_{longO\text{-}O}$=2.406Å) existing in the ternary symmetry axis of the octahedral, an orientation of the magnetic pointing one 'in-plane' vertex of a Co(II) octahedral can be assumed (**Fig. S17**).

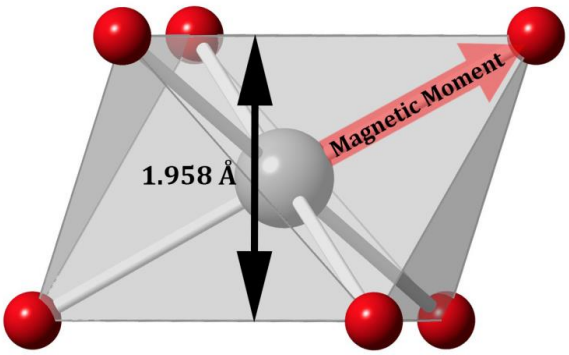

Figure S17. Depiction of the orientation of the magnetic moment in a coordination octahedra. Red arrow shows the real orientation (center to vertex) of the moment. A vision compatible with an Ising model can be obtained by averaging all the possible orientations in the xy plane.

The calculation considers an isolated magnetic moment pointing to a square layer containing a certain number of similar moments, distributed according to the geometry and distances of the experimental system (see Eq. 2). Both the lateral size dimension of the layer and its distance are variables that have been explored. The lateral length of the sheet was increased from 1.5 nm (5x5 atoms) to 300 nm (1000x1000 atoms), while the interlayer distance was varied from 5 to 50 Å (covering the whole range of experimental values that get to a maximum of 34 Å).

$$\overrightarrow{E_z} = \sum_{i=1}^{n} \frac{\mu_{ref} \cdot \mu_i}{4\pi\varepsilon_0} \cdot \frac{1}{r^3} \cdot (1 - 3cos^2\theta) \quad (2)$$

In order to compare the values obtained with this model such coming from the semiempirical fitting, the dipolar energy has been normalized to mimic the six-atom platelet. The results of these calculations are shown in main text, **Fig. 5**.

These results deserve a particularly detailed analysis. Specifically, it is necessary to highlight some revealing statements. Note that in order to avoid the overparametrization of the fitting to affect these conclusions we have only extracted them from this purely dipolar model.

The first idea can be summarized as: the net dipolar interaction between two infinite ferromagnetic layers is zero. Furthermore, the magnetic field generated by a single infinite ferromagnetic layer is also zero at every point of the space. This can be understood trivially by substituting each spin with a minuscule square loop through which a finite current circulates. In this case, an infinite layer of ferromagnetic spins would then be equivalent to an infinitely large loop through which a finite current circulates, and this generates an infinitesimal magnetic field. The key is, infinite ferromagnetic layers do not exist in the real world. Real layers, even if they can be synthesized to display extremely large horizontal dimensions, are eventually broken down into discrete magnetic domains. This principle produces a vital corollary: the major factor governing the dipolar interaction between magnetic layers is the layer size, or, if they are broken up into domains, the domain size. As can be seen from our numerical results presented above, this is, in practice, much more important than the interlayer distance, except for tiny domain sizes (of the order of 5 nm). Descending into the details, for domain sizes of tens of nm and interlayer distances between 5 and 50 nm, the intensity of the interaction falls exponentially with the domain size and is constant up to perhaps a 10% with the layer distance. This behaviour is shocking, considering the known third-order dependence of dipolar coupling, and thus needs an explanation.[5]

Let us focus on a magnetic ion placed at the centre of the bottom layer and looking vertically up towards the upper layer. We can picture the cone defined by the magic angle (54.7º from the vertical where $3\cos^2\theta = 1$, and thus the dipolar coupling varies from positive to negative or *viceversa*) as a lantern shining on the metal ions of the upper layer. (**Fig. S18**) All these enlighted ions are coupled ferromagnetically to our initial ion in the bottom layer due to the dipolar coupling, with all dark ions being

coupled antiferromagnetically. The quasi-constant dipolar coupling results from the compensation of two effects that work in opposite directions: (1) the dipolar coupling between two given centers falls with the cube of distance (here the metaphor is not quantitative, as the intensity of a light beam decreases with the square of the distance), but at the same time (2) the ratio of ferromagnetic to antiferromagnetic interactions rises rapidly as the light shines upon a larger part of the upper layer, with a receding "dark" external ring that contributes antiferromagnetically.

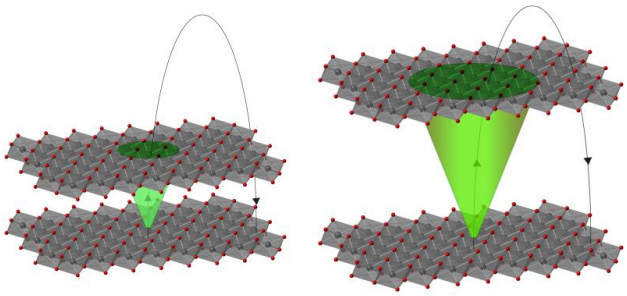

Figure S18. Schematic view of the flashlight effect produced by a single Co ion dipolar field at two different interlayer distances. Note the change in the number of shadowed atoms in the upper layer that have their magnetic moments aligned parallel with such field while the rest are antiparallel to it.

Finally a connection within this theory and the semiempirical fitting theories is also possible. With the obtained relation between domain size and previously found interlayer interactions we can deduce in a first approximation the domain size in our particular cases. These results point to domain sizes in the range of 30–60nm. Although these parameters are in the usual range for anisotropic Co(II) complexes, one should note that the model employed for each layer in our fitting procedure is quite crude and this should definitively not be considered a firm prediction of the domain size. Presumably, fits using models of larger sizes would eventually converge into the best possible value of the parameters and also a more precise value for the domain size. Unfortunately, this is computationally expensive, because the cost of the calculations rises exponentially. Thus, we consider that no reasonable increase in computing power would be able to cope with a proper description of the individual layer.

The second principle can be stated as: dipolar interaction between layers at increasing distances can never result in a change in the sign of the magnetic coupling between single-domain layers. If the magnetic momentum is perpendicular to the layer plane, the interaction will always be ferromagnetic. Conversely, if the momentum is parallel to the plane, the interaction will always be antiferromagnetic. Here we are dealing with the former case, *i.e*. ferromagnetic interactions. As we have shown, as the size of the domain tends to infinity, the interaction tends to zero. Nevertheless, for a multidomain layer it is in principle possible that at small distances the dipolar interaction favours antiferromagnetic coupling of neighbouring domains within each layer, while at larger distance the same interaction favours ferromagnetic coupling of neighbouring domains within each layer. Exploring this exciting possibility is nevertheless outside the scope of the present work, and would require the coupling of the models we propose herein to the model proposed by Drillon and Panissod.[6,7] In fact, to put our work in perspective, it is useful to recall the work these authors did in the same direction but for different systems –monometallic layered hydroxides.[6,8] Compared with our own work, the Drillon-Panissod model is more focused on large, multi-domain layers, instead of considering single-domain layers. Their calculations were based on a vertical pile of square checkerboards with a given in-plane ferromagnetic correlation length, where nearest squares in a plane couple antiferromagnetically, whereas directly vertically aligned squares couple ferromagnetically via dipolar interactions. Every (multispin) square was treated as a superspin. As a practical advantage, they were able to produce equations conceived to predict the critical temperature of the system. Compared with these efforts, our approach, which is more microscopical, has both limitations and advantages. Our dipolar model between individual spins is adequate to understand and analyze the effect of the layer size for single-domain layers, which we found to be more important than the effect of interlayer distance in the single-domain approximation. Our effective Hamiltonian model, which in principle enables a more realistic study of both intralayer and interlayer phenomena, is used to reproduce and rationalize the dc magnetic susceptibility data. The combination of the two models presented in this work serves to estimate the effective lateral dimension of spin-correlated layers. As a common limitation, it is worth to remark here that both our models and the one by Drillon-Panissod assume rigid layers, but the flexibility of LDHs could strongly affect the resulting magnetic behaviour.[9–11]

Section III. References.

(1) Marvilliers, A.; Parsons, S.; Rivière, E.; Audière, J.-P.; Kurmoo, M.; Mallah, T. Structure, Magnetic Properties and Magnetic Phase Diagram of a Layered, Bimetallic, Cyanide-Bridged CrIII-NiII Metamagnet. *Eur. J. Inorg. Chem.* **2001**, *2001*, 1287–1293.

(2) Gingsberg, A. P. Magnetic Exchange in Transition Metal Complexes vi: Aspects of Exchange Coupling in Magnetic Cluster Complexes. *Inorganica Chim. Acta Rev.* **1971**, *5*, 45–68.

(3) Lines, M. E. Orbital Angular Momentum in the Theory of Paramagnetic Clusters. *J. Chem. Phys.* **1971**, *55*, 2977–2984.

(4) Ginsberg, A. P.; Lines, M. E. Magnetic Exchange in Transition Metal Complexes. VIII. Molecular Field Theory of Intercluster Interactions in Transition Metal Cluster Complexes. *Inorg. Chem.* **1972**, *11*, 2289–2290.

(5) Rabu, P.; Delahaye, E.; Rogez, G. Hybrid Interfaces in Layered Hydroxides: Magnetic and Multifunctional Superstructures by Design. *Nanotechnol. Rev.* **2015**, *4*, 557–580.

(6) Drillon, M.; Panissod, P. Long-Range Ferromagnetism in Hybrid Compounds: The Role of Dipolar Interactions. *J. Magn. Magn. Mater.* **1998**, *188*, 93–99.

(7) Rabu, P.; Drillon, M. Layered Organic–Inorganic Materials: A Way towards Controllable Magnetism. *Adv. Eng. Mater.* **2003**, *5*, 189–210.

(8) Rabu, P.; Rouba, S.; Laget, V.; Hornick, C.; Drillon, M. Ferro/Antiferromagnetism Mediated by Interlayer Organic Spacers in Layered Copper(II) Compounds. *Chem. Commun.* **1996**, *10*, 1107–1108.

(9) Thyveetil, M.-A.; Coveney, P. V.; Suter, J. L.; Greenwell, H. C. Emergence of Undulations and Determination of Materials Properties in Large-Scale Molecular Dynamics Simulation of Layered Double Hydroxides. *Chem. Mater.* **2007**, *19*, 5510–5523.

(10) Li, B.; He, J.; Evans, D. G. Experimental Investigation of Sheet Flexibility of Layered Double Hydroxides: One-Pot Morphosynthesis of Inorganic Intercalates. *Chem. Eng. J.* **2008**, *144*, 124–137.

(11) Abellán, G.; Coronado, E.; Martí-Gastaldo, C.; Ribera, A.; Jordá, J. L.; García, H. Photo-Switching in a Hybrid Material Made of Magnetic Layered Double Hydroxides Intercalated with Azobenzene Molecules. *Adv. Mater.* **2014**, *26*, 4156–4162.

Chapter 3:

Exfoliation and Functionalization of Layered Double Hydroxides

3.1. Introduction.

One of the main features of LDHs is their ability to be exfoliated into 2D nanosheets as they retain the properties of the pristine bulk precursor such as redox behaviour or 2D magnetism.[1] Therefore, they can be used as macromolecular building blocks in the design of more complex architectures. Because of the electrostatic interlayer interactions, absent in other layered materials such as graphene, chalcogenides or layered pnictogens,[2–7] LDHs can hardly be exfoliated under soft conditions. In addition, anion exchange reactions are mandatory to minimize the electrostatic interactions by distancing the cationic sheets, and anionic surfactants, such as SDS, are intercalated for achieving this task.[8] Their aliphatic tails favour the formation of micelles surrounding the layers, creating the perfect scenario for the dispersion in a polar solvent that can solvate the hydrophobic tails of the intercalated surfactant.[9] Hence, organic solvents such as butanol, acrylates, carbon tetrachloride, toluene or formamide are usually employed in order to obtain the nanosheet dispersion.[1] Among these solvents, formamide stands out as one of the main choices in the exfoliation of LDHs.[10–12] Formamide allows the spontaneous exfoliation without the need of additional heating or refluxing treatment in a wide range of different LDHs (MgAl-, CoAl-, ZnAl-, NiAl- or NiFe-, among others),[13–15] consequently acting as a general delaminating agent. This universal feature can be related to the fact that this solvent can be accommodated itself in the interlayer space. Furthermore, it is suggested that the driving force for the swelling of LDHs may be ascribed with the hydrogen bonding. In this context, formamide presents electronegative elements (O and N) that lead to the formation of H-bonds between them and the hydroxide sheets after its penetration into the gallery space of the LDH, followed by the subsequent break of the H-bonding network among the cationic sheets, the interlayer anion and the water molecules.[16,17] As a result, the LDH sheets distance themselves in a swollen phase and are finally exfoliated using sonication or shaking methods (**Fig 3.1**). Best exfoliated nanosheets are obtained from LDHs synthesized with the addition of urea or hexamethylenetetramine as hydrolysis agents that favour the basic media and lead to high-quality crystallites.[16,18,19]

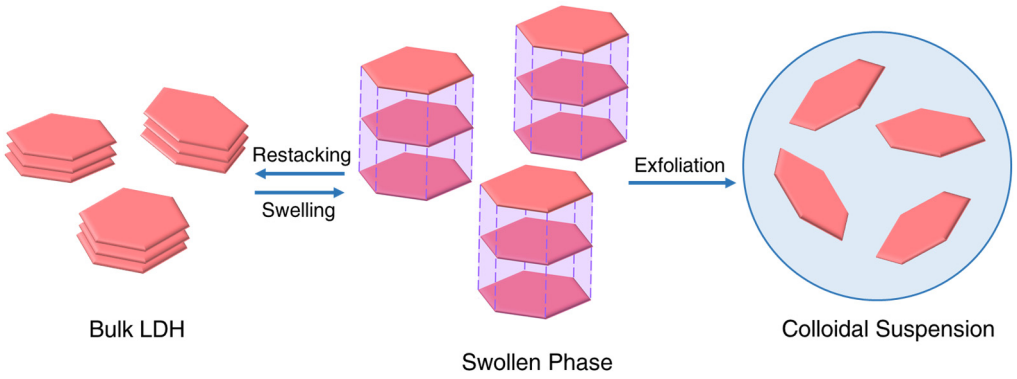

Figure 3.1. Schematic view of the swelling of a LDH material after dispersing in a solvent such as formamide. From the swollen phase, one can exfoliate the system via sonication or mechanical stirring methods in order to obtain a colloidal suspension of nanosheets.

Nevertheless, the use of formamide has some disadvantages due to its toxicity and later deposition on substrates. The high boiling point or the formamide (210 ºC) makes difficult to evaporate the solvent without damaging the sample. Hence, it is an important task to find out good alternatives to formamide in the delamination of LDHs. Gardner *et al.* reported aqueous transparent colloidal suspensions of LDH particles that exhibit increased surface-to-surface interactions, therefore suggesting the exfoliation of the material into nanosheets.[20,21] The methodology is based on the synthesis of alkoxide-intercalated LDHs that undergo complete hydrolysis in water giving rise to colloidal suspensions.[22] This synthetic procedure leads to crystal sizes below 100 nm, in stark contrast with the micrometric sizes obtained with the most traditional ARR methodologies. Concerning the magnetism of the system, this nanometric size leads to superparamagnetic behaviour and influences on the electrochemical properties of the material.[22–24] This approach is later explored for the fabrication of thin films of magnetic LDHs.

Regarding the delamination methodology, liquid phase exfoliation is the most used among the LDHs, standing out mechanical stirring or bath sonication as the preferred options among the different possibilities.[10,12,16,25] Nevertheless, more attention should be payed to the use of techniques such as ultrasonic tip sonication for liquid phase exfoliation. For inorganic layered materials such as transition metal dichalcogenides, layered simple hydroxides, antimonene or black phosphorous,

among others, tip sonication exhibits higher production rates than bath sonication, as well as better quality in the exfoliated material, in terms of overall dimensions, thickness and yields.[2–4,26–30] No studies on exfoliation of LDHs *via* tip sonication are reported in literature.

Finally, covalent functionalization of 2D materials is also a topic of interest in this area.[31–34] The main advantages of the covalent functionalization relies in three key points: (i) processability *via* the reinforcement of the interfacial interactions between material and substrate,[32] (ii) the enhancement of the dispersibility of the samples[35] and (iii) the control of molecular orientation.[36] In order to covalently graft molecules on substrates, aminosilanes stand out as one of the most promising candidates because of their ability to bind themselves on oxide surfaces mediated the formation of a covalent Si-O-Si bond when the hydroxyl group of the surface displace the alkoxide group of the silane. In addition, the versatility of primary amine groups allow subsequent coupling reactions (see **Fig. 3.2** for a schematic view).[37] LDHs are not unaware of this topic and some reports have been published using silanes such as (3-Aminopropyl)triethoxysilane (APTS) as the anchoring molecule to achieve the covalent bonding to the cationic sheet of the LDH material.[38,39] However, further research needs to be done in this field yet the reported studies are very scarce and have never addressed aspects such as the influence of the covalent bonding in the overall magnetism of the LDH or thorough studies on the enhanced deposition on film substrates thanks to the grafted molecules.

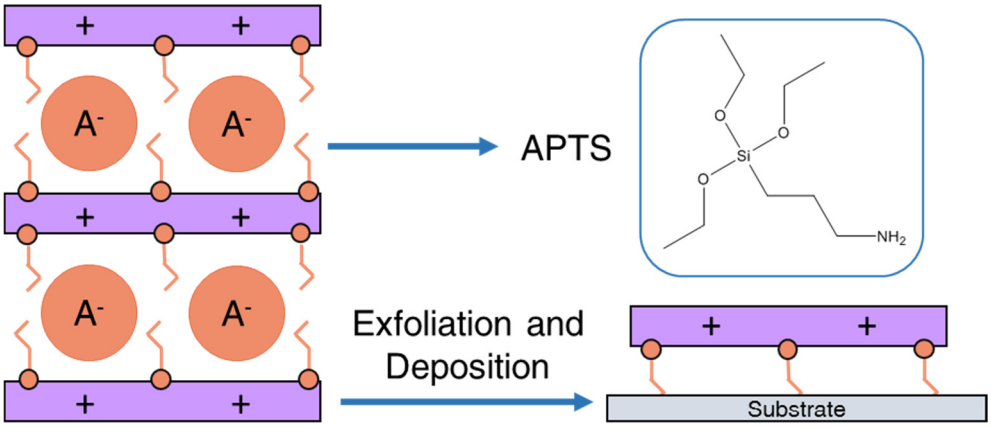

Figure 3.2. Schematic illustration of the cationic sheets of the LDH (purple) covalently grafted to APTS molecules, and how affects the deposition on film substrates. Interlayer anion is depicted by the orange circle between the layers.

3.2. Summary of the most important results.

The main objectives of the present chapter are to improve the exfoliation of LDHs into nanosheets with reduced thickness, as well as the study of functionalized LDHs. The conventional aqueous coprecipitation and hydrothermal methods lead to the synthesis of highly crystalline micrometric LDHs with strong interlayer electrostatic interactions, therefore hindering the exfoliation procedure under mild conditions. In order to overcome this problem, a different synthetic approach was employed, *via* a non-aqueous synthesis (alcoholic media) that leads to nanosized LDHs that undergo complete hydrolysis in water giving rise to colloidal suspensions.[20,21]

A methanolic synthesis was carried out on CoFe- and NiFe-LDHs with M^{2+}/M^{3} ratio of 3:1 and 2:1, respectively, in order to explore the advantages of the alkoxide-LDHs regarding the exfoliation procedures and electrochemical applications of the nanosheet suspension.[23,24] The metallic ratio was chosen to be suitable for electrochemical applications.[25,40–42] A schematic illustration of the LDHs can be found in **Fig. 2.3**. The resulting LDHs presented methoxide (-OMe) as the interlayer anion. The formation of the LDH phase was initially confirmed by powder XRD, exhibiting broader peaks than the ones found after a conventional synthesis (coprecipitation or hydrothermal method). The broadness is ascribed to the presence of nanometric size, in stark contrast with micrometric LDHs. NiFe-OMe LDH was characterised with thermogravimetric analysis coupled with a mass spectrometer (TG-MS), identifying the alkoxide group between the layers for the first time *via* TG-MS. Furthermore, the mass fragments, corresponding to the decomposition of the methoxide moiety, were detected at 270 ºC, 200 ºC higher than the boiling point of methanol (65 ºC). This suggests a strong bonding of the molecule to the LDH layer. In addition, scanning transmission electron microscopy and electron energy-loss spectroscopy (STEM-EELS) was employed to gain further information on the microstructure of the nanosized LDHs. Nanocrystals with an average lateral size of *ca.* 26 and 110 nm were observed for CoFe- and NiFe-OMe LDH, respectively. Moreover, the images pointed out the high quality crystalline structure, in spite of the presence of some stacking faults alongside with occasional lacks of periodicity in the atomic chains. This effect may be related with the presence of

disruptions in the cation ordering through the layers.[43,44] Exfoliation in water was also tested thanks to the hydrolysis of the interlayer alkoxide moiety of the samples. We were able to obtain nanosheets with average lateral sizes of *ca.* 20 (CoFe-OMe LDH) and 50 nm (NiFe-OMe LDH) and a low thickness of *ca.* 4 nm determined by AFM for both samples. Besides, NiFe-OMe homogeneous ultrathin films with a thickness of few nanometers (lower than 3 nm) were obtained after sonication and dispersion of the sample in a mixture of formamide and butanol. The activation of the silicon substrate with O_2-plasma revealed crucial for achieving a complete coverage of the film. Regarding magnetic measurements, it was observed that the small size of the alkoxide-LDHs affected the overall magnetism of the material. Both samples depicted superparamagnetic behaviour and lower blocking temperature than their micrometric counterparts. Furthermore, the frequency dependence can be estimated with the Mydosh parameter (ϕ), related with the spin glass nature of the samples.[45] Alkoxide samples displayed Mydosh values in the range of spin glass-like material (0.06 – 0.08), in line with the expected size effects, while hydrothermal NiFe-LDH was in the range close to canonical spin glasses (0.005 – 0.018). By fitting the frequency dependence to an Arrhenius law, we extracted the energy barrier of the system, with values of 117 and 276 K for CoFe-OMe and NiFe-OMe LDHs, respectively, related to the presence of a superparamagnetic behaviour.[45] This is in clear contrast with NiFe-LDH synthesized by a hydrothermal method, which showed an energy barrier of 1400 K. All results highlighted the crucial role of the nanometric size and low dimensionality of these systems in stark contrast with the micrometric ones.[46]

Finally, electrochemical measurements were tested on both materials in a standard three-electrode cell. CoFe-OMe LDH exhibited good results as a supercapacitive material, with large discharge capacity of *ca.* 145 F g^{-1} at a current density of 1 A g^{-1} in 6 M KOH, overpassing the reported data for a similar CoFe-OMe LDH phase.[47] This capacity retention was studied for the first 100 cycles with no apparent loss. OER performance was measured in a CoFe-LDH for the first time, depicting excellent results in basic media, with overpotentials of *ca.* 397 and 310 mV for hydroxide oxidation at 0.1 and 1 M KOH, respectively. Regarding the electrochemistry of NiFe-OMe LDH, it was focused on the OER activity, with an

overpotential of 340 mV at 1 M KOH. Interestingly, by growing the LDH directly on the Ni-foam the overpotential was decreased to 249 mV. In addition, the electrocatalytic activity was evaluated by calculating the turnover frequency (TOF) of the sample, assuming that all the transition metal ions are contributing to the reaction. NiFe-OMe LDH exhibited a TOF value of 0.01 s^{-1} at an overpotential of 0.3 V, slightly higher than that observed for the hydrothermal-synthesized NiFe-LDH. The results on both samples competed favourably with those reported for other NiFe-LDHs.[25,48] In summary, gathered data suggested that the two samples are promising earth-abundant candidates for both energy storage and as OER electrocatalysts, overcoming the economic limitation showed by the most traditional Ir or Ru oxides have.

Besides, some unpublished studies of exfoliation *via* ultrasonic tip sonication and covalent functionalization of CoAl-LDHs were carried out to shed further insights on the topic. Regarding the sonication and exfoliation, CoAl-CO_3 and CoAl-DS samples were synthesized with the coprecipitation and anion exchange methodology depicted in Article 3, Chapter 2. Studying their solubility based on Hildebrand parameters,[26,49] we found that N-Cyclohexyl-2-pyrrolidone (CHP) and 1-Pentanol were good candidates for the dispersion and exfoliation of CoAl-CO_3 and CoAl-DS samples, respectively. Deposition of the nanosheet dispersions on SiO_2 substrates *via* spin coating at 5000 rpm gave rise to nanosheets with *ca*. 15 and 6 nm in thickness for CoAl-CO_3 and CoAl-DS, respectively (**Fig. 3.3**). It is worth noting that direct exfoliation of CoAl-CO_3 (without previous anion exchange) was unprecedent.

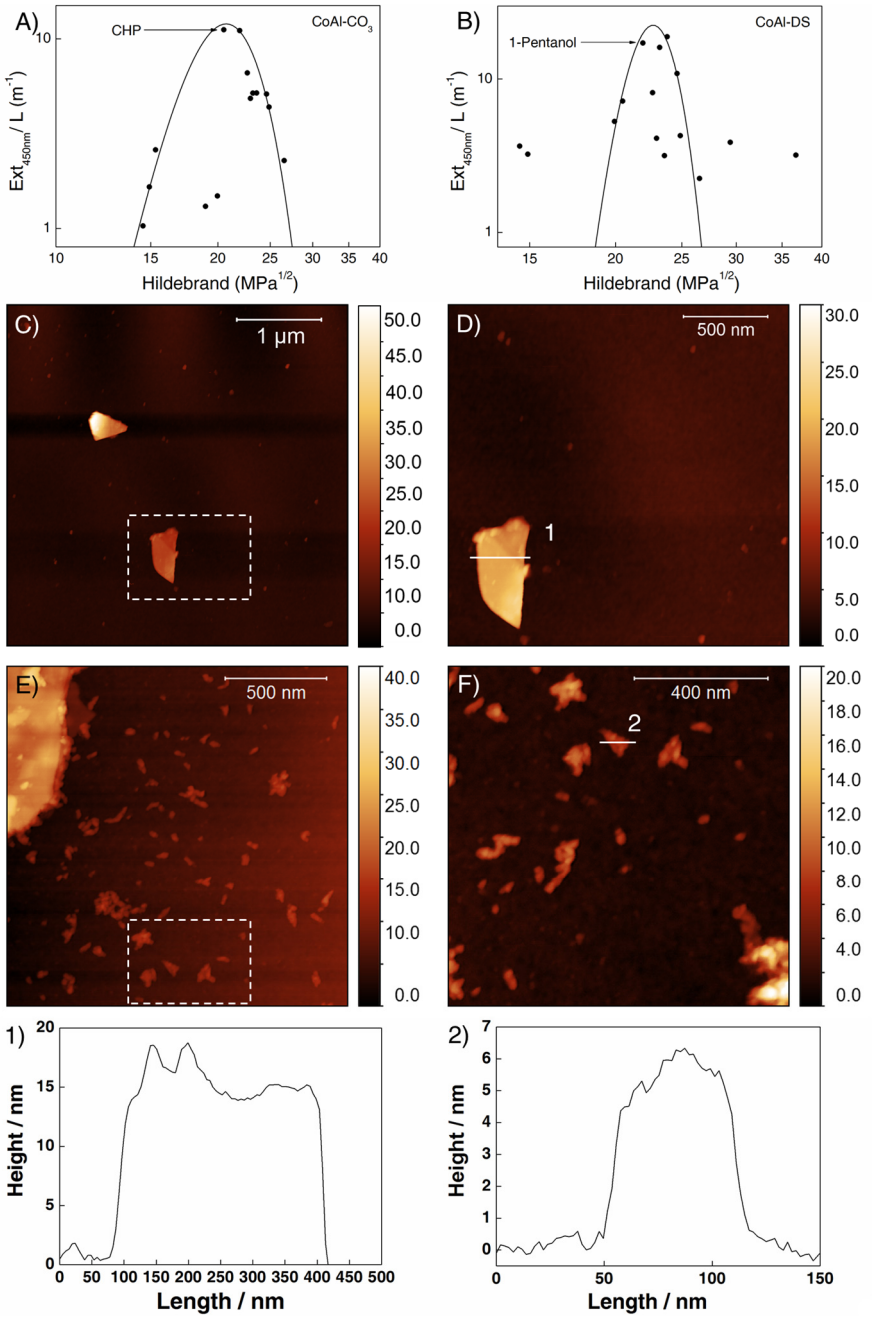

Figure 3.3. Solubility curves based on the Hildebrand parameter in order to discriminate among the most suitable solvents for CoAl-CO_3 (A) and CoAl-DS (B). AFM images of CoAl-CO_3 (C and D) and CoAl-DS (E and F) deposited on SiO_2 films. Profiles of CoAl-CO_3 (1) and CoAl-DS (2).

The covalent functionalization for the CoAl-LDH was approached following a modification of the method described by Kim and coworkers,[39] starting from CoAl-DS and substituting the interlayer anion by (3-Aminopropyl)triethoxysilane (APTS). We can expect a covalent bonding of the silane molecule to the LDH cationic sheets through O-bonding (**Fig. 3.4A**).

XRPD analysis (**Fig. 3.4B**) confirmed the LDH phase of the CoAl-APTS sample, with the main three characteristic basal reflections (003), (006) and (009). The (003) peak is related with the basal space of the LDH, therefore this peak will shift to lower 2-theta values as well as the size of the interlamellar anion increases.[50,51] The basal spaces found for the CoAl-LDH samples are 7.5, 25.6 and 27.0 Å for -CO_3, -DS and -APTS form, respectively. As stated previously in Chapter 1, (00*l*) peaks are related with the stacking among the layers, whereas (*h*0*l*) and (*hk*0) reflections indicate the presence of in-plane turbostatic structures and disorder effects,[52,53] found at *ca.* 40º and 60º for the functionalized sample, respectively. The FTIR spectra depict the presence of the APTS molecule in the LDH structure (**Fig. 3.4C**). The bands at *ca.* 3300 and 300 cm^{-1} are related with the O–H vibration of the hydroxyl group of the LDH or absorbed water molecules, and the N–H vibration found in the APTS molecule, respectively. No presence of the C–H band of the -DS intermediate is found in the -APTS intercalated spectra. At lower wavenumbers, the bands at *ca.* 1600, 1480, 1050 and 650 cm^{-1} are related to additional N–H, C–H, Si–O–C and Si–O bands found in the APTS molecule, respectively.[54,55] Microscopy measurements were carried out in order to study the morphology of the system, as well as how is affected after the anion exchange reactions. **Fig. 3.4D** shows the FESEM image of the CoAl-APTS sample. We observe that the sample shows a well-defined hexagonal morphology, as expected for this kind of LDHs.[56] Moreover, the morphology is not affected after the exchange reactions, and all samples (from the pristine CoAl-CO_3 to CoAl-APTS) presents the same morphology and dimensions. Lateral dimensions were found to be of *ca.* 6 μm. ^{29}Si NMR was measured for the CoAl-APTS functionalized LDH. A broad structure was observed with a total width of more than a thousand ppm. The broadening is caused by the strong dipole-dipole interaction of the Si nuclei, indicating that the APTS molecule is covalently bonded between the hydroxyl layers.

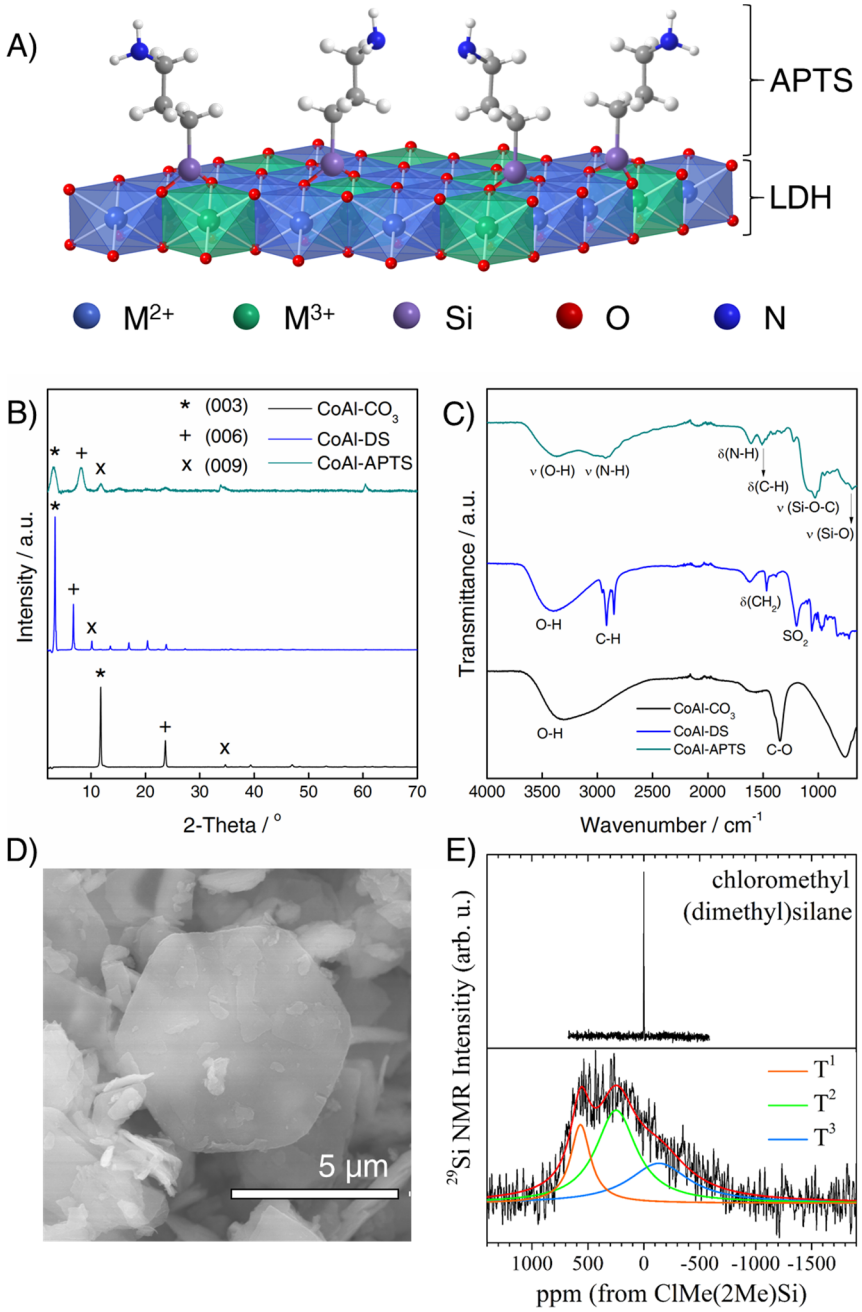

Figure 3.4. Schematic illustration of a LDH functionalized with APTS molecules, bonded *via* O atoms (A). Powder XRD (B) and FTIR spectra (C) of the CoAl-LDH family. FESEM image of CoAl-APTS sample (D). ^{29}Si NMR spectra of CoAl-APTS (bottom) and chloromethyl(dimethyl)silane as reference (top) (E).

The ^{29}Si NMR structure can be decomposed into 3 Lorentzian curves (colored lines, noted with T^1, T^2 and T^3 in **Fig. 3.4E**), following the notation of Q. Tao *et al.*[57], which can be associated with the different siloxane bond structures (1, 2 or 3 Si are present in the chain). Unfortunately, the broadening hinders the exact geometry.

Covalent functionalization was also carried out on NiFe-LDH, starting from the pristine material NiFe-Anthraquinone (NiFe-AQ), synthesized according to the topochemical oxidation method reported elsewhere.[58,59] Afterwards, NiFe-DS intermediate was obtained *via* anion exchange reaction[59] and NiFe-APTS sample was synthesized following a modification of the method described by Kim and coworkers.[39] As stated for the CoAl-APTS, physical characterization of the functionalized NiFe-APTS indicated the covalent bonding of the silane molecule (**Fig. 3.5**). XRPD (**Fig. 3.5A**) and FTIR (**Fig. 3.5B**) spectra confirmed the successful synthesis of the different intermediates, and the electronic microscopy highlighted a less defined morphology in contrast to that found for the CoAl-APTS counterpart (**Fig. 3.5C**). ^{29}Si NMR exhibited a broad structure due to the strong dipole-dipole interaction of the Si nuclei, which is an indication of the covalent boding of the silane molecule between the layers (**Fig. 3.5D**).

In overall, direct exfoliation of CoAl-CO_3 and CoAl-DS have been achieved *via* ultrasonic tip sonication. It is the first time this methodology is used for LDHs, as well as the first time that a carbonate LDH is exfoliated directly in absence of additional anion exchange reactions. Moreover, covalent functionalization of CoAl- and NiFe-LDH have been identified by anchoring a silane molecule to the layered material. In view of these results, LDHs stand out as promising candidates in both topics and an optimistic future can be envisioned.

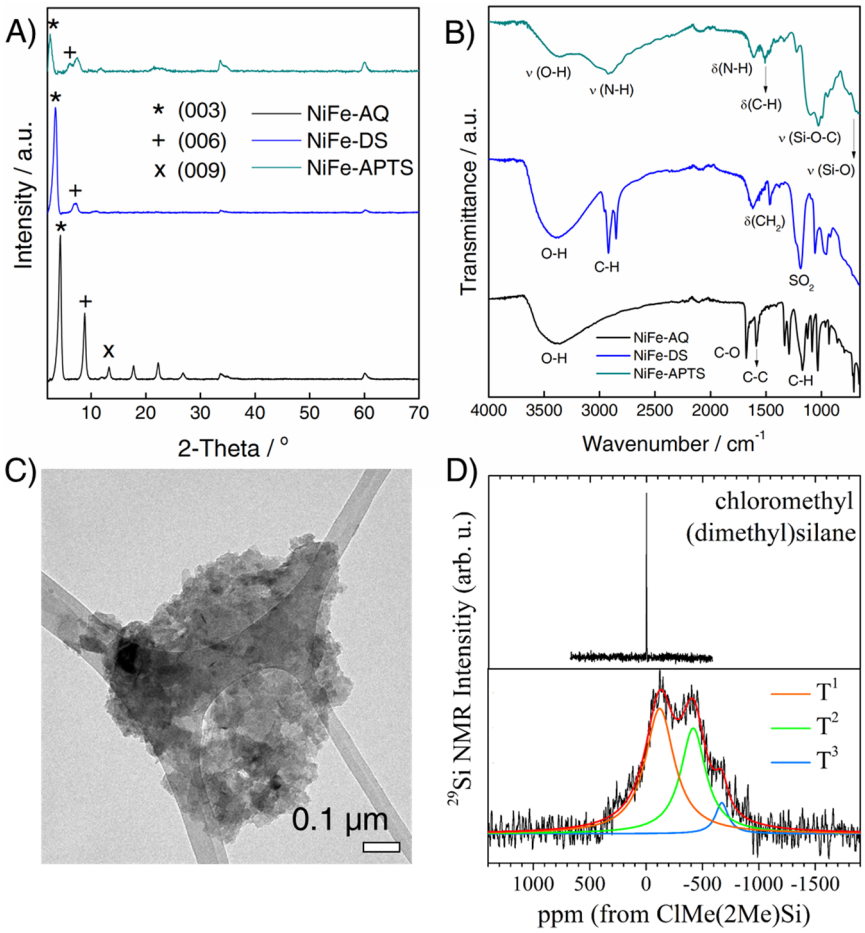

Figure 3.5. Physical characterization of a NiFe-LDH functionalized with APTS molecules: Powder XRD (A) and FTIR spectra (B) of the NiFe-LDH family. HRTEM image of NiFe-APTS sample (C). ^{29}Si NMR spectra of NiFe-APTS (bottom) and chloromethyl(dimethyl)silane as reference (top) (D).

3.3. Contribution of the author.

3.3.1. Article 4: "*Alkoxide-intercalated CoFe-Layered Double Hydroxides as Precursors of Colloidal Nanosheet Suspensions: Structural, Magnetic and Electrochemical Properties*."

The main contribution of this work was the non-aqueous synthesis of pure magnetic alkoxide-intercalated CoFe-LDH. This nanosized LDH was able to be partially exfoliated in water through the hydrolysis of the alkoxide molecules, achieving nanosheets of *ca.* 4 nm in thickness. In addition, the microstructure of the material was unveiled by aberration-corrected STEM-EELS, exhibiting a high quality crystalline structure with some stacking faults. Superparamagnetic size effects were observed due to the reduced dimensions of the flakes (*ca.* 12 – 18 nm). Finally, electrochemical measurements demonstrated the electrode functionality of the sample as a supercapacitive material as well as an excellent performance as OER electrocatalyst in basic media that was reported for the first time in a CoFe-LDH.

The author synthesized, characterised and discussed the results of all samples except the STEM-EELS and electrochemistry measurements, carried out by other authors. The author wrote the paper in collaboration with the other authors.

3.3.2. Article 5: "*Alkoxide-intercalated NiFe-Layered Double Hydroxides Magnetic Nanosheets as Efficient Water Oxidation Electrocatalysts*."

In this paper, we synthesized highly crystalline nanosized NiFe-LDH by means of a non-aqueous methanolic route. Microstructure was revealed with STEM analysis, and the methoxide intercalation was confirmed *via* TG-MS for the first time. This material was exfoliated both in water and in a mixture of buthanol and formamide, resulting in the formation of ultrathin films with a thickness of few nanometers. Activation of the substrates with O_2-plasma became crucial to achieve the best deposition. Magnetic measurements highlighted the superparamagnetic size effects of the LDH with lower ordering temperature than the one found for the most typical micrometric NiFe-LDH. Furthermore, this material exhibited an outstanding

performance as water oxidation electrocatalyst in basic media, therefore confirming its great potential in the field of energy storage and conversion.

The author synthesized, characterised and discussed the results of all samples except the STEM-EELS, TG-MS and electrochemistry measurements, carried out by other authors. The author wrote the paper in collaboration with the other authors.

Note about the papers: Article 5 was selected to be the inside front cover of its respective issue:

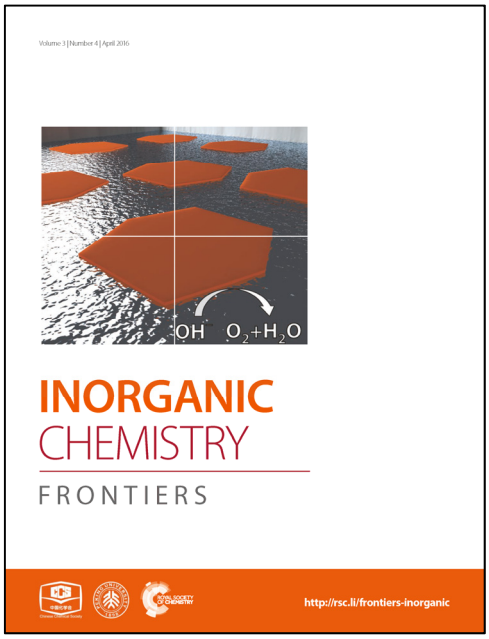

3.4. References.

(1) Wang, Q.; O'Hare, D. Recent Advances in the Synthesis and Application of Layered Double Hydroxide (LDH) Nanosheets. *Chem. Rev.* **2012**, *112*, 4124–4155.

(2) Gholamvand, Z.; McAteer, D.; Backes, C.; McEvoy, N.; Harvey, A.; Berner, N. C.; Hanlon, D.; Bradley, C.; Godwin, I.; Rovetta, A.; et al. Comparison of Liquid Exfoliated Transition Metal Dichalcogenides Reveals $MoSe_2$ to Be the Most Effective Hydrogen Evolution Catalyst. *Nanoscale* **2016**, *8*, 5737–5749.

(3) Coleman, J. N.; Lotya, M.; O'Neill, A.; Bergin, S. D.; King, P. J.; Khan, U.; Young, K.; Gaucher, A.; De, S.; Smith, R. J.; et al. Two-Dimensional Nanosheets Produced by Liquid Exfoliation of Layered Materials. *Science* **2011**, *331*, 568–571.

(4) Backes, C.; Berner, N. C.; Chen, X.; Lafargue, P.; LaPlace, P.; Freeley, M.; Duesberg, G. S.; Coleman, J. N.; McDonald, A. R. Functionalization of Liquid-Exfoliated Two-Dimensional 2H-MoS_2. *Angew. Chem. Int. Ed.* **2015**, *54*, 2638–2642.

(5) Miró, P.; Audiffred, M.; Heine, T. An Atlas of Two-Dimensional Materials. *Chem. Soc. Rev.* **2014**, *43*, 6537–6554.

(6) Gusmão, R.; Sofer, Z.; Bouša, D.; Pumera, M. Pnictogen (As, Sb, Bi) Nanosheets for Electrochemical Applications Are Produced by Shear Exfoliation Using Kitchen Blenders. *Angew. Chem. Int. Ed.* **2017**, *56*, 14417–14422.

(7) Duong, D. L.; Yun, S. J.; Lee, Y. H. Van der Waals Layered Materials: Opportunities and Challenges. *ACS Nano* **2017**, *11*, 11803–11830.

(8) Wang, C. J.; Wu, Y. A.; Jacobs, R. M. J.; Warner, J. H.; Williams, G. R.; O'Hare, D. Reverse Micelle Synthesis of Co−Al LDHs: Control of Particle Size and Magnetic Properties. *Chem. Mater.* **2011**, *23*, 171–180.

(9) Almgren, M.; Swarup, S.; Loefroth, J. E. Effect of Formamide and Other Organic Polar Solvents on the Micelle Formation of Sodium Dodecyl Sulfate. *J. Phys. Chem.* **1985**, *89*, 4621–4626.

(10) Song, F.; Hu, X. Exfoliation of Layered Double Hydroxides for Enhanced Oxygen Evolution Catalysis. *Nat. Commun.* **2014**, *5*, 4477.

(11) Ma, R.; Liu, Z.; Li, L.; Iyi, N.; Sasaki, T. Exfoliating Layered Double Hydroxides in Formamide: A Method to Obtain Positively Charged Nanosheets. *J. Mater. Chem.* **2006**, *16*, 3809–3913.

(12) Ma, R.; Sasaki, T. Nanosheets of Oxides and Hydroxides: Ultimate 2D Charge-Bearing Functional Crystallites. *Adv. Mater.* **2010**, *22*, 5082–5104.

(13) Abellán, G.; Coronado, E.; Martí-Gastaldo, C.; Pinilla-Cienfuegos, E.; Ribera, A. Hexagonal Nanosheets from the Exfoliation of Ni^{2+}-Fe^{3+} LDHs: A Route towards Layered Multifunctional Materials. *J. Mater. Chem.* **2010**, *20*, 7451–7455.

(14) Hibino, T.; Jones, W. New Approach to the Delamination of Layered Double Hydroxides. *J. Mater. Chem.* **2001**, *11*, 1321–1323.

(15) Guo, Y.; Zhang, H.; Zhao, L.; Li, G.-D.; Chen, J.-S.; Xu, L. Synthesis and Characterization of Cd–Cr and Zn–Cd–Cr Layered Double Hydroxides Intercalated with Dodecyl Sulfate. *J. Solid State Chem.* **2005**, *178*, 1830–1836.

(16) Liu, Z.; Ma, R.; Osada, M.; Iyi, N.; Ebina, Y.; Takada, K.; Sasaki, T. Synthesis, Anion Exchange, and Delamination of Co−Al Layered Double Hydroxide: Assembly of the Exfoliated Nanosheet/Polyanion Composite Films and Magneto-Optical Studies. *J. Am. Chem. Soc.* **2006**, *128*, 4872–4880.

(17) Hibino, T. Delamination of Layered Double Hydroxides Containing Amino Acids. *Chem. Mater.* **2004**, *16*, 5482–5488.

(18) Adachi-Pagano, M.; Forano, C.; Besse, J.-P. Synthesis of Al-Rich Hydrotalcite-like Compounds by Using the Urea Hydrolysis Reaction – Control of Size and Morphology. *J. Mater. Chem.* **2003**, *13*, 1988–1993.

(19) Iyi, N.; Matsumoto, T.; Kaneko, Y.; Kitamura, K. A Novel Synthetic Route to Layered Double Hydroxides Using Hexamethylenetetramine. *Chem. Lett.* **2004**, *33*, 1122–1123.

(20) Gardner, E.; Huntoon, K. M.; Pinnavaia, T. J. Direct Synthesis of Alkoxide-Intercalated Derivatives of Hydrocalcite-like Layered Double Hydroxides: Precursors for the Formation of Colloidal Layered Double Hydroxide Suspensions and Transparent Thin Films. *Adv. Mater.* **2001**, *13*, 1263–1266.

(21) Gursky, J. A.; Blough, S. D.; Luna, C.; Gomez, C.; Luevano, A. N.; Gardner, E. A. Particle−Particle Interactions between Layered Double Hydroxide Nanoparticles. *J. Am. Chem. Soc.* **2006**, *128*, 8376–8377.

(22) Latorre-Sanchez, M.; Atienzar, P.; Abellán, G.; Puche, M.; Fornés, V.; Ribera, A.; García, H. The Synthesis of a Hybrid Graphene–nickel/Manganese Mixed Oxide and Its Performance in Lithium-Ion Batteries. *Carbon* **2012**, *50*, 518–525.

(23) Abellán, G.; Carrasco, J. A.; Coronado, E.; Romero, J.; Varela, M. Alkoxide-Intercalated CoFe-Layered Double Hydroxides as Precursors of Colloidal Nanosheet Suspensions: Structural, Magnetic and Electrochemical Properties. *J. Mater. Chem. C* **2014**, *2*, 3723–3731.

(24) Carrasco, J. A.; Romero, J.; Varela, M.; Hauke, F.; Abellán, G.; Hirsch, A.; Coronado, E. Alkoxide-Intercalated NiFe-Layered Double Hydroxides Magnetic Nanosheets as Efficient Water Oxidation Electrocatalysts. *Inorg. Chem. Front.* **2016**, *3*, 478–487.

(25) Ma, W.; Ma, R.; Wang, C.; Liang, J.; Liu, X.; Zhou, K.; Sasaki, T. A Superlattice of Alternately Stacked Ni–Fe Hydroxide Nanosheets and Graphene for Efficient Splitting of Water. *ACS Nano* **2015**, *9*, 1977–1984.

(26) Backes, C.; Higgins, T. M.; Kelly, A.; Boland, C.; Harvey, A.; Hanlon, D.; Coleman, J. N. Guidelines for Exfoliation, Characterization and Processing of Layered Materials Produced by Liquid Exfoliation. *Chem. Mater.* **2017**, *29*, 243–255.

(27) Backes, C.; Szydłowska, B. M.; Harvey, A.; Yuan, S.; Vega-Mayoral, V.; Davies, B. R.; Zhao, P.; Hanlon, D.; Santos, E. J. G.; Katsnelson, M. I.; et al. Production of Highly Monolayer Enriched Dispersions of Liquid-Exfoliated Nanosheets by Liquid Cascade Centrifugation. *ACS Nano* **2016**, *10*, 1589–1601.

(28) Hanlon, D.; Backes, C.; Doherty, E.; Cucinotta, C. S.; Berner, N. C.; Boland, C.; Lee, K.; Harvey, A.; Lynch, P.; Gholamvand, Z.; et al. Liquid Exfoliation of Solvent-Stabilized Few-Layer Black Phosphorus for Applications beyond Electronics. *Nat. Commun.* **2015**, *6*, 8563.

(29) Harvey, A.; He, X.; Godwin, I. J.; Backes, C.; McAteer, D.; Berner, N. C.; McEvoy, N.; Ferguson, A.; Shmeliov, A.; Lyons, M. E. G.; et al. Production of $Ni(OH)_2$ Nanosheets by Liquid Phase Exfoliation: From Optical Properties to Electrochemical Applications. *J. Mater. Chem. A* **2016**, *4*, 11046–11059.

(30) Gibaja, C.; Rodriguez-San-Miguel, D.; Ares, P.; Gómez-Herrero, J.; Varela, M.; Gillen, R.; Maultzsch, J.; Hauke, F.; Hirsch, A.; Abellán, G.; et al. Few-Layer Antimonene by Liquid-Phase Exfoliation. *Angew. Chem. Int. Ed.* **2016**, *55*, 14345–14349.

(31) Georgakilas, V.; Otyepka, M.; Bourlinos, A. B.; Chandra, V.; Kim, N.; Kemp, K. C.; Hobza, P.; Zboril, R.; Kim, K. S. Functionalization of Graphene: Covalent and Non-Covalent Approaches, Derivatives and Applications. *Chem. Rev.* **2012**, *112*, 6156–6214.

(32) Yang, H.; Li, F.; Shan, C.; Han, D.; Zhang, Q.; Niu, L.; Ivaska, A. Covalent Functionalization of Chemically Converted Graphene Sheets via Silane and Its Reinforcement. *J. Mater. Chem.* **2009**, *19*, 4632–4638.

(33) Chou, S. S.; De, M.; Kim, J.; Byun, S.; Dykstra, C.; Yu, J.; Huang, J.; Dravid, V. P. Ligand Conjugation of Chemically Exfoliated MoS_2. *J. Am. Chem. Soc.* **2013**, *135*, 4584–4587.

(34) Zhou, L.; He, B.; Yang, Y.; He, Y. Facile Approach to Surface Functionalized MoS_2 Nanosheets. *RSC Adv.* **2014**, *4*, 32570–32578.

(35) Ma, P. C.; Kim, J.-K.; Tang, B. Z. Effects of Silane Functionalization on the Properties of Carbon Nanotube/Epoxy Nanocomposites. *Compos. Sci. Technol.* **2007**, *67*, 2965–2972.

(36) Sargeant, T. D.; Rao, M. S.; Koh, C.-Y.; Stupp, S. I. Covalent Functionalization of NiTi Surfaces with Bioactive Peptide Amphiphile Nanofibers. *Biomaterials* **2008**, *29*, 1085–1098.

(37) Zhang, F.; Srinivasan, M. P. Self-Assembled Molecular Films of Aminosilanes and Their Immobilization Capacities. *Langmuir* **2004**, *20*, 2309–2314.

(38) Guo, W.; Zhao, Y.; Zhou, F.; Yan, X.; Fan, B.; Li, R. Silylated Layered Double Hydroxide Nanosheets Prepared by a Large-Scale Synthesis Method as Hosts for Intercalation of Metal Complexes. *Appl. Catal. Gen.* **2016**, *522*, 101–108.

(39) Park, A.-Y.; Kwon, H.; Woo, A. J.; Kim, S.-J. Layered Double Hydroxide Surface Modified with (3-Aminopropyl) Triethoxysilane by Covalent Bonding. *Adv. Mater.* **2005**, *17*, 106–109.

(40) Ma, R.; Liang, J.; Takada, K.; Sasaki, T. Topochemical Synthesis of Co−Fe Layered Double Hydroxides at Varied Fe/Co Ratios: Unique Intercalation of Triiodide and Its Profound Effect. *J. Am. Chem. Soc.* **2011**, *133*, 613–620.

(41) Ma, K.; Cheng, J. P.; Zhang, J.; Li, M.; Liu, F.; Zhang, X. Dependence of Co/Fe Ratios in Co-Fe Layered Double Hydroxides on the Structure and Capacitive Properties. *Electrochim. Acta* **2016**, *198*, 231–240.

(42) Kim, S. J.; Lee, Y.; Lee, D. K.; Lee, J. W.; Kang, J. K. Efficient Co–Fe Layered Double Hydroxide Photocatalysts for Water Oxidation under Visible Light. *J. Mater. Chem. A* **2014**, *2*, 4136–4139.

(43) Cadars, S.; Layrac, G.; Gérardin, C.; Deschamps, M.; Yates, J. R.; Tichit, D.; Massiot, D. Identification and Quantification of Defects in the Cation Ordering in Mg/Al Layered Double Hydroxides. *Chem. Mater.* **2011**, *23*, 2821–2831.

(44) Abellán, G.; Coronado, E.; Martí-Gastaldo, C.; Waerenborgh, J.; Ribera, A. Interplay between Chemical Composition and Cation Ordering in the Magnetism of Ni/Fe Layered Double Hydroxides. *Inorg. Chem.* **2013**, *52*, 10147–10157.

(45) Mydosh, J. A. *Spin Glasses: An Experimental Introduction*; Taylor & Francis: London ; Washington, DC, 1993.

(46) Abellán, G.; Coronado, E.; Gómez-García, C. J.; Martí-Gastaldo, C.; Ribera, A. Intercalation of Cobalt(II)-Tetraphenylporphine Tetrasulfonate Complex in Magnetic NiFe-Layered Double Hydroxide. *Polyhedron* **2013**, *52*, 216–221.

(47) Xu, Z. P.; Li, L.; Cheng, C.-Y.; Ding, R.; Zhou, C. High Capacitance Electrode Materials Based on Layered Double Hydroxides Prepared by Non-Aqueous Precipitation. *Appl. Clay Sci.* **2013**, *74*, 102–108.

(48) Lu, Z.; Xu, W.; Zhu, W.; Yang, Q.; Lei, X.; Liu, J.; Li, Y.; Sun, X.; Duan, X. Three-Dimensional NiFe Layered Double Hydroxide Film for High-Efficiency Oxygen Evolution Reaction. *Chem. Commun.* **2014**, *50*, 6479–6482.

(49) Hansen, C. M. 50 Years with Solubility Parameters—past and Future. *Prog. Org. Coat.* **2004**, *51*, 77–84.

(50) Ogawa, M.; Hiramine, M. Direct Correlation between Nanostructure and Particle Morphology during Intercalation. *Cryst. Growth Des.* **2014**, *14*, 1516–1519.

(51) Zhang, C.; Tsuboi, T.; Namba, H.; Einaga, Y.; Yamamoto, T. Enhancement of the Coercivity in Co–Ni Layered Double Hydroxides by Increasing Basal Spacing. *Dalton Trans.* **2016**, *45*, 13324–13331.

(52) *Layered Double Hydroxides*; Duan, X., Evans, D. G., Eds.; Structure and Bonding; Springer-Verlag: Berlin/Heidelberg, 2006; Vol. 119.

(53) Carrasco, J. A.; Abellán, G.; Coronado, E. Influence of Morphology in the Magnetic Properties of Layered Double Hydroxides. *J. Mater. Chem. C* **2018**, *6*, 1187–1198.

(54) Wang, J.; Stevens, L. A.; Drage, T. C.; Wood, J. Preparation and CO_2 Adsorption of Amine Modified Mg–Al LDH via Exfoliation Route. *Chem. Eng. Sci.* **2012**, *68*, 424–431.

(55) Salili, S. M.; Ataie, A.; Barati, M. R.; Sadighi, Z. Characterization of Mechano-Thermally Synthesized Curie Temperature-Adjusted $La_{0.8}Sr_{0.2}MnO_3$ Nanoparticles Coated with (3-Aminopropyl) Triethoxysilane. *Mater. Charact.* **2015**, *106*, 78–85.

(56) Arai, Y.; Ogawa, M. Preparation of Co–Al Layered Double Hydroxides by the Hydrothermal Urea Method for Controlled Particle Size. *Appl. Clay Sci.* **2009**, *42*, 601–604.

(57) Tao, Q.; Zhu, J.; Wellard, R. M.; Bostrom, T. E.; Frost, R. L.; Yuan, P.; He, H. Silylation of Layered Double Hydroxides via an Induced Hydrolysis Method. *J. Mater. Chem.* **2011**, *21*, 10711–10719.

(58) Lee, J.-H.; O'Hare, D.; Jung, D.-Y. Topochemical Oxidation of Transition Metals in Layered Double Hydroxides by Anthraquinone-2-Sulfonate. *Bull. Korean Chem. Soc.* **2012**, *33*, 725–727.

(59) Ma, W.; Ma, R.; Wang, C.; Liang, J.; Liu, X.; Zhou, K.; Sasaki, T. A Superlattice of Alternately Stacked Ni–Fe Hydroxide Nanosheets and Graphene for Efficient Splitting of Water. *ACS Nano* **2015**, *9*, 1977–1984.

Article 4:

Alkoxide-intercalated CoFe-Layered Double Hydroxides as Precursors of Colloidal Nanosheet Suspensions: Structural, Magnetic and Electrochemical Properties

Journal of Materials Chemistry C **2014**, *2*, 3723–3731

Journal of Materials Chemistry C

PAPER

View Article Online
View Journal | View Issue

Cite this: J. Mater. Chem. C, 2014, 2, 3723

Alkoxide-intercalated CoFe-layered double hydroxides as precursors of colloidal nanosheet suspensions: structural, magnetic and electrochemical properties†

Gonzalo Abellán,[a] Jose A. Carrasco,[a] Eugenio Coronado,*[a] Jorge Romero[a] and María Varela[bc]

Received 28th December 2013
Accepted 18th February 2014

DOI: 10.1039/c3tc32578d

www.rsc.org/MaterialsC

Alkoxide-intercalated CoFe-layered double hydroxides (CoFe–LDHs) were synthesized *via* the non-aqueous methanolic route. According to powder X-ray diffraction and field emission scanning electron microscopy, they exhibit a nanosized plate-like morphology with a basal space of 9.21 Å. The hydrolysis of the material in water leads to colloidal suspensions of nanosheets with lateral dimensions of about 20 nm and thicknesses of *ca.* 4 nm as demonstrated by atomic force microscopy and dynamic light scattering. Atomic resolution scanning transmission electron microscopy combined with electron energy-loss spectroscopy confirm the high crystalline quality of the crystals and the proper Co/Fe stoichiometry. The magnetic properties of the CoFe–LDH have been investigated by means of DC and AC magnetic susceptibility measurements and isothermal magnetisation, showing a low-temperature magnetic ordering below *ca.* 7 K with a size-dependent spin-glass like behaviour, and displaying hysteresis cycles at 2 K with a coercive field of 402 G. Moreover, the sample has been tested as an electrode material for supercapacitors in a three-electrode system by means of cyclic voltammetry and galvanostatic charge–discharge experiments, showing high capacitances and stability. Finally, we have explored the electrocatalytic behaviour towards water oxidation, demonstrating its efficient and persistent performance at basic pHs, highlighting their tremendous potential in energy storage devices.

1. Introduction

Two-dimensional (2D) materials have attracted increasing interest in the last few years due to their unique morphology and properties and their use in a variety of applications, ranging from electronics to gas storage or separation, catalysis, high performance sensors or inert protective coatings, among others.[1] Beyond graphene (G),[2] layered chalcogenides,[3] phosphates,[4] titanates,[5] perovskites[6] and metal oxides or hydroxides[7] appear as promising alternatives to this ubiquitous 2D material, displaying complementary physical properties, that open the door for the development of new hybrid multifunctional materials.[8–10]

Layered double hydroxides (LDHs) are a family of inorganic 2D layered materials that have attracted increasing attention because of their interest in catalysis, adsorption, drug delivery, sensors, magnetism or energy storage.[11,12] These lamellar compounds can be described by the general formula $[M^{II}_{1-x}M^{III}_{x}(OH)_2]^{x+}(X^{n-})_{x/m}\cdot nH_2O$ in which M^{II} and M^{III} are divalent and trivalent metals (M^{II} = Mg, Zn, Ni, Co *etc.* and M^{III} = Al, Fe, Cr, Mn *etc.*) and X^{n-} is the interlayer anion (typically carbonate, nitrate, chloride *etc.*) compensating the positive charge of the layers.

The conventional methods for synthesizing LDH-based materials are the coprecipitation at variable or constant pH, and the most recently reported procedures based on ammonia releasing reagents (ARR), which enable the synthesis of highly crystalline micrometric-sized particles. All these synthetic routes were developed in aqueous solutions, leading to LDHs with strong interlayer electrostatic interactions, which can hardly be exfoliated under mild conditions. Thus, organic polar solvents like formamide are often required to obtain unilamellar nanosheets.[13] The obtention of positively charged monolayers (*ca.* 0.8 nm in thickness) of LDHs is a topic of utmost importance, as these nanometric entities can be employed as extremely useful building blocks in the design of novel heterostructured materials.[1,7,13]

[a]Instituto de Ciencia Molecular (ICMol), Universidad de Valencia, Catedrático José Beltrán 2, 46980, Valencia, Paterna, Spain. E-mail: eugenio.coronado@uv.es; Fax: +34 96 354 3273; Tel: +34 96 354 4415

[b]Oak Ridge National Laboratory, Materials Science and Technology Division, Oak Ridge, TN 37830-6071, USA

[c]Universidad Complutense de Madrid, Dpt. Física Aplicada III & Instituto Pluridisciplinar, Madrid 28040, Spain

† Electronic supplementary information (ESI) available. See DOI: 10.1039/c3tc32578d

Gardner *et al.* have reported aqueous transparent colloidal suspensions of LDH particles that exhibit increased surface-to-surface interactions.[14,15] This procedure consists in the non-aqueous synthesis of Al-containing alkoxide-intercalated LDHs that undergo complete hydrolysis in water forming colloidal solutions. This synthetic procedure leads to crystals with sizes below 100 nm, in sharp contrast to the micrometric crystals obtained by ARR methodologies. The nanometric sizes exhibited by these alkoxide-intercalated LDHs could have a significant influence on the magnetic behaviour or electrochemical properties of LDHs, due to some size-dependent magnetic phenomena or an increase in the specific surface area, respectively. This innovative synthetic route has been scarcely employed to date.[13] Indeed, the only reported examples are the NiMn–LDHs, successfully used in the development of high capacity hybrid Li-ion batteries,[16] and more recently, hybrid NiCo–LDHs[17] and Co- or Mn-containing LDHs,[18] which have been tested as electrode materials for supercapacitors, exhibiting high specific capacity. Remarkably, to the best of our knowledge, no magnetic studies have been performed on these alkoxide-containing LDH materials.

Herein, we have synthesized and thoroughly characterized (*via* scanning transmission electron microscopy (STEM) techniques, atomic force microscopy (AFM) and magnetic measurements) alkoxide-intercalated CoFe–LDHs of *ca.* 20 nm size, and these materials exhibit low-temperature magnetism. More interestingly their electrochemical behaviour makes them useful as electrode materials for supercapacitors and as Oxygen Evolution Reaction (OER) electrocatalysts.

2. Experimental section

2.1 Chemicals

Poly(vinylidene fluoride), $(CH_2CF_2)_n$ (PVDF, Sigma Aldrich); carbon black, acetylene 50% compressed (Alfa Aesar, 99.9%); $CoCl_2\cdot 6H_2O$, $FeCl_3\cdot 6H_2O$ (Sigma-Aldrich); lithium perchlorate, $LiClO_4$ (Aldrich); sodium nitrate, $NaNO_3$ (Merck); potassium hydroxide, KOH (Panreac, 99%); methanol (Panreac, 99.9%); and ethanol (Panreac, 98%) were used as received; ultrapure water was obtained from a Millipore Milli-Q equipment.

2.2 Synthesis of CoFe–LDH

CoFe–LDH was synthesized following a modified method described by Gardner *et al.*[14,15]

In a typical procedure, chloride salts of the metals with a stoichiometry ratio of 3 : 1, $CoCl_2\cdot 6H_2O$ (30 mM, 714 mg) and $FeCl_3\cdot 6H_2O$ (10 mM, 270 mg) were added into a three-neck flask and then dissolved with 100 mL of methanol, reaching a total metal cation concentration of 40 mM. The solution was then stirred and heated at 65 °C for 1 h. Afterwards, a solution containing 3.8 g of NaOH in 100 mL of MeOH was slowly added to the previous solution (the addition should last for around 2–3 minutes) and the mixture was left for 72 h under stirring at 65 °C. A constant pressure of an Ar atmosphere was employed to avoid the carbonate contamination and the evaporation of the MeOH. Finally, the resultant brown fine powder product was filtered, washed with MeOH and dried in a vacuum.

$[Co_{0.75}Fe_{0.25}(OH)_{1.3}(OMe)_{0.7}](Cl)_{0.25}\cdot 0.6H_2O$: (C, H, N, calc.: 7.1, 2.1, 0; found: 7.12, 2.34, 0.16).

2.3 Exfoliation of CoFe–LDH

In order to exfoliate the CoFe–LDH platelets in water, typically 10 mg of the sample were dissolved in 10 mL of Milli-Q water and then the mixture was sonicated during 30 min. Afterwards, the solution was centrifuged at 2000 rpm for 10 minutes and sonicated again for 30 min more. The colloidal suspension was then taken to carry out the measurements over the exfoliated platelets.

2.4 Synthesis of a CoFe–LDH-coprecipitate

A CoFe–LDH-coprecipitate was synthesized following the method described by Rives *et al.*[19]

In a typical procedure, the nitrate salts of the metals, 0.012 mol of $Co(NO_3)_2\cdot 6H_2O$ and 0.006 mol of $Fe(NO_3)_3\cdot 9H_2O$, were dissolved in 25 mL of Milli-Q water (previously boiled in a microwave (MW) and stored under an argon atmosphere for 1 hour) and then the solution was added dropwise (*ca.* 30 drops per min) to a solution containing 0.031 mol Na_2CO_3 in 50 mL of Milli-Q water (previously boiled in a MW and stored under an argon atmosphere for 1 hour). The resulting mixture was stirred at 70 °C for 30 h under an argon atmosphere (with the system sealed hermetically). After that, the light brown fine powder was filtered, washed thoroughly with Milli-Q water and EtOH and dried in a vacuum. Further characterization can be found in ESI 1.†

2.5 Physical characterization

Real space studies of the samples were carried out by aberration corrected scanning transmission electron microscopy (STEM) and electron energy-loss spectroscopy (EELS) in a JEOL JEM-ARM200CF electron microscope equipped with a spherical aberration corrector and a Gatan Quantum EEL spectrometer, operated at 200 kV. Samples were prepared by dropping a colloidal suspension of the fresh sample in Milli-Q water on a holey carbon-coated copper grid for STEM-EELS observation. Field emission scanning electron microscopy (FESEM) studies were performed on a Hitachi S-4800 microscope operating at an accelerating voltage of 20 kV and without metallization of the samples. Thermogravimetric analysis (TGA) of all compounds were carried out with a Mettler Toledo TGA/SDTA 851 apparatus in the 25–800 °C temperature range at a 10 °C min^{-1} scan rate and an air flow of 30 mL min^{-1}. X-ray diffraction (XRD) patterns were obtained using a Philips X'Pert diffractometer using the copper radiation (Cu-Kα = 1.54178 Å). Infrared spectra were recorded in a FT-IR Nicolet 5700 spectrometer in the 4000–400 cm^{-1} range with a nominal resolution of 0.4 cm^{-1}. Atomic force microscopy (AFM) measurements were collected in a Multimode atomic force microscope (Veeco Instruments, Inc.). Typically, a freshly diluted emulsion resulting from the hydrolysis of CoFe–LDH samples in water was deposited onto a clean Si wafer by spin coating at 5000 rpm. The images were obtained with a Si tip (frequency and K of $\approx$300 kHz and 42 N m^{-1},

respectively) using the tapping-mode in air at room temperature. Images were recorded with 512 × 512 pixels and a 0.5–1 Hz scan rate. Processing and analysis of the images were carried out using the Nanotec WSXM-4.0 Beta 6.5 software (http://www.nanotec.es).[20] Dynamic light scattering (DLS) measurements were recorded at 25 °C with a Zetasizer Nano ZS instrument (Malvern Instrument Ltd) on a freshly exfoliated sample as described before. Magnetic measurements were carried out with a Quantum Design superconducting quantum interference device (SQUID) MPMS-XL-5. The susceptibility data were corrected from the diamagnetic contributions of the atomic constituents of the samples as deduced from Pascal's constant tables and the sample holder. The dc data were collected under an external applied field of 100 or 1000 G in the 2–300 K temperature range. Magnetization studies were performed between −5 and +5 T at a constant temperature of 2 K.

2.6 Electrochemical measurements

The electrochemical experiences were executed using an Autolab electrochemical workstation (PGSTAT-100 potentiostat/galvanostat) connected to a personal computer that uses GPES electrochemical software.

The materials were mixed with acetylene black and PVDF at a mass ratio of 80 : 10 : 10 in ethanol and deposited on a nickel foam electrode. The as-prepared nickel foam electrodes were dried overnight at 70 °C and pressed. Each working electrode contained about 1 mg of an electroactive material and had a geometric surface area of about 1 cm^2. A typical three-electrode experimental cell equipped with a stainless steel plate having 4 cm^2 of surface area as the counter electrode and a Metrohm Ag/AgCl (3 M KCl) as the reference electrode were used for the electrochemical characterization of the nanocomposite materials trapped by the working electrodes.

The electrochemical measurements were carried out in aqueous KOH solutions as the electrolyte at the indicated concentrations. Ultrapure water was obtained from Milli-Q equipment. The specific capacitance (C), was calculated from the cyclic chronopotentiometric curves according to eqn (1):

$$C = I\Delta t/m\Delta V \quad (1)$$

where I is the charge/discharge current, Δt is the time for a full charge or discharge, m is the weight in grams of the active material in the electrode layer, and ΔV is the voltage change after a full charge or discharge.

The electrocatalytic properties were studied in the aforementioned working electrodes, measuring the cyclic voltammograms at a scan rate of 5 mV s^{-1} in 0.1 M and 1 M aqueous KOH solutions. In addition, chronoamperometric studies were performed at constant potentials (0.83 V for 0.1 M KOH and 0.75 V for 1 M KOH). All potentials reported in this manuscript were converted to the NHE reference scale using $E(\mathrm{NHE}) = E^{\circ}(\mathrm{Ag/AgCl}) + 0.197$ V.

3. Results and discussion

The synthesis of the CoFe–LDH was performed in non-aqueous media by following a modified synthetic method reported by Gardner *et al.*[14] In this synthesis, a methanolic solution including the metal chloride salts was mixed with a NaOH solution at 65 °C. After 72 h a brown precipitate was obtained; then the particles were filtered and washed thoroughly with methanol. The dark-brown powder was then placed in a vacuum chamber in order to avoid the carbonate contamination. On the basis of microanalysis, thermogravimetric analysis and elemental analysis, the proposed chemical formula was estimated to be: $[Co_{0.75}Fe_{0.25}(OH)_{1.3}(OMe)_{0.7}](Cl)_{0.25}\cdot 0.6H_2O$; Co/Fe = 3 : 1.

The formation of the LDH phase was confirmed by powder X-ray diffraction (PXRD), exhibiting the typical hydrotalcite-like profile with (00l) basal reflections at low angles and the characteristic (110) doublet at around 60° in 2θ. The estimated basal space is of 9.21 Å, in excellent accordance with that reported for an MgAl–Cl–MeOH LDH.[14] The broadness of the peaks indicates that the sample is composed of nanometric particles, in clear contrast to that expected for traditional coprecipitated LDHs. In this sense, for comparative purposes Fig. 1 shows the PXRD pattern of a sample synthesized by means of the traditional coprecipitation approach (CoFe–LDH Cop).[19] In this case, well-defined sharp peaks could be observed, with a basal space of 7.59 Å indicating the sole presence of carbonate as interlamellar anions (ESI 1†).[19]

Fourier transform infrared (FT-IR) spectroscopy was also used for studying the nature of the intercalated moieties. In addition to the characteristic M–O bands related to the brucite-like structure at low frequencies, significant bands appeared at around 2926 and 1070 cm^{-1}, indicative of C–H bonds and C–O bonds, respectively, confirming the presence of methoxide in the interlamellar space of the CoFe hydroxide layers (Fig. 1B). Moreover, the broad band centred at *ca.* 3416 cm^{-1} is related to the combination of the stretching vibrations of the hydroxide groups in the layers and the interlayer water molecules (ν_{OH}). Interestingly, if the sample is stored in the presence of air for several days, a band corresponding to CO_3^{2-} absorption appeared at around 1448 cm^{-1} (C═O asymmetric stretching vibrations), as previously reported for several LDH-based hybrids by Iyi and co-workers, demonstrating the high CO_2 affinity of these alkoxide-intercalated LDHs (see Fig. 1B).[21]

Thermogravimetric analysis (Fig. 1C) was also performed in air showing an initial loss (*ca.* 10 wt%) of physisorbed water molecules at low temperatures. As the temperature is increased to 300 °C, an abrupt mass loss (*ca.* 14 wt%) corresponding to the elimination of interlamellar chemisorbed water, followed by decomposition of the organic moiety and the dehydroxylation of the layers, takes place (300–500 °C), accounting for a weight loss of about 34% in total.[21]

The morphology of the CoFe–LDHs was examined by FESEM. The inset in Fig. 1C shows homogeneous samples displaying weak contrast consisting of small platelet-like particles with nanometric lateral dimensions. The nanoparticles seem to be well oriented in a plane-to-plane disposition, in clear contrast to that expected for higher aspect ratio relationship samples several hundreds of nanometers in size, in accordance with that reported for MgAl–LDHs by Gardner[15] or Hibino[22] and co-workers. The Fe/Co atomic ratio was confirmed by means of

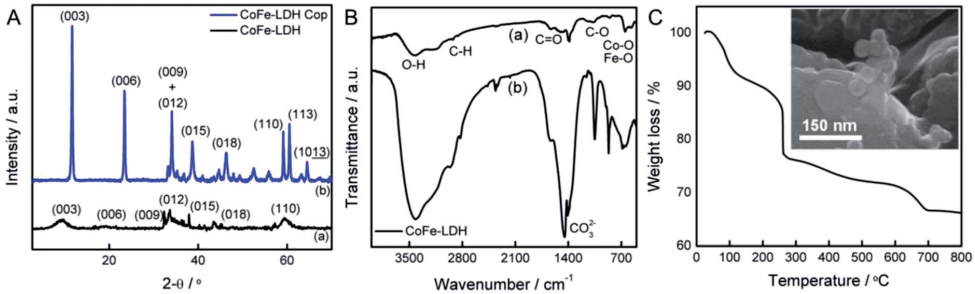

Fig. 1 (A) PXRD patterns of nanosized alkoxide intercalated CoFe–LDH (a) and carbonate intercalated CoFe–LDH Cop synthesized *via* conventional coprecipitation route (b), showing the characteristic reflections of the LDH phase. (B) FT-IR spectra of freshly prepared CoFe–LDH (a) and the powder stored open to the ambient air (b), highlighting the carbonate incorporation into the LDH. (C) Thermogravimetric analysis of CoFe–LDH. The inset represents a FESEM image of CoFe–LDH nanoplates.

EDAX microanalysis, showing an experimental value of 0.34, in excellent accordance with the nominal composition. Thus, in the series of FESEM images of the CoFe–LDH sample, a homogeneous distribution of Co and Fe atoms at the nanometric scale can be seen (Fig. S2†).

To gain further insight on the microstructure of the nanoparticles, we analyzed the sample by aberration-corrected STEM-EELS. Fig. 2A shows a low magnification high angle annular dark field (HAADF) STEM image of the particles. The platelet-like nanocrystals have an average lateral size of 12–18 nm. Fig. 2B shows an EELS spectrum obtained while illuminating a crystal while scanning the electron beam in order to minimize beam induced damage. The O K edge, Fe $L_{2,3}$ edge and Co $L_{2,3}$ edges are visible, near 530 eV, 709 eV and 779 eV, respectively. The quantification of the spectrum using the routine available in the Gatan Digital Micrograph software (and Hartree–Slater cross-sections) yields a Fe/Co atomic ratio of 0.31 ± 0.04, in good agreement with EDAX microanalysis. High magnification atomic resolution images show a high quality crystalline structure (Fig. 2C). Some stacking faults are observed along with occasional lacks of periodicity in the atomic chains, probably related to some disruptions in the cation ordering of the samples.[23,24]

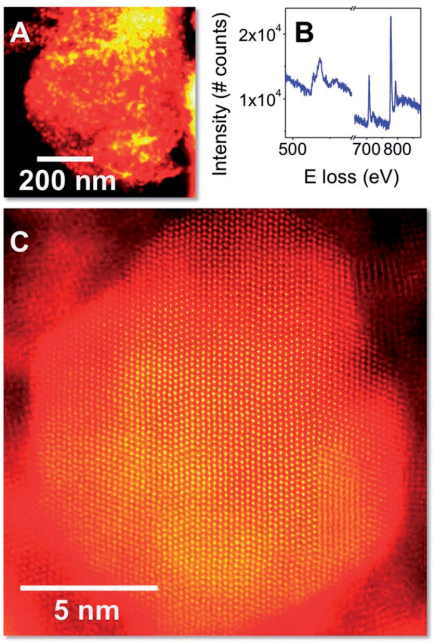

Fig. 2 (a) Low magnification HAADF image. (b) EEL spectrum showing the O K edge, Fe $L_{2,3}$ edge and Co $L_{2,3}$ edges. (c) Atomic resolution HAADF image of a 2D platelet crystal, obtained at 200 kV.

At this point, the ability of other alkoxyde intercalated LDHs to serve as precursors of colloidal nanosheet suspensions after their aqueous hydrolysis is well known.[14–16] In this sense, we have explored the hydrolysis of our sample suspending *ca.* 10 mg of CoFe–LDH in 10 mL of Milli-Q water. The suspension was successively sonicated and centrifuged before characterizing the resulting colloidal suspension. After initial sonication, the Tyndall effect (indicative of the light scattering of nanometric particles) can be clearly observed, showing a translucent colloidal solution brown in color, as previously reported by Sasaki and co-workers for micrometric $Co^{2+}Fe^{3+}$–LDHs exfoliated in formamide (Fig. 3).[25] Direct information of the size of the colloidal suspension in water was obtained from Dynamic Light Scattering (DLS) experiments (Fig. 3A). We observe that the average hydrodynamic diameter, that is a complex function of both the diameter and the particle size for anisotropic materials like LDHs, describes a Gaussian distribution of the size of the particles centred on *ca.* 26 nm in excellent agreement with the electron microscopy observations. In addition, we always observe a less intense peak of particle aggregates at about 530 nm.

Furthermore, we investigated the particle size and thickness by means of tapping mode AFM taking advantage of the topological precision of this technique. We decorated a SiO_2 substrate by spin-coating with our colloidal aqueous suspension, and afterwards we studied its morphology. Fig. 3B exhibits a 3D AFM image of 550 nm × 550 nm area showing

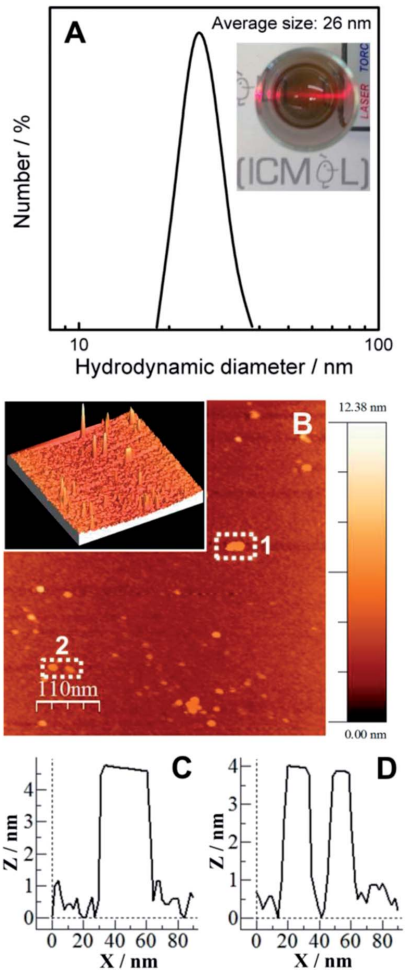

Fig. 3 (A) Distribution of sizes as extracted from DLS measurements for the CoFe–LDH. The inset shows the clearly visible Tyndall effect, resulting from the scattering of the irradiated beam by the particles in solution, confirming the presence of exfoliated LDH nanosheets. (B) AFM topography image of the hydrolysed CoFe–LDH nanosheets deposited on a silicon wafer substrate by spin coating. The inset represents the corresponding three-dimensional image. (C) and (D) height profiles of the selected areas 1 and 2, respectively.

well-dispersed single particles. The cross-sectional analysis corresponding to the highlighted areas 1 and 2 in the topography image shows small nanoparticles with a thickness of about 4 nm and smooth rounded shapes of *ca.* 37, 18 and 13 nm, respectively (Fig. 3C and D). From the analysis of several exfoliated crystals we have measured an average particle size and height of 25.7 ± 8.6 nm and 4.6 ± 0.8 nm, respectively (see ESI 3†). Therefore, we can consider the exfoliated particles as a few-layers of CoFe–LDHs. With the lateral dimensions extracted from electron microscopy and the thickness observed in AFM studies corresponding to 5–8 monolayers, we can estimate an aspect ratio relationship of 4 that is even smaller than that observed for submicrometric MgAl–LDH nanoplatelets suspended in water as reported by Xu *et al.*[26,27]

As previously reported for several magnetic LDHs, CoFe–LDHs are expected to behave as ferrimagnets due to the coexistence of ferromagnetic Co–OH–Co superexchange interactions and antiferromagnetic Co–OH–Fe or Fe–OH–Fe interactions mediated by the –OH bridges.[24,28,29] Static magnetic measurements were performed in a superconducting quantum interference device (SQUID) with freshly prepared powdered samples. DC susceptibility exhibits an abrupt step jump at around 50 K indicative of cooperative magnetic interactions (Fig. 4A). The corresponding thermal variation of the product of the molar magnetic susceptibility times the temperature ($\chi_M T$) decreases regularly from 2.48 emu Kmol^{-1} at 300 K to a minimum of 1.98 emu Kmol^{-1} at 55 K. Afterwards, the $\chi_M T$ product exhibits a sharp increase upon cooling reaching a maximum value of 5.55 emu Kmol^{-1} at 6.7 K, and then sharply decreases to a value of 2.0 emu Kmol^{-1} at 2 K (Table 1 and inset in Fig. 4A). The fitting of the dc data to the Curie–Weiss law above 50 K yields a negative value of the Weiss constant (Θ) of −14.7 K indicative of strong AF interactions within the layers, and a Curie constant value (C) of 2.57 emu Kmol^{-1} in good agreement with that expected for a magnetically diluted combination of Co^{2+} ($S = 3/2$) and Fe^{3+} ($S = 5/2$) ions in the ratio previously determined by electron probe microanalysis (inset in Fig. 4A). Field cooled (FC) and zero-field cooled (ZFC) experiments indicated the presence of cooperative magnetism, presenting a clear bifurcation below an irreversible temperature ($T_{irr} = 4.8$ K) and a ZFC broad maximum at *ca.* 4.4 K (Fig. 4B).

The long-range magnetism was further confirmed by ac dynamic measurements, showing the onset of spontaneous magnetization (T_M) at *ca.* 7.0 K (Fig. 4C). This value is smaller than that exhibited by NiFe–LDH and NiCr–LDH synthesized by ARR methodologies (16.5–16.8 K and 19.5–21 K, respectively) and is indicative of size effects.[24,30] Otherwise, the CoFe–LDH T_M value is slightly higher than those reported for any NiAl– or CoAl–LDHs (<7 K), independent of the particle size and the synthetic methodology used, indicative of a higher extent of F and AF magnetic interactions.[26,28,31,32] Moreover, both the in-phase and out-of-phase signals of the ac data exhibit frequency dependence. The frequency dependence of the χ'_M maxima was quantified with the frequency-shift parameter introduced by Mydosh.[33] Thus, this peak shows a frequency dependence whose normalized variation, measured as the peak shift per decade of frequency, $\Delta T_{max}/T_{max}\Delta(\log \nu)$, is 0.058–0.063 (depending on the T_{max} value used). It is worth mentioning that this value is much larger than the typical values observed in canonical spin glasses (0.005–0.018) and is similar to that observed for spin-glass like materials (0.06–0.08) such as nanosized NiAl– and CoAl–LDHs,[31] $CoAl(OH)_6(DDS)_x$–LDH nanoplatelets[26] and NiFe–CoTPPS hybrids.[34] Furthermore, the fitting of the frequency dependence of χ'_M to an Arrhenius law yields a value for the energy barrier of $\Delta/k_B = 116.9$ K, which is consistent with that of a superparamagnet.[33] This activated behaviour in the CoFe–LDH nanoparticles is probably related to

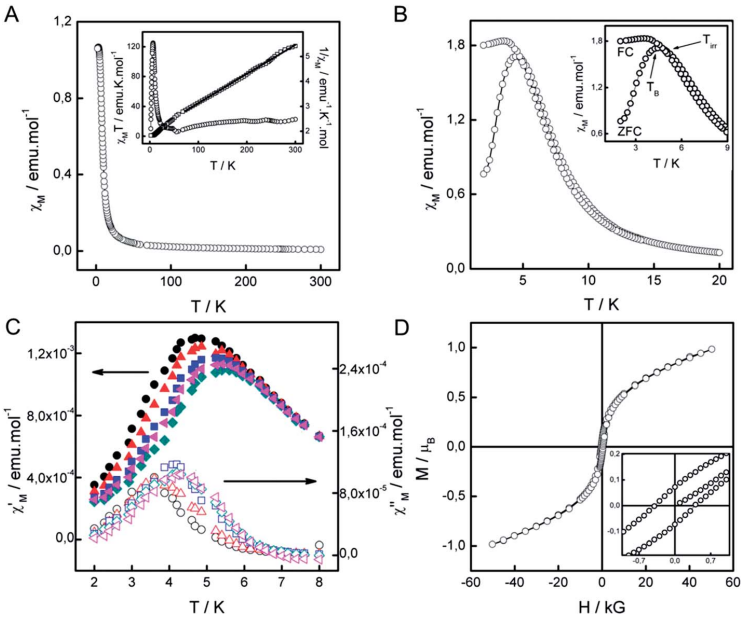

Fig. 4 Magnetic properties of CoFe–LDH. (A) χ_M *vs.* *T* plot. The inset represents the temperature dependence of the $\chi_M T$ product and the fitting (solid line) of the magnetic susceptibility data to a Curie–Weiss law. (B) ZFC-FC molar magnetization. The inset highlights the low temperature region showing the bifurcation point (T_{irr}) and the blocking temperature (T_B). (C) Thermal dependence of the in-phase (χ_M') and out-of-phase (χ_M'') signals at different frequencies from 1 to 997 Hz. (D) Hysteresis cycle at 2 K. The inset shows the low field region.

Table 1 Main magnetic data and parameters for CoFe–LDH[a]

χT_{rt} (emu Kmol^{-1})	C_{SO} (emu Kmol^{-1})	C (emu Kmol^{-1})	Θ (K)	T_{irr} (K)	T_B (K)	T_M (K)	M_S (50 kG) (μ_B)	M_R (μ_B)	H_{Coer} (G)	Δ/k_B (K)	ν_0 (Hz)	ϕ
2.48	2.50	2.57	−14.69	4.8	4.4	7.0	0.98	0.07	402	116.9	3.8×10^{14}	0.063

[a] χT value at room temperature [χT_{rt} (emu Kmol^{-1})]; expected spin-only value of the Curie constant [C_{so} (emu Kmol^{-1})]; experimental Curie constant [C, (emu Kmol^{-1})]; Weiss constant (Θ); temperature of the divergence of the ZFC and FC magnetic susceptibility (T_{irr}); blocking temperature extracted from the ZFC curve (T_B); temperature for the onset of spontaneous magnetization extracted from the χ'' plot (T_M); saturation magnetization (M_S); remnant magnetization (M_R); coercive field at 2 K (H_{Coer}); energy barrier (Δ/k_B) and frequency factor (ν_0), resulting from the fitting of the magnetic susceptibility to the Arrhenius law; Mydosh parameter (ϕ). $S(Co^{2+}) = 3/2$, $S(Fe^{3+}) = 5/2$.

a superparamagnetic size effect,[26,35] in addition to the spin-glass like nature intrinsic to LDHs,[24] indicating that the nanometric dimensions play a crucial role in the magnetic properties of the LDHs. In this sense, the magnetic behaviour of the CoFe–LDH Cop sample whose average size is of several hundred nanometers (see ESI 1.IV†) was also measured, showing the presence of extrinsic impurities and a higher T_M value of *ca.* 11 K (see Fig. S4† for further details). Moreover, Fig. 4D exhibits the field-dependent magnetization at 2 K under an applied field of up to 5 T, showing a small coercive field of *ca.* 402 G, which indicates the soft magnetic character of this nanomaterial.

One of the most relevant aspects of LDHs is their applicability in energy storage devices like Li-ion batteries, supercapacitors (SCs) or water splitting devices.[36] In this context, SCs represent an avenue worth exploring due to the potential to deliver high power densities in short periods of time with high cyclability and durability.[37] SCs are mainly utilized for industrial stationary applications, automotive transportation and portable electronic applications.[38]

We tested the CoFe–LDH sample as the electrode material for SCs in a conventional three-electrode cell. The CoFe–LDH powdered sample was mixed with acetylene black and polyvinylidene fluoride at a mass ratio of 80 : 10 : 10 with ethanol.[39] The resulting slurry was cast on a 1 cm^2 Ni-foam, dried and pressed to minimize the loss of the active material during the electrochemical testing. The electrochemical properties were measured by means of cyclic voltammetry (CV) using 6 M KOH as the electrolyte under an applied voltage range of −0.4 to 0.4 V (*vs.* Ag/AgCl). CV in Fig. 5A reveals a pseudocapacitive behaviour with peaks related to the oxidation of Co (*e.g.* from Co^{2+} to Co^{3+} and then to Co^{4+}) while cathodic peaks indicate the reduction of Co (*e.g.* Co^{4+} to Co^{3+} and then to Co^{2+}). In addition, the effect of

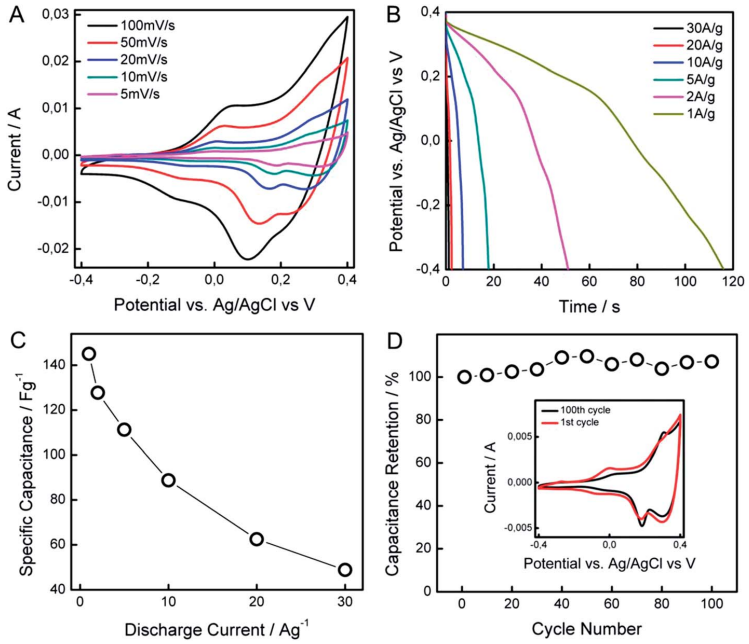

Fig. 5 Electrochemical properties of CoFe–LDH. (A) CV curves at various scan rates in a 6 M KOH aqueous solution. (B) Galvanostatic discharge curves and (C) specific capacitance of the material at different discharge current densities. (D) Specific capacitance *vs.* cycle number at a current density of 10 A g^{-1}. The inset represents the CV curves corresponding to the 1st and the 100th cycles at 10 mV s^{-1}.

the scan rate was also studied; Fig. S5† shows that the cathodic and anodic peak currents (i_p) exhibit an almost linear relationship with the square root of the scan rate ($\nu^{1/2}$), indicating a diffusion-controlled process, in which the electrolyte plays an important role in the pseudocapacitance.[40] All these results support the use of these nanoparticles as electrode materials for supercapacitive devices.[18]

Galvanostatic charge–discharge cycling was also measured in order to study the specific capacitance of this material (Fig. 5B). A large discharge capacity of *ca.* 145 F g^{-1} was obtained for a current density of 1 A g^{-1} (Fig. 5C), overpassing that recently reported (138 F g^{-1} at 20 mA g^{-1}) for a similar CoFe–LDH phase.[18] Moreover, a comparison with other recently reported Co-containing LDH materials reveals that CoFe–LDH presents good specific capacity values if compared with CoNiAl–LDH (90 F g^{-1} at 1 A g^{-1}) or Co_2Al–LDH (190 F g^{-1} at 1 A g^{-1}) synthesized by the traditional coprecipitation method.[41] The CoFe–LDH exhibits a multi-site pseudo-capacitive behaviour similar to that reported by Mousty and co-workers for CoAl–LDHs,[36,41] and is quite similar to that reported for novel layered parallel folding Co_3O_4 nanostructures, in which the formation of superficial cobalt oxyhydroxide (CoOOH) plays a crucial role in the pseudocapacitive behaviour, yielding values close to 200 F g^{-1} at 1 A g^{-1}.[42] The capacity retention was also studied for the first 100 cycles, yielding excellent values with no apparent loss of capacity after the first 100 cycles as depicted in Fig. 5D. It is worth noting that large measuring periods lead to partial loss of the active material. Interestingly, the CoFe–LDH Cop sample exhibits an excellent behaviour as an electrode material for supercapacitors with remarkably higher values of specific capacitance, *e.g.* 505 F g^{-1} at 2 A g^{-1}. This enhanced performance is probably related to the presence of active extrinsic impurities, different particle sizes, porosity and/or crystallinity. Works in progress are trying to clarify these aspects (see further details in Fig. S6†).

Finally, it is believed that the inclusion of active metals like Co or Fe in the LDH layers could promote the electrocatalytic behaviour of these moieties towards the oxygen evolution reaction (OER).[43,44] In fact, preliminary data indicated that the CoFe–LDH nanosheets evolve oxygen under an applied anodic potential. Along this front, we explored the linear sweep voltammetry (LSV) curves at basic pH (0.1 M and 1 M KOH) at a slow scan rate of 5 mV s^{-1} in order to avoid diffusion limitations and minimize the capacitive currents, showing the onset of the oxygen evolution around 0.60 V (pH = 13; 0.797 V *vs.* NHE) and 0.51 V (pH = 14; 0.710 V *vs.* NHE), which represents required overpotentials of *ca.* 397 mV and 310 mV for hydroxide oxidation at 0.1 and 1 M KOH, respectively (Fig. 6A):

$$4OH^- \leftrightarrow O_2 + 2H_2O + 4e^-;\ E^0 = 0.40\ V$$

The catalytic activity towards water oxidation at 1.0 V yields current densities (that is a measure of the catalytic activity) of

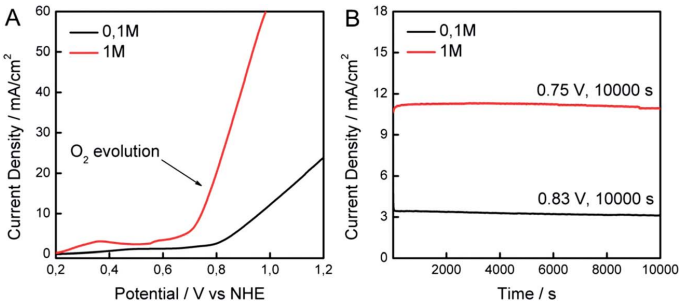

Fig. 6 Electrochemical performance of a CoFe–LDH OER electrocatalyst. (A) LSV curves in 0.1 M and 1 M KOH. (B) Current–time curves obtained for water oxidation reaction at 0.83 V (0.1 M) and 0.75 V (1 M) *vs.* NHE.

12.43 and 62.69 mA cm^{-2}, respectively. These values are higher than those reported for ZnCo–LDHs[43] (11.6 mA cm^{-2}, pH = 13) or CoNi–LDHs[45] (1 mA cm^{-2} at 1.4 V_{NHE}, pH = 7), and surpass that exhibited by Co_3O_4 (ref. 43) (2.90 mA cm^{-2}, pH = 13) as recently reported by Asefa and co-workers. LSV measurements of the CoFe–LDH Cop sample have also been performed, exhibiting a similar behaviour as depicted in Fig. S7.† The onset of the oxygen evolution appears at around 0.57 V (pH = 13; 0.767 V *vs.* NHE) and 0.50 V (pH = 14; 0.697 V *vs.* NHE), respectively. Besides, the values of the current densities at 1.0 V are 8.86 mA cm^{-2} (pH = 13) and 74.36 mA cm^{-2} (pH = 14). In addition, Fig. 6B depicts the chronoamperometric curve of the CoFe–LDH-catalysed water oxidation reaction over 10 000 s at 0.83 V *vs.* NHE at pH = 13 and 0.75 V *vs.* NHE at pH = 14, showing current densities higher than 3 and 10 mA cm^{-2}, respectively. The current–time plot reveals the persistence of the electrocatalytic activity in the studied timescale. This assumption was further confirmed by measuring the LSV after the long reaction period that exhibits an almost similar profile, indicative of an excellent performance towards OER (see Fig. S8†).

The combination of Co and Fe in molecular-based materials for OER electrocatalysis has been recently reported for CoFe Prussian blues analogues, which in fact, exhibited very similar CV curves.[46] This preliminary result highlights the growing importance of LDHs as electrocatalytic materials as recently demonstrated for NiFe–LDH,[44] CoNi–LDH,[45] MnAl–LDH[47] or ZnCo–LDH.[43] Further work is still needed in order to improve the OER activity, optimize the metal ratio composition and/or hybridize these materials with conducting counterparts that could help to enhance the electron transport.[48,49]

4. Conclusions

In summary, we have shown how the use of a non-aqueous route for the synthesis of alkoxide-intercalated CoFe–LDH leads to crystalline anisotropic particles with a Fe : Co atomic ratio of 1 : 3 that exhibit some structural disorder as revealed by STEM, and can be partially exfoliated in water through the hydrolysis of the alkoxide moieties. Our CoFe–LDH nanosheets exhibit superparamagnetic size effects with a temperature for the onset of the spontaneous magnetization of *ca.* 7 K, with no signal of extrinsic magnetic impurities. Finally, electrochemical measurements have demonstrated their electrode functionality as a supercapacitive material, exhibiting high specific capacitance values, and furthermore their excellent performance as OER electrocatalysts in basic media. Our results suggest that aqueous colloidal suspensions of CoFe–LDH nanosheets are good candidates for being used as building blocks in the development of more sophisticated hybrid nanostructures, for example, by hybridizing with carbon nanostructures.[48] Moreover, these layered Co-containing systems can be envisaged as good electrode materials for supercapacitors, Li-ion batteries[13,16] or effective electrocatalysts towards the oxygen evolution reaction,[36,44,50] underscoring a promising future to these earth-abundant nanostructured alkoxide-intercalated LDHs.

Acknowledgements

Financial support from the EU (Projects HINTS and ERC Advanced Grant SPINMOL), the Spanish MINECO (Projects Consolider-Ingenio in Molecular Nanoscience, MAT2011-22785, and CTQ-2011-26507), and the Generalitat Valenciana (Prometeo Program, ISIC-Nano and Gerónimo Forteza Program) is gratefully acknowledged. Support from VLC/CAMPUS and INNCIDE program through Vicerectorat d'Investigació i Política Científica of the University of Valencia is also acknowledged. We also acknowledge E. Tormos and A. López for their help with the experimental work, and J. M. Martínez and G. Agustí for magnetic measurements. This research was sponsored by the Office of Basic Energy Sciences, Division of Materials Sciences and Engineering, U.S. Department of Energy (M.V.). Electron microscopy was performed at the Centro Nacional de Microscopia Electrónica (UCM) sponsored by the ERC Starting Investigator Award STEMOX#239739.

References

1 R. Mas-Ballesté, C. Gómez-Navarro, J. Gómez-Herrero and F. Zamora, *Nanoscale*, 2011, **3**, 20–30.
2 A. K. Geim and K. S. Novoselov, *Nat. Mater.*, 2007, **6**, 183–191.

3 Q. H. Wang, K. Kalantar-Zadeh, A. Kis, J. N. Coleman and M. S. Strano, *Nat. Nanotechnol.*, 2012, **7**, 699–712.
4 A. Clearfield, *Comments Inorg. Chem.*, 1990, **10**, 89–128.
5 T. Sasaki, M. Watanabe, H. Hashizume, H. Yamada and H. Nakazawa, *J. Am. Chem. Soc.*, 1996, **118**, 8329–8335.
6 Y.-S. Han, I. Park and J.-H. Choy, *J. Mater. Chem.*, 2001, **11**, 1277–1282.
7 R. Ma and T. Sasaki, *Adv. Mater.*, 2010, **22**, 5082–5104.
8 P. Gómez-Romero and C. Sanchez, *Functional Hybrid Materials*, John Wiley & Sons, 2006.
9 G. Rogez, C. Massobrio, P. Rabu and M. Drillon, *Chem. Soc. Rev.*, 2011, **40**, 1031–1058.
10 M. Clemente-León, E. Coronado, C. Martí-Gastaldo and F. M. Romero, *Chem. Soc. Rev.*, 2011, **40**, 473–497.
11 V. Rives, *Layered Double Hydroxides: Present and Future*, Nova Publishers, 2001.
12 X. Duan and D. G. Evans, *Layered Double Hydroxides*, Springer, 2006.
13 Q. Wang and D. O'Hare, *Chem. Rev.*, 2012, **112**, 4124–4155.
14 E. Gardner, K. M. Huntoon and T. J. Pinnavaia, *Adv. Mater.*, 2001, **13**, 1263–1266.
15 J. A. Gursky, S. D. Blough, C. Luna, C. Gomez, A. N. Luevano and E. A. Gardner, *J. Am. Chem. Soc.*, 2006, **128**, 8376–8377.
16 M. Latorre-Sanchez, P. Atienzar, G. Abellán, M. Puche, V. Fornés, A. Ribera and H. García, *Carbon*, 2012, **50**, 518–525.
17 H. Chen, L. Hu, M. Chen, Y. Yan and L. Wu, *Adv. Funct. Mater.*, 2014, **24**, 934–942.
18 Z. P. Xu, L. Li, C.-Y. Cheng, R. Ding and C. Zhou, *Appl. Clay Sci.*, 2013, **74**, 102–108.
19 M. del Arco, R. Trujillano and V. Rives, *J. Mater. Chem.*, 1998, **8**, 761–767.
20 I. Horcas, R. Fernández, J. M. Gómez-Rodríguez, J. Colchero, J. Gómez-Herrero and A. M. Baro, *Rev. Sci. Instrum.*, 2007, **78**, 013705.
21 N. Iyi, Y. Ebina and T. Sasaki, *Langmuir*, 2008, **24**, 5591–5598.
22 T. Hibino and M. Kobayashi, *J. Mater. Chem.*, 2005, **15**, 653–656.
23 S. Cadars, G. Layrac, C. Gérardin, M. Deschamps, J. R. Yates, D. Tichit and D. Massiot, *Chem. Mater.*, 2011, **23**, 2821–2831.
24 G. Abellán, E. Coronado, C. Martí-Gastaldo, J. Waerenborgh and A. Ribera, *Inorg. Chem.*, 2013, **52**, 10147–10157.
25 R. Ma, Z. Liu, K. Takada, N. Iyi, Y. Bando and T. Sasaki, *J. Am. Chem. Soc.*, 2007, **129**, 5257–5263.
26 C. J. Wang, Y. A. Wu, R. M. J. Jacobs, J. H. Warner, G. R. Williams and D. O'Hare, *Chem. Mater.*, 2011, **23**, 171–180.
27 Z. P. Xu, G. S. Stevenson, C.-Q. Lu, G. Q. (Max) Lu, P. F. Bartlett and P. P. Gray, *J. Am. Chem. Soc.*, 2006, **128**, 36–37.
28 E. Coronado, J. R. Galán-Mascarós, C. Martí-Gastaldo, A. Ribera, E. Palacios, M. Castro and R. Burriel, *Inorg. Chem.*, 2008, **47**, 9103–9110.
29 G. Abellán, J. A. Carrasco and E. Coronado, *Inorg. Chem.*, 2013, **52**, 7828–7830.
30 J. J. Almansa, E. Coronado, C. Martí-Gastaldo and A. Ribera, *Eur. J. Inorg. Chem.*, 2008, **2008**, 5642–5648.
31 J. Pérez-Ramírez, A. Ribera, F. Kapteijn, E. Coronado and C. J. Gómez-García, *J. Mater. Chem.*, 2002, **12**, 2370–2375.
32 G. Abellán, F. Busolo, E. Coronado, C. Martí-Gastaldo and A. Ribera, *J. Phys. Chem. C*, 2012, **116**, 15756–15764.
33 J. A. Mydosh, *Spin glasses: an experimental introduction*, Taylor & Francis, London, Washington, DC, 1993.
34 G. Abellán, E. Coronado, C. J. Gómez-García, C. Martí-Gastaldo and A. Ribera, *Polyhedron*, 2013, **52**, 216–221.
35 J. D. Rall and M. S. Seehra, *J. Phys.: Condens. Matter*, 2012, **24**, 076002.
36 C. Mousty and F. Leroux, *Recent Pat. Nanotechnol.*, 2012, **6**, 174–192.
37 G. Wang, L. Zhang and J. Zhang, *Chem. Soc. Rev.*, 2012, **41**, 797–828.
38 X. Li and B. Wei, *Nano Energy*, 2013, **2**, 159–173.
39 G. Abellán, E. Coronado, C. Martí-Gastaldo, A. Ribera and T. F. Otero, *Part. Part. Syst. Charact.*, 2013, **30**, 853–863.
40 E. Scavetta, B. Ballarin, M. Gazzano and D. Tonelli, *Electrochim. Acta*, 2009, **54**, 1027–1033.
41 P. Vialat, F. Leroux, C. Taviot-Gueho, G. Villemure and C. Mousty, *Electrochim. Acta*, 2013, **107**, 599–610.
42 D. Wang, Q. Wang and T. Wang, *Inorg. Chem.*, 2011, **50**, 6482–6492.
43 X. Zou, A. Goswami and T. Asefa, *J. Am. Chem. Soc.*, 2013, **135**, 17242–17245.
44 M. Gong, Y. Li, H. Wang, Y. Liang, J. Z. Wu, J. Zhou, J. Wang, T. Regier, F. Wei and H. Dai, *J. Am. Chem. Soc.*, 2013, **135**, 8452–8455.
45 Y. Zhang, B. Cui, C. Zhao, H. Lin and J. Li, *Phys. Chem. Chem. Phys.*, 2013, **15**, 7363–7369.
46 S. Pintado, S. Goberna-Ferrón, E. C. Escudero-Adán and J. R. Galán-Mascarós, *J. Am. Chem. Soc.*, 2013, **135**, 13270–13273.
47 S. Werner, V. W. Lau, S. Hug, V. Duppel, H. Clausen-Schaumann and B. V. Lotsch, *Langmuir*, 2013, **29**, 9199–9207.
48 M.-Q. Zhao, Q. Zhang, J.-Q. Huang and F. Wei, *Adv. Funct. Mater.*, 2012, **22**, 675–694.
49 Y. Liang, Y. Li, H. Wang and H. Dai, *J. Am. Chem. Soc.*, 2013, **135**, 2013–2036.
50 H. Wang and H. Dai, *Chem. Soc. Rev.*, 2013, **42**, 3088–3113.

Supplementary Information

Alkoxide-intercalated CoFe-layered double hydroxides as precursors of colloidal nanosheet suspensions: structural, magnetic and electrochemical properties

Gonzalo Abellán,[a] Jose A. Carrasco,[a] Eugenio Coronado,[a,*] Jorge Romero,[a] María Varela,[b,c]

[a] *Instituto de Ciencia Molecular (ICMol), Universidad de Valencia, Catedrático José Beltrán 2, 46980, Paterna, Valencia, Spain.*

[b] *Oak Ridge National Laboratory, Materials Science and Technology Division, Oak Ridge, TN 37830-6071, USA.*

[c] *Universidad Complutense de Madrid, Dpt. Fisica Aplicada III & Instituto Pluridisciplinar. Madrid 28040, Spain.*

Contents

SI 1: Physical Characterization of CoFe-LDH synthesized *via* coprecipitation route.

SI 1.I: Chemical Composition.

Metallic atomic composition of bulk samples was determined by means of electron probe microanalysis (EPMA) performed in a Philips SEM-XL30 equipped with an EDAX microprobe. Carbon, hydrogen and nitrogen contents were determined by microanalytical procedures using an EA 1110 CHNS-O elemental analyzer from CE Instruments. The proposed chemical formula was estimated to be: $[Co_{0.67}Fe_{0.33}(OH)_2](CO_3)_{0.16}\cdot 0.2H_2O$; Co/Fe = 2 / 1. (C,H,N, calc: 1.9, 2.3, 0; found: 1.56, 2.44, 0.14).

SI 1.II: FT-IR Spectra.

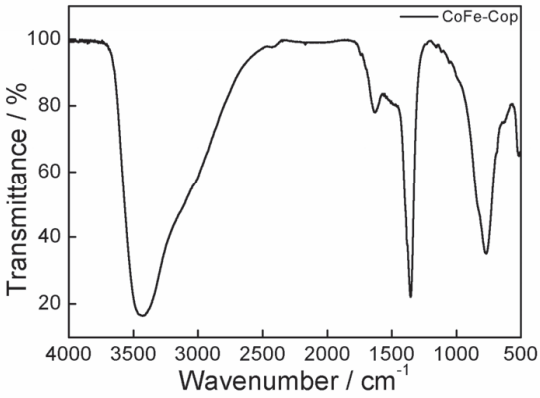

SI 1.III: Thermogravimetric Analysis.

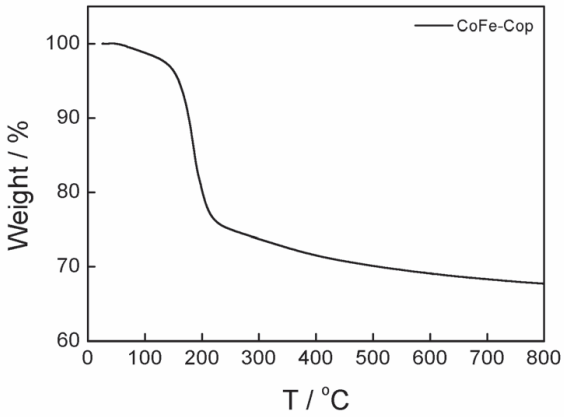

SI 1.IV: FESEM images of CoFe-LDH Cop.

FESEM images of the CoFe-LDH Cop sample show a wide distribution of sizes of several hundred nanometers.

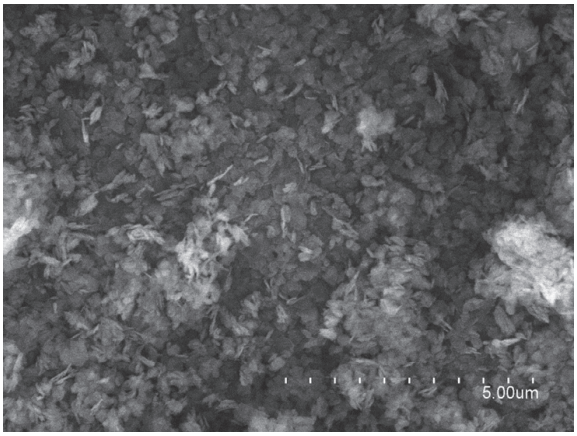

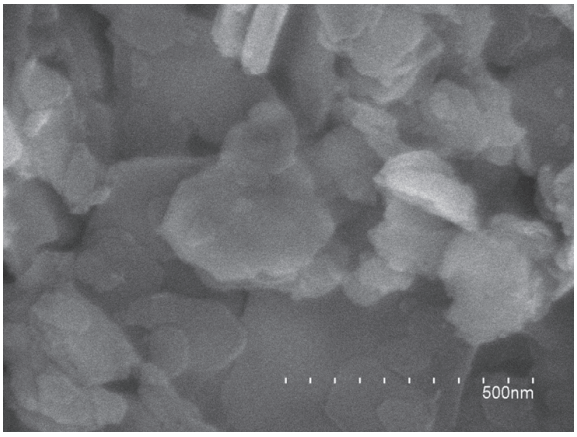

SI 2. FESEM-EDS study of CoFe-LDH.

(A and B) Field-emission scanning electron microscopy with elemental mapping (FESEM-EDS) images of CoFe-LDH measured at different magnifications can be observed in (A) and (B), showing the homogeneous distribution of Co (purple) and Fe (green) in the sample, discarding the presence of segregated phases.

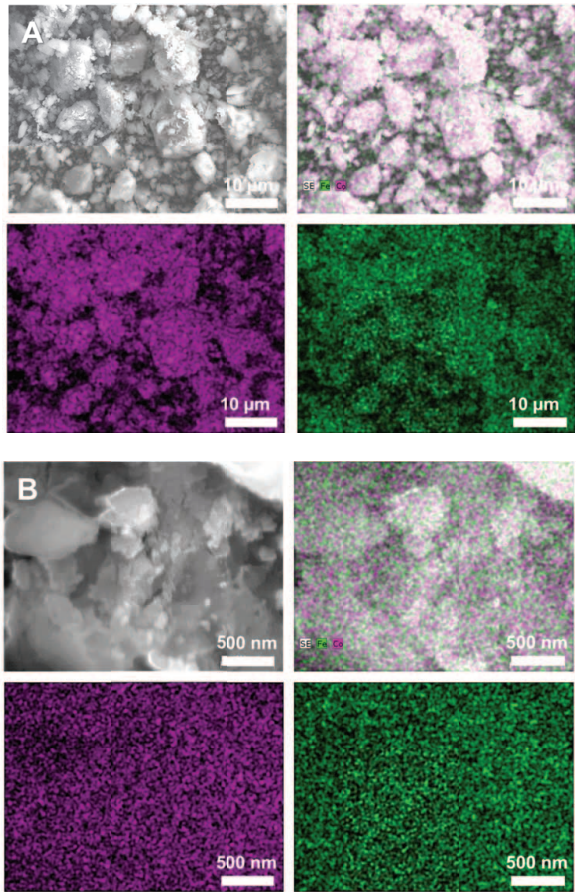

SI 3. AFM study of exfoliated CoFe-LDH.

In order to further determine the lateral dimensions and height of our LDH nanosheets we have measured several exfoliated CoFe-LDHs. The following Figure shows the corresponding AFM histograms of the exfoliated particles in water, depicting the (A) particle-size data and (B) the corresponding particle-height.

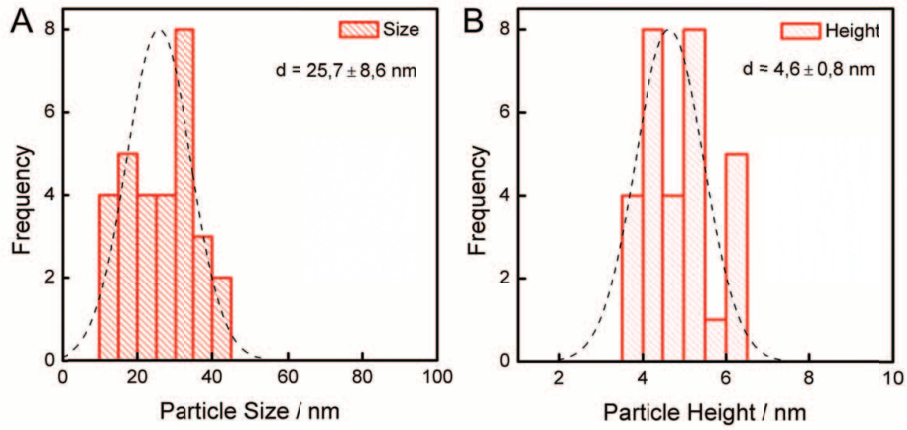

Control experiment on SiO_2 prepared by the same procedure with its height profile.

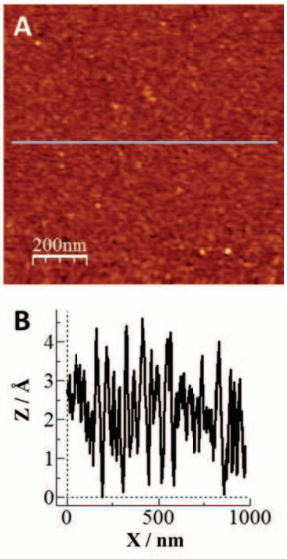

SI 4. Magnetic properties of CoFe-LDH synthesized *via* coprecipitation route.

(A) The temperature-dependent magnetic susceptibility, χ, reported as, χT' versus T shows an almost linear increase above ca. 25 K for the CoFe-LDH Cop sample, whilst no increase was observed for the CoFe-LDH sample (Figure 4 main text). In both cases (CoFe-LDH and CoFe-LDH Cop), the drop observed below 20 K defining a maximum corresponds to the intrinsic cooperative magnetism in the LDH layers. (B) The measurements of the ac susceptibility revealed a temperature for the onset of the spontaneous magnetization (TM) of ca. 11 K, 4 K higher that that exhibited by the pure CoFe-LDH (Table 1 main text), indicative of size effects, with an average size of several hundred nanometers for the CoFe-LDH Cop platelets in contrast with the homogeneous distribution of sizes for the CoFe-LDH, as depicted in the FESEM measurements.

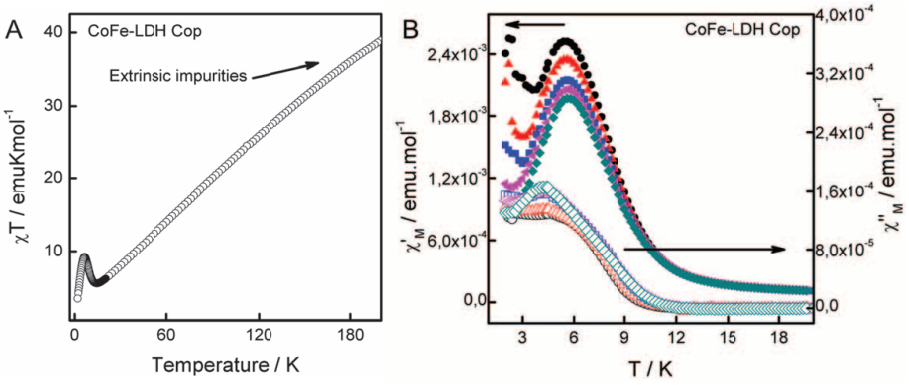

SI 5: Diffusional behaviour of CoFe-LDH: peak current (i_p) *vs.* square root of scan rate ($\nu^{1/2}$) plots.

Cyclic voltammograms of CoFe-LDH at different scan rates (left) indicating the fitted peaks.

Plot of the peak current *vs*. square root of scan rate ($\nu^{1/2}$) for peaks P1 and P2 (right).

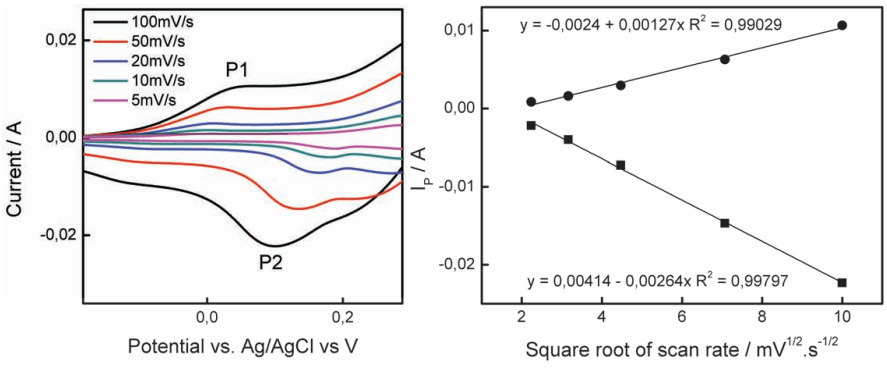

SI 6: Electrochemical properties of CoFe-LDH Cop

(A) CV curves at various scan rates in 6 M KOH aqueous solution. (B) Galvanostatic discharge curves and (C) specific capacitance of the material at different discharge current densities. (D) Specific capacitance *vs*. cycle number at a current density of 40 Ag^{-1}.

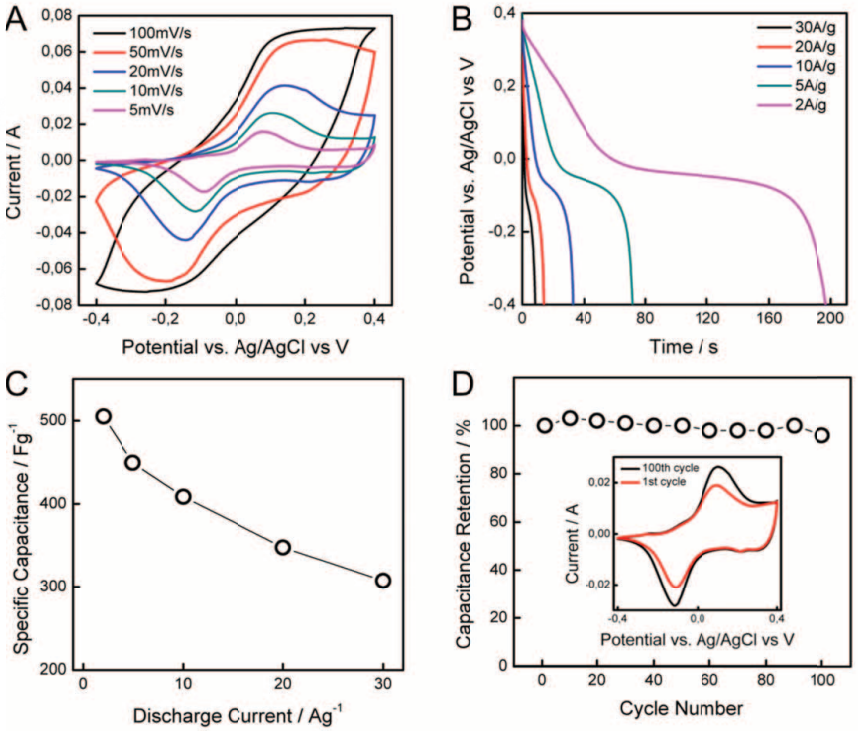

SI 7. Comparison of LSV curves for CoFe-LDH and CoFe-LDH Cop in 0.1 M and 1 M KOH.

The direct comparison between CoFe-LDH and CoFe-LDH Cop leads to a similar behaviour strongly dependent on pH, with some differences probably arising from the extrinsic sources as well as the different particle size and/or morphology. Further studies are needed in order to clarify these differences on the electrocatalytic behaviour.

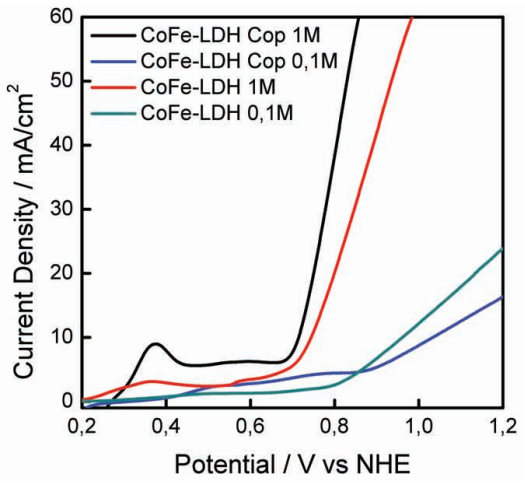

SI 8: Linear sweep voltammetry curves of CoFe-LDH.

LSV curves obtained with freshly prepared CoFe-LDH and 10000 s after use under chronoamperometric measurements at 0.83 V (0.1 M) and 0.75 V (1 M) vs ENH.

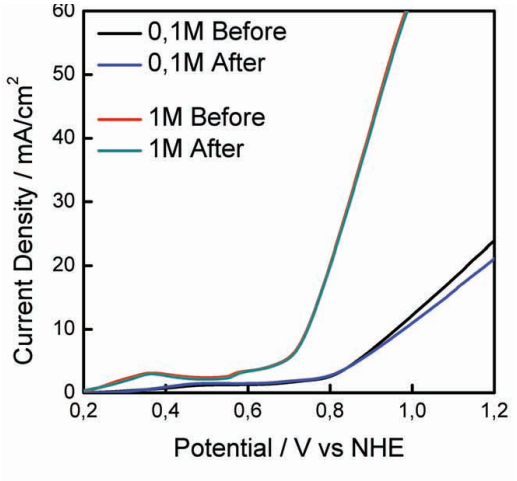

Article 5:

Alkoxide-intercalated NiFe-Layered Double Hydroxides Magnetic Nanosheets as Efficient Water Oxidation Electrocatalysts

Inorganic Chemistry Frontiers **2016**, 3, 478–487

Note about the paper: After the publication of the article, we found that caption for Fig. 7 was provided incorrectly. Correction can be found with the DOI: 10.1039/C6QI90013E. Here we include the original paper and its correction.

Volume 3 | Number 4 | April 2016

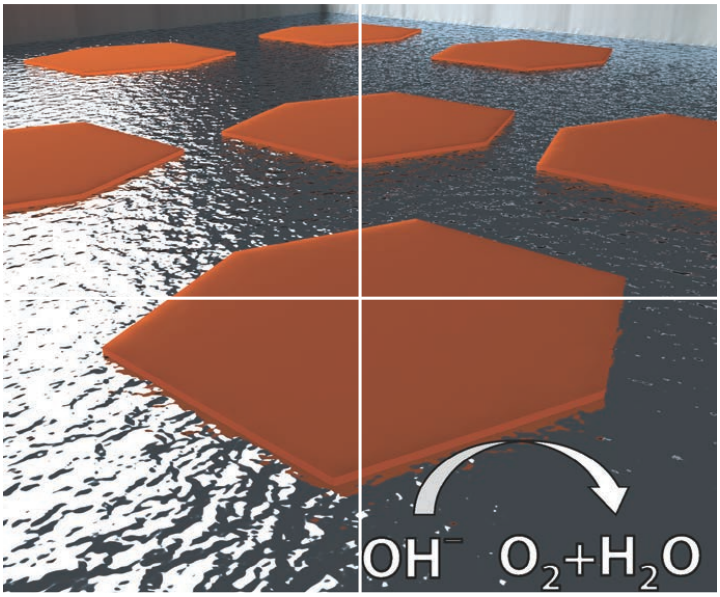

INORGANIC CHEMISTRY

FRONTIERS

Chinese Chemical Society
PEKING UNIVERSITY 1898
ROYAL SOCIETY OF CHEMISTRY

http://rsc.li/frontiers-inorganic

INORGANIC CHEMISTRY
FRONTIERS

RESEARCH ARTICLE

View Article Online
View Journal | View Issue

Cite this: *Inorg. Chem. Front.*, 2016, **3**, 478

Alkoxide-intercalated NiFe-layered double hydroxides magnetic nanosheets as efficient water oxidation electrocatalysts†

Jose A. Carrasco,[a] Jorge Romero,[a] María Varela,[b] Frank Hauke,[c] Gonzalo Abellán,*[a,c] Andreas Hirsch[c] and Eugenio Coronado*[a]

Received 13th January 2016,
Accepted 11th February 2016

DOI: 10.1039/c6qi00009f

rsc.li/frontiers-inorganic

Alkoxide-intercalated NiFe-layered double hydroxides were synthesized *via* the nonaqueous methanolic route. These nanoplatelets exhibit high crystalline quality as demonstrated by atomic resolution scanning transmission electron microscopy combined with electron energy-loss spectroscopy. Moreover, the presence of the alkoxide moieties has been unambiguously demonstrated by means of thermogravimetric analysis coupled to a mass spectrometer. These NiFe-LDHs can be exfoliated in water or organic solvents and processed into homogeneous ultra-thin films (<3 nm thick) with the assistance of O_2-plasma. The study of their behaviour as water oxidation electrocatalysts has shown an outstanding performance at basic pHs (small overpotential of *ca.* 249 mV and Tafel slopes in the range of 52–55 mV per decade).

[a]*Instituto de Ciencia Molecular (ICMol), Universidad de Valencia, Catedrático José Beltrán 2, 46980 Paterna, Valencia, Spain. E-mail: gonzalo.abellan@fau.de*
[b]*Universidad Complutense de Madrid, Dpt. Fisica Aplicada III & Instituto Pluridisciplinar, Madrid 28040, Spain*
[c]*Department of Chemistry and Pharmacy and Institute of Advanced Materials and Processes (ZMP), University Erlangen-Nürnberg, Henkestr. 42, 91054 Erlangen and Dr.-Mack Str. 81, 90762 Fürth, Germany*
†Electronic supplementary information (ESI) available. See DOI: 10.1039/c6qi00009f

Gonzalo Abellán

Gonzalo Abellán was born in Orihuela (Spain). He obtained his Ph.D. in the group of Prof. E. Coronado at the Institute of Molecular Science (ICMol – University of Valencia) in 2014 in the field of hybrid magnetic materials based on layered double hydroxides. Currently he is a Marie Curie Fellow at the University of Erlangen-Nuremberg in the group of Prof. Andreas Hirsch, working in the chemical functionalization of graphene and related 2D materials. Gonzalo is the recipient of several awards including the E-MRS Graduate Student Award or the Valencia Idea Prize in Energy and Environmental, among others. He is pursuing his independent career focused on the chemistry of 2D materials, hybrid materials, magnetism and energy storage and conversion.

Introduction

Since the discovery of graphene,[1] two dimensional (2D) materials have attracted widespread attention from the scientific community,[2] including layered chalcogenides,[3] boron nitride[4] or black phosphorus.[5] In addition to these van der Waals layered solids, other compounds formed by ionic layers can also provide examples of these 2D materials. An extensive family of this type is provided by the layered double hydroxides (LDHs), a class of anionic clays known the since the mid-19th century[6] which have been of interest in catalysis, sensing or magnetism.[7–10]

LDH can be formulated as $[M^{II}_{1-\chi}M^{III}_{\chi}(OH)_2]^{\chi+}(A^{n-})_{\chi/n}\cdot mH_2O$, in which M^{II} and M^{III} are divalent and trivalent metals, respectively (like $M^{II} = Mg^{2+}$, Zn^{2+}, Ni^{2+}, Co^{2+}, and Fe^{2+} or $M^{III} = Al^{3+}$, Fe^{3+}, Co^{3+}, Ni^{3+} or Cr^{3+}), and A^{n-} is the interlayer anion which can be organic or inorganic and is placed between the cationic hydroxide sheets in order to compensate the excess of positive charge. One of the main features of these systems is their high chemical tunability, which allows them to be synthesized with different metallic compositions without altering their structure, leading to a wide range of properties. Moreover, the facile exfoliation of these LDH into monolayer nanosheets has boosted the attention paid to these materials.[11]

Among all the different possible compositions they exhibit, the combination of Ni and Fe (NiFe-LDHs) seems to be the most promising on the basis of its recent successful application as a highly efficient carbon monoxide (CO) oxidation catalyst,[12] their excellent behaviour as electroactive material in the water photolysis,[13–15] their use on high performance

batteries[16,17] or as catalytic precursors for the CVD synthesis of novel carbon nanoforms.[18–21]

The synthesis and exfoliation of pure NiFe-LDHs with high crystallinity and well-defined hexagonal shapes have remained elusive so far.[22,23] Currently, there are two main routes for the synthesis of pure NiFe-LDHs that can be exfoliated into 2D nanosheets, namely the hydrothermal approach using urea as ammonium releasing reagent and triethanolamine as chelating reagent,[23,24] and the use of anthraquinone-2-sulfate that favors the topochemical oxidation of the metals during the layer formation.[25,26] These aqueous methodologies avoid the Fe oxidation, leading to NiFe-LDHs without spinel impurities.[27] When it comes to non-aqueous routes Gardner *et al.* described a synthetic procedure to obtain nanometric alkoxide-intercalated Al-containing LDHs using alcohols as solvents.[28,29] In this sense, we recently applied this method to synthesize pure CoFe-LDHs that can be exfoliated in water and exhibit excellent electrochemical properties.[30]

In the present work, we have extended this non-aqueous route for the synthesis of NiFe-LDHs, obtaining alkoxide-intercalated nanoplatelets that exhibit size-dependent magnetic properties. Furthermore, we have explored their exfoliation in water and developed their processing into ultra-thin films with homogeneous coverage. Finally, we have characterized their electrochemical behavior as OER electrocatalysts showing an outstanding performance in alkaline solution.

Experimental

Chemicals

$NiCl_2{\cdot}6H_2O$, $FeCl_3{\cdot}6H_2O$, $Ni(NO_3)_2{\cdot}6H_2O$, $Fe(NO_3)_3{\cdot}9H_2O$, $C_6H_{15}NO_3$, $CO(NH_2)_2$, NaOH 97%, 1-butanol, and poly(vinylidene fluoride) (PVDF) were purchased from Sigma-Aldrich. Ethanol absolute, methanol (99.9%), and potassium hydroxide KOH (99.99%) were purchased from Panreac. Carbon black, acetylene 50% compressed, was obtained from Alfa Aesar (99.9%) and iridium(IV) oxide from Stream chemicals. All chemicals were used as received. Ultrapure water was obtained from Millipore Milli-Q equipment.

Synthesis of NiFe alkoxide (NiFe-A)

The synthesis of the main sample was carried out following the method described by Gardner *et al.*[28,29] In a typical procedure, Ni and Fe salts were mixed in 100 mL of solvent (MeOH) in a molar ratio of 2 : 1 for a total of 40 mmol of metal cations. This solution was stirred and heated up to 65 °C for 1 h under Ar in a round bottom flask equipped with a reflux condenser. Afterwards, 3.8 g of NaOH dissolved in 100 mL of the MeOH was added dropwise to the initial mixture over a 2–3 min time span. The final mixture was left during 72 h at 65 °C and under magnetic stirring. Finally, the solution was filtered, washed thoroughly with MeOH and dried in vacuum. The final sample was labelled as NiFe-A.

$[Ni_{0.66}Fe_{0.33}(OH)_{1.55}(OMe)_{0.45}](Cl)_{0.33}{\cdot}1H_2O$: (C, H, N, calc.: 4.2, 2.8, 0; found: 4.2, 3.1, 0.1).

Synthesis of NiFe by hydrothermal approach (NiFe-HT)

In a typical procedure, the nitrate salts were dissolved in 50 mL of Milli-Q water together with TEA, reaching a total metal cation concentration of 20 mM, with a ratio Ni : Fe of 2 : 1. TEA concentration was equimolar with Fe one. After that, 50 mL of an aqueous solution of urea (35 mM) was added. The final mixture was placed in a 125 mL stainless steel Teflon lined autoclave and heated up to 125 °C in an oven for 48 h. Afterwards, the autoclave was cooled to room temperature and the powder was filtered, washed with Milli-Q water and ethanol and dried in vacuum. The final sample was labelled as NiFe-HT.

$[Ni_{0.69}Fe_{0.31}(OH)_2](CO_3)_{0.155}{\cdot}0.5H_2O$: (C, H, N, calc.: 2.0, 3.2, 0; found: 2.0, 3.6, 0.3).

Exfoliation and deposition on SiO_2-Si substrates

Tipically, SiO_2-Si substrates were cleaned and treated with oxygen plasma.[31]

For the deposition of exfoliated platelets in water, 1 mg of the sample was dissolved in 10 mL of Milli-Q water and sonicated for 30 min. Then, two approaches were considered, drop casting and spin coating (5000 rpm) of the solution onto the previously cleaned and treated with O_2 plasma SiO_2-Si wafer. On the other hand, for a complete coverage of the substrate a different approach was followed.[31] Typically, 10 mg of the NiFe-A LDHs were dissolved in a mixture of 20 mL of 1-BuOH and 10 mL of formamide in a covered flask. The solution was placed in an ultrasonic bath for 30 min. Then, the SiO_2-Si substrate was submerged into the solution for 5 min, followed by 1 min in a solution of 1-BuOH to remove the excess of LDH platelets. Afterwards, the substrates were dried at 70 °C overnight and stored in vacuum.

Instrumentation

X-ray powder diffraction (XRPD) patterns were obtained with a Philips X'Pert diffractometer using the copper radiation (Cu-Kα = 1.54178 Å). Field emission scanning electron microscopy (FESEM) studies were carried out on a Hitachi S-4800 microscope at an accelerating voltage of 20 kV and 30 seconds of Au/Pd metallization of the samples. ATR Infrared spectra were recorded with an Agilent Cary 630 FTIR spectrometer in the 4000–650 cm^{-1} range with no need of KBr pellets. Scanning transmission electron microscopy and electron energy-loss spectroscopy (STEM/EELS) characterization of the samples was carried out with a JEOL ARM200cF at University Complutense of Madrid, Spain, equipped with an aberration corrector, a cold field emission gun, and a Gatan Quantum spectrometer. Samples were prepared by dropping a colloidal suspension of the fresh sample in EtOH on a holey carbon-coated copper grid for STEM-EELS observation. Thermogravimetric analysis (TGA) coupled with a mass spectrometer (MS) was performed on a Netzsch STA 409 CD instrument equipped with a Skimmer QMS 422 mass spectrometer (MS/EI) with the following programmed time-dependent temperature profile: 25–500 °C with 10 °C min^{-1} gradient and cooling

to room temperature. The initial sample weights were about 5 mg, and the whole experiment was performed under helium with a gas flow of 80 mL min^{-1}. Atomic force microscopy (AFM) measurements were performed with a Multimode atomic force microscope (Veeco Instruments, Inc.). The images were obtained with a Si tip (frequency and K of ≈300 kHz and 42 N m^{-1}, respectively) using the tapping-mode in air at room temperature. Images were recorded with 512 × 512 pixel and a 0.5–1 Hz scan rate. Processing and analysis of the images were carried out using the Nanotec WSXM-5.0 Develop 6.0 software (http://www.nanotec.es).[32] Dynamic light scattering (DLS) measurements were recorded at 25 °C with a Zetasizer Nano ZS instrument from Malvern Instrument Ltd on the aqueous suspensions previously described. Magnetic data were collected with a Quantum Design superconducting quantum interference device (SQUID) MPMS-XL-5. The susceptibility data were corrected from the diamagnetic contributions of the atomic constituents of the samples as deduced from Pascal's constant tables and the sample holder. The dc data were obtained under an external applied field of 100 or 1000 Oe in the 2–300 K temperature range. Magnetization studies were performed between −5 and +5 T at constant temperatures of 2 and 20 K.

Electrochemical measurements

The electrochemical experiments were performed using an Autolab electrochemical workstation (PGSTAT-100 potentiostat/galvanostat) connected to a personal computer that uses GPES electrochemical software.

The powdered materials were mixed with acetylene black and PVDF in a mass ratio of 80 : 10 : 10 in ethanol and deposited on a nickel foam electrode. The as-prepared nickel foam electrodes were dried overnight at 80 °C and pressed. Each working electrode contained about 0.25–0.5 mg of electroactive material and had a geometric surface area of about 1 cm^2. The synthesis of the *in situ* grown films was performed by following the same experimental procedure described for NiFe-A but replacing the magnet used for the stirring with Ni foam leading to the direct growth of NiFe-A on this material.[33] A typical three-electrode experimental cell equipped with a stainless steel plate having 4 cm^2 of surface area as the counter electrode, and a Metrohm Ag/AgCl (3 M KCl) as the reference electrode was used for the electrochemical characterization of the working electrodes. All measurements were carried out with magnetic agitation and nitrogen bubbling.

The electrochemical properties were studied measuring the CV at different scan rates in 1 M KOH aqueous solutions. In addition, chronoamperometric studies were performed at a constant overpotential (j = 0.3 V), and chronopotentiometric studies at constant current densities of 5 and 10 mA cm^{-2}. All potentials reported in this manuscript were converted to the RHE reference scale using E(RHE) = E(NHE) + 0.059 pH = $E°$(Ag/AgCl) + 0.197 V + 0.059 pH. The turnover frequency (TOF) values were calculated from the equation:

$$\mathrm{TOF} = JA/4Fm$$

where J is the current density at a given overpotential of 0.3 V, A is the surface area of the working electrode, F is the Faraday constant and m is the number of moles of metal loaded on the electrode.

Results and discussion

The synthesis of NiFe-LDH alkoxide (NiFe-A) was carried out using a methanolic solution including the metal chloride salts under basic pH at 65 °C, following a modified method reported by Gardner and co-workers.[28–30] After the 72 h of synthesis, the resulting brown precipitate was filtered and washed thoroughly with MeOH, dried in a vacuum chamber and stored under vacuum in order to avoid carbonate contamination.

The synthesis of the LDH phase was confirmed by X-ray powder diffraction (XRPD) analysis (Fig. 1A), showing the characteristic (110) doublet at around 60° in 2θ, and the main basal reflection (003) at around 2θ = 9–9.5°, providing a basal space of *ca.* 9.3 Å, in good agreement with the expected values for MeO-intercalated LDH.[28] For the sake of comparison the XRPD spectrum of the NiFe-LDH obtained by hydrothermal approach (NiFe-HT) was also depicted (Fig. 1A), showing the (003) reflection at a 11.4° indicative of the presence of carbonate anions in the interlamellar space.[20,23]

The Fourier transform infrared spectra (FTIR) of NiFe-A and NiFe-HT are compared in Fig. 1B. There are two bands in the former case at *ca.* 2950 and 1070 cm^{-1}, related to C–H and C–O stretching vibrations, respectively, which are absent in the

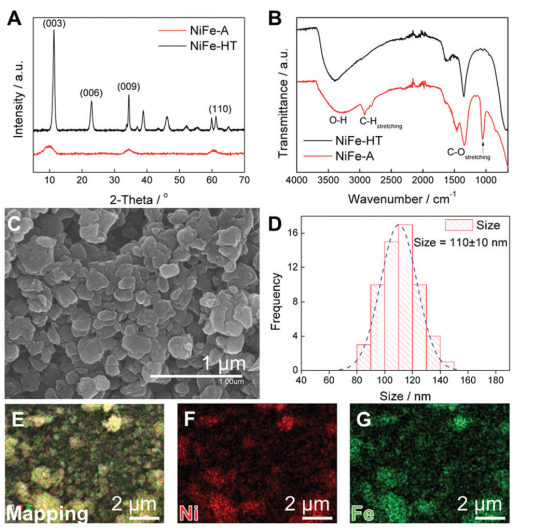

Fig. 1 XRPD (A) and FTIR spectra (B) of the NiFe-A and NiFe-HT samples. FESEM image of NiFe-A (C). Histogram showing the average particle size distribution for the NiFe-A sample (D). Mapping analysis of the NiFe-A highlighting the homogeneous distribution of Ni and Fe in the layers (E, F, and G).

carbonate-intercalated sample, supporting the presence of the alkoxide anion in the interlamellar space.[34]

FESEM measurements were carried out to unveil the morphology of both samples (Fig. 1C). NiFe-A depicts homogeneous lateral dimensions of around 110 nm, in clear contrast to NiFe-HT, which depicts micrometric sizes (see ESI 1 and 2† for additional FESEM images).[24] It is worth to remark that, whereas the morphology of the NiFe-HT consists on well-defined hexagonal shapes, NiFe-A does not show this good definition, resulting into more irregular flakes.

Similar dimensions have been reported for the MgAl derivative by Gursky *et al.*,[29] or conventional NiAl-HT.[35] For CoFe-A synthesized with our non-aqueous method, values of *ca.* 20 nm were reported.[30] EDAX mapping confirmed the expected 2 : 1 Ni : Fe ratio showing a homogeneous distribution of the two metals throughout the whole sample (Fig. 1E–G). Furthermore, elemental analysis, microanalysis, and thermogravimetric analysis of the sample allowed us to estimate the following molecular formula for NiFe-A: $[Ni_{0.66}Fe_{0.33}(OH)_{1.55}(OMe)_{0.45}](Cl^-)_{0.33}\cdot 1H_2O$.

Direct information of the microstructure of the nanoplatelets can be obtained by aberration-corrected STEM-EELS. Fig. 2A shows a high angle annular dark field (HAADF) STEM image of a single NiFe-A flake. The platelet-like nanocrystal has a lateral dimension of ~35 nm, the smaller size is related with the rupture of the flake after the sonication used for the preparation of the TEM grid. Fig. 2B depicts a high magnification atomic resolution image showing a high quality crystalline structure. In order to confirm the chemical composition of the sample, the corresponding EEL spectrum was obtained working at 80 kV and illuminating a crystal while scanning the electron beam in order to minimize the beam-induced damage. The O K, Fe $L_{2,3}$ and Ni $L_{2,3}$ edges are visible, near 530 eV, 708 eV, and 855 eV, respectively. The quantification of the spectra using the routine available in the Gatan Digital Micrograph software (and hydrogenic-white line cross-sections) yields a Ni : Fe atomic ratio of 1 : (0.61 ± 0.09), in good agreement with EDAX microanalysis.

To provide further insight into the chemical nature of the intercalated species we have characterised, for the first time, the NiFe-LDH samples with thermogravimetric analysis coupled with a mass spectrometer (TG-MS) under an inert atmosphere of helium (Fig. 3). This powerful technique allows us to unambiguously identify the interlamellar anions, confirming the intercalation of the alkoxide groups.[36] Analysis of NiFe-HT from room temperature to 500 °C revealed the presence of carbonate (CO_2, *m*/*z* 44) with a continuous mass loss peaking at *ca.* 280 °C. With respect to the H_2O (*m*/*z* 18), a first intense mass loss attributed to the weakly physisorbed water appeared between room temperature and *ca.* 180 °C, then a

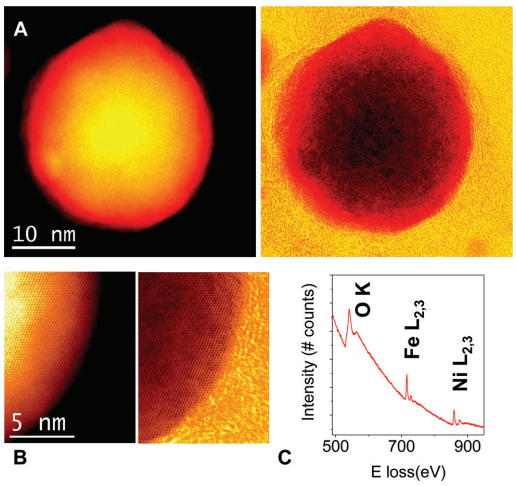

Fig. 2 (A) Annular dark field (ADF) and simultaneously acquired annular bright field (ABF) low magnification images –left and right respectively– of a small NiFe-A flake. The flake is monocrystalline and the crystal quality is very high. (B) High magnification ADF (left) and ABF (right) images of the flake edge, exhibiting a high degree of crystallinity. No major defects are observed. (C) EEL spectra of a flake, showing the O K, Fe $L_{2,3}$ and the Ni $L_{2,3}$ absorption edges. STEM images acquired at an acceleration voltage of 200 kV, EEL spectrum measured at 80 kV on a different flake.

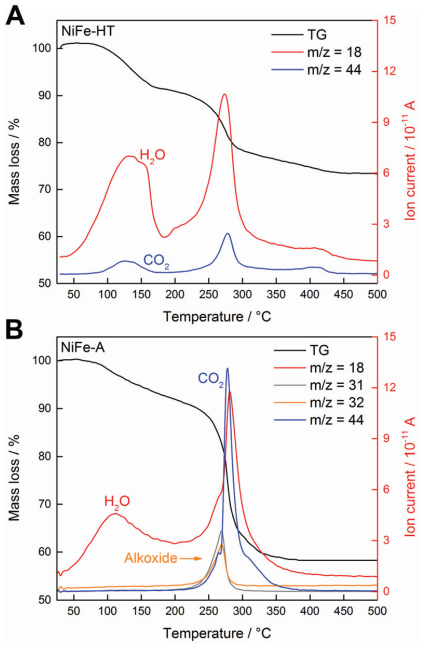

Fig. 3 (A) TGA-MS analysis of NiFe-HT using a heating rate of 10 K min^{-1} under helium. The mass traces corresponding to H_2O (*m*/*z* 18) and CO_2 (*m*/*z* 44) are highlighted. The intense peak mass loss takes place at 278 °C. (B) TGA-MS analysis of NiFe-A showing, in addition to the H_2O and CO_2, the MS traces attributed to the intercalated methoxide fragments – *m*/*z* 31 and 32.

second and more intense mass loss takes place at around 274 °C and is correlated with the dehydroxylation of the layers as well as with the detachment of chemisorbed water present in the interlamellar space (Fig. 3A).[36] In the case of NiFe-A the continuous MS enabled the allocation of the molecular fragments corresponding to the alkoxide moiety, *m*/*z* 31 and 32, at around 270 °C, a temperature remarkably higher than that of the pristine MeOH (*ca*. 65 °C). Interestingly, no signal of CO_2 was detected till the appearance of a tiny peak centered at *ca.* 264 °C, indicative for the residual character of the carbonate contamination in the alkoxide-intercalated samples as recently observed for other hybrid MgAl- and ZnAl-LDHs.[36] Its worth to remark that the CO_2 signal of NiFe-A at higher temperature is also related with the combustion of the organic anions (Fig. 3B).

One of the main features of LDH is their ability to be exfoliated in appropriate solvents.[11] In the case of the alkoxide-intercalated LDH is also possible to perform the exfoliation in water. Indeed, by suspending 1 mg of LDH in 10 mL of Milli-Q water and sonicating during 30 min, a clear colloidal suspension showing Tyndall-Faraday effect can be prepared. Dynamic light scattering measurements provided an average hydrodynamic diameter of *ca.* 140 nm in excellent agreement with the FESEM studies (Fig. 4). The exfoliation and further deposition of the NiFe-A sample on SiO_2-Si substrates was also confirmed *via* AFM measurements. We firstly performed a typical drop casting of the NiFe-A water suspension observing the accretion of the platelets into clusters of *ca.* 10–20 nm in thickness (Fig. 4A and B). This situation can be overcome by spin coating the same solution at 5000 rpm (two times) lowering the thickness to *ca.* 2.5 nm (Fig. 4C).

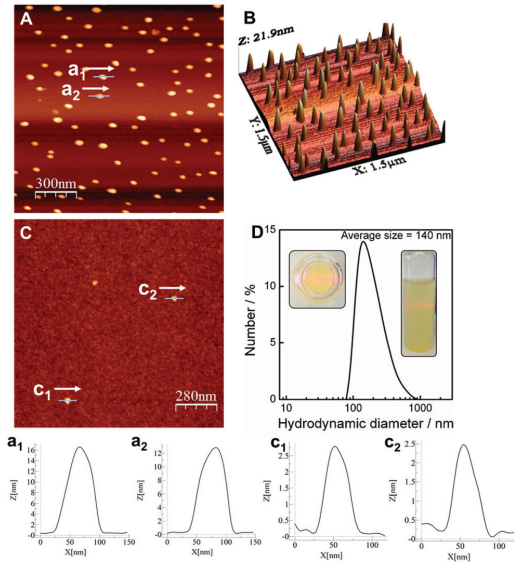

Fig. 4 (A) AFM images of a solution of water exfoliated NiFe-A deposited by drop casting onto a SiO_2-Si substrate and (B) its 3D representation. (C) Topographic AFM image of a spin coating deposition of the previous solution. (D) DLS and Tyndall effect of the NiFe-A sample exfoliated in water. Profiles of the marked regions in A (a_1, a_2) and C (c_1, c_2).

The processability of LDH into thin films is one of the most rapidly growing areas in this field, as the large-scale correct disposition of the LDH platelets would facilitate their application in energy storage and conversion devices.[20,37] Along this front, we checked the formation of continuous thin films by physical deposition. The first attempts with the water suspensions were unsatisfactory due to an inhomogeneous coverage even after using O_2-plasma cleaning for the activation of the substrates (Fig. 4). To face this challenge we used a solvent mixture of 1-buthanol and formamide, following a slight modification of the method reported by Jung *et al.*[31] including O_2-plasma activation. As seen in Fig. 5, complete coverage of the substrate was achieved, with lateral sizes of *ca.* 50–100 nm for the platelets and small RMS values of 0.83 nm. The average height of the coverage is 2.67 nm, revealing a highly homogeneous film. The scratch of the film gave us an approximate thickness value, resulting in *ca.* 1 nm (average of the measurement in different points), very close to that expected for a monolayer. This film is remarkably thinner than that previously synthesized by *in situ* growth of the NiFe-LDH on glass substrates (*ca*. 138–170 nm).[20] A control experiment on a cleaned substrate including its RMS value is depicted in the ESI 3.† The role exerted by the oxygen plasma is crucial. Indeed, control experiments without using the O_2-plasma revealed poor deposition of the LDH, with higher thickness values that might be attributed to some agglomeration of the platelets (Fig. 5D). The plasma treatment allows us to activate the silicon substrate with negative charges,[38,39] leading to a better bonding with the positive LDH cationic sheets, and resulting in a homogeneous and large coverage (additional images can be seen in ESI 4†).

The chemical integrity of the resulting films was confirmed by XPS. Fig. 5E and F shows the high-resolution Ni 2p and Fe 2p XPS spectra of the film confirming the presence of Ni(II) and Fe(III) in the samples. The Ni 2p spectrum exhibit two main peaks at 855 and 873 eV, related to the spin–orbit splitting of the Ni ($2p_{3/2}$) and Ni ($2p_{1/2}$), respectively. In the case of Fe 2p, two peaks are centred at binding energies of 713 and 726 eV, indicative for Fe ($2p_{3/2}$) and Fe ($2p_{1/2}$), respectively. These binding energy values are in good agreement with those expected for NiFe-LDH phases.[14,20,40] Our new synthetic route represents a straightforward way for the preparation of homogeneous ultrathin films of NiFe-LDH.

The overall magnetism of a LDH system is controlled by two main contributions.[10] On the one hand the intralayer magnetic superexchange interactions between metallic centres through the hydroxyl (OH–) bridges across the cationic sheets. On the other hand, the less intense dipolar interactions, which take place in the space between the magnetic LDH layers (interlayer nature). In our specific case, NiFe-LDHs behave as low-temperature ferrimagnets due to the coexistence between ferromagnetic Ni–OH–Ni superexchange interactions along

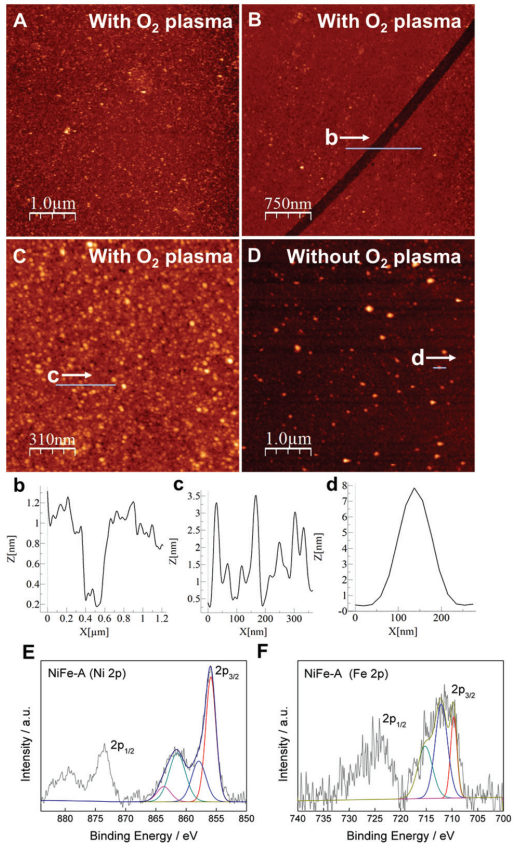

Fig. 5 AFM images of the SiO_2-Si substrate after being covered with NiFe-A LDH dissolved in a mixture of formamide and butanol in the presence (A, B, C) or absence (D) of O_2 plasma activation of the film prior the deposition. Image (B) highlights a scratch in the surface revealing the overall thickness of the film. Profiles corresponding to the marked regions in B (b), C (c) and D (d). XPS analysis of the film highlighting the Ni 2p (E) and Fe 2p (F) high-resolution spectra.

with antiferromagnetic Ni–OH–Fe and Fe–OH–Fe interactions.[20,24,27,30,41] All magnetic measurements were carried out in a SQUID with freshly prepared powdered samples. The main magnetic data and parameters have been summarized in Table 1, including NiFe-HT[24] and CoFe-A[30] for comparative purposes. The DC susceptibility measurements (χ_M) depict a sharp increase near 50 K, reaching a maximum value of 0.63 emu mol^{-1} at 4.5 K, indicative of cooperative magnetic interactions (Fig. 6A). On the other hand, the thermal variation of $\chi_M T$ decreases from a value of 1.93 emu K mol^{-1} at room temperature to 1.86 emu K mol^{-1} at 70 K. After that, $\chi_M T$ exhibits a sharp increase upon cooling to its maximum value of 4 emu K mol^{-1} at 8.1 K, followed by an abrupt decrease to 1.23 emu K mol^{-1} at 2 K (Fig. 6A). Fitting the DC data to the Curie–Weiss law above 50 K gives rise to a Curie constant (C) of 1.95 emu K mol^{-1} consistent with that expected for the spin only value of a magnetically diluted combination of Ni^{2+} (S = 1) and Fe^{3+} (S = 5/2) ions (Table 1).[24] Moreover, the positive value (4.74 K) of the Weiss constant (θ) is indicative for the predominance of ferromagnetic interactions throughout the layers, although its value is remarkably smaller than in the NiFe-HT. Field cooled and zero field cooled (FC/ZFC) measurements allowed us to extract both blocking and irreversible temperatures, resulting in T_B = 4.8 K and T_{irr} = 5 K, respectively (Fig. 6B). Hysteresis loop were also recorded at 2 and 20 K – below and above the blocking temperature (Fig. 6C), confirming the presence of spontaneous magnetization at low temperatures. The coercive field increases as long as we decrease the temperature, as expected, with a H_c of 690 Oe at 2 K and 30 Oe for 20 K. These H_c values are always lower than 1000 Oe, concluding that this NiFe-A LDH is a soft magnet, in good agreement with what is found for the CoFe-A.[24,30] On the other hand, micrometric NiFe-HT depicted a higher coercive field of *ca.* 3600 Oe for the 2 : 1 ratio, as well as a much higher irreversible temperature (15.1 K) pointing towards superparamagnetic behaviour of the NiFe-A due to the dramatic decrease in the particle size.[24]

AC dynamic susceptibility measurements in the presence of an external field of 3.95 Oe oscillating at different frequencies in the 1–10 000 Hz interval were carried out in order to confirm the cooperative magnetism in the sample (Fig. 6D). In both cases, the in-phase (χ'_M) and the out-of-phase (χ''_M) signals exhibit a defined peak at low temperatures.

Table 1 Main magnetic data and parameters for the magnetic LDH[a]

Sample	χT_{rt} (emu K mol^{-1})	C_{so} (emu K mol^{-1})	C (emu K mol^{-1})	θ (K)	T_{irr} (K)	T_M (K)	T_{Hys} (K)	M_S (μ_B)	H_c (Oe)	Δ/k_B (K)	ν_0 (Hz)	ϕ	Ref.
NiFe-A	1.93	2.10	1.95	4.74	5.0	7.8	2; 20	0.97; 0.74	690; 30	275.7	9.1×10^{24}	0.043	This work
CoFe-A	2.48	2.50	2.57	−14.69	4.8	7.0	2.0	0.98	402	116.9	3.8×10^{14}	0.063	30
NiFe-HT	2.29	2.10	2.56	29.11	15.1	16.8	2.0	0.76	3600	1381.5	2.01×10^{40}	0.021	24

[a] χT_{rt} value at room temperature; expected spin-only value of the Curie constant (C_{so}); experimental Curie constant (C); Weiss constant (θ); temperature of the divergence of the ZFC and FC magnetic susceptibility (T_{irr}); temperature for the onset of spontaneous magnetization extracted from the χ''_M plot (T_M); measured hysteresis temperature (T_{Hys}); saturation magnetization (M_S); coercive field (H_{Coer}); energy barrier (Δ/k_B) and frequency factor (ν_0), resulting from the fitting of the magnetic susceptibility to the Arrhenius law; Mydosh parameter (ϕ). $S(Ni^{2+}) = 1$, $S(Fe^{3+}) = 5/2$.

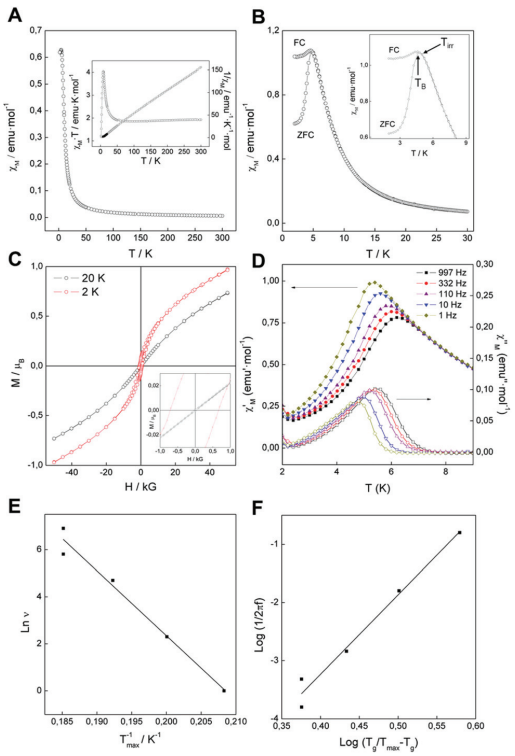

Fig. 6 Magnetic properties of the NiFe-A sample. (A) χ_M *vs.* *T* plot. The inset in represents the temperature dependence of the $\chi_M T$ product and the fitting of the magnetic data to a Curie–Weiss law. (B) FC/ZFC plot, the inset remarks the low field region highlighting the irreversible (bifurcation point) and blocking temperature. (C) Hysteresis cycle at 2 and 20 K. The inset highlights the low field region. (D) Thermal dependence of the χ'_M (in-phase) and χ''_M (out-of-phase) signals at 1, 10, 110, 332 and 997 Hz. (E) Arrhenius fitting of the χ''_M signal. (F) Frequency dependence of χ''_M fitted with the 3D scaling low model $\tau = \tau_0 \cdot [T_g/(T_g/T_{max} - T_g)]^{z\nu}$.

From the out-of-phase signal we can extract the temperature for the onset of the spontaneous magnetization (T_M), set as the point where $\chi''_M \neq 0$. For the NiFe-A T_M = 7.8 K, remarkably lower than that observed for NiFe-HT (T_M = 16.8 K), which is indicative of size effects.[42] As the experimental ratio is 2 : 1 between Ni : Fe (χ = 0.33), the Fe^{3+} clustering cannot be avoided, as previously demonstrated by Mössbauer spectroscopy for NiFe-HT, leading to a glassy magnetic behaviour.[24] Along with that, both signals χ'_M and χ''_M exhibit a significant frequency dependence. The frequency dependence of the χ''_M maxima can be estimated with the calculation of the frequency shift parameters defined by Mydosh:[43,44]

$$\Phi = \Delta T_{max}/[T_{max}\Delta(\log \nu)] \quad (1)$$

For NiFe-A, the value $\Phi \approx 0.043$ is higher than that observed for canonical spin glasses (0.005–0.018)[43] and within the range of values associated to spin glass-like materials (0.06–0.08). Notice that nanosized NiAl-, CoAl-[45] and CoFe-LDHs,[30] exhibit Φ values in this range, in line with the expected size effects. In contrast, in NiFe-HT Φ is in the range of values associated close to canonical spin glasses ($\Phi \approx 0.021$).[24] Further information of the spin relaxation in these materials can be obtained by fitting the frequency dependence of χ''_M to both an Arrhenius law and a 3D critical scaling law.

The Arrhenius law for a thermally activated process is described by the following equation:

$$\nu = \nu_0 \exp(-E_a/k_B T) \quad (2)$$

where ν_0 is the frequency factor, E_a the activation energy and k_B the Boltzmann constant.

For NiFe-A a fitting of the frequency dependence of χ''_M to this law gives a value for energy barrier of E_a/k_B = 276 K, which can be ascribed to the presence of a superparamagnetic behaviour,[43] in clear contrast to the NiFe-HT sample that exhibits a higher value of *ca.* 1400 K. These results highlight the crucial role of the nanometric size and low dimensionality of these LDH systems in sharp contrast with the micrometric ones.[46]

Finally, we have fitted the frequency dependence of χ''_M to the 3D critical scaling law for spin dynamics,[47,48] which is described by the following equation:

$$\tau = \tau_0[T_g/(T_g/T_{max} - T_g)]^{z\nu} \quad (3)$$

where T_g is the critical glass temperature, τ_0 the attempt time and $z\nu$ a critical exponent. For 3D model spin glasses, the relaxation time diverges at finite temperature ($T_g \neq 0$ K). For NiFe-A the best fit of our data to a linear form of the eqn (3) (Fig. 7F) was obtained for T_g = 3.8 K, $\tau_0 = 1.99 \times 10^{-9}$ s and a $z\nu$ = 13.7. Whereas the obtained τ_0 value falls in the range for canonical spin glasses (from 10^{-7} to 10^{-12}), $z\nu$ is out of this range (from 4 to 12).[43]

A similar behaviour was reported by Layrac *et al.* for different magnetic LDHs intercalated with cyano-bridged coordination polymers.[47] For NiFe-HT, the best fit (see ESI 5†) was found for T_g = 14.9 K, $\tau_0 = 2.55 \times 10^{-7}$ s and $z\nu$ = 2.7.[48] In overall, these results indicate a spin-glass like behaviour for these NiFe-LDHs, with superparamagnetic effects in the NiFe-A derivative arising from the nanometric size of the samples.[44,47]

To demonstrate the applicability of these novel NiFe-LDHs in the field of energy storage and conversion, we have investigated their performance as OER electrocatalysts for the multielectron reaction: $4OH^- \leftrightarrow O_2 + 2H_2O + 4e^-$, in alkaline media.[49–51] Beyond other compositions, the catalysts containing earth-abundant Ni and Fe cations are among the most efficient reported so far.[52,53] Along this front, the performance exhibited by NiFe-LDH and its corresponding carbon hybrids have been studied.[14,15,26,54,55–57]

The electrocatalytic OER activity of NiFe-LDH was tested in a basic medium (1 M KOH) in a standard three-electrode cell. For comparative purposes we have prepared working electrodes consisting on NiFe-A and NiFe-HT, as well as commercial IrO_2 catalyst as a reference, using powdered samples coated on

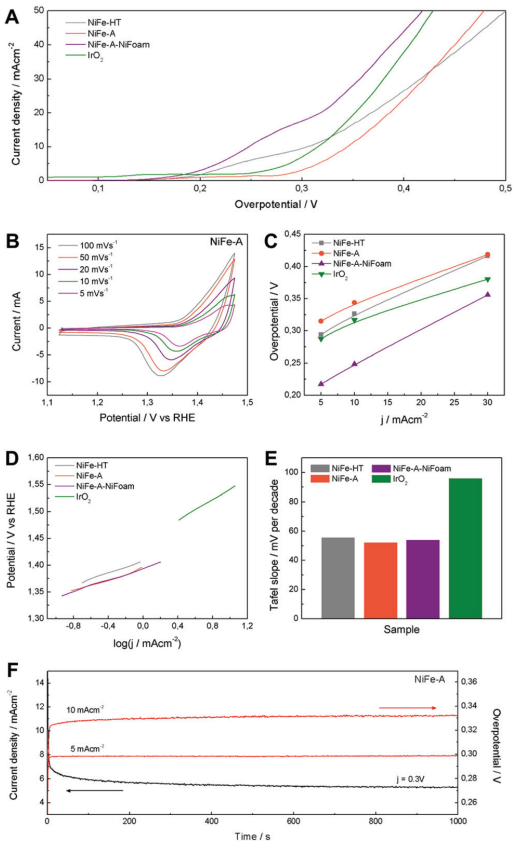

Fig. 7 (A) Cyclic voltammetry at different scan rates of NiFe-A in 1 M KOH solution. (B) Polarization curves of NiFe-LDHs and commercial IrO_2. (C) Overpotential required at different current densities. (D) Onset values of the different NiFe-LDHs and the comercial IrO_2 corresponding to the polarization curves. (E) Tafel plots and (F) the histogram of corresponding values of Tafel slopes. (G) The potentiostatic and galvanostatic stability testing under a certain potential or current density.

Ni-foam collectors. Moreover, to overcome the intrinsic insulating behaviour of LDH, avoid the detachment of the active material due to the exfoliation in water and in order to improve their catalytic performance and stability, we have directly grown 3D porous films of NiFe-A on Ni-foam – hereinafter: NiFe-A-NiFoam – following a modified procedure previously described in the literature (see ESI 6†).[13,33] The cyclic voltammetry at different scan rates of NiFe-A (Fig. 7A) reveals the presence of a redox peak around 1.35 V *vs.* RHE, that can be assigned to the Ni(II)/Ni(III or IV) redox processes, probably related with the transformation between $Ni_{1-x}Fe_x(OH)_2$ and $Ni_{1-x}Fe_xOOH$ (see ESI 7† for additional CVs of the other the samples).[14,33,58] Moreover, the anodic wave of the NiFe-A catalyst is nearly merged with the catalytic wave but a distinct cathodic feature is evident, in excellent accordance with previous reports (see ESI 7† for pristine Ni-foam blank experiments and additional CVs of the other sample).[58,59]

The catalytic materials were measured by linear sweep voltammetry, showing the lowest onset potential for the NiFe-A-NiFoam (1.51 V *vs.* RHE), followed by the NiFe-HT and the pristine NiFe-A (Fig. 7B and ESI 7†). Different parameters were calculated to quantify the improvements of activity: the overpotential (η) at different current densities (5, 10 and 30 mA cm^{-2}), the current density (j) at η = 300 mV and the Tafel slopes (the performance of the different samples have been summarized in ESI 8†). The current density of 10 mA cm^{-2} was chosen because it represents the current density from a device with 12% solar to hydrogen efficiency, considered as a realistic measure of the catalytic activity.[15]

As presented in Fig. 7C, an overpotential of *ca.* 0.249 V is required at j = 10 mA cm^{-2} for NiFe-A-NiFoam, a value much smaller than that of NiFe-HT (more than 0.32 V) or NiFe-A (0.34 V) and similar to that previously published by Lu and coworkers.[33] In Fig. 7D it can be seen that the overpotential is decreased by 60–80 mV by growing the LDH directly on the Ni-foam. The excellent catalytic activity of the as-synthesized NiFe-LDHs is also reflected in the Tafel slopes, showing values in the range of 52–55 mV per decade, much smaller that that exhibited by the commercial IrO_2 (we should indicate that the Tafel slopes not solely reflect the kinetic information of water oxidation but a combined process of redox reactions and OER).

To further evaluate their electrocatalytic activity, the values of the turnover frequency (TOF) of the powdered samples were calculated by assuming that all the transition metal ions in the catalysts are contributing to the reaction, which also confirm that NiFe-A has the highest TOF of 0.01 s^{-1} at an overpotential of 0.3 V, nearly of NiFe-HT (0.007). It is worth to keep in mind that these TOF values compete favourably with those recently reported for others NiFe-LDHs.[26,33]

The stability and durability of the NiFe-A powdered catalyst was tested at constant current densities j of 5 and 10 mA cm^{-2} and with a constant overpotential of η 300 mV for 1000 s. In Fig. 7G, we can see a very high stability in both cases. When increasing the current density from 5 to 10 mA cm^{-2} the overpotential correspondingly increases to *ca.* 0.03 V (see ESI 7† for additional measurements). These results are in good accordance with NiFe-LDH nanosheets synthesized using the topochemical approach having the same composition (Ni : Fe 2 : 1).[26] It is worth to remark here that the spin-glass magnetic behaviour exhibited by these NiFe-LDH can be correlated to the presence of Fe-clustering, and this may play a role in their OER behaviour. Indeed, as recently pointed out by M. A. Oliver-Tolentino *et al.* the superexchange interactions could exert a big influence in the electrocatalytic activity.[60] When compared to $Ni(OH)_2$, the more complex local environment around Ni–O pairs in NiFe-LDHs plays a crucial role in the OER activity, increasing the NiOOH conductivity >30-fold. In fact, Fe exerts a partial-charge transfer activation effect on the Ni atoms, improving the catalytic activity.[58] Moreover, operando Mössbauer spectroscopic studies demonstrated the

exclusive formation of Fe^{4+} in NiFe, but not in Fe-only catalysts, as a result of the stabilizing effect of the local NiOOH lattice, most probably on the edges, corners or defects.[59] In any case, the role of the particle size and defect sites in the OER behaviour of NiFe-LDH catalysts remains an open question. These results illustrate the great potential exhibited by NiFe-A as a cheap electrocatalyst for the OER, and opens the door for its hybridization with organic counterparts like graphene or carbon nanotubes in order to further improve its electrochemical performance.

Conclusions

In summary, we have demonstrated the synthesis of alkoxide-intercalated NiFe-layered double hydroxide exhibiting lateral dimensions of *ca.* 110 nm with a high crystalline quality as revealed by STEM analysis. Moreover, we studied *via* TG-MS measurements its interlamellar composition, proving the methoxide intercalation. Their successful exfoliation in water and 1-BuOH/formamide mixtures has also been performed showing the easy formation of homogeneous ultrathin films with thicknesses in the range of a few nanometers. The magnetic measurements revealed the role exerted by the nanometric dimensions of the platelets, exhibiting superparamagnetic size effects and spin-glass like behaviour with T_M temperatures of *ca.* 8 K. Finally, we have investigated their possible application as water oxidation electrocatalysts. They exhibit an outstanding performance similar to those recently reported for other NiFe-LDHs. This work illustrates the great potential of these earth-abundant 2D materials not only in magnetism or as building blocks for the development of hybrid materials, but also as excellent candidates in the field of energy storage and conversion.

Acknowledgements

Financial support from the EU (FET-OPEN 2D-INK, grant agreement 664878, Graphene Flagship, grant agreement 604391 and ERC Starting Investigator Award STEMOX, grant agreement 239739), the Spanish MINECO (Project MAT2014-56143-R and Excellence Unit Maria de Maeztu, MDM-2015-0538) and the Generalitat Valenciana (Prometeo and ISIC-Nano Programs) is gratefully acknowledged. Co-funding from UE is also acknowledged. Electron microscopy observations carried out at the Centro Nacional de Microscopía Electrónica, Universidad Complutense de Madrid. We thank the Universidad de Valencia for support from VLC/CAMPUS and INNCIDE program, and for a predoctoral grant (to J. A. C.). G. A. thanks the EU for a Marie Curie Fellowship (FP7/2013-IEF-627386).

Notes and references

1 A. K. Geim and K. S. Novoselov, *Nat. Mater.*, 2007, **6**, 183–191.
2 A. K. Geim and I. V. Grigorieva, *Nature*, 2013, **499**, 419–425.
3 Q. H. Wang, K. Kalantar-Zadeh, A. Kis, J. N. Coleman and M. S. Strano, *Nat. Nanotechnol.*, 2012, **7**, 699–712.
4 V. Nicolosi, M. Chhowalla, M. G. Kanatzidis, M. S. Strano and J. N. Coleman, *Science*, 2013, **340**, 1226419.
5 D. Hanlon, C. Backes, E. Doherty, C. S. Cucinotta, N. C. Berner, C. Boland, K. Lee, A. Harvey, P. Lynch, Z. Gholamvand, S. Zhang, K. Wang, G. Moynihan, A. Pokle, Q. M. Ramasse, N. McEvoy, W. J. Blau, J. Wang, G. Abellan, F. Hauke, A. Hirsch, S. Sanvito, D. D. O'Regan, G. S. Duesberg, V. Nicolosi and J. N. Coleman, *Nat. Commun.*, 2015, **6**, 8563.
6 S. M. Auerbach, K. A. Carrado and P. K. Dutta, *Handbook of Layered Materials*, CRC Press, 2004.
7 *Layered double hydroxides: present and future*, ed. V. Rives, Nova Science Publishers, Huntington, N.Y, 2001.
8 F. Li and X. Duan, in *Layered Double Hydroxides*, ed. X. Duan and D. G. Evans, Springer, Berlin, Heidelberg, 2006, pp. 193–223.
9 V. Rives, M. del Arco and C. Martín, *Appl. Clay Sci.*, 2014, **88–89**, 239–269.
10 G. Abellán, C. Martí-Gastaldo, A. Ribera and E. Coronado, *Acc. Chem. Res.*, 2015, **48**, 1601–1611.
11 Q. Wang and D. O'Hare, *Chem. Rev.*, 2012, **112**, 4124–4155.
12 G. Chen, Y. Zhao, G. Fu, P. N. Duchesne, L. Gu, Y. Zheng, X. Weng, M. Chen, P. Zhang, C.-W. Pao, J.-F. Lee and N. Zheng, *Science*, 2014, **344**, 495–499.
13 J. Luo, J.-H. Im, M. T. Mayer, M. Schreier, M. K. Nazeeruddin, N.-G. Park, S. D. Tilley, H. J. Fan and M. Grätzel, *Science*, 2014, **345**, 1593–1596.
14 M. Gong, Y. Li, H. Wang, Y. Liang, J. Z. Wu, J. Zhou, J. Wang, T. Regier, F. Wei and H. Dai, *J. Am. Chem. Soc.*, 2013, **135**, 8452–8455.
15 F. Song and X. Hu, *Nat. Commun.*, 2014, **5**, 4477.
16 H. Wang, Y. Liang, M. Gong, Y. Li, W. Chang, T. Mefford, J. Zhou, J. Wang, T. Regier, F. Wei and H. Dai, *Nat. Commun.*, 2012, **3**, 917.
17 Y. Li, M. Gong, Y. Liang, J. Feng, J.-E. Kim, H. Wang, G. Hong, B. Zhang and H. Dai, *Nat. Commun.*, 2013, **4**, 1805.
18 G. Abellán, E. Coronado, C. Martí-Gastaldo, A. Ribera and J. F. Sánchez-Royo, *Chem. Sci.*, 2012, **3**, 1481–1485.
19 G. Abellán, E. Coronado, C. Martí-Gastaldo, A. Ribera and T. F. Otero, *Part. Part. Syst. Charact.*, 2013, **30**, 853–863.
20 G. Abellán, J. A. Carrasco, E. Coronado, J. P. Prieto-Ruiz and H. Prima-García, *Adv. Mater. Interfaces*, 2014, **1**, 1400184.
21 J. A. Carrasco, H. Prima-Garcia, J. Romero, J. Hernández-Saz, S. I. Molina, G. Abellán and E. Coronado, *J. Mater. Chem. C*, 2016, **4**, 440–448.
22 Y. Han, Z.-H. Liu, Z. Yang, Z. Wang, X. Tang, T. Wang, L. Fan and K. Ooi, *Chem. Mater.*, 2008, **20**, 360–363.
23 G. Abellán, E. Coronado, C. Martí-Gastaldo, E. Pinilla-Cienfuegos and A. Ribera, *J. Mater. Chem.*, 2010, **20**, 7451–7455.
24 G. Abellán, E. Coronado, C. Martí-Gastaldo, J. Waerenborgh and A. Ribera, *Inorg. Chem.*, 2013, **52**, 10147–10157.

25 J.-H. Lee, D. O'Hare and D.-Y. Jung, *Bull. Korean Chem. Soc.*, 2012, **33**, 725–727.
26 W. Ma, R. Ma, C. Wang, J. Liang, X. Liu, K. Zhou and T. Sasaki, *ACS Nano*, 2015, **9**, 1977–1984.
27 G. Abellán, J. A. Carrasco and E. Coronado, *Inorg. Chem.*, 2013, **52**, 7828–7830.
28 E. Gardner, K. M. Huntoon and T. J. Pinnavaia, *Adv. Mater.*, 2001, **13**, 1263–1266.
29 J. A. Gursky, S. D. Blough, C. Luna, C. Gomez, A. N. Luevano and E. A. Gardner, *J. Am. Chem. Soc.*, 2006, **128**, 8376–8377.
30 G. Abellán, J. A. Carrasco, E. Coronado, J. Romero and M. Varela, *J. Mater. Chem. C*, 2014, **2**, 3723–3731.
31 J. H. Lee, S. W. Rhee and D.-Y. Jung, *Chem. Mater.*, 2004, **16**, 3774–3779.
32 I. Horcas, R. Fernández, J. M. Gómez-Rodríguez, J. Colchero, J. Gómez-Herrero and A. M. Baro, *Rev. Sci. Instrum.*, 2007, **78**, 013705–013708.
33 Z. Lu, W. Xu, W. Zhu, Q. Yang, X. Lei, J. Liu, Y. Li, X. Sun and X. Duan, *Chem. Commun.*, 2014, **50**, 6479–6482.
34 G. Boehm and M. Dwyer, *J. Chem. Educ.*, 1981, **58**, 809–811.
35 G. Abellán, P. Amo-Ochoa, J. L. G. Fierro, A. Ribera, E. Coronado and F. Zamora, *Polymers*, 2016, **8**, 5.
36 E. Conterosito, L. Palin, D. Antonioli, D. Viterbo, E. Mugnaioli, U. Kolb, L. Perioli, M. Milanesio and V. Gianotti, *Chem. – Eur. J.*, 2015, **21**, 14975–14986.
37 X. Guo, F. Zhang, D. G. Evans and X. Duan, *Chem. Commun.*, 2010, **46**, 5197–5210.
38 S. Bhattacharya, A. Datta, J. M. Berg and S. Gangopadhyay, *J. Microelectromech. Syst.*, 2005, **14**, 590–597.
39 K. S. Kim, K. H. Lee, K. Cho and C. E. Park, *J. Membr. Sci.*, 2002, **199**, 135–145.
40 H. W. Nesbitt, D. Legrand and G. M. Bancroft, *Phys. Chem. Miner.*, 2000, **27**, 357–366.
41 P. Rabu, E. Delahaye and G. Rogez, *Nanotechnol. Rev.*, 2015, **4**, 557–580.
42 J. J. Almansa, E. Coronado, C. Martí-Gastaldo and A. Ribera, *Eur. J. Inorg. Chem.*, 2008, **2008**, 5642–5648.
43 J. A. Mydosh, *Spin glasses: an experimental introduction*, Taylor & Francis, London, Washington, DC, 1993.
44 C. J. Wang, Y. A. Wu, R. M. J. Jacobs, J. H. Warner, G. R. Williams and D. O'Hare, *Chem. Mater.*, 2011, **23**, 171–180.
45 J. Pérez-Ramírez, A. Ribera, F. Kapteijn, E. Coronado and C. J. Gómez-García, *J. Mater. Chem.*, 2002, **12**, 2370–2375.
46 G. Abellán, E. Coronado, C. J. Gómez-García, C. Martí-Gastaldo and A. Ribera, *Polyhedron*, 2013, **52**, 216–221.
47 G. Layrac, D. Tichit, J. Larionova, Y. Guari and C. Guérin, *J. Phys. Chem. C*, 2011, **115**, 3263–3271.
48 G. Abellán Sáez, *Hybrid magnetic materials based on layered double hydroxides: from the chemistry towards the applications*, PhD Thesis, 2014.
49 Y. Liang, Y. Li, H. Wang and H. Dai, *J. Am. Chem. Soc.*, 2013, **135**, 2013–2036.
50 J. Xie, R. Wang, J. Bao, X. Zhang, H. Zhang, S. Li and Y. Xie, *Inorg. Chem. Front.*, 2014, **1**, 751–756.
51 P. Chen, K. Xu, Y. Tong, X. Li, S. Tao, Z. Fang, W. Chu, X. Wu and C. Wu, *Inorg. Chem. Front.*, 2016, **3**, 236–242.
52 M. Gong and H. Dai, *Nano Res.*, 2014, 1–17.
53 J. R. Galán-Mascarós, *ChemElectroChem*, 2015, **2**, 37–50.
54 X. Long, J. Li, S. Xiao, K. Yan, Z. Wang, H. Chen and S. Yang, *Angew. Chem., Int. Ed.*, 2014, **126**, 7714–7718.
55 R. Chen, G. Sun, C. Yang, L. Zhang, J. Miao, H. B. Tao, H. Yang, J. Chen, P. Chen and B. Liu, *Nanoscale Horiz.*, 2016, DOI: 10.1039/C5NH00082C.
56 C. Tang, H.-S. Wang, H.-F. Wang, Q. Zhang, G.-L. Tian, J.-Q. Nie and F. Wei, *Adv. Mater.*, 2015, **27**, 4516–4522.
57 Y. Li, H. He, W. Fu, C. Mu, X.-Z. Tang, Z. Liu, D. Chi and X. Hu, *Chem. Commun.*, 2016, **52**, 1439–1442.
58 L. Trotochaud, S. L. Young, J. K. Ranney and S. W. Boettcher, *J. Am. Chem. Soc.*, 2014, **136**, 6744–6753.
59 J. Y. C. Chen, L. Dang, H. Liang, W. Bi, J. B. Gerken, S. Jin, E. E. Alp and S. S. Stahl, *J. Am. Chem. Soc.*, 2015, **137**, 15090–15093.
60 M. A. Oliver-Tolentino, J. Vázquez-Samperio, A. Manzo-Robledo, R. de G. González-Huerta, J. L. Flores-Moreno, D. Ramírez-Rosales and A. Guzmán-Vargas, *J. Phys. Chem. C*, 2014, **118**, 22432–22438.

INORGANIC CHEMISTRY
FRONTIERS

CORRECTION

Cite this: *Inorg. Chem. Front.*, 2016, **3**, 556

Correction: Alkoxide-intercalated NiFe-layered double hydroxides magnetic nanosheets as efficient water oxidation electrocatalysts

Jose A. Carrasco,[a] Jorge Romero,[a] María Varela,[b] Frank Hauke,[c] Gonzalo Abellán,*[a,c] Andreas Hirsch[c] and Eugenio Coronado*[a]

DOI: 10.1039/c6qi90013e
rsc.li/frontiers-inorganic

Correction for 'Alkoxide-intercalated NiFe-layered double hydroxides magnetic nanosheets as efficient water oxidation electrocatalysts' by Jose A. Carrasco, *et al.*, *Inorg. Chem. Front.*, 2016, DOI: 10.1039/c6qi00009f.

The authors regret that the caption for Fig. 7 was provided incorrectly. The correct version of Fig. 7 and the associated caption are provided below.

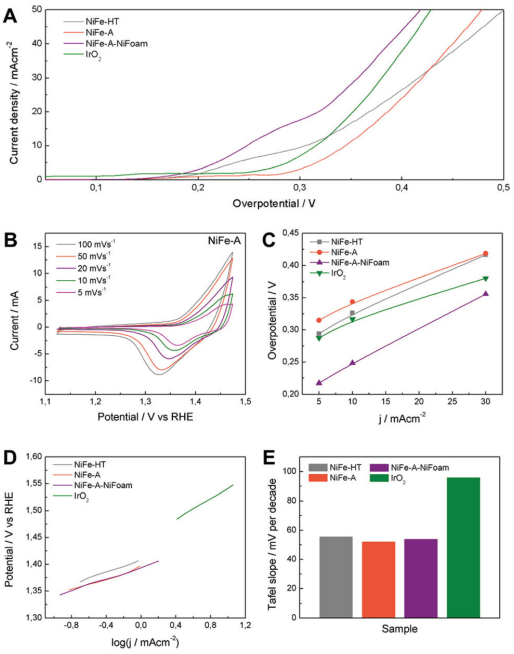

[a]*Instituto de Ciencia Molecular (ICMol), Universidad de Valencia, Catedrático José Beltrán 2, 46980 Paterna, Valencia, Spain. E-mail: gonzalo.abellan@fau.de*
[b]*Universidad Complutense de Madrid, Dpt. Fisica Aplicada III & Instituto Pluridisciplinar, Madrid 28040, Spain*
[c]*Department of Chemistry and Pharmacy and Institute of Advanced Materials and Processes (ZMP), University Erlangen-Nürnberg, Henkestr. 42, 91054 Erlangen and Dr.-Mack Str. 81, 90762 Fürth, Germany*

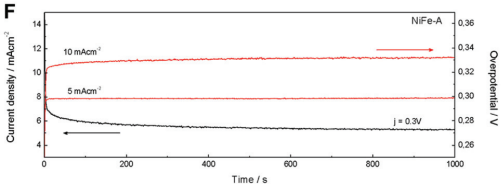

Fig. 7 (A) Polarization curves of NiFe-LDHs and commercial IrO_2. (B) Cyclic voltammetry at different scan rates of NiFe-A in 1 M KOH solution. (C) Overpotential required at different current densities. (D) Tafel plots and (E) the histogram of corresponding values of Tafel slopes. (F) The potentiostatic and galvanostatic stability testing under a certain potential or current density.

In addition, the authors regret that any citations to Fig. 7 within the article text are incorrect. Correct versions of the affected text are provided below.

For page 7 of the article:

For NiFe-A the best fit of our data to a linear form of the eqn (3) (Fig. 6F) was obtained for T_g = 3.8 K, $\tau_0 = 1.99 \times 10^{-9}$ s and a $z\nu$ = 13.7.

For page 8 of the article:

The cyclic voltammetry at different scan rates of NiFe-A (Fig. 7B) reveals the presence of a redox peak around 1.35 V *vs.* RHE, that can be assigned to the Ni(II)/Ni(III or IV) redox processes, probably related with the transformation between $Ni_{1-x}Fe_x(OH)_2$ and $Ni_{1-x}Fe_xOOH$ (see ESI 7† for additional CVs of the other samples).[14,33,58] Moreover, the anodic wave of the NiFe-A catalyst is nearly merged with the catalytic wave but a distinct cathodic feature is evident, in excellent accordance with previous reports (see ESI 7† for pristine Ni-foam blank experiments and additional CVs of the other sample).[58,59]

The catalytic materials were measured by linear sweep voltammetry, showing the lowest onset potential for the NiFe-A-NiFoam (1.51 V *vs.* RHE), followed by the NiFe-HT and the pristine NiFe-A (Fig. 7A and ESI 7†). Different parameters were calculated to quantify the improvements of activity: the overpotential (η) at different current densities (5, 10 and 30 mA cm^{-2}), the current density (j) at η = 300 mV and the Tafel slopes (the performance of the different samples have been summarized in ESI 8†). The current density of 10 mA cm^{-2} was chosen because it represents the current density from a device with 12% solar to hydrogen efficiency, considered as a realistic measure of the catalytic activity.[15]

As presented in Fig. 7C, an overpotential of *ca.* 0.249 V is required at j = 10 mA cm^{-2} for NiFe-A-NiFoam, a value much smaller than that of NiFe-HT (more than 0.32 V) or NiFe-A (0.34 V) and similar to that previously published by Lu and co-workers.[33] In Fig. 7C it can be seen that the overpotential is decreased by 60–80 mV by growing the LDH directly on the Ni-foam. The excellent catalytic activity of the as-synthesized NiFe-LDHs is also reflected in the Tafel slopes, showing values in the range of 52–55 mV per decade, much smaller than that exhibited by the commercial IrO_2 (we should indicate that the Tafel slopes not solely reflect the kinetic information of water oxidation but a combined process of redox reactions and OER).

To further evaluate their electrocatalytic activity, the values of the turnover frequency (TOF) of the powdered samples were calculated by assuming that all the transition metal ions in the catalysts are contributing to the reaction, which also confirm that NiFe-A has the highest TOF of 0.01 s^{-1} at an overpotential of 0.3 V, nearly of NiFe-HT (0.007). It is worth to keep in mind that these TOF values compete favourably with those recently reported for others NiFe-LDHs.[26,33]

The stability and durability of the NiFe-A powdered catalyst was tested at constant current densities j of 5 and 10 mA cm^{-2} and with a constant overpotential of η 300 mV for 1000 s. In Fig. 7F, we can see a very high stability in both cases. When increasing the current density from 5 to 10 mA cm^{-2} the overpotential correspondingly increases to *ca.* 0.03 V (see ESI 7† for additional measurements).

The Royal Society of Chemistry apologises for these errors and any consequent inconvenience to authors and readers.

Supplementary Information

Alkoxide-intercalated NiFe-layered double hydroxides magnetic nanosheets as efficient water oxidation electrocatalyst

Jose A. Carrasco,[a] Jorge Romero,[a] María Varela,[b] Frank Hauke[c], Gonzalo Abellán[a,c,*], Andreas Hirsch[c] and Eugenio Coronado[a,*]

[a] Instituto de Ciencia Molecular (ICMol), Universidad de Valencia, Catedrático José Beltrán 2, 46980, Paterna, Valencia, Spain

[b] Universidad Complutense de Madrid, Dpt. Fisica Aplicada III & Instituto Pluridisciplinar, Madrid 28040, Spain

[c] Department of Chemistry and Pharmacy and Institute of Advanced Materials and Processes (ZMP), University Erlangen-Nürnberg, Henkestr. 42, 91054 Erlangen and Dr.-Mack Str. 81, 90762 Fürth, Germany.

Contents

SI 1. FESEM image of the NiFe-A sample.

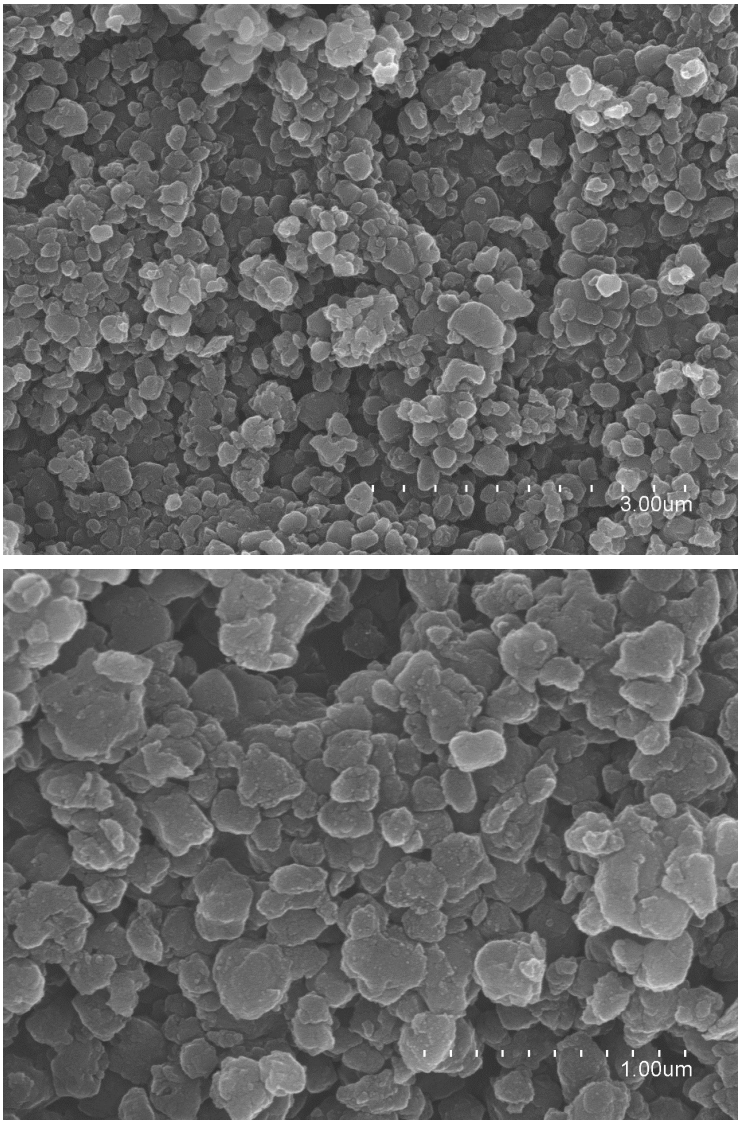

SI 2. FESEM image of the NiFe-HT sample.

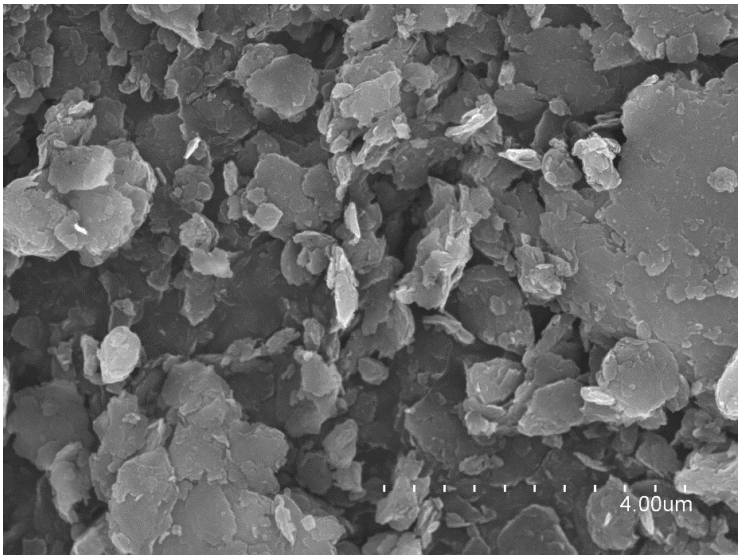

SI 3. AFM images highlighting the coverage of the NiFe-A sample.

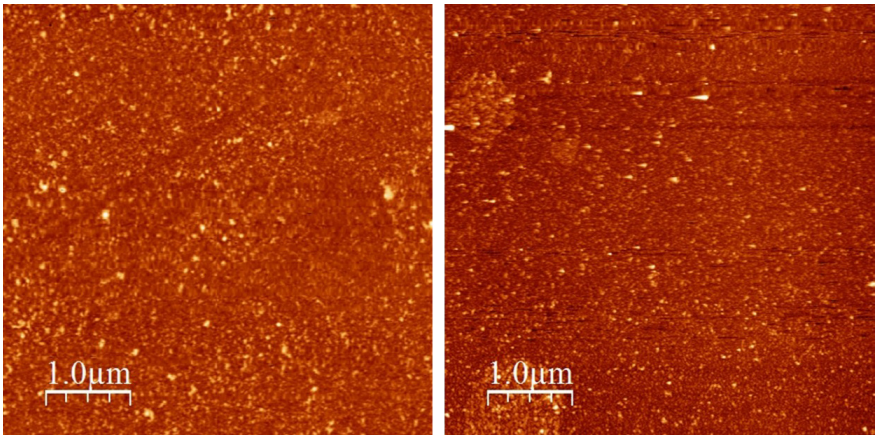

As explained in the main text, the deposition procedure has been carried out with a mixture of formamide/BuOH and with a SiO_2-Si substrate previously activated with O_2 plasma.

SI 4. AFM characterization of a SiO_2-Si substrate (blank).

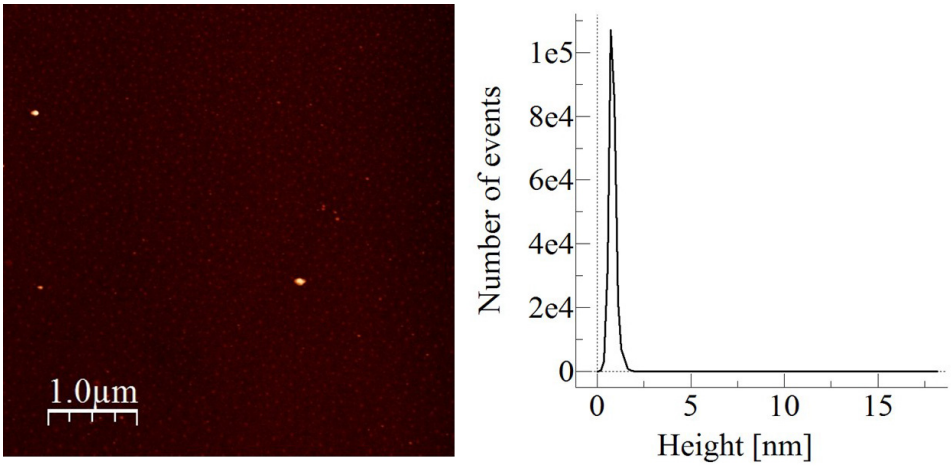

RMS value = 0.15 nm.

Average height = 0.90 nm

SI 5. Arrhenius plot and 3D scaling law model of the spin dynamics for the NiFe-HT sample.

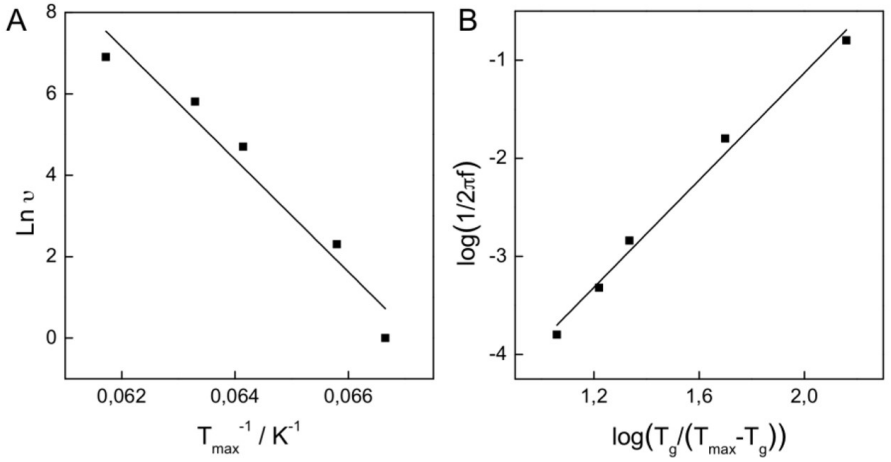

(A) Arrhenius fitting of the χ''_M signal for the NiFe-HT sample. (B) Frequency dependence of χ''_M fitted with the 3D scaling low model $\tau = \tau_0 \cdot [T_g/(T_g/T_{max} - T_g)]^{zv}$.

SI 6. SEM images of the NiFe-A-NiFoam sample.

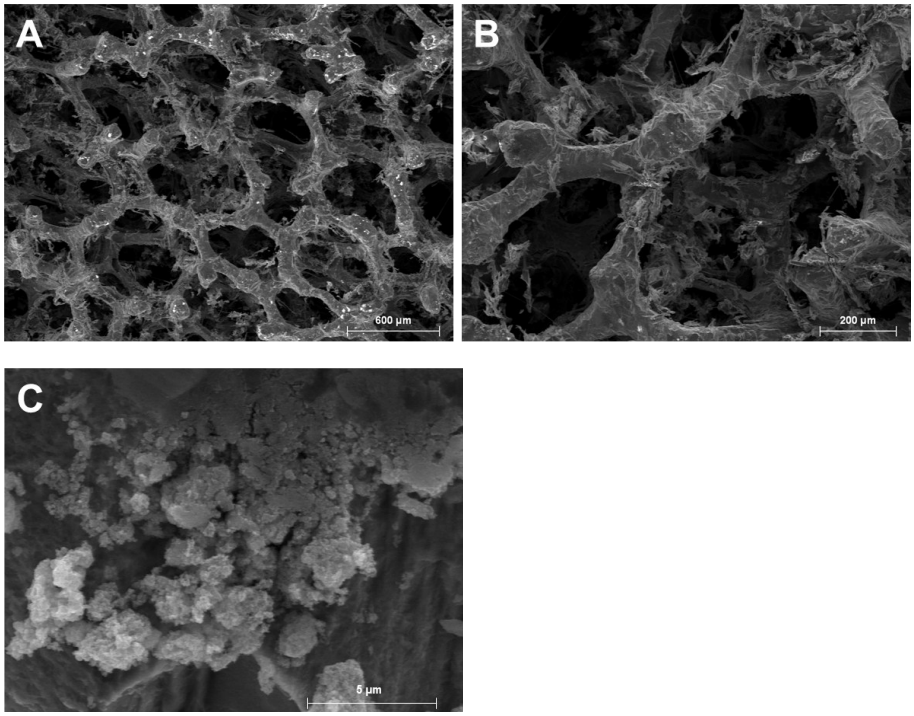

SI 7. Electrochemical measurements

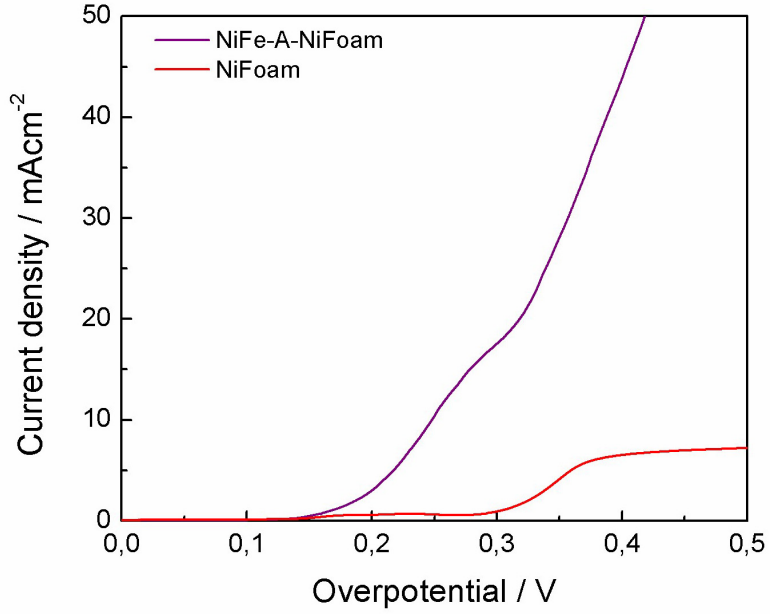

Figure SI 7.1. Blank experiment showing the LSV of the pristine Ni-foam versus the NiFe-A-NiFoam sample.

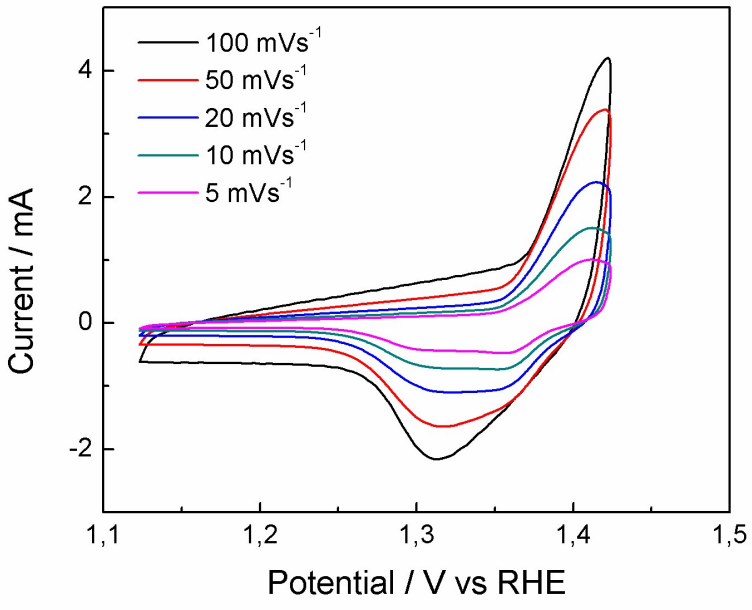

Figure SI 7.2. CV of NiFe-A-NiFoam at different scan rates.

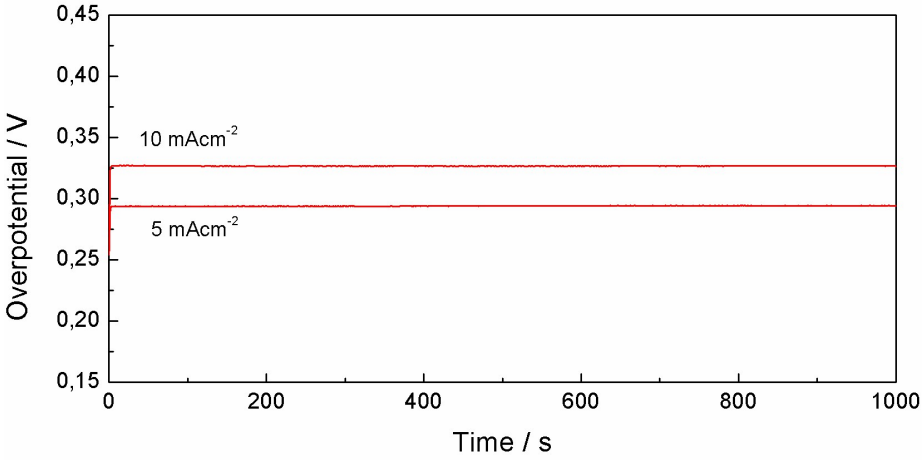

Figure SI 7.3. Potentiostatic stability testing of NiFe-A-NiFoam under a certain current density.

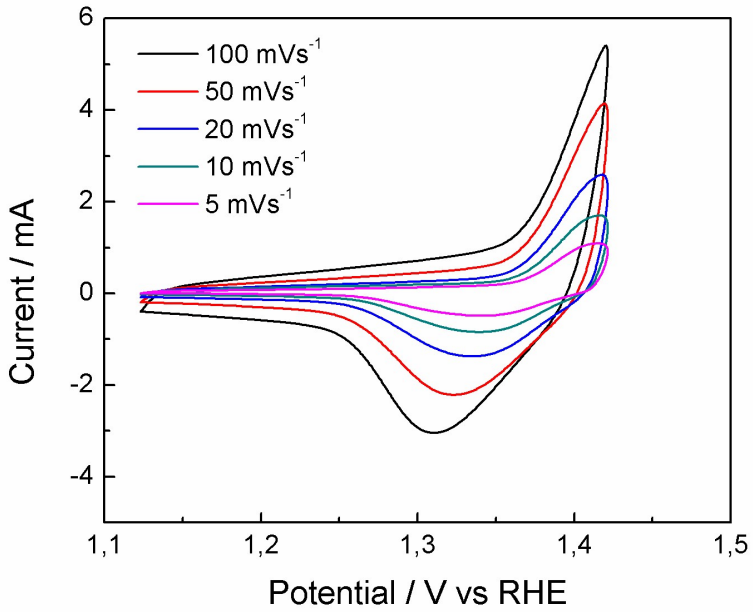

Figure SI 7.4. CV of NiFe-HT at different scan rates.

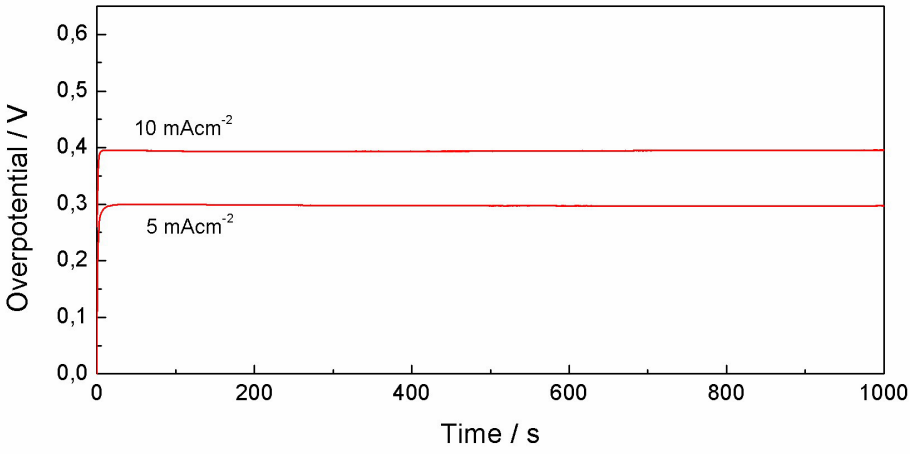

Figure SI 7.5. CV Potentiostatic stability testing of NiFe-HT under a certain current density.

SI 8. Comparison of catalytic performance of NiFe-LDHs.

Supplementary Table 2: Comparison of our NiFe-LDHs and others reported.

	Onset	Overpotential with a 5 mVs^{-1} CV (V)			Current at 0,3V OP ($mAcm^{-2}$)	TOF (s^{-1})	Tafel Slope (mV per decade)
	(vs RHE)	5 $mAcm^{-2}$	10 $mAcm^{-2}$	30 $mAcm^{-2}$			
NiFe-HT	1,530	0,294	0,327	0,417	9,490	0,007	55,5
NiFe-A	1,534	0,315	0,344	0,419	3,140	0,010	52,0
NiFe-A-NiFoam	1,509	0,217	0,249	0,356	17,800	-	53,7
IrO_2	1,561	0,288	0,317	0,380	7,360	0,009	96,6
NiFe-LDH [1]	-	-	0,347	-	2,070	0,050	67,0
NiFe-LDH [2]	-	-	0,310	-	-	~ 0,010	76,0
NiFe-LDH [3]	~ 1,55	-	0,240	-	-	0,004	65,0

[1] Fang Song, Xile Hu; Nature Comunications, 2014, 5:4477

[2] Wei Ma, Renzhi Ma, Chengxiang Wang, Jianbo Liang, Xiaohe Liu, Kechao Zhou, and Takayoshi Sasaki; ACS Nano, 2015, 9 (2), pp 1977–1984

[3] Z. Lu, L. Qian, Y. Tian, Y. Li, X. Sun and X. Duan, Chem. Commun., 2016, 52, 908-911

Chapter 4:
Applications of Layered Double Hydroxides

4.1. Introduction.

LDHs have a wide range of applications as functional materials that can vary from catalysis to magnetism, adsorbents, ion exchange, electrochemistry, biochemistry or environmental approach, among others (**Fig. 4.1**).[1–4] That fact is precisely due to their chemical versatility, anion exchange properties and relative low cost synthesis,[5,6] that this kind of material can be tuned to achieve the desired properties. Furthermore, thanks to their layered nature and, in combination with specific anions that minimize the interactions among the layers (such as some surfactants), it is also possible to produce stable colloidal suspensions consisting of exfoliated LDHs with surface areas up to *ca*. 1000 cm^2 g^{-1}. In that sense, LDHs can act as inorganic building blocks in the design of hybrid nanocomposites with both organic or inorganic counterparts.[7–11]

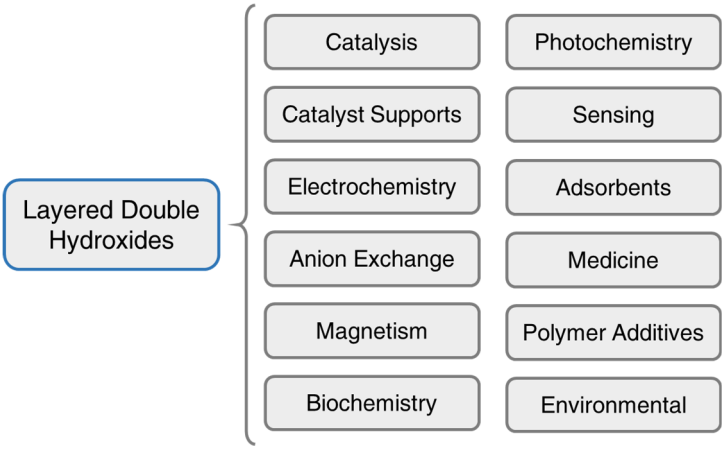

Figure 4.1. Main applications of LDH materials.

Some of the most relevant applications nowadays arise in the field of catalysis and electrochemistry, both as in the pristine LDH material as well as in a composite form.[12] As pristine materials, a great variety of LDH-based catalysts have been reported so far: from solid base catalysts to nanocatalysts based on LDH nanosheets, intercalation catalysts,[13] mixed metal oxides or supported metal catalysts, among others. Different synthetic routes need to be developed to include such a wide range of catalysts, like rehydration or reduction after calcination, intercalation or delamination procedures.[13] All of these processes rely in two of the

most important features of a LDH material: the flexible tunability of its metallic composition and its anion exchange ability. For example, MgAl-LDH has been reported to act as a solid base catalyst in the transesterification of long-chain triglycerides;[14] and NiFe-LDH was found to catalyse the formation of carbon nanoforms (CNFs) at lower temperatures while exhibiting a higher degree of selectivity.[15,16] In this context, **Table 4.1** depicts the most typical LDH compositions and their capability for synthesizing the main CNFs. Electrocatalysis is another important field of action, where LDHs can replace the more expensive alternatives based on precious metals such as Ir or Ru. As an example, ZnCo-LDH has been reported to act as an electrocatalyst for water and alcohol oxidation, with a turnover frequency of *ca.* 10 times higher than that found for $Co(OH)_2$ and Co_3O_4 species at the same potentials.[17] In line with that, CoNi-LDH was found to be a good candidate for oxygen evolution reaction in absence of any sacrificial agent.[18] The total performance of a LDH material in electrocatalysis relies on the metallic composition of the LDH and its morphology. In fact, it has been demonstrated that a porous 3D morphology (instead of the typical 2D planar structure) facilitates the electron transport process, electrolyte penetration and enhances the electrochemically active surface area.[19–21] **Fig. 4.2** schematises a schematic view of the main catalytic applications of LDHs.

Table 4.1. Most representative LDH compositions and their capability for synthesizing the main CNFs: G (graphene), T (carbon nanotubes), F (fullerene), QD (carbon quantum dots), CS (carbon spheres) and F (carbon fibers).

M^{3+},M^{4+}/M^{2+},M^{+}	Fe^{2+}	Co^{2+}	Ni^{2+}	Cu^{2+}	Zn^{2+}	Ca^{2+}	Mg^{2+}	Mn^{2+}	Li^{+}
Fe^{3+}		G, T, F	G, T, QD, CS						
Co^{3+}			G, T, F		G				
Ni^{3+}		F							
Al^{3+}		G, T, CS, F	G, T, QD, CS		G, T		G, T, F, CS	G	

Cr^{3+}					G				
Mn^{3+}		T, F	G, T						
Ga^{3+}									
In^{3+}									
Ti^{4+}			G						

	Synthesized catalytic LDH		LDHs without catalytic activity for nanocarbon growth		Not synthesized

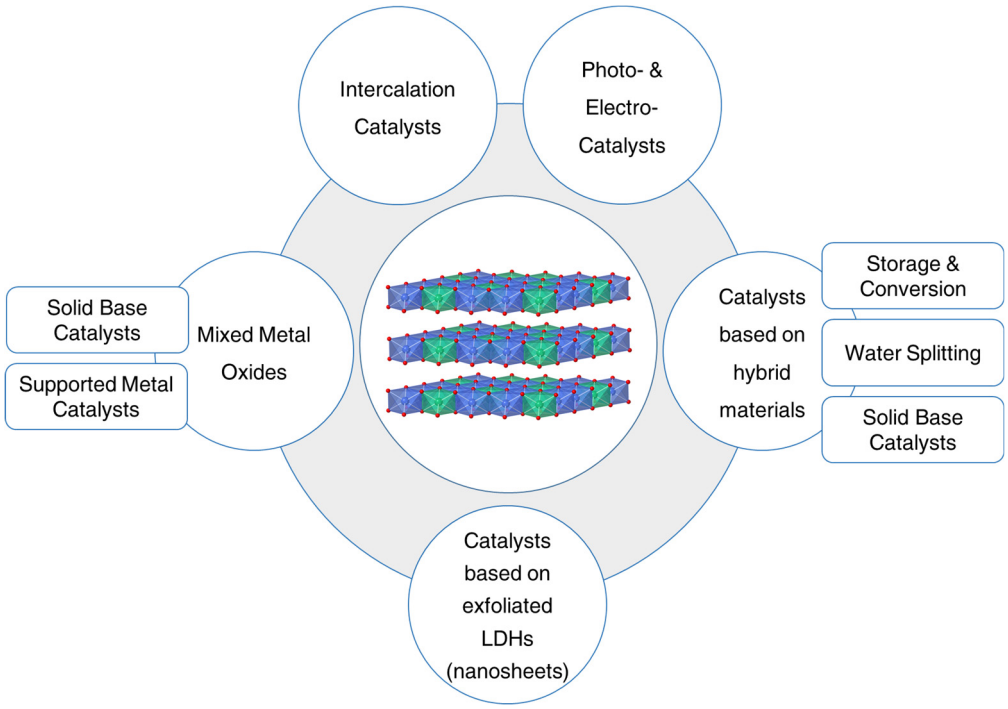

Figure 4.2. Main catalytic applications of LDH materials.

On the other hand, LDH nanocomposites based on carbon nanoforms have been also widely studied. The carbon-based materials gather a wide variety of different forms and allotropes of carbon that comprise all kind of dimensionalities:

0D fullerenes or carbon spheres, 1D carbon nanotubes, 2D graphene or 3D graphite, to mention some representative examples.[22] **Table 4.2** shows some properties of the most representative carbon materials and compare them with the ones of a LDH. This versatility proclaims CNFs as one of the most appealing building block for the synthesis of nanocomposites,[12,23–26] and that fact is relevant to the LDH field.[27–29] The synthesis of hybrid LDH materials relies in the anion exchange features of the pristine system, capable of accommodating a great variety of different molecules and of achieving the coexistence and even interaction of the properties between the LDH host and the guest molecule.[8,30–32] **Fig. 4.3** shows a schematic illustration with the main CNF/LDH nanocomposites reported in the literature.[12]

Table 4.2. Properties of different carbon materials and LDHs.

Properties	**Fullerenes**[33–35]	**CNTs**[36–42]	**Graphene**[43–46]	**Graphene oxide**[47–52]	**LDHs**[7]
Young´s Modulus /GPa	15.9	0.27 – 1.25	*ca.* 1.0	380 – 470	/
Tensile Strength /Gpa	/	11 – 63	130	130	/
Band Gap /ev	1.5 – 2.0	0 – 1.9	0	0.1 – 4	/
Electrical Conductivity / S cm^{-1}	10^{-14} – $6 \cdot 10^{-8}$	0.17 – $2 \cdot 10^{5}$	*ca.* 10^{6}	$1 \cdot 10^{-3}$ – 2	Insulating (~62 S cm^{-1} for calcined CoNi-LDH)
Thermal Conductivity / W m^{-1} K^{-1}	0.4	3000 – 6600	3000 – 5000	*ca.* 5000	/
Specific Surface Area /m^2 g^{-1}	/	150 – 1315	2630	736.6	20 – 365
Chemical Reactivity	Active	Active	Active	Active (redox)	Active (redox)

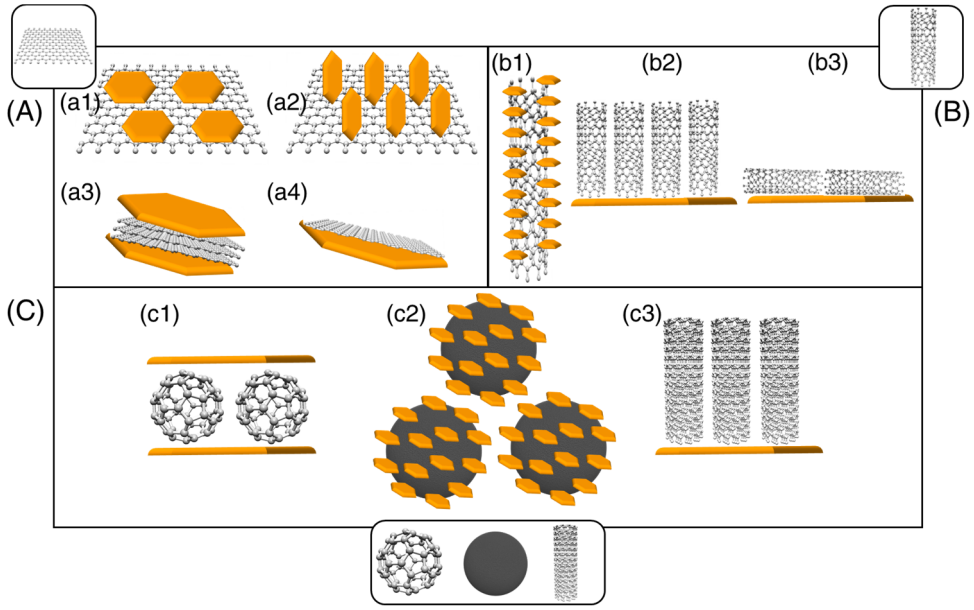

Figure 4.3. Schematic illustration with some of the most typical nanocomposites between LDH and CNFs. Nanocomposites with graphene (A): *in situ* growth of LDH flakes parallel (a1) or vertically (a2) aligned to the graphene layer, intercalation of graphene layers into the interlayer space of the LDH (a3) and graphene directly grown on the surface of the LDH crystallite (a4). Nanocomposites with carbon nanotubes (B): *in situ* growth of LDH flakes on the surface of CNTs (b1), *in situ* growth of CNTs vertically (b2) or parallel (b3) aligned to the surface of the LDH. Nanocomposites with, from left to right, fullerene, carbon spheres and carbon fibres (C): directly assembled between LDH flakes and fullerenes located into the interlayer space (c1), *in situ* growth of LDH crystallites on the surface of carbon spheres (c2) and *in situ* growth of carbon fibres vertically aligned to the surface of the LDH flakes (c3).

The main synthetic approaches to prepare these CNF/LDH nanocomposites are three: firstly, *via* strong electrostatic interactions between the positively charged exfoliated LDH nanosheets and the negatively charged CNFs, which lead to the reassembly of both nanocarbons and LDH in the final hybrid.[53] Secondly, we can take advantage of the strong adsorption ability of the negatively charged CNFs for metal cations, therefore acting as an ideal template for the direct seed nucleation and growth of LDH flakes mediated coprecipitation or hydrothermal synthesis under basic pH.[15,54,55] Lastly, the catalytic properties of LDHs can be useful to act as either a catalytic support for the subsequent *in situ* growth of CNFs (by means of chemical

vapour deposition, CVD, with a carbon source such as ethylene), or acting as nanoreactors. In this case, carbon-enriched molecules are intercalated within the interlayer space of the LDH system and then the hybrid carbon material is formed upon calcination of the intercalated carbon-rich LDH.[9,15,56,57] Furthermore, after the calcination procedure, the LDH phase usually evolves into a mixture of metallic oxides and nanoparticles, hence enhancing the catalytic properties of the calcined material.[15,58] Whereas the 2D structure of LDHs is lost after calcination,[59] the layered structure is kept in case of LDH synthesized by means of ARR, giving rise to the formation of metallic nanoparticles. For NiFe-LDHs, the formation of $FeNi_3$ nanoparticles are observed within the LDH structure,[15] a magnetic alloy that becomes crucial for its superior magnetic properties and thermal stability,[60,61] as well as in the enhancement of the electrochemical properties.[62,63] Regarding their applications, CNF/LDH nanocomposites are present in a great variety of fields, mainly related with electrochemistry and catalysis. **Table 4.3** depicts some examples of CNF/LDH nanocomposites as well as their synthetic method and field of application.

Table 4.3. Overview of some of CNF/LDH nanocomposites reported in literature, highlighting the synthetic method and field of application.

Nanocomposite	Synthetic Method	Applications	Ref.
Graphene oxide/CoAl-LDH	Layer by layer assembly	Films with enhanced electrical conductivity	64
Graphene/NiAl-LDH	Hydrothermal	Supercapacitor	65
Reduced graphene oxide/NiCo-LDH	Hydrothermal	Supercapacitor	66
Graphene oxide/CoAl-LDH	Coprecipitation	Supercapacitor	67
Graphene/MgAl-LDH	Hydrothermal	Cr (VI) removal	68
Reduced graphene oxide/NiFe-LDH	Hydrothermal	Water oxidation	69
Graphene/MgAl-LDH	CVD		70

Graphene/NiFe-LDH	Hydrothermal	Flame retardant	71
Graphene/NiMn-LDH	Coprecipitation	Li-ion batteries	72
Graphene oxide/MgAl-LDH	Coprecipitation	CO_2 adsorbent	73
Graphene/CoAl-LDH	Coprecipitation	Supercapacitor	74
Graphene/CNT/CoMgAl-LDH	CVD	Supercapacitor	75
Graphene/CNT/FeMgAl-LDH	CVD		76
CNT/ZnAl-LDH	Hydrothermal		77
CNT/MgAl-LDH	Self-assembly	CO_2 adsorbent	29
CNT/NiFe-LDH	Hydrothermal	Water oxidation	78
CNT/NiMn-LDH	Hydrothermal	Supercapacitor	79
Carbon spheres/CoAl-LDH	CVD	Super-hydrophobicity	80
Carbon spheres/MgAl-LDH	Self-assembly	Water treatment	81
Fullerene/MgAl-LDH	Self-assembly		82
Carbon quantum dot/NiFe-LDH	Hydrothermal	Water oxidation	83
Carbon fiber/CoAl-LDH	Hydrothermal	Supercapacitor	84
Carbon nanoring/CoAl-LDH	CVD	Li-storage	85
Carbon nanobelt/CoAl-LDH	Hydrothermal		86

Electrochemical applications are related with energy storage and conversion processes, *i.e.*, batteries, supercapacitors and water splitting. Carbon/LDH nanocomposites have demonstrated to be very good candidates for batteries with

long life and high power and energy density, as well as both environmental friendly and low cost alternative if compared with Pb or Ni batteries.[87–89,89] Different authors have reported how these nanocomposites enhance the electrochemical activity after the thermal transformation of the LDH in a mixture of metal oxides and metal nanoparticles,[72,90] achieving higher discharge capacity than that observed for carbon-only materials.[91] Electrochemical supercapacitors (ultracapacitors) have also attracted the aim among the scientific community for their long lifecycle and high power density, among other features.[92] Into this field, one can find a division between two kinds of supercapacitors: the electrical double layer capacitors (EDLC), in which the capacitance comes from the charge accumulation, and the pseudocapacitors, where the electro-active species perform the fast faradic processes.[93] Carbon materials are usually used as electrodes in EDLCs thanks to their flexibility, high surface area, good conductivity and electrocatalytic active sites, therefore allowing the production of redox reactions.[94] Mixing CNFs with LDHs lead to the assembly of high-performance supercapacitators at basic pH, combining the full use of the double layer capacitance as well as a high activity of the faradic reactions.[27] For example, CNT/LDH nanocomposites have demonstrated to be very good supercapacitors with small losses of *ca.* 10% after 400 cycles and better values of specific capacitance than that observed for the pristine LDH material.[79,95] Finally, electrocatalytic water splitting is a process that consists in the conversion of water into hydrogen, erecting as one of the most promising source of clean, renewable and limitless energy. The oxygen evolution reaction (OER) is the limiting step process as it is energetically disfavoured by the thermodynamic stability of water.[96,97] Nowadays, the main electrocatalyst for OER is based on precious metal oxides such as IrO_2 or RuO_2.[98] However, their high cost and scarcity have encouraged the scientific community in the search of less expensive and more abundant alternatives. In this context, LDHs have raised as one of the candidates offering a very efficient bimetallic earth-abundant electrocatalysts. For example, NiFe-LDHs display an excellent OER activity in basic pH.[99,100] In this sense, the hybridization with CNFs dramatically improves the global performance of the resulting material. For example, CNT/NiFe-LDH nanocomposites have been reported exhibiting higher OER activity than that observed for Ir-based catalysts, which are also surpassed in economic

cost.[78] The key point is the synergy between cooperation of the OER activity of the initial NiFe-LDH and the electron transport properties of the CNT, giving rise to enhanced OER values that equal or overcome those obtained by the Ir/C catalyst.[78]

Regarding the catalytic properties, LDH nanocomposites are usually employed in photocatalysis, photodegradation of pollutants, water oxidation and removal of NO_x and SO_x contaminant emissions, among others.[13,101,102] As reported by different authors, CNF/LDH hybrids depict catalytic properties due to the fact that the carbonaceous matrix increases the catalytic behaviour of the LDH, therefore favouring mass transfer, dispersion and heat processes.[27] Hence, the global catalytic activity of the mixed material is usually enhanced. One of the main advantages on the synthesis of these hybrids is the fact that the hierarchical architectures formed after the assembly or calcination of the initial materials allow a more efficient distribution of the catalytic active sites through the internal structure of the hierarchical nanocomposite. That is possible thanks to the new pores (macro-, meso- or micro-) created during the formation of the hierarchical nanocomposite.[15,16,27] Finally, other applications such as environment protection (mainly as removal agents of contaminant anions or molecules[103–105]), drug delivery[106,107] or polymer additives[108,109] have also been reported for CNF/LDH hybrid materials.

4.2. Summary of the most important results.

The two articles here presented are focused on the catalytic applications of NiFe-LDHs towards the synthesis of carbon nanoforms, as well as on the processability of the material over film substrates. **Fig. 4.4** shows the schematic view of a NiFe-LDH with a Ni^{2+}/Fe^{3+} ratio of 3:1.

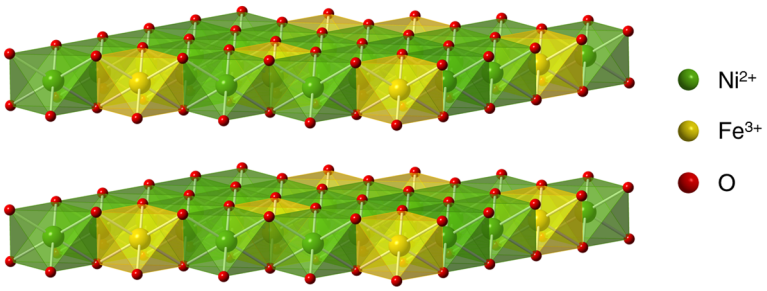

Figure 4.4. Schematic illustration of a NiFe-LDH with Ni^{2+}/Fe^{3+} ratio of 3:1.

The synthesis of the NiFe-LDH was carried out by using a hydrothermal approach thoroughly developed by our group. Then, the nitrate salts of the metals are combined in presence of a chelating agent such as triethanolamine and urea to achieve both the slowly release of Fe^{3+} cations to the media and the basic media prior to the formation of the LDH phase, respectively. By carefully controlling the synthetic parameters, such as reaction time and temperature, we can obtain the pure LDH phase of the desired 3:1 composition, which is the one with the highest catalytic activity.[110,111] In order to shed light in the formation of a LDH material, we study the growing mechanism in function of time of samples deposited on film substrates. We observe a formation route based on the circle-like growth motion mechanism, which starts with FeO_x nanoparticles until the complete formation of the hexagonal layer. Meanwhile, we are able to decipher the evolution selection mechanism that is used as time reaction increases, from an initial parallel orientation of the ab-planes of the flakes to the substrate for the initial times (24 and 48 h), to a perpendicular alignment of them at 72 h.[15] Parallel films exhibit a thickness of *ca.* 140 – 170 nm. In this context, a low roughness of the substrate (suprasil quartz substrate, with a root mean square [RMS] roughness of *ca.* 0.79 nm), is required to successfully study the deposition of the flakes, since a typical quartz substrate (RMS value of *ca.* 1.25 nm)

gives rise to a more irregular arrangement of the material and the perpendicular alignment was found at earlier stages. Magnetic measurements of a calcined film sample exhibit a magnetic exchange bias phenomenon with a bias field of *ca.* 100 G, in good agreement with previous results.[112,113] This effect is ascribed to the interfacial exchange coupling that occurs between the ferromagnetic $NiFe_2O_4$ spinel nanoparticles and the antiferromagnetic NiO matrix, and is a signature of the successful transformation of the precursor LDH.[112] Furthermore, contact angle measurements (CA) are studied to evaluate the hydrophilic/hydrophobic behaviour of the LDH films and correlate the morphological arrangement of the flakes with that property, since this kind of technique is a macroscopic evidence of the hierarchy of the sample. As expected, low contact angle values are observed for the films with parallel alignment (*ca.* 18º), implying hydrophilic behaviour (CA < 90º), while higher values are found for the perpendicular oriented ones (*ca.* 96º), which are therefore related with a hydrophobic nature (CA ≥ 90º). No super-hydrophobicity is found in any case (CA ≥ 150º). With both bulk and film samples, chemical vapour deposition processes (CVD) are carried out to investigate the catalytic properties of the NiFe-LDH after the calcination procedure, preceded by an exhaustive study of the calcination parameter (maximum temperature and scan rate) to achieve optimum values. Ethylene is chosen as the carbon source. A low temperature of 550 ºC is selected for the film samples giving rise to a selectively synthesis of a hierarchical growing of bamboo-like carbon nanotubes, with a diameter of *ca.* 40 nm. In this film, contact angle measurement is about 95º, resulting in a hydrophobic coating of the carbon nanotubes. It is worth noting that if we perform the CVD procedure in absence of H_2 (catalytic CVD), no major differences are observed. Furthermore, the arrangement of the LDH flakes throughout the film surface is kept after the calcination process. On the other hand, CVD at 550 ºC is also tested on the bulk samples. In this case, there is no evidence of selectivity and a mixture of CNFs is obtained, which is composed by few-layer graphene, carbon fibers and multi-wall carbon nanotubes. A higher temperature of 900 ºC is tested also for the bulk material, resulting in the gram-scale synthesis of carbon spheres with a diameter of *ca.* 740 nm.[16] These spheres exhibit a higher degree of graphitization (order) based on the Raman spectrum of the sample. For carbonaceous materials, D and G bands

in the Raman spectra are related with the defects and disorder-induced modes (D band), on one hand, and on the other hand, with the in-plane E_{2g} zone-centre mode, like the vibration of sp^2 carbon atoms in the 2D hexagonal lattice. By calculating the ratio between both intensities (stated as I_D/I_G), one can estimate the degree of graphitization of the carbon material. For the present case, I_D/I_G ratio is found to be *ca.* 0.80, which is lower than that observed for other carbon spheres reported to date, therefore involving a higher degree of order.[114,115] Focused ion beam scanning electron microscopy (FIB-SEM) is employed in order to unveil the internal structure of the carbon spheres and determine if the sphere presented a solid or a hollow structure. Cross-section images highlight the existence of a solid inner structure of the spheres, made by concentric graphitic planes. Moreover, one of the main problems of these materials is the aggregation processes that happen among the spheres resulting in clusters of several microns. This effect is ascribed to the presence of reactive dangling bonds on the surface of the spheres, enhancing their surface reactivity.[114] We find out that sonication and dispersion of the clusters in toluene is able to avoid this aggregation effect. High-resolution transmission electron microscopy (HRTEM) allows us to obtain images of isolated spheres. Regarding the electrochemical properties, a supercapacitive behaviour is observed, even though the absence of mesoporosity of these spheres, therefore indicating an active surface. According to transport measurements, the registered data can be fitted to a Mott variable range hopping (Mott VRH) model. This model of conductivity relies on a phonon-assisted mechanism of charge transport and is usually related with amorphous semiconductors, semiconductor glasses and amorphous carbon. Finally, a positive and non-saturated magnetoresistance effect of *ca.* 72% at low temperature (2 K) is also observed. As long as temperature is increased, magnetoresistance falls dramatically until no signal is observed above 100 K.

Fig. 4.5 exhibits a scheme with the different CNFs obtained after the CVD processes of NiFe-LDHs here depicted. In summary, the starting NiFe-LDH material can be *in situ* grown on suprasil quartz substrates, giving rise to ultrathin films which undergo CVD procedures at 550 ^oC, resulting in the selectively growth of bamboo-like CNTs. On the contrary, from the bulk material we can apply a CVD

process at low temperature (500 ºC), achieving a mixture of CNFs, or at a high temperature (900 ºC), which results in the synthesis of carbon spheres.

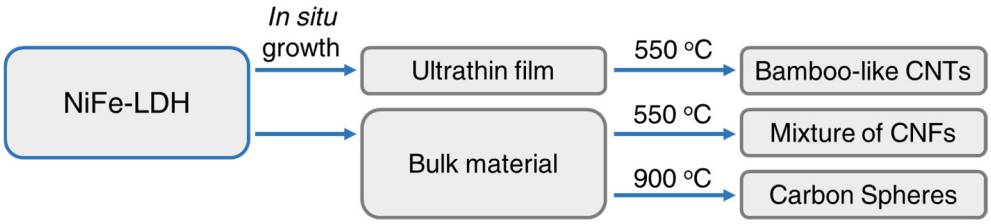

Figure 4.5. Scheme with the CNFs obtained after the CVD procedure of NiFe-LDHs, both in bulk and deposited on ultrathin film substrates.

4.3. Contribution of the author.

4.3.1. Article 6: "*In-situ Growth of Ultrathin Films of NiFe-LDHs: Towards a Hierarchical Synthesis of Bamboo-Like Carbon Nanotubes.*"

The main contribution of this publication to the field of LDHs was the study of the influence of reaction times in the growing mechanism as well as the crucial role of the quality of the substrate in terms of the arrangement of the LDH flakes throughout the film. We were able to synthesized ultrathin films of NiFe-LDH with a thickness of *ca.* 138 – 170 nm *via* an *in situ* hydrothermal approach on suprasil quartz substrates. We study different reaction times during the synthesis (24, 48 and 72 h) and characterize them, observing an initial parallel growing of the LDH flakes (circle-like growth motion mechanism) which evolves to a perpendicular one as long as the reaction time is increased (dense stacking growth) on the substrate. This sequence is based on the evolution selection mechanism. In line with that, the quality of the substrate plays a crucial role in this growing mechanism, finding out that typical quartz substrate with higher roughness values leads to a perpendicular arrangement at lower reaction times. We also found that the arrangement of the crystallites is kept after the calcination procedure. In line with that, both CVD and catalytic CVD at low temperature (550 ^{o}C) reactions were carried out on the ultrathin films of NiFe-LDHs giving rise to a selectively hierarchical growth of bamboo-like carbon nanotubes. This result is in stark contrast with the lack of selectivity observed after the calcination of the bulk LDH, which gives rise to the synthesis of a mixture of carbon nanoforms.

The author synthesized, characterised and discussed the results of all samples. The author wrote the paper in collaboration with the other authors.

4.3.2. Article 7: "*CVD Synthesis of Carbon Spheres using NiFe-LDHs as Catalytic Precursors: Structural, Electrochemical and Magnetoresistive Properties.*"

In this publication, we used NiFe-LDHs as catalyst precursor in order to achieve the gram-scale synthesis of carbon spheres by means of a CVD procedure. In this reaction, the presence of $FeNi_3$ nanoparticles (after the calcination of the LDH) revealed their crucial role in giving rise to both a monodisperse sample and a higher graphitization degree than that observed in other spheres reported. Furthermore, the inner structure of the carbon spheres was thoroughly studied by FIB-SEM exhibiting a solid structure composed by concentric graphitic planes. Finally, giant magnetoresistance of *ca.* 72% at 2 K was found for these materials. All these features make these carbon spheres good candidates in polymer science as functional reinforcement agents.

The author synthesized, characterised and discussed the results of all samples except the FIB-SEM, electrochemistry, transport and magnetoresistance measurements, carried out by other authors. The author wrote the paper in collaboration with the other authors.

Note about the papers: Both articles were selected to be the front cover of their respectives issues:

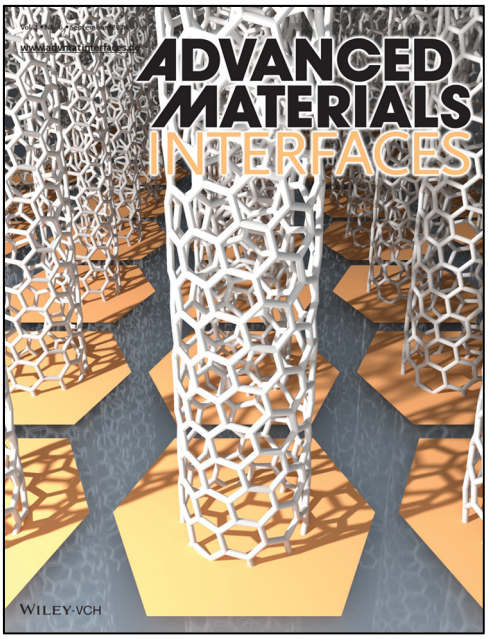

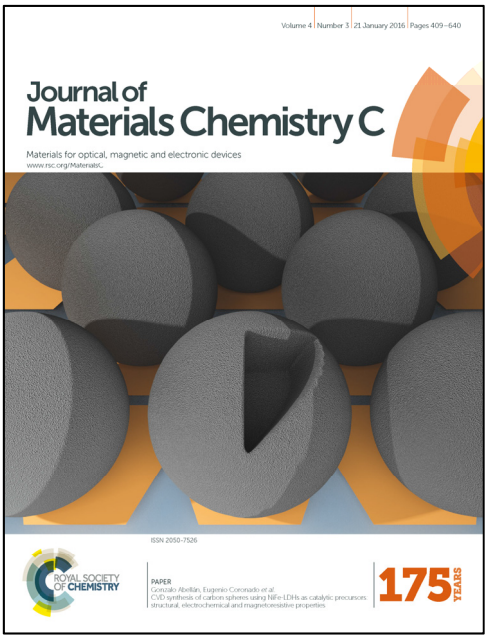

In addition to the articles, book chapter "*Layered Double Hydroxide Nanocomposites Based on Carbon Nanoforms*", Chapter 9 in Layered Double Hydroxide Polymer Nanocomposites; Ed. Woodhead Publishing, Cambridge, 2019, is included.

The author wrote the book chapter supervised by his thesis directors.

4.4. References.

(1) Tian, R.; Liang, R.; Wei, M.; Evans, D. G.; Duan, X. Applications of Layered Double Hydroxide Materials: Recent Advances and Perspective; Springer Berlin Heidelberg: Berlin, Heidelberg, 2015.

(2) Goh, K.-H.; Lim, T.-T.; Dong, Z. Application of Layered Double Hydroxides for Removal of Oxyanions: A Review. *Water Res.* **2008**, *42*, 1343–1368.

(3) Khan, A. I.; O'Hare, D. Intercalation Chemistry of Layered Double Hydroxides: Recent Developments and Applications. *J Mater. Chem.* **2002**, *12*, 3191–3198.

(4) Wang, Q.; O'Hare, D. Recent Advances in the Synthesis and Application of Layered Double Hydroxide (LDH) Nanosheets. *Chem. Rev.* **2012**, *112*, 4124–4155.

(5) *Layered Double Hydroxides: Present and Future*; Rives, V., Ed.; Nova Science Publishers: Huntington, N.Y, 2001.

(6) *Layered Double Hydroxides*; Duan, X., Evans, D. G., Eds.; Structure and Bonding; Springer-Verlag: Berlin/Heidelberg, 2006; Vol. 119.

(7) Chen, C.; Wangriya, A.; Buffet, J.-C.; O'Hare, D. Tuneable Ultra High Specific Surface Area Mg/Al-CO_3 Layered Double Hydroxides. *Dalton Trans.* **2015**, *44*, 16392–16398.

(8) Abellán, G.; Jordá, J. L.; Atienzar, P.; Varela, M.; Jaafar, M.; Gómez-Herrero, J.; Zamora, F.; Ribera, A.; García, H.; Coronado, E. Stimuli-Responsive Hybrid Materials: Breathing in Magnetic Layered Double Hydroxides Induced by a Thermoresponsive Molecule. *Chem. Sci.* **2015**, *6*, 1949–1958.

(9) Abellán, G.; Coronado, E.; Martí-Gastaldo, C.; Ribera, A.; Sánchez-Royo, J. F. Layered Double Hydroxide (LDH)–organic Hybrids as Precursors for Low-Temperature Chemical Synthesis of Carbon Nanoforms. *Chem. Sci.* **2012**, *3*, 1481–1485.

(10) Abellán, G.; Busolo, F.; Coronado, E.; Martí-Gastaldo, C.; Ribera, A. Hybrid Magnetic Multilayers by Intercalation of Cu(II) Phthalocyanine in LDH Hosts. *J. Phys. Chem. C* **2012**, *116*, 15756–15764.

(11) Newman, S. P.; Jones, W. Synthesis, Characterization and Applications of Layered Double Hydroxides Containing Organic Guests. *New J. Chem.* **1998**, *22*, 105–115.

(12) Carrasco, J.A.; Abellán, G.; Coronado, E. Layered Double Hydroxide Nanocomposites Based on Carbon Nanoforms, Chapter 9 in *Layered Double Hydroxide Polymer Nanocomposites*; Ed. Woodhead Publishing, Cambridge, 2019.

(13) Fan, G.; Li, F.; Evans, D. G.; Duan, X. Catalytic Applications of Layered Double Hydroxides: Recent Advances and Perspectives. *Chem. Soc. Rev.* **2014**, *43*, 7040–7066.

(14) Woodford, J. J.; Dacquin, J.-P.; Wilson, K.; Lee, A. F. Better by Design: Nanoengineered Macroporous Hydrotalcites for Enhanced Catalytic Biodiesel Production. *Energy Environ. Sci.* **2012**, *5*, 6145–6150.

(15) Abellán, G.; Carrasco, J. A.; Coronado, E.; Prieto-Ruiz, J. P.; Prima-García, H. In-Situ Growth of Ultrathin Films of NiFe-LDHs: Towards a Hierarchical Synthesis of Bamboo-Like Carbon Nanotubes. *Adv. Mater. Interfaces* **2014**, *1*, 1400184.

(16) Carrasco, J. A.; Prima-Garcia, H.; Romero, J.; Hernández-Saz, J.; Molina, S. I.; Abellán, G.; Coronado, E. CVD Synthesis of Carbon Spheres Using NiFe-LDHs as Catalytic Precursors: Structural, Electrochemical and Magnetoresistive Properties. *J. Mater. Chem. C* **2016**, *4*, 440–448.

(17) Zou, X.; Goswami, A.; Asefa, T. Efficient Noble Metal-Free (Electro)Catalysis of Water and Alcohol Oxidations by Zinc–Cobalt Layered Double Hydroxide. *J. Am. Chem. Soc.* **2013**, *135*, 17242–17245.

(18) Zhang, Y.; Cui, B.; Zhao, C.; Lin, H.; Li, J. Co–Ni Layered Double Hydroxides for Water Oxidation in Neutral Electrolyte. *Phys. Chem. Chem. Phys.* **2013**, *15*, 7363–7369.

(19) Lu, Z.; Xu, W.; Zhu, W.; Yang, Q.; Lei, X.; Liu, J.; Li, Y.; Sun, X.; Duan, X. Three-Dimensional NiFe Layered Double Hydroxide Film for High-Efficiency Oxygen Evolution Reaction. *Chem. Commun.* **2014**, *50*, 6479–6482.

(20) Lu, Z.; Yang, Q.; Zhu, W.; Chang, Z.; Liu, J.; Sun, X.; Evans, D. G.; Duan, X. Hierarchical Co_3O_4@Ni-Co-O Supercapacitor Electrodes with Ultrahigh Specific Capacitance per Area. *Nano Res.* **2012**, *5*, 369–378.

(21) Lang, X.; Hirata, A.; Fujita, T.; Chen, M. Nanoporous Metal/Oxide Hybrid Electrodes for Electrochemical Supercapacitors. *Nat. Nanotechnol.* **2011**, *6*, 232–236.

(22) Delgado, J. L.; Herranz, M.; Martín, N. The Nano-Forms of Carbon. *J. Mater. Chem.* **2008**, *18*, 1417–1426.

(23) Zhao, Z.; Sun, Y.; Dong, F. Graphitic Carbon Nitride Based Nanocomposites: A Review. *Nanoscale* **2015**, *7*, 15–37.

(24) Moniruzzaman, M.; Winey, K. I. Polymer Nanocomposites Containing Carbon Nanotubes. *Macromolecules* **2006**, *39*, 5194–5205.

(25) Kim, H.; Abdala, A. A.; Macosko, C. W. Graphene/Polymer Nanocomposites. *Macromolecules* **2010**, *43*, 6515–6530.

(26) Thostenson, E. T.; Ren, Z.; Chou, T.-W. Advances in the Science and Technology of Carbon Nanotubes and Their Composites: A Review. *Compos. Sci. Technol.* **2001**, *61*, 1899–1912.

(27) Zhao, M.-Q.; Zhang, Q.; Huang, J.-Q.; Wei, F. Hierarchical Nanocomposites Derived from Nanocarbons and Layered Double Hydroxides - Properties, Synthesis, and Applications. *Adv. Funct. Mater.* **2012**, *22*, 675–694.

(28) Daud, M.; Kamal, M. S.; Shehzad, F.; Al-Harthi, M. A. Graphene/Layered Double Hydroxides Nanocomposites: A Review of Recent Progress in Synthesis and Applications. *Carbon* **2016**, *104*, 241–252.

(29) Wang, J.; Huang, L.; Zheng, Q.; Qiao, Y.; Wang, Q. Layered Double Hydroxides/Oxidized Carbon Nanotube Nanocomposites for CO_2 Capture. *J. Ind. Eng. Chem.* **2016**, *36*, 255–262.

(30) Abellán, G.; Martí-Gastaldo, C.; Ribera, A.; Coronado, E. Hybrid Materials Based on Magnetic Layered Double Hydroxides: A Molecular Perspective. *Acc. Chem. Res.* **2015**, *48*, 1601–1611.

(31) Clemente-León, M.; Coronado, E.; Martí-Gastaldo, C.; Romero, F. M. Multifunctionality in Hybrid Magnetic Materials Based on Bimetallic Oxalate Complexes. *Chem. Soc. Rev.* **2011**, *40*, 473–497.

(32) Abellán, G.; Coronado, E.; Martí-Gastaldo, C.; Ribera, A.; Jordá, J. L.; García, H. Photo-Switching in a Hybrid Material Made of Magnetic Layered Double Hydroxides Intercalated with Azobenzene Molecules. *Adv. Mater.* **2014**, *26*, 4156–4162.

(33) Shi, X. D.; Kortan, A. R.; Williams, J. M.; Kini, A. M.; Savall, B. M.; Chaikin, P. M. Sound Velocity and Attenuation in Single-Crystal C_{60}. *Phys. Rev. Lett.* **1992**, *68*, 827–830.

(34) Haddon, R. C.; Perel, A. S.; Morris, R. C.; Palstra, T. T. M.; Hebard, A. F.; Fleming, R. M. C_{60} Thin Film Transistors. *Appl. Phys. Lett.* **1995**, *67*, 121–123.

(35) Yu, R. C.; Tea, N.; Salamon, M. B.; Lorents, D.; Malhotra, R. Thermal Conductivity of Single Crystal C_{60}. *Phys. Rev. Lett.* **1992**, *68*, 2050–2053.

(36) Krishnan, A.; Dujardin, E.; Ebbesen, T. W.; Yianilos, P. N.; Treacy, M. M. J. Young's Modulus of Single-Walled Nanotubes. *Phys. Rev. B* **1998**, *58*, 14013–14019.

(37) Yu, M. Strength and Breaking Mechanism of Multiwalled Carbon Nanotubes Under Tensile Load. *Science* **2000**, *287*, 637–640.

(38) Yu, M.-F.; Files, B. S.; Arepalli, S.; Ruoff, R. S. Tensile Loading of Ropes of Single Wall Carbon Nanotubes and Their Mechanical Properties. *Phys. Rev. Lett.* **2000**, *84*, 5552–5555.

(39) Wilder, J. W.; Venema, L. C.; Rinzler, A. G.; Smalley, R. E.; Dekker, C. Electronic Structure of Atomically Resolved Carbon Nanotubes. *Nature* **1998**, *391*, 59–62.

(40) Ebbesen, T. W.; Lezec, H. J.; Hiura, H.; Bennett, J. W.; Ghaemi, H. F.; Thio, T. Electrical Conductivity of Individual Carbon Nanotubes. *Nature* **1996**, *382*, 54–56.

(41) Berber, S.; Kwon, Y.-K.; Tománek, D. Unusually High Thermal Conductivity of Carbon Nanotubes. *Phys. Rev. Lett.* **2000**, *84*, 4613–4616.

(42) Peigney, A.; Laurent, C.; Flahaut, E.; Bacsa, R. R.; Rousset, A. Specific Surface Area of Carbon Nanotubes and Bundles of Carbon Nanotubes. *Carbon* **2001**, *39*, 507–514.

(43) Geim, A. K.; Novoselov, K. S. The Rise of Graphene. *Nat. Mater.* **2007**, *6*, 183–191.

(44) Lee, C.; Wei, X.; Kysar, J. W.; Hone, J. Measurement of the Elastic Properties and Intrinsic Strength of Monolayer Graphene. *Science* **2008**, *321*, 385–388.

(45) Chen, J.-H.; Jang, C.; Xiao, S.; Ishigami, M.; Fuhrer, M. S. Intrinsic and Extrinsic Performance Limits of Graphene Devices on SiO_2. *Nat. Nanotechnol.* **2008**, *3*, 206–209.

(46) Seol, J. H.; Jo, I.; Moore, A. L.; Lindsay, L.; Aitken, Z. H.; Pettes, M. T.; Li, X.; Yao, Z.; Huang, R.; Broido, D.; et al. Two-Dimensional Phonon Transport in Supported Graphene. *Science* **2010**, *328*, 213–216.

(47) Montes-Navajas, P.; Asenjo, N. G.; Santamaría, R.; Menéndez, R.; Corma, A.; García, H. Surface Area Measurement of Graphene Oxide in Aqueous Solutions. *Langmuir* **2013**, *29*, 13443–13448.

(48) Compton, O. C.; Nguyen, S. T. Graphene Oxide, Highly Reduced Graphene Oxide, and Graphene: Versatile Building Blocks for Carbon-Based Materials. *Small* **2010**, *6*, 711–723.

(49) Dreyer, D. R.; Park, S.; Bielawski, C. W.; Ruoff, R. S. The Chemistry of Graphene Oxide. *Chem. Soc. Rev.* **2010**, *39*, 228–240.

(50) Liu, L.; Zhang, J.; Zhao, J.; Liu, F. Mechanical Properties of Graphene Oxides. *Nanoscale* **2012**, *4*, 5910–5916.

(51) Suk, J. W.; Piner, R. D.; An, J.; Ruoff, R. S. Mechanical Properties of Monolayer Graphene Oxide. *ACS Nano* **2010**, *4*, 6557–6564.

(52) Gómez-Navarro, C.; Weitz, R. T.; Bittner, A. M.; Scolari, M.; Mews, A.; Burghard, M.; Kern, K. Electronic Transport Properties of Individual Chemically Reduced Graphene Oxide Sheets. *Nano Lett.* **2007**, *7*, 3499–3503.

(53) Li, L.; Ma, R.; Ebina, Y.; Iyi, N.; Sasaki, T. Positively Charged Nanosheets Derived via Total Delamination of Layered Double Hydroxides. *Chem. Mater.* **2005**, *17*, 4386–4391.

(54) Du, M.; Ye, W.; Fu, H.; Lv, W.; Zheng, Q. Direct Growth of Layered Double Hydroxides in an Aqueous Suspension of Carbon Nanotubes and Their Application as Fillers in Polypropylene. *Compos. Sci. Technol.* **2014**, *105*, 28–36.

(55) Okamoto, K.; Iyi, N.; Sasaki, T. Factors Affecting the Crystal Size of the MgAl-LDH (Layered Double Hydroxide) Prepared by Using Ammonia-Releasing Reagents. *Appl. Clay Sci.* **2007**, *37*, 23–31.

(56) Wang, B.; Williams, G. R.; Chang, Z.; Jiang, M.; Liu, J.; Lei, X.; Sun, X. Hierarchical NiAl Layered Double Hydroxide/Multiwall Carbon Nanotube/Nickel Foam Electrodes with Excellent Pseudocapacitive Properties. *ACS Appl. Mater. Interfaces* **2014**, *6*, 16304–16311.

(57) Xu, Z. P.; Xu, R.; Zeng, H. C. Sulfate-Functionalized Carbon/Metal-Oxide Nanocomposites from Hydrotalcite-like Compounds. *Nano Lett.* **2001**, *1*, 703–706.

(58) Hobbs, C.; Jaskaniec, S.; McCarthy, E. K.; Downing, C.; Opelt, K.; Güth, K.; Shmeliov, A.; Mourad, M. C. D.; Mandel, K.; Nicolosi, V. Structural Transformation of Layered Double Hydroxides: An in Situ TEM Analysis. *Npj 2D Mater. Appl.* **2018**, *2*.

(59) Zhao, X.; Zhang, F.; Xu, S.; Evans, D. G.; Duan, X. From Layered Double Hydroxides to ZnO-Based Mixed Metal Oxides by Thermal Decomposition: Transformation Mechanism and UV-Blocking Properties of the Product. *Chem. Mater.* **2010**, *22*, 3933–3942.

(60) Jia, J.; Yu, J. C.; Wang, Y.-X. J.; Chan, K. M. Magnetic Nanochains of $FeNi_3$ Prepared by a Template-Free Microwave-Hydrothermal Method. *ACS Appl. Mater. Interfaces* **2010**, *2*, 2579–2584.

(61) Liao, Q.; Tannenbaum, R.; Wang, Z. L. Synthesis of $FeNi_3$ Alloyed Nanoparticles by Hydrothermal Reduction. *J. Phys. Chem. B* **2006**, *110*, 14262–14265.

(62) Abellán, G.; Coronado, E.; Martí-Gastaldo, C.; Ribera, A.; Otero, T. F. Magnetic Nanocomposites Formed by $FeNi_3$ Nanoparticles Embedded in Graphene. Application as Supercapacitors. *Part. Part. Syst. Charact.* **2013**, 853–863.

(63) Abellán, G.; Carrasco, J. A.; Coronado, E.; Prima-García, H. Synthesis of $FeNi_3$ Nanoparticles in Benzyl Alcohol and Their Electrical and Magnetic Properties. *J. Sol-Gel Sci. Technol.* **2014**, *70*, 292–299.

(64) Chen, D.; Wang, X.; Liu, T.; Wang, X.; Li, J. Electrically Conductive Poly(Vinyl Alcohol) Hybrid Films Containing Graphene and Layered Double Hydroxide Fabricated via Layer-by-Layer Self-Assembly. *ACS Appl. Mater. Interfaces* **2010**, *2*, 2005–2011.

(65) Gao, Z.; Wang, J.; Li, Z.; Yang, W.; Wang, B.; Hou, M.; He, Y.; Liu, Q.; Mann, T.; Yang, P.; et al. Graphene Nanosheet/Ni^{2+}/Al^{3+} Layered Double-Hydroxide Composite as a Novel Electrode for a Supercapacitor. *Chem. Mater.* **2011**, *23*, 3509–3516.

(66) Chen, H.; Hu, L.; Chen, M.; Yan, Y.; Wu, L. Nickel-Cobalt Layered Double Hydroxide Nanosheets for High-Performance Supercapacitor Electrode Materials. *Adv. Funct. Mater.* **2014**, *24*, 934–942.

(67) Huang, S.; Zhu, G.-N.; Zhang, C.; Tjiu, W. W.; Xia, Y.-Y.; Liu, T. Immobilization of Co–Al Layered Double Hydroxides on Graphene Oxide Nanosheets: Growth Mechanism and Supercapacitor Studies. *ACS Appl. Mater. Interfaces* **2012**, *4*, 2242–2249.

(68) Yuan, X.; Wang, Y.; Wang, J.; Zhou, C.; Tang, Q.; Rao, X. Calcined Graphene/MgAl-Layered Double Hydroxides for Enhanced Cr(VI) Removal. *Chem. Eng. J.* **2013**, *221*, 204–213.

(69) Youn, D. H.; Park, Y. B.; Kim, J. Y.; Magesh, G.; Jang, Y. J.; Lee, J. S. One-Pot Synthesis of NiFe Layered Double Hydroxide/Reduced Graphene Oxide Composite as an Efficient Electrocatalyst for Electrochemical and Photoelectrochemical Water Oxidation. *J. Power Sources* **2015**, *294*, 437–443.

(70) Sun, J.; Liu, H.; Chen, X.; Evans, D. G.; Yang, W.; Duan, X. Synthesis of Graphene Nanosheets with Good Control over the Number of Layers within the Two-Dimensional Galleries of Layered Double Hydroxides. *Chem. Commun.* **2012**, *48*, 8126–8128.

(71) Wang, X.; Zhou, S.; Xing, W.; Yu, B.; Feng, X.; Song, L.; Hu, Y. Self-Assembly of Ni–Fe Layered Double Hydroxide/Graphene Hybrids for Reducing Fire Hazard in Epoxy Composites. *J. Mater. Chem. A* **2013**, *1*, 4383–4390.

(72) Latorre-Sanchez, M.; Atienzar, P.; Abellán, G.; Puche, M.; Fornés, V.; Ribera, A.; García, H. The Synthesis of a Hybrid Graphene–nickel/Manganese Mixed Oxide and Its Performance in Lithium-Ion Batteries. *Carbon* **2012**, *50*, 518–525.

(73) Garcia-Gallastegui, A.; Iruretagoyena, D.; Gouvea, V.; Mokhtar, M.; Asiri, A. M.; Basahel, S. N.; Al-Thabaiti, S. A.; Alyoubi, A. O.; Chadwick, D.; Shaffer, M. S. P. Graphene Oxide as Support for Layered Double Hydroxides: Enhancing the CO_2 Adsorption Capacity. *Chem. Mater.* **2012**, *24*, 4531–4539.

(74) Zhang, L.; Zhang, X.; Shen, L.; Gao, B.; Hao, L.; Lu, X.; Zhang, F.; Ding, B.; Yuan, C. Enhanced High-Current Capacitive Behavior of Graphene/CoAl-Layered Double Hydroxide Composites as Electrode Material for Supercapacitors. *J. Power Sources* **2012**, *199*, 395–401.

(75) Zhao, M.-Q.; Zhang, Q.; Huang, J.-Q.; Tian, G.-L.; Chen, T.-C.; Qian, W.-Z.; Wei, F. Towards High Purity Graphene/Single-Walled Carbon Nanotube Hybrids with Improved Electrochemical Capacitive Performance. *Carbon* **2013**, *54*, 403–411.

(76) Zhao, M.-Q.; Peng, H.-J.; Zhang, Q.; Huang, J.-Q.; Tian, G.-L.; Tang, C.; Hu, L.; Jiang, H.-R.; Cai, H.-Y.; Yuan, H.-X.; et al. Controllable Bulk Growth of Few-Layer Graphene/Single-Walled Carbon Nanotube Hybrids Containing Fe@C Nanoparticles in a Fluidized Bed Reactor. *Carbon* **2014**, *67*, 554–563.

(77) Qiao, Z.; Gao, C.; Sun, B.; Ai, S. Synthesis and Characterization of Functionalized Multi-Walled Carbon Nanotubes/Exfoliated Layered Double Hydroxide Nanosheets Hybrids via Electrostatic Force. *J. Inorg. Organomet. Polym. Mater.* **2013**, *23*, 871–876.

(78) Gong, M.; Li, Y.; Wang, H.; Liang, Y.; Wu, J. Z.; Zhou, J.; Wang, J.; Regier, T.; Wei, F.; Dai, H. An Advanced Ni–Fe Layered Double Hydroxide Electrocatalyst for Water Oxidation. *J. Am. Chem. Soc.* **2013**, *135*, 8452–8455.

(79) Zhao, J.; Chen, J.; Xu, S.; Shao, M.; Zhang, Q.; Wei, F.; Ma, J.; Wei, M.; Evans, D. G.; Duan, X. Hierarchical NiMn Layered Double Hydroxide/Carbon Nanotubes Architecture with Superb Energy Density for Flexible Supercapacitors. *Adv. Funct. Mater.* **2014**, *24*, 2938–2946.

(80) Hima, H. I.; Xiang, X.; Zhang, L.; Li, F. Novel Carbon Nanostructures of Caterpillar-like Fibers and Interwoven Spheres with Excellent Surface Super-Hydrophobicity Produced by Chemical Vapor Deposition. *J. Mater. Chem.* **2008**, *18*, 1245–1252.

(81) Gong, J.; Liu, T.; Wang, X.; Hu, X.; Zhang, L. Efficient Removal of Heavy Metal Ions from Aqueous Systems with the Assembly of Anisotropic Layered Double Hydroxide Nanocrystals@Carbon Nanosphere. *Environ. Sci. Technol.* **2011**, *45*, 6181–6187.

(82) Fortner, J. D.; Solenthaler, C.; Hughes, J. B.; Puzrin, A. M.; Plötze, M. Interactions of Clay Minerals and a Layered Double Hydroxide with Water Stable, Nano Scale Fullerene Aggregates (nC_{60}). *Appl. Clay Sci.* **2012**, *55*, 36–43.

(83) Tang, D.; Liu, J.; Wu, X.; Liu, R.; Han, X.; Han, Y.; Huang, H.; Liu, Y.; Kang, Z. Carbon Quantum Dot/NiFe Layered Double-Hydroxide Composite as a Highly Efficient Electrocatalyst for Water Oxidation. *ACS Appl. Mater. Interfaces* **2014**, *6*, 7918–7925.

(84) Zhao, J.; Lu, Z.; Shao, M.; Yan, D.; Wei, M.; Evans, D. G.; Duan, X. Flexible Hierarchical Nanocomposites Based on MnO_2 Nanowires/CoAl Hydrotalcite/Carbon Fibers for High-Performance Supercapacitors. *RSC Adv* **2013**, *3*, 1045–1049.

(85) Sun, J.; Liu, H.; Chen, X.; Evans, D. G.; Yang, W.; Duan, X. Carbon Nanorings and Their Enhanced Lithium Storage Properties. *Adv. Mater.* **2013**, *25*, 1125–1130.

(86) Su, L.; Gong, L.; Qu, B.; Zhang, X. Synthesis of Carbon Nanobelts Using a Colloidal Suspension of Co–Al Layered Double Hydroxide Nanosheets. *Carbon* **2011**, *49*, 4950–4952.

(87) Li, H.; Wang, Z.; Chen, L.; Huang, X. Research on Advanced Materials for Li-Ion Batteries. *Adv. Mater.* **2009**, *21*, 4593–4607.

(88) Liu, C.; Li, F.; Ma, L.-P.; Cheng, H.-M. Advanced Materials for Energy Storage. *Adv. Mater.* **2010**, *22*, E28–E62.

(89) Gray, H. B. Powering the Planet with Solar Fuel. *Nat. Chem.* **2009**, *1*, 7–7.

(90) Cheng, X.-B.; Tian, G.-L.; Liu, X.-F.; Nie, J.-Q.; Zhao, M.-Q.; Huang, J.-Q.; Zhu, W.; Hu, L.; Zhang, Q.; Wei, F. Robust Growth of Herringbone Carbon Nanofibers on Layered Double Hydroxide Derived Catalysts and Their Applications as Anodes for Li-Ion Batteries. *Carbon* **2013**, *62*, 393–404.

(91) Fan, Z.-J.; Yan, J.; Wei, T.; Ning, G.-Q.; Zhi, L.-J.; Liu, J.-C.; Cao, D.-X.; Wang, G.-L.; Wei, F. Nanographene-Constructed Carbon Nanofibers Grown on Graphene Sheets by Chemical Vapor Deposition: High-Performance Anode Materials for Lithium Ion Batteries. *ACS Nano* **2011**, *5*, 2787–2794.

(92) Wang, G.; Zhang, L.; Zhang, J. A Review of Electrode Materials for Electrochemical Supercapacitors. *Chem. Soc. Rev.* **2012**, *41*, 797–828.

(93) Zhang, L. L.; Zhao, X. S. Carbon-Based Materials as Supercapacitor Electrodes. *Chem. Soc. Rev.* **2009**, *38*, 2520–2531.

(94) Pandolfo, A. G.; Hollenkamp, A. F. Carbon Properties and Their Role in Supercapacitors. *J. Power Sources* **2006**, *157*, 11–27.

(95) Su, L.-H.; Zhang, X.-G.; Liu, Y. Electrochemical Performance of Co–Al Layered Double Hydroxide Nanosheets Mixed with Multiwall Carbon Nanotubes. *J. Solid State Electrochem.* **2008**, *12*, 1129–1134.

(96) Oliver-Tolentino, M. A.; Vázquez-Samperio, J.; Manzo-Robledo, A.; González-Huerta, R. de G.; Flores-Moreno, J. L.; Ramírez-Rosales, D.; Guzmán-Vargas, A. An Approach to Understanding the Electrocatalytic Activity Enhancement by Superexchange Interaction toward OER in Alkaline Media of Ni–Fe LDH. *J. Phys. Chem. C* **2014**,*118*, 22432–22438.

(97) Dau, H.; Limberg, C.; Reier, T.; Risch, M.; Roggan, S.; Strasser, P. The Mechanism of Water Oxidation: From Electrolysis via Homogeneous to Biological Catalysis. *ChemCatChem.* **2010**, *2*, 724–761.

(98) Walter, M. G.; Warren, E. L.; McKone, J. R.; Boettcher, S. W.; Mi, Q.; Santori, E. A.; Lewis, N. S. Solar Water Splitting Cells. *Chem. Rev.* **2010**, *110*, 6446–6473.

(99) Gong, M.; Li, Y.; Wang, H.; Liang, Y.; Wu, J. Z.; Zhou, J.; Wang, J.; Regier, T.; Wei, F.; Dai, H. An Advanced Ni–Fe Layered Double Hydroxide Electrocatalyst for Water Oxidation. *J. Am. Chem. Soc.* **2013**, *135*, 8452–8455.

(100) Li, Y.; Gong, M.; Liang, Y.; Feng, J.; Kim, J.-E.; Wang, H.; Hong, G.; Zhang, B.; Dai, H. Advanced Zinc-Air Batteries Based on High-Performance Hybrid Electrocatalysts. *Nat. Commun.* **2013**, *4*, 1805.

(101) Xu, Z. P.; Zhang, J.; Adebajo, M. O.; Zhang, H.; Zhou, C. Catalytic Applications of Layered Double Hydroxides and Derivatives. *Appl. Clay Sci.* **2011**, *53*, 139–150.

(102) Choudary, B. M.; Madhi, S.; Chowdari, N. S.; Kantam, M. L.; Sreedhar, B. Layered Double Hydroxide Supported Nanopalladium Catalyst for Heck-, Suzuki-, Sonogashira-, and Stille-Type Coupling Reactions of Chloroarenes. *J. Am. Chem. Soc.* **2002**, *124*, 14127–14136.

(103) Hsu, L. C.; Wang, S. L.; Tzou, Y. M.; Lin, C. F.; Chen, J. H. The Removal and Recovery of Cr(VI) by Li/Al Layered Double Hydroxide (LDH). *J. Hazard. Mater.* **2007**, *142*, 242–249.

(104) Seida, Y.; Nakano, Y. Removal of Phosphate by Layered Double Hydroxides Containing Iron. *Water Res.* **2002**, *36*, 1306–1312.

(105) Chuang, Y. H.; Tzou, Y. M.; Wang, M. K.; Liu, C. H.; Chiang, P. N. Removal of 2-Chlorophenol from Aqueous Solution by Mg/Al Layered Double Hydroxide (LDH) and Modified LDH. *Ind. Eng. Chem. Res.* **2008**, *47*, 3813–3819.

(106) Liu, Z.; Tabakman, S.; Welsher, K.; Dai, H. Carbon Nanotubes in Biology and Medicine: In Vitro and in Vivo Detection, Imaging and Drug Delivery. *Nano Res.* **2009**, *2*, 85–120.

(107) Sun, X.; Liu, Z.; Welsher, K.; Robinson, J. T.; Goodwin, A.; Zaric, S.; Dai, H. Nano-Graphene Oxide for Cellular Imaging and Drug Delivery. *Nano Res.* **2008**, *1*, 203–212.

(108) Costa, F. R.; Saphiannikova, M.; Wagenknecht, U.; Heinrich, G. Layered Double Hydroxide Based Polymer Nanocomposites. In *Wax Crystal Control · Nanocomposites · Stimuli-Responsive Polymers*; Springer Berlin Heidelberg: Berlin, Heidelberg, 2007; Vol. 210, pp 101–168.

(109) Coleman, J. N.; Khan, U.; Gun'ko, Y. K. Mechanical Reinforcement of Polymers Using Carbon Nanotubes. *Adv. Mater.* **2006**, *18*, 689–706.

(110) Friebel, D.; Louie, M. W.; Bajdich, M.; Sanwald, K. E.; Cai, Y.; Wise, A. M.; Cheng, M.-J.; Sokaras, D.; Weng, T.-C.; Alonso-Mori, R.; et al. Identification of Highly Active Fe Sites in (Ni,Fe)OOH for Electrocatalytic Water Splitting. *J. Am. Chem. Soc.* **2015**, *137*, 1305–1313.

(111) Fan, K.; Chen, H.; Ji, Y.; Huang, H.; Claesson, P. M.; Daniel, Q.; Philippe, B.; Rensmo, H.; Li, F.; Luo, Y.; et al. Nickel–vanadium Monolayer Double Hydroxide for Efficient Electrochemical Water Oxidation. *Nat. Commun.* **2016**, *7*, 11981.

(112) Zhao, X.; Xu, S.; Wang, L.; Duan, X.; Zhang, F. Exchange-Biased $NiFe_2O_4$/NiO Nanocomposites Derived from NiFe-Layered Double Hydroxides as a Single Precursor. *Nano Res.* **2010**, *3*, 200–210.

(113) Lüders, U.; Barthélémy, A.; Bibes, M.; Bouzehouane, K.; Fusil, S.; Jacquet, E.; Contour, J.-P.; Bobo, J.-F.; Fontcuberta, J.; Fert, A. $NiFe_2O_4$: A Versatile Spinel Material Brings New Opportunities for Spintronics. *Adv. Mater.* **2006**, *18*, 1733–1736.

(114) Nieto-Márquez, A.; Romero, R.; Romero, A.; Valverde, J. L. Carbon Nanospheres: Synthesis, Physicochemical Properties and Applications. *J. Mater. Chem.* **2011**, *21*, 1664–1672.

(115) Nieto-Márquez, A.; Toledano, D.; Lazo, J. C.; Romero, A.; Valverde, J. L. Carbon Nanospheres as Novel Support in the Nickel Catalyzed Gas Phase Hydrogenation of Butyronitrile. *Appl. Catal. Gen.* **2010**, *373*, 192–200.

Article 6:

In-situ Growth of Ultrathin Films of NiFe-LDHs: Towards a Hierarchical Synthesis of Bamboo-Like Carbon Nanotubes

Advanced Materials Interfaces **2014**, *1*, 1400184

Vol. 1 • No. 6 • September • 2014
www.advmatinterfaces.de

ADVANCED MATERIALS INTERFACES

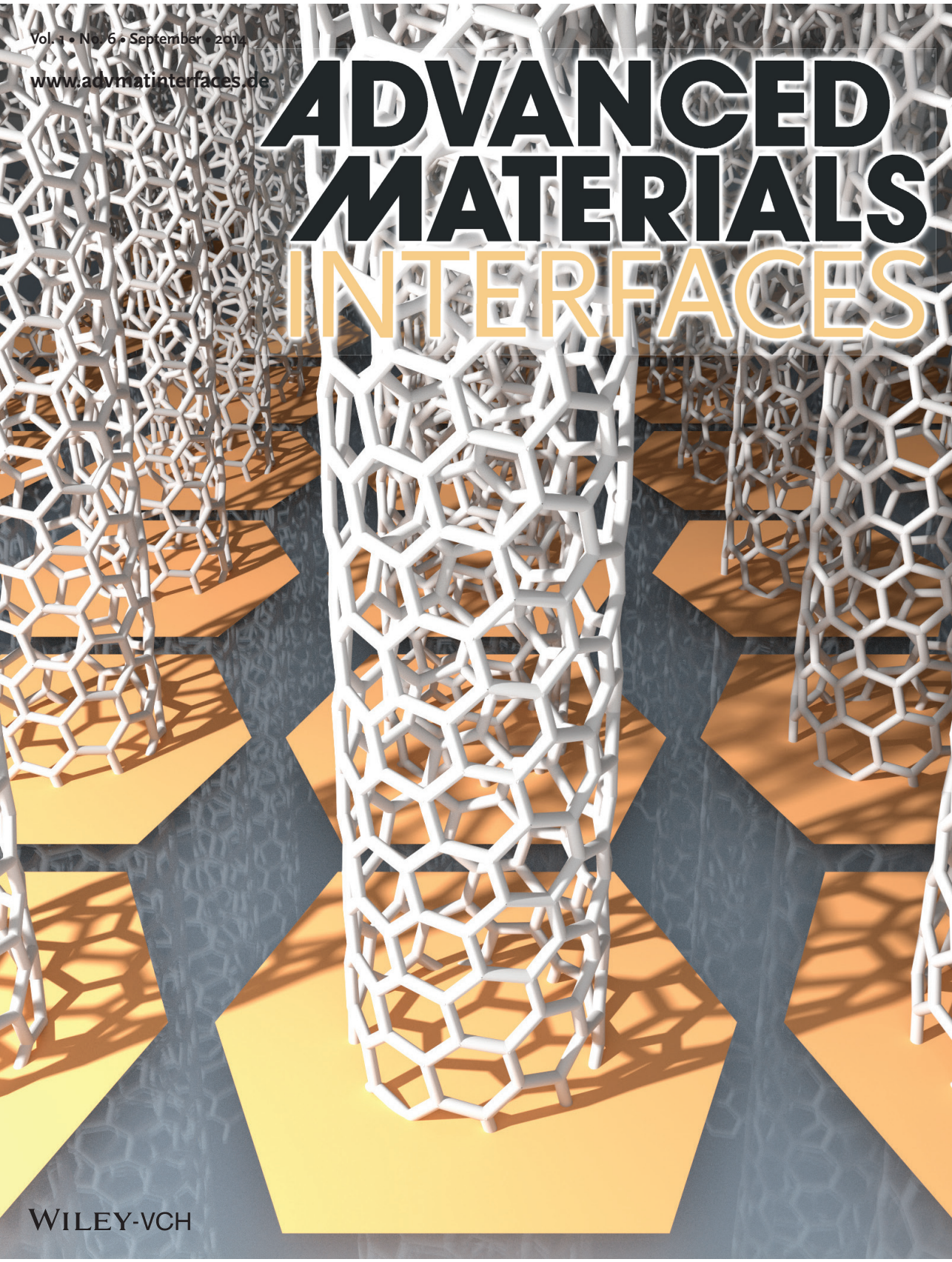

WILEY-VCH

ADVANCED MATERIALS INTERFACES
www.advmatinterfaces.de

In-Situ Growth of Ultrathin Films of NiFe-LDHs: Towards a Hierarchical Synthesis of Bamboo-Like Carbon Nanotubes

Gonzalo Abellán, Jose A. Carrasco, Eugenio Coronado, Juan P. Prieto-Ruiz, and Helena Prima-García*

The synthesis of ultrathin films (UTFs) of NiFe-LDHs has been achieved by means of an in situ hydrothermal approach, leading to a flat disposition of the LDH crystallites on the substrate, in clear contrast to the most common perpendicular orientation reported to date. Experimental factors like time of synthesis or the nature of the substrate, seem to play a crucial role during the growing process. The 2D morphology of the NiFe-LDH crystallites was kept after a calcination procedure, leading to a topotactic transformation into mixed-metal oxide platelets. Hereby, in order to study the catalytic behavior of our samples, a chemical vapor deposition process is explored upon the as-synthesized films. In presence of a carbon source (ethylene), these films catalyze a preferential low-temperature (550 °C) growth of bamboo-like carbon nanotubes, in stark contrast to the different mixture of carbon nanoforms obtained from the bulk samples. This work opens the door for the development of UTFs based on LDHs, which may be of utmost importance in a wide range of potential applications ranging from magnetic storage, catalysis or biomedical applications, to electrochemical batteries, anti-corrosion and superhydrophobic coatings.

1. Introduction

Layered Double Hydroxides (LDHs) are a class of synthetic 2D nanostructured anionic clays that can be represented by the general formula: $[M^{II}_{1-x}M^{III}_{x}(OH)_2](A^{n-})_{x/n}\cdot mH_2O$, in which the two metals (M^{II}, M^{III}), the interlayer anion (A^{n-}) and the value of the stoichiometric coeficient x can be varied over a wide range giving rise to a large variety of isostructural layered systems.[1,2] The intrinsic flexibility of these materials has allowed their application in different fields of great importance like catalysis, absorbents, sensors, separation or environmental remediation.[3] Concerning LDHs, one of the most rapidly growing areas of research is that related with their processability in films.[4] The correct disposition of LDH platelets or nanosheets into well-oriented films has allowed their advanced physical characterization allowing their application in different fields ranging from solar cells, gas sensors, electrochemical energy storage, magnetism or catalysis.[5]

The in situ direct crystallization of LDH platelets on different surfaces is scalable and probably the most straightforward synthetic methodology.[4] Unfortunately, there is a lack of control over the orientation of the crystals on the surfaces, resulting in dense films with intricate morphologies that deliver gross thickness of at least one micron.[6–9] The crystallites orientation in these films exhibits a disordered growth with the ab-planes perpendicular to the substrates. Some efforts have been made using PVA polymers for directing the growing of MgAl-LDHs and obtaining crystals with the ab-planes of the crystallites parallel to the films surface,[10] but examples regarding this topic are very scarce. Besides, the control of the metal composition to avoid the Al-containing LDHs is an additional but rewarding challenge.[11] In this sense, magnetic NiFe-LDHs are a special class of hydroxides that exhibit the highest catalytic metals concentration allowed by these layered entities.[12] Still, their application in direct nanocarbon formation remains unexplored.[13] Furthermore, their excellent magnetic properties as precursors of $NiO/NiFe_2O_4$ heterostructures beating the superparamagnetic limit,[14,15] and their electrocatalytic activity towards oxygen evolution reaction,[16] makes their processability into well-organized films an issue of great interest in catalysis, energy storage and spintronics. Unfortunately, when the traditional coprecipitation route is used to prepare the NiFe-LDH films, upon heating thick disordered nano composites were obtained.[17,18]

Herein, we have synthesized UTFs of NiFe-LDHs, taking advantage of our recently reported synthesis of highly crystalline and well-defined hexagonal-shaped NiFe-LDHs using trietanolamine (TEA) as chelating reagent.[11,19] Moreover, we have observed under thermal treatment the topochemical conversion into 2D platelet-like $NiO/NiFe_2O_4$ heterostructures that exhibits room temperature magnetism. Fourier transform infrared spectroscopy (FT-IR), X-ray diffraction (XRD), X-ray photoelectron spectroscopy (XPS), atomic force microscopy (AFM), ellipsometry, field emission electron microscopy (FE-SEM), high-resolution electron microscopy (HRTEM), conductivity and magnetic measurements have been used to elucidate the growing mechanism and exhaustively characterize the UTFs.

G. Abellán, J. A. Carrasco, Prof. E. Coronado, J. P. Prieto-Ruiz, Dr. H. Prima-García
Instituto de Ciencia Molecular (ICMol)
Universidad de Valencia
C/Catedrático José Beltrán, 2, 46980-, Paterna, Spain
E-mail: Eugenio.coronado@uv.es

DOI: 10.1002/admi.201400184

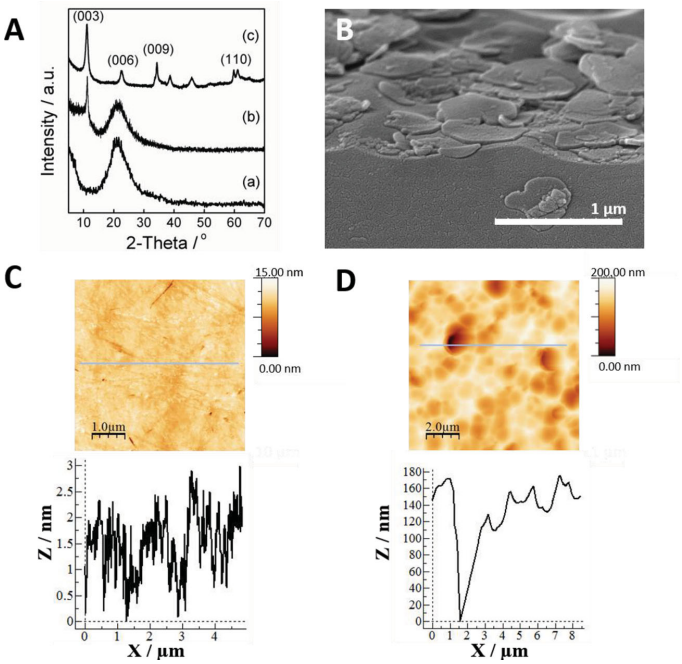

Figure 1. (A) XRD pattern of (a) the suprasil quartz substrate, (b) the **48h-LDH film** and (c) the NiFe-LDH powder scraped from the film. (B) Cross-sectional FE-SEM image of the sample. AFM images with height profile from both (C) suprasil quartz substrate and (D) **48h-LDH film**. The RMS values are 0.79 nm and 24 nm, respectively.

Furthermore, to illustrate the potential of these hierarchical organized UTFs in the catalytic formation of carbon nanoforms, and based on recent reports on LDHs by Wei, Li and co-workers,[9,13,20,21] we have explored the chemical vapor deposition (CVD) growth process, obtaining a preferential low-temperature (550 °C) formation of bamboo-like carbon nanotubes arrays on the surface of the films, in clear contrast with what is observed in bulk samples. The experiments have shown that the preferential orientation of the crystallites plays a crucial role on the catalytic growth of the carbon nanoforms. These vertically aligned bamboo-like carbon nanotubes are highly compatible with microfabrication, facilitating their incorporation as functional components on a large variety of devices with applications as electron field emitters, energy storage, composite materials, biosensors, electrochemical probes, etc.[22]

2. Results and Discussion

The possibility of processing highly crystalline hexagonal NiFe-LDHs can be very appealing to add new records to the long list of applications that these kind of materials have. The easiest way one can imagine would be to synthesize directly the desired film on the surface, permitting the complete coverage of the sample in a uniform way. On this basis, we developed a one step, reproducible and quite simple methodology by which the LDH films are fabricated by a modified urea hydrolysis method using TEA as additional chelating reagent. This method was previously described for the synthesis of bulk NiFe-LDH samples.[19] The cleaned suprasil quartz substrate was put into a Teflon-lined autoclave containing $Ni(NO_3)_2 \cdot 6H_2O$, $Fe(NO_3)_3 \cdot 9H_2O$, urea and TEA. The resulting films were removed from the autoclave after hydrothermal reaction at 150 °C for 48 h (denoted as **48h-LDH film**).

We characterized the **48h-LDH film** (**Figure 1**) by XRD. Interestingly, it only shows a basal (*003*) reflection of an LDH peak appearing as a broad line at low angles as reported for other thin films.[10] Note that no reflections were observed in the XRD pattern of the previous reported films. That is an indication of the better quality of our film. The absence of non-basal reflections (h, $k \neq 0$) at high angles is a sign of the partially *c*-oriented growth of LDH crystallites on the surface and the thinness of the film.[10]

FE-SEM studies of the **48h-LDH film** confirmed that the LDH platelets show a preferred *c*-oriented growth on the surface. Atomic force microscopy (AFM) was also used to elucidate the roughness and the morphology of the surface of the film (Figure 1). The topography image is consistent with the FE-SEM studies, confirming the in plane growth of the film. AFM measurements showed a root-mean-squared (RMS) roughness of 24 nm indicative of a relatively smooth surface. Moreover, the analysis of the height profiles revealed an average thickness of ca. 170 nm, whilst ellipsometry yielded a thickness value of ca. 138 nm (vide infra). For the sake of comparison, Zhao et al. reported the preparation of CoFe-LDH films with ca. 6 µm in thickness by solvent evaporation.[23] F. Li and co-workers[17] described a coprecipitation route yielding NiFe-LDH films of 0.8 µm in thickness, whereas micrometric (ca. 1–2 µm) NiFe-LDH films were prepared by direct casting by Zhang et al.[18] Therefore, to the best of our knowledge, the hydrothermal approach herein reported depicts the lowest thickness found in the literature for an in situ grown LDH film (see SI 1 for further details).

Furthermore, the successful formation of NiFe-LDH on the surface of the quartz substrate was demonstrated by XPS. **Figure 2** shows the Ni 2p and Fe 2p high resolution XPS spectra of the NiFe-LDH powder scraped from the film, revealing the presence of Ni(II) and Fe(III). Ni 2p spectra displayed two dominant peaks between 856 and 880 eV which can be assigned to the spin-orbit splitting of the $Ni(2p_{3/2})$ and $Ni(2p_{1/2})$, with a splitting energy of 17.2 eV. Each peak was accompanied by a less intense satellite peak at ca. 6 eV higher BEs, in agreement with that expected for Ni^{2+} ions.[24] As for the Fe 2p XPS spectra, two dominant peaks centered at BEs of approximately 712 and 725 eV were observed as expected for these materials.[16]

In order to clarify the growing mechanism of these films, we studied first the role of the synthesis time in the final disposition of the LDH platelets throughout the suprasil quartz

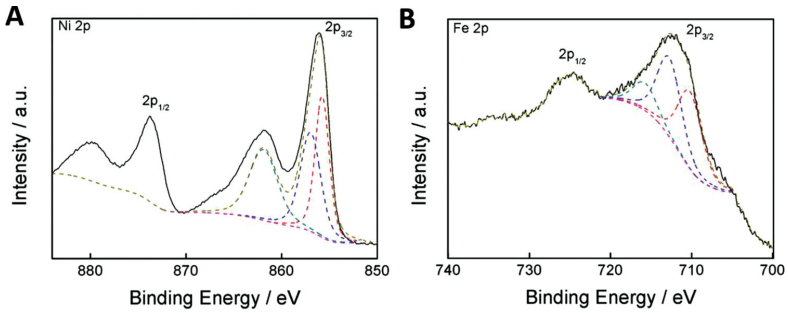

Figure 2. XPS analysis. High-resolution XPS spectra of (A) Ni 2p and (B) Fe 2p for the NiFe-LDH powder scraped from the film.

surface. Three different samples varying the reaction time from 24 h to 72 h (namely **24h-LDH film**, **48h-LDH film** and **72h-LDH film**) were synthesized. A detailed observation of FE-SEM images of the different films revealed that the growing time exerts a strong influence on the morphology, orientation and crystallites distribution (**Figure 3**).

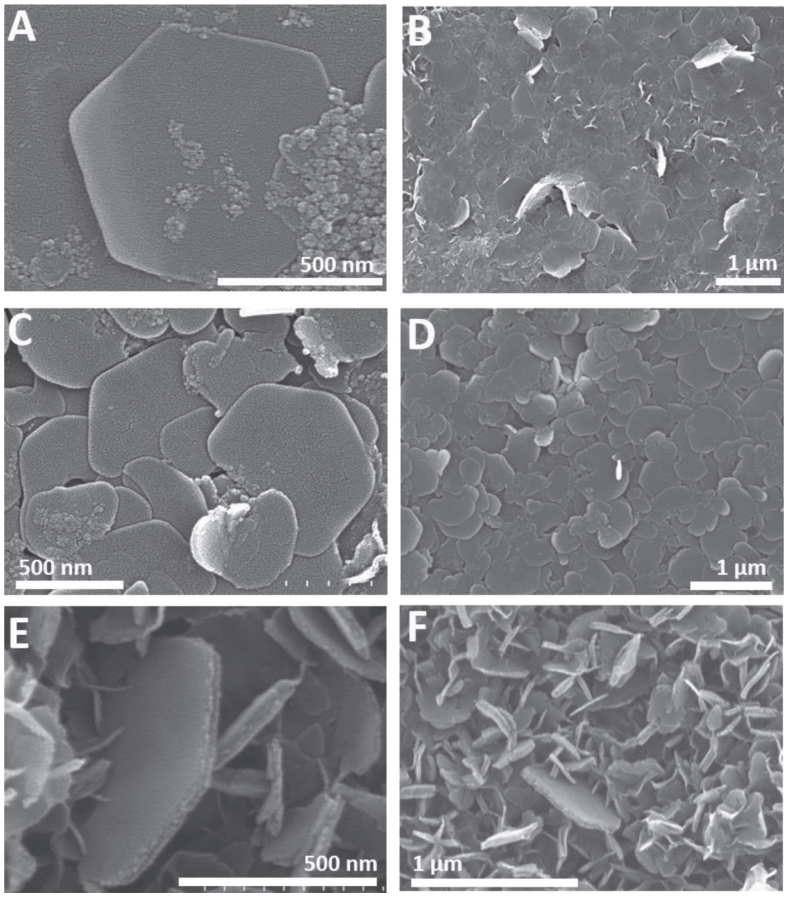

Figure 3. FE-SEM images of the films synthesized with different reaction times: (A and B) 24 h, (C and D) 48 h, and (E and F) 72 h.

All the samples showed the growth of hexagonal LDH crystallites of about 800 nm in size and ca. 15-20 nm in thickness on the whole surface of the quartz substrate. For the first two experiments, 24 h and 48 h, the LDH platelets showed a preferred orientation with their ab-planes parallel to the substrate, whilst for longer reaction times (72 h), the disposition of the ab-planes was amended into a perpendicular one. This change can be rationalized in terms of the "evolution selection" mechanism firstly described by Van der Drift,[25] in good agreement with previous reports on LDHs.[26] It is worth to mention that, to the best of our knowledge, there are no works reporting the obtaining of a parallel disposition of LDH crystals on unmodified surfaces. In contrast, the dense perpendicular disposition is always reported even at the early growing stages.

Hereby we can suggest that the observed hexagonal morphology begins to take form on the basis of a circle-like growth motion mechanism[27] as depicted in **Figure 4** (where the LDH crystal grows in a circular manner until the hexagonal form is reached and the depletion of the seed occurs, i.e. at 48 hours). These early growing crystals evolve by increasing their diameter as long as we increase the synthesis time, giving rise to the typical perpendicular dense-stacking growth.[10] This statement is supported by the fact that for **24h-LDH film** there are some platelets with imperfect morphologies and the presence of several FeO_x seeds (Figure 4). Further insights on the interface between FeO_x seeds and growing LDH layers can be obtained via HRTEM experiments. In fact, detailed images of the powder scrapped from the **24h-LDH film** revealed the presence of higher contrast small FeO_x nanoparticles of ca. 5 nm in intimate contact with the surface of LDH sheets. Moreover, a different set of lattice fringes corresponding to iron oxide nanoparticles can be measured.[16,28] Electron diffraction also shows the presence of several diffraction peaks corresponding to LDH and FeO_x phases. (**Figure 5**). For **48h-LDH film** the crystals have finally grown and showed the hexagonal morphology.

EDAX analysis of the powder scraped from the films show a Ni:Fe ratio of ca. 3:1, in perfect agreement with that expected from the synthetic gel (we were unable to carry out an accurate EDAX measurement directly from the film surface because of the low intensity signals of Ni and Fe, masked by the presence of Si).

Furthermore, the influence of the chelating reagent (TEA) has been also studied for the 48 h film. In this case, the powder obtained during the film synthesis (without TEA) was attracted by a magnet at room temperature, whilst pure NiFe-LDH only exhibits magnetism at low temperature, as we recently reported.[19,29] This phenomenon is ascribed to the presence of extrinsic impurities, similar to those reported by Faivre and coworkers on the nucleation and growth of amorphous magnetite nanoparticles from solution.[28]

The influence of the substrate was studied in order to check if the surface roughness plays any role in the growing mechanism. In line with this, we measured the RMS value of the high quality suprasil quartz substrate employed in this work, obtaining very small values of ca. 0.79 nm. Interestingly, by using a typical quartz substrate (RMS of ca. 1.25 nm) for the synthesis of a new film (keeping the same experimental conditions), we observed the characteristic perpendicular disposition of the LDH crystallites with their ab-planes perpendicular to the surface. Selected

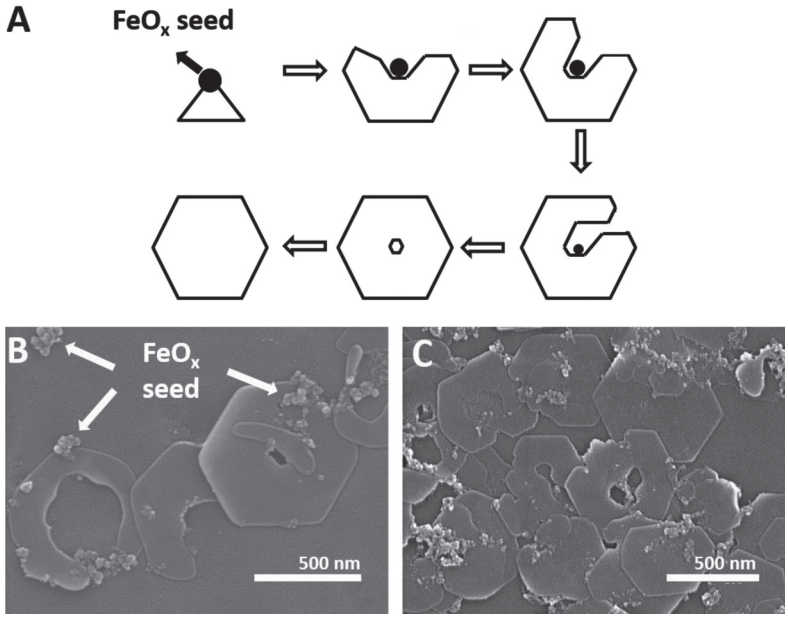

Figure 4. (A) Formation route of an LDH crystal on the basis of the circle-like growth motion mechanism, adapted from Okamoto et al.[27] (B and C) FE-SEM images of the 24 h film sample, showing the imperfect morphology and the FeO_x nanoparticles according with the proposed growing mechanism.

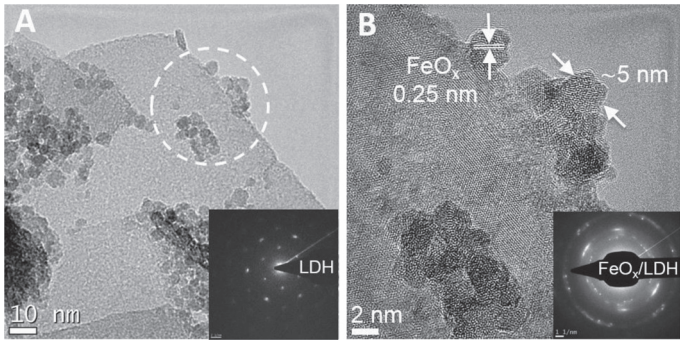

Figure 5. (A) HRTEM image of the powder scraped from the **24h-LDH film** showing the presence of several FeO_x nanoparticles on the surface of a growing LDH. (B) A higher magnification image of the selected area in (A). The inset in (A) shows the selected area electron diffraction (SAED) pattern of the LDH layer in absence of FeO_x. The inset in (B) corresponds to the SAED pattern of the selected area in (A) showing the polycrystalline structure of the FeO_x nanoparticles in addition to the LDH contribution.

images of this film highlight the strong influence of the surface roughness in the growing of LDHs (**Figure 6**).

In order to determine the influence of the calcination procedure on the morphology of the pristine film, we selected the **48h-LDH film** sample and submitted it to a thermal treatment at 550 °C (**48h-LDH film C**). Electron microscopy confirmed that the hexagonal-shaped 2D morphology of the flakes was kept after the calcination procedure. AFM measurements corroborated this assumption showing 2D crystals with an overall smaller thickness due to the sinterization process. This can be correlated with a lower RMS value of ca. 20 nm (**Figure 7**).

We performed the optical characterization and evaluated the thickness of the films by ellipsometry (see SI 2.1). In this technique the interference effects observed in the polarized light are used to determine the overall thickness and refraction index of materials prepared as thin films.[30] The refraction index of the LDH films has been modelled by using the uniaxial anisotropic Cauchy model and 5 harmonic oscillators. The thickness of the film was comprised in the 138–146 nm range, in good accordance with the values obtained by AFM. For further details on the ellipsometry characterization, see SI 2.1.

To further corroborate the retention of the intrinsic physical properties of the NiFe-LDHs films, we measured the magnetic properties before and after the calcination of the 72 h film (**Figure 8**). For clarity, it is worthwhile introducing some aspects related with the general magnetism in LDHs. Their magnetic behaviour is controlled by two main contributions: (i) the intralayer magnetic superexchange between metallic centers mediated by –OH bridges throughout the cationic sheets, and (ii) the less intense dipolar interactions operating through the space between the magnetic layers. As previously reported for several magnetic LDHs, NiFe-LDHs are expected to behave as ferrimagnets due to the coexistence of ferromagnetic Ni-OH-Ni superexchange interactions and antiferromagnetic Ni-OH-Fe or Fe-OH-Fe interactions mediated by the –OH bridges.[19,29,31]

In our experiments, magnetization was expressed in electromagnetic units (emu) since the exact mass cannot be measured precisely due to the low thickness of the film.[23] For the pristine NiFe-LDH film, a low-temperature spontaneous magnetization below 50 K has been observed in excellent accordance with other magnetic LDHs.[19,29,31] Moreover, field-dependent magnetization at 2 K showed the typical magnetic behaviour of a NiFe-LDH with a coercive field of 3000 G, a value which was higher than that observed for the bulk sample.[19] After the topochemical transformation of the LDH to NiO-$NiFe_2O_4$ mixed oxides at 550 °C, we observed the presence of room temperature magnetic properties.[14] In fact, a hysteresis cycle at 400 K can be observed, confirming the transformation and illustrating the great potential of these 2D films in magnetism. The coercive field at 2K turned out to be ca. 300 G, in good accordance with the values reported for bulk NiO-$NiFe_2O_4$ nanocomposites.[14] In addition, we have measured the FC-ZFC hysteresis at 2 K after cooling down from 400 K, in order to observe the exchange bias phenomenon. Hence, the hysteresis loop shifts negatively upon the field axis under an applied field (FC) whilst it keeps central symmetry in the ZFC process, implying a change of the coercivity when the sample is cooled under an applied field.[23] The value of the exchange bias field (H_E) calculated as $H_E = -(H_1 + H_2)/2$, where H_1 and H_2 are the left and the right coercive fields, is about 99.8 G, in agreement with previous results.[14,15] This behaviour is due to the interfacial exchange coupling between the ferrimagnetic $NiFe_2O_4$ nanoparticles and the antiferromagnetic NiO matrix, and is a signature of the successful transformation of the precursor as previously reported by Zhao et al.[14]

Moreover, the electrical conductivity of the LDH films was measured before and after the calcination process at 550 °C. The pristine film is essentially insulating as expected for hydroxides, with a conductivity value of $6.3 \cdot 10^{-12}$ $S \cdot cm^{-1}$. After the thermal treatment the conductivity increased up to $1.2 \cdot 10^{-10}$ $S \cdot cm^{-1}$, which is in agreement with

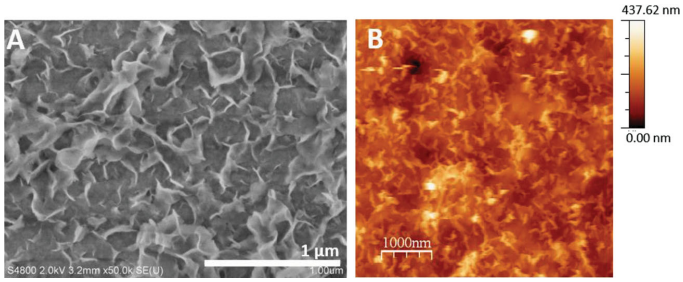

Figure 6. FE-SEM (A) and (B) AFM image of an LDH film grown on common quartz. The RMS value is 48 nm, indicative of a perpendicular disposition of the LDH crystals.

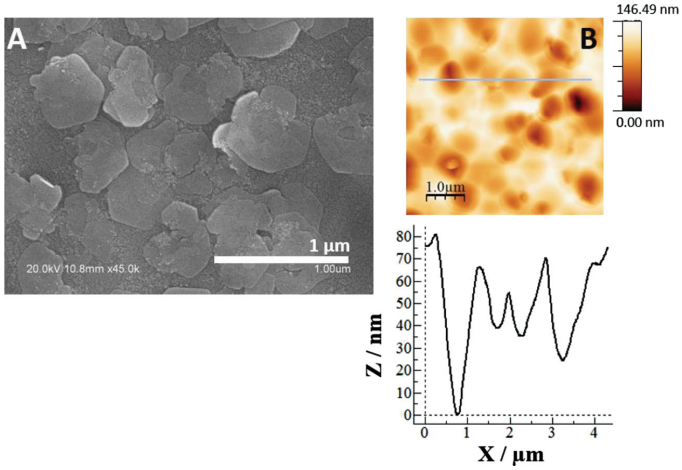

Figure 7. FE-SEM (A) and (B) AFM image and its corresponding height profile for the calcined film. The RMS value is ca. 20 nm, indicative of crystals with smooth edges.

the topotactic transformation of the hydroxide into spinel, as recently reported by Wu et al. for CoNi-LDHs.[32] See SI 2.2 for further details on the electrical conductivity.

In order to demonstrate the potential applications of these hierarchical films, chemical vapor deposition (CVD) and catalytic chemical vapor deposition (CCVD) experiments were performed. These procedures have demonstrated to be very useful in the synthesis of different carbon nanoforms such as carbon nanotubes in the gas phase.[33] After the decomposition at high temperature of a carbon source (ethylene in this work), its structural units rearrange into carbonaceous species. These reactions can be catalyzed, among others, by LDHs on film surfaces.[9] We selected the **48h-LDH film** sample as catalyst, fixing the CVD temperature at 550 °C (which is lower than the temperature used in other related works[9]. Moreover, we have also studied the influence of the H_2 on the catalytic growth of carbon nanoforms. These samples were labelled as **CVD-48h-LDH film** and **CCVD-48h-LDH film**. The optimum CVD conditions were previously optimized in bulk samples. The study of CVD control experiments by XRPD revealed a mixture of $NiFe_2O_4$, NiO and $FeNi_3$ phases. A specific thermal scan rate (1 and 5 ºC·min^{-1}) study showed that $NiFe_2O_4$/NiO and $FeNi_3$ phases exhibited different crystallization dynamics. Furthermore, a control experiment carried out in absence of both H_2 and ethylene allowed us to conclude that the $FeNi_3$ alloy is the catalytic specie responsible of the carbon nanoform growing. For further information about these experiments, see SI 3.

Figure 9 shows a collection of selected FE-SEM images exhibiting the preferential synthesis of bamboo-like[33] carbon nanotubes (BLCNTs), i.e., a special class of multi-wall carbon nanotubes (MWCNT), with multishell and periodic bamboo-like structure. In the growing of these BLCNTs, there is a continual growth and renucleation mechanism[34] which gives rise to the stacking of the graphitic shells. As can be clearly seen in Figure 9, the presence of H_2 does not imply any major difference in the final results. This is probably due to the high catalytic behaviour of the NiFe-LDH platelets, as previously demonstrated for NiFe-sebacate intercalated hybrids acting as catalytic nanoreactors.[12]

Hereby, the ordered disposition of the LDH platelets on the film surface leads to a preferential synthesis of BLCNTs. This is in sharp contrast to what is obtained when CVD on randomly oriented bulk samples is performed, which leads to a mixture of carbon nanoforms formed by few-layers graphene, carbon fibers and multi-wall carbon nanotubes (**Figure 10**).[9] See SI 3.2 for further characterization of these samples.

The as-synthesized BLCNTs exhibit similar size and morphology in both CVD and CCVD films, with an average length of ca. 250 nm and a thickness of about 40 nm (**Figure 11**). Moreover, as highlighted in Figure 11A, an interlayer spacing of 0.34 nm

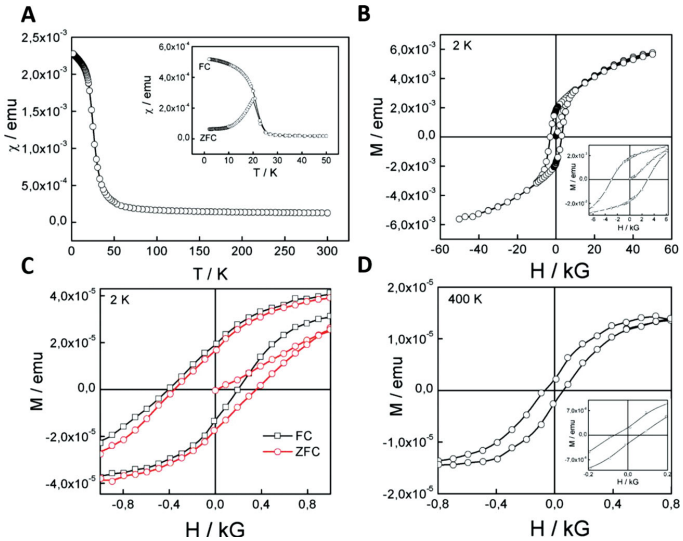

Figure 8. Magnetic properties of the NiFe-LDH films. (A) χ vs T plot for the pristine film. The inset represents the FC-ZFC magnetization. (B) Hysteresis cycle at 2 K for the pristine film. The inset represents the low field region. (C) Hysteresis cycle for the calcined film at 2 K highlighting the exchange bias phenomenon. (D) Hysteresis cycle at 400 K. The insets show the low field region.

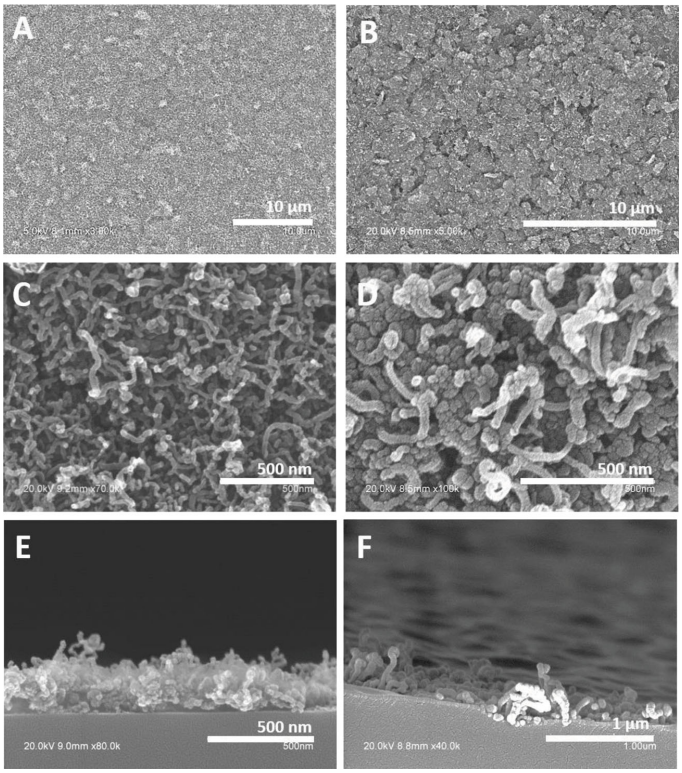

Figure 9. FE-SEM images for the (A), (C), (E) **CVD-48h-LDH film** and the (B), (D), (F) **CCVD-48h-LDH film**.

has been measured, in agreement with the expected value for a (*002*) plane of graphite.

Raman spectroscopy is a useful technique for determining the nature of carbon nanoforms. In this sense, the characteristic D and G bands are related with the disorder (carbon atom vibrations with the dangling bonds) and order (vibration of sp^2-bonded carbon atoms in a 2D hexagonal framework) of the system, respectively. The Raman spectrum of the **CVD-48h-LDH film** shows a D band centered at ca. 1350 cm^{-1}, a G band at ca. 1590 cm^{-1}, and a 2D band –overtone of the disorder (D) band– at ca. 2707 cm^{-1} (Figure 11B). The I_D/I_G ratio is related with the graphitic ordering in carbon materials. Therefore, high I_D/I_G ratio involves a low degree of graphitization (order) in the carbonaceous system, and vice versa.[35] We have observed an I_D/I_G ratio of ca. 1.07 slightly better than other related examples.[36] It is worth noting that in general, these BLCNTs show stronger D bands as well as larger I_D/I_G than other CNTs due to the presence of defects, curves and dislocations of the graphitic sheets.[37]

We have further evaluated the hydrophilic/hydrophobic behaviour of the as-prepared films by means of contact angle (CA) studies (**Figure 12**). This type of measurement is a direct and macroscopic evidence of the hierarchy of our samples. According to the Cassie and Baxter theory,[38] a rougher surface leads to a high hydrophobicity (CA ≥ 90°) of the system, whereas a soft film will be hydrophilic (low CA values). Furthermore, for CA greater than 150° we are dealing with super-hydrophobicity.[39] Therefore, a film with their ab-planes parallel to the surface, like those synthesized in the present work, will show a hydrophilic behavior.

Herein, we have observed low CA values for both the **48h-LDH film** (ca. 18°) and the **48h-LDH film C** (ca. 28°), i.e., the calcined one, indicative of a highly hydrophilic behavior. In contrast, the growth of the LDHs with their ab-planes perpendicular to the surface observed for the **72h-LDH film**, revealed an increase in the CA up to ca. 96° and so depicting hydrophobicity. This observation is a clear evidence of the increase in the roughness of the system.

In addition, regarding the **CVD-48h-LDH film**, we observed a CA of ca. 95° (Figure 12D). This value is slightly higher than those reported for unmodified films consisting on CNT forests (84–86°), in which the water droplets quickly penetrates into the samples due to the high surface energy of the nanotubes.[40]

It is important to note that our films have not been modified with any extrinsic material like ZnO or Na-laureate as reported in other works,[7,41] with which can easily reach values of CA in CNT films close to 160º, depicting super-hydrophobic properties. On the other hand, for LDH films grown on other substrates than suprasil quartz (like alumina oxide or AEBA glass) we can find values of CA of about 120°,[8,42] related with a dense and complete perpendicular disposition of the LDH platelets.

3. Conclusions

In the present work, we have successfully synthesized homogeneous ultrathin films of NiFe-LDHs (metal ratio of $x = 0.25$ and a thickness of ca. 138–170 nm) on suprasil quartz substrates by means of an in situ hydrothermal method. The study of the influence of reaction times in these systems has allowed us to clarify their growing mechanism from a parallel orientation of the ab-planes of the platelets (circle-like growth motion mechanism) to a perpendicular one (dense stacking growth). This sequence is produced by means of the "evolution selection" mechanism. A key factor in the final arrangement of the crystallites is the quality of the substrate. In fact, the same reaction time for different substrates may lead to a different final disposition depending on the roughness of the surface. Moreover, our *as*-synthesized films retain their 2D morphology and parallel disposition after a calcination procedure. In overall, that opens the possibility of processing this sort of material in a

ADVANCED MATERIALS INTERFACES
www.advmatinterfaces.de

Materials Views
www.MaterialsViews.com

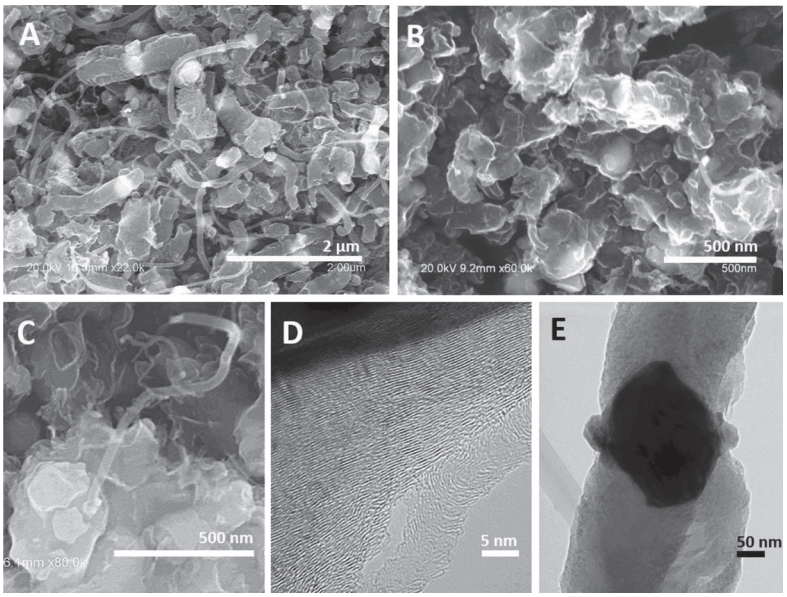

Figure 10. Electron microscopy studies for bulk samples. FE-SEM image of (A) the sample, (B) a selected area showing the formation of some few-layers graphene, and a (C) carbon nanotube. HRTEM images highlighting the morphology of (D, E) a graphitic carbon fiber, and the growth on both sides of the catalytic particle.

one-pot synthesis. Furthermore, to check the catalytic behaviour of these films, both CVD and CCVD procedures at 550 °C have been carried out over the samples, depicting a hierarchical growth of bamboo-like carbon nanotubes with a thickness of ca. 250 nm. In contrast, the study of bulk samples has led to different results, displaying a wide variety of carbon nanoforms such as few-layers graphene, carbon fibers and MWCNTs. Comparing film and bulk results, it is clearly seen that the preferential orientation of the LDH platelets on the film surface leads to an exclusive formation of CNTs, and so the hierarchical structure imposes a specific growth. These systems exhibit a tremendous potential in different fields such as energy storage, microelectronics or sensing. Further studies on the in situ synthesis and characterization of different ultrathin films of LDHs such as CoFe-, NiAl-, CoAl-LDH or ternary-LDHs will be carried out. In this sense, preliminary results indicate that these films behave as excellent electrocatalysts for water oxidation.

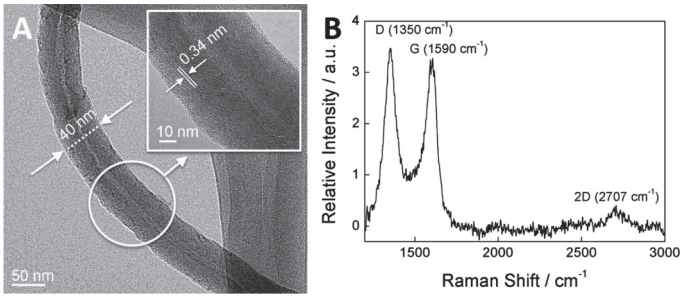

Figure 11. (A) HRTEM image highlighting the thickness of a BLCNT and (B) Raman spectrum of the **CVD-48h-LDH film**.

4. Experimental Section

Chemicals: All chemical reagents $Ni(NO_3)_2.6H_2O$ (Aldrich); $Fe(NO_3)_3.9H_2O$ (Sigma-Aldrich); triethanolamine (TEA), $C_6H_{15}NO_3$ (Sigma-Aldrich); urea, $CO(NH_2)_2$ (Fluka) and ethanol absolute (Panreac, 99.9%) were used as received without further purification. Ultrapure water was obtained from a Millipore Milli-Q equipment. Suprasil quartz slides of 9 × 30 mm and a thickness of 0.3 mm were used as substrates for the film growth. N_2, H_2/Ar (10%) and ethylene (C_2H_4) were purchased from Linde Material Handling.

Synthesis of NiFe-CO_3 LDHs: NiFe-CO_3 LDH were synthesized following a modified homogeneous precipitation method by using urea and TEA as ammonium releasing reagent (ARR) and chelating agent, respectively.[11] In a typical synthesis, the nitrate salts of the metals were dissolved in 50 mL of deionized purged water together with TEA, in order to reach a total metal cation concentration of 20 mM in the final solution, with a Ni:Fe ratio of 3:1 (x = 0.25, being $x = [Fe^{3+}]/([Fe^{3+}] + [Ni^{2+}])$, and a TEA concentration equimolar with the iron concentration (5 mM). Next, 50 mL of an aqueous solution of urea (35 mM) were added. The excess of urea was fixed to be 1.75 times the total metal concentration. The resulting dark brown mixture was placed in a 125 cm^3 stainless steel Teflon-lined autoclave

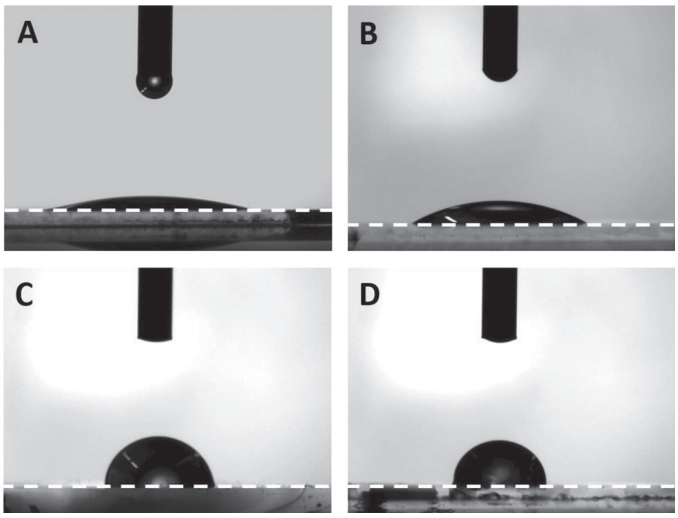

Figure 12. Contact angle measurements for (A) **48h-LDH film**, (B) **48h-LDH film C**, (C) **72h-LDH film** and (D) **CVD-48h-LDH film**.

and heated up to 150 °C in a previously heated oven. After 48 h, the autoclave was left to cool down at room temperature and the final yellowish fine powder was filtered and dried in a vacuum. The pH value of the remaining solution was found to be around 8.

Synthesis of NiFe-CO_3 LDH Films: The syntheses were carried out by using an in situ growth method. This direct growth was developed in suprasil quartz substrates with a very low RMS roughness. After cleaning the surface (first with soap, and then immersed in an ultrasonic bath with EtOH for 10 min, and finally with deionized Milli-Q water for another 10 min), these substrates were immersed perpendicularly in the Teflon-lined autoclave containing the reaction mixture, and then sealed and heated at 150 °C in a conventional oven. After cooled to room temperature (once the reaction is finished), the substrate is taken out, cleaned with Milli-Q water and dried at room temperature in a desiccator. We also studied the influence of time of synthesis and the presence/absence of the chelating reagent in order to elucidate the parameters underlying the growing of the LDHs on the substrates. These variations were pointed and discussed later.

Calcination Procedure: In a typical calcination, the sample was heated up to 550 °C under a 1 °C·min^{-1} scan rate with a synthetic air flow atmosphere of 100 mL·min^{-1} during 12 h and then cooled to room temperature at the same scan rate.

Chemical Vapor Deposition (CVD) Procedure: In a typical CVD process, either the NiFe-LDH or the suprasil quartz substrate, were placed in a quartz tubular reactor inserted into a furnace at atmospheric pressure. After that, the furnace was heated under flowing N_2 (100 mL·min^{-1}) up to 550 °C in a 1 °C·min^{-1} scan rate. When this temperature was reached, a reduction treatment with H_2 (50 mL·min^{-1}, mixture of H_2 10 % in Ar) was performed into the reactor 5 min before switching the gas for the carbon source, ethylene (C_2H_4, 100 mL·min^{-1}), during 5 more min at the desirable temperature. Then, the furnace was cooled to room temperature under N_2 protection. Finally, samples were collected in order to study them. In catalytic chemical vapor deposition processes (CCVD), no H_2 was supplied. Any variation of these settings were pointed out when it was necessary.

Physical Characterization: Sample morphologies were studied by means of field emission scanning electron microscopy (FE-SEM) performed on a Hitachi S-4800 microscope operating at an accelerating voltage of 20 kV over metallized samples with a mixture of gold and palladium for 30 s. FE-SEM measurements of the films were done at an accelerating voltage of 20 kV over metallized samples for 120 s due to the lower conductivity of the suprasil quartz substrate. X-ray powder diffraction (XRPD) patterns were obtained using a PANalytical Empyrean X-ray powder diffractometer with hybrid monochromator using the copper radiation (Cu-Kα = 1.54178 Å) and equipped with a PIXcel detector XRPD for capillary and flat plate measurements. Samples were mounted on a flat sample plate. Profiles were collected in the 2.5° < 2θ < 70° range (2.5° < 2θ < 90° for some of the bulk samples) with a step size of 0.05°. X-ray photoelectron spectroscopy (XPS) measurements were performed in an ultra-high vacuum system ESCALAB210 (base pressure 1.0×10-10 mbar) from Thermo VG Scientific. Photoelectrons were excited by using the Mg-Kα line (1253.6 eV). All spectra were referred to the Fermi level. Atomic Force Microscopy (AFM) measurements were collected in a Multimode atomic force microscope from Veeco, using tapping mode in air at room temperature. Processing and analysis of the images were carried out using the Nanotec WSxM 6.0 software.[43] Film thickness was determined using an Ambios XP1 profilometer and a GES5E variable angle spectroscopic ellipsometer from Sopralab, with a wavelength range from 198 nm to 1200 nm, a continuously adjustable incident angle, and a focused spot size of approximately (0.350 × 0.450) mm. The Raman measurements (Jobin-Yvon LabRam HR 800 Raman Microscope) were carried out at room temperature with the 532 nm line of an Ar ion laser as an excitation source. High resolution transmission electron microscopy (HRTEM) studies were carried out on a Technai G2 F20 microscope operating at 200 kV. Samples were prepared by dipping a sonicated suspension of the sample in ethanol on a carbon-coated copper grid. Metallic atomic composition of bulk samples was determined by means of electron probe microanalysis (EPMA) performed in a Philips SEM-XL30 equipped with an EDAX microprobe. Carbon, nitrogen and hydrogen contents were determined by microanalytical procedures by using a LECO CHNS. Infrared spectra were recorded in a FT-IR Nicolet 5700 spectrometer in the 4000–400 cm^{-1} range using powdered samples diluted in KBr pellets. These pellets were prepared just before their use, in order to avoid possible contamination of the sample from an anionic exchange reaction. Contact angle (CA) measurements were carried out in a ramé-hart contact angle goniometer instrument with a NET GmbH 1394 Digital Camera, using the Drop image program (v 2.3.0) to calculate the average CA. Average CA was obtained with the measurements of a 3 μL of Milli-Q water droplet over the same sample at five different positions, each one being measured for 120 times in a 1 minute interval. The electrical conductivity measurements were carried out by using a standard two-probe contacts method with Pt wires in a physical property measurement system (PPMS-9) by Quantum Design. Magnetic measurements were obtained with a Quantum Desing superconducting quantum interference device (SQUID) MPMS-XL-5. The susceptibility data were corrected from the diamagnetic contributions of the atomic constituents of the samples, as deducted from Pascal's constant tables and the sample holder. The dc data were collected under an external applied field of 100 or 1000 G in the 2–300 K range. Magnetization studies were preformed between –5 and +5 T at a constant temperature of 2 or 300 K, depending on the sample.

Supporting Information

Supporting Information is available from the Wiley Online Library or from the author.

Acknowledgements

Financial support from the EU (Projects HINTS and ERC Advanced Grant SPINMOL), the Spanish MINECO (Projects Consolider-Ingenio in Molecular Nanoscience, MAT-2011-22785, and CTQ-2011-26507), and the Generalitat Valenciana (Prometeo Program and ISIC-Nano) is gratefully acknowledged. Support from VLC/CAMPUS and INNCIDE program through Vicerectorat d'Investigació i Política Científica of the University of Valencia is also acknowledge. J.A.C. acknowledges the support of the Vicerectorat d'Investigació i Política Científica of the University of Valencia for a predoctoral grant in the "Atracció de Talent" subprogram. The authors specially thank E. Navarro Raga and S. Agouram of the SCSIE (UV) for their kind assistance with electron microscopies. We also acknowledge E. Tormos and A. López for his help with the experimental work, and J. M. Martínez and G. Agustí for magnetic measurements.

Received: April 11, 2014
Revised: May 14, 2014
Published online: July 9, 2014

[1] X. Duan, *Layered double hydroxides*, Springer-Verlag GmbH, Berlin Heidelberg, **2006**.
[2] Q. Wang, D. O'Hare, *Chem. Rev.* **2012**, *112*, 4124.
[3] F. Bergaya, B. K. G. Theng, G. Lagaly, *Handbook of clay science*, Elsevier, Amsterdam; London, **2006**.
[4] X. Guo, F. Zhang, D. G. Evans, X. Duan, *Chem. Commun.* **2010**, *46*, 5197.
[5] F. Li, X. Duan, In *Layered Double Hydroxides*, X. Duan, D. G. Evans, Eds.; Springer-Verlag, Berlin/Heidelberg, Vol. *119*, pp. 193–223.
[6] H. Chen, F. Zhang, T. Chen, S. Xu, D. G. Evans, X. Duan, *Chem. Eng. Sci.* **2009**, *64*, 2617.
[7] H. Chen, F. Zhang, S. Fu, X. Duan, *Adv. Mater.* **2006**, *18*, 3089.
[8] Z.-L. Hsieh, M.-C. Lin, J.-Y. Uan, *J. Mater. Chem.* **2011**, *21*, 1880.
[9] M.-Q. Zhao, G.-L. Tian, Q. Zhang, J.-Q. Huang, J.-Q. Nie, F. Wei, *Nanoscale* **2012**, *4*, 2470.
[10] X. Guo, F. Zhang, S. Xu, D. G. Evans, X. Duan, *Chem. Commun.* **2009**, 6836.
[11] G. Abellán, E. Coronado, C. Martí-Gastaldo, E. Pinilla-Cienfuegos, A. Ribera, *J. Mater. Chem.* **2010**, *20*, 7451.
[12] G. Abellán, E. Coronado, C. Martí-Gastaldo, A. Ribera, J. F. Sánchez-Royo, *Chem. Sci.* **2012**, *3*, 1481.
[13] M.-Q. Zhao, Q. Zhang, J.-Q. Huang, F. Wei, *Adv. Funct. Mater.* **2012**, *22*, 675.
[14] X. Zhao, S. Xu, L. Wang, X. Duan, F. Zhang, *Nano Res.* **2010**, *3*, 200.
[15] U. Lüders, A. Barthélémy, M. Bibes, K. Bouzehouane, S. Fusil, E. Jacquet, J.-P. Contour, J.-F. Bobo, J. Fontcuberta, A. Fert, *Adv. Mater.* **2006**, *18*, 1733.
[16] M. Gong, Y. Li, H. Wang, Y. Liang, J. Z. Wu, J. Zhou, J. Wang, T. Regier, F. Wei, H. Dai, *J. Am. Chem. Soc.* **2013**, *135*, 8452.
[17] G. Fan, X. Xiang, J. Fan, F. Li, *J. Mater. Chem.* **2010**, *20*, 7378.
[18] Y. Zhang, F. Zhang, Y. Lu, T. Chen, L. Yang, *J. Phys. Chem. Solids* **2010**, *71*, 604.
[19] G. Abellán, E. Coronado, C. Martí-Gastaldo, J. Waerenborgh, A. Ribera, *Inorg. Chem.* **2013**, *52*, 10147.
[20] H. I. Hima, X. Xiang, L. Zhang, F. Li, *J. Mater. Chem.* **2008**, *18*, 1245.
[21] M.-Q. Zhao, Q. Zhang, G.-L. Tian, J.-Q. Huang, F. Wei, *ACS Nano* **2012**, *6*, 4520.
[22] K. L. Klein, A. V. Melechko, T. E. McKnight, S. T. Retterer, P. D. Rack, J. D. Fowlkes, D. C. Joy, M. L. Simpson, *J. Appl. Phys.* **2008**, *103*, 061301.
[23] X. Zhao, Y. Zhang, S. Xu, X. Lei, F. Zhang, *J. Phys. Chem. C* **2012**, *116*, 5288.
[24] H. W. Nesbitt, D. Legrand, G. M. Bancroft, *Phys. Chem. Miner.* **2000**, *27*, 357.
[25] A. Van der Drift, *Philips Res Rep* **1967**, *22*, 267.
[26] J. Liu, Y. Li, X. Huang, G. Li, Z. Li, *Adv. Funct. Mater.* **2008**, *18*, 1448.
[27] K. Okamoto, N. Iyi, T. Sasaki, *Appl. Clay Sci.* **2007**, *37*, 23.
[28] J. Baumgartner, A. Dey, P. H. H. Bomans, C. Le Coadou, P. Fratzl, N. A. J. M. Sommerdijk, D. Faivre, *Nat. Mater.* **2013**, *12*, 310.
[29] G. Abellán, J. A. Carrasco, E. Coronado, *Inorg. Chem.* **2013**, *52*, 7828.
[30] R. Todorov, A. Paneva, K. Petkov, *Thin Solid Films* **2010**, *518*, 3280.
[31] G. Abellán, J. A. Carrasco, E. Coronado, J. Romero, M. Varela, *J. Mater. Chem. C* **2014**, *2*, 3723.
[32] L. Hu, L. Wu, M. Liao, X. Hu, X. Fang, *Adv. Funct. Mater.* **2012**, *22*, 998.
[33] J. Wu, B. El Hamaoui, J. Li, L. Zhi, U. Kolb, K. Müllen, *Small* **2005**, *1*, 210.
[34] H. Cui, O. Zhou, B. R. Stoner, *J. Appl. Phys.* **2000**, *88*, 6072.
[35] R. Saito, G. Dresselhaus, M. S. Dresselhaus, In *Physical properties of carbon nanotubes*, Imperial College Press, London, **1998**; pp. 183–203.
[36] B. Xue, R. Liu, W.-Z. Huang, Y.-F. Zheng, Z.-D. Xu, *J. Mater. Sci.* **2009**, *44*, 4040.
[37] S. Shanmugam, A. Gedanken, *J. Phys. Chem. B* **2006**, *110*, 2037.
[38] A. B. D. Cassie, S. Baxter, *Trans. Faraday Soc.* **1944**, *40*, 546.
[39] L. Feng, S. Li, Y. Li, H. Li, L. Zhang, J. Zhai, Y. Song, B. Liu, L. Jiang, D. Zhu, *Adv. Mater.* **2002**, *14*, 1857.
[40] K. K. S. Lau, J. Bico, K. B. K. Teo, M. Chhowalla, G. A. J. Amaratunga, W. I. Milne, G. H. McKinley, K. K. Gleason, *Nano Lett.* **2003**, *3*, 1701.
[41] L. Huang, S. P. Lau, H. Y. Yang, E. S. P. Leong, S. F. Yu, S. Prawer, *J. Phys. Chem. B* **2005**, *109*, 7746.
[42] F. Yang, B. Y. Xie, J. Z. Sun, J. K. Jin, M. Wang, *Mater. Lett.* **2008**, *62*, 1302.
[43] I. Horcas, R. Fernández, J. M. Gómez-Rodríguez, J. Colchero, J. Gómez-Herrero, A. M. Baro, *Rev. Sci. Instrum.* **2007**, *78*, 013705.

ADVANCED MATERIALS INTERFACES

Supporting Information

for *Adv. Mater. Interfaces,* DOI: 10.1002/admi.201400184

In-Situ growth of Ultrathin Films of NiFe-LDHs: Towards a Hierarchical Synthesis of Bamboo-Like Carbon Nanotubes

Gonzalo Abellán, Jose A. Carrasco, Eugenio Coronado, Juan P. Prieto-Ruiz, and Helena Prima-García*

Supporting Information

In-situ **growth of Ultrathin Films of NiFe-LDHs: Towards a Hierarchical Synthesis of Bamboo-like Carbon Nanotubes**

Gonzalo Abellán, Jose A. Carrasco, Eugenio Coronado, Juan P. Prieto-Ruiz and Helena Prima-García*

Instituto de Ciencia Molecular (ICMol), Universidad de Valencia. C/ Catedrático José Beltrán, 2, 46890 Paterna, Spain. Fax: +34 96 354 3273. Telf: +34 96 354 4415. E-mail: eugenio.coronado@uv.es.

Contents

SI 1. Structural and synthetic characteristics of some *in situ* growth LDH films

Material	Synthetic Methodology	Particle dimensions (lateral size/thickness)	Film thickness	Reference
NiFe-LDH	Hydrothermal TEA-assisted	1 µm / 20 nm	138 – 170 nm	This work
MgAl-LDH	Hydrothermal PVA-modified substrates	1 – 2 µm / 100 nm	–	[1]
MgAl-LDH	Hydrothermal	1 – 2 µm / 100 nm	0.8 µm	[1]
NiFe-LDH	Coprecipitation	–	0.8 µm	[2]
FeMoMgAl-LDH	Coprecipitation	1 µm / 20 nm	–	[3]
NiAl-LDH	Hydrothermal	– / 60 – 80 nm	2.4 µm	[4]
CoFe-LDH	Hydrothermal	6 µm / 60 nm	several microns	[5]

SI 2. Further characterization on film samples

SI 2.1. Ellipsometry study

(A) Refractive index and (B) extinction coefficient for both calcined and non-calcined films as measured by ellipsometry.

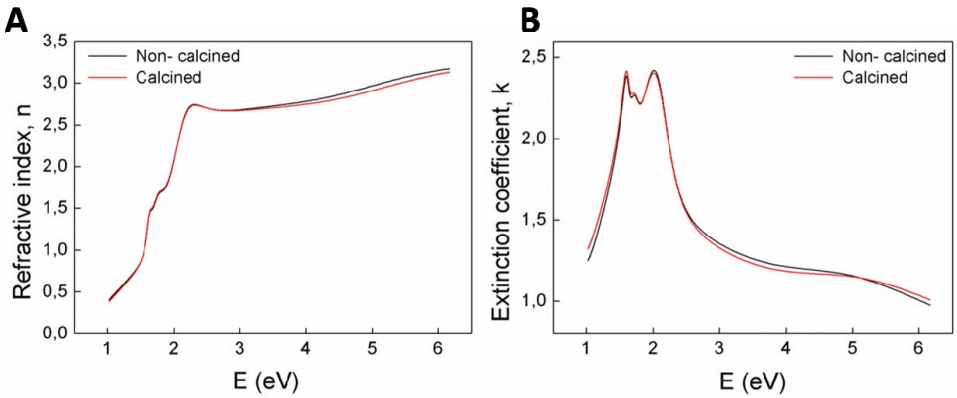

Both films (pristine and calcined) showed absorption in all the visible spectra from 1.5 to 3.0 eV, as well as in some of the infrared, being the UV region the one which depicts the lowest extinction coefficient yet without reaching the total transparency (k = 0).

SI 2.2. Conductivity measurements

I-V curves (A) before and (B) after the calcination procedure. Gold pads electrodes were evaporated on top of the film with a distance between them of 50 µm.

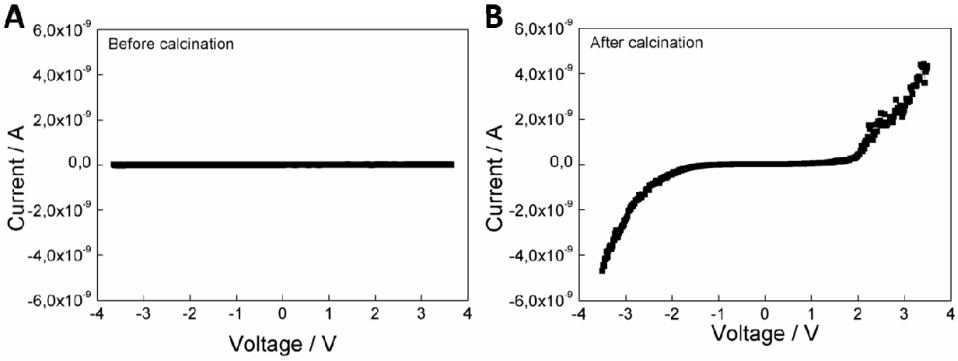

SI 3. Control experiments

SI 3.1. CVD control experiments without C_2H_4

Several control experiments of the CVD process at different temperatures and scan rates were carried out in order to optimize the experimental settings for the films.

B1: Blank 1 (with H_2; without C_2H_4); CVD maximum T of 900 ^oC; 5 ^oC min^{-1} scan rate.

B2: Blank 2 (with H_2; without C_2H_4); CVD maximum T of 900 ^oC; 1 ^oC min^{-1} scan rate.

B3: Blank 3 (with H_2; without C_2H_4); CVD maximum T of 550 ^oC; 5 ^oC min^{-1} scan rate.

B4: Blank 4 (with H_2; without C_2H_4); CVD maximum T of 550 ^oC; 1 ^oC min^{-1} scan rate.

FE-SEM images showed a well-defined bidimensional structure for the blanks calcined at low temperature, **B3** and **B4**. Some of the particle edges seemed to be broken, probably due to structural damages after the H_2 reduction process. On the other hand, the 2D structure disappeared with increasing the temperature to 900 ^oC (**B1** and **B2**).

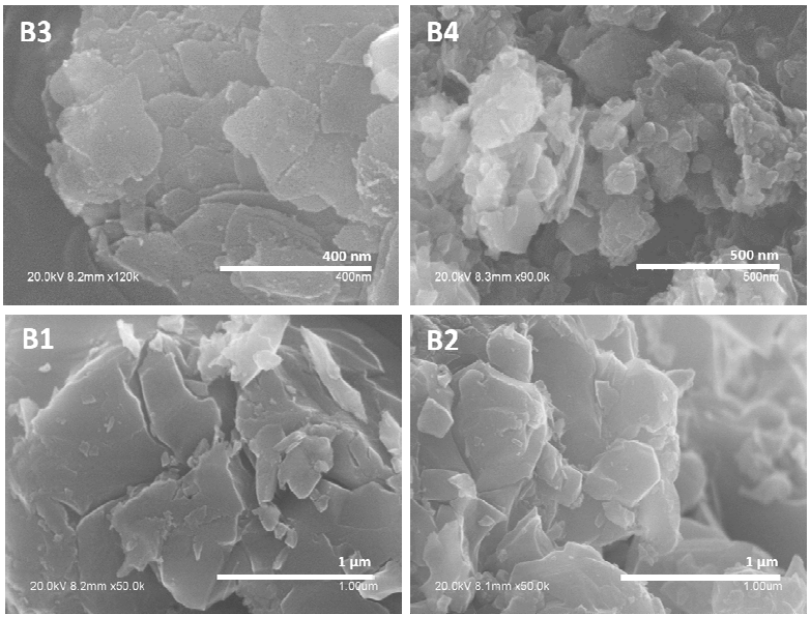

SI 3.1.1. XRPD characterization of the control experiments without C_2H_4

XRPD spectra of all **B1, B2, B3** and **B4** were employed to elucidate the different species in which the NiFe-LDH decomposes after the CVD process. Comparing our XRPD spectra and displaying theoretical patterns with CrystalMaker 2.5 for different species, we found that $FeNi_3$[6], $NiFe_2O_4$[7] and NiO[8] matched with the observed peaks and their relative intensities. As detailed in the theoretical patterns and the associated table, when NiO and $NiFe_2O_4$ spectra are compared, it can be observe that some peaks are superposed between the two species. These peaks are, for the NiO phase, the (*111*), (*200*) and (*220*), and for the $NiFe_2O_4$ phase, the (*222*), (*400*) and (*440*).[9]

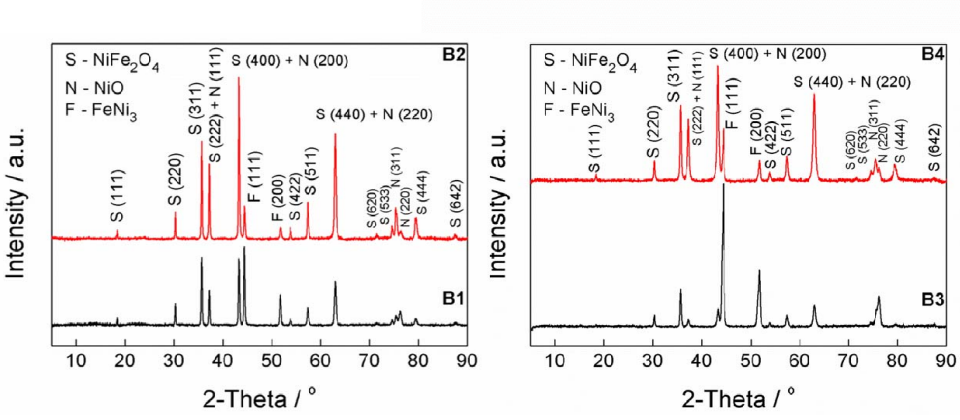

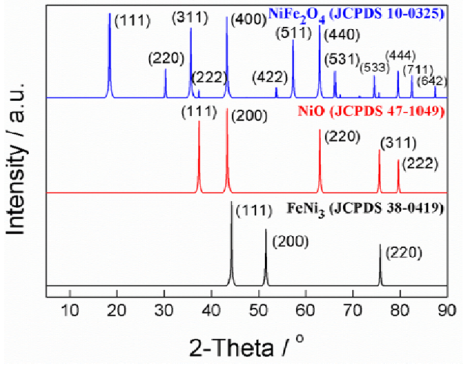

$FeNi_3$	
(*hkl*)	2-Theta / °
(*111*)	44.21
(*200*)	51.51
(*220*)	75.84

NiO	
(*hkl*)	2-Theta / °
(*111*)	37.33
(*200*)	43.38
(*220*)	63.02
(*311*)	75.59
(*222*)	79.60

$NiFe_2O_4$	
(*hkl*)	2-Theta / °
(*111*)	18.40
(*220*)	30.26
(*311*)	35.65
(*222*)	37.29
(*400*)	43.33
(*422*)	53.76
(*511*)	57.32
(*440*)	62.95
(*531*)	66.19
(*533*)	74.49
(*444*)	79.50
(*711*)	82.47
(642)	87.37

The influence of the heating scan rate on the crystallization played an important role in these CVD procedures. In fact, the 5 ^{o}C min^{-1} scan rate favored the concomitant crystallization of the $FeNi_3$ alloy at expense of the $NiFe_2O_4$/NiO mixture. On the other hand, the (*220*) peak of $FeNi_3$ shows a little shift to high theta values when the scan rate is increased. Comparing the same scan rate at 900 ºC, it revealed an increase in the intensity of the $NiFe_2O_4$/NiO peaks. This observation can be ascribed to the fact that in these systems the crystallization of the spinel phase is favored thermodynamically, whilst the alloy crystallization is controlled kinetically.[10]

We selected the lowest calcination temperature (550 ^{o}C) for performing the CVD experiments in films on the basis of the preserved 2D morphology, as seen in FE-SEM images. Furthermore, we carried out a control sample namely as **B5** (scan rate of 1 ^{o}C min^{-1}), in the absence of H_2 and C_2H_4, *i.e.* a calcination of a NiFe-LDH, to confirm the nature of the catalytic specie.

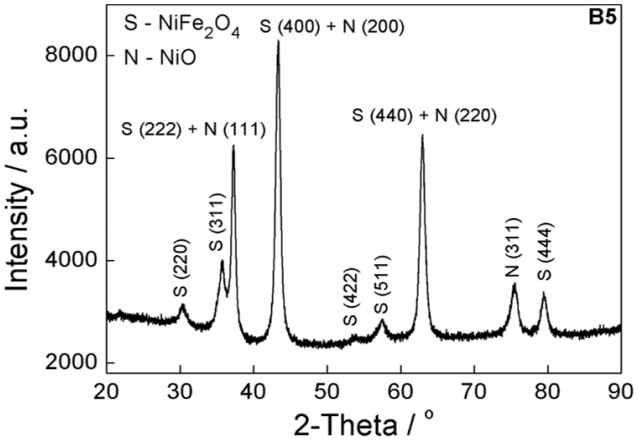

As expected, the XRPD spectrum of **B5** displays a collection of peaks related with both $NiFe_2O_4$ and NiO phases, concluding that $FeNi_3$ alloy is the active catalytic specie in the CVD reaction, responsible of the carbon nanoform growing.

SI 3.2. CVD control experiments with C_2H_4

We studied the CVD process on bulk samples at 550 ^oC and at scan rates of 5 and 1 $^oC\ min^{-1}$ for **S1** and **S2**, respectively.

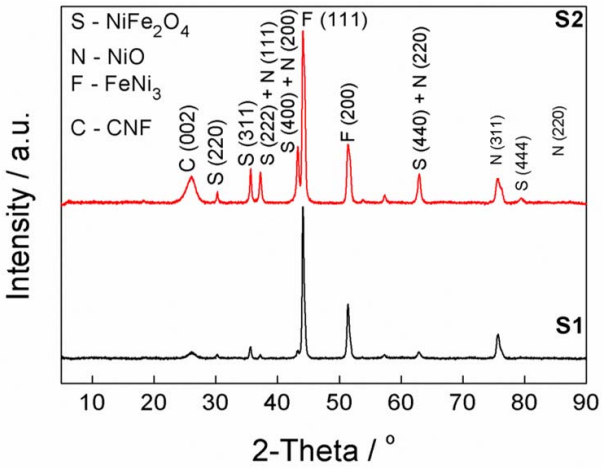

XRPD spectra of both **S1** and **S2**, showing the same pattern as seen before for the control experiments. However, a new peak appears at *ca.* 26^o, related with the presence of carbon nanoforms. It is worth noting that, even for the slower scan rate, the $FeNi_3$ alloy shows always the highest intensity (contrary to that observed for the control experiments without C_2H_4).

SI 4. Additional References.

[1] X. Guo, F. Zhang, S. Xu, D. G. Evans, X. Duan, *Chem. Commun.* **2009**, 6836.

[2] G. Fan, X. Xiang, J. Fan, F. Li, *J. Mater. Chem.* **2010**, *20*, 7378.

[3] M.-Q. Zhao, G.-L. Tian, Q. Zhang, J.-Q. Huang, J.-Q. Nie, F. Wei, *Nanoscale* **2012**, *4*, 2470.

[4] H. Chen, F. Zhang, S. Fu, X. Duan, *Adv. Mater.* **2006**, *18*, 3089.

[5] J. Jiang, J. Zhu, R. Ding, Y. Li, F. Wu, J. Liu, X. Huang, *J. Mater. Chem.* **2011**, *21*, 15969.

[6] Z. Ahmed, *Mineral. Mag.* **1981**, *44*, 225.

[7] P. Priyadharsini, A. Pradeep, P. S. Rao, G. Chandrasekaran, *Mater. Chem. Phys.* **2009**, *116*, 207.

[8] R. W. Cairns, E. Ott, *J. Am. Chem. Soc.* **1933**, *55*, 527.

[9] Y. Zhang, F. Zhang, Y. Lu, T. Chen, L. Yang, *J. Phys. Chem. Solids* **2010**, *71*, 604.

[10] X. G. Liu, B. Li, D. Y. Geng, W. B. Cui, F. Yang, Z. G. Xie, D. J. Kang, Z. D. Zhang, *Carbon* **2009**, *47*, 470.

Article 7:

CVD Synthesis of Carbon Spheres using NiFe-LDHs as Catalytic Precursors: Structural, Electrochemical and Magnetoresistive Properties

Journal of Materials Chemistry C **2016**, *4*, 440–448

Volume 4 | Number 3 | 21 January 2016 | Pages 409–640

Journal of Materials Chemistry C

Materials for optical, magnetic and electronic devices

www.rsc.org/MaterialsC

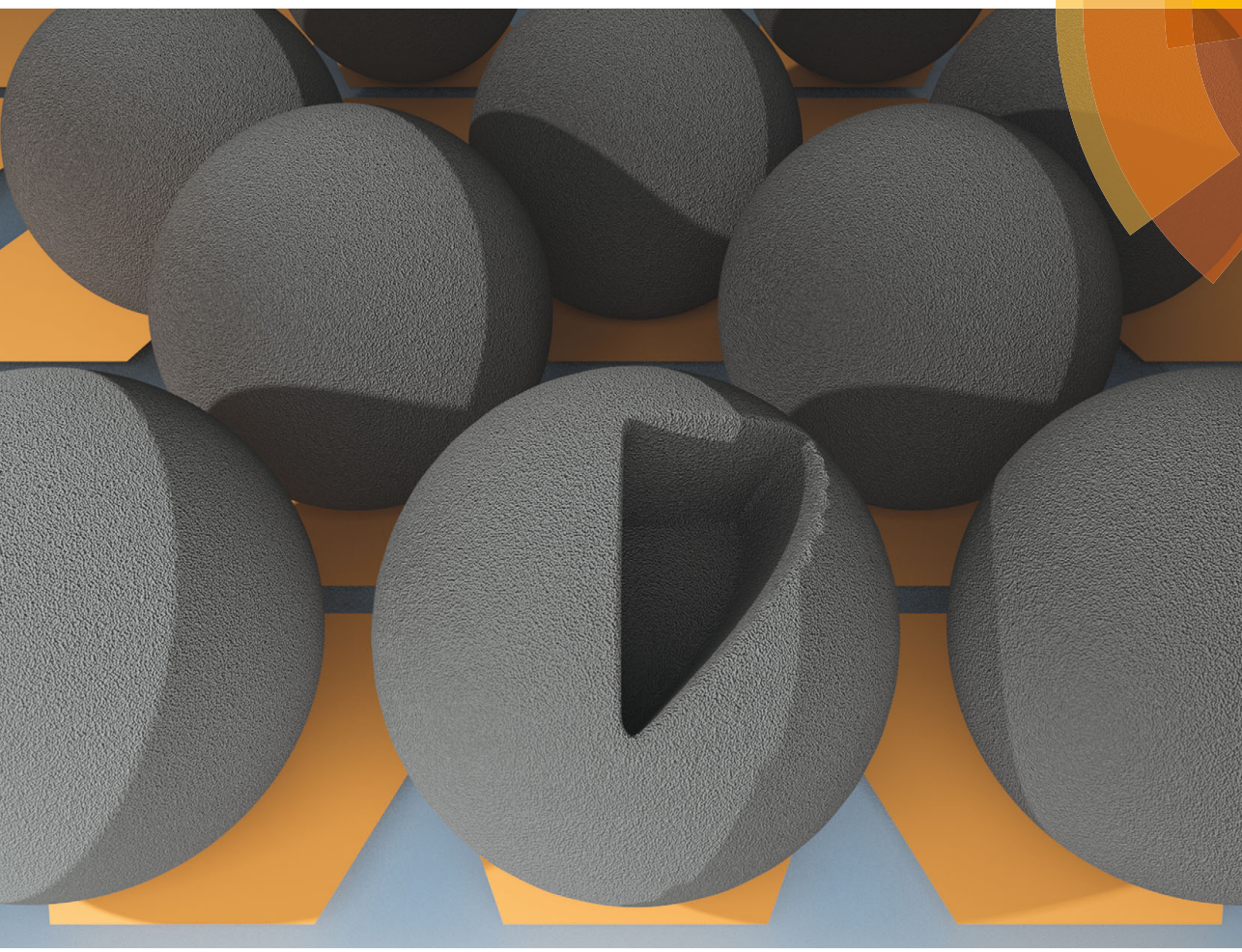

ISSN 2050-7526

ROYAL SOCIETY OF CHEMISTRY

PAPER

Gonzalo Abellán, Eugenio Coronado *et al.*

CVD synthesis of carbon spheres using NiFe-LDHs as catalytic precursors: structural, electrochemical and magnetoresistive properties

175 YEARS

Journal of Materials Chemistry C

PAPER

View Article Online
View Journal | View Issue

Cite this: J. Mater. Chem. C, 2016, 4, 440

CVD synthesis of carbon spheres using NiFe-LDHs as catalytic precursors: structural, electrochemical and magnetoresistive properties†

Jose A. Carrasco,[a] Helena Prima-Garcia,[a] Jorge Romero,[a] Jesús Hernández-Saz,[b] Sergio I. Molina,[b] Gonzalo Abellán*[ac] and Eugenio Coronado*[a]

Received 11th September 2015,
Accepted 9th November 2015

DOI: 10.1039/c5tc02861b

www.rsc.org/MaterialsC

The gram-scale synthesis of carbon spheres with a diameter of *ca.* 740 nm has been achieved by means of a chemical vapour deposition method using NiFe-layered double hydroxides as a solid catalytic precursor. The presence of the catalyst ($FeNi_3$) allows controlling the final size distribution, resulting in a monodisperse sample. Their structural properties exhibited a high degree of graphitization according to their I_D/I_G ratio. In addition, their morphological features were unveiled by FIB-SEM and HRTEM, showing that they are formed by solid inner cores, and presenting labile chain-like structures due to accretion procedures. The solution and posterior sonication of the samples in toluene gave rise to the well-defined isolated spheres. The textural and electrochemical properties of the spheres have been tested showing non-mesoporous structures with a good behaviour as electrode materials for supercapacitors due to the presence of redox functionalities on their surface. Finally, magneto-transport measurements have been carried out, demonstrating semiconductor behaviour, as well as a positive magnetoresistance effect (*ca.* 72%) for the lowest studied temperature (2 K).

1. Introduction

Since the discovery of fullerenes (C_{60}) by Kroto *et al.* in 1985,[1] many studies have been published in the field of the so-called carbon nanoforms (CNF). These carbon-based materials include a wide variety of sizes and shapes ranging from C_{60} to metallofullerenes, carbon fibers, nanotubes (single-wall, multi-wall…), nano-onions, nanohorns, nanobuds, spheres or graphene, among others.[2] The interest in different synthetic carbon allotropes relies on their outstanding properties and applications, as recently highlighted by the ubiquitous graphene. Among this family, spherical carbon structures like C_{60}, or carbon nano-onions have attracted increasing attention in the last few years. One of these forms are carbon spheres (CS), formerly known as carbon blacks.[3] The curved structure of CS is a consequence of the presence of pentagonal and heptagonal rings within the hexagonal framework of carbon, allowing the system to adopt their characteristic morphology.[4]

Carbon spheres can be classified according to different parameters, like their size, nanometric texture or internal structure.[5–8] Recently, Deshmukh *et al.* reviewed different techniques employed for the synthesis of CS, pointing out chemical vapour deposition (CVD) as one of the most versatile synthetic approaches.[9]

These carbonaceous forms show a wide range of potential applications due to their thermal stability, electronic properties, high surface area or low density. Furthermore, their unclosed graphitic flakes give rise to dangling bonds throughout the surface of the spheres, increasing their reactivity and boosting their applicability in adsorption, lubricants, tribological coatings, catalysis, batteries, supercapacitors or fuel cells among others.[10–15] Conversely, when it comes to their transport and magnetic properties, the list of examples is very scarce,[16,17] despite their potential for use as electronically active reinforcing agents of functional composites.[18,19] Indeed, the recent discovery of organic magnetoresistance (OMAR) in graphene and other related nanocarbons has significantly attracted increasing attention to these systems, as they are promising materials for flexible, low-cost and transparent electronics.[20–25] Therefore, the cost-effective production of magnetoresistive CS is of great interest in the development of new hybrid composites and functional polymers.

Herein, we have synthesized monodisperse carbon spheres in a gram-scale by means of a CVD procedure using NiFe-layered

[a] Instituto de Ciencia Molecular (ICMol), Universidad de Valencia, Catedrático José Beltrán 2, 46980, Paterna, Valencia, Spain. E-mail: eugenio.coronado@uv.es; Fax: +34 96 354 3273; Tel: +34 96 354 4415
[b] Departamento de Ciencia de los Materiales e Ingeniería Metalúrgica y Química Inorgánica, IMEYMAT, Universidad de Cádiz, 11510 Puerto Real, Cádiz, Spain
[c] Department of Chemistry and Pharmacy and Institute of Advanced Materials and Processes (ZMP), University Erlangen-Nürnberg, Henkestr. 42, 91054 Erlangen and Dr.-Mack Str. 81, 90762 Fürth, Germany. E-mail: gonzalo.abellan@fau.de; Fax: +49 911 65078 65015; Tel: +49 911 65078 65031

† Electronic supplementary information (ESI) available. See DOI: 10.1039/c5tc02861b

double hydroxides (LDHs) as catalytic precursors.[26] The NiFe-LDH materials have demonstrated their utility as catalysts in the low-temperature synthesis of several carbon nanoforms, including carbon nano-onions,[27] bamboo-like carbon nanotubes[28] or even graphene – when they are used as precursors for the preparation of hybrid $FeNi_3$–graphene nanocomposites.[28–30]

We have thoroughly characterized the as-obtained spheres by means of XRD, Raman, FT-IR, TG, FESEM, FIB-SEM, HRTEM, DLS, N_2 isotherms, XPS and Electrochemistry. Furthermore, their magneto-transport properties revealed a semiconducting behaviour with an intrinsic large MR of *ca.* 72%.

2. Experimental methods

2.1. Chemicals

All chemical reagents $Ni(NO_3)_2{\cdot}6H_2O$ (Aldrich); $Fe(NO_3)_3{\cdot}9H_2O$ (Sigma-Aldrich); triethanolamine (TEA), $C_6H_{15}NO_3$ (Sigma-Aldrich); urea, $CO(NH_2)_2$ (Fluka) and ethanol absolute (Panreac, 99.9%) were used as received without further purification. Ultrapure water was obtained from Millipore Milli-Q equipment. N_2, H_2/Ar (10%) and ethylene (C_2H_4) were purchased from Linde Material Handling.

2.2. Synthesis of NiFe-CO_3 LDHs

NiFe-CO_3 LDHs were synthesized following a modified homogeneous precipitation method by using urea and TEA as an ammonium releasing reagent (ARR) and a chelating agent, respectively.[31]

In a typical synthesis, the nitrate salts of the metals were dissolved in 50 mL of deionized pure water together with TEA, in order to reach a total metal cation concentration of 20 mM in the final solution, with a Ni : Fe ratio of 3 : 1 (x = 0.25, with $x = [Fe^{3+}]/([Fe^{3+}] + [Ni^{2+}])$), and a concentration of TEA equimolar with the iron concentration (5 mM). Next, 50 mL of aqueous solution of urea (35 mM) were added. The excess of urea was fixed to be 1.75 times the total metal concentration. The resulting dark brown mixture was placed in a 125 cm^3 stainless steel Teflon-lined autoclave and heated up to 150 °C in a previously heated oven. After 48 h, the autoclave was left to cool down at room temperature and the final yellowish fine powder was filtered and dried under a vacuum. The pH value of the remaining solution was found to be around 8.

2.3. Synthesis of carbon spheres

Carbon spheres were synthesized by means of a chemical vapour deposition process (CVD). In a typical procedure, 25 mg of NiFe-LDHs were placed at the centre of a horizontal quartz tube, which was inserted into a tubular furnace at atmospheric pressure. The furnace was heated under flowing N_2 (100 mL min^{-1}) up to 900 °C at a 5 °C min^{-1} scan rate. When the temperature was reached, reduction with H_2 (50 mL min^{-1}, mixture of H_2 10% in Ar) was performed for 5 min before switching the gas for the carbon source, ethylene (C_2H_4, 100 mL min^{-1}), during 60 more min at 900 °C. Then, the furnace was cooled to room temperature under N_2 protection, and the sample was collected from the quartz tube. Control experiments in the absence of NiFe-LDHs were also carried out under the same experimental conditions.

2.4. Thermal treatment

The as-synthesized carbon spheres were annealed at 800 °C in order to eliminate organic impurities. In a typical procedure, the sample was placed in a holder at the centre of a horizontal quartz tube inserted into a furnace at atmospheric pressure. The furnace was heated up to 800 °C under a N_2 atmosphere (100 mL min^{-1}) at a 2 °C min^{-1} scan rate. When the temperature was reached, the system was cooled to room temperature under N_2 protection. Finally, the annealed spheres were collected from the holder.

2.5. Physical characterization

X-ray powder diffraction (XRPD) patterns were obtained using a PANalytical Empyrean X-ray powder diffractometer under copper radiation (Cu-Kα = 1.54178 Å). Samples were mounted on a flat sample plate. Profiles were collected in the $2.5^\circ < 2\theta < 90^\circ$ range with a step size of 0.05°. Raman measurements (Jobin-Yvon LabRam HR 800 Raman Microscope) were carried out at room temperature with the 532 nm line of an Ar ion laser as an excitation source. The morphology of spheres was studied by means of field emission scanning electron microscopy (FESEM) performed on a Hitachi S-4800 microscope operating at an accelerating voltage of 20 kV over metallized samples with a mixture of gold and palladium for 30 s. FEI dual-beam FIB-SEM Quanta 200 3D equipment operating at 30 kV was used to mill the spheres and observe their inner structure and prepare lamellae by using an *in situ* lift-out method.[32] High-resolution transmission electron microscopy (HRTEM) studies were carried out on Tecnai G2 F20 and Jeol 2100 microscopes operating at 200 kV. Samples were prepared by dipping a sonicated suspension of the sample in toluene on a carbon-coated copper grid. Metallic atomic composition of bulk samples was determined by means of electron probe microanalysis (EPMA) performed on a Philips SEM-XL30 equipped with an EDAX microprobe. Carbon, nitrogen and hydrogen contents were determined by microanalytical procedures by using a LECO CHNS. Infrared spectra were recorded on a FT-IR Nicolet 5700 spectrometer in the 4000–400 cm^{-1} range using powdered samples diluted in KBr pellets. Thermogravimetric analysis of the compounds were carried out using a Mettler Toledo TGA/SDTA 851 apparatus in the 25–800 °C temperature range at a 10 °C min^{-1} scan rate and under an air flow of 30 mL min^{-1}. The porous texture was characterized by N_2 adsorption at 77 K in an AUTOSORB-6 apparatus. The samples were previously degassed for 4 h at 523 K and 5×10^{-5} bar. Dynamic light scattering (DLS) measurements were recorded at 25 °C using a Zetasizer Nano ZS instrument (Malvern Instrument Ltd) on a freshly prepared sample (1 mg of CS in 10 mL of toluene and sonicated for 30 min). The electrical conductivity and magneto-resistance measurements were carried out by using a standard four-probe contact method with Pt wire in a physical property measurement system (PPMS-9) by Quantum Design. The resistivity data were taken from 300 to 2 K and from 0 to 8 T, with Keithley 2450 as a current source and a

Keitley 6514 as an electrometer. The measurements were performed in a pressed pellet of the CS with a size of 2.4×10^{-4} cm^2.

2.6. Electrochemical measurements

The electrochemical analyses were performed using an Autolab electrochemical workstation (PGSTAT-100 potentiostat/galvanostat) connected to a personal computer that uses GPES electrochemical software.

The materials were mixed with acetylene black and PVDF at a mass ratio of 80 : 10 : 10 in ethanol and deposited on a nickel foam electrode. The as-prepared nickel foam electrodes were dried overnight at 70 °C and pressed. Each working electrode contained about 1 mg of electroactive material and had a geometric surface area of about 1 cm^2. A typical three-electrode experimental cell equipped with a stainless steel plate having 4 cm^2 of surface area as the counter electrode and a Metrohm Ag/AgCl (3 M KCl) as the reference electrode were used for the electrochemical characterization of the materials trapped by working electrodes.

The electrochemical measurements were carried out in aqueous 6 M KOH solutions as the electrolyte. Ultrapure water was obtained from Milli-Q equipment. The specific capacitance (C) was calculated from the cyclic chronopotentiometric curves according to eqn (1):

$$C = I\Delta t/m\Delta V \quad (1)$$

where I is the charge/discharge current, Δt is the time for a full charge or discharge, m is the mass in grams of the active material in the electrode layer, and ΔV is the voltage change after a full charge or discharge.

Electrochemical impedance spectroscopy measurements were carried out by applying an AC amplitude of 10 mV in the frequency range of 0.01–10^6 Hz at an open circuit potential with the help of an impedance spectrum analyser (GAMRY interface 1000 potentiostat). The electrochemical cell was placed in a Faradaic cage. Data were analysed with the help of Gamry Echem Analyst v. 6.03 software.

3. Results and discussion

The synthesis of carbon spheres was achieved by means of a catalytic CVD process at 900 °C using NiFe-LDHs as catalytic precursors and ethylene as a carbon source for a period of 60 min. After the CVD process, a black solid with metallic brilliance was formed using a quartz tube. The sample was collected from the inner part of the quartz reactor, powdered and submitted to a subsequent annealing process at 800 °C under an inert atmosphere in order to eliminate possible organic impurities. The final product was a black powder light in weight, hereinafter named as CS. Further characterization of pristine spheres is depicted in the ESI† (see SI 1).

As recently reported by our group, NiFe-LDHs are excellent catalysts for the synthesis of carbon nanoforms.[26,28] Moreover, we have demonstrated that the calcinated NiFe-LDH preserves the structural integrity, with the *in situ* formed $FeNi_3$ nanoparticles being the main catalytic seeds.[27] Herein, control experiments consisting of the calcination of NiFe-LDHs at 900 °C, supplying H_2 but in the absence of a carbon source, gave rise to a mixture of $NiFe_2O_4$, NiO and $FeNi_3$ phases as revealed by XRPD (see SI 2.1, ESI†). However, further experiment with neither H_2 nor ethylene depicted the presence of only a mixture of $NiFe_2O_4$ and NiO, concluding that the $FeNi_3$ alloy is the active catalytic species in the CVD reaction, responsible for the growth of carbon nanoforms. Indeed, a low-temperature CVD process at 550 °C with bulk samples leads to a mixture of carbon nanoforms formed by few-layer graphene, carbon fibers and multi-wall carbon nanotubes (see ref. 28 for further information). According to Li and co-workers, these graphitic structures could evolve towards the formation of carbon spheres for larger times of feeding.[33] Herein, the presence of the catalyst is reflected in a decrease in the starting synthesis temperature towards *ca.* 800 °C, allowing the gram-scale formation of monodisperse CS (*vide infra*). In contrast, carbon sphere control experiments without the presence of a catalyst leads to an increase in the temperature to 900 °C yielding a lower amount of CS with a wide range of dimensions and morphologies, highlighting the crucial role of NiFe-LDHs (Fig. SI 2.2, ESI†).[34]

Inagaki[6,7] reported that the most probable mechanism for the formation of carbon spheres consists of the dissociation of ethylene (carbon source) at 900 °C into C and H. After that C starts to polymerize forming the so-called basic structural units (BSUs), whilst methane and hydrogen are also formed. Usually, the arrangement of these BSUs leads to three different textures in these carbon forms: concentric, radial and random.[7] The final disposition of these units depends on the precursor, heating treatment, feeding time and the interface between the carbon atoms and their surroundings during the thermal process.[7,35,36] Anyway, the exact role of the catalyst in the formation of spheres mediated by CVD procedures is not yet fully revealed. It seems that the $FeNi_3$ catalyst may act as a template, providing nucleation sites for the subsequent formation of spheres. Another possibility is its role in the modification and deposition of carbon radicals which are formed in the gas phase, *i.e.*, helping the decomposition of the carbon source instead of the polymerization reaction.[9]

The XRPD spectrum in CS was recorded in order to study the graphitic structure of the sample. Fig. 1A exhibits the presence of a main peak centred at *ca.* 25° and a secondary peak at *ca.* 43.8°, related to the (002) and the (100) planes of graphite, respectively. The common broadness of the peaks in the carbon sphere spectra indicates a low range in the structural order.[10,28] According to Bragg's equation, the interlayer spacing d_{002} of our CS is 0.356 nm, which agrees with the literature,[30,31] with a low deviation for the ideal d_{002} space (0.343 nm) in a graphitic structure (JCPDS-ICDD Card No. 41-1487). This value is intermediate between those measured for a carbon fiber (d_{002} = 0.342) and activated carbon atoms (d_{002} = 0.363), which is indicative of a relatively well-organised carbon structure.[5]

Raman spectra have been recorded to disclose the graphitic ordering of CS. Fig. 1B shows a representative Raman spectrum with the characteristic D and G bands centred at 1354 cm^{-1}, and 1590 cm^{-1}, respectively. The D band is related to the defects and disorder-induced modes, and the G band is associated with

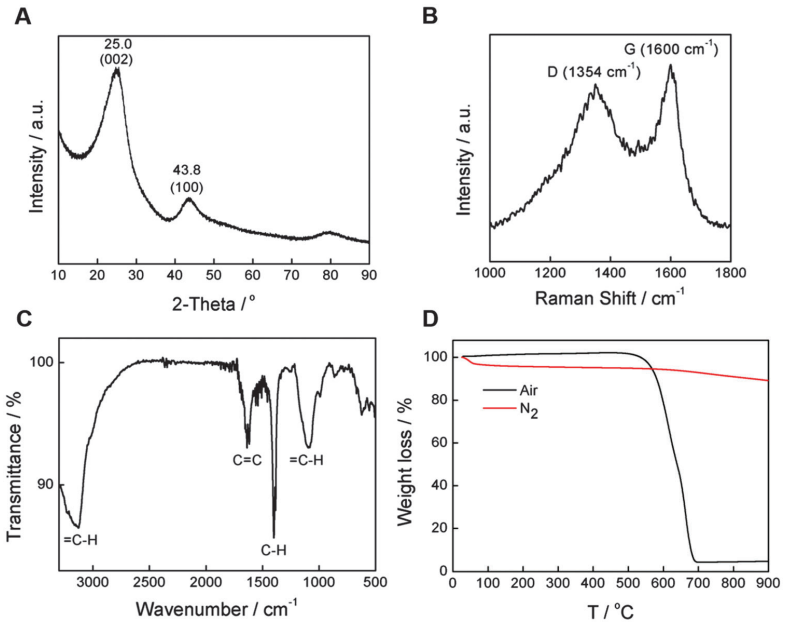

Fig. 1 (A) XRPD, (B) Raman and (C) FT-IR spectra of CS. (D) TGA of CS in air (black line) and a nitrogen atmosphere (red).

the in-plane E_{2g} zone-centre mode, *i.e.* the vibration of sp^2-bonded carbon atoms in a two-dimensional hexagonal lattice. The I_D/I_G ratio is related to graphitic ordering in carbon materials, and a high I_D/I_G ratio involves a low degree of graphitization (order) in the carbon system, and *vice versa*. In our sample we measured a I_D/I_G ratio of *ca.* 0.80, showing a higher degree of graphitization (lower I_D/I_G) than most of the other CVD carbon spheres reported to date.[10,33,37,38] Lower I_D/I_G ratios can be achieved in the presence of MnO_2 or Ni doping.[39,40] In any case, our results are in accordance with the graphitization trend reported by Nieto-Márquez *et al.*: graphite > carbon nanotubes/nanofibers > carbon nanospheres > activated carbon.[10] A further comparison of all the synthesized spheres in this work can be found in SI 3 (ESI†).

FT-IR (Fig. 1C) confirmed the presence of C=C (1637 cm^{-1}) and =C–H groups (3100 and 1080 cm^{-1}, stretching and bending modes, respectively) in the CS, supporting the presence of an sp^2 structure. Among these, another band at *ca.* 1400 cm^{-1} can be found, related to the C–H bending mode.[34]

Furthermore, thermogravimetric analysis (TGA) and differential thermal analysis (DTA) experiments in air and under a N_2 atmosphere up to 900 °C were carried out. The thermogravimetric profile reveals that CS are stable in air below 530 °C; at *ca.* 560 °C they exhibit an abrupt mass loss of *ca.* 95% which ended at 700 °C (Fig. 1D). According to Serp *et al.* classification of carbon nanoforms based on the maximum of the gasification rate,[5] our sample is located in the range of carbon nano-spheres with a combustion temperature of *ca.* 630 °C depicted in the DTA (see SI 4, ESI†). In turn, the experiment in N_2 exhibits a stable thermal behaviour, showing only a weight loss of *ca.* 10% when 900 °C is reached. It is worth noting that in the presence of air, a slight increase of mass (*ca.* 105%) is observed just before thermal decomposition; this is attributed to the oxidizing process of graphitic flakes into oxidized graphite. In contrast, this effect is not seen in N_2.[34,41]

After studying the structural properties of the spheres, their morphology was unveiled by means of FESEM and HRTEM, depicting the spherically characteristic shape of CS, with a large quantity of them usually forming aggregates (Fig. 2). The accretion of spheres into clusters of several microns (see SI 5, ESI†) was described by Kroto *et al.* for feeding times higher than 10 min,[34] or by Pol and co-workers as a result of cooling the system from high temperature to room temperature.[35] Anyway, it is worth noting that this coalescence is related to the presence of reactive dangling bonds on the surface, which gives them a high surface reactivity.[4,10] Indeed, the EDAX analysis of the sample revealed a carbon content of 93.2 atomic% and an oxygen content of 6.8%. These results are corroborated by C, H, N elemental analysis, with a carbon content of 93.3% (atomic ratio) and 0.4% of H. No N was detected. Atomic percentages were also confirmed by XPS (see SI 6.1, ESI†). Furthermore, the XPS spectrum of C_{1s} clearly exhibits a main peak which can be deconvoluted into sp^2 and sp^3 components. No trace of the catalyst (Ni and Fe) was found in the spectra of the CS (SI 6.2, ESI†). Finally, the synthesis of carbon spheres at a higher temperature (1000 °C) depicted a decrease of *ca.* 1% in the O atomic percentage (a decrease of *ca.* 11% of the total oxygen content). The N signal remains residual (SI 6.1, ESI†).

The particle size distribution was determined by measuring 50 spheres in the SEM images, giving rise to an average diameter of 740 ± 42 nm. This is in sharp contrast with the

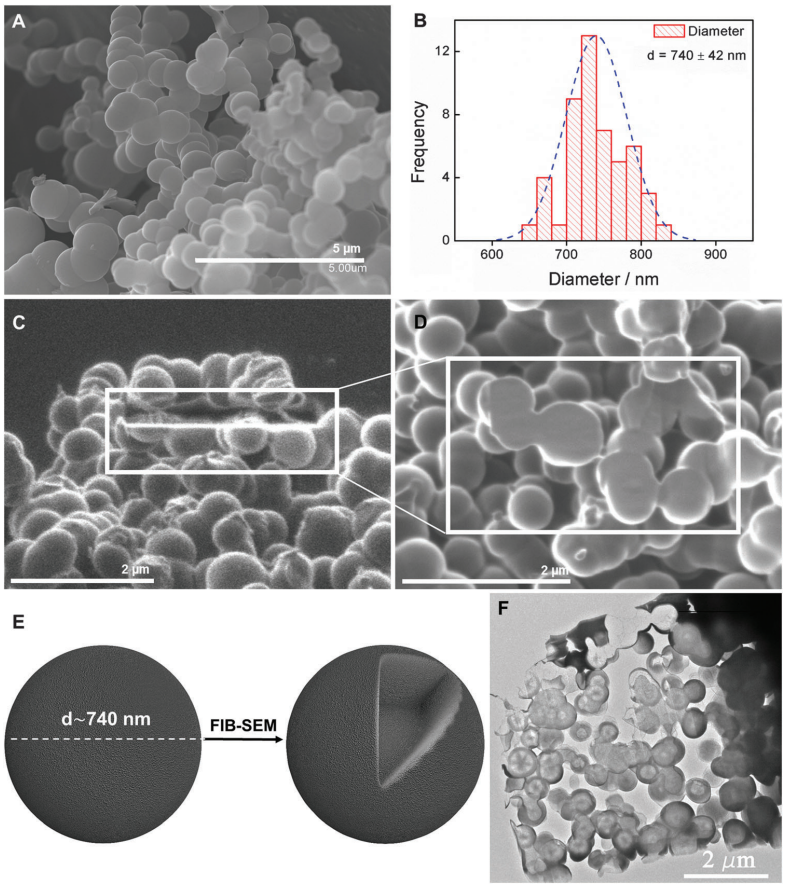

Fig. 2 (A) FESEM image of CS. (B) Histogram displaying the average diameter taken from FESEM images. (C) FIB-SEM image of the milled region, it is remarked within the white square. (D) FIB-SEM cross-section image of the same region of (C) depicting a solid inner structure. (E) Idealized 3D representation of a sphere before and after the FIB, highlighting the solid inner structure. (F) Bright field TEM image of electron-transparent lamella prepared by FIB-SEM. The porosity between the carbon spheres can be clearly seen.

wide range of diameters obtained in the control experiments (see SI 2, ESI†), and highlights the role played by the NiFe-LDH catalytic precursor in controlling the size distribution of the spheres.

In order to determine directly whether the spheres are hollow or not, we have taken advantage of a dual beam focused ion beam-SEM instrument. Precise milling was carried out over several spheres. An example of a typical zone where the focused ion milling process has been applied is shown in Fig. 2C. The cross-section acquired after the milling process supplies detailed information of the specimen subsurface, highlighting the existence of a solid inner structure in the spheres, as depicted in Fig. 2D and E.

Furthermore, a lamella thinned down to electron-transparency has been studied by TEM showing the absence of mesopores and porosity between the carbon spheres (*vide infra*) (Fig. 2F). The preparation of these lamellae is detailed in SI 7 (ESI†).

HRTEM images displayed nearly perfect spherical morphologies with an average diameter of *ca.* 700–800 nm (Fig. 3A), disposed usually in a chain-like structure due to the accretion effect. These diameters are in good accordance with the value extracted from FESEM studies. A deeper look into their internal structure revealed a concentric arrangement of the graphitic planes (as demonstrated by HRTEM *vide infra*).[6] In addition, the distance between the graphitic planes also matches with that calculated from Bragg's equation according to the XRPD spectrum (*vide supra*).

Interestingly, these chain-like structures can be disassembled by sonication, obtaining relatively stable suspensions of CS exhibiting the characteristic Tyndall–Faraday effect. Concretely, by suspending the powder in toluene (1 mg of CS in 10 mL) and submitting it to bath sonication for 30 min, almost all of the aggregates can be individualized. Fig. 3B and C depict an HRTEM image showing the presence of isolated and monodisperse spheres, retaining their

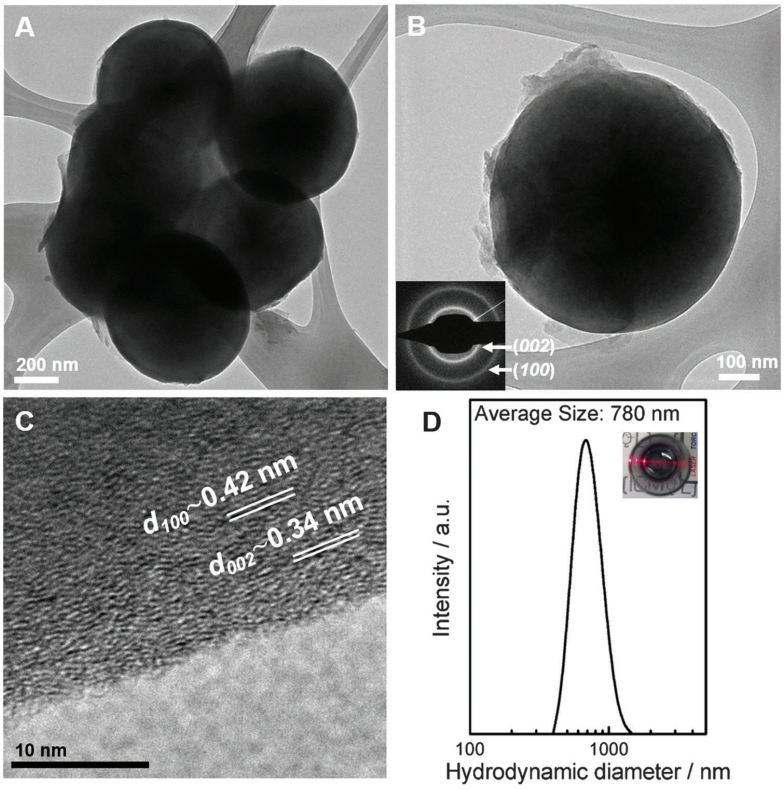

Fig. 3 HRTEM image depicting (A) a cluster of spheres, disposed in a chain-like structure, and (B) a single sphere from the CS sample after a sonication procedure in toluene. The inset in (B) shows the selected area electron diffraction (SAED) pattern displaying two rings corresponding to (002) and (100) planes. (C) High magnification image of the interface from a single sphere, highlighting the (002) and (100) planes and the distance between crystallographic lattices (D). Distribution of sizes extracted from DLS measurements for CS. Its inset shows the visible Tyndall–Faraday effect, resulting from the scattering of the irradiated beam by the particles in a toluene solution.

intrinsic structure. In their spherical surface, some broken edges can be seen, due to the disaggregation of the clusters after the sonication process. Furthermore, Dynamic Light Scattering (DLS) was carried out with this suspension, in order to further study the size distribution of the sample (Fig. 3D), as well as the possible presence of bigger clusters. We observed that the average hydrodynamic diameter – a complex function that describes a Gaussian distribution – is centred at *ca.* 780 nm, in good agreement with the electron microscopy observations and the classification proposed by Serp *et al.*[5]

In order to determine the surface texture of the spheres, N_2 adsorption–desorption isotherms were measured. The CS showed a BET surface area value of 16.2 $m^2\ g^{-1}$, indicative of the absence of mesoporosity on its surface, in accordance with previously published studies.[10] In contrast, carbon spheres with a mesoporous structure depicted larger BET surface areas of *ca.* 1400–1600 $m^2\ g^{-1}$.[36,37] It is worth saying that this value is slightly higher than that exhibited by the pristine spheres (3.6 $m^2\ g^{-1}$), as a consequence of annealing. In line with that, differential pore volume distribution of the spheres by DFT has been calculated, suggesting the presence of ultramicropores (see SI 8, ESI†).[42–44]

One of the most important fields of application of CS and related nanomaterials is the energy storage and conversion.[45,46] Among others, supercapacitors (SCs) are attracting increasing attention due to their potential to deliver high power densities in short periods of time with high cyclability and durability.[47] In this sense, the graphitic character, porosity, conductivity or the presence of oxygen functionalities could greatly affect the properties of SCs, providing us with important information about the presence of oxygen functionalities on the surface.

For comparative purposes, we have tested the electrochemical properties of the CS as electrode materials for SCs in a conventional three-electrode cell. The powdered sample was mixed with acetylene black and poly-vinylidene fluoride at a mass ratio of 80:10:10 with ethanol. The mixture was cast on a 1 cm^2 Ni-foam collector, dried and pressed to minimize the loss of the active material during electrochemical testing. The electrochemical properties

were measured by means of cyclic voltammetry (CV) using 6 M KOH (99.99%) as the electrolyte in an applied voltage range of 0 to −1 V (*vs.* Ag/AgCl). Fig. 4A shows the quasi-rectangular cyclic voltammograms recorded at different scan rates, in which the large areas suggest an appropriate supercapacitive behaviour, although these CS are not porous, indicative of an activated surface.[48] Moreover, galvanostatic charge–discharge cycling was also measured in order to study the specific capacitance of these CS (Fig. 4B). A relatively large discharge capacity of *ca.* 132 F g^{-1} was obtained for a current density of 1 A g^{-1} (inset in Fig. 4B), overpassing that recently reported for related microporous CS,[49] a clear indication of the improved graphitic quality of the as-synthesized materials and the presence of an oxidized shell in accordance with the EDAX and elemental analysis results (*vide supra*). Because the oxygen content has a close relationship with carbonization temperature, the electrochemical properties of CS synthesized at 1000 °C were measured, exhibiting lower values of capacitances as seen in SI 9 (ESI†). This fact can be related to the minor presence of oxygen on the surface of those spheres, as revealed by XPS (SI 6.1, ESI†).

The potential electrochemical impedance spectroscopy (EIS) shows Nyquist plots with a nearly vertical line, typical of capacitive behaviour. In the inset of Fig. 4 a minor increase in the imaginary part can be seen due to electrolyte resistance. The corresponding conductance shows a typical behaviour, with values close to zero at low frequencies increasing with the increasing frequency, with a maximum of 1.3 S.[50]

A complete physical characterization of CS has been done measuring the transport properties using the four-probe method. The CS exhibited a nonmetallic behaviour as can be observed in the thermal evolution of resistance (Fig. 5). Fig. 5 shows characteristic non-linear and symmetrical *I–V* curves for the whole studied temperature range. The non-linearity increases when the temperature is reduced, observing semiconductor behaviour. The electrical conductivity at room temperature is 1.92×10^{-2} S cm^{-1} and it is reduced by four orders of magnitude when the temperature decreases, which is 1.32×10^{-6} S cm^{-1} at 2 K (Fig. 5). Furthermore, the conductivity matches perfectly with other values reported in the literature for CS.[16,17]

Studies dealing with the electrical properties of CS are very scarce. To the best of our knowledge, the first work that has measured the electrical properties of the CS is from Coville *et al.*,[16,17] where they studied the electrical transport mechanisms in nitrogen and boron-doped carbon spheres. These studies show that the dominant conduction mechanism in pristine CS is Mott variable range hopping (Mott VRH). In our case, this model provides a good description of the thermal dependence of electrical conductivity in the 300–2 K temperature range (Fig. SI 10, ESI†). Thus, the experimental behaviour is well fitted by the expression $\sigma(T) = \sigma_0 \cdot \exp[-(T_0/T)^n]$, with $n = 1/4$. The VRH model of conductivity represents a phonon-assisted mechanism of charge transport and it is normally associated with amorphous semiconductors, semiconductor glasses[51,52] and more recently with amorphous carbon.[17]

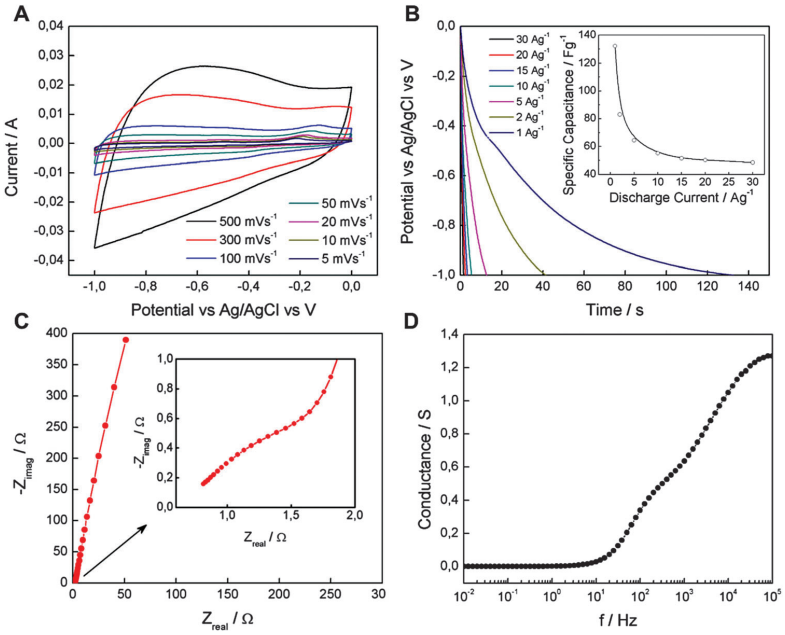

Fig. 4 Electrochemical properties of CS. (A) CV curve at various scan rates in a 6 M KOH aqueous solution. (B) Galvanostatic discharge curves at different discharge current densities. The inset represents the specific capacitance of the material at different discharge current densities. Electrochemical impedance spectra of CS in a 6 M KOH electrolyte. (C) Nyquist plots and (D) the response of conductance at different frequencies. The inset shows the high-frequency region.

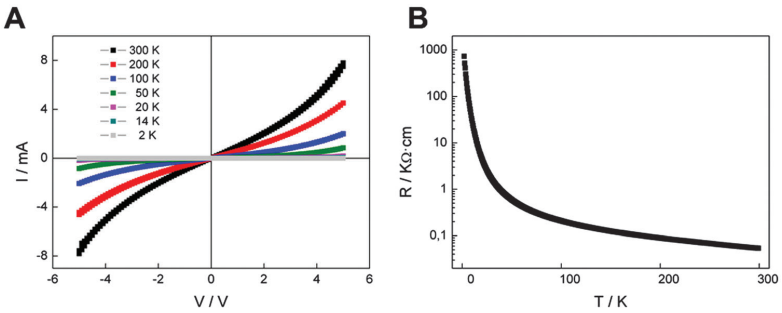

Fig. 5 (A) *I–V* curves for a temperature range from 300 K to 2 K. The electrical conductivity at room temperature is 1.92×10^{-2} S cm^{-1}. (B) Thermal resistance dependence of the CS.

We also measured the magnetoresistance (MR) properties of CS in the applied fields of 8 T in a PPMS system, revealing an intrinsic magnetoresistance (MR) of *ca.* 72% at low temperatures (Fig. 6). MR is calculated as MR (%) = $[R(H) - R(0)/R(0)] \times 100$, where $R(H)$ is the resistivity under the magnetic field B and $R(0)$ is the resistivity without any magnetic field. As long as we increase the temperature, the MR falls dramatically until no signal is observed above 100 K.

Fig. 6 shows a positive and non-saturated MR that decreases dramatically when the temperature increases for all the temperature range studied (from 50 K to 2 K). This positive, non-saturated MR behavior has also been found for other crystalline and amorphous nanocarbons and carbon composites.[20–25] All the experimental data of the Fig. 6 were fitted with the relation of MR $\propto (\mu_0 \cdot \mu \cdot |H|)^2$ (Fig. SI 10, ESI†). The quadratic term is related to the ordinary MR (OMR)[20] due to the curving of electron trajectories in the carbon plane, which results in a positive MR, and has a quadratic magnetic dependence of MR $\propto (\mu_0 \cdot \mu \cdot |H|)^2$, where μ is mobility.[20–24] The magnetic measurements revealed a very small magnetic phase in the CS (Fig. SI 11, ESI†). This magnetic phase probably comes from a small rest of the catalyst. However, the XPS analysis of CS showed the absence of the catalyst on the sample surface, highlighting the residual character of the catalyst present in the CS (Fig. SI 6.2, ESI†). Therefore, the influence of the magnetic rest of the catalyst in the MR is very weak, and almost negligible.

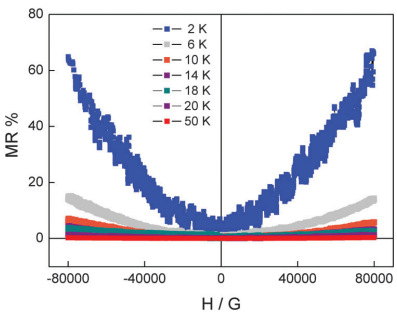

Fig. 6 MR dependence on the temperature of the CS.

Finally, the dramatic temperature dependence of the MR (Fig. SI 12, ESI†) is an indication of the predominant contribution of the OMR to the MR observed in the CS. These results pave the way for using CS not only as a reinforcing agent of polymers, but also as electronically active building blocks in the design of hybrid multifunctional composites.

4. Conclusions

Carbon spheres with a diameter of *ca.* 740 nm have been synthesized in gram-scale proportions by means of a CVD method using NiFe-LDHs as catalyst precursors. Control experiments revealed that the presence of the $FeNi_3$ catalyst allows us to control the size distribution, giving rise to a monodisperse sample. XRPD and Raman spectroscopy demonstrate their graphitic nature, with an I_D/I_G ratio of *ca.* 0.80, therefore exhibiting a higher degree of graphitization than other spheres reported to date. Moreover, these CS can be individualized in toluene by means of sonication, beating the accretion effects. Furthermore, FIB-SEM experiments show that the inner structure of the spheres is solid and consists of concentric graphitic planes. Concerning their surface properties, nitrogen adsorption, XPS and electrochemical testing revealed the presence of redox functionalities on their surface behaving as appropriated electrode materials for supercapacitors despite their intrinsic non-mesoporous nature.

Finally, their transport properties have also been studied, exhibiting a semiconducting behaviour at low temperatures and a giant magnetoresistance of *ca.* 72% at 2 K and a voltage of 3 V. The MR was strongly dependent on the temperature and principally has a quadratic dependence, following an ordinary MR behaviour. These CS are promising candidates for polymer reinforcement and as building blocks for preparing more complex hybrid composites.

Acknowledgements

Financial support from the EU (FET-OPEN 2D-INK. Grant agreement 648786), the Spanish MINECO (Project MAT2014-56143-R), the Junta de Andalucía (PAI research group TEP-946 INNANOMAT) and the Generalitat Valenciana (Prometeo and ISIC-Nano Programs) is gratefully acknowledged. Co-funding from UE is also acknowledged. TEM measurements were carried

out at DME-SCCYT-UCA. We also acknowledge E. Bandiello for his help with the EIS experiments. We thank the Universidad de Valencia for support from VLC/CAMPUS and INNCIDE program, and for a predoctoral grant (to J. A. C.). G. A. thanks the EU for a Marie Curie Fellowship (FP7/2013-IEF-627386).

References

1 H. W. Kroto, J. R. Heath, S. C. O'Brien, R. F. Curl and R. E. Smalley, *Nature*, 1985, **318**, 162–163.
2 J. L. Delgado, M. Herranz and N. Martín, *J. Mater. Chem.*, 2008, **18**, 1417–1426.
3 A. W. Francis, *Ind. Eng. Chem.*, 1931, **23**, 612–617.
4 Z. C. Kang and Z. L. Wang, *J. Phys. Chem.*, 1996, **100**, 5163–5165.
5 P. Serp, R. Feurer, P. Kalck, Y. Kihn, J. L. Faria and J. L. Figueiredo, *Carbon*, 2001, **39**, 621–626.
6 M. Inagaki, *Solid State Ionics*, 1996, **86**, 833–839.
7 M. Inagaki, *Carbon*, 1997, **35**, 711–713.
8 Y. Xia, B. Gates, Y. Yin and Y. Lu, *Adv. Mater.*, 2000, **12**, 693–713.
9 A. A. Deshmukh, S. D. Mhlanga and N. J. Coville, *Mater. Sci. Eng., R*, 2010, **70**, 1–28.
10 A. Nieto-Márquez, R. Romero, A. Romero and J. L. Valverde, *J. Mater. Chem.*, 2011, **21**, 1664–1672.
11 *Carbon materials for catalysis*, ed. P. Serp and J. L. Figueiredo, John Wiley & Sons, Hoboken, N.J, 2009.
12 N. Fleischer, M. Genut and A. Gorodnev, *Am. Ceram. Soc. Bull.*, 2006, **85**, 27–28.
13 X. He, F. Wu and M. Zheng, *Diamond Relat. Mater.*, 2007, **16**, 311–315.
14 Y. Z. Jin, Y. J. Kim, C. Gao, Y. Q. Zhu, A. Huczko, M. Endo and H. W. Kroto, *Carbon*, 2006, **44**, 724–729.
15 F. P. Hu, Z. Wang, Y. Li, C. Li, X. Zhang and P. K. Shen, *J. Power Sources*, 2008, **177**, 61–66.
16 W. P. Wright, V. D. Marsicano, J. M. Keartland, R. M. Erasmus, S. M. A. Dube and N. J. Coville, *Mater. Chem. Phys.*, 2014, **147**, 908–914.
17 K. C. Mondal, A. M. Strydom, Z. Tetana, S. D. Mhlanga, M. J. Witcomb, J. Havel, R. M. Erasmus and N. J. Coville, *Mater. Chem. Phys.*, 2009, **114**, 973–977.
18 Y. Z. Jin, C. Gao, H. W. Kroto and T. Maekawa, *Macromol. Rapid Commun.*, 2005, **26**, 1133–1139.
19 H. Ismail, P. K. Freakley and E. Sheng, *Eur. Polym. J.*, 1995, **31**, 1049–1056.
20 H. Gu, X. Zhang, H. Wei, Y. Huang, S. Wei and Z. Guo, *Chem. Soc. Rev.*, 2013, **42**, 5907–5943.
21 C. Bosch-Navarro, F. Busolo, E. Coronado, Y. Duan, C. Martí-Gastaldo and H. Prima-Garcia, *J. Mater. Chem. C*, 2013, **1**, 4590–4598.
22 J. Wang, X. Zhang, C. Wan, J. Vanacken and V. V. Moshchalkov, *Carbon*, 2013, **59**, 278–282.
23 Z.-M. Liao, H.-C. Wu, S. Kumar, G. S. Duesberg, Y.-B. Zhou, G. L. W. Cross, I. V. Shvets and D.-P. Yu, *Adv. Mater.*, 2012, **24**, 1862–1866.
24 Y.-B. Zhou, B.-H. Han, Z.-M. Liao, H.-C. Wu and D.-P. Yu, *Appl. Phys. Lett.*, 2011, **98**, 222502.
25 J. Zhu, Z. Luo, S. Wu, N. Haldolaarachchige, D. P. Young, S. Wei and Z. Guo, *J. Mater. Chem.*, 2012, **22**, 835–844.
26 G. Abellán, C. Martí-Gastaldo, A. Ribera and E. Coronado, *Acc. Chem. Res.*, 2015, **48**, 1601–1611.
27 G. Abellán, E. Coronado, C. Martí-Gastaldo, A. Ribera and J. F. Sánchez-Royo, *Chem. Sci.*, 2012, **3**, 1481–1485.
28 G. Abellán, J. A. Carrasco, E. Coronado, J. P. Prieto-Ruiz and H. Prima-García, *Adv. Mater. Interfaces*, 2014, **1**, 1400184.
29 G. Abellán, J. G. Martínez, T. F. Otero, A. Ribera and E. Coronado, *Electrochem. Commun.*, 2014, **39**, 15–18.
30 G. Abellán, E. Coronado, C. Martí-Gastaldo, A. Ribera and T. F. Otero, *Part. Part. Syst. Charact.*, 2013, 853–863.
31 G. Abellán, E. Coronado, C. Martí-Gastaldo, E. Pinilla-Cienfuegos and A. Ribera, *J. Mater. Chem.*, 2010, **20**, 7451–7455.
32 R. Langford and C. Clinton, *Micron*, 2004, **35**, 607–611.
33 Y. Li, J. Chen, Q. Xu, L. He and Z. Chen, *J. Phys. Chem. C*, 2009, **113**, 10085–10089.
34 Y. Z. Jin, C. Gao, W. K. Hsu, Y. Zhu, A. Huczko, M. Bystrzejewski, M. Roe, C. Y. Lee, S. Acquah, H. Kroto and D. R. M. Walton, *Carbon*, 2005, **43**, 1944–1953.
35 V. G. Pol, M. Motiei, A. Gedanken, J. Calderon-Moreno and M. Yoshimura, *Carbon*, 2004, **42**, 111–116.
36 L. C. Yang, Y. Shi, Q. S. Gao, B. Wang, Y. P. Wu and Y. Tang, *Carbon*, 2008, **46**, 1816–1818.
37 A. Nieto-Márquez, D. Toledano, J. C. Lazo, A. Romero and J. L. Valverde, *Appl. Catal., A*, 2010, **373**, 192–200.
38 H. Qian, F. Han, B. Zhang, Y. Guo, J. Yue and B. Peng, *Carbon*, 2004, **42**, 761–766.
39 M. Liu, L. Gan, W. Xiong, Z. Xu, D. Zhu and L. Chen, *J. Mater. Chem. A*, 2014, **2**, 2555–2562.
40 M. Liu, L. Gan, W. Xiong, F. Zhao, X. Fan, D. Zhu, Z. Xu, Z. Hao and L. Chen, *Energy Fuels*, 2013, **27**, 1168–1173.
41 Y. J. Kim, M. I. Kim, C. H. Yun, J. Y. Chang, C. R. Park and M. Inagaki, *J. Colloid Interface Sci.*, 2004, **274**, 555–562.
42 W. Li, D. Chen, Z. Li, Y. Shi, Y. Wan, G. Wang, Z. Jiang and D. Zhao, *Carbon*, 2007, **45**, 1757–1763.
43 D. Fujikawa, M. Uota, T. Yoshimura, G. Sakai and T. Kijima, *Chem. Lett.*, 2006, **35**, 432–433.
44 M. Liu, J. Qian, Y. Zhao, D. Zhu, L. Gan and L. Chen, *J. Mater. Chem. A*, 2015, **3**, 11517–11526.
45 M. Liu, X. Ma, L. Gan, Z. Xu, D. Zhu and L. Chen, *J. Mater. Chem. A*, 2014, **2**, 17107–17114.
46 D. Zhu, Y. Wang, L. Gan, M. Liu, K. Cheng, Y. Zhao, X. Deng and D. Sun, *Electrochim. Acta*, 2015, **158**, 166–174.
47 F. Beguin and E. Frackowiak, *Supercapacitors: Materials, Systems and Applications*, John Wiley & Sons, 2013.
48 X. Ma, L. Gan, M. Liu, P. K. Tripathi, Y. Zhao, Z. Xu, D. Zhu and L. Chen, *J. Mater. Chem. A*, 2014, **2**, 8407–8415.
49 W. Yang, Y. Feng, D. Xiao and H. Yuan, *Int. J. Energy Res.*, 2015, **39**, 805–811.
50 Y. Gao, Y. S. Zhou, M. Qian, X. N. He, J. Redepenning, P. Goodman, H. M. Li, L. Jiang and Y. F. Lu, *Carbon*, 2013, **51**, 52–58.
51 N. F. Mott, *Philos. Mag.*, 1969, **19**, 835–852.
52 N. F. Mott and M. Kaveh, *Adv. Phys.*, 1985, **34**, 329–401.

Supplementary Information

CVD Synthesis of Carbon Spheres using NiFe-LDHs as Catalytic Precursors. Structural, electrochemical and magnetoresistive properties.

Jose A. Carrasco,[a] Helena Prima-Garcia,[a] Jorge Romero,[a] Jesús Hernández-Saz,[b] Sergio I. Molina,[b] Gonzalo Abellán,[a,c,*] and Eugenio Coronado[a,*]

[a] *Instituto de Ciencia Molecular (ICMol), Universidad de Valencia, Catedrático José Beltrán 2, 46980, Paterna, Valencia, Spain.*

[b] *Departamento de Ciencia de los Materiales e Ingeniería Metalúrgica y Química Inorgánica, IMEYMAT, Universidad de Cádiz, 11510 Puerto Real, Cádiz, Spain.*

[c] *Department of Chemistry and Pharmacy and Institute of Advanced Materials and Processes (ZMP), University Erlangen-Nürnberg, Henkestr. 42, 91054 Erlangen and Dr.-Mack Str. 81, 90762 Fürth, Germany.*

Contents

SI 1. Characterization of carbon spheres before the annealing process.

SI 1.1. FESEM and HRTEM microscopy.

(A) Selected FESEM image of the original (before the thermal treatment) carbon spheres. (B) HRTEM showing the chain-like disposition due to accretion effects. (C) Histogram of 50 spheres displaying the average diameter taken from FESEM images.

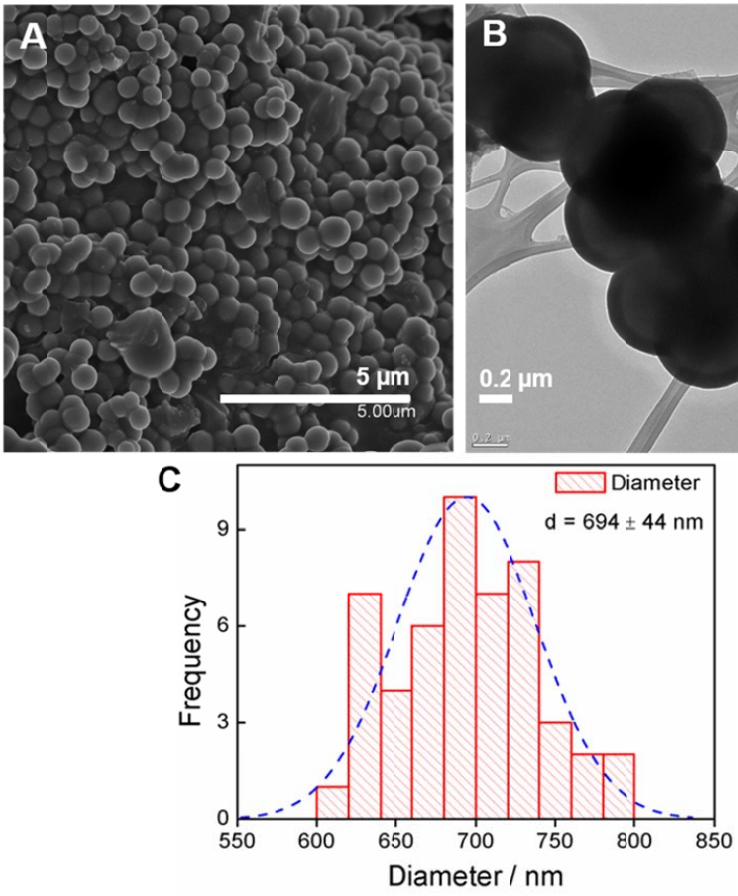

SI 1.2. XRPD.

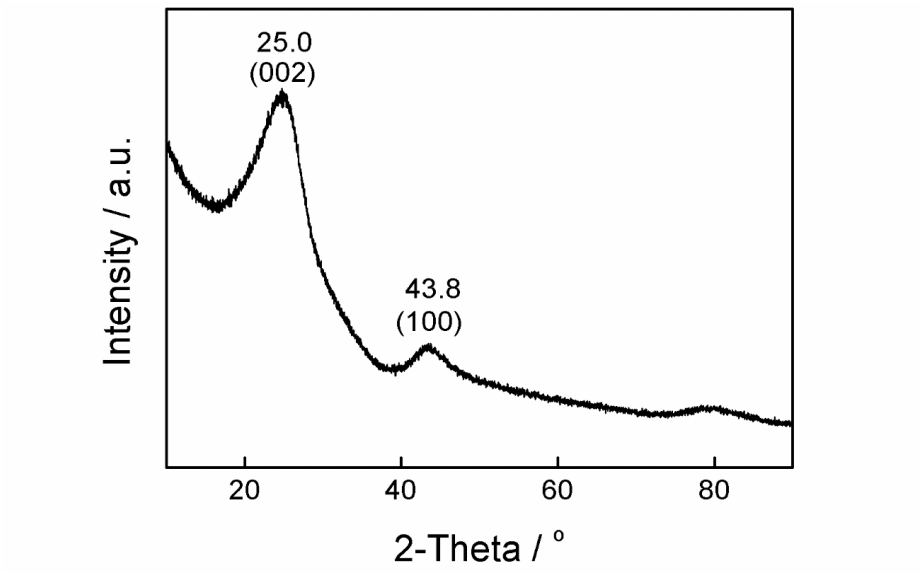

SI 1.3. Thermogravimetric analysis (TGA) in air and N_2.

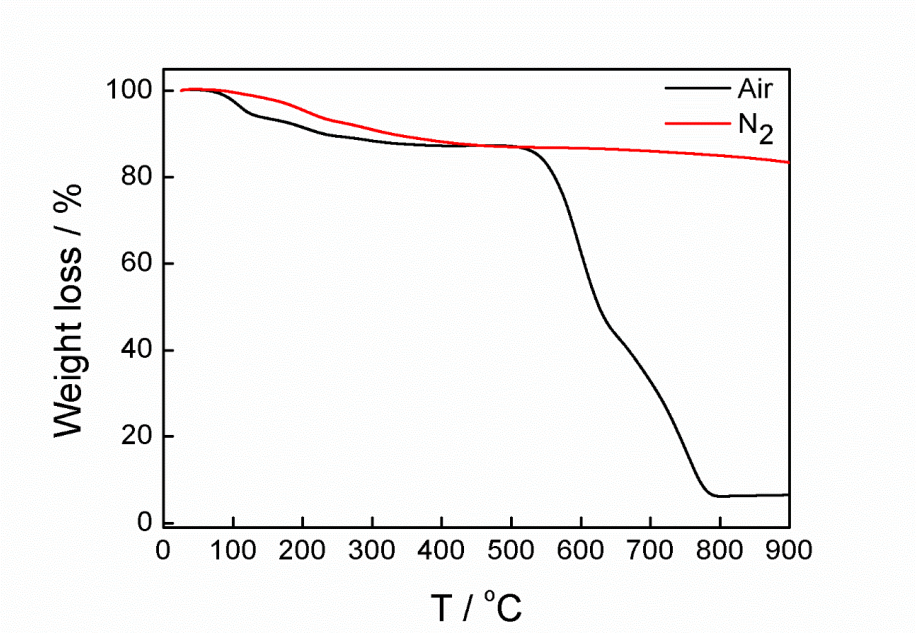

In air atmosphere, the combustion temperature of *ca.* 595 ^{o}C, as obtained from the DTA, is in good agreement within the range of carbon nano-spheres based on the classification of Serp *et al*. according to the maximum of gasification rate.[1]

SI 2. Characterization of control experiments.

SI 2.1. Calcination of NiFe-LDH.

A control experiment at 900 ^{o}C with a scan rate of 5 $^{o}C \cdot min^{-1}$ was carried out in absence of ethylene (therefore only supplying H_2 as the reducing agent) to elucidate the species formed after the calcination procedure. The following XRPD spectrum compares both the pristine and the calcined LDH:

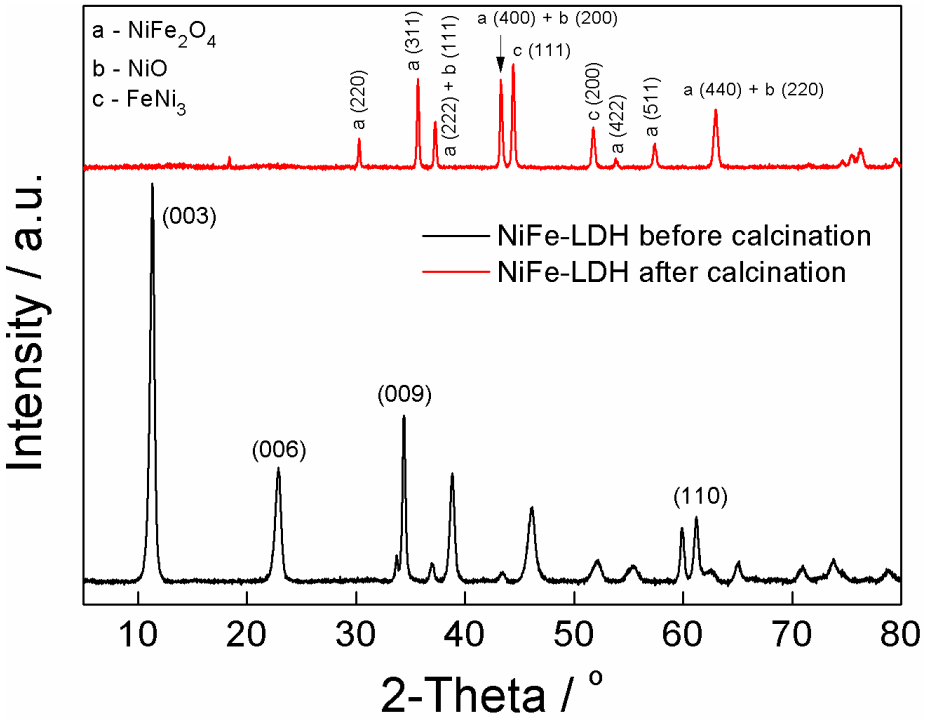

The spectra exhibit the formation of a mixture of three phases: $NiFe_2O_4$, NiO and $FeNi_3$ alloy.

Another control experiment in absence of both H_2 and C_2H_4 only depicts the presence of $NiFe_2O_4$ and NiO:

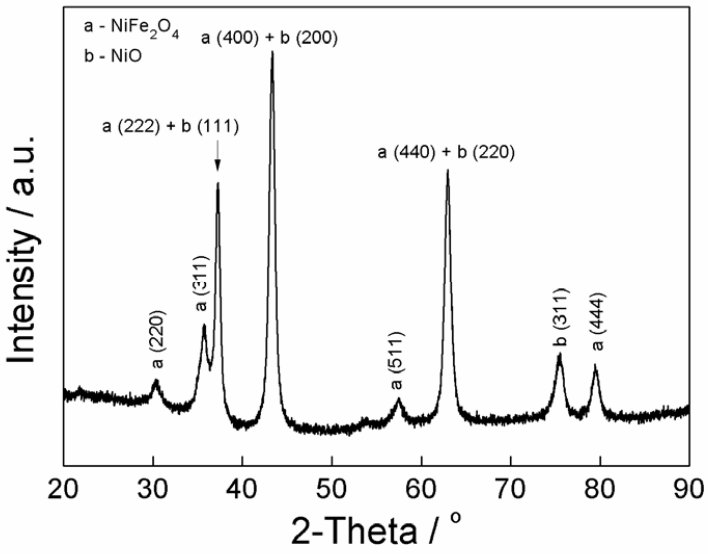

Since the $FeNi_3$ alloy only appears in the presence of a reduction agent, we can conclude that is the main catalytic specie responsible for the carbon nanoform growing. For further information in the characterization and study of related control experiments, see ref [2].

SI 2.2. Carbon Spheres

SI 2.2.1. FESEM microscopy.

Both images depict the formation of carbon spheres with a wide range of diameters, from *ca.* 700 – 800 nm for the smallest ones to several microns for the biggest spheres. The latter ones are formed by accumulation effects, displaying a caterpillar-like morphology.

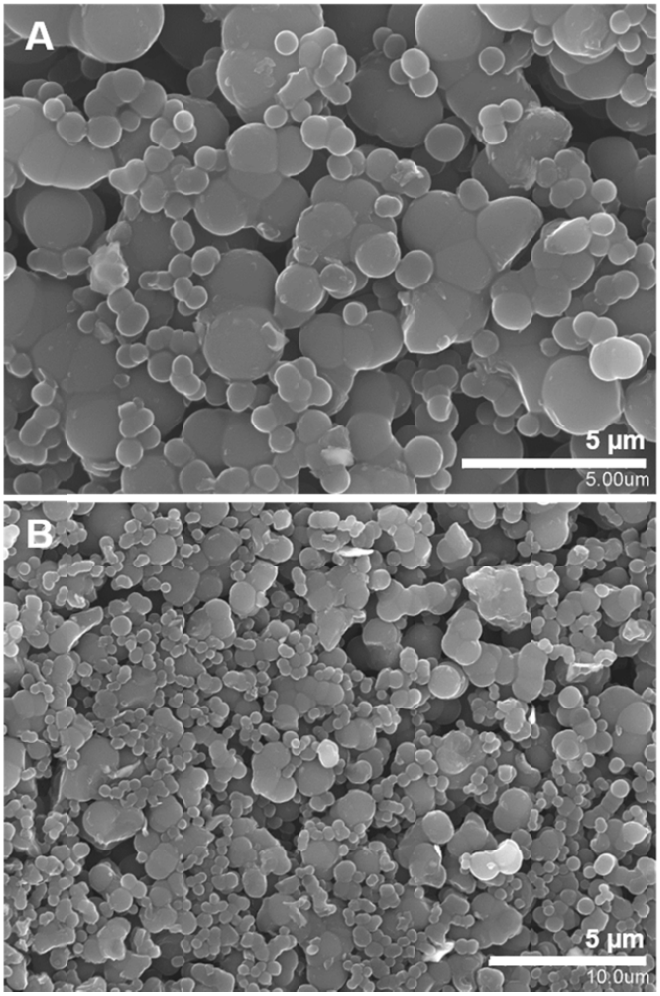

SI 2.2.2. XRPD

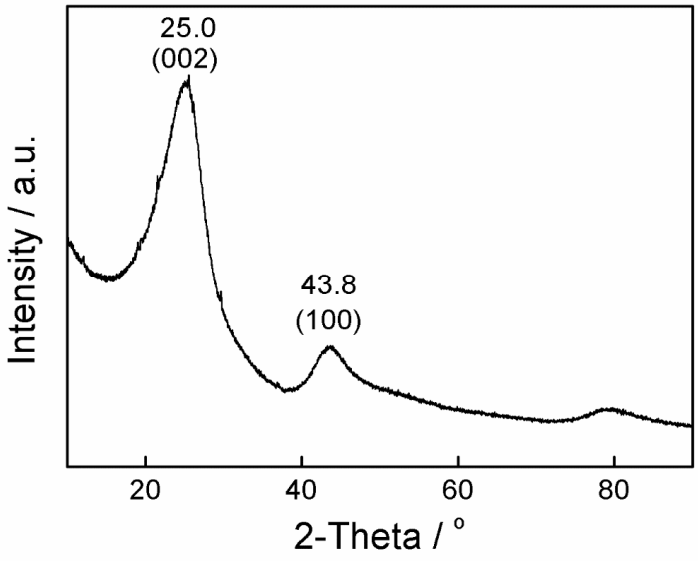

SI 2.2.3. Thermogravimetric analysis (TGA) in air and N_2.

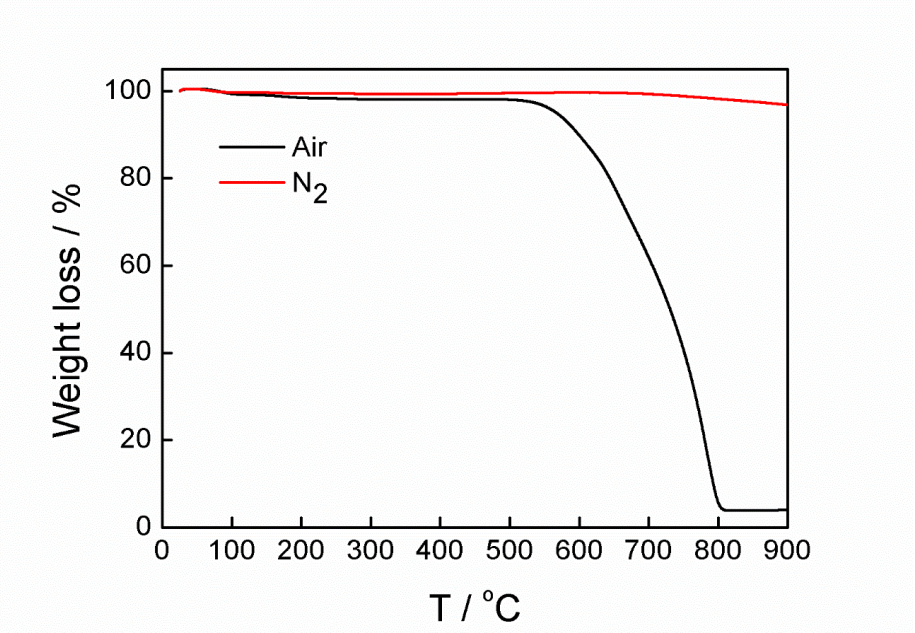

The combustion temperature of *ca.* 600 °C in air atmosphere (obtained from the DTA), is in good agreement within the range of carbon nano-spheres according to the classification of Serp *et al*. on the basis of the maximum of gasification rate.[1]

SI 3. **Raman spectra comparison.**

Raman spectra for (a) the control experiment at 900 ºC and the carbon spheres (b) before and (c) after the thermal treatment at 800 ºC. All spectra for the different samples display two peaks centered at *ca.* 1354 and 1600 cm^{-1}, related with the D (disorder) and G (order) band, and an I_D/I_G of *ca.* 0.8.

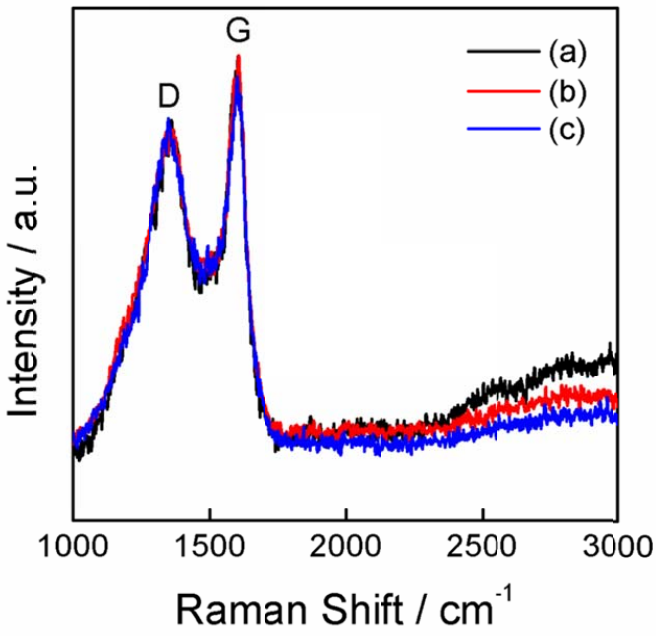

SI 4. DTA analysis of CS in air.

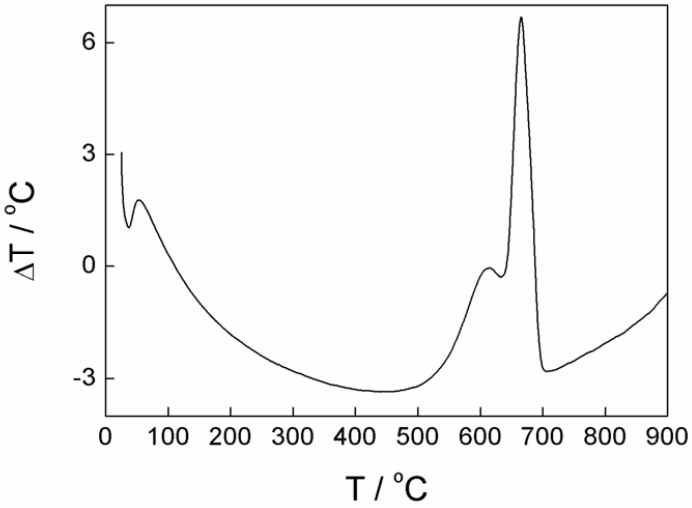

SI 5. Additional microscopy images of CS and accretion effects.

(A) FESEM image showing the average diameter of the spheres of *ca.* 700 – 800 nm, as depicted in the main article. (B) FESEM image in low magnification (3000x) displaying a large selected area of carbon spheres and highlighting some bigger spheres formed by an accretion process. The average diameter of the accreted carbon spheres is about 1.5 – 2.0 µm. (C) FIB-SEM image showing a milled region. (D) FIB-SEM cross-section image of the same region of (C) depicting the solid inner structure.

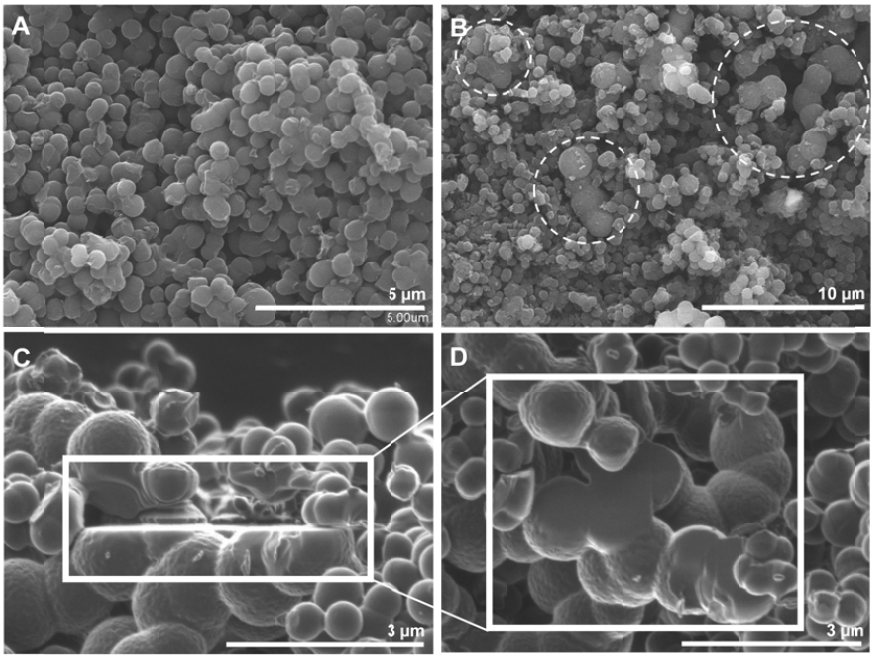

SI 6. XPS of carbon spheres.

SI 6.1. XPS of carbon spheres synthesized at 900 °C and 1000 °C.

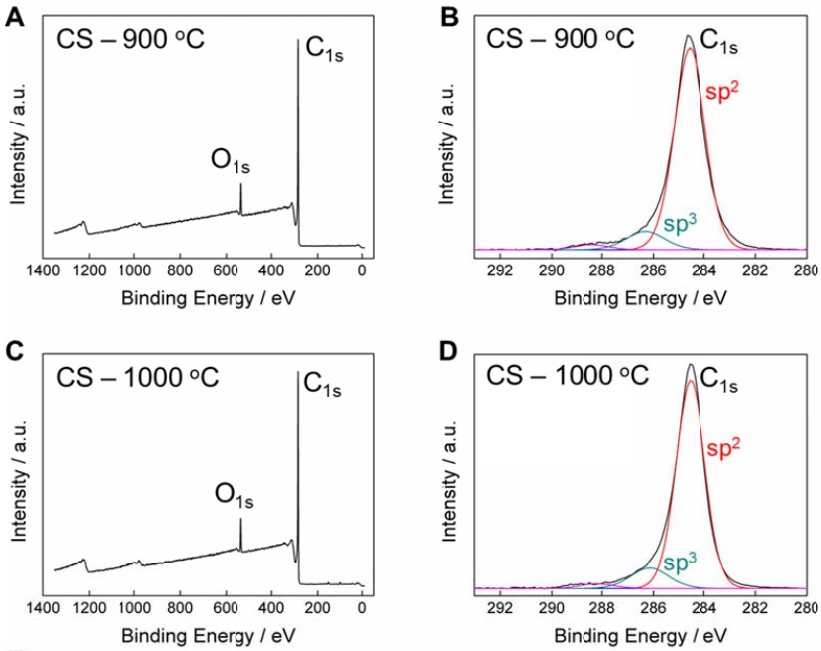

E

Atomic %	CS – 900 °C	CS – 1000 °C
C	91,66	92,68
N	0,36	0,24
O	7,98	7,09

(A) Survey and (B) C_{1s} spectrum of carbon spheres synthesized at 900 °C. (C) Survey and (D) C_{1s} spectrum of carbon spheres synthesized at 1000 °C. (E) Comparative table with atomic percentages between both spheres.

SI 6.2. XPS spectra of the Fe 2p and Ni 2p core-levels in **CS** (900 ^{o}C).

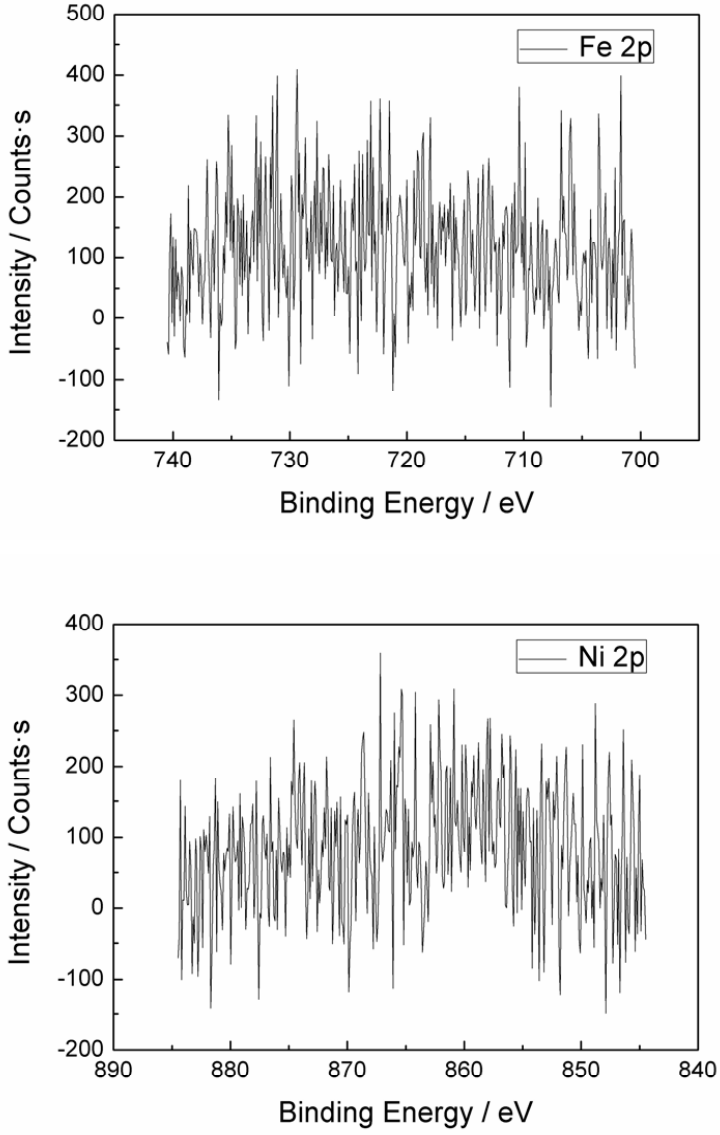

SI 7. FIB-SEM sequential steps of the lift-out procedure.

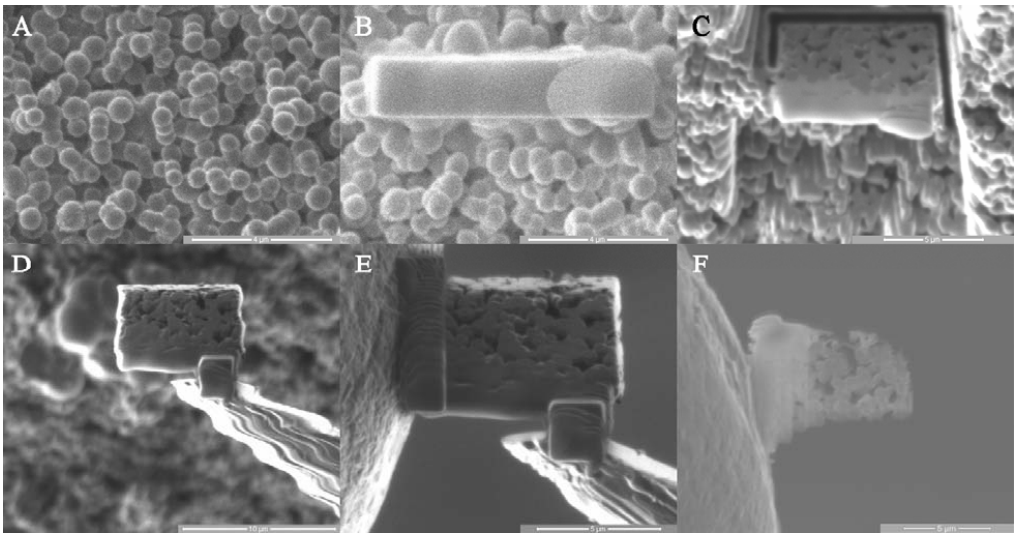

(A) select a localization, (B) deposit a platinum layer, (C) mill trenches (tilted view), (D) lamella attached to the micromanipulator, (E) lamella attached to the TEM grid and the micromanipulator and (F) lamella thinned down to electron-transparency. From (A) to (E) are FIB images and (F) is a SEM image.

SI 8. Differential pore volume distribution by DFT of CS.

DFT method summary

Pore volume = 0.009 $cc \cdot g^{-1}$

Surface area = 14.684 $m^2 \cdot g^{-1}$

Lower confidence limit = 10.960 Å

Fitting error = 0.410 %

Pore width (Mode) = 10.960 Å

The model which has been used is "QSDFT-N_2-carbon adsorption branch at 77 K based on a slit/cylinder pores" obtained from www.quantachrome.com/technical/dft.html, and in good agreement with similar samples in literature.[3,4] Differential pore volume distribution by DFT is represented in the following plot:

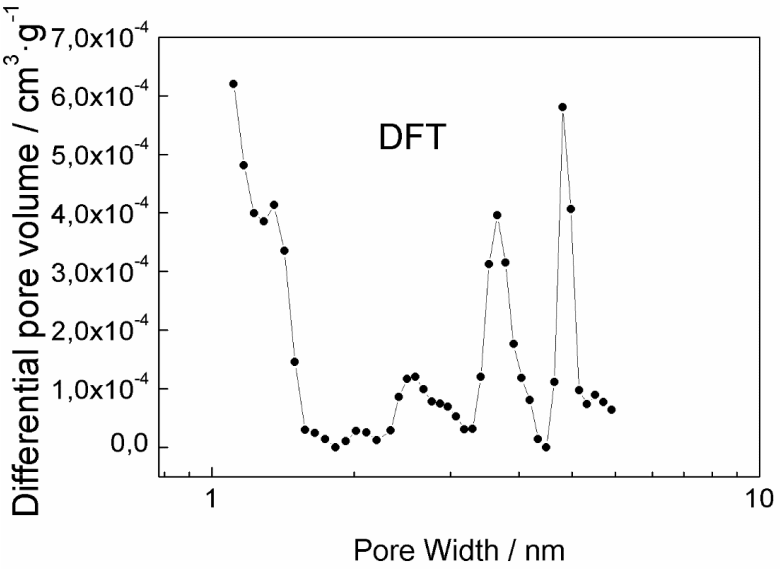

The low value of pore volume suggests the presence of ultramicropores. [3,4]

SI 9. Electrochemical properties of carbon spheres synthesized at 1000 ^{o}C.

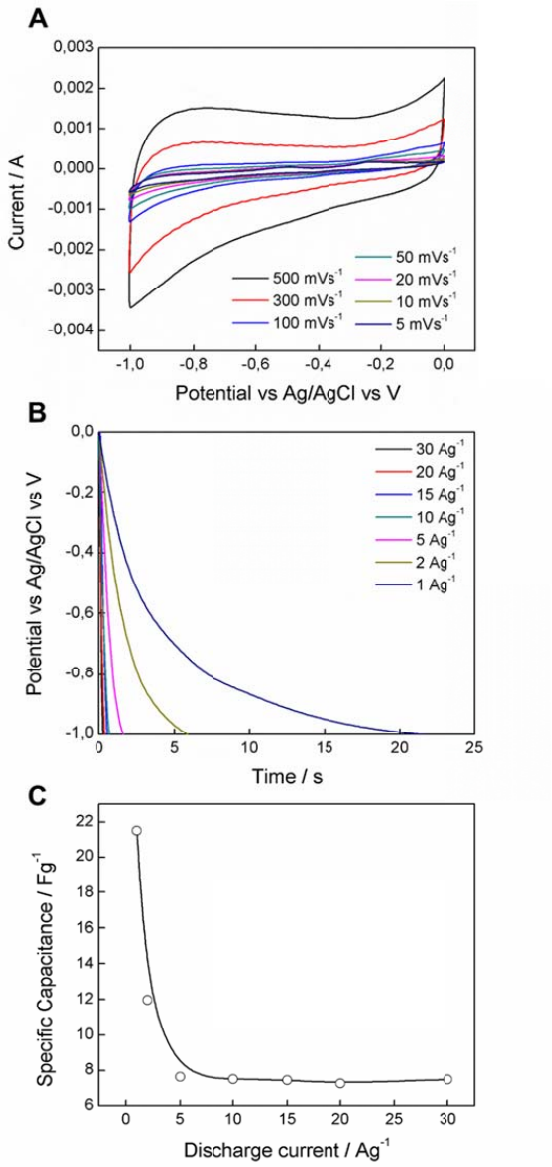

(A) CV curve at various scan rates in a 6 M KOH aqueous solution. (**B**) Galvanostatic discharge curves at different discharge current densities. (C) Specific capacitance of the material at different discharge current densities.

SI 10. Fit the magnetoresistance curves with the relation MR ∝ $(\mu_0 \cdot \mu \cdot |H|)^2$.

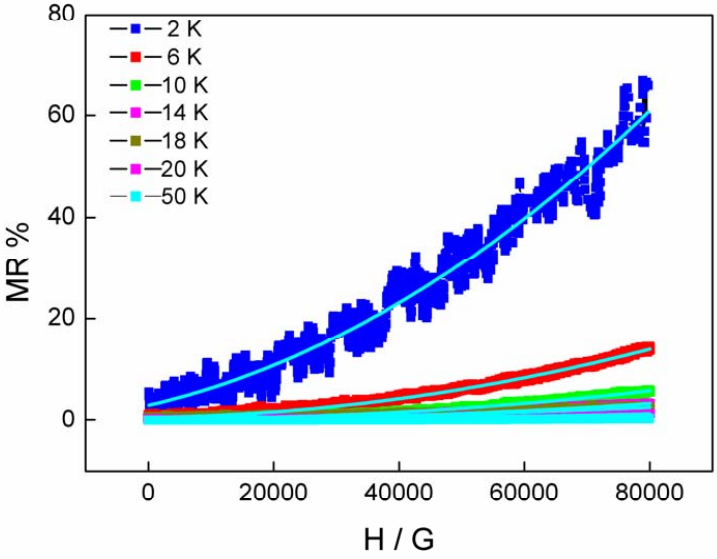

SI 11. Magnetic temperature dependence of CS.

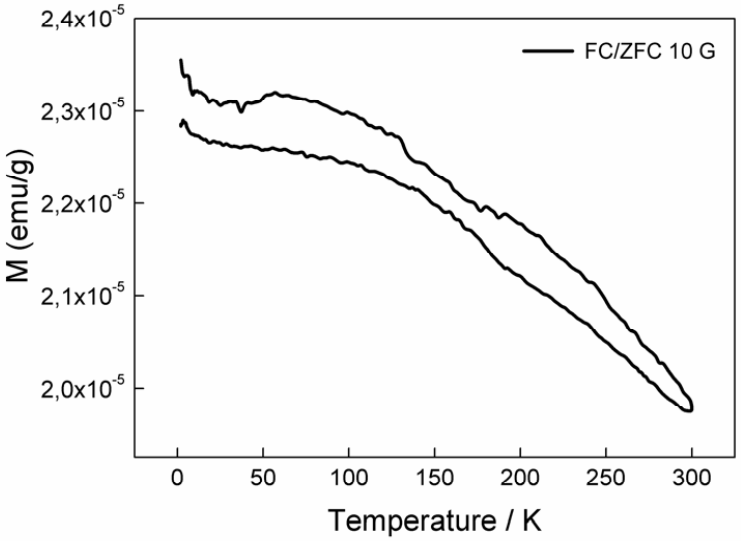

SI 12. Magnetoresistance dependence with the temperature.

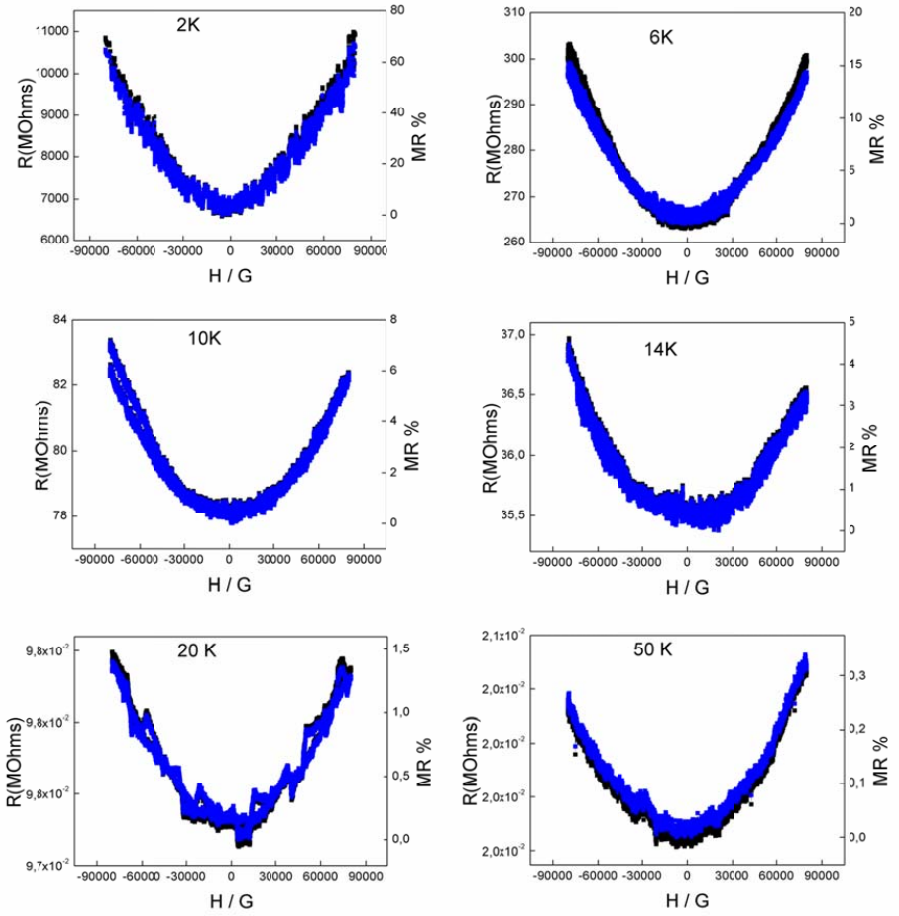

SI 13. Additional References.

1 P. Serp, R. Feurer, P. Kalck, Y. Kihn, J. L. Faria and J. L. Figueiredo, *Carbon*, 2001, **39**, 621–626.

2 G. Abellán, J. A. Carrasco, E. Coronado, J. P. Prieto-Ruiz and H. Prima-García, *Adv. Mater. Interfaces*, 2014, **1**, 1400184.

3 Y. Han, X. Dong, C. Zhang and S. Liu, *J. Power Sources*, 2012, **211**, 92–96.

4 N. P. Wickramaratne, J. Xu, M. Wang, L. Zhu, L. Dai and M. Jaroniec, *Chem. Mater.*, 2014, **26**, 2820–2828.

Book Chapter**:**

Layered Double Hydroxide Nanocomposites Based on Carbon Nanoforms

Chapter 9 in *Layered Double Hydroxide Polymer Nanocomposites;*
Ed. Woodhead Publishing, Cambridge, **2019**

Book Chapter is currently in copyediting process. Therefore, an acceptance letter is included.

Elsevier
The Officers' Mess Business Centre
Royston Road
Duxford
Cambridge
CB22 4QH

07.06.2018

Dear Jose Alberto Carrasco

The purpose of this letter is to confirm your recent contribution to one of our titles in the Woodhead Publishing Series in Composites Science and Engineering. The book, '*Layered Double Hydroxide Polymer Nanocomposites',* edited by Sabu Thomas, Saju Daniel, ISBN 9780081022610, is now in production and the planned pub date is January 2019.

I can confirm that you are one of the named authors of the chapter Layered Double Hydroxide Nanocomposites Based on Carbon Nanoforms,' comprising of approximately 14,747 words.

I would like to take this opportunity to thank you for your hard work to reach this point, producing a first-rate title and a distinguished addition to the Woodhead Publishing list.

Kind Regards,

Andrea Gallego Ortiz, PhD
Senior Editorial Project Manager | ELSEVIER
The Officers' Mess Business Centre, Royston Road, Duxford, Cambridge, CB22 4QH, UK
Tel: + 44 (0)1223 381625 | **Email:** a.gallegoortiz@elsevier.com

Layered Double Hydroxide Nanocomposites Based on Carbon Nanoforms

Gonzalo Abellán, Jose A. Carrasco and Eugenio Coronado*

1. A general introduction to carbon nanoforms/LDH nanocomposites.

Layered Double Hydroxides (LDHs) are anionic clays built from the stacking of positively charged brucite-type inorganic layers interleaved with anions. They can be formulated as $[M^{z+}_{1-x}M^{y+}_{x}(OH)_2]^{x+}[A^{n-}]_{x/n}\cdot mH_2O$ (M^{z+}, z = 1 or 2; M^{y+}, y = 3 or 4; A^{n-} = organic or inorganic anions). Synthetic LDHs are quite promising based on their low cost, chemical versatility and anion exchange capabilities, which allows for tuning of their composition and properties in a wide range.[1,2] Thanks to their layered nature, they can be also exfoliated in polar organic solvents by intercalation of suitable anions that minimize the interaction between layers to produce stable colloids containing single and few-layers LDHs, which possess ultrahigh surface areas of ca. 1000 $cm^2\cdot g^{-1}$ in theory.[3] These positively charged nanosheets can then be used as inorganic building blocks in the design of hybrid nanocomposites when mixed with other organic or molecular materials. In this context, an interesting ingredient of these nanocomposites is provided by the so-called carbon nanoforms (CNFs). These carbon-based materials include a wide variety of sizes and shapes ranging from C_{60} to metallofullerenes, carbon fibers, nanotubes, nano-onions, nanohorns, nanobuds, spheres or graphene, among others.[4] Owing to their low-dimensional nature and sp^2 hybridization of carbon atoms, and because of the sheer multitude of their aesthetically pleasing structures, 0D fullerenes, 1D carbon nanotubes (CNTs), and 2D graphene, exhibit excellent physical and chemical properties, and stands as one of the most appealing building blocks in the development of nanocomposites. For instance, graphene,[5,6] a one-atom-thick layer of graphite, is a semimetal, gapless two-dimensional (2D) semiconductor with unprecedented properties including ultrahigh room-temperature carrier mobility, or specific surface area (2630 $m^2\cdot g^{-1}$, in theory). Moreover, graphene is an elastic film, with a high Young's modulus (*ca*. 1.0 GPa),[7] it is transparent like (or better than) plastic,[5] and possesses outstanding electrical (*ca*. 10^6 $S\cdot cm^{-1}$)[8] and thermal (3000–5000 $W\cdot m^{-1}\cdot K^{-1}$)[9] conductivities, better than any metal. Additionally, it behaves as an impermeable membrane,[10] and can be considered as both a solid and a macromolecule with molecular weights of more than 10^6–10^7 $g\cdot mol^{-1}$.[11] Graphene also exhibits a rich chemical phenomenology that ranges from supramolecular to covalent functionalization, endowing them with improved processability as well as allowing to controllably engineer the bandgap structure, create novel architectures, and manipulate the interfacial characteristics of this monolayer material.[11–15]

When it comes to nanocomposite formation, the limited solubility of pristine graphene is one of the main drawbacks. Along this front, negatively charged graphene oxide (GO) is usually employed as a very effective alternative. GO is a single layer of graphite oxide.

During the formation of graphite oxide, the graphene layers in graphite become intercalated by an acid to form a stage 1 intercalation compound, with all layers being intercalated.[11] Subsequent oxygenation of such stage1 intercalation compounds occurs on both sides of the basal plane and in this way graphite oxide is formed. Delamination of single layers of graphite oxide leads to GO. The exact nature of the functional groups in GO strongly depends on the reaction conditions, such as preparation time and temperature as well as on the work-up procedure. Typically, GO consists of about 45 mass% carbon. Although several structure models have been proposed, GO is a rather polydisperse material, whose exact structure is very difficult to precisely define. The mobility of charge carriers depends on the density of defects and therefore, mobility values range between 0.1 and 1000 $cm^2\ V^{-1}\ s^{-1}$, a very limited values compared to that of pristine graphene, which usually exceeds 15000 $cm^2 \cdot V^{-1} \cdot s^{-1}$. In any case, its excellent processability has allowed the development of the first examples of graphene/LDH hybrid nanocomposites.

With respect to 1D CNTs –which can exists with various flavours (*i.e.* broad variation of helicities, single walled, multiwalled)– they possess a low bandgap of 0–1.9 eV, high electrical conductivity of $0.17–2 \cdot 10^5\ S \cdot cm^{-1}$,[16] and high thermal conductivity of 3000–6600 $W \cdot m^{-1} \cdot K^{-1}$.[17] In addition, their excellent mechanical properties with Young's moduli of 0.27–1.25 GPa and a tensile strength of 11–63 GPa,[18] makes them excellent candidates for functional nanocomposite reinforcement.

In stark contrast, LDHs exhibit an insulating behaviour, low to moderate specific surfaces areas ranging from 20–365 $m^2 \cdot g^{-1}$, but a rich redox chemical behaviour.[3] The incorporation of transition metals in synthetic LDHs endowed them with excellent redox properties, extremely interesting in energy conversion and storage. Moreover, they can accommodate different metals in a well-defined atomic arrangement within the layers, a property that has been extensively used in heterogeneous catalysis. But LDH are not only interesting as active materials *per se*, but also as functional precursors of layered mixed metal oxides or spinels, of utmost importance in catalysis or magnetism.[19,20]

Probably, the most interesting property of LDHs is their anion-exchange ability.[1] LDH are capable of accommodating a multitude of inorganic and organic anions, including complex macrocycles, polymers, or even DNA strands.[2] This allows the synthesis of hybrid functional materials with the coexistence, and in some cases, even interaction of different properties.[20–23] Additionally, LDH submitted to calcination at moderate temperatures exhibit the so called "memory effect", enabling the reconstruction of the initial solids in the presence of anions. This effect has been extensively used for environmental remediation and controlled delivery of anions.[24]

The intrinsic limitations of LDH, mainly due to its poor conductivity, can be overcome by its combination with highly conducting carbon nanoforms, in the same way as the rich chemical reactivity of LDH perfectly complements the limited redox behaviour of carbon nanoforms. In this sense, the design and synthesis of hierarchical nanocomposites is one of the most interesting approaches for combining their distinguishing properties together creating multifunctional hybrid materials endowed with high mechanical strength and hierarchical porosities, as well as improved heat and mass transfer properties.[25,26] The combination of LDH with different carbon nanoforms have attracted an increasing level of attention during the last years due to their outstanding properties in different fields ranging from polymer reinforcement and environmental remediation, to catalysis or energy storage and conversion.

Table 1 summarizes some properties of CNFs and LDHs, and **Figure 1** depicts a schematic illustration of a LDH material combined with the most typical CNFs. Along this line, **Table 2** depicts the most typical LDH combination of metals and the capability of these inorganic layers to be mixed with CNFs giving rise to nanocomposites.

Table 1. Properties of different carbon nanoforms materials and LDHs. Adapted from Ref. 27 and extended with new data for graphene oxide.

Properties	Fullerenes[28–30]	CNTs[18,31–36]	Graphene[5,7–9]	Graphene Oxide[37–42]	LDHs[3]
Young´s modulus /GPa	15.9	0.27 – 1.25	*ca.* 1.0	380 – 470	/
Tensile strength /GPa	/	11 – 63	130	130	/
Band gap /eV	1.5 – 2.0	0 – 1.9	0	0.1 – 4	/
Electrical conductivity /S·cm^{-1}	10^{-14} – $6{\cdot}10^{-8}$	0.17 – $2{\cdot}10^{5}$	*ca.* 10^{6}	$1{\cdot}10^{-3}$ – 2	Insulating (~62 S·cm^{-1} for calcined CoNi-LDH)
Thermal conductivity /W·m^{-1}·K^{-1}	0.4	3000 – 6600	3000 – 5000	*ca.* 5000	/
Specific surface area /m^2·g^{-1}	/	150 – 1315	2630	736.6	20 – 365
Chemical reactivity	Active	Active	Active	Active (redox)	Active (redox)

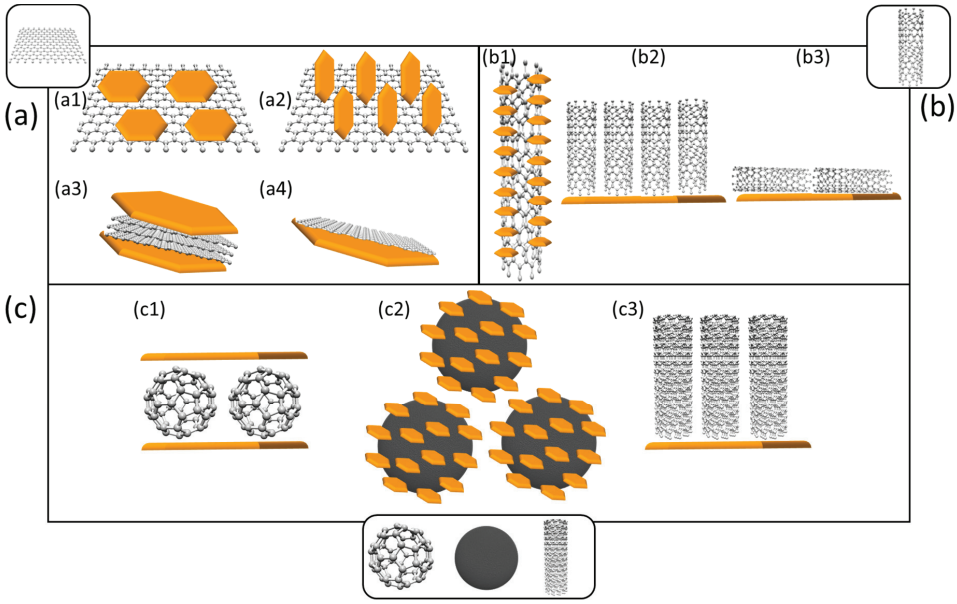

Figure 1. Schematic illustration with some of the most typical nanocomposites between LDH and CNFs. (a) Nanocomposites with graphene: (a1) *in situ* growth of LDH flakes parallel or (a2) vertical to the graphene layer, (a3) intercalation of graphene layers into the interlayer space of the LDH and (a4) graphene growth on the surface of the LDH crystallite. (b) Nanocomposites with carbon nanotubes: (b1) *in situ* growth of LDH flakes in the surface of CNTs, (b2) *in situ* growth of CNTs vertical or (b3) parallel aligned to the LDH surface. (c) Nanocomposites with, from left to right, fullerene, carbon spheres and carbon fibers: (c1) direct assembly between LDH flakes and fullerenes located into the interlayer space, (c2) *in situ* growth of LDH crystallites on the surface of carbon spheres and (c3) *in situ* growth of carbon fibers vertical aligned to the surface of the LDH flakes.

Table 2. Most representative LDH compositions and its capability for synthesizing the main CNFs are labelled as follows: G (graphene), T (carbon nanotubes), F (fullerene), QD (carbon quantum dots), CS (carbon spheres) and F (carbon fibers).

M^{3+},M^{4+}/M^{2+},M^{+}	Fe^{2+}	Co^{2+}	Ni^{2+}	Cu^{2+}	Zn^{2+}	Ca^{2+}	Mg^{2+}	Mn^{2+}	Li^{+}
Fe^{3+}		G, T, F	G, T, QD, CS						
Co^{3+}			G, T, F		G				
Ni^{3+}		F							
Al^{3+}		G, T, CS, F	G, T, QD, CS		G, T		G, T, F, CS	G	
Cr^{3+}					G				
Mn^{3+}		T, F	G, T						
Ga^{3+}									
In^{3+}									
Ti^{4+}			G						

	Synthesized catalytic LDH		LDHs without catalytic activity for nanocarbon growth		Not synthesized

There are different synthetic approaches for the preparation of carbon nanoform/LDH hybrids.[27] We can divide them into three main families, graphene/LDH; CNT/LDH, and other nanocomposites combining LDHs with carbon nanoforms like fullerenes, carbon spheres or mesoporus carbons. **Figure 1** summarizes the most common synthetic approaches pursued in the literature to prepare these systems. Firstly, based on the strong electrostatic interactions between exfoliated positively charged LDH nanosheets[43] and negatively charged CNFs, the reassembly of nanocarbons and LDH is one of the most extensively used approaches for the synthesis of LDH/carbon hybrids.

Secondly, owing to the strong adsorption ability of negatively charged CNFs for metal cations, their surface is perfectly suited for the direct seed nucleation and growth of LDH crystallites under basic pHs by means of coprecipitation or hydrothermal methods.[19,44,45]

Finally, LDH can act as either as a catalytic support for the in-situ formation of CNFs (employing chemical vapour deposition (CVD) using a carbon source like ethylene), or even as multilayer nanoreactors, where carbon-rich molecules are intercalated within LDH; the calcination of these systems leads to the formation of hybrid nanocomposites.[19,46–48]

In the first part of this review we will discuss in detail the synthetic routes pursued to prepare LDH/Carbon nanocomposites focusing first on 2D graphene, then on 1D CNT, and finally on other CNFs. In the second part we will give an overview of the main applications of these nanocomposites in areas like energy storage and conversion and catalysis

2. Graphene and graphene oxide/LDH Nanocomposites.

As previously mentioned, all the examples of graphene/LDH nanocomposites developed in the literature using the reassembly of 2D building blocks have employed graphene oxide (GO) instead of pristine graphene, owing to its good processability and negatively charged surface. The reduction of GO can be performed by thermal or chemical treatment with reducing reagents like hydrazine, leading to rGO. The exfoliation of LDH leads to positively charged nanosheets with a unilamellar thickness (<1 nm) and ultimate 2D anisotropy (aspect ratio >100). The ideal perfect assembly should consists of electrostatic face-to-face stacking of positively charged LDH nanosheets and negatively charged GO in alternating sequence at a molecular scale. However, due to the large disparity of particle sizes and intrinsic polydisperse nature of GO, a perfect sandwich-like hybrid remains a big challenge.[49,50]

The first self-assembled graphene/LDH nanocomposite ever described was developed in 2010.[51] In that work, Li *et al.* synthesized a film of graphene and CoAl-LDH. Both halves were previously exfoliated and delaminated and then reassembled into the final nanocomposite. Graphene/LDH nanocomposites with different compositions such as NiAl-,[49] NiCo-[52] or CoAl-[53] have been described and applied as feasible supercapacitors, giving rise to excellent performance in terms of energy storage behaviour, higher specific capacitance and longer life cycles than the expected for the separated materials.

2.1. Synthesis.

As mentioned above, we can classify the synthetic methods in three main branches namely, reassembly of LDHs and graphene, direct growth of LDH on graphene and formation of graphene in LDH layers:

2.1.1. Reassembly of graphene and LDHs.

This synthetic methodology lies in the self-assembly of pre-exfoliated 2D building blocks in solution leading to the final restacked material, or in a layer-by-layer assembly on selected substrates[54,55] (**Figure 2**).

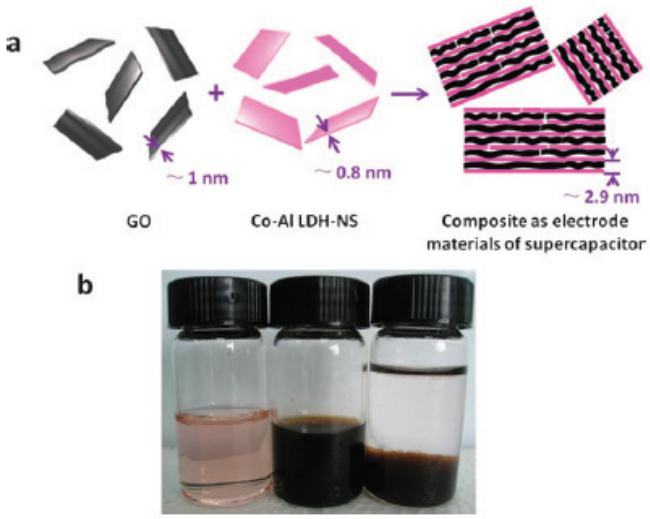

Figure 2. (a) Scheme with the formation of a CoAl-LDH and graphene oxide (GO) nanocomposite. (b) Digital photographs of an aqueous dispersion of CoAl-LDH (left), of GO (middle) and the GO/CoAl-LDH nanocomposite (right). Reproduced from Ref. 53 with permission from the Royal Society of Chemistry.

The exfoliation-restacking synthesis is based on the delamination of LDH previously intercalated with labile anions such as chlorides, nitrates or surfactants prior to the combination with GO through electrostatic interactions.[56] The main problem associated to the delamination of LDHs is the great facility in which the exfoliated nanosheets tend to reassemble, due to the electrostatic interactions between the cationic hydroxide layers and the interlamellar anions.[57] At the moment, no exhaustive studies have been carried out on the full optimization of the liquid-phase exfoliation (LPE)[58,59] of LDHs, in contrast with the exfoliation of other 2D materials like graphene, transition metal dichalcogenides or simple metal hydroxides which have been fully addressed.[60] To avoid the inherent

problems LDHs have in terms of delamination, polar aprotic solvents like formamide[61] or bulky amphiphilic interlamellar anions such as surfactant molecules (specially dodecyl sulfate)[62] are commonly used in order to enable the delamination of cationic nanosheets to be thermodynamically favourable, preventing unwanted aggregation. At this point, It is worth to remark that the conventional aqueous synthetic routes for LDHs usually leads to carbonate-intercalated LDH that requires further anion exchange processes to weaken the interlamellar interactions, and allow a proper exfoliation in solvents such as formamide or dimethylformamide. When it comes to non-aqueous routes, Gardner *et al*. described a synthetic procedure to obtain nanometric alkoxide-intercalated Al-containing LDHs using alcohols as solvents.[63,64] Recently, this methodology has been successfully extended to synthesize pure phases like: NiMn-, CoFe- NiCo- and NiFe-LDH, which can be exfoliated in water due to the hydrolysis of the interlamellar alkoxide groups (**Figure 3**).[52,58,59,65–67] These chemical compositions are of utmost importance in magnetism, Li-ion batteries or water splitting.

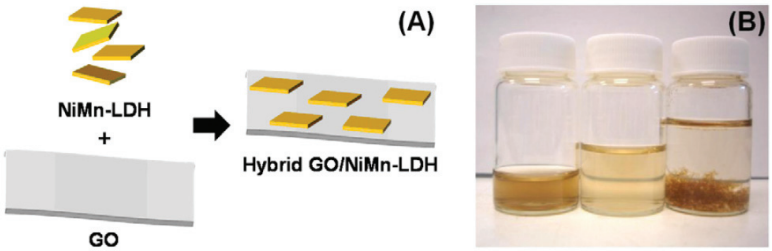

Figure 3. (A) Idealized illustration of the preparation and structure of the hybrid GO/NiMn-LDH. The scheme remarks size of the sheets and the large particle surface of GO on which the smaller NiMn-LDH nanosheets are supported. (B) Digital photographs of the aqueous dispersions of GO (left), NiMn-LDH (middle) and the hybrid GO/NiMn-LDH formed immediately after mixing the previous components (right). Reproduced from Ref. 58 with permission from Elsevier.

Along this line, Latorre-Sánchez *et al.* reported the first synthesis in water of a GO/NiMn-LDH with superparamagnetic behavior and high capacity values when used as anode in Li-ion batteries.[58]

The negative nature of GO reveals to be crucial for combining with the positive LDH layers in the final nanocomposite. Controlling the GO synthetic process can modify the amount of negative charges. On the other hand, by differing the atomic ratio it is possible to modulate the positive charge in LDH to a certain extent. **Figure 4** (extracted from the work of Zou *et al.*)[56] exhibits the schematic process for mixing GO (reduced with hydrazine) with LDH in a unique material, as well as electronic microscopy images that further corroborate this assembly.

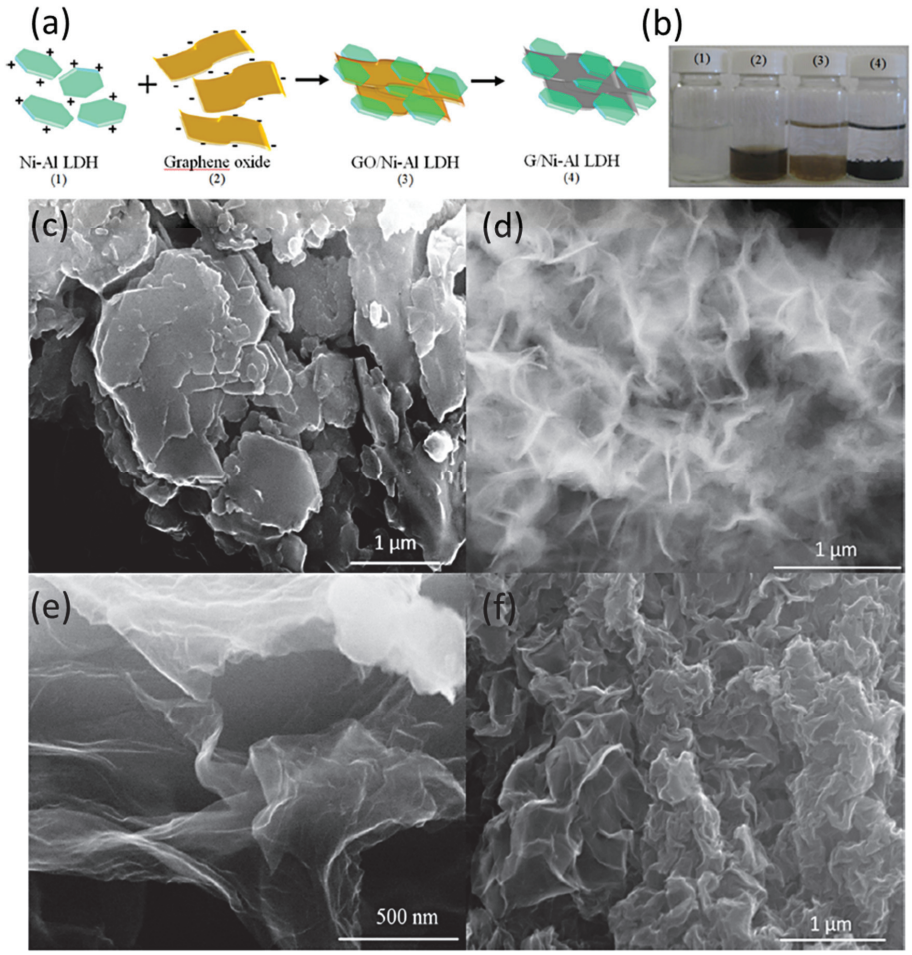

Figure 4. (a) Schematic procedure for the synthesis of a graphene/NiAl-LDH nanocomposite and (b) the corresponding digital photographs of the different steps. Scanning electron microscopy (SEM) images of (c) NiAl-LDH platelets, (d) exfoliated NiAl-LDH nanosheets, (e) graphene nanosheets and (f) graphene/NiAl-LDH nanocomposite. Reproduced from Ref. 56 with permission from Elsevier.

Recently Ma and co-workers have revisited the synthesis of rGO/LDH hybrids by means of a fine control of the graphene/LDH mass ratios and adjusting the charge density of GO/rGO nanosheets, improving the stacking of the layers, which results in superlattice structures up to 20 layers in the best case. Exploiting this strategy, the preparation of rGO/CoAl, rGO/MgAl, rGO/NiFe and rGO/NiMn-LDH hybrids has been successfully developed, exhibiting great potential in supercapacitors, water splitting and membranes.[62,68–70] (**Figure 5**).

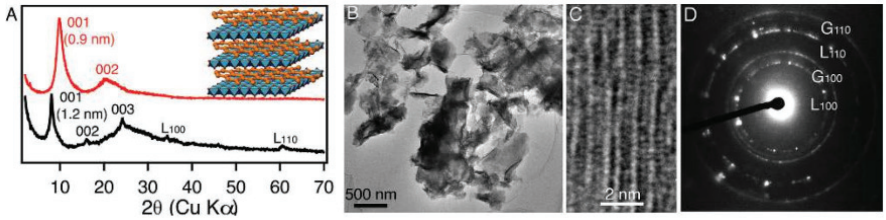

Figure 5. (A) XRD patterns of LDH nanosheets flocculated with GO (black trace) and rGO (red trace) nanosheets, respectively. Indices *00l* are basal series of superlattice lamellar composites whereas L_{100} and L_{110} are in-plane diffraction peaks from LDH nanosheets. (Inset) Schematic illustration of sandwiched LDH nanosheets and graphene. (B) TEM observations of the lamellar nanocomposites. (C) High-resolution image showing lamellar lattice fringes with different contrast. (D) Electron diffraction indexed to be in-plane diffraction rings of LDH (L_{100} and L_{110}) and graphene (G_{100} and G_{110}), respectively. Reproduced from Ref. 68 with permission from Wiley.

On the other hand, the hydrogen-bonding layer-by-layer (LbL) technique has been successfully applied in the assembly between positive hydroxide and negative GO nanosheets. The main difference with the exfoliation and restacking approach relies on the usage of substrates and a polymeric solution to assists the layer-by-layer assembly. In the work of Liu *et al.*,[51] the authors prepare the GO nanosheets by a slightly modification of the Hummers method, and the CoAl-NO_3 LDH is delaminated in formamide. For the LbL assembly, polyvinyl alcohol (PVA) is dissolved in deionized water in order to obtain an aqueous solution of PVA 1% in weight. After preparing the different components, cleaned quartz glass slides (using H_2SO_4/H_2O_2, which introduces some negative charges in the SiO_2 surface) are submerged first in a suspension of LDH nanosheets, followed by dipping the substrates in the PVA solution, then in the exfoliated GO and finally again in the PVA solution. Between each step, a thoroughly rinsing with deionized water is carried out. The complete cycle is repeated several times to obtain the final nanocomposite film. The reduction of GO to rGO has been performed by immersing the final film in hydrazine/N,N-dimethylformamide (0.5 at 50%/30 vol. ratio) solution. (**Figure 6**) Similar assemblies have been obtained between CoAl-LDH exfoliated in formamide and aqueous GO suspensions using PDDA-coated ITO (where PDDA= poly(diallyldimethylammonium chloride) and ITO = indium tin oxide) and flexible PET substrates. In this case an iterative self-assembly process has been developed without using a polymer between the different building blocks. The reduction is obtained by heating at 200 °C for 2 h under H_2 atmosphere (**Figure 6**).

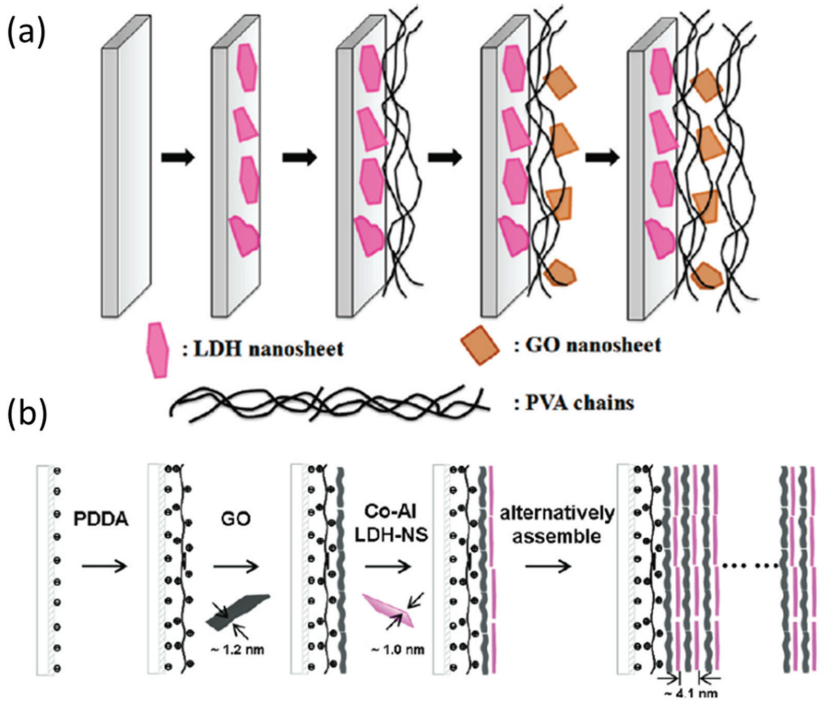

Figure 6. (a) Schematic procedure of a layer-by-layer assembly of LDH and GO nanosheets mediated through PVA chains. Reproduced with permission from Ref. 51. Copyright 2010 American Chemical Society. (b) Scheme of LbL assembly for the synthesis of multilayer films of GO/CoAl-LDH nanocomposite. Reproduced with permission from Ref. 71. Copyright 2012 American Chemical Society.

LBL is a promising technique as other driving forces than electrostatic interactions can be used for directing the self-assembly of LDH and carbon nanoforms, such as hydrophobic interactions or hydrogen bonding.

2.1.2. LDH growth on graphene.

Two main approaches have been used for the direct growth of LDH on graphene. On the one hand, the co-precipitation of LDH starting from the selected precursor salts (M^{2+}/M^{3+}) in the presence of ultrasonicated GO under controlled pH conditions. On the other hand, the hydrothermal approach using stainless steel Teflon-lined autoclaves. Reducing agents like urea, hydrazine, glucose or sodium sulphide are commonly used to adjust the pH and reduce the GO to rGO.[72] In this approach, GO acts as a template for the precipitation of the LDH, due to the adsorption capacity of the cations added during the precipitation process, thus limiting the final LDH particle size. Heating at moderate temperatures triggers the hydrolysis of urea that progressively increases the

pH up to a final value close to 8. This enables the *in situ* reduction of GO layers into rGO, whilst assisting the formation of the LDH phase. **Figure 7** shows the first report on the synthesis of LDH-rGO hybrids.[50]

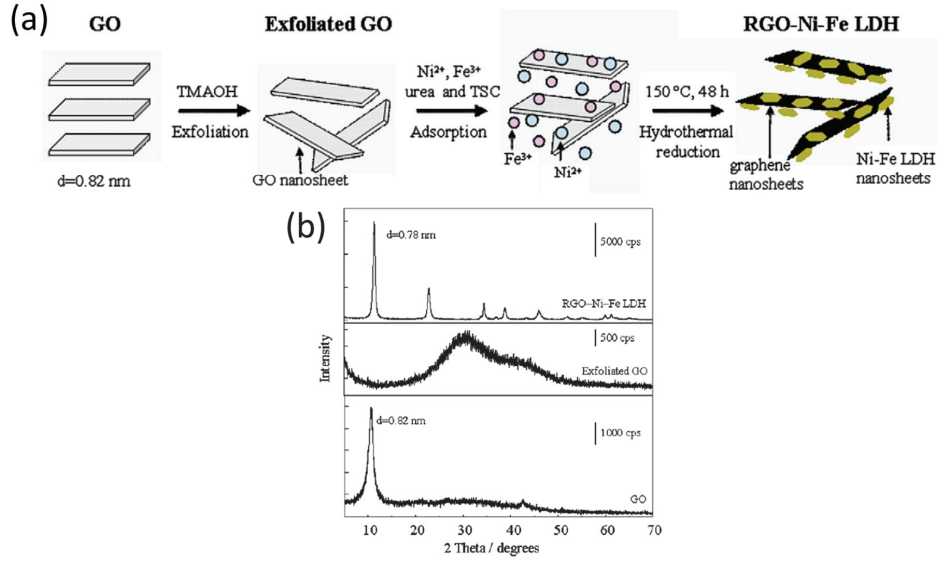

Figure 7. (a) Schematic representation of the synthetic procedure of the hybrid rGO/NiFe-LDH hybrid. (b) XRPD patterns of the precursor GO, the delaminated form and the nanocomposite. The precursor GO exhibit a basal space of 0.82 nm, implying a complete oxidation of graphite into GO. The exfoliated sheets display a broad peak in the range 20º – 40º, related with scattering effects between the exfoliated sheets and water as solvent. Lastly, the pattern of the hybrid material matches with a NiFe-LDH phase and no peaks of graphite is observed, therefore the restacking of the *as*-reduced graphene sheets is prevented. Reproduced from Ref. 50 with permission from Elsevier.

By following this synthesis, graphene/LDH nanocomposites of different compositions have been described, from the conventional CoAl-LDH[73] and MgAl-LDH[74] to more sophisticated ZnCr-LDH,[75] NiFe-LDH[76] or even ternary LDHs like NiCoAl-LDH.[77] The work of Liu *et al.*[49] depicts a modified synthetic procedure in the formation of a graphene/NiAl-LDH nanocomposite. In this case, graphite oxide is exfoliated by ultrasonication and glucose is used as reducing agent in order to obtain a graphene nanosheet suspension prior to the *in situ* growth of the LDH, avoiding the use hydrazine due to its high toxicity.[78] After that, the suspension of graphene nanosheets is introduced in an autoclave where Ni and Al salts are present, as well as urea as pH controlling agent.[79] The final nanocomposite has been successfully prepared after 24 h at 95 ºC (**Figure 8**).[49]

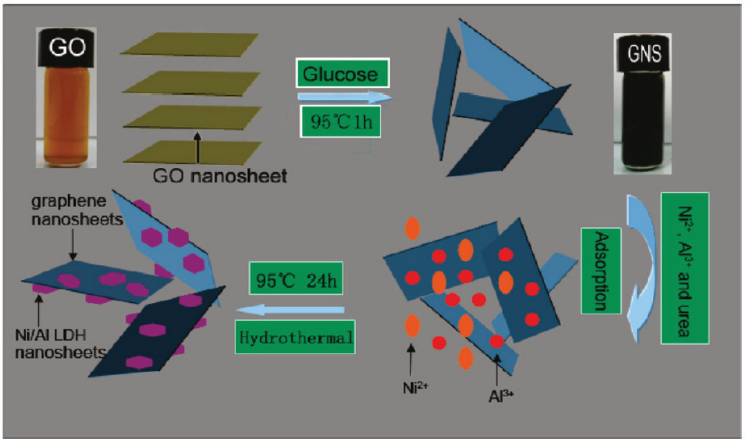

Figure 8. Scheme with the formation of a graphene/LDH nanocomposite. Reproduced with permission from Ref. 49. Copyright 2011 American Chemical Society.

The annealing temperature is another important parameter that has to be optimized in order to avoid metal reduction at expense of graphene that can act as a sacrificial reducing agent being converted into CO and CO_2 (**Figure 9**).[59]

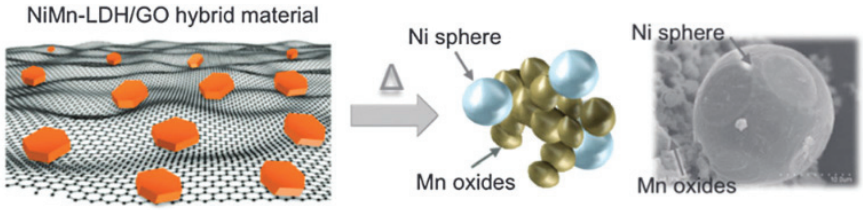

Figure 9. Idealized structure of the GO/NiMn-LDH hybrid. The remarkable difference in size between NiMn-LDH (*ca*. 100 nm) and GO (*ca*. 3 μm) is illustrated, as well as how the thermal treatment affects the segregation of Ni NP and Mn oxides. The right panel shows an FESEM image of a Ni NP of *ca*. 20 μm formed in the nanometallurgic process. Reproduced from Ref. 59 with permission from the Royal Society of Chemistry.

In general, the direct growth of LDH on GO leads to strong interactions at the interface.[80] Indeed, XANES measurements have been employed by Dai and co-workers to study the nature of these interactions. They observe for a related NiFe-LDH/CNT hybrid the formation of M−O−C (M = Ni, Fe) bonding via the carboxyl group, leading to large perturbations to the carbon atoms in the carbonyl groups. The same is expected in the case of GO.[81]

The main limitation of the direct nucleation and growth of the LDH phases on GO is the restricted accessibility of electrolyte to the active metal centres due to the formation

of thicker flakes compared to the exfoliation and restacking approach. On the other hand, the strong interaction between both phases leads to a dramatic improvement of the electrical properties of LDH.

2.1.3 Graphene formation in LDH layers.

Owing to its unusual anion intercalation property, noncatalytic systems like MgAl-LDH can act as "nanoreactors" for the formation of carbon nanoforms within their interlamellar space. Indeed, Yang *et al.*[82] described a way to synthesize graphene nanosheets with a certain control over their thickness after the calcination of MgAl-LDH intercalated with dodecyl sulfonate (DSO) and methyl methacrylate (MMA) anions (see **Figure 10** extracted from Ref. 82). These small and slightly oxidized graphene flakes can be isolated and characterized after acid etching of the nanocomposite.

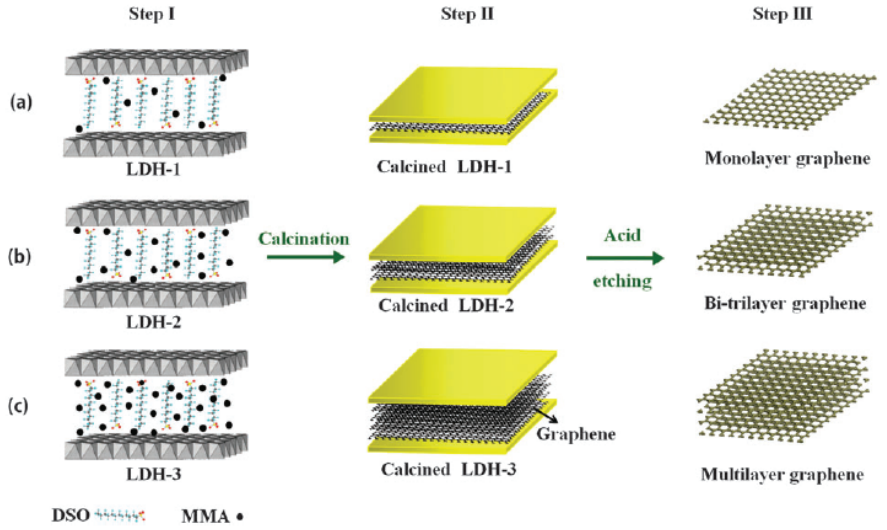

Figure 10. Scheme with the formation of MMA-derived graphene nanosheets with different number of layers in the interlamellar space of a LDH. (a) Monolayer, (b) bi- and trilayer and (c) multilayer graphene nanosheets after acid treatment of LDH-1, 2 and 3, respectively. Reproduced from Ref. 82 with permission from the Royal Society of Chemistry.

On the other hand, by template-directed CVD it is possible to use MgAl-LDH as precursors for the synthesis of mesoporous MgAl- layered double oxides (LDOs) nanosheets consisting of MgO and $MgAl_2O_4$. The mesoporus structure arises from the Kirkendall diffusion of Mg^{2+} during the transformation of octahedral Mg–O into tetrahedral Mg–O via dehydration of the interfacial –OH groups. These layered oxides have been proven excellent for actively decompose CH_4 (or related carbon sources) and deposit single-layer graphene due to the exposed oxygen atoms on their surface. In contrast to

monometallic hydroxides like $Mg(OH)_2$ –which after calcination lead to the formation of MgO layers– the use of MgAl-LDH gives rise to an uninterrupted and uniform unstacked graphene layer with protuberances rather than an aggregate of graphene nanocages.[83] This is mainly due to the presence of mesopores (**Figure 11**).[84]

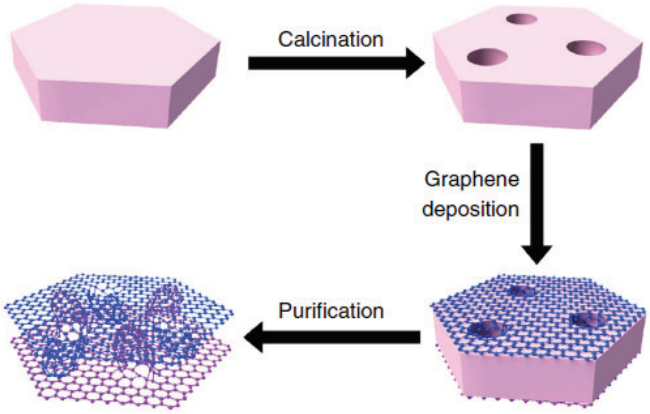

Figure 11. Scheme for the synthesis of unstacked double-layer template graphene. A mesoporous oxide derived from the calcination of a LDH is used as a template, followed by its removal by acid etching. Reproduced from Ref. 84 with permission from Nature publishing group.

Aside from catalytically "innocent" metals like Mg, Zn or Al, LDH can be excellent catalysts precursors. Indeed a wide variety of carbon nanoforms have been synthesized using the metal oxides or the metal nanoparticles obtained after calcination and/or reduction of LDH having Fe, Ni or Co atoms.[47,85] A thorough revision can be encountered in the work of Wei *et al.*, indeed using this methodology several graphene-containing hierarchical systems have been synthesized, including SWCNT/graphene hybrids (*vide infra*).[27] Authors like Zhang *et al.* have used methane as carbon source combined with different LDHs to obtain a mixture of graphene and carbon nanotubes hybrids with LDHs.[86,87] **Figure 12** depicts part of the characterization of the nanocomposite graphene/SWCNT/CoAlMg-LDH extracted from Ref. 86.

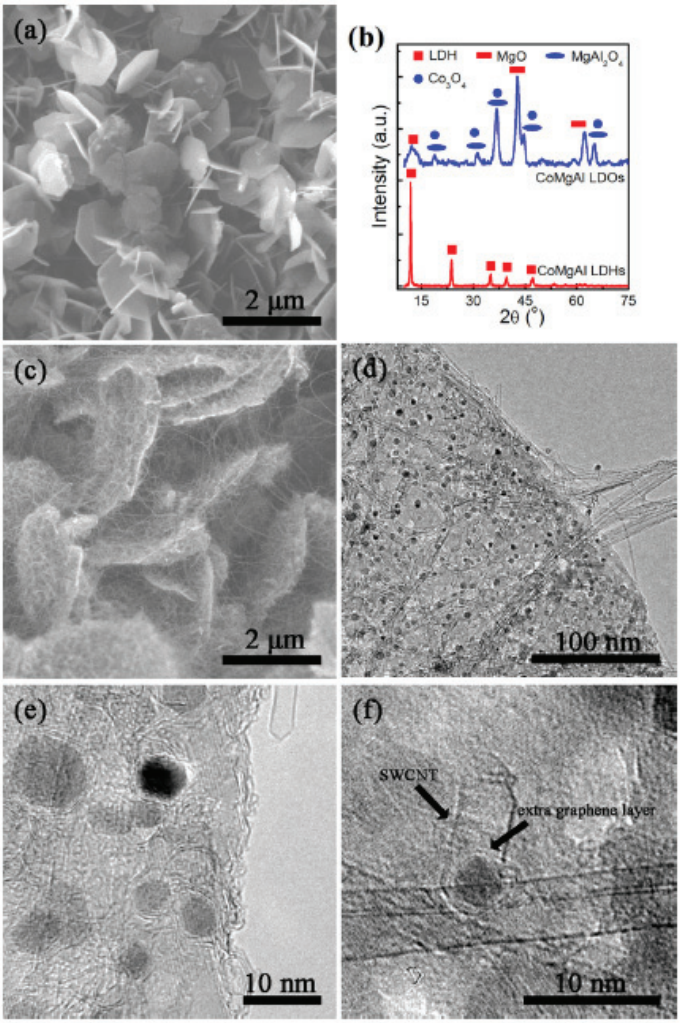

Figure 12. (a) SEM image of CoMgAl-LDH platelets, (b) XRPD patterns for the CoMgAl-LDH and LDO, (c) SEM, (d) TEM and (e,f) HRTEM images for the graphene/single-walled CNT/CoMgAl-LDO nanocomposite. Reproduced from Ref. 86 with permission from Elsevier.

Despite the aforementioned efforts, the directed controlled synthesis of high quality graphene within the interlamellar space of LDH remains an open challenge. In any case, the rich chemical versatility of LDH assures a promising future in the design of new graphene synthetic concepts.

3. Carbon Nanotubes/LDH Nanocomposites.

As introduced in the previous section, the first works reported in the literature were related to the use of LDH phases as catalysts for the formation of CNF, and the subsequent elimination of the LDH phase by acid leaching. Indeed, since 1997 several works have explored the influence of composition, size, surface reactivity and calcination temperatures in the CVD growth of CNF using LDH as catalytic precursors. As a matter of fact, Wei *et al.* reported the use of different LDHs as catalysts for the large-scale synthesis of high quality single-walled CNTs by means of a fluidized-bed catalytic CVD procedure.[88] Other examples where LDH have been used as catalysts can be found elsewhere.[89–93]

In 2008 the first CNT/LDH nanocomposite was described by Zhang *et al.*[94] In that work, a MWCNT/CoAl-LDH nanocomposite was synthesized by means of homogeneous precipitation, and used as electrode material for supercapacitor purposes at high currents, leading to improved performances. Similarly, in 2010, a CNT/NiAl-LDH nanocomposite with controllable LDH mass ratio was described by Li and co-workers, showing LDH platelets with lateral size of 10–15 nm.[95,96] At that time the important influence of the functionalization degree of CNTs was pointed out paving the way for future works.[96]

3.1. Synthesis.

The two main approaches for the synthesis of these nanocomposites are the LDH formation directly on CNTs and the *in situ* growth of the CNTs on the LDH structure. The reassembly of both halves is not usually chosen as a synthetic method but some examples can be found in the literature.

3.1.1 Reassembly of CNTs and LDHs.

Has been carried out by authors like Ai *et al.*[97] and Wang *et al.*[98] In both cases, the LDH material was delaminated in formamide, followed by the addition of a NaOH[97] or aqueous solution[98] with functionalized CNT. Electrostatic interactions between opposing charges (cationic sheets of LDH and anionic groups in the CNT) are the driving force for the self-assembly process. **Figure 13**, extracted from Ref. 97 represents a schematic description of the procedure.

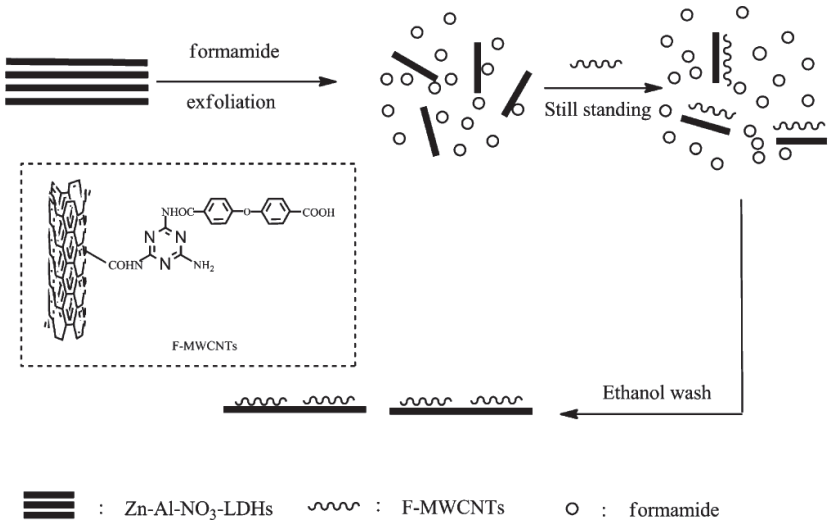

Figure 13. Scheme of the formation of multi-walled CNT/LDH nanosheets nanocomposites. Reproduced from Ref. 97 with permission from Springer.

3.1.2. LDH formation on CNTs.

It is the most typical way of synthesis for CNT/LDH nanocomposites, where the LDH phase has been usually synthesized by means of a coprecipitation or solvothermal method. In 2013, Dai and co-workers described the synthesis of a NiFe-LDH/CNT hybrid with an excellent electrocatalytic activity for the oxygen evolution reaction (OER), which boosted the research on NiFe applications in water splitting. [81] They used the nucleation and growth of NiFe-LDH on the surface of dispersed oxidized CNTs at moderate temperatures (85 ^{o}C), and then the solvothermal growth at 160 ^{o}C obtaining crystalline NiFe-LDH platelets strongly interacting with partially reduced CNTs. However, this synthetic approach leads to the formation of spinel impurities, a typical problem associated to the aqueous synthesis of non-Al containing LDH, like NiFe- or CoFe-, for example.[99,100] A similar work was developed by Qiu *et al.*[101], this time combining a ternary NiCoAl-LDH with activated multi-wall CNTs *via* homogeneous urea precipitation method. The resulting nanocomposite exhibited high specific capacitances and good results in rate capability or cyclic stability. Wei *et al*.[102] explored the formation of a nanocomposite between NiMn-LDH or CoMn-LDH and CNTs previously treated with HNO_3. The formation of the hybrid material was achieved by mixing the corresponding metal salts and the functionalized CNT by an *in situ* coprecipitation method (**Figure 14**, extracted from the work of Wei *et al*.[102] depicts a scheme of the procedure). The resulting nanocomposite was tested as an electrode material in supercapacitors, giving rise to excellent cyclability and high specific capacitance.

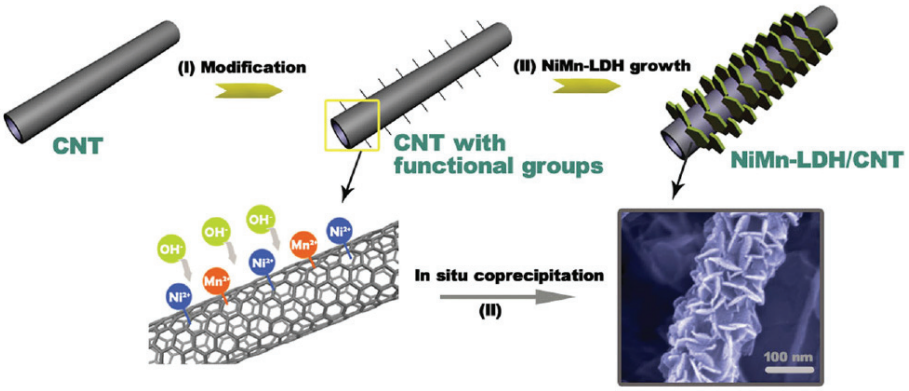

Figure 14. Scheme with the formation of CNT/NiMn-LDH nanocomposite. Step (I): surface modification of the CNT by functional groups such as –OH-, –CO or –COO-). Step (II): grafting of the NiMn-LDH nanosheets to the CNT structure by an in situ growth method. Reproduced from Ref. 102 with permission from Wiley.

3.1.3. CNTs formation on LDHs.

This approach relies in using CVD procedures, which usually give rise to a mixture of carbon species like graphene, carbon spheres or CNTs.[19,103,104] The work of Li *et al.*[103] clearly defines how the CVD conditions affect directly on the final carbon nanoforms (see **Figure 15** extracted from that work). The authors stated that the different CNFs may arise from an overgrowth of the initially formed 1D tubular structures, which gain volume as long as the CVD time is increased. This fact also affects the wettability properties of the nanocomposite, leading to super-hydrophobic films in the case of the longest growing times.

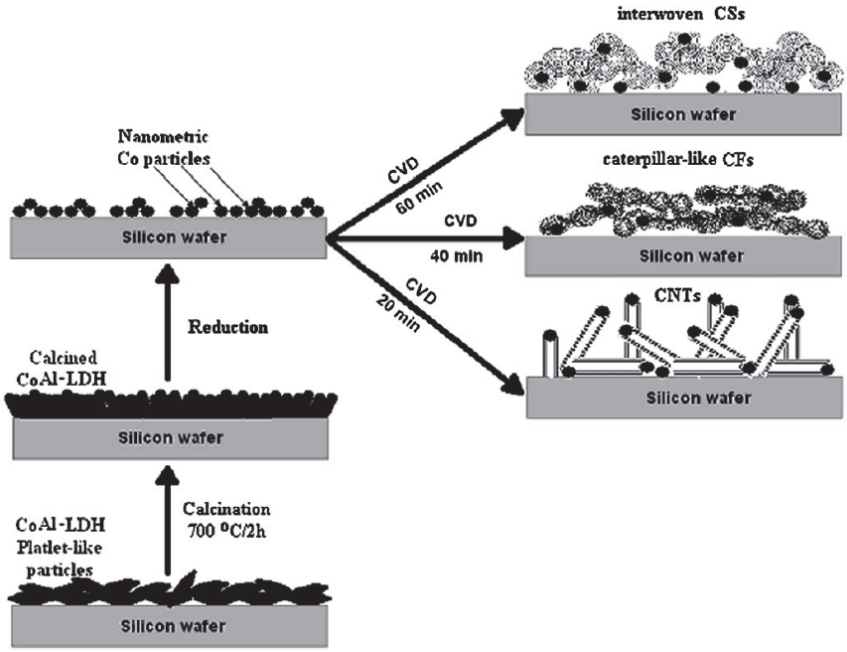

Figure 15. Schematic formation of different nanocomposites of carbon structures after using CoAl-LDH particles as catalysts. Interwoven carbon spheres, caterpillar-like carbon fibers and carbon nanotubes are reported. Reproduced from Ref. 103 with permission from the Royal Society of Chemistry.

The selective formation of a specific CNF is governed by several factors, being the size and surface density ($NP \cdot m^{-1}$) of the catalytic nanoparticles (e.g. Fe NPs) generated *in situ*, one of the most important parameters. The fine-tuning of the size by using FeMgAl-LDH intercalated with MoO_4^{2-}, which act as pinning centre for the Fe NPs generated after calcination, can lead to the selective formation of SWCNT and more complex helical structures.[105] Another factor that was revealed as very important in the specific growth of CNT was the final disposition of the 2D crystallites. In this sense, magnetic NiFe-LDHs are a special class of hydroxides that exhibit the highest catalytic metals concentration allowed by these layered entities. However, it was not until 2014 that their application in direct nanocarbon formation was first studied.[19] Interestingly, bulk NiFe-LDH led to a wide variety of carbon nanoforms such as few-layers graphene, carbon fibers and MWCNTs, whereas ultrathin films of *ca*. 150 nm thick with parallel orientation of the crystallites conduces to a hierarchical growth of bamboo-like carbon nanotubes with a thickness of *ca*. 250 nm at relatively low temperatures (550 °C).[19] (**Figure 16**).

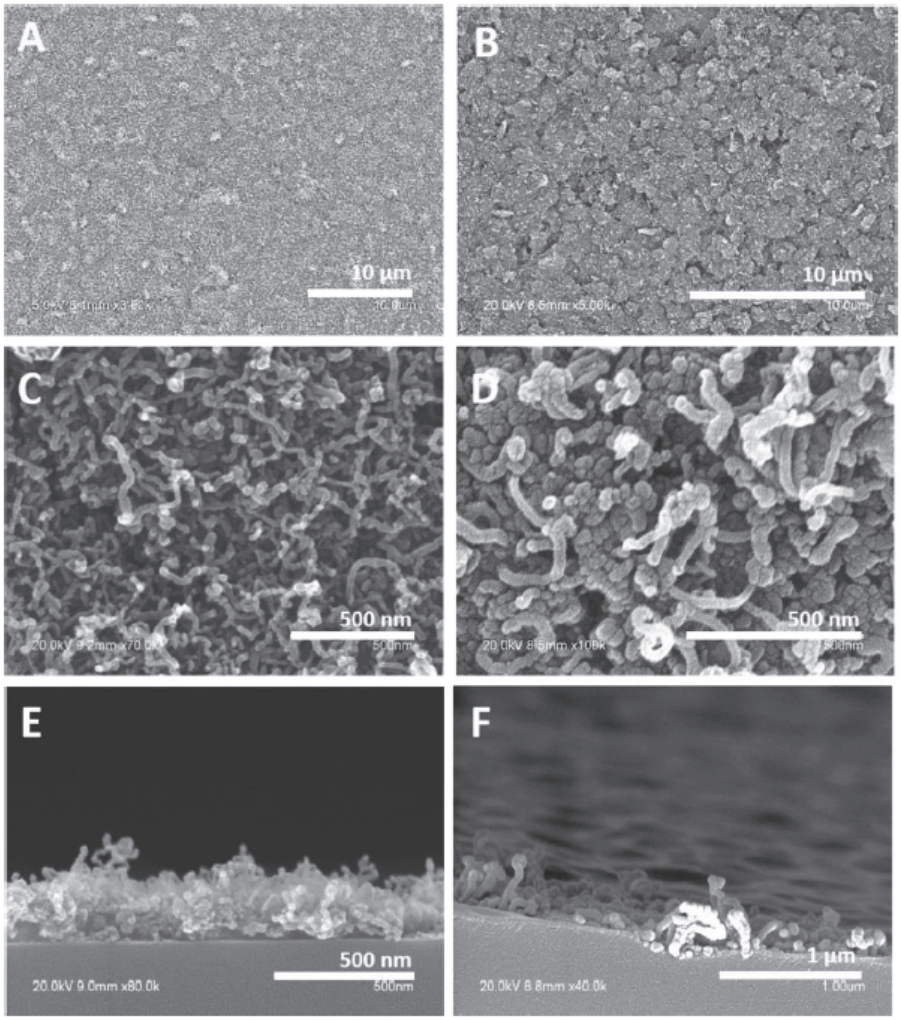

Figure 16. FESEM images of bamboo-like CNT growth over NiFe-LDH platelets after a (A, C, E) chemical vapor deposition (CVD) and a (B, D, F) catalytic CVD (in absence of H_2) procedures. Reproduced from Ref. 19 with permission from Wiley.

4. Other Carbon Nanoforms/LDH Nanocomposites.

Despite the fact that graphene/LDH and CNT/LDH nanocomposites are the most studied families of hybrid materials consisting of LDHs and carbon species, nanocomposites based on LDHs and other CNFs like fullerene, carbon spheres, nanofibers, carbon dots or carbon rings have been reported:

4.1. Fullerene/LDH Nanocomposites.

This type of materials has been described by authors like Liu *et al.*[106,107] and Plötze *et al.*[108] The first example of C_{60}/LDH nanocomposite dates from 1996, and was synthesized by simply mixing powders of dodecyl sulphate-intercalated MgAl-LDH with C_{60} solutions in toluene or hexane. The hydrophobic character of the interlamellar space of the alkyl-functionalized LDH allowed the diffusion of the C_{60} molecules within the layers, and the ulterior calcination of the system led to the decomposition of dodecyl molecules forming the final C_{60}/LDH nanocomposite.[109] A few recent examples were reported using the anion exchange capacity of the LDHs, *e.g.* by preparing benzoic acid-intercalated LDHs from NO_3-LDHs and then adding the fullerene in the interlamellar space by means of ultrasonic treatment.[107] It is worth to remark that no thorough characterization studies have been reported for this family of hybrids, being still unknown its physical and chemical properties. **Figure 1.c1**, exhibits a schematic representation of the C_{60}/LDH nanocomposite.

4.2. Carbon quantum dot/LDH Nanocomposites.

These nanocomposites were firstly reported in 2014 by Kang *et al*. They decorated NiFe-LDH with 0D carbon quantum dots (CQDs) of *ca*. 5 nm in a three-step synthetic process consisting on mixing first the metal salts and CQD solutions at 85 ^{o}C for 4 hours. Then, they transferred the mixture to a solvothermal reaction at 120 ^{o}C for 12 h, followed by a final solvothermal process at 160 ^{o}C for 2 h. A similar approach was developed by both Liu *et al.* and Zhang *et al.*[110,111] for the synthesis of hybrids with MgAl and NiAl-LDH, respectively. **Figure 17**, extracted from Ref. 112, exhibits some part of the characterization of the CQD/NiFe-LDH nanocomposite. The hybrids were tested as electrocatalysts for water oxidation as well as a supercapacitors, with good results due to the synergy between both parts of the material.

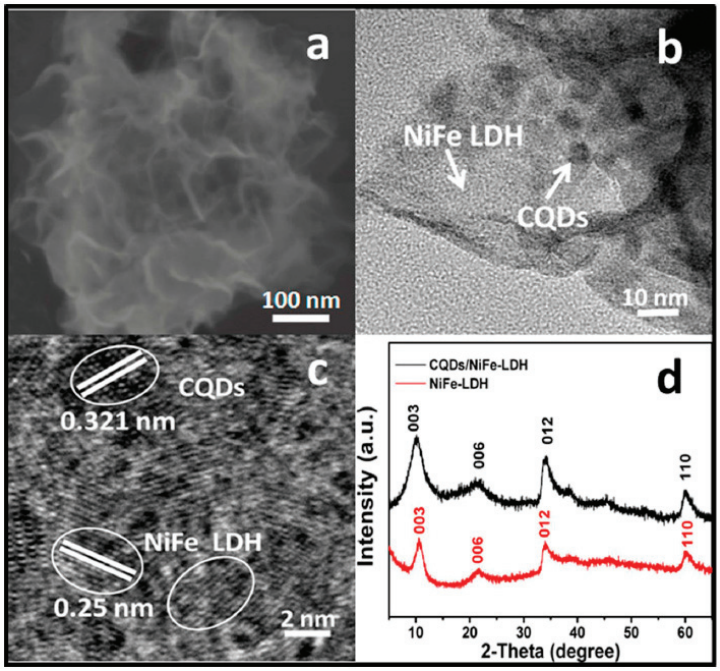

Figure 17. (a) SEM, (b) TEM and (c) HRTEM images of a carbon quantum dot/NiFe-LDH nanocomposite. (d) XRPD spectra of the nanocomposite and the pure LDH phase. Reproduced with permission from Ref. 112. Copyright 2014 American Chemical Society.

4.3. Carbon Spheres/LDH Nanocomposites.

These nanocomposites were synthesized by authors like Zhang[113] or He[114] *et. al.,* with the aim of exploring their electrochemical applications since in this field carbon spheres have demonstrated to be of interest.[115,116] Regarding the synthetic methodology, the direct reassembly of the spheres and LDHs has been explored by means of ultrasonication procedures, preparing both building blocks separately and then mixing them at the same time,[113] whereas the most typical approximation of synthesizing these hybrids are by CVD process, using the LDH material as a catalyst and a carbon source like ethylene[117] for the formation of the spheres at high temperatures (*e.g.* 900 ºC).[118] **Figure 18** depicts the schematic formation by direct assembly of a carbon sphere/LDH nanocomposite.[113]

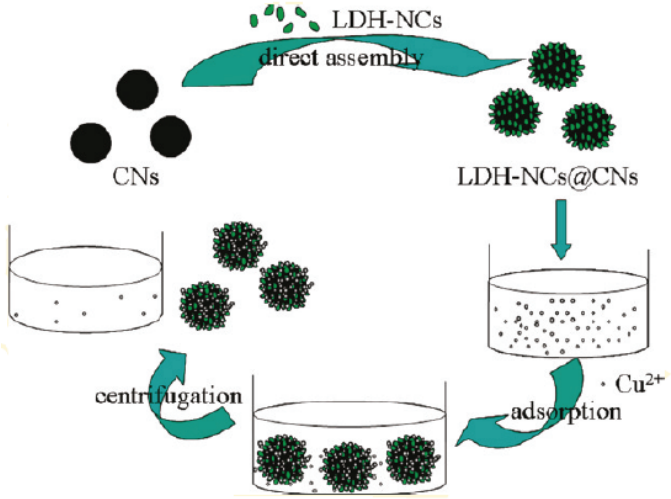

Figure 18. Schematic procedure for the synthesis of a carbon sphere/LDH nanocomposite through a direct assembly approach. Reproduced with permission from Ref. 113. Copyright 2011 American Chemical Society.

4.4. Carbon (Nano)Fibers/LDH Nanocomposites.

The main approach pursued to obtain this kind of nanocomposites is the *in situ* LDH formation on carbon fibers.[119–122] In a typical procedure, the LDH is synthesized by means of a hydrothermal method, adding the carbon fibers to the mixture. Liu *et al.*[121] prepared a mixture of bohemite AlOOH/carbon nanofibers and then a Ni salt plus urea were added to the aqueous solution. After some time, the final solution was transferred to an autoclave and the reaction was set at 100 ºC for 48 h. The resulting nanocomposite was collected after a centrifugation process. Authors like Wei *et. al.*[120] also used MnO_2 nanowires to enhance the supercapacitive properties of the nanocomposite (see **Figure 19** extracted from Ref. 120).

The main driving force in the development of these hybrids were their applications related with electrochemistry, especially for supercapacitors in this case.[121]

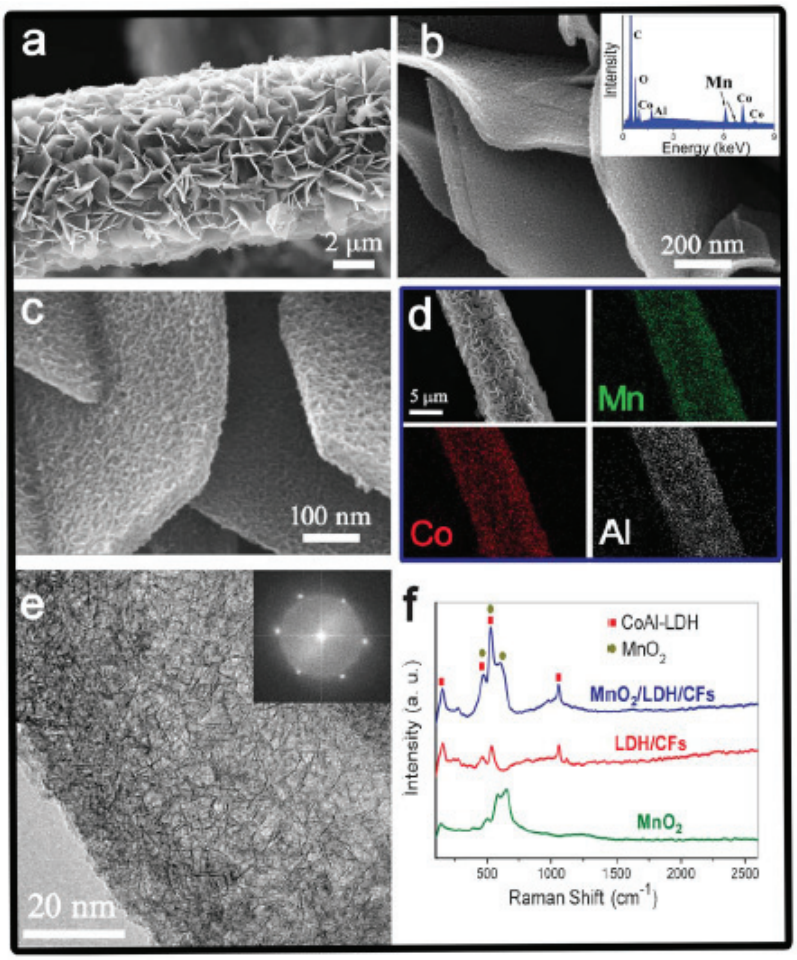

Figure 19. (a, b, c) SEM images of the MnO_2/LDH/carbon fibers nanocomposite. The inset in (b) corresponds to the EDS results. (d) EDS mapping of a single nanostructure. (e) TEM image of an individual MnO_2/LDH composite (the inset corresponds to the FFT pattern). (f) Raman spectra of MnO_2, carbon fiber/LDH and the MnO2/LDH/carbon fibers nanocomposite. Reproduced from Ref. 120 with permission from the Royal Society of Chemistry.

In addition to the previously described LDH nanocomposites, there are also some punctual examples of hybrids with other CNF. For example, **carbon nanorings or nano onions/LDH** have been synthesized by the groups of Zeng,[48] Coronado[47] (**Figure 20**) or Yang[123] using Ni, Co or Fe-containing LDHs as catalytic nanoreactors. Indeed the pioneering works of Zeng and co-workers revealed that the *in situ* generated low-valence-state cobalt oxides during the calcination of terephthalate anions (TA^{2-})-intercalated CoMgAl-LDH led to the formation of MWCNT with a diameter of 10–35 nm and a length of 20–200 nm.[124] The intercalation of poly(vinyl sulfonate)-intercalated

CoAl-LDH led to the formation of sulphate-doped CNF.[48] It is worth mentioning that since 1995 several efforts have been developed for the synthesis of meso/microporous 3D carbons using LDH as containers.[125–130] More recently, the thermal decomposition of a NiFe-LDH intercalated with sebacate molecules, acting as carbon source, enables the low-temperature formation of carbon nano-onions (CNOs) and multiwalled nanotubes (MWNTs) through a simple reaction.[47] This process benefits from the catalytic activity of the $FeNi_3$ nanoparticles formed *in situ*, which facilitate the decomposition of the confined sebacate molecules to produce CNFs embedded into a graphitic shell via a bottom-up approach. Remarkably, this was the first example of low-temperature (400 °C) formation of CNFs and metal alloy nanoparticles, instead of LDO using LDH hybrids as precursors.[47,117,131] By following similar approaches carbon nanorings have been reported by Yang and co-workers.[123]

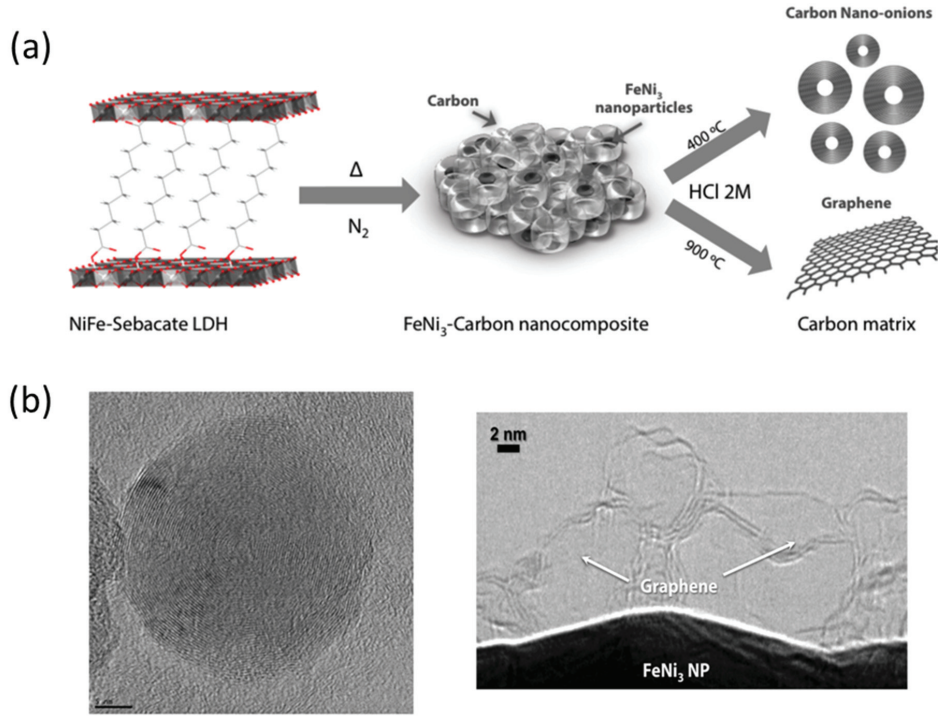

Figure 20. (a) Schematic illustration of the formation of $FeNi_3$-carbon nanocomposites and their corresponding carbon nanoforms after the acid leaching procedure. (b) HRTEM images of some carbon nanoforms and the $FeNi_3$ nanoparticles acting as catalysts. Reproduced from Ref. 131 with permission from the Royal Society of Chemistry.

Iwasaki *et al.*[132] reported a nanocomposite with **nanocoils** (also known as helical carbon nanotubes) applying a CVD process using NiFe-LDH as a catalyst precursor and

acetonitrile as the carbon and nitrogen source for doping the nanocoils. On the other hand, **nanobelts/LDH** were observed by Zhang *et al.*[133] This time, the composite was prepared by the *in situ* synthesis of the nanobelts in the CoAl-LDH phase after submitting a delaminated CoAl-dodecyl sulfate LDH colloidal suspension to a solvothermal technique (120 ^{o}C for 24 h in a stainless steel Teflon-lined autoclave). The final hybrid was collected after filtering the resulting solution. Finally, other carbon/LDH (activated carbon, carbon cloth or carbon dots) nanocomposites were reported by several authors.[134–136] For example, carbon dot/LDH hybrids were prepared by direct reassembly of LDH and the carbon dot solution, and the resulting hybrid was tested for catalysis due to its peroxidase-like activity[137], and also as adsorbents to methyl blue due to the electrostatic interactions and hydrogen bonding that are established between the dye and the composite.[134] Mizuhata *et al.*[138] synthesized a carbon/NiAl-LDH by liquid phase deposition (LDH formation on carbon black), whereas Frackowiak *et al.*[136] prepared a similar hybrid by means of a homogeneous coprecipitation method. In both cases the resulting composites were electrochemically tested. Carbon black/LDH nanocomposites have also been reported by authors such as Debdipta *et al.* in the synthesis of elastomer composites.[139] Lastly, a carbon cloth/LDH was reported by the group of Mai[135] with a honecomb-like structure by means of a hydrothermal approach, which increases the electrochemically active sites for redox reactions, giving rise to excellent behaviour for energy storage applications.[140]

4.5. Graphene/single-walled CNT/LDH Nanocomposites.

These nanocomposites have also been reported in the work of Wei *et al.*[141] In that work, a novel mildly oxidized graphene/single-walled CNT/NiFe-LDH electrocatalyst was synthesized by incorporating LDH crystallites into a carbon network by means of an *in situ* growth and defect-anchored nucleation (**Figure 21**). The synergy between the properties of the different parts of the nanocomposite gave rise to a superior OER performance in basic media, highlighting the fact that the oxidized carbonaceous matrix allowed the LDH phase to grow in a highly uniform and fully accessible arrangement, which enhances the utilization efficiency of the active sites.

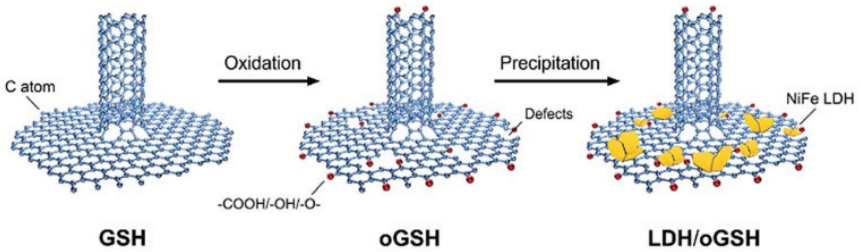

Figure 21. Synthesis of the mildly oxidized graphene/single-walled CNT/NiFe-LDH electrocatalysts with a dual-sized distribution of the LDH platelets. Reproduced from Ref. 141 with permission from the Royal Society of Chemistry.

5. Applications.

The CNF/LDH nanocomposites have been used for several applications, **Table 3** reports a brief overview of the most representative systems, detailing their preparation and highlighting their applications. In the following, we briefly summarize the most important achievements obtained with these nanocomposites in the different fields of application.

Table 3. Overview of some of the carbon material/LDH nanocomposites reported in literature, highlighting the precursor salts used for the synthesis of the LDH phase, the synthetic method for obtaining the nanocomposite, the reducing agent, if used, and the main application of the nanocomposite.

Nanocomposite	Precursor salts	Synthetic Method	Reducing Agent	Applications	Ref.
Graphene oxide/CoAl-LDH	Chlorides	Layer by layer assembly		Films with enhanced electrical conductivity	51
Graphene/NiAl-LDH	Nitrates	Hydrothermal	Glucose	Supercapacitor	49
Reduced graphene oxide/NiCo-LDH	Nitrate and chloride	Hydrothermal	Heating at 150 °C	Supercapacitor	52
Graphene oxide/CoAl-LDH	Chlorides	Coprecipitation	Hydrazine	Supercapacitor	73
Graphene/MgAl-LDH	Nitrates	Hydrothermal		Cr (VI) removal	74
Reduced graphene oxide/NiFe-LDH	Acetate and nitrate	Hydrothermal	Hydrazine	Water oxidation	76
Graphene/MgAl-LDH	Nitrates	CVD			82
Graphene/NiFe-LDH	Nitrates	Hydrothermal		Flame retardant	142
Graphene oxide/MgAl-LDH	Nitrates	Coprecipitation		CO_2 adsorbent	143

Graphene/CoAl-LDH	Chlorides	Coprecipitation	Urea	Supercapacitor	144
Graphene/CNT/CoMgAl-LDH	Nitrates	CVD		Supercapacitor	86
Graphene/CNT/FeMgAl-LDH	Nitrates	CVD			87
CNT/ZnAl-LDH	Nitrates	Hydrothermal			97
CNT/MgAl-LDH	Nitrates	Self-assembly		CO_2 adsorbent	98
CNT/NiFe-LDH	Acetate and nitrate	Hydrothermal		Water oxidation	81
CNT/NiMn-LDH	Nitrates	Hydrothermal		Supercapacitor	102
Carbon spheres/CoAl-LDH	Nitrates	CVD		Super-Hydrophobicity	103
Carbon spheres/MgAl-LDH	Nitrates	Self-assembly		Water treatment	113
Fullerene/MgAl-LDH	Nitrates	Self-assembly			108
Carbon quantum dot/NiFe-LDH	Acetate and nitrate	Hydrothermal		Water oxidation	112
Carbon fiber/CoAl-LDH	Nitrates	Hydrothermal		Supercapacitor	120
Carbon nanoring/CoAl-LDH	Nitrates	CVD		Li-storage	123
Carbon nanobelt/CoAl-LDH	Nitrates	Hydrothermal			133

5.1. Energy Storage and Conversion.

As previously seen, energy storage and conversion rise as two of the most appealing applied topics for LDH/Carbon nanocomposites. In fact, preparation of efficient catalysts based on LDH nanosheets has been restricted by their tendency to aggregate, insulating nature, and poor stability, etc. The hybridization with different CNF has been erected as the most effective solution for boosting the energy-related applications of LDH/CNF nanocomposites. Hereafter, we will succinctly summarize the most prominent examples in this field. We can divide this general topic in three subthemes, namely batteries, supercapacitors and water splitting electrocatalysts.

5.1.1. Batteries.

We can define a battery as a device composed by different electrochemical cells connected between them, therefore providing the required voltage or capacity when they are connected in series or in parallel, respectively.[110] The electropositivity of Li (highest value of the periodic table with -3.04 V *vs* standard hydrogen electrode), as well as its lightness, makes that element an ideal metal as anode in a battery device. The main advantages of Li-ion batteries (LIBs) rely on its high energy density, long cycling life, high voltage and their relatively good environmental compatibility, especially if compared with Pb and Ni batteries.[146,147] Nevertheless, the rapid increase in energy demand in recent years has prompted the search of low-cost alternatives for energy storage and conversion.[148,149], There is a demand for better batteries with longer life, higher power and higher energy density. In this context, carbon and its related allotropes have proved to be excellent electrode materials. It has been extensively reported that the synergy between carbon materials with metallic species and derivatives to form nanocomposites can improve the activity and performance for acting as Li-ion batteries,[146] due to the optimized diffusion processes of metal atoms in a carbonaceous matrix and the redox properties of metallic species. In this context, carbon/LDH nanocomposites have provided a good opportunity. The first example was reported in 2012 by García and co-workers[58] showing that a NiMn-LDH/GO can act as a precursor for the formation of mixed metal oxides covered and wrapped by rGO layers. They showed a maximum capacity of 1030 $mAh \cdot g^{-1}$ during the first discharge when used as anode in LIBs and these values were kept higher than 400 $mAh \cdot g^{-1}$ after 10 cycles. Zhang *et al*.[150] reported a carbon nanofibers/NiAl-LDH nanocomposite as anode for Li-ion batteries with an enhanced electrochemical activity after the thermal transformation of the LDH in a mixture of metal oxides and metal nanoparticles. The hybrid, synthesized at 550 ^{o}C, exhibited a cycle discharge of 374 $mAh \cdot g^{-1}$ and a charge capacity of 330 $mAh \cdot g^{-1}$, higher than that observed for carbon-only materials.[151] Along with that, a reversible discharge capacity of 374 $mAh \cdot g^{-1}$ at a charge-discharge current of 0.2 ^{o}C and 119 $mAh \cdot g^{-1}$ at 5.0 ^{o}C were found. **Figure 22,** extracted from Ref. 150, exhibit the Li-ion storage performance of the hybrid material. Moreover, carbon nanotubes/LDH nanocomposites have been tested as anode materials for Ni-Zn secondary batteries,[152,153] with an average discharge capacity of about 385 $mAh \cdot g^{-1}$ and high cycle stability with a capacity maintenance of 95% after 200 cycles.

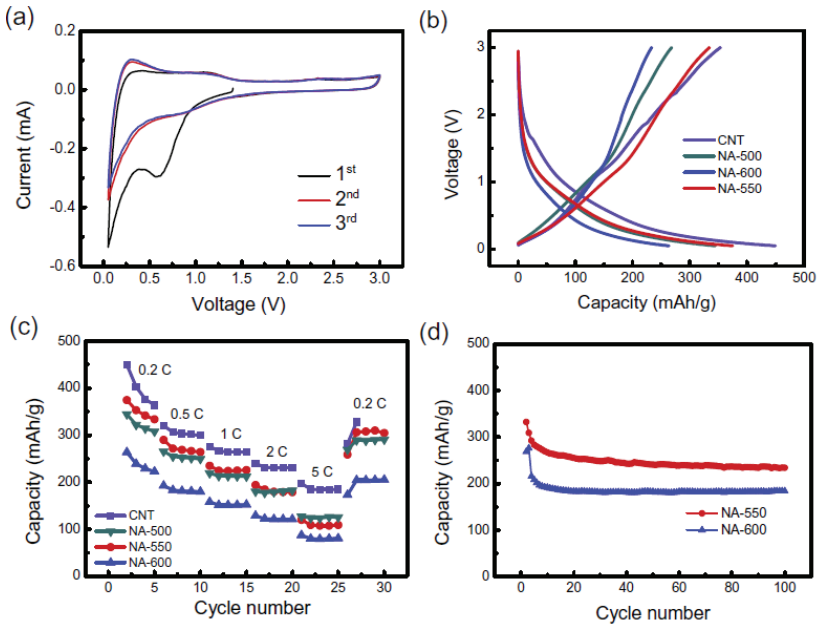

Figure 22. Li-ion storage performance of the herringbone carbon nanofibers and nanotubes obtained using LDHs as catalysts. (a) CV profiles, (b) voltage profiles of the galvanostatic charge-discharge at a current of 0.2 ºC, (c) discharge capacities at different current densities and (d) cycling performance of the carbon nanofibers at 0.5 ºC. Reproduced from Ref. 150 with permission from Elsevier.

Another type of promising energy storage device, which has emerged in the last few years, is the high-power lithium-sulphur batteries. In this line, unstacked graphene layers separated by a large amount of mesosized protuberances synthesized using MgAl-LDH as templates exhibited an excellent performance even after 1,000 cycles, with high reversible capacities of *ca*. 530 $mAh \cdot g^{-1}$ and 380 $mAh \cdot g^{-1}$ which were retained at 5.0 C and 10.0 C, respectively.[84]

5.1.2. Supercapacitors.

Electrochemical supercapacitors, also known as ultracapacitors, have gained increasing interest in the scientific community due to their high power density and long lifecycle, among other properties.[154] Supercapacitors can be divided in two main different types, the electrical double layer capacitors (EDLC), where the capacitance comes from the charge accumulation, thus being, dependent of the surface area of the electrode materials which is accessible to the electrolyte ions, and the *pseudo*-capacitors, where reversible and fast faradic processes are generated due to the presence of electro-active species.[155] Carbonaceous materials like CNTs, graphene or activated carbon are often

used as electrodes (mainly in EDLC) due to their good conductivity, flexibility, high surface area and electrocatalytic active sites allowing the generation of redox reactions.[156] Combining CNF with LDH gives rise to very promising nanocomposites for creating high-performance supercapacitors working at basic pHs, owing to their full use of the double-layer capacitance and high activity of the faradaic reactions.[27]

Some of the first examples of CNF/LDH nanocomposites as supercapacitors were developed using CNTs. Thus, a CNT/LDH was described in 2008 by Zhang *et al*.[94] It exhibits better values of specific capacitance than the pure LDH (CoAl-LDH in that work) –342 $F \cdot g^{-1}$ in the hybrid compared to 192 $F \cdot g^{-1}$ in the pure material– with a small loss of its capacitance of 10% after 400 cycles. The enhancement of the electrochemical properties relies in the high surface area and good electronic conductivity provided by the carbon nanotubes. Wei *et al.*[102] reported a hybrid of CNT/NiMn-LDH reaching a high specific capacitance (measured by galvanostatic charge-discharge curves) of 2960 $F \cdot g^{-1}$ at 1.5 $A \cdot g^{-1}$, which is 1.8 times higher than that observed for a simple CNT/$Ni(OH)_2$ composite. Even at high current densities such as 30 $A \cdot g^{-1}$, the 79.5% of the capacitance was retained. Moreover, as the stability of these hybrid materials in alkaline solutions is crucial for developing commercial alkaline batteries, cycling life tests were measured at 12 $A \cdot g^{-1}$, exhibiting a loss of *ca.* 3% after 2000 cycles. **Figure 23,** extracted from Ref. 102 displays the electrochemical performance of the CNT/NiMn-LDH nanocomposite.

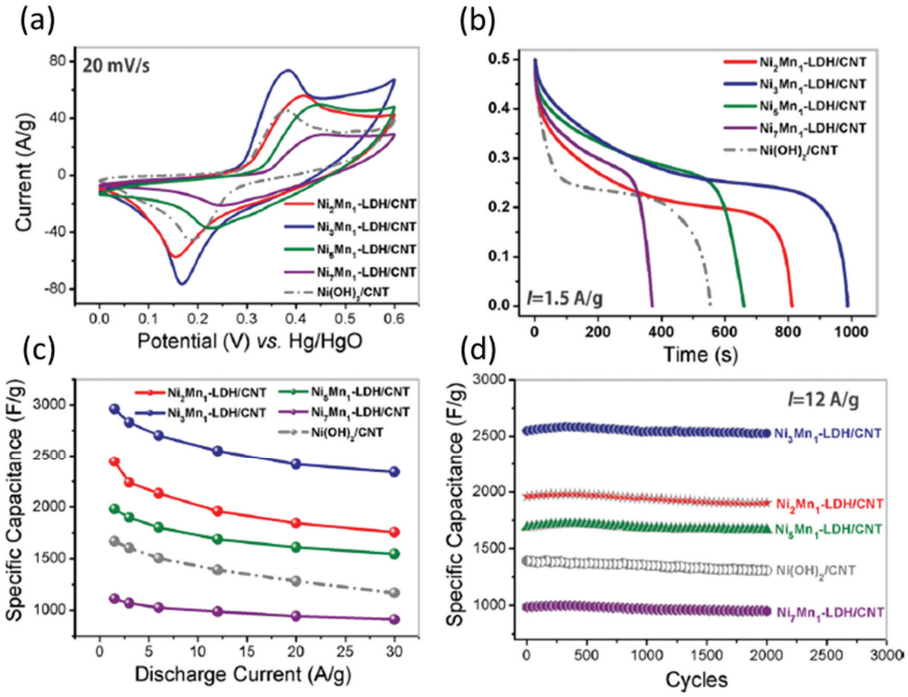

Figure 23. Electrochemical performance of the CNT/NiMn-LDH and the CNT/$Ni(OH)_2$ nanocomposites. (a) CV curves, (b) galvanostatic discharge curves, (c) specific capacitance and (d) cycle stability. Reproduced from Ref. 102 with permission from Wiley.

As far as the graphene is concerned, the first examples were developed using self-assembled exfoliated CoAl-LDH and NiAl-LDH, and GO nanosheets, as detailed in previous section 3. These nanocomposites exhibited specific capacitances up to 1031 $F \cdot g^{-1}$ at a current density of 1 $A \cdot g^{-1}$. Additionally, CoAl- and CoNi-LDH/rGO hybrids have been reported showing capacities as high as *ca.* 650 $F \cdot g^{-1}$.[68] Other nanocomposites with good results were observed by authors like Zhang *et al.*, with a carbon quantum dot/LDH nanocomposite[111], or Wang *et al.*[157], who reported the synthesis of a CNT/NiAl-LDH/rGO nanocomposite with high capacitances (1869, 1796 and 1562 $F \cdot g^{-1}$ at 1, 2.5 and 5 $mA \cdot cm^2$, respectively). A complete revision of the various LDH/carbon nanocomposites acting as supercapacitors can be found in the work of Cao *et al.*[55] The research interest in the field of CNF/LDH supercapacitors is constantly increasing. However, it is well-known that a test fixture configuration –like a two-electrode cell using big amounts (> 10 mg) of active materials in order to obtain reliable measurements– is more closely related to the performance of commercially available packaged cells than other conventional lab-scale configurations.[158,159]

Along this front, several efforts have still to be made in order to achieve the commercial application of CNF/LDH hybrids into the market.

5.1.3. Water splitting.

Electrocatalytic water splitting (WS) drives the conversion of water into hydrogen fuels and arguably qualifies as the most promising source of limitless, clean, renewable energy. The OER ($2\ H_2O \rightarrow O_2 + 4H^+ + 4e^-$) is the key limiting process as it is energetically disfavoured by the thermodynamic stability of water.[160,161]

It involves the transfer of 4-electron per molecule with a complex mechanism affecting the overall energy conversion efficiency.[162] Practical electrochemical H_2 production is generally limited by the high overpotentials necessary, imposed by the slow kinetics of O_2 evolution, and the poor stability of electrode materials under alkali conditions. To date, the dominant electrocatalysts for OER are based on oxides of precious metals like Iridium (IrO_2) or Ruthenium (RuO_2) oxides based on their efficiency and sustainability.[163] Their high cost and scarcity nonetheless has hindered integration into commercial electrolysers and prompted the search of inexpensive, more abundant alternatives featuring similar efficiencies —high current densities at low overpotentials— and chemical stabilities. LDHs have been postulated as very efficient bimetallic earth-abundant electrocatalysts. Indeed, nanosheets of NiFe-LDH display very high OER activity in alkali solutions and has been proposed as excellent electrodes for ultrafast Zn-air batteries.[164,165166,167] However, their poor electrical conductivity and tendency of the layers to re-pack might compromise the stability of the electrode featuring poor sustainability. This can be overcome by hybridization with conducting CNF, dramatically improving its performance. The surface exposure and the direct interfacial contact of all transition metal atoms and CNFs is very favourable in expediting the redox reaction due to a fast proton-coupled electron transfer process, and significantly shorter diffusion distances of the reactants.

CNF/LDH nanocomposites have been tested recently by some authors focusing in this application. Dai *et al.* reported a CNT/NiFe-LDH nanocomposite with higher OER activity and stability than Ir-based catalyst, to whom also beats in economic cost.[81] The key of that activity is the growth of LDH nanoplatelets on the surface of the CNTs, therefore combining the OER activity of pristine NiFe-LDH[66] with the electron transport properties of CNT. The OER activity of the hybrid was studied under alkaline solutions in a three-electrode cell, and the onset potential was 1.50 V *vs* the reversible hydrogen electrode (RHE) in 0.1 M KOH. The Ir/C catalyst exhibits a similar value, whereas its OER current density value is lower than that of the CNT/NiFe-LDH at *ca.* 1.52 V. In 1 M KOH, the OER onset potential of the nanocomposite was *ca.* 1.45 V vs RHE. The

durability of the CNT/NiFe-LDH composite was also studied, resulting in good values under alkaline solutions. At 2.5 and 5 mA·cm^{-2} the catalyst showed a nearly constant potential in 0.1 M KOH, whereas in 1 M KOH there was a decrease in the working potential at a current density of 5 mA·cm^{-2}. **Figure 24**, extracted from the work of Dai,[81] displays the electrochemical performance of this material as OER catalyst in comparison with the Ir/C catalyst.

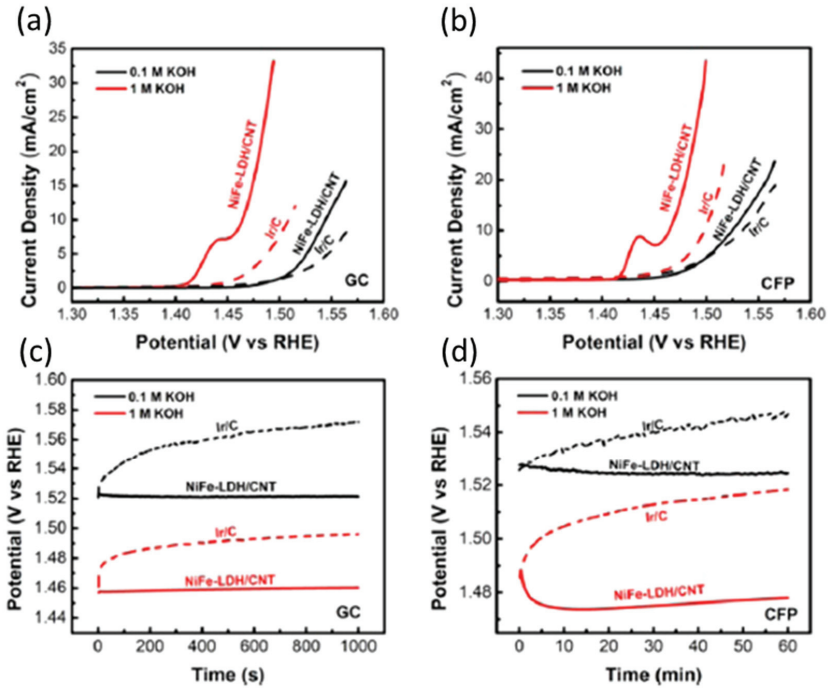

Figure 24. Electrochemical performance of the CNT/NiFe-LDH nanocomposite as a OER catalyst. (a) iR-corrected polarization curves of the nanocomposite and Ir/C catalyst on GC electrode in basic media. (b) iR-corrected polarization curves of the nanocomposite and Ir/C catalyst on carbon fiber paper. (c) Chronopotentiometry curves of the nanocomposite and Ir/C catalyst on GC electrode at a current density of 2.5 mA·cm^{-2}. (d) Chronopotentiometry curves of the nanocomposite and Ir/C catalyst on CFP at a current density of 5 mA·cm^{-2}. Reproduced with permission from Ref. 81. Copyright 2013 American Chemical Society.

Another CNT/LDH nanocomposite based on CNT/CoMn-LDH was described by Qiu *et al.*[168] It exhibited an excellent OER performance with an overpotential of 355 mV at 10 mA·cm^{-2} in 0.1 M KOH and good values of electrochemical durability, resulting in a performance similar to that of RuO_2. Furthermore, Wei *et al.* also synthesized a nanocarbon/NiFe-LDH hybrid (graphene and single-walled CNT),[141] whose OER performance exhibited a small onset overpotential of *ca.* 240 mV and a low overpotential

of 350 mV at 10 $mA \cdot cm^{-2}$ in 0.1 M KOH. Since 2013, systematic effort has been devoted to the design and synthesis of high-performance CNF/NiFe-LDH hybrids. However, several improvements are still required as, for exemple, a precise determination of the catalytic activity (the onset potential and the Tafel slopes are difficult to determine unambiguously due to the overlap of the Ni^{2+}/Ni^{3+} redox current and OER current), the precise control over the mass ratio between the components and, in operando insights on the underlying mechanism of the catalytic behavior. Moreover, an unambiguous control over the interfacial interactions through controlled covalent chemistry remains almost unexplored. A thorough revision of all the NiFe-LDH based catalysts can be found elsewhere.[169–171]

5.2. Catalysis.

LDHs have been widely used in the field of catalysis as supports or as active materials in different forms and for different purposes. CNF/LDH nanocomposites have been used as photocatalysts, in water oxidation, photodegradation of some pollutants and for the elimination of NO_x and SO_x contaminant emissions, to name a few.[172–174] Moreover, combined with CVD processes, LDHs can act as a catalyst for the synthesis of carbon nanoforms (using a carbon source that can be extrinsically added as a gas into the reactor, or be present as anions in the interlamellar space of the LDH).[19,47,117] As previously shown, the fact that the LDH phase evolves into a combination of metallic oxides and nanoparticles enhance the catalytic properties of the calcined material.[19] CNF/LDH nanocomposites are also reported as feasible catalysts, where the carbonaceous matrix increases the catalytic activity of the LDH, favoring the dispersion, mass transfer and heat processes.[27] Li *et al.*[175] prepared multi-walled CNT/NiAl-LDH which was calcined giving rise to a mixed Ni/Al oxide supported by the CNTs. The resulting nanocomposite was set again in a furnace and reduced with H_2 at high temperature, followed by the addition of propylene as carbon source for the synthesis of new multi-walled CNTs, therefore allowing the formation of more CNTs in relatively high quantity that can be later easily isolated after removing the mixed oxide catalyst through acidic treatment.

Abellán *et al.*[117] reported the synthesis of carbon spheres using NiFe-LDHs as catalytic precursors. **Figure 25**, depicts an electronic microscopic characterization of carbon spheres synthesized by CVD using NiFe-LDHs as catalysts.

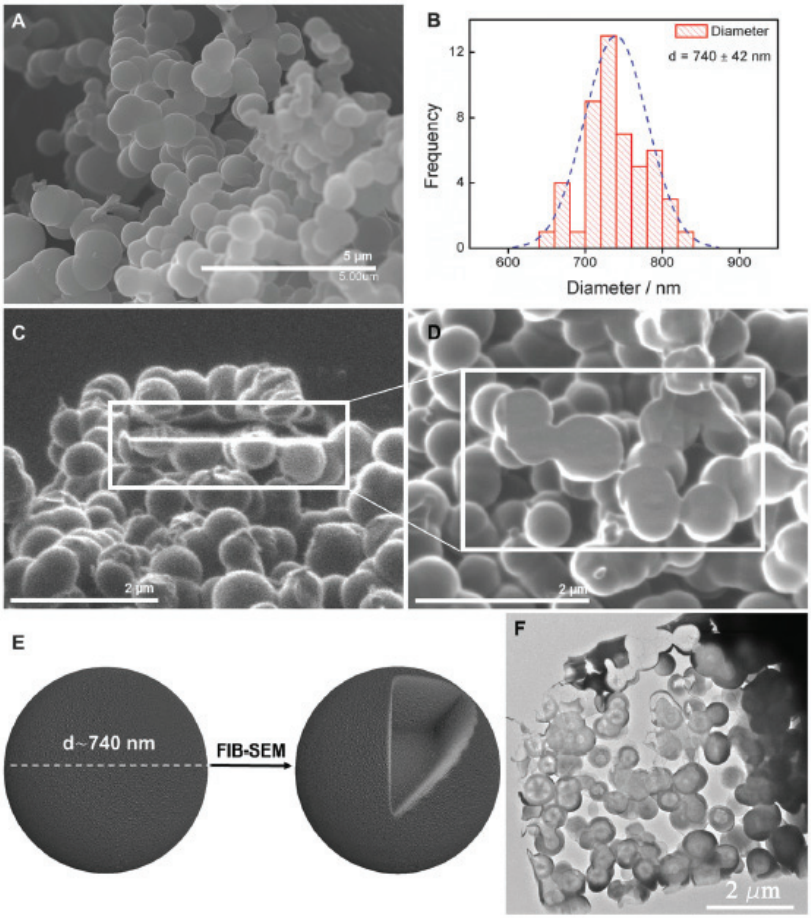

Figure 25. (A) FESEM image of carbon spheres synthesized after a CVD procedure using NiFe-LDH as catalyst. (B) Histogram displaying the average size of the spheres. (C, D) Focused Ion Beam (FIB) SEM images of the milled region and a cross-section of the spheres, respectively. (E) 3D representation before and after the FIB, remarking the solid inner structure. (F) Bright field TEM image of an electron-transparent lamella prepared by FIB-SEM, highlighting the porosity between the carbon spheres. Reproduced from Ref. 117 with permission from the Royal Society of Chemistry.

Photocatalysis has also been reported for some hybrids.[176] Fan *et al.* prepared a graphene/ZnCr-LDH nanocomposite by dispersing the LDH nanoplatelets on exfoliated graphene sheets.[75] The hybrid was tested in the photodegradation of Rhodamine B under visible light irradiation. Comparing the composite with the pure LDH phase, it was observed that the graphene matrix improved the transport and separation of the photogenerated charge carriers, therefore leading to better photodegradation results (see **Figure 26**, extracted from Ref. 75).

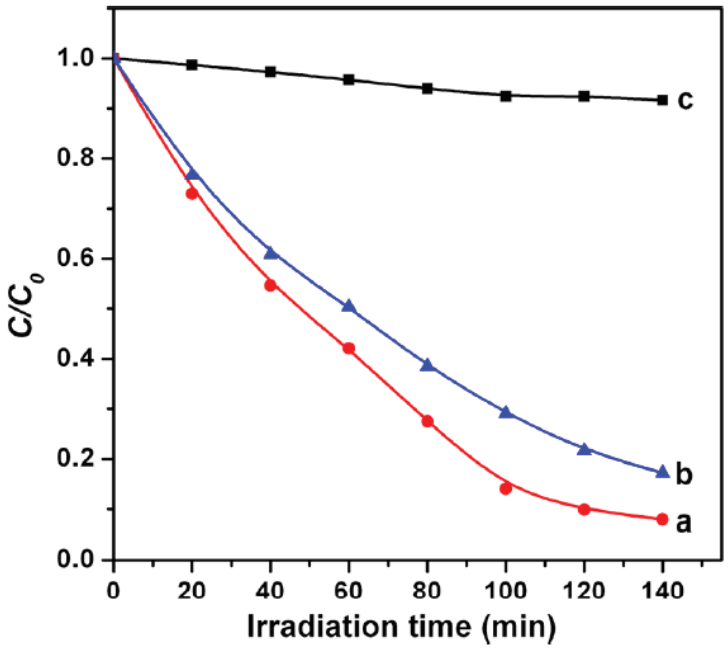

Figure 26. Photodegradation of Rhodamine B over graphene/ZnCr-LDH nanocomposite; (a) alone, (b) in presence of 1 mM benzoquinone and (c) in presence of 10 mM *t*-BuOH. Reproduced with permission from Ref. 75. Copyright 2014 American Chemical Society.

5.3. Miscellanea.

Despite the fact that electrochemistry and catalysis are the main applications studied for these nanocomposites, other fields such as environmental remediation, materials science or drug delivery have been explored for the application of LDH/CNF nanocomposites.

5.3.1. Environment Protection.

Thanks to the inherent anion exchange features of the LDHs,[72] these materials have been widely used as removal agents for different anions such as Cr (VI),[177] phosphates[178] or 2-Chlorophenol.[179] In this context, added to the fact that some carbon nanoforms such as CNT or graphene have shown good results in the adsorption of organic pollutants due to their porous structure,[180] CNF/LDH nanocomposites are perfectly suited for this application. Yang and co-workers prepared a CNT/mixed metal oxide nancomposite derived from a LDH for the adsorption of Congo red dye.[181] The LDH with terephtalic anions in its interlamellar space was pyrolysed under N_2 atmosphere, giving rise to the CNT/Mg(Al)O nanocomposite. Its adsorptive properties were tested regarding Congo red dye, giving rise to a peak of 1250 mg/g (pH = 7, adsorbent dosage of 30 mg). This value

is higher than that exhibited by other adsorbents like FeOOH hollow spheres (275 mg·g^{-1}), activated carbon fibers (557 mg·g^{-1}) or functionalized CNTs (882 mg·g^{-1}).[181] The main responsible of the high values is the interaction between the functionalized CNT surface and the dye, combined with the electrostatic attraction between the positively charged metallic components and the negatively charged Congo red ions.

Wang *et al.* and Liu *et al.* reported the synthesis of graphene/LDH nanocomposites for the efficient removal of As (V)[182] and methyl orange.[183] The first one (graphene/MgAl-LDH hybrid) exhibited adsorption peaks of 183.11 mg/g, higher than that observed for other adsorbents such as rGO/magnetite (5.83 mg·g^{-1}), α-FeOOH (58 mg/g) or Zr (IV)-loaded orange waste gel (88.0 mg·g^{-1}).[182] **Figure 27**, extracted from Ref. 182 depicts the adsorption behavior of this hybrid. The second one, a graphene/NiAl-LDH composite transformed in graphene/NiAl mixed oxides after the calcination of the material, presented a maximum adsorption of 210.8 mg·g^{-1} for methyl orange, in line with that observed for porous materials.[184]

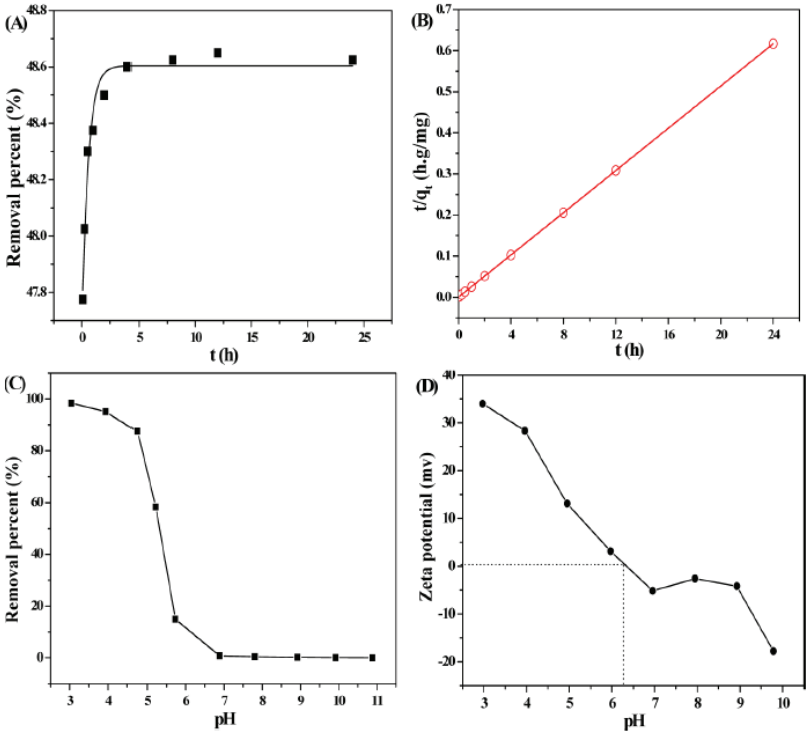

Figure 27. (A) Time profile for the adsorption of As (V) on GO/MgAl-LDH; (B) pseudo-second-order kinetic plots of t / qt vs t; (C) Effect of the pH on the adsorption of the As (V); (D) Zeta-potential of the nanocomposite as a function of pH. All experiments were tested in m / V = 0.5 g·L-1 and I = 0.01 M $NaNO_3$ polyethylene test tubes. Reproduced with permission from Ref. 182. Copyright 2013 American Chemical Society.

To sum up, due to the improved adsorption capacities of graphene/LDH nanocomposites, they have been used in CO_2 adsoprtion showing excellent results.[143] As a matter of fact, Shaffer and co-workers showed that the adsorption capacity of MgAl-LDH can be improved by 62 % just by hybridization with rGO (7 wt.%).[143]

5.3.2. Drug Delivery.

It is widely reported in the literature that carbon nanoforms such as graphene or CNTs can be used as efficient drug delivery vectors because of their large surface area and electronic properties. Drugs with aromatic groups can be bonded through π-π interactions to the surface of nanocarbons.[185,186] LDHs can also be used in this context due to their anion exchange capabilities. Different LDHs such as MgAl-, ZnAl- LiAl- or FeAl-LDH have been tested as host materials for drug delivery, conforming drug-LDH host-guest supramolecular interactions.[187] For these reasons, CNF/LDH nanocomposites are expected to be good candidates for acting as nanovectors in drug delivery. However, reports regarding this topic are very scarce. Zhang *et al.*[188] prepared films of graphene/MgAl-LDH nanocomposite with oxide-benzylpenicilin as the interlamellar anion. They observed a first-order kinetic regarding the controlled release of the drug. Moreover, the effectiveness in the release is enhanced as long as the density of the composite films is increased.

5.3.3. Materials Science.

Carbon/LDH nanocomposites have also been used in the field of polymers mainly in the form of CNT/LDH or graphene/LDH hybrids, taking advantage of the combination of properties of the two counterparts.[189,190] Fang and co-workers synthesized a CNT/NiAl-LDH nanocomposite by direct formation of the LDH on the CNTs.[96] The resulting hybrid was tested as flame retardant for polyprolylene. Attending to the heat release curves of polyprolylene, the nanocomposite material exhibited better results than those found for the separated building blocks, with a peak heat release rate of the hybrid of *ca.* 540 $kW \cdot m^{-2}$. This effect can be ascribed to the combination of the free radical trapping effect of the CNTs network and the barrier effect. The layered structure of the CNTs with the LDH shields the polymers from external radiation and heat feedback, while acting as excellent thermal insulator layers.[191] Huang *et al.* reported the use of a graphene/LDH nanocomposite as flame retardant for poly(methyl methacrylate).[192] The results depicted an improvement of the thermal stability of the polymer, as well as a reduction of the heat release rate, CO and smoke production if compared with the individual parts. Furthermore, the production of volatile compounds such as hydrocarbons or carbonyl compounds was also diminished. The enhancement of the

properties from the composite was ascribed to the combination of the barrier effect of the graphene and the catalytic carbonization of the LDH. **Figure 28**, extracted from Ref. 192, exhibits the heat release rate for the poly(methyl methacrylate) combined with the LDH, the rGO and the composite.

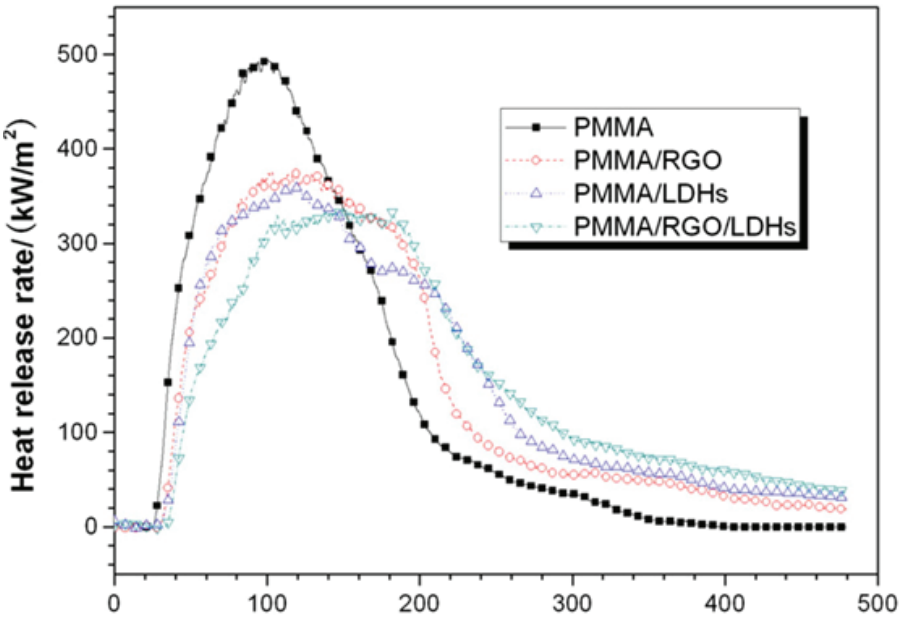

Figure 28. Heat release rate curve for the PMMA alone and hybridized with different components. Reproduced from Ref. 192 with permission from Elsevier.

6. Conclusions.

CNF/LDH nanocomposites have been widely studied in the recent years thanks to the adequate combination of the properties of both LDH and Carbon nanomaterials. In some cases they can exhibit newly improved or unexpected properties as a consequence of their hierarchical structures. Overall, three main approaches are reported to prepare the nanocomposites: reassembly of nanocarbons and LDH, direct formation of LDHs on the nanocarbon materials or the direct synthesis of nanocarbons on the LDH phase. The first one is usually achieved by means of liquid phase exfoliation and dispersion of the materials separately, followed by the self-assembly of both parts driven by electrostatic interactions. Secondly, the direct growth of LDH on the surface of nanocarbons is carried out generally by means of a coprecipitation or hydrothermal method where the carbonaceous material is added to a reaction mixture with the selected metallic salts. Lastly, the *in situ* growth of nanocarbons on the inorganic materials is usually accomplished by CVD procedures, where the carbon source can be present in the form

of carbon-rich intercalated anions in the interlamellar space of the LDH, or added in a gaseous phase (like ethylene) into the furnace. As far as their properties are concerned, the CNF/LDH nanocomposites exhibit improved conductivity, mechanical properties and redox reactivity; moreover, the hybridization confers hierarchical porosities and better dispersion to the final materials. These hybrids are of fundamental interest in several fields, but they can also be used in a plethora of practical applications including batteries, supercapacitors, water splitting, catalysts, flame retardants, drug delivery or environment protection. In summary, these classes of nanocomposites are expected to be of major importance because of their wide chemical versatility, straightforward synthesis, low cost and excellent behaviour towards very demanding topics such as energy storage and conversion or catalysis.

7. Perspectives.

CNF/LDH nanocomposites are very promising candidates for their application in emergent and very demanding areas such as Li-ion batteries, supercapacitors or water splitting. Indeed, great results have been achieved, like in water oxidation reaction, surpassing the performance of benchmark materials based on precious metals like Ir or Ru oxides. Moreover, these nanocomposites represent one of the most promising alternatives so far reported for ultrafast nickel-iron or metal-air batteries. In addition, the large porous structure of the employed carbon materials such as graphene or CNTs combined with the catalytic properties of some LDHs could give rise to hybrids very suitable for the heterogeneous catalysis in polymerization processes. Furthermore, although topics like drug delivery or environment protection have started to be explored, further advances are required in those fields for increasing the capacity of adsorbing and transporting anions in these CNF/LDH hybrids.

However, despite the great advances, several synthetic challenges should still be faced, as the development of high-quality defect-free graphene hybrids, the control over the metal distribution within the LDH layers and the stability of some LDH phases, or the synthesis of LDH nanocomposites with novel CNFs with promising properties like nanodiamonds or nanohorns. Moreover, hybridization with heteroatom-doped CNF is also a topic of utmost importance for several electrochemical applications.

In this sense, a more precise chemical control for tuning the particle size, the morphology of the building blocks and the final nanocomposites, or their processability, would boost the development of well-established applications, as well as new ones such as magnetism, nanoelectronics or sensing, to name a few.

Finally, the controlled assembly of functionalized LDH and CNF to create tailor-made hybrid architectures remains completely unexplored.

8. Acknowledgements.

Authors want to acknowledge the financial support from the European Commission (ERC Proof of Concept grant HyMAC, 713704), the Spanish MINECO –Ministerio de Economia, Industria y Competitividad– (Unit of Excellence Maria de Maeztu MDM-2015-0538 Grant and MAT2014-56143-R co-financed by FEDER) and the Generalitat Valenciana (Prometeo Program). In addition, the research leading to these results has received partial funding from the European Union Seventh Framework Program under Grant Agreement No. 604391 Graphene Flagship (G. A.). G. A. wants to also acknowledge Deutsche Forschungsgemeinschaft (DFG-SFB 953 "Synthetic Carbon Allotropes", Project A1) for its economic support. J.A.C. thanks the University of Valencia for a doctoral fellowship *Atracció de Talent*.

9. References.

(1) *Layered double hydroxides: present and future*; Rives, V., Ed.; Nova Science Publishers: Huntington, N.Y, 2001.

(2) *Layered Double Hydroxides*; Duan, X., Evans, D. G., Eds.; Structure and Bonding; Springer-Verlag: Berlin/Heidelberg, 2006; Vol. 119.

(3) Chen, C.; Wangriya, A.; Buffet, J.-C.; O'Hare, D. *Dalton Trans* **2015**, *44* (37), 16392.

(4) Delgado, J. L.; Herranz, M.; Martín, N. *J. Mater. Chem.* **2008**, *18* (13), 1417.

(5) Geim, A. K.; Novoselov, K. S. *Nat. Mater.* **2007**, *6* (3), 183.

(6) Geim, A. K. *Science* **2009**, *324* (5934), 1530.

(7) Lee, C.; Wei, X.; Kysar, J. W.; Hone, J. *Science* **2008**, *321* (5887), 385.

(8) Chen, J.-H.; Jang, C.; Xiao, S.; Ishigami, M.; Fuhrer, M. S. *Nat. Nanotechnol.* **2008**, *3* (4), 206.

(9) Seol, J. H.; Jo, I.; Moore, A. L.; Lindsay, L.; Aitken, Z. H.; Pettes, M. T.; Li, X.; Yao, Z.; Huang, R.; Broido, D.; Mingo, N.; Ruoff, R. S.; Shi, L. *Science* **2010**, *328* (5975), 213.

(10) Abraham, J.; Vasu, K. S.; Williams, C. D.; Gopinadhan, K.; Su, Y.; Cherian, C. T.; Dix, J.; Prestat, E.; Haigh, S. J.; Grigorieva, I. V.; Carbone, P.; Geim, A. K.; Nair, R. R. *Nat. Nanotechnol.* **2017**, *12*, 546.

(11) Eigler, S.; Hirsch, A. *Angew. Chem. Int. Ed.* **2014**, *53* (30), 7720.

(12) Hirsch, A.; Englert, J. M.; Hauke, F. *Acc. Chem. Res.* **2013**, *46* (1), 87.

(13) Paulus, G. L. C.; Wang, Q. H.; Strano, M. S. *Acc. Chem. Res.* **2013**, *46* (1), 160.

(14) Criado, A.; Melchionna, M.; Marchesan, S.; Prato, M. *Angew. Chem. Int. Ed.* **2015**, *54* (37), 10734.

(15) Abellán, G.; Schirowski, M.; Edelthalhammer, K. F.; Fickert, M.; Werbach, K.; Peterlik, H.; Hauke, F.; Hirsch, A. *J. Am. Chem. Soc.* **2017**, *139*, 5175.
(16) Baughman, R. H. *Science* **2002**, *297* (5582), 787.
(17) Kim, P.; Shi, L.; Majumdar, A.; McEuen, P. L. *Phys. Rev. Lett.* **2001**, *87* (21).
(18) Yu, M. *Science* **2000**, *287* (5453), 637.
(19) Abellán, G.; Carrasco, J. A.; Coronado, E.; Prieto-Ruiz, J. P.; Prima-García, H. *Adv. Mater. Interfaces* **2014**, *1* (6), 1400184.
(20) Abellán, G.; Martí-Gastaldo, C.; Ribera, A.; Coronado, E. *Acc. Chem. Res.* **2015**, 48, 1601.
(21) Clemente-León, M.; Coronado, E.; Martí-Gastaldo, C.; Romero, F. M. *Chem. Soc. Rev.* **2011**, *40* (2), 473.
(22) Abellán, G.; Jordá, J. L.; Atienzar, P.; Varela, M.; Jaafar, M.; Gómez-Herrero, J.; Zamora, F.; Ribera, A.; García, H.; Coronado, E. *Chem Sci* **2015**, *6* (3), 1949.
(23) Abellán, G.; Coronado, E.; Martí-Gastaldo, C.; Ribera, A.; Jordá, J. L.; García, H. *Adv. Mater.* **2014**, *26* (24), 4156.
(24) Goh, K.-H.; Lim, T.-T.; Dong, Z. *Water Res.* **2008**, *42* (6–7), 1343.
(25) Abellán, G.; Coronado, E.; Martí-Gastaldo, C.; Pinilla-Cienfuegos, E.; Ribera, A. *J. Mater. Chem.* **2010**, *20* (35), 7451.
(26) Coronado, E.; Martí-Gastaldo, C.; Navarro-Moratalla, E.; Ribera, A.; Blundell, S. J.; Baker, P. J. *Nat. Chem.* **2010**, *2* (12), 1031.
(27) Zhao, M.-Q.; Zhang, Q.; Huang, J.-Q.; Wei, F. *Adv. Funct. Mater.* **2012**, *22* (4), 675.
(28) Shi, X. D.; Kortan, A. R.; Williams, J. M.; Kini, A. M.; Savall, B. M.; Chaikin, P. M. *Phys. Rev. Lett.* **1992**, *68* (6), 827.
(29) Haddon, R. C.; Perel, A. S.; Morris, R. C.; Palstra, T. T. M.; Hebard, A. F.; Fleming, R. M. *Appl. Phys. Lett.* **1995**, *67* (1), 121.
(30) Yu, R. C.; Tea, N.; Salamon, M. B.; Lorents, D.; Malhotra, R. *Phys. Rev. Lett.* **1992**, *68* (13), 2050.
(31) Krishnan, A.; Dujardin, E.; Ebbesen, T. W.; Yianilos, P. N.; Treacy, M. M. J. *Phys. Rev. B* **1998**, *58* (20), 14013.
(32) Yu, M.-F.; Files, B. S.; Arepalli, S.; Ruoff, R. S. *Phys. Rev. Lett.* **2000**, *84* (24), 5552.
(33) Wilder, J. W.; Venema, L. C.; Rinzler, A. G.; Smalley, R. E.; Dekker, C. *Nature* **1998**, *391* (6662), 59.
(34) Ebbesen, T. W.; Lezec, H. J.; Hiura, H.; Bennett, J. W.; Ghaemi, H. F.; Thio, T. *Nature* **1996**, *382* (6586), 54.
(35) Berber, S.; Kwon, Y.-K.; Tománek, D. *Phys. Rev. Lett.* **2000**, *84* (20), 4613.
(36) Peigney, A.; Laurent, C.; Flahaut, E.; Bacsa, R. R.; Rousset, A. *Carbon* **2001**, *39* (4), 507.

(37) Montes-Navajas, P.; Asenjo, N. G.; Santamaría, R.; Menéndez, R.; Corma, A.; García, H. *Langmuir* **2013**, *29* (44), 13443.
(38) Compton, O. C.; Nguyen, S. T. *small* **2010**, *6* (6), 711.
(39) Dreyer, D. R.; Park, S.; Bielawski, C. W.; Ruoff, R. S. *Chem Soc Rev* **2010**, *39* (1), 228.
(40) Liu, L.; Zhang, J.; Zhao, J.; Liu, F. *Nanoscale* **2012**, *4* (19), 5910.
(41) Suk, J. W.; Piner, R. D.; An, J.; Ruoff, R. S. *ACS Nano* **2010**, *4* (11), 6557.
(42) Gómez-Navarro, C.; Weitz, R. T.; Bittner, A. M.; Scolari, M.; Mews, A.; Burghard, M.; Kern, K. *Nano Lett.* **2007**, *7* (11), 3499.
(43) Li, L.; Ma, R.; Ebina, Y.; Iyi, N.; Sasaki, T. *Chem. Mater.* **2005**, *17* (17), 4386.
(44) Du, M.; Ye, W.; Fu, H.; Lv, W.; Zheng, Q. *Compos. Sci. Technol.* **2014**, *105*, 28.
(45) Okamoto, K.; Iyi, N.; Sasaki, T. *Appl. Clay Sci.* **2007**, *37* (1–2), 23.
(46) Wang, B.; Williams, G. R.; Chang, Z.; Jiang, M.; Liu, J.; Lei, X.; Sun, X. *ACS Appl. Mater. Interfaces* **2014**,*6* (18), 16304.
(47) Abellán, G.; Coronado, E.; Martí-Gastaldo, C.; Ribera, A.; Sánchez-Royo, J. F. *Chem. Sci.* **2012**, *3* (5), 1481.
(48) Xu, Z. P.; Xu, R.; Zeng, H. C. *Nano Lett.* **2001**, *1* (12), 703.
(49) Gao, Z.; Wang, J.; Li, Z.; Yang, W.; Wang, B.; Hou, M.; He, Y.; Liu, Q.; Mann, T.; Yang, P.; Zhang, M.; Liu, L. *Chem. Mater.* **2011**, *23* (15), 3509.
(50) Li, H.; Zhu, G.; Liu, Z.-H.; Yang, Z.; Wang, Z. *Carbon* **2010**, *48* (15), 4391.
(51) Chen, D.; Wang, X.; Liu, T.; Wang, X.; Li, J. *ACS Appl. Mater. Interfaces* **2010**, *2* (7), 2005.
(52) Chen, H.; Hu, L.; Chen, M.; Yan, Y.; Wu, L. *Adv. Funct. Mater.* **2014**, *24* (7), 934.
(53) Wang, L.; Wang, D.; Dong, X. Y.; Zhang, Z. J.; Pei, X. F.; Chen, X. J.; Chen, B.; Jin, J. *Chem. Commun.* **2011**, *47* (12), 3556.
(54) Daud, M.; Kamal, M. S.; Shehzad, F.; Al-Harthi, M. A. *Carbon* **2016**, *104*, 241.
(55) Cao, Y.; Li, G.; Li, X. *Chem. Eng. J.* **2016**, *292*, 207.
(56) Wimalasiri, Y.; Fan, R.; Zhao, X. S.; Zou, L. *Electrochimica Acta* **2014**, *134*, 127.
(57) Wang, Q.; O'Hare, D. *Chem. Rev.* **2012**, *112* (7), 4124.
(58) Latorre-Sanchez, M.; Atienzar, P.; Abellán, G.; Puche, M.; Fornés, V.; Ribera, A.; García, H. *Carbon* **2012**, *50* (2), 518.
(59) Abellán, G.; Latorre-Sánchez, M.; Fornés, V.; Ribera, A.; García, H. *Chem. Commun.* **2012**, *48* (93), 11416.
(60) Backes, C.; Higgins, T. M.; Kelly, A.; Boland, C.; Harvey, A.; Hanlon, D.; Coleman, J. N. *Chem. Mater.* **2017**, *29* (1), 243.
(61) Huang, Z.; Wang, S.; Wang, J.; Yu, Y.; Wen, J.; Li, R. *Electrochimica Acta* **2015**, *152*, 117.

(62) Ma, W.; Ma, R.; Wang, C.; Liang, J.; Liu, X.; Zhou, K.; Sasaki, T. *ACS Nano* **2015**, *9* (2), 1977.
(63) Gardner, E.; Huntoon, K. M.; Pinnavaia, T. J. *Adv. Mater.* **2001**, *13* (16), 1263.
(64) Gursky, J. A.; Blough, S. D.; Luna, C.; Gomez, C.; Luevano, A. N.; Gardner, E. A. *J. Am. Chem. Soc.* **2006**, *128* (26), 8376.
(65) Abellán, G.; Carrasco, J. A.; Coronado, E.; Romero, J.; Varela, M. *J. Mater. Chem. C* **2014**, *2* (19), 3723.
(66) Carrasco, J. A.; Romero, J.; Varela, M.; Hauke, F.; Abellán, G.; Hirsch, A.; Coronado, E. *Inorg Chem Front* **2016**, *3* (4), 478.
(67) Xu, Z. P.; Li, L.; Cheng, C.-Y.; Ding, R.; Zhou, C. *Appl. Clay Sci.* **2013**, *74*, 102.
(68) Ma, R.; Liu, X.; Liang, J.; Bando, Y.; Sasaki, T. *Adv. Mater.* **2014**, *26* (24), 4173.
(69) Ma, W.; Ma, R.; Wu, J.; Sun, P.; Liu, X.; Zhou, K.; Sasaki, T. *Nanoscale* **2016**, *8*, 10425.
(70) Sun, P.; Ma, R.; Ma, W.; Wu, J.; Wang, K.; Sasaki, T.; Zhu, H. *NPG Asia Mater.* **2016**, *8* (4), e259.
(71) Dong, X.; Wang, L.; Wang, D.; Li, C.; Jin, J. *Langmuir* **2012**, *28* (1), 293.
(72) Liu, Z.; Ma, R.; Osada, M.; Iyi, N.; Ebina, Y.; Takada, K.; Sasaki, T. *J. Am. Chem. Soc.* **2006**, *128* (14), 4872.
(73) Huang, S.; Zhu, G.-N.; Zhang, C.; Tjiu, W. W.; Xia, Y.-Y.; Liu, T. *ACS Appl. Mater. Interfaces* **2012**, *4* (4), 2242.
(74) Yuan, X.; Wang, Y.; Wang, J.; Zhou, C.; Tang, Q.; Rao, X. *Chem. Eng. J.* **2013**, *221*, 204.
(75) Lan, M.; Fan, G.; Yang, L.; Li, F. *Ind. Eng. Chem. Res.* **2014**, *53* (33), 12943.
(76) Youn, D. H.; Park, Y. B.; Kim, J. Y.; Magesh, G.; Jang, Y. J.; Lee, J. S. *J. Power Sources* **2015**, *294*, 437.
(77) He, F.; Hu, Z.; Liu, K.; Guo, H.; Zhang, S.; Liu, H.; Xie, Q. *J. Solid State Electrochem.* **2015**, *19*, 607.
(78) Zhu, C.; Guo, S.; Fang, Y.; Dong, S. *ACS Nano* **2010**, *4* (4), 2429.
(79) Huang, J.; Lei, T.; Wei, X.; Liu, X.; Liu, T.; Cao, D.; Yin, J.; Wang, G. *J. Power Sources* **2013**, *232*, 370.
(80) Wang, H.; Dai, H. *Chem. Soc. Rev.* **2013**, *42* (7), 3088.
(81) Gong, M.; Li, Y.; Wang, H.; Liang, Y.; Wu, J. Z.; Zhou, J.; Wang, J.; Regier, T.; Wei, F.; Dai, H. *J. Am. Chem. Soc.* **2013**, *135* (23), 8452.
(82) Sun, J.; Liu, H.; Chen, X.; Evans, D. G.; Yang, W.; Duan, X. *Chem. Commun.* **2012**, *48* (65), 8126.
(83) Xie, K.; Qin, X.; Wang, X.; Wang, Y.; Tao, H.; Wu, Q.; Yang, L.; Hu, Z. *Adv. Mater.* **2012**, *24* (3), 347.

(84) Zhao, M.-Q.; Zhang, Q.; Huang, J.-Q.; Tian, G.-L.; Nie, J.-Q.; Peng, H.-J.; Wei, F. *Nat. Commun.* **2014**, *5*.
(85) Evans, D. G.; Duan, X. *Chem. Commun.* **2006**, No. 5, 485.
(86) Zhao, M.-Q.; Zhang, Q.; Huang, J.-Q.; Tian, G.-L.; Chen, T.-C.; Qian, W.-Z.; Wei, F. *Carbon* **2013**, *54*, 403.
(87) Zhao, M.-Q.; Peng, H.-J.; Zhang, Q.; Huang, J.-Q.; Tian, G.-L.; Tang, C.; Hu, L.; Jiang, H.-R.; Cai, H.-Y.; Yuan, H.-X.; Wei, F. *Carbon* **2014**, *67*, 554.
(88) Zhao, M.-Q.; Zhang, Q.; Huang, J.-Q.; Nie, J.-Q.; Wei, F. *Carbon* **2010**, *48* (11), 3260.
(89) Li, F.; Tan, Q.; Evans, D. G.; Duan, X. *Catal. Lett.* **2005**, *99* (3–4), 151.
(90) Xiang, X.; Zhang, L.; Hima, H.; Li, F.; Evans, D. *Appl. Clay Sci.* **2009**, *42* (3–4), 405.
(91) Cao, Y.; Zhao, Y.; Li, Q.; Jiao, Q. *J. Chem. Sci.* **2009**, *121* (2), 225.
(92) Zhao, Y.; Jiao, Q.; Li, C.; Liang, J. *Carbon* **2007**, *45* (11), 2159.
(93) Xue, R.; Sun, Z.; Su, L.; Zhang, X. *Catal. Lett.* **2010**, *135* (3–4), 312.
(94) Su, L.-H.; Zhang, X.-G.; Liu, Y. *J. Solid State Electrochem.* **2008**, *12* (9), 1129.
(95) Wang, H.; Xiang, X.; Li, F. *J. Mater. Chem.* **2010**, *20* (19), 3944.
(96) Du, B.; Fang, Z. *Nanotechnology* **2010**, *21* (31), 315603.
(97) Qiao, Z.; Gao, C.; Sun, B.; Ai, S. *J. Inorg. Organomet. Polym. Mater.* **2013**, *23* (4), 871.
(98) Wang, J.; Huang, L.; Zheng, Q.; Qiao, Y.; Wang, Q. *J. Ind. Eng. Chem.* **2016**, *36*, 255.
(99) Abellán, G.; Coronado, E.; Martí-Gastaldo, C.; Waerenborgh, J.; Ribera, A. *Inorg. Chem.* **2013**, *52* (17), 10147.
(100) Abellán, G.; Carrasco, J. A.; Coronado, E. *Inorg. Chem.* **2013**, *52* (14), 7828.
(101) Yang, J.; Yu, C.; Fan, X.; Ling, Z.; Qiu, J.; Gogotsi, Y. *J. Mater. Chem. A* **2013**, *1* (6), 1963.
(102) Zhao, J.; Chen, J.; Xu, S.; Shao, M.; Zhang, Q.; Wei, F.; Ma, J.; Wei, M.; Evans, D. G.; Duan, X. *Adv. Funct. Mater.* **2014**, *24* (20), 2938.
(103) Hima, H. I.; Xiang, X.; Zhang, L.; Li, F. *J. Mater. Chem.* **2008**, *18* (11), 1245.
(104) Pacuła, A.; Nowak, P.; Makowski, W.; Socha, R. P. *Microporous Mesoporous Mater.* **2015**, *201*, 1.
(105) Zhao, M.-Q.; Zhang, Q.; Zhang, W.; Huang, J.-Q.; Zhang, Y.; Su, D. S.; Wei, F. *J. Am. Chem. Soc.* **2010**, *132* (42), 14739.
(106) Liu, X. L.; Wang, Q.; Geng, D. G.; Wei, M.; Duan, X. *Asian J. Chem.* **2012**, *24* (1), 101.
(107) Xiao Lei Liu. *Asian J. Chem.* **2013**, *25* (8).

(108) Fortner, J. D.; Solenthaler, C.; Hughes, J. B.; Puzrin, A. M.; Plötze, M. *Appl. Clay Sci.* **2012**, *55*, 36.

(109) Tseng, W.-Y.; Lin, J.-T.; Mou, C.-Y.; Cheng, S.; Liu, S.-B.; Chu, P. P.; Liu, H.-W. *J. Am. Chem. Soc.* **1996**, *118* (18), 4411.

(110) Liu, W.; Xu, S.; Li, Z.; Liang, R.; Wei, M.; Evans, D. G.; Duan, X. *Chem. Mater.* **2016**, *28* (15), 5426.

(111) Wei, Y.; Zhang, X.; Wu, X.; Tang, D.; Cai, K.; Zhang, Q. *RSC Adv* **2016**, *6* (45), 39317.

(112) Tang, D.; Liu, J.; Wu, X.; Liu, R.; Han, X.; Han, Y.; Huang, H.; Liu, Y.; Kang, Z. *ACS Appl. Mater. Interfaces* **2014**, *6* (10), 7918.

(113) Gong, J.; Liu, T.; Wang, X.; Hu, X.; Zhang, L. *Environ. Sci. Technol.* **2011**, *45* (14), 6181.

(114) Xu, J.; He, F.; Gai, S.; Zhang, S.; Li, L.; Yang, P. *Nanoscale* **2014**, *6* (18), 10887.

(115) Chen, X.; Kierzek, K.; Cendrowski, K.; Pelech, I.; Zhao, X.; Feng, J.; Kalenczuk, R. J.; Tang, T.; Mijowska, E. *Colloids Surf. Physicochem. Eng. Asp.* **2012**, *396*, 246.

(116) Wickramaratne, N. P.; Xu, J.; Wang, M.; Zhu, L.; Dai, L.; Jaroniec, M. *Chem. Mater.* **2014**, *26* (9), 2820.

(117) Carrasco, J. A.; Prima-Garcia, H.; Romero, J.; Hernández-Saz, J.; Molina, S. I.; Abellán, G.; Coronado, E. *J Mater Chem C* **2016**, *4* (3), 440.

(118) Jin, Y. Z.; Gao, C.; Hsu, W. K.; Zhu, Y.; Huczko, A.; Bystrzejewski, M.; Roe, M.; Lee, C. Y.; Acquah, S.; Kroto, H.; Walton, D. R. M. *Carbon* **2005**, *43* (9), 1944.

(119) Yu, C.; Liu, Z.; Han, X.; Huang, H.; Zhao, C.; Yang, J.; Qiu, J. *Carbon* **2016**, *110*, 1.

(120) Zhao, J.; Lu, Z.; Shao, M.; Yan, D.; Wei, M.; Evans, D. G.; Duan, X. *RSC Adv* **2013**, *3* (4), 1045.

(121) He, F.; Hu, Z.; Liu, K.; Zhang, S.; Liu, H.; Sang, S. *J. Power Sources* **2014**, *267*, 188.

(122) Warsi, M. F.; Shakir, I.; Shahid, M.; Sarfraz, M.; Nadeem, M.; Gilani, Z. A. *Electrochimica Acta* **2014**, *135*, 513.

(123) Sun, J.; Liu, H.; Chen, X.; Evans, D. G.; Yang, W.; Duan, X. *Adv. Mater.* **2013**, *25* (8), 1125.

(124) Xu, Z. P.; Zeng, H. C. *J. Phys. Chem. B* **2000**, *104* (44), 10206.

(125) Putyera, K.; Bandosz, T. J.; Jagiełło, J.; Schwarz, J. A. *Appl. Clay Sci.* **1995**, *10* (1–2), 177.

(126) Putyera, K.; Bandosz, T. J.; Jagieo, J.; Schwarz, J. A. *Carbon* **1996**, *34* (12), 1559.

(127) Hibino, T. *Clays Clay Miner.* **1996**, *44* (1), 151.

(128) Leroux, F.; Dubois, M. *J. Mater. Chem.* **2006**, *16* (46), 4510.
(129) Leroux, F.; Raymundo-Piñero, E.; Nedelec, J.-M.; Béguin, F. *J Mater Chem* **2006**, *16* (21), 2074.
(130) Prévot, V.; Géraud, E.; Stimpfling, T.; Ghanbaja, J.; Leroux, F. *New J Chem* **2011**, *35* (1), 169.
(131) Abellán, G.; Coronado, E.; Martí-Gastaldo, C.; Ribera, A.; Otero, T. F. *Part. Part. Syst. Charact.* **2013**, 853.
(132) Iwasaki, T.; Tomisawa, M.; Nakamura, H.; Watano, S. *Chem. Vap. Depos.* **2013**, *19* (10-11–12), 323.
(133) Su, L.; Gong, L.; Qu, B.; Zhang, X. *Carbon* **2011**, *49* (14), 4950.
(134) Zhang, M.; Yao, Q.; Lu, C.; Li, Z.; Wang, W. *ACS Appl. Mater. Interfaces* **2014**, *6* (22), 20225.
(135) Shi, L.; Sun, P.; Du, L.; Xu, R.; He, H.; Tan, S.; Zhao, C.; Huang, L.; Mai, W. *Mater. Lett.* **2016**, *175*, 275.
(136) Malak-Polaczyk, A.; Vix-Guterl, C.; Frackowiak, E. *Energy Fuels* **2010**, *24* (6), 3346.
(137) Guo, Y.; Liu, X.; Wang, X.; Iqbal, A.; Yang, C.; Liu, W.; Qin, W. *RSC Adv* **2015**, *5* (116), 95495.
(138) Béléké, A. B.; Higuchi, E.; Inoue, H.; Mizuhata, M. *J. Power Sources* **2013**, *225*, 215.
(139) Basu, D.; Das, A.; Stöckelhuber, K. W.; Wagenknecht, U.; Heinrich, G. *Prog. Polym. Sci.* **2014**, *39* (3), 594.
(140) Liu, W.; Xu, S.; Liang, R.; Wei, M.; Evans, D. G.; Duan, X. *J Mater Chem C* **2017**, *5*, 3536.
(141) Zhu, X.; Tang, C.; Wang, H.-F.; Zhang, Q.; Yang, C.; Wei, F. *J Mater Chem A* **2015**, *3* (48), 24540.
(142) Wang, X.; Zhou, S.; Xing, W.; Yu, B.; Feng, X.; Song, L.; Hu, Y. *J. Mater. Chem. A* **2013**, *1* (13), 4383.
(143) Garcia-Gallastegui, A.; Iruretagoyena, D.; Gouvea, V.; Mokhtar, M.; Asiri, A. M.; Basahel, S. N.; Al-Thabaiti, S. A.; Alyoubi, A. O.; Chadwick, D.; Shaffer, M. S. P. *Chem. Mater.* **2012**, *24* (23), 4531.
(144) Zhang, L.; Zhang, X.; Shen, L.; Gao, B.; Hao, L.; Lu, X.; Zhang, F.; Ding, B.; Yuan, C. *J. Power Sources* **2012**, *199*, 395.
(145) Tarascon, J.-M.; Armand, M. *Nature* **2001**, *414* (6861), 359.
(146) Li, H.; Wang, Z.; Chen, L.; Huang, X. *Adv. Mater.* **2009**, *21* (45), 4593.
(147) Liu, C.; Li, F.; Ma, L.-P.; Cheng, H.-M. *Adv. Mater.* **2010**, *22* (8), E28.
(148) Lewis, N. S.; Nocera, D. G. *Proc. Natl. Acad. Sci.* **2006**, *103* (43), 15729.

(149) Gray, H. B. *Nat. Chem.* **2009**, *1* (1), 7.
(150) Cheng, X.-B.; Tian, G.-L.; Liu, X.-F.; Nie, J.-Q.; Zhao, M.-Q.; Huang, J.-Q.; Zhu, W.; Hu, L.; Zhang, Q.; Wei, F. *Carbon* **2013**, *62*, 393.
(151) Fan, Z.-J.; Yan, J.; Wei, T.; Ning, G.-Q.; Zhi, L.-J.; Liu, J.-C.; Cao, D.-X.; Wang, G.-L.; Wei, F. *ACS Nano* **2011**, *5* (4), 2787.
(152) Yang, B.; Yang, Z.; Wang, R.; Wang, T. *Electrochimica Acta* **2013**, *111*, 581.
(153) Yang, B.; Yang, Z. *RSC Adv.* **2013**, *3* (31), 12589.
(154) Wang, G.; Zhang, L.; Zhang, J. *Chem. Soc. Rev.* **2012**, *41* (2), 797.
(155) Zhang, L. L.; Zhao, X. S. *Chem. Soc. Rev.* **2009**, *38* (9), 2520.
(156) Pandolfo, A. G.; Hollenkamp, A. F. *J. Power Sources* **2006**, *157* (1), 11.
(157) Yang, W.; Gao, Z.; Wang, J.; Ma, J.; Zhang, M.; Liu, L. *ACS Appl. Mater. Interfaces* **2013**, *5* (12), 5443.
(158) *Supercapacitors: Materials, Systems, and Applications*; Béguin, F., Frąckowiak, E., Eds.; Wiley-VCH Verlag GmbH & Co. KGaA: Weinheim, Germany, 2013.
(159) Stoller, M. D.; Ruoff, R. S. *Energy Environ. Sci.* **2010**, *3* (9), 1294.
(160) Oliver-Tolentino, M. A.; Vázquez-Samperio, J.; Manzo-Robledo, A.; González-Huerta, R. de G.; Flores-Moreno, J. L.; Ramírez-Rosales, D.; Guzmán-Vargas, A. *J. Phys. Chem. C* **2014**, *118* (39), 22432.
(161) Dau, H.; Limberg, C.; Reier, T.; Risch, M.; Roggan, S.; Strasser, P. *ChemCatChem* **2010**, *2* (7), 724.
(162) Liang, Y.; Li, Y.; Wang, H.; Dai, H. *J. Am. Chem. Soc.* **2013**, *135* (6), 2013.
(163) Walter, M. G.; Warren, E. L.; McKone, J. R.; Boettcher, S. W.; Mi, Q.; Santori, E. A.; Lewis, N. S. *Chem. Rev.* **2010**, *110* (11), 6446.
(164) Gong, M.; Li, Y.; Wang, H.; Liang, Y.; Wu, J. Z.; Zhou, J.; Wang, J.; Regier, T.; Wei, F.; Dai, H. *J. Am. Chem. Soc.* **2013**, *135* (23), 8452.
(165) Li, Y.; Gong, M.; Liang, Y.; Feng, J.; Kim, J.-E.; Wang, H.; Hong, G.; Zhang, B.; Dai, H. *Nat. Commun.* **2013**, *4*, 1805.
(166) Gray, H. B. *Nat. Chem.* **2009**, *1* (1), 7.
(167) Lu, Y.-C.; Xu, Z.; Gasteiger, H. A.; Chen, S.; Hamad-Schifferli, K.; Shao-Horn, Y. *J. Am. Chem. Soc.* **2010**, *132* (35), 12170.
(168) Liu, Z.; Yu, C.; Han, X.; Yang, J.; Zhao, C.; Huang, H.; Qiu, J. *ChemElectroChem* **2016**, *3* (6), 906.
(169) Gong, M.; Dai, H. *Nano Res.* **2015**, *8* (1), 23.
(170) Jia, X.; Zhao, Y.; Chen, G.; Shang, L.; Shi, R.; Kang, X.; Waterhouse, G. I. N.; Wu, L.-Z.; Tung, C.-H.; Zhang, T. *Adv. Energy Mater.* **2016**, *6*, 1502585.
(171) Tang, C.; Wang, H.-F.; Zhu, X.-L.; Li, B.-Q.; Zhang, Q. *Part. Part. Syst. Charact.* **2016**, *33* (8), 473.

(172) Fan, G.; Li, F.; Evans, D. G.; Duan, X. *Chem Soc Rev* **2014**, *43* (20), 7040.

(173) Xu, Z. P.; Zhang, J.; Adebajo, M. O.; Zhang, H.; Zhou, C. *Appl. Clay Sci.* **2011**, *53* (2), 139.

(174) Choudary, B. M.; Madhi, S.; Chowdari, N. S.; Kantam, M. L.; Sreedhar, B. *J. Am. Chem. Soc.* **2002**, *124* (47), 14127.

(175) Li, C.-H.; Zhao, Y.; Yao, K.-F.; Liang, J. *Carbon* **2003**, *41* (12), 2443.

(176) Huang, Z.; Wu, P.; Gong, B.; Fang, Y.; Zhu, N. *J. Mater. Chem. A* **2014**, *2* (15), 5534.

(177) Hsu, L. C.; Wang, S. L.; Tzou, Y. M.; Lin, C. F.; Chen, J. H. *J. Hazard. Mater.* **2007**, *142* (1–2), 242.

(178) Seida, Y.; Nakano, Y. *Water Res.* **2002**, *36* (5), 1306.

(179) Chuang, Y. H.; Tzou, Y. M.; Wang, M. K.; Liu, C. H.; Chiang, P. N. *Ind. Eng. Chem. Res.* **2008**, *47* (11), 3813.

(180) Zhao, M.-Q.; Huang, J.-Q.; Zhang, Q.; Luo, W.-L.; Wei, F. *Appl. Clay Sci.* **2011**, *53* (1), 1.

(181) Yang, S.; Wang, L.; Zhang, X.; Yang, W.; Song, G. *Chem. Eng. J.* **2015**, *275*, 315.

(182) Wen, T.; Wu, X.; Tan, X.; Wang, X.; Xu, A. *ACS Appl. Mater. Interfaces* **2013**, *5* (8), 3304.

(183) Yang, Z.; Ji, S.; Gao, W.; Zhang, C.; Ren, L.; Tjiu, W. W.; Zhang, Z.; Pan, J.; Liu, T. *J. Colloid Interface Sci.* **2013**, *408*, 25.

(184) Haque, E.; Lee, J. E.; Jang, I. T.; Hwang, Y. K.; Chang, J.-S.; Jegal, J.; Jhung, S. H. *J. Hazard. Mater.* **2010**, *181* (1–3), 535.

(185) Liu, Z.; Tabakman, S.; Welsher, K.; Dai, H. *Nano Res.* **2009**, *2* (2), 85.

(186) Sun, X.; Liu, Z.; Welsher, K.; Robinson, J. T.; Goodwin, A.; Zaric, S.; Dai, H. *Nano Res.* **2008**, *1* (3), 203.

(187) Li, B.; He, J.; Gevans, D.; Duan, X. *Appl. Clay Sci.* **2004**, *27* (3–4), 199.

(188) Wang, Y.; Zhang, D.; Bao, Q.; Wu, J.; Wan, Y. *J. Mater. Chem.* **2012**, *22* (43), 23106.

(189) Costa, F. R.; Saphiannikova, M.; Wagenknecht, U.; Heinrich, G. In *Wax Crystal Control · Nanocomposites · Stimuli-Responsive Polymers*; Springer Berlin Heidelberg: Berlin, Heidelberg, 2007; Vol. 210, pp 101–168.

(190) Coleman, J. N.; Khan, U.; Gun'ko, Y. K. *Adv. Mater.* **2006**, *18* (6), 689.

(191) Kashiwagi, T.; Du, F.; Douglas, J. F.; Winey, K. I.; Harris, R. H.; Shields, J. R. *Nat. Mater.* **2005**, *4* (12), 928.

(192) Huang, G.; Chen, S.; Song, P.; Lu, P.; Wu, C.; Liang, H. *Appl. Clay Sci.* **2014**, *88–89*, 78.

General Conclusions

This thesis addresses the field of layered double hydroxides from three different perspectives. First of all, the study and comprehension of distinct factors that affect the magnetic nature of LDHs. The necessity of a meticulous synthesis in order to avoid impurities that can mislead in the magnetic response, the influence of the distortion on the internal magnetic disorder of the material or the effect of the interlayer distance on the dipolar interactions are studied from the fundamental basis. These studies help in unveiling the fundaments that relies beneath the magnetic behaviour of these systems. Afterwards, a new non-aqueous route was approached in the synthesis of magnetic LDHs, giving rise to nanometric alkoxide-intercalated materials that undergo complete hydrolysis and therefore exfoliation in water. These samples exhibited superparamagnetic behaviour, electrochemical properties and improved possibilities regarding exfoliation procedures, overcoming processability problems related to the most common delaminating reagents. Furthermore, unpublished studies on covalent functionalization and ultrasonic tip exfoliation were also carried out. Finally, the catalytic applications of LDHs towards the synthesis of carbon nanoforms were tested on bulk and ultrathin film samples, highlighting a great variety of possibilities according to the temperature and the arrangement of the samples, that range from the controllable synthesis of bamboo-like carbon nanotubes or carbon spheres to a mixture of different carbon nanoforms.

In summary, and thanks to the study of distinct magnetic LDH compositions (CoAl-, CoFe- and NiFe-, highlighting the -Fe^{3+} LDHs for its difficult synthesis), this thesis depicts an overall and in-depth vision of features linked to these materials such as magnetism, exfoliation, functionalization and applications. The final purpose is to extend the boundaries on the LDH field by contributing with new results that lead to a greater knowledge for these promising materials.

Resumen de la Tesis Doctoral

Introducción.

Tras el descubrimiento del grafeno en 2004, los materiales bidimensionales han generado un interés creciente por parte de la comunidad científica que se prolonga hasta nuestros días. Junto a este material constituido por delgadas láminas de carbono, también existen materiales bidimensionales de naturaleza inorgánica entre los que predominan aquellos basados en fuerzas de van der Waals. Dicalcogenuros metálicos, fósforo negro o antimoneno son algunos de estos ejemplos. Sin embargo, también existen materiales 2D formados por láminas iónicas, donde son las fuerzas electrostáticas las que ejercen un papel fundamental en cuanto a la organización y estructura de dichos sistemas. Este es el caso de los hidróxidos dobles laminares (LDHs).

Los LDHs son una familia de arcillas aniónicas bidimensionales con estructura laminar que presentan un espaciado interlaminar donde se alojan los aniones que compensan el exceso de carga positiva de las láminas catiónicas, así como moléculas de solvatación. Su estructura química es análoga a la observada para el mineral natural hidrotalcita, $Mg_6Al_2(OH)_{16}(CO_3)\cdot 4H_2O$, siendo la fórmula de un LDH la siguiente: $[M^{2+}_{1-x}\, M^{3+}_{x}\, (OH)_2][A^{n-}]_{x/n}\cdot yH_2O$, donde M hace referencia a los cationes metálicos y A al anión interlaminar. Una de las principales características de estos materiales es su gran versatilidad desde el punto de vista estructural y de composición, permitiendo el uso de diferentes cationes, así como un conjunto de posibilidades en cuanto a la naturaleza del anión interlaminar. Además, una de las propiedades fundamentales de estos sistemas es su capacidad de exfoliarse en láminas bidimensionales manteniendo las propiedades del material prístino, tales como su magnetismo o propiedades redox. Esto les permite ejercer como unidades básicas en el ensamblado de estructuras más complejas, como es el caso de los materiales híbridos o heteroestructuras.

Generalmente, los cationes divalentes más habituales son Mg^{2+}, Ni^{2+}, Co^{2+}, Fe^{2+}, Zn^{2+}, Ca^{2+}, Cu^{2+} o Mn^{2+}, mientras que los trivalentes varían entre Al^{3+}, Fe^{3+}, Ni^{3+}, Cr^{3+}, Fe^{3+}, Ga^{3+}, Mn^{3+} o In^{3+}. En la lámina, estos cationes ocupan los centros de entornos de coordinación octaédricos, y quedan conectados con cationes vecinos a través de los grupos hidroxilos compartidos presentes en los vértices de estos

octaedros, conformando así la estructura bidimensional global infinita. Pese a que la presencia de un catión divalente y otro trivalente es el escenario más habitual en la síntesis de LDHs, existen también otras composiciones que pueden ir desde LDHs ternarios o cuaternarios hasta el uso de cationes monovalentes como el Li^{+} o tetravalentes como el Ti^{4+}. Respecto a la relación estequiométrica entre cationes, χ suele oscilar entre 0.2 – 0.4, lo que corresponde con una relación M^{2+}/M^{3+} entre 4:1 hasta 1.5:1. En relación al anión interlaminar, las posibilidades van desde aniones inorgánicos hasta orgánicos. Por ejemplo, se pueden emplear haluros (Cl^{-}, F^{-}, etc.), oxoaniones no metálicos (CO_3^{2-}, NO_3^{2-}, SO_4^{2-}, BrO_4^{-}, ClO_4^{-}, AsO_4^{3-}, etc.), oxometalatos (CrO_4^{2-}, MnO_4^{-}, $Cr_2O_7^{2-}$, VO_4^{3-}, etc.), surfactantes y aniones orgánicos ($C_2O_4^{2-}$, $C_6H_5SO_3^{-}$, CH_3COO^{-}, $C_6H_5COO^{-}$, $C_{12}H_{25}SO_4^{-}$ etc.) o bien ejemplos más exóticos como porfirinas, polímeros aniónicos, moléculas biológicas o moléculas fotoactivas, entre otros. Estos aniones pueden ser intercalados a través de reacciones de intercambio aniónico, que resultan fundamentales para modificar propiedades químicas, electrónicas, ópticas o incluso magnéticas del sistema global. En este contexto, la facilidad o dificultad de dichas reacciones depende de la densidad de carga de las láminas, así como de los aniones, observándose que aniones como el carbonato presentan una de las mayores afinidades por su elevada densidad de carga negativa, apareciendo de forma predominante en síntesis realizadas en atmósfera de aire. La sustitución de este anión por otros de menor densidad de carga tales como el nitrato o surfactantes es prácticamente imperativo para posteriores procesos de delaminación, donde la formación de micelas derivadas del uso de surfactantes favorece el proceso de exfoliación.

Desde el punto de vista sintético, los LDHs presentan varias alternativas respecto a su preparación. La más empleada estriba en el método de coprecipitación, donde las sales metálicas se disuelven en agua en presencia de un compuesto básico que favorezca un pH determinado para la formación de la fase hidróxido. Habitualmente es el método sintético escogido para LDHs en cuya composición se encuentra el catión Al^{3+}, cuyo carácter anfótero favorece la formación del hidróxido doble. El uso de agentes reguladores de pH tales como la urea está altamente recomendado para obtener mejores resultados de morfología y homogeneidad de tamaños de partícula. El empleo de esta metodología deriva en la obtención de láminas hexagonales y de

elevada cristalinidad, las cuales comienzan su nucleación a partir de una semilla de óxido o hidróxido del metal trivalente y forman el cristal completo mediante un crecimiento circular alrededor de la semilla.

Para las composiciones que no presentan Al^{3+} como metal trivalente (tales como NiCo-, CoFe- o NiFe-LDHs) se requiere el empleo de síntesis alternativas a la coprecipitación para asegurar la pureza y calidad cristalina de las muestras. En este contexto se emplean principalmente los tratamientos hidrotermales o solvotermales así como el uso de agentes quelantes que permitan la liberación progresiva del M^{3+} tales como la trietanolamina, o bien llevar a cabo aproximaciones sintéticas topotácticas. Junto a estas metodologías más convencionales también existen opciones minoritarias fundamentadas en microondas, ultrasonidos o electrosíntesis, entre otras. Cabe señalar que la adición de reactivos tales como etilenglicol o el empleo de rutas no acuosas da lugar a fuertes variaciones en la morfología y estructura interna del LDH, obteniéndose morfologías en forma de flores o de tamaños nanométricos, respectivamente, con una influencia directa sobre diversas propiedades del material tales como el comportamiento magnético.

A lo largo del presente trabajo se exponen y profundiza en tres aspectos fundamentales de estos materiales. Inicialmente, se estudiarán las propiedades magnéticas de los LDHs y cómo pueden verse afectadas respecto a tres factores: la necesidad de llevar a cabo una síntesis meticulosa para evitar posibles impurezas magnéticas que induzcan a error en cuanto a la respuesta magnética registrada, la modificación de la morfología y el distanciamiento de las láminas que componen el LDH. A continuación, se estudiará el campo de la exfoliación y la funcionalización covalente de estos materiales, y cómo el empleo de una ruta no acuosa da lugar a LDHs con alcóxidos intercalados que se hidrolizan en presencia de agua, favoreciendo así la formación de suspensiones coloidales y la posterior deposición sobre sustratos. Del mismo modo, estos nuevos LDHs de tamaño nanométrico presentan comportamientos superparamagnéticos y unas propiedades electroquímicas diferentes a sus análogos micrométricos. Junto a ello se presentan resultados prometedores no publicados tanto en lo relativo a la exfoliación a través de punta de sonicación así como la funcionalización covalente de las láminas catiónicas con silanos. Por último, se abordarán las posibles aplicaciones catalíticas

de estos sistemas tanto en polvo como depositados formando films ultradelgados en reacciones catalíticas de deposición química en fase vapor a diferentes temperaturas. Los resultados obtenidos evidenciarán una respuesta distinta en función de la organización del LDH así como de la temperatura empleada.

En resumen, este trabajo expande los límites estudiados en estos sistemas en cuanto a aspectos tales como el magnetismo, la funcionalización y exfoliación o aplicaciones, remarcando la importancia de los LDHs en el campo de la ciencia de los materiales como sistemas con un presente brillante y un futuro prometedor.

Motivación.

La presente tesis está motivada por el creciente interés en el campo de la ciencia de los materiales, especialmente en cuanto a los recientes avances en materiales bidimensionales. Inspirados tras el descubrimiento e investigación del grafeno, los materiales bidimensionales de naturaleza inorgánica están generando un gran interés por parte de la comunidad científica. En concreto, los hidróxidos dobles laminares están experimentando un gran auge debido fundamentalmente a sus excepcionales resultados en campos de actualidad como la catálisis y la electroquímica, convirtiéndose en este caso en alternativas mucho más económicas que otras opciones tradicionales basadas en metales como el Ir o el Ru. No obstante, todavía existen numerosos aspectos y terrenos inexplorados que requieren del entendimiento de estos materiales.

Este trabajo está dividido en tres capítulos principales, los cuales presentan una misma estructura: una introducción respecto al estado del arte del tema en cuestión, seguido por un resumen de los principales resultados obtenidos durante el desarrollo de la tesis doctoral y concluyendo con las contribuciones del autor al campo en cuestión, esto último apoyado con la inclusión de las publicaciones más relevantes durante el desarrollo de la tesis doctoral.

Aspectos como la naturaleza magnética de los LDHs, con matices que requerían de un estudio metódico y sistemático, la funcionalización y posterior exfoliación de las mismas o sus aplicaciones catalíticas se abordan en detalle a lo largo de los diferentes capítulos, aportando nuevos resultados que nos permiten aumentar el

conocimiento global de estos materiales y conocer al detalle nuevos entresijos hasta ahora inexplorados que permitan avanzar en el campo de los LDHs desarrollando nuevas aplicaciones y sistemas híbridos. Tal es el caso de los LDHs de NiFe- y CoFe- puros y exfoliables sintetizados durante la tesis.

Respecto a los artículos incluidos en esta tesis, estos han sido seleccionados en función del tema central de los mismos. Así pues, el Capítulo 1 incluye tres artículos que versan sobre el comportamiento magnético de los LDHs: "*Room Temperature Magnetism in Layered Double Hydroxides due to Magnetic Nanoparticles*" (*Inorg. Chem.* **2013**, *52*, 7828–7830), "*Influence of Morphology in the Magnetic Properties of Layered Double Hydroxides*" (*J. Mater. Chem. C* **2018**, *6*, 1187–1198) y "*Deciphering the Role of Dipolar Interactions in Magnetic Layered Double Hydroxides*" (*Inorg. Chem.* **2018**, *57*, 2013–2022). El Capítulo 2 se centra en la funcionalización, exfoliación y propiedades electroquímicas de las nanoláminas exfoliadas, presentando dos artículos basados en la síntesis no acuosa de LDHs de tamaño nanométrico: "*Alkoxide-intercalated CoFe-Layered Double Hydroxides as Precursors of Colloidal Nanosheet Suspensions: Structural, Magnetic and Electrochemical Properties*" (*J. Mater. Chem. C* **2014**, *2*, 3723–3731) y "*Alkoxide-intercalated NiFe-Layered Double Hydroxides Magnetic Nanosheets as Efficient Water Oxidation Electrocatalysts*" (*Inorg. Chem. Front.* **2016**, *3*, 478–487). Para terminar, el Capítulo 3 aborda las aplicaciones catalíticas de NiFe-LDHs respecto a la síntesis de nanoformas de carbono, tanto en polvo como depositados en films: "*In-Situ Growth of Ultrathin Films of NiFe-LDHs: Towards a Hierarchical Synthesis of Bamboo-Like Carbon Nanotubes*" (*Adv. Mater. Interfaces* **2014**, *1*, 1400184) y "*CVD Synthesis of Carbon Spheres Using NiFe-LDHs as Catalytic Precursors: Structural, Electrochemical and Magnetoresistive Properties*" (*J. Mater. Chem. C* **2016**, *4*, 440–448). Junto a ellos, se incluye el capítulo de libro "*Layered Double Hydroxide Nanocomposites Based on Carbon Nanoforms*" (Capítulo 9 del libro *Layered Double Hydroxide Polymer Nanocomposites*; Ed. Woodhead Publishing, Cambridge, 2019).

Magnetismo en LDHs.

Una de las principales características de los LDHs es su potencial como materiales magnéticos, y cuyo magnetismo se conserva tras la exfoliación en nanoláminas de espesor reducido. De este modo se permite el acceso a sistemas magnéticos bidimensionales de composición y propiedades controladas. Todo ello les otorga la capacidad de actuar como unidades magnéticas básicas en el diseño de arquitecturas más complejas. El comportamiento magnético de los LDHs presenta dos contribuciones principales. Por un lado, las interacciones de supercanje magnético que tienen lugar entre centros metálicos vecinos de una misma lámina (interacciones intralaminares) mediante los puentes hidroxo que los unen. Por otra parte, se encuentran las interacciones dipolares (interlaminares), las cuales tienen lugar entre láminas catiónicas adyacentes y son de menor intensidad respecto a las intralaminares. Pese a que el carácter magnético de este tipo de materiales ha demostrado ser de gran utilidad tanto desde el punto de vista del material prístino como de sus híbridos (los cuales heredan el carácter magnético del LDH o lo combinan de forma sinérgica con el otro componente), el número de trabajos existentes en la literatura que abordan la naturaleza de dicho magnetismo o la influencia de determinados factores sobre él es muy escaso.

En concreto se estudiaron tres factores determinantes en el comportamiento magnético de estos sistemas. En primer lugar, la importancia de llevar a cabo una síntesis que permita obtener la muestra sin impurezas magnéticas, ya que estas pueden conducir a resultados erróneos al asignar una respuesta magnética al LDH cuando es en realidad debido a contribuciones extrínsecas a su magnetismo. En segundo lugar, se estudió cómo un cambio en la morfología de las láminas puede afectar al comportamiento magnético global dando lugar a un sistema más desordenado desde un punto de vista magnético. Por último, se analizó el efecto de la distancia interlaminar sobre las interacciones dipolares y por consiguiente sobre el magnetismo completo del sistema, utilizando LDHs de dimensiones y morfología controladas.

Pese a que los LDHs presentan magnetización espontánea a bajas temperaturas, no existe ningún indicio que indique una posible magnetización a

temperatura ambiente. No obstante, algunos autores han descrito LDHs con Fe^{3+} que presentan dicha característica. Mediante un análisis exhaustivo de la metodología sintética, se observó que dicha propiedad era debida a la presencia de impurezas en forma de nanopartículas de espinelas u óxidos metálicos que se formaban durante la síntesis, puesto que, ante una fase pura, esta magnetización a temperatura ambiente era inexistente. La obtención de impurezas se encuentra ligada a la mayor complejidad sintética de obtener LDHs sin Al^{3+}, debido a la ausencia de un comportamiento anfótero por parte de los cationes de metales de transición. La obtención de fases puras se consigue mediante variación del tradicional método de coprecipitación o con la adición de agentes quelantes durante la síntesis. El estudio se llevó a cabo con dos familias de LDHs conteniendo Fe^{3+} en su estructura: NiFe- y CoFe-LDHs. Sintetizando ambas familias tanto en forma pura como impura, se observó, para el segundo caso, la aparición de partículas de ferrihidrita (FeOOH) así como de maghemita (Fe_2O_3) o magnetita (Fe_3O_4). Para el caso de CoFe-LDH también se produjo la formación de espinelas de $Co^{2+}Co^{3+}{}_2O_4$, $Co^{2+}Fe^{3+}{}_3O_4$ o $Co^{2+}Co^{3+}Fe^{3+}O_4$ debido a la oxidación parcial del Co^{2+} a Co^{3+}. Son estas partículas las que otorgan el carácter magnético a temperatura ambiente al material. La dificultad de detectar estas impurezas magnéticas estriba en que en ocasiones son invisibles a la caracterización por rayos X, por lo que se debe recurrir a microscopía de alta resolución para poder detectarlas decorando las láminas de LDHs. La caracterización magnética mediante corriente directa y alterna es extremadamente sensible a la presencia de dichas impurezas, observándose, para las muestras impuras, ciclos de histéresis a temperaturas superiores a la temperatura crítica del LDH en fase pura. Una forma macroscópica y sencilla de diferenciar una muestra pura de una impura es acercando un imán a ellas. La muestra impura será atraída por él mientras que la pura permanecerá inalterada.

La morfología también juega un papel fundamental en el magnetismo global del sistema. Gracias a la naturaleza flexible de los LDHs, estos se pueden obtener en formas diferentes a la convencional hexagonal mediante la modificación de sus parámetros sintéticos. Estas formas más exóticas pueden ser conos, espirales e incluso flores, entre otras, fruto de plegamientos y alteración de los bordes de las láminas. Sin embargo, no existían trabajos relacionados sobre cómo este cambio

de morfología podía alterar el ordenamiento magnético. Para llevar a cabo dicho estudio, se sintetizaron dos familias diferentes de LDHs con una relación M^{2+}/M^{3+} de 2:1, NiFe- y CoAl-, en dos morfologías enfrentadas, la clásica hexagonal y en forma de flor. Para ello se empleó un método de síntesis hidrotermal (en presencia de etilenglicol para las muestras de flores). Ambas morfologías fueron obtenidas satisfactoriamente a la luz de las imágenes de microscopía electrónica y otras técnicas de caracterización como rayos X o isotermas de adsorción, comprobándose que las flores estaban formadas por láminas de LDHs de menor tamaño presentando un elevado grado de flexibilidad. Estas pequeñas láminas se agrupaban a modo de pétalos dando lugar a la estructura superior de una flor. Mientras que las técnicas clásicas de caracterización física no mostraban grandes diferencias (salvo mayor anchura y asimetría de picos en los difractogramas para las muestras de flores, factor relacionado con un sistema más desordenado, evidenciándose el desorden turbostático de estas muestras), la caracterización magnética sí resultó determinante a la hora de dilucidar el magnetismo de ambas morfologías, con diferencias que se evidenciaban independientemente de la composición metálica del LDH. Se observó que los sistemas de flores presentaban unos acoplamientos de carácter más antiferromagnéticos (menor valor de la constante de Weiss), junto con una temperatura de ordenamiento magnético mayor a la observada en la morfología hexagonal. También presentaban un mayor valor de la magnetización de saturación (aproximadamente un 50% superior a su análogo hexagonal). Estas variaciones, reportadas por primera vez en la presente tesis, están relacionadas con un aumento en el desorden del sistema desde el punto de vista magnético, efecto que vuelve a evidenciarse a través del cálculo del parámetro de Mydosh y la obtención de la energía de activación del sistema mediante ajustes de la señal fuera de fase (en la medida de corriente alterna). Respecto al rango obtenido por Mydosh, los sistemas distorsionados presentaron valores más bajos a los hexágonos, y por tanto más próximos a los mostrados por vidrios de espín canónicos. La energía de activación de los sistemas de flores también resultó en valores más elevados, en concordancia con dicho carácter más próximo a un vidrio de espín. De nuevo, todo ello pone de manifiesto cómo la distorsión de las láminas

debido al cambio de la morfología induce un desorden magnético en el sistema global.

El último factor sometido a estudio fue la influencia de la distancia interlaminar sobre las interacciones dipolares y por tanto sobre el magnetismo del sistema, análisis no realizado hasta la fecha. Para ello, se sintetizaron una serie de CoAl-LDHs cuyo espaciado interlaminar se aumentaba mediante reacciones de intercambio aniónico sucesivas, introduciendo surfactantes entre las láminas. De este modo se obtuvieron una serie de cinco miembros de CoAl-LDHs cristalinos de morfología idéntica con espacios basales desde 7.5 hasta 34 Å, correspondientes a las formas carbonato y octadecil sulfato, respectivamente. Tras confirmar que las reacciones de intercambio aniónico se produjeron satisfactoriamente (mediante rayos X, infrarrojo y análisis termogravimétrico), y que la morfología se mantenía inalterada (observándose hexágonos regulares de tamaño micrométrico), se llevó a cabo un exhaustivo estudio magnético sobre todas las muestras. Inicialmente, se esperaba que la distancia interlaminar tuviera un efecto importante sobre las interacciones dipolares, de modo que aumentar la distancia de separación entre láminas afectara al magnetismo global del sistema. No obstante, los resultados obtenidos fueron muy diferentes. Los datos experimentales mostraban un escenario magnético donde únicamente el campo coercitivo presentaba una dependencia con la distancia interlaminar en forma de incremento directo, mientras que el resto de factores no mostraban ninguna relación respecto a dicha distancia. Se llevaron a cabo estudios teóricos simplificados que nos permitieron arrojar algo de luz a dichos resultados, concluyéndose que el factor que realmente controla las interacciones dipolares en un sistema LDH no es la distancia interlaminar sino el tamaño de la lámina, íntimamente relacionado con el tamaño de dominio magnético. Únicamente para dominios pequeños la distancia interlaminar juega un papel determinante, aspecto que se demostró sintetizando un CoAl-LDH nanométrico mediante síntesis no acuosa (en metanol). Estas conclusiones concuerdan con resultados previos donde se ha observado que factores como el tamaño de partícula, la flexibilidad de las láminas o el agrupamiento catiónico contribuyen directamente sobre el magnetismo global del sistema. Respecto a extender este estudio sobre LDHs con dos metales magnéticos (como los NiFe-LDHs), cabría esperar un mayor efecto de

la distancia interlaminar sobre las interacciones dipolares debido a la presencia de interacciones magnéticas adicionales o efectos de frustración de espín.

Exfoliación y Funcionalización de LDHs.

Una de las características más interesantes de los LDHs estriba en su capacidad de conservar sus propiedades principales tras ser exfoliadas en nanoláminas bidimensionales. Propiedades como su carácter magnético o naturaleza redox se ven inalteradas tras el proceso de delaminación. Sin embargo, debido a la presencia de interacciones electrostáticas entre las láminas y los aniones interlaminares, los procesos de exfoliación requieren condiciones diferentes a las observadas en otros materiales bidimensionales cuyas interacciones predominantes son fuerzas de van der Waals, generalmente de menor intensidad (un orden de magnitud) que las electrostáticas. Este es el caso de materiales como el grafeno, el nitruro de boro, los dicalcogenuros metálicos o el fósforo negro, entre otros. Respecto a los LDHs, estos procesos de separación de láminas se llevan a cabo generalmente empleando formamida como agente delaminante, debido a su capacidad para ubicarse entre las láminas catiónicas y distanciarlas, disminuyendo así la intensidad de las fuerzas electrostáticas que las mantienen unidas y facilitando su posterior exfoliación tras aplicar un proceso de sonicación y agitación mecánica o magnética. Cabe mencionar que, con el objetivo de facilitar la delaminación por parte de la formamida, se requiere un proceso de intercambio aniónico previo que facilite el distanciamiento entre las láminas y el debilitamiento de sus interacciones interlaminares. Para ello se recurre habitualmente al uso de surfactantes tales como el dodecilsulfato de sodio por sus largas cadenas alifáticas que benefician la formación de micelas que a su vez favorecerán el proceso de dispersión y posterior delaminación.

A pesar de las ventajas de este disolvente, existen inconvenientes respecto a su toxicidad y a la procesabilidad de las dispersiones, debido a la dificultad de eliminar los restos de formamida tras la deposición sobre sustratos (films), principalmente a causa de su elevado punto de ebullición de 210 ºC. Es por ello que resulta vital explorar nuevas alternativas de exfoliación de LDHs. Una de las principales alternativas consiste en sintetizar LDHs a través de una ruta no acuosa, sino alcohólica, de modo que los materiales resultantes intercalados con los

correspondientes alcóxidos puedan hidrolizarse en presencia de agua dando lugar a dispersiones coloidales. En concreto, se ha empleado una síntesis en metanol de LDHs de CoFe- y NiFe- (relación M^{2+}/M^{3+} de 3:1 y 2:1, respectivamente) con el objetivo de estudiar las ventajas de esta metodología sintética sobre LDHs magnéticos, así como estudiar sus propiedades electroquímicas. Los LDHs así obtenidos, presentaron el ión metóxido (-OMe) como anión interlaminar y evidenciaron unas dimensiones nanométricas en base a los difractogramas y microscopía electrónica. Entre las diferentes técnicas de microscopía empleadas, destaca la microscopía electrónica de transmisión de barrido acoplada con espectroscopia de pérdida de energía de electrones (STEM-EELS), la cual exhibió tamaños de los nanocristales de los LDHs en torno a 26 y 110 nm para los CoFe- y NiFe-OMe, respectivamente, así como una elevada cristalinidad a lo largo de las láminas.

Gracias a la presencia de metóxido como anión interlaminar, se llevó a cabo un proceso de dispersión y exfoliación en agua, obteniéndose nanoláminas con dimensiones laterales de 20 (CoFe-OMe) y 50 nm (NiFe-OMe), así como espesores menores a 4 nm en ambos casos. También se estudió la importancia de la activación del sustrato con plasma de O_2, que mejoraba la deposición de las nanoláminas, alcanzándose un recubrimiento homogéneo a lo largo del film con un espesor menor a 3 nm para una dispersión de NiFe-OMe en una mezcla de formamida y butanol.

Desde el punto de vista magnético, el tamaño nanométrico de estos sistemas se ve reflejado en las menores temperaturas de ordenamiento del material, su naturaleza superparamagnética o el menor carácter de vidrio de espín en contraste con las muestras análogas de tamaño micrométrico sintetizadas por metodologías más convencionales. Entre otros factores, para el NiFe-OMe, se observó una temperatura de ordenamiento de 8 K frente a los 17 K del equivalente micrométrico o una energía de activación tras el ajuste de la señal fuera de fase en medidas de corriente alterna a una ecuación de Arrhenius de 276 K frente a los 1400 K del NiFe-LDH convencional, entre otros factores.

También se caracterizó por primera vez la electroquímica de estas dispersiones acuosas, observándose buenos resultados tanto en el campo de los

supercapacitores como en procesos de electrolisis del agua en medio básico, resultando en alternativas de electrocatálisis mucho más económicas que los tradicionales óxidos de Ir o Ru. Se llevó a cabo también el crecimiento directo del NiFe-OMe sobre espuma de Ni, disminuyéndose así el sobrepotencial respecto a la reacción de evolución de oxígeno (OER) de 340 a 249 mV frente a una concentración de KOH 1 M y pH = 14.

Para concluir, se realizaron estudios de exfoliación (no publicados) mediante punta de sonicación y funcionalización covalente sobre CoAl-LDHs sintetizados mediante métodos de coprecipitación convencionales. Respecto al proceso de exfoliación con punta de sonicación, se llevó a cabo un estudio de solubilidad en base a los parámetros de Hildebrand para localizar los disolventes óptimos, seguido de una deposición sobre sustratos de SiO_2 mediante centrifugación de las dispersiones a 5000 rpm. Las nanoláminas así obtenidas presentaron espesores de 15 y 6 nm para las muestras estudiadas, CoAl-CO_3 y CoAl-dodecilsulfato, respectivamente. Cabe resaltar que esta es la primera vez que se reporta la exfoliación directa de la forma carbonato sin realizar un intercambio aniónico previo. Por último, en lo concerniente a la funcionalización covalente, se lograron anclar moléculas de (3-aminopropil)trietoxisilano (APTS) a las láminas catiónicas tanto de un CoAl-LDH como de un NiFe-LDH. La caracterización por técnicas de rayos X, infrarrojo y esencialmente resonancia magnética nuclear de ^{29}Si en estado sólido sugirieron la unión covalente de las moléculas de APTS a las láminas catiónicas a través de los átomos de oxígeno. En base a los resultados obtenidos en los campos de exfoliación mediante punta de sonicación y funcionalización covalente, los LDHs se erigen como candidatos prometedores a tener en cuenta en ambos campos.

Aplicaciones de los LDHs.

Los LDHs presentan aplicaciones en diversos campos tales como magnetismo, catálisis, bioquímica, medicina, electroquímica o intercambio aniónico, entre otros. Este amplio rango se debe a la versatilidad química respecto a sus metales constituyentes, sus propiedades de intercambio aniónico y sus bajos costes de síntesis, que nos permiten modificar los materiales en función de la aplicación deseada. Actualmente, las aplicaciones que más interés están atrayendo en estos

materiales por parte de la comunidad científica son la catálisis y la electroquímica, tanto para los LDHs puras como en forma de híbridos. En concreto, muchos de estos híbridos se realizan junto con nanoformas de carbono, dando lugar a nuevas especies combinadas que potencian las propiedades catalíticas o electroquímicas de sus elementos por separado gracias a la sinergia entre las partes.

Entre los distintos LDHs, los compuestos por NiFe-LDHs han demostrado tener una excelente actividad catalítica en relación a la síntesis de nanoformas de carbono, en concreto aquellos con una relación Ni^{2+}/Fe^{3+} de 3:1. Dicha actividad se manifiesta tanto en muestras en polvo como organizadas sobre sustratos (films). En lo que respecta a las muestras en polvo, estas se sometieron a un proceso de calcinación mediante deposición química en fase vapor (con etileno como fuente de carbono) a alta temperatura de 900 ^{o}C, dando lugar a la síntesis de varios gramos de esferas de carbono con un diámetro aproximado de 740 nm. En base a la espectroscopia Raman, estas esferas mostraron un mayor grado de grafitización (cristalinidad) en comparación con esferas obtenidas en ausencia de catalizador de LDH. Por otra parte, se llevó a cabo un estudio de microscopia electrónica mediante haz de iones focalizados, permitiendo observar la estructura interna de las esferas, constituida por planos grafíticos organizados de manera concéntrica. Uno de los principales problemas en la síntesis de estos materiales es su tendencia a la formación de agregados debido a la elevada reactividad en la superficie de las esferas. Para evitar este efecto, se llevó a cabo la dispersión y posterior sonicación en tolueno, permitiendo obtener así esferas aisladas que fueron caracterizadas mediante microscopía de alta resolución. Por último, se estudiaron el comportamiento electroquímico así como la magnetorresistencia por primera vez de dichos materiales en aras de encontrar posibles aplicaciones favorecidas además por la facilidad de síntesis a gran escala. Respecto a los resultados electroquímicos, las esferas presentaron un comportamiento supercapacitor incluso en ausencia de mesoporosidad, mientras que en lo referente a magnetorresistencia gigante, se registró un efecto positivo y no saturado del 72% a baja temperatura (2 K), que disminuye drásticamente con el aumento de la misma, hasta no observarse señal a partir de 100 K.

Respecto a la organización en films ultradelgados, se realizó por primera vez un estudio exhaustivo sobre la formación y crecimiento de las láminas en función del tiempo empleando sustratos de cuarzo suprasil de alta calidad y baja rugosidad. Para ello, se realizó la síntesis *in situ* de NiFe-LDHs mediante método hidrotermal, situando el sustrato de cuarzo en el interior del autoclave. Los tiempos de reacción estudiados fueron de 24, 48 y 72 h. A raíz del estudio mediante microscopia electrónica de barrido se comprobó cómo el crecimiento paulatino de LDHs sobre los films está basado en un crecimiento circular, empezando con la formación de nanopartículas de FeO_x que crecen hasta dar lugar a la lámina hexagonal. La formación de dichas láminas se produce con estas alineadas paralelamente a la superficie del film, cuya organización óptima se alcanza a las 48 h de reacción, con un recubrimiento de NiFe-LDH en todo el sustrato y un espesor de 140 – 170 nm. Al aumentar el tiempo de síntesis hasta 72 h se observa cómo el tipo de organización de las láminas deriva hacia una alineación perpendicular respecto al sustrato. Únicamente empleando sustratos de baja rugosidad como el cuarzo suprasil (rugosidad promedio de 0.79 nm) se pueden observar claramente las diferentes etapas de crecimiento, puesto que con sustratos convencionales de cuarzo (rugosidad media de 1.25 nm) la disposición es más irregular y la alineación paralela no llega a apreciarse. La morfología hexagonal se mantiene tras someter los films a procesos de calcinación. El estudio magnético de films calcinados mostró el fenómeno de *exchange bias* debido al acoplamiento magnético que tiene lugar entre la fase ferromagnética de la espinela de $NiFe_2O_4$ con la matriz antiferromagnética de NiO. Ambas especies indican la transformación de la fase LDH en sus derivados calcinados. Al mismo tiempo, medidas mediante ángulo de contacto permitieron dilucidar el carácter hidrófilo o hidrófobo de los films, con valores inferiores a 90º (comportamiento hidrófilo) para los films con disposición paralela de las láminas de LDHs y mayores a 90º (comportamiento hidrófobo) en la disposición perpendicular.

Por último, se estudiaron las posibles aplicaciones catalíticas de estos films a bajas temperaturas (550 ºC) mediante procesos de deposición química en fase vapor (usando etileno como fuente de carbono), tanto en presencia como en ausencia de H_2 como agente reductor. Se observó indistintamente para ambos

casos la formación jerárquica de nanotubos de carbono de tipo bambú, un tipo concreto de nanotubos multicapa que presentaban un diámetro aproximado de 40 nm. El ángulo de contacto de este film resultó ser de 95º, indicativo de una naturaleza hidrofóbica. La misma temperatura de 550 ºC se escogió para la calcinación de muestras en polvo mediante deposición química en fase vapor, observándose en este caso una amalgama de diferentes nanoformas de carbono, entre ellas láminas de grafeno, fibras de carbono o nanotubos multicapa. Frente a la selectividad de las muestras en films, aquí se observó una mezcolanza de sistemas. Esta misma muestra en polvo calcinada a 900 ºC fue la base para la síntesis de las esferas de carbono descritas anteriormente, así pues mostrando un conjunto de posibilidades catalíticas para el mismo NiFe-LDH en función de su organización (polvo o film) y la temperatura de calcinación escogida.

Conclusiones.

En conclusión, la presente tesis doctoral aborda el campo de los hidróxidos dobles laminares desde tres perspectivas diferentes. Por una parte, el estudio de diversos factores que afectan a la naturaleza y comportamiento magnético de los LDHs. Factores como una correcta síntesis para evitar impurezas, la influencia de la morfología sobre el desorden magnético del sistema y el efecto de la distancia interlaminar así como los tamaños de dominios magnéticos sobre las interacciones dipolares son tratados desde el punto de vista más fundamental y sirven para ahondar en la casuística que subyace al carácter magnético de estos sistemas, permitiendo diseñar nuevos y mejores sistemas en el futuro empleando estos criterios. A continuación, se exploraron nuevas vías no acuosas de síntesis orientadas a mejorar y ampliar las posibilidades de exfoliación de estos materiales, unido a la funcionalización de sus láminas y a la repercusión de todo ello sobre las propiedades electroquímicas debido al tamaño nanométrico de estos LDHs con alcóxidos como anión interlaminar. Asimismo, la intercalación de alcóxidos permitió la exfoliación en agua gracias a la hidrólisis de los mismos, evitando los problemas de procesabilidad y toxicidad inherentes al uso de disolventes más convencionales en exfoliación como formamida. En última instancia, se analizaron las propiedades catalíticas frente a la síntesis de nanoformas de carbono tanto sobre muestras en

polvo como tras su procesado en films de espesor ultradelgados, encontrando una amplia gama de posibilidades en función de la temperatura empleada y el ordenamiento de las láminas. Respecto a las muestras en films, se trabajó con sustratos de baja rugosidad que permitió descifrar el mecanismo de crecimiento de las láminas en función del tiempo de síntesis.

En conjunto, y gracias al empleo de diferentes composiciones de LDHs estudiados (CoAl-, CoFe- y NiFe-, destacándose aquellos compuestos por -Fe^{3+} debido a su mayor dificultad sintética), esta tesis ofrece una visión global y desarrollada de tres aspectos vinculados a estos materiales como son magnetismo, exfoliación y funcionalización y por último aplicaciones, cuyo propósito es ampliar los límites de los mismos aportando nuevos resultados que repercutan en el mayor conocimiento y desarrollo de estos materiales.

Resum de la Tesi Doctoral

Introducció.

Després del descobriment del grafè a l'any 2004, els material bidimensional han generat un interès creixent per la comunitat científica que s'estén fins als nostres dies. Junt amb aquest material constituït per primes làmines de carboni, també hi ha materials bidimensionals de naturalesa inorgànica entre els que predominen aquells basats en forces de van der Waals. Dicalcogenurs metàl·lics, fòsfor negre, o antimoneno són alguns d'estos exemples. No obstant això, també hi ha materials 2D formats per làmines iòniques, on són les forces electrostàtiques les que exerceixen un paper fonamental en quant a l'organització i estructura d'aquests sistemes. Este és el cas dels hidròxids dobles laminars (LDHs).

Els LDHs són una família d'argiles aniòniques bidimensional amb estructura laminar que presentant un espaiat interlaminar on s'allotgen els anions que compensen l'excés de càrrega positiva de les làmines catiòniques, així com les molècules de solvatació. La seua estructura química és anàloga a l'observada per al mineral natural hidrotalcita, $Mg_6Al_2(OH)_{16}(CO_3)\cdot 4H_2O$ sent la fórmula d'un LDH la següent: $[M^{2+}_{1-x}\, M^{3+}_{x}\, (OH)_2][A^{n-}]_{x/n}\cdot yH_2O$, on M fa referència als cations metàl·lics i A a l'anió interlaminar. Una de les principals característiques d'estos materials és la seua gran versatilitat des del punt de vista estructural i de composició, permetent l'ús de diferents cations, així com un conjunt de possibilitats en quant a la naturalesa de l'anió interlaminar. A més, una de les propietats fonamentals d'estos sistemes és la seua capacitat d'exfoliar-se en làmines bidimensionals i mantindre les propietats del material pristi, com ara el seu magnetisme o propietats redox. Açò els permet exercir com a unitats bàsiques en l'acoblament d'estructures més complexes, com és el cas dels materials híbrids o les heteroestructures.

Generalment, els cations divalents més comuns són Mg^{2+}, Ni^{2+}, $Co^{2+}Fe^{2+}$, Zn^{2+}, Ca^{2+}, Cu^{2+} o Mn^{2+}, mentre que els trivalents varien entre Al^{3+}, Fe^{3+}, Ni^{3+}, Cr^{3+}, Fe^{3+}, Ga^{3+}, Mn^{3+} o In^{3+}. En la làmina, estos cations ocupen els centres d'entorns de coordinació octaèdrics, i queden connectats amb cations veïns a través dels grups hidroxils compartits presents en els vèrtexs d'estos octaedres, conformant així l'estructura bidimensional global infinita. A pesar que la presència d'un catió divalent i un altre trivalent és l'escenari més habitual en la síntesi d'LDHs, existeixen també

altres composicions que poden anar des d'LDHs ternaris o quaternaris fins a l'ús de cations monovalents com el Li^+ o tetravalent com el Ti^{4+}. Respecte a la relació estequiomètrica entre cations, χ sol oscil·lar entre 0.2 – 0.4, la qual cosa correspon amb una relació M^{2+}/M^{3+} entre 4:1 fins a 1.5:1. En relació a l'anió interlaminar, les possibilitats van des d'anions inorgànics fins a orgànics. Per exemple, es poden emprar halurs (Cl^-, F^-, etc..), oxoanions no metàl·lics (CO_3^{2-}, NO_3^{2-}, SO_4^{2-}, BrO_4^-, ClO_4^-, AsO_4^{3-}, etc.), oxometalats (CrO_4^{2-}, MnO_4^-, $Cr_2O_7^{2-}$, VO_4^{3-}, etc.) surfactants i anions orgànics ($C_2O_4^{2-}$, $C_6H_5SO_3^-$, CH_3COO^-, $C_6H_5COO^-$, $C_{12}H_{25}SO_4^-$ etc.) o bé exemples més exòtics com porfirines, polímers aniònics, molècules biològiques o molècules fotoactives, entre altres. Estos anions poden ser intercalats a través de reaccions d'intercanvi aniònic, que resulten fonamentals per a modificar propietats químiques, electròniques, òptiques i fins i tot magnètiques del sistema global. En aquest context, la facilitat o dificultat de dites reaccions depèn de la densitat de càrrega de les làmines, així com dels anions, i s'observa que anions com el carbonat presenten una de les majors afinitats per la seua elevada densitat de càrrega negativa, i apareixen de forma predominant en les síntesis realitzades en atmosfera d'aire. La substitució d'este anió per altres de menor densitat de càrrega com ara el nitrat o surfactants és pràcticament imperatiu per a posteriors processos de delaminació, on la formació de micel·les derivades de l'ús de surfactants afavoreix el procés d'exfoliació.

Des del punt de vista sintètic, els LDHs presenten diverses alternatives respecte a la seua preparació. La més emprada consisteix en el mètode de coprecipitació, on les sals metàl·liques es dissolen en aigua en presència d'un compost bàsic que afavoreix un pH determinat per a la formació de la fase hidròxid. Habitualment és el mètode sintètic triat per a LDHs en la composició dels quals es troba el catió Al^{3+}, amb un caràcter amfòter que afavoreix la formació de l'hidròxid doble. L'ús d'agents reguladors de pH com ara la urea està altament recomanat per obtindre millors resultats de morfologia i homogeneïtat de grandàries de partícula. L'ús d'esta metodologia deriva en l'obtenció de làmines hexagonals i d'elevada cristal·linitat, les quals comencen la seua nucleació a partir d'una llavor d'òxid o hidròxid del metall trivalent i formen el cristall complet per mitjà d'un creixement circular al voltant de la llavor.

Per a les composicions que no presenten Al^{3+} com a metall trivalent (com ara NiCo-, CoFe- o NiFe-LDHs) es requereix l'ús de síntesis alternatives a la coprecipitació per a assegurar la puresa i qualitat cristal·lina de les mostres. En este context s'emprèn principalment els tractaments hidrotermals o solvotermals així com l'ús d'agents quelants que permeten l'alliberament progressiu del M^{3+} com ara la trietanolamina, o bé dur a terme aproximacions sintètiques topotàctiques. Junt amb estes metodologies més convencionals també hi ha opcions minoritàries fonamentades en microones, ultrasons o electrosíntesi, entre altres. Cal assenyalar que l'addició de reactius com ara etilenglicol o l'ocupació de rutes no aquoses dóna lloc a fortes variacions en la morfologia i estructura interna de l'LDH, obtenint-se morfologies en forma de flors o de grandàries nanomètriques, respectivament, amb una influència directa sobre diverses propietats del material com ara el comportament magnètic.

Al llarg del present treball s'exposen i aprofundeix en tres aspectes fonamentals d'estos materials. Inicialment, s'estudiaran les propietats magnètiques dels LDHs i com poden veure's afectades respecte a tres factors: la necessitat de dur a terme una síntesi meticulosa per a evitar possibles impureses magnètiques que indueixin a error quant a la resposta magnètica registrada, la modificació de la morfologia i el distanciament de les làmines que componen l'LDH. A continuació, s'estudiarà el camp de l'exfoliació i la funcionalització covalent d'estos materials, i com l'ús d'una ruta no aquosa dóna lloc a LDHs amb alcóxids intercalats que s'hidrolitzen en presència d'aigua, afavorint així la formació de suspensions col·loïdals i la posterior deposició sobre substrats. De la mateixa manera, estos nous LDHs de grandària nanomètrica presenten comportaments superparamagnètics i unes propietats electroquímiques diferents dels seus anàlegs micromètrics. Així mateix, es presenten resultats prometedors no publicats tant pel que fa a l'exfoliació a través de punta de sonicació així com la funcionalització covalent de les làmines catiòniques amb silans. Finalment, s'abordaran les possibles aplicacions catalítiques d'estos sistemes tant en pols com depositats en films ultraprims en reaccions catalítiques de deposició química en fase vapor a diferents temperatures. Els resultats obtinguts evidenciaran una resposta distinta en funció de l'organització de l'LDH així com de la temperatura emprada.

En resum, este treball expandeix els límits estudiats en estos sistemes quant a aspectes com ara el magnetisme, la funcionalització i exfoliació o aplicacions, i remarca la importància dels LDHs al camp de la ciència dels materials com a sistemes amb un present brillant i un futur prometedor.

Motivació.

La present tesi està motivada pel creixent interès en el camp de la ciència dels materials, especialment quant als recents avanços en materials bidimensionals. Inspirats després del descobriment i investigació del grafè, els materials bidimensionals de naturalesa inorgànica estan generant un gran interès per part de la comunitat científica. En concret, els hidròxids dobles laminars estan experimentant un gran auge degut fonamentalment als seus excepcionals resultats en camps d'actualitat com la catàlisi i l'electroquímica, convertint-se en este cas en alternatives molt més econòmiques que altres opcions tradicionals basades en metalls com l'Au o el Ru. No obstant això, encara hi ha nombrosos aspectes i terrenys inexplorats que requereixen de l'enteniment d'estos materials.

Aquest treball està dividit en tres capítols principals, els quals presenten una mateixa estructura: una introducció respecte a l'estat de l'art del tema en qüestió, seguit per un resum dels principals resultats obtinguts durant el desenvolupament de la tesi doctoral i una conclusió amb les contribucions de l'autor al camp en qüestió, açò últim recolzat amb la inclusió de les publicacions més rellevants durant el desenvolupament de la tesi doctoral.

Aspectes com la naturalesa magnètica dels LDHs, la funcionalització i posterior exfoliació dels mateixos o les seues aplicacions catalítiques s'aborden en detall al llarg dels diferents capítols, aportant nous resultats que ens permeten augmentar el coneixement global d'estos materials i conèixer al detall nous amagatalls fins ara inexplorats que permeten avançar en el camp dels LDHs i desenvolupar noves aplicacions així com sistemes híbrids. Tal és el cas dels LDHs de NiFe- i CoFe- purs i exfoliables sintetitzats durant la tesi.

Pel que fa als articles inclosos en esta tesi, estos han sigut seleccionats en funció del tema central dels mateixos. Així doncs, el Capítol 1 inclou tres articles que

tracten sobre el comportament magnètic dels LDHs: "*Room Temperature Magnetism in Layered Double Hydroxides due to Magnetic Nanoparticles*" (*Inorg. Chem.* **2013**, *52*, 7828–7830), "*Influence of Morphology in the Magnetic Properties of Layered Double Hydroxides*" (*J. Mater. Chem. C* **2018**, *6*, 1187–1198) i "*Deciphering the Role of Dipolar Interactions in Magnetic Layered Double Hydroxides*" (*Inorg. Chem.* **2018**, *57*, 2013–2022). El Capítol 2 se centra en la funcionalització, exfoliació i propietats electroquímiques de les nanolàmines exfoliades, i presenta dos articles basats en la síntesi no aquosa d'LDHs de grandària nanomètrica: "*Alkoxide-intercalated CoFe-Layered Double Hydroxides as Precursors of Colloidal Nanosheet Suspensions: Structural, Magnetic and Electrochemical Properties*" (*J. Mater. Chem. C* **2014**, *2*, 3723–3731) i "*Alkoxide-intercalated NiFe-Layered Double Hydroxides Magnetic Nanosheets as Efficient Water Oxidation Electrocatalysts*" (*Inorg. Chem. Front.* **2016**, *3*, 478–487). Per a acabar, el Capítol 3 aborda les aplicacions catalítiques de NiFe-LDHs respecte a la síntesi de nanoformes de carboni, tant en pols com depositats en films: "*In-Situ Growth of Ultrathin Films of NiFe-LDHs: Towards a Hierarchical Synthesis of Bamboo-Like Carbon Nanotubes*" (*Adv. Mater. Interfaces* **2014**, *1*, 1400184) i "*CVD Synthesis of Carbon Spheres Using NiFe-LDHs as Catalytic Precursors: Structural, Electrochemical and Magnetoresistive Properties*" (*J. Mater. Chem. C* **2016**, *4*, 440–448). Amb ells s'inclou el capítol de llibre "*Layered Double Hydroxide Nanocomposites Based on Carbon Nanoforms*" (Capitol 9 del llibre *Layered Double Hydroxide Polymer Nanocomposites*; Ed. Woodhead Publishing, Cambridge, 2019).

Magnetisme en LDHs.

Una de les principals característiques dels LDHs és el seu potencial com a materials magnètics, el magnetisme dels quals es conserva després de l'exfoliació en nanolàmines de grossària reduïda. D'esta manera es permet l'accés a sistemes magnètics bidimensionals de composició i propietats controlades. Tot això els atorga la capacitat d'actuar com a unitats magnètiques bàsiques en el disseny d'arquitectures més complexes. El comportament magnètic dels LDHs presenta dues contribucions principals. D'una banda, les interaccions de supercanvi magnètic que tenen lloc entre centres metàl·lics veïns d'una mateixa làmina (interaccions

intralaminars) per mitjà dels ponts hidroxo que els uneixen. D'altra banda, es troben les interaccions dipolars (interlaminars), les quals tenen lloc entre làmines catiòniques adjacents i són de menor intensitat respecte a les intralaminars. Tot i que el caràcter magnètic d'este tipus de materials ha demostrat ser de gran utilitat tant des del punt de vista del material pristi com dels seus híbrids (els quals hereten el caràcter magnètic de l'LDH o ho combinen de forma sinèrgica amb l'altre component), el nombre de treballs existents en la literatura que aborden la naturalesa del magnetisme o la influència de determinats factors sobre ell és molt escàs.

Es van estudiar tres factors determinants en el comportament magnètic d'estos sistemes. En primer lloc, la importància de dur a terme una síntesi que permet obtenir la mostra sense impureses magnètiques, ja que estes poden conduir a resultats erronis a l'assignar una resposta magnètica a l'LDH quan és en realitat a causa de contribucions extrínseques al seu magnetisme. En segon lloc, es va estudiar com un canvi en la morfologia de les làmines pot afectar el comportament magnètic global i dóna lloc a un sistema més desordenat des d'un punt de vista magnètic. Finalment, es va analitzar l'efecte de la distància interlaminar sobre les interaccions dipolars i per consegüent sobre el magnetisme complet del sistema, utilitzant LDHs de dimensions i morfologia controlades.

Tot i que els LDHs presenten magnetització espontània a baixes temperatures, no hi ha cap indici que indiqui una possible magnetització a temperatura ambient. No obstant això, alguns autors han descrit LDHs amb Fe^{3+} que presenten dita característica. Per mitjà d'una anàlisi exhaustiva de la metodologia sintètica, es va observar que la dita propietat era deguda a la presència d'impureses en forma de nanopartícules d'espinel·les o òxids metàl·lics que es formaven durant la síntesi, ja que, davant d'una fase pura, esta magnetització a temperatura ambient era inexistent. L'obtenció d'impureses es troba lligada a la major complexitat sintètica d'obtindre LDHs sense Al^{3+}, a causa de l'absència d'un comportament amfòter per part dels cations de metalls de transició. L'obtenció de fases pures s'aconsegueix per mitjà de variació del tradicional mètode de coprecipitació o amb l'addició d'agents quelants durant la síntesi. L'estudi es va dur a terme amb dos famílies d'LDHs que contenen Fe^{3+} en la seua estructura: NiFe- i CoFe-LDHs. Amb la síntesi

d'ambdues famílies tant en forma pura com impura, es va observar, per al segon cas, l'aparició de partícules de ferrihidrita (FeOOH) així com de maghemita (Fe_2O_3) o magnetita (Fe_3O_4). Per al cas de CoFe-LDH també es va veure la formació d'espinel·les de $Co^{2+}Co^{3+}{}_2O_4$, $Co^{2+}Fe^{3+}{}_3O_4$ o $Co^{2+}Co^{3+}Fe^{3+}O_4$ a causa de l'oxidació parcial de Co^{2+} a Co^{3+}. Són estes partícules les que atorguen el caràcter magnètic a temperatura ambient al material. La dificultat de detectar estes impureses magnètiques consisteix en el fet pel qual de vegades són invisibles a la caracterització per rajos X, per la qual cosa s'ha d'emprar microscòpia d'alta resolució per a poder detectar-les decorant les làmines d'LDHs. La caracterització magnètica per mitjà de corrent directe i alterna és extremadament sensible a la presència de les dites impureses, i s'observa, per a les mostres impures, cicles d'histèresi a temperatures superiors a la temperatura crítica de l'LDH en fase pura. Una forma macroscòpica i senzilla de diferenciar una mostra pura d'una impura és acostant un imant a elles. La mostra impura serà atreta per ell mentre que la pura romandrà inalterada.

La morfologia també juga un paper fonamental en el magnetisme global del sistema. Gràcies a la naturalesa flexible dels LDHs, estos es poden obtindre en formes diferents de la convencional hexagonal per mitjà de la modificació dels seus paràmetres sintètics. Estes formes més exòtiques poden ser cons, espirals i fins i tot flors, entre altres, a causa de plegaments i alteració dels bords de les làmines. No obstant això, no existien treballs relacionats sobre com este canvi de morfologia podia alterar l'ordenament magnètic. Per a dur a terme l'estudi, es van sintetitzar dues famílies diferents d'LDHs amb una relació M^{2+}/M^{3+} de 2:1, NiFe- i CoAl-, en dues morfologies enfrontades, la clàssica hexagonal i en forma de flor. Per a això es va emprar un mètode de síntesi hidrotermal (en presència d'etilenglicol per a les mostres de flors). Ambdues morfologies van ser obtingudes satisfactòriament a la llum de les imatges de microscòpia electrònica i altres tècniques de caracterització com a rajos X o isotermes d'adsorció, i es va comprobar que les flors estaven formades per làmines d'LDHs més xicotetes presentant un elevat grau de flexibilitat. Estes xicotetes làmines s'agrupaven a manera de pètals i donan lloc a l'estructura superior d'una flor. Mentre que les tècniques clàssiques de caracterització física no mostraven grans diferències (excepte major amplària i asimetria de pics en els

difractogrames per a les mostres de flors, factor relacionat amb un sistema més desordenat), la caracterització magnètica sí va resultar determinant a l'hora de dilucidar el magnetisme d'ambdues morfologies, amb diferències que s'evidenciaven independentment de la composició metàl·lica de l'LDH. Es va observar que els sistemes de flors presentaven uns acoblaments de caràcter més antiferromagnètic (menor valor de la constant de Weiss), amb una temperatura d'ordenament magnètic major a l'observada en la morfologia hexagonal. També presentaven un valor més gran de la magnetització de saturació (aproximadament un 50% superior al seu anàleg hexagonal) . Estes variacions, reportades per primera vegada en la present tesi, estan relacionades amb un augment en el desordre del sistema des del punt de vista magnètic, efecte que torna a evidenciar-se mitjançant del càlcul del paràmetre de Mydosh i l'obtenció de l'energia d'activació del sistema per mitjà d'ajustos del senyal fora de fase (en la mesura de corrent alterna). Pel que fa al rang obtingut per Mydosh, els sistemes distorsionats van presentar valors més baixos als hexàgons, i per tant més pròxims als mostrats per vidres d' espí canònics. L'energia d'activació dels sistemes de flors també va resultar en valors més elevats, en concordança amb el caràcter més pròxim a un vidre d'espí. De nou, tot això posa de manifest com la distorsió de les làmines a causa del canvi de la morfologia indueix un desordre magnètic en el sistema global.

L'últim factor sotmès a estudi va ser la influència de la distància interlaminar sobre les interaccions dipolars i per tant sobre el magnetisme del sistema, anàlisi no realitzat fins a la data. Per a això, es van sintetitzar una sèrie de CoAl-LDHs l'espaiat interlaminar dels quals s'augmentava per mitjà de successives reaccions d'intercanvi aniònic, i es van introduir surfactants entre les làmines. D'esta manera es van obtindre una sèrie de cinc membres de CoAl-LDHs cristal·lins de morfologia idèntica amb espais basals des de 7.5 fins a 34 Å, corresponents a les formes carbonat i octadecil sulfat, respectivament. Després de confirmar que les reaccions d'intercanvi aniònic es van produir satisfactòriament (per mitjà de rajos X, infraroig i anàlisi termogravimètric), i que la morfologia roman inalterada (observant-se hexàgons regulars de grandària micromètrica) , es va dur a terme un exhaustiu estudi magnètic sobre totes les mostres. Inicialment, s'esperava que la distància interlaminar tinguera un efecte important sobre les interaccions dipolars, de manera

que augmentar la distància de separació entre làmines afectara el magnetisme global del sistema. No obstant això, els resultats obtinguts van ser molt diferents. Les dades experimentals mostraven un escenari magnètic on únicament el camp coercitiu presentava una dependència amb la distància interlaminar en forma d'increment directe, mentre que la resta de factors no mostraven cap relació respecte a la dita distància. Es van dur a terme estudis teòrics simplificats per comprendre millor els resultats, i es va concloure que el factor que controla les interaccions dipolars en un sistema LDH no és la distància interlaminar sinó la grandària de la làmina, íntimament relacionat amb la grandària de domini magnètic. Únicament per a dominis xicotets la distància interlaminar juga un paper determinant, aspecte que es va demostrar sintetitzant un CoAl-LDH nanomètrica per mitjà de síntesi no aquosa (en metanol). Estes conclusions concorden amb resultats previs on s'ha observat que factors com la grandària de partícula, la flexibilitat de les làmines o l'agrupament catiònic contribuïxen directament sobre el magnetisme global del sistema. Respecte a estendre este estudi sobre LDHs amb dos metalls magnètics (com els NiFe-LDHs), cabria esperar un major efecte de la distància interlaminar sobre les interaccions dipolars a causa de la presència d'interaccions magnètiques addicionals o efectes de frustració d'espí.

Exfoliació i Funcionalització d'LDHs.

Una de les característiques més interessants dels LDHs consisteix en la seua capacitat de conservar les seues propietats després de ser exfoliades en nanolàmines bidimensionals. Propietats com el seu caràcter magnètic o naturalesa redox es veuen inalterades després del procés de delaminació. No obstant això, a causa de la presència d'interaccions electrostàtiques entre les làmines i els anions interlaminars, els processos d'exfoliació requereixen condicions diferents de les observades en altres materials bidimensionals on les interaccions predominants són forces de van der Waals, generalment de menor intensitat (un orde de magnitud) que les electrostàtiques. Este és el cas de materials com el grafè, el nitrur de bor, els dicalcogenurs metàl·lics o el fòsfor negre. Pel que fa als LDHs, estos processos de separació de làmines es duen a terme generalment emprant formamida com a agent delaminant, a causa de la seua capacitat per a ubicar-se entre les làmines

catiòniques i distanciar-les, de manera que disminueixen la intensitat de les forces electrostàtiques que les mantenen unides i faciliten la posterior exfoliació després d'aplicar un procés de sonicació i agitació mecànica o magnètica. Cal mencionar que, amb l'objectiu de facilitar la delaminació per part de la formamida, es requereix un procés d'intercanvi aniònic previ que facilita el distanciament entre les làmines i el debilitament de les seues interaccions interlaminars. Per a això s'empra habitualment a l'ús de surfactants com ara el dodecilsulfat de sodi per les seues llargues cadenes alifàtiques que beneficien la formació de micel·les al seu torn, ide manera que s'afavoreix el procés de dispersió i posterior delaminació.

Malgrat els avantatges d'aquest dissolvent, hi ha inconvenients pel que fa a la seua toxicitat i a la processabilitat de les dispersions, a causa de la dificultat d'eliminar les restes de formamida després de la deposició sobre substrats (films), principalment a causa del seu elevat punt d'ebullició de 210 ^{o}C. És per això que resulta vital explorar noves alternatives d'exfoliació d'LDHs. Una de les principals alternatives consisteix a sintetitzar LDHs mitjançant una ruta no aquosa, sinó alcohòlica, de manera que els materials resultants intercalats amb els corresponents alcòxids puguin hidrolitzar-se en presència d'aigua i donar lloc a dispersions col·loïdals. En concret, s'ha emprat una síntesi en metanol d'LDHs de CoFe- i NiFe- (relació M^{2+}/M^{3+} de 3:1 i 2:1, respectivament) amb l'objectiu d'estudiar els avantatges d'esta metodologia sintètica en LDHs magnètics, així com estudiar les seues propietats electroquímiques. Els LDHs així obtinguts van presentar l'ió metòxid (-OMe) com a anió interlaminar, i van evidenciar unes dimensions nanomètriques d'acord amb els difractogrames i microscòpia electrònica. Entre les diferents tècniques de microscòpia emprades destaca la microscòpia electrònica de transmissió d'agranat acoblada amb espectroscòpia de pèrdua d'energia d'electrons (STEM-EELS), la qual va exhibir grandàries dels nanocristals dels LDHs al voltant de 26 i 110 nm per als CoFe- i NiFe-OMe, respectivament, així com una elevada cristal·linitat al llarg de les làmines.

Gràcies a la presència de metòxid com a anió interlaminar, es va dur a terme un procés de dispersió i exfoliació en aigua, i es van obtindre nanolàmines amb dimensions laterals de 20 (CoFe-OMe) i 50 nm (NiFe-OMe), així com grossàries menors a 4 nm en ambdós casos. També es va estudiar la importància de l'activació

del substrat amb plasma d'O_2, que millorava la deposició de les nanolàmines i aconseguia un recobriment homogeni al llarg del film amb una grossària menor a 3 nm per a una dispersió de NiFe-OMe en una mescla de formamida i butanol.

Des del punt de vista magnètic, la grandària nanomètrica d'estos sistemes es veu reflectada en les menors temperatures d'ordenament del material, la seua naturalesa superparamagnètica o el menor caràcter de vidre d'espí en contrast amb les mostres anàlogues de grandària micromètrica sintetitzades per metodologies més convencionals. Entre altres factors, per al NiFe-OMe, es va observar una temperatura d'ordenament de 8 K enfront dels 17 K de l'equivalent micromètric o una energia d'activació després de l'ajust del senyal fora de fase en mesures de corrent alterna a una equació d'Arrhenius de 276 K enfront dels 1400 K del NiFe-LDH convencional, entre altres factors.

També es va caracteritzar per primera vegada l'electroquímica d'estes dispersions aquoses, i es van observar bons resultats tant en el camp dels supercapacitors com en processos d'electròlisi de l'aigua en medi bàsic, resultant en alternatives d'electrocatàlisi molt més econòmiques que els tradicionals òxids d'Au o Ru. Es va dur a terme també el creixement directe del NiFe-OMe sobre escuma de Ni, disminuint-se així el sobrepotencial respecte a la reacció d'evolució d'oxigen (OER) de 340 a 249 mV enfront d'una concentració de KOH 1 M i pH = 14.

Per concloure, es van realitzar estudis d'exfoliació (no publicats) mitjançant punta de sonicació i funcionalització covalent en CoAl-LDHs sintetitzats per mètodes de coprecipitació convencionals. Respecte al procés d'exfoliació amb punta de sonicació, es va dur a terme un estudi de solubilitat basat en els paràmetres de Hildebrand per a localitzar els dissolvents òptims, seguit d'una deposició sobre substrats de SiO_2 per mitjà de centrifugació de les dispersions a 5000 rpm. Les nanolàmines així obtingudes van presentar grossàries de 15 i 6 nm per a les mostres estudiades, CoAl-CO_3 i CoAl-dodecilsulfat, respectivament. Cal ressaltar que aquesta és la primera vegada que es reporta l'exfoliació directa de la forma carbonat sense realitzar un intercanvi aniònic previ. Finalment, pel que fa a la funcionalització covalent, es van aconseguir ancorar molècules de (3-aminopropil)trietoxisilà (APTS) a les làmines catiòniques tant d'un CoAl-LDH com d'un NiFe-LDH. La caracterització

per tècniques de rajos X, infraroig i essencialment ressonància magnètica nuclear de ^{29}Si en estat sòlid van suggerir la unió covalent de les molècules d'APTS a les làmines catiòniques a través dels àtoms d'oxigen. Amb en els resultats obtinguts en els camps d'exfoliació amb punta de sonicació i funcionalització covalent, els LDHs s'erigeixen com a candidats prometedors a tindre en compte en ambdues àrees.

Aplicacions dels LDHs.

Els LDHs presenten aplicacions en diversos camps com ara magnetisme, catàlisi, bioquímica, medicina, electroquímica o intercanvi aniònic, entre altres. Este ampli rang es deu a la versatilitat química respecte als seus metalls constituents, les seues propietats d'intercanvi aniònic i els seus baixos costos de síntesi, que ens permeten modificar els materials en funció de l'aplicació desitjada. Actualment, les aplicacions de més interès en estos materials per part de la comunitat científica són la catàlisi i l'electroquímica, tant per als LDHs pures com en forma d'híbrids. En concret, molts d'estos híbrids es realitzen en combinació amb nanoformes de carboni, i donen lloc a noves espècies que potencien les propietats catalítiques o electroquímiques dels seus elements per separat gràcies a la sinergia entre les parts.

Entre els distints LDHs, els compostos per NiFe-LDHs han demostrat tindre una excel·lent activitat catalítica en relació a la síntesi de nanoformes de carboni, en concret aquells amb una relació Ni^{2+}/Fe^{3+} de 3:1. La dita activitat es manifesta tant en mostres en pols com organitzades sobre substrats (films). Pel que fa a les mostres en pols, estes es van sotmetre a un procés de calcinació per mitjà de deposició química en fase vapor (amb etilè com a font de carboni) a alta temperatura de 900 ºC, i va donar lloc a la síntesi de diversos grams d'esferes de carboni amb un diàmetre aproximat de 740 nm. D'acord amb l'espectroscòpia Raman, estes esferes van mostrar un major grau de grafitització (cristal·linitat) en comparació amb esferes obtingudes en absència de catalitzador d'LDH. D'altra banda, es va dur a terme un estudi de microscòpia electrònica per mitjà de feix d'ions focalitzats, el qual permet observar l'estructura interna de les esferes, constituïda per plans grafítics organitzats de manera concèntrica. Un dels principals problemes en la síntesi d'estos materials és la seua tendència a la formació d'agregats a causa de l'elevada

reactivitat en la superfície de les esferes. Per a evitar este efecte, es va dur a terme la dispersió i posterior sonicació en toluè, i es van obtindre així esferes aïllades que van ser caracteritzades mitjançant microscòpia d'alta resolució. Finalment, es van estudiar per primera vegada el comportament electroquímic així com la magnetoresistència dels materials a fi de trobar possibles aplicacions afavorides per la seua facilitat de síntesi a gran escala. Respecte als resultats electroquímics, les esferes van presentar un comportament supercapacitor inclús en absència de mesoporositat, mentre que pel que fa a magnetoresistència gegant, es va registrar un efecte positiu i no saturat del 72% a baixa temperatura (2 K), que disminuïx dràsticament amb l'augment d'aquesta, fins no observar-se senyal a partir de 100 K.

Pel que fa a l'organització en films ultraprims, es va realitzar per primera vegada un estudi exhaustiu sobre la formació i creixement de les làmines en funció del temps emprant substrats de quars suprasil d'alta qualitat i baixa rugositat. Per dur-ho a terme, es va realitzar la síntesi *in situ* de NiFe-LDHs per mitjà de mètode hidrotermal, que situa el substrat de quars en l'interior de l'autoclau. Els temps de reacció estudiats van ser de 24, 48 i 72 h. Arran de l'estudi de microscòpia electrònica d'agranat es va comprovar com el creixement gradual d'LDHs sobre els films està basat en un creixement circular, començant amb la formació de nanopartículas d'FeO_x que creixen fins a donar lloc a la làmina hexagonal. La formació de les dites làmines es produïx amb estes alineades paral·lelament a la superfície del film, l'organització òptima de la qual s'aconsegueix a les 48 h de reacció, amb un recobriment d'NiFe-LDH en tot el substrat i una grossària de 140 – 170 nm. A l'augmentar el temps de síntesi fins a 72 h s'observa com el tipus d'organització de les làmines deriva cap a una alineació perpendicular respecte al substrat. Únicament emprant substrats de baixa rugositat com el quars suprasil (rugositat mitjana de 0.79 nm) es poden observar clarament les diferents etapes de creixement, ja que amb substrats convencionals de quars (rugositat mitjana de 1.25 nm) la disposició és més irregular i l'alineació paral·lela no arriba a apreciar-se. La morfologia hexagonal es manté després de sotmetre els films a processos de calcinació. L'estudi magnètic de films calcinats va mostrar el fenomen d'*exchange bias* a causa de l'acoblament magnètic que té lloc entre la fase ferromagnètica de

l'espinel·la de $NiFe_2O_4$ amb la matriu antiferromagnètica d'NiO. Ambdues espècies indiquen la transformació de la fase LDH en els seus derivats calcinats. Al mateix temps, mesures per mitjà d'angle de contacte van permetre dilucidar el caràcter hidròfil o hidròfob dels films, amb valors inferiors a 90º (comportament hidròfil) per als films amb disposició paral·lela de les làmines de LDHs i majors a 90º (comportament hidròfob) en la disposició perpendicular.

Finalment, es van estudiar les possibles aplicacions catalítiques d'estos films a baixes temperatures (550 ºC) per mitjà de processos de deposició química en fase vapor (usant etilè com a font de carboni), tant en presència com en absència d'H_2 com a agent reductor. Es va observar indistintament per a ambdós casos la formació jeràrquica de nanotubs de carboni de tipus bambú, un tipus concret de nanotubs multicapa que presentaven un diàmetre aproximat de 40 nm. L'angle de contacte d'este film va resultar ser de 95º, indicatiu d'una naturalesa hidrofòbica. La mateixa temperatura de 550 ºC es va triar per a la calcinació de mostres en pols per mitjà de deposició química en fase vapor, i es va observar en aquest cas una amalgama de diferents nanoformes de carboni, entre elles làmines de grafè, fibres de carboni o nanotubs multicapa. Enfront de la selectivitat de les mostres en films, ací es va observar una mescladissa de sistemes. Esta mostra en pols calcinada a 900 ºC va ser la base per a la síntesi de les esferes de carboni descrites anteriorment, així doncs mostrant un conjunt de possibilitats catalítiques per al mateix NiFe-LDH en funció de la seua organització (pols o film) i la temperatura de calcinació triada.

Conclusions.

En conclusió, la present tesi doctoral aborda el camp dels hidròxids dobles laminars des de tres perspectives diferents. D'una banda, l'estudi de diversos factors que afecten la naturalesa i comportament magnètic dels LDHs. Factors com una correcta síntesi per a evitar impureses, la influència de la morfologia sobre el desordre magnètic del sistema i l'efecte de la distància interlaminar així com les grandàries de dominis magnètics sobre les interaccions dipolars són tractats des del punt de vista més fonamental i serveixen per aprofundir en la casuística subjacent al caràcter magnètic d'estos sistemes, i ens permet dissenyar nous i millors sistemes en el futur emprant estos criteris. A continuació, es van explorar noves vies no

aquoses de síntesi orientades a millorar i ampliar les possibilitats d'exfoliació d'estos materials, unit amb la funcionalització de les seues làmines i a la repercussió de tot això sobre les propietats electroquímiques a causa de la grandària nanomètrica d'estos LDHs amb alcòxids com a anió interlaminar. Així mateix, la intercalació d'alcòxids va permetre l'exfoliació en aigua gràcies a la hidròlisi dels mateixos, i evita els problemes de processabilitat i toxicitat inherents a l'ús de dissolvents més convencionals en exfoliació com la formamida. Per acabar, es van analitzar les propietats catalítiques derivades de la síntesi de nanoformes de carboni tant sobre mostres en pols com després del seu processat en films de grossària ultraprims, i es va trobar una àmplia gamma de possibilitats en funció de la temperatura emprada i l'ordenament de les làmines. Respecte a les mostres en films, es va treballar amb substrats de baixa rugositat que va permetre desxifrar el mecanisme de creixement de les làmines en funció del temps de síntesi.

En conjunt, i gràcies a l'estudi de diferents composicions d'LDHs (CoAl-, CoFe- i NiFe-, on cal destacar els compostos per -Fe^{3+} a causa de la major dificultat sintètica), esta tesi ofereix una visió global i desenvolupada de tres aspectes vinculats a estos materials com són magnetisme, exfoliació i funcionalització i finalment aplicacions, amb l'aportació de nous resultats que repercutisquen en el major coneixement i desenvolupament d'estos materials.

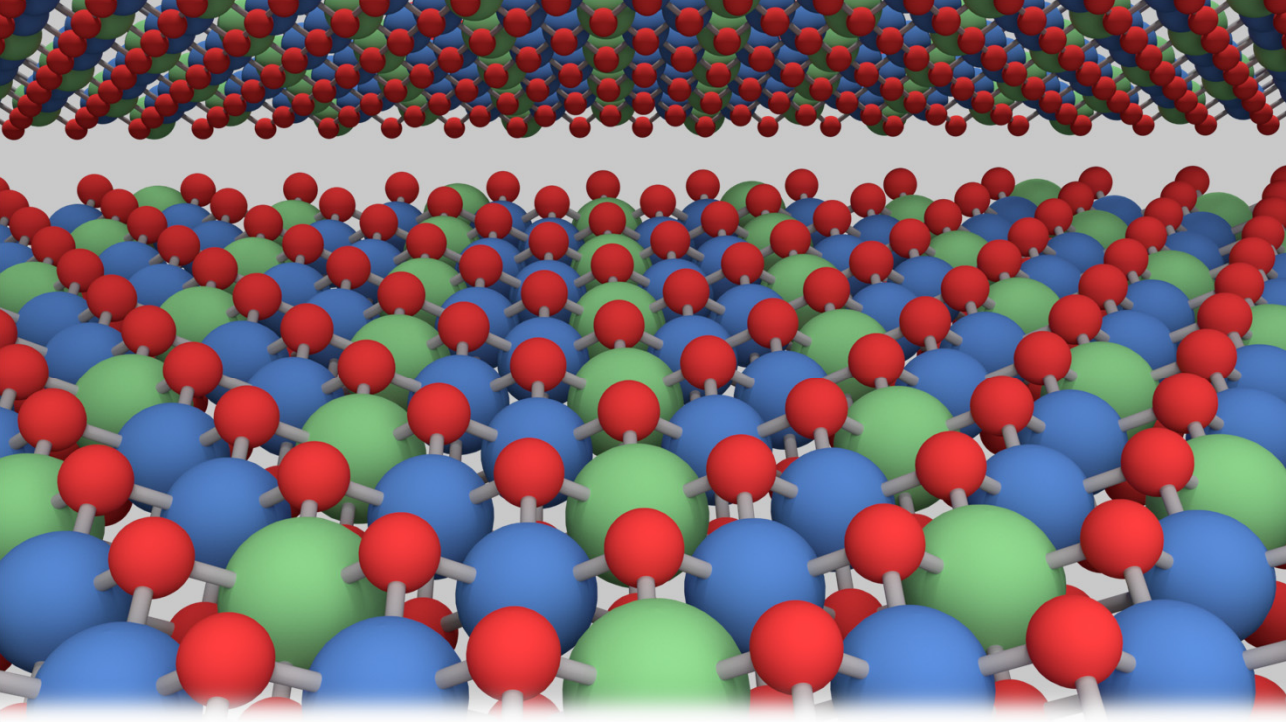

Layered Double Hydroxides (LDHs) are a class of inorganic compounds that have raised an increasing interest in the field of materials science. Thanks to their chemical tunability and versatility, these anionic clays have shown to be useful in several domains such as catalysis, anion exchange, electrochemistry or pharmaceutical applications, among others. The present thesis focuses on magnetic LDHs, guiding the reader through their essential structural and magnetic features, on the post synthetic modification of these layered materials through liquid phase exfoliation and chemical functionalization and, finally, on their electrochemical applications.

Instituto de Ciencia Molecular

ICMOL

VNIVERSITAT DE VALÈNCIA